Alma Mater Studiorum
Università di Bologna

Scuola di Dottorato in Ingegneria Civile ed Architettura

Dottorato di Ricerca in Ingegneria Civile e Ambientale

Tesi di Dottorato

Shape memory and elastoplastic materials: from constitutive and numerical to fatigue modeling

Settore Concorsuale di Afferenza 08/B2
Settore Scientifico Disciplinare ICAR/08

Relatore:
Chiar.mo Prof. Ing. **Francesco Ubertini**

Candidato:
Giulia Scalet

Correlatore:
Chiar.mo Prof. Ing. **Ferdinando Auricchio**

Coordinatore di Dottorato:
Chiar.mo Prof. Ing. **Alberto Lamberti**

Esame Finale Anno 2014 - Ciclo XXVI

To my grandfather Ovidio

Acknowledgments

These years of PhD have provided me the opportunity to carry out several scientific activities, but also have contributed to my personal growth. I would like to thank several people whose great experience and long-lasting support have kept my motivation high during these years.

I wish to express my most sincere gratitude to my advisors, Professors Ferdinando Auricchio and Francesco Ubertini, for their valuable teachings, both academic and personal, as well as for their important advices and constant encouragement during the course of this thesis. I have really learnt more than a lot from their enthusiasm for research and professional experience.

I would like to thank Professor Andrei Constantinescu for introducing me into the fascinating research field of fatigue and fracture and for being a valuable guidance during my stay in France.

I am particularly grateful to Professors Dimitris C. Lagoudas and Darren J. Hartl for giving me the great opportunity of a fantastic and fruitful experience in the USA and for their precious teachings in the complex field of shape memory alloys.

I sincerely thank Professor Elena Bonetti who has always been available to support me and to settle my mathematical doubts during these years.

I also wish to thank Professor Joze Korelc for his help and support into the numerical modeling.

I would like to thank all the collaborators of SAES Getters and of the Basic Chemicals and Plastics Research Center in Versalis (ENI), who have contributed to the experimental part of this thesis.

Many thanks to my colleagues at DICAM and DICAr, who provided me with advices, support, and most of all friendship. Many thanks to Dottor Michele Conti for his constant support and contribution to the biomedical simulations of this thesis.

I would like to thank with all my heart my mother Fiorella, my grandmother Maria and my grandfather Ovidio who is enjoying this day from Paradise. Without their love and constant support it would have been impossible every step up to now.

Last but not least, I would like to thank Alberto for his understanding, endless patience and encouragement when it was most required.

Abstract

Shape memory materials, which include shape memory alloys, shape memory ceramics and shape memory polymers, represent an important class of multi-phase smart materials that have the ability to return from a deformed state to their original shape. Such a property is typically induced by an external stimulus such as heat, electricity or magnetism.
Thanks to such a unique property, shape memory materials are utilized in a wide range of innovative commercial applications. As an example, shape memory alloys find the most successful applications in the biomedical, robotic as well as automotive areas, thanks to their properties known as pseudo-elasticity, one-way and two-way shape memory effects. On the contrary, shape memory polymers have a promising future for interesting applications as, e.g., actuators, packaging, films with insulating properties, biomedical devices, and damping elements, thanks to their large elastic deformations, low energy consumption, cost and density, biocompatibility, biodegradability, and manufacturability.

The increasing number of shape memory material based applications and the consequent growing involvement of industrial players in the field have motivated researchers to formulate constitutive models able to catch the complex thermo-mechanical behavior of these materials and to develop robust computational tools for advanced design purposes. However, such a research field is still under progress, especially in the prediction of shape memory polymer behavior as well as of several important effects characterizing shape memory alloy based applications.
Moreover, the frequent use of shape memory and metallic materials in biomedical devices, particularly in cardiovascular stents, which are permanently implanted in the human body and experience millions of in-vivo cycles induced by the pulsing blood pressure, clearly indicates the need for a deeper understanding of fatigue and fracture failure in microsize components. In particular, the development of a reliable stent design procedure against fatigue is still an open and debated subject in scientific literature.

Motivated by the described framework, the thesis is dedicated to several research issues involving the advanced constitutive, numerical and fatigue modeling of elastoplastic and shape memory materials.

Starting from the constitutive modeling, the present thesis proposes to develop refined and flexible one-dimensional and three-dimensional phenomenological models for reliable descriptions of shape memory alloy and polymer behaviors.

Then, concerning the numerical modeling, the present thesis proposes to implement the introduced models into numerical software through the development of appropriate implicit and explicit time-integration algorithms, to guarantee robust computational tools, which could be effectively utilized for practical purposes. Since the structure of the equations proposed to describe shape memory alloy and polymer behavior is very similar to that characterizing rate-independent plasticity models, the thesis first presents a detailed and critical analysis of several computational approaches for classical plasticity in order to investigate possible solution algorithms to be applied to shape memory material models.

The described constitutive and numerical modeling activities are completed by two experimental investigations on shape memory alloy actuator springs as well as on low-density and high-density polyethylene-based polymers, that are being considered for packaging applications. The comparison between numerical predictions and experimental data allows to quantitatively validate the proposed models as well as to assess

the robustness and efficiency of their numerical counterparts.

Finally, regarding the fatigue modeling, the thesis proposes the introduction of a reliable, general and complete computational approach for the fatigue-life assessment of a classical coronary balloon-expandable stent design, in order to exploit computer-based simulations to prevent undesired failures and modify stent design, without making and testing numerous physical devices. To this purpose, the present thesis combines advanced computational methods and fatigue-life prediction methodologies with available material fatigue data to lay down the basis for the prediction of fatigue-controlled service life of balloon-expandable stents as well as to provide useful information either to be used for product improvements or for clinicians to make life-saving decisions.

Key-words: plasticity, shape memory alloys, shape memory polymers, constitutive modeling, numerical integration, fatigue modeling, biomedical applications, high-cycle fatigue, experimental campaign

Sommario

I materiali a memoria di forma, che includono leghe, ceramiche e polimeri a memoria di forma, rappresentano un'importante classe di materiali intelligenti multi-fase, caratterizzati da inusuali proprietà meccaniche. La loro caratteristica principale è quella di essere in grado di recuperare la forma iniziale, dopo essere stati deformati, tramite l'applicazione di uno stimolo esterno come il calore, l'elettricità od un campo magnetico.
Grazie a questa proprietà, i materiali a memoria di forma trovano impiego in una vasta gamma di interessanti ed innovative applicazioni commerciali. A titolo di esempio, le leghe a memoria di forma vengono notevolmente sfruttate in campo biomedico, robotico e dell'automazione, grazie alle loro proprietà note come pseudoelasticità ed effetto a memoria di forma ad una ed a due vie. Al contrario, i polimeri a memoria di forma hanno un futuro promettente per applicazioni come attuatori, imballaggi, pellicole isolanti, dispositivi biomedici o smorzatori, grazie a proprietà quali elevate deformazioni elastiche, basso consumo energetico, bassi costi, bassa densità, biocompatibilità, biodegradabilità e facile producibilità.

Il crescente numero di applicazioni che sfruttano materiali a memoria di forma ed il conseguente aumento di partner industriali coinvolti in tale ambito hanno spinto i ricercatori a formulare modelli costitutivi in grado di descrivere il complesso comportamento termo-meccanico di questi materiali ed a sviluppare robusti strumenti computazionali da utilizzare per la progettazione di componenti strutturali e dispositivi reali. Tuttavia, quest'ambito di ricerca necessita a tutt'oggi di ulteriori approfondimenti, specialmente in relazione alla modellazione sia di polimeri a memoria di forma sia di effetti rilevanti per le applicazioni che sfruttano leghe a memoria di forma.
Inoltre, il frequente impiego di materiali a memoria di forma e metallici in dispositivi biomedici, come stent cardiovascolari, che sono permanentemente impiantati nel corpo umano e di conseguenza sottoposti a milioni di cicli di carico indotti dalla pressione sanguigna, rende evidente la necessità di uno studio più profondo ed accurato dei problemi di fatica e frattura in queste componenti microscopiche. In particolare, lo sviluppo di un'affidabile procedura di progettazione a fatica per stents è tuttora un problema aperto nella lettetura scientifica.

La presente tesi si colloca nel quadro descritto, dedicandosi a diversi temi di ricerca che coinvolgono una sofisticata modellazione costitutiva, numerica e a fatica di materiali elastoplastici e a memoria di forma.

Partendo dalla modellazione costitutiva, la tesi propone lo sviluppo di raffinati e flessibili modelli costitutivi macroscopici monodimensionali e tridimensionali in grado di descrivere in modo affidabile il comportamento di leghe e polimeri a memoria di forma.

Per quanto riguarda la modellazione numerica, la tesi si propone di implementare i modelli proposti in software di calcolo attraverso lo sviluppo di appropriati schemi di integrazione nel tempo impliciti ed espliciti, al fine di sviluppare un potente strumento computazionale, efficacemente utilizzabile ai fini pratici. Data la somiglianza tra le equazioni proposte per descrivere il comportamento di leghe e polimeri a memoria di forma e quelle per materiali elastoplastici *rate-independent*, la tesi presenta inizialmente un'analisi dettagliata e critica di vari approcci computazionali per la plasticità classica, per valutare possibili algoritmi da applicare ai modelli per materiali a memoria di forma.

Le attività di modellazione costitutiva e numerica, sopra descritte, sono completate da due campagne

sperimentali condotte su molle in leghe a memoria di forma per attuatori e su polimeri di polietilene a bassa ed alta densità impiegati in applicazioni di packaging. Il confronto tra risultati numerici e sperimentali consente di validare quantitativamente i modelli proposti e di verificare l'affidabilità, la robustezza e l'efficienza dei relativi algoritmi numerici.

Infine, per quanto riguarda la modellazione a fatica, la presente tesi si propone l'introduzione di un approccio computazionale affidabile, generale e completo per la valutazione della vita a fatica di un generico stent coronarico, che consenta l'impiego di simulazioni numeriche in attività di design e di prevenzione da rotture indesiderate, senza la necessità di onerose prove sperimentali. A questo scopo, la tesi combina metodi computazionali innovativi e metodologie di previsione della vita a fatica con appropriati dati sperimentali disponibili in letteratura, allo scopo sia di creare un approccio numerico in grado di predire la vita a fatica di stents di tipo *balloon-expandable* sia di fornire informazioni utili ai medici o ai produttori che si occupano dell'ottimizzazione di tali dispositivi.

Parole-chiave: plasticità, leghe a memoria di forma, polimeri a memoria di forma, modellazione costitutiva, integrazione numerica, modellazione a fatica, dispositivi biomedici, fatica ad alto numero di cicli, campagna sperimentale

Contents

List of Tables **XIV**

List of Figures **XXI**

Thesis motivations and organization **1**

PART I: Constitutive and numerical modeling of elastoplastic and shape memory materials **5**

1 Continuum Mechanics and Elasticity **7**
1.1 Review on notation . . . 7
1.2 Kinematics of a material body . . . 11
1.3 Equilibrium for a material body . . . 15
1.3.1 Static equilibrium . . . 15
1.3.2 Dynamic equilibrium . . . 16
1.4 Constitutive equation . . . 17
1.4.1 Linear elastic material body . . . 17
1.4.2 Isotropic elastic material body . . . 18
1.5 Thermodynamic setting for Elasticity . . . 19
1.5.1 Linear elastic material body . . . 21
1.6 IBVP of equilibrium in Elasticity . . . 22

2 Elastoplasticity theory **23**
2.1 Thermodynamic setting for elastoplasticity . . . 23
2.1.1 Isothermal behavior . . . 23
2.1.2 Rate-independence . . . 24
2.1.3 Internal variables . . . 24
2.1.4 Thermodynamic assumptions . . . 24
2.1.5 Additive decomposition of strain . . . 25
2.1.6 Free-energy as a function of elastic strain and internal variables . . . 26
2.1.7 Plastic incompressibility . . . 27
2.1.8 Yield surface . . . 27
2.1.9 Associative plasticity . . . 27
2.1.10 Kuhn-Tucker complementary inequality conditions . . . 28
2.2 von-Mises yield criterion . . . 30
2.3 IBVP of equilibrium in J_2 elastoplasticity . . . 32
2.4 The principle of maximum plastic dissipation . . . 33
2.5 Elastoplasticity in a convex-analytic setting . . . 37

2.5.1 Pseudo-potential of dissipation for J_2 perfect plasticity . . . 37
2.6 Complementarity problem functions . . . 40
2.6.1 Fischer-Burmeister complementarity problem function . . . 40
2.6.2 A different form of complementarity problem function . . . 42

3 Integration algorithms for J_2 elastoplasticity 47
3.1 Literature review . . . 47
3.2 The notion of closest point projection . . . 50
3.2.1 Outline of the discrete equations for J_2 elastoplasticity . . . 50
3.2.2 Return-mapping algorithm . . . 51
3.2.3 Geometric interpretation of closest point projection . . . 51
3.3 The principle of maximum plastic dissipation . . . 55
3.3.1 Augmented Lagrangian formulation . . . 56
3.3.2 Penalty formulation . . . 56
3.4 The energy minimization problem . . . 57
3.5 Complementarity problem functions . . . 60
3.5.1 Fischer-Burmeister complementarity problem function . . . 60
3.5.2 A different form of complementarity problem function . . . 60

4 Numerical tests for J_2 elastoplasticity 61
4.1 Outline of the governing equations for J_2 elastoplasticity . . . 61
4.2 Numerical test setup . . . 62
4.2.1 Mixed stress-strain loading histories . . . 63
4.2.2 IBVPs . . . 67
4.2.3 Discussion on results . . . 69

5 Introduction to SMAs 71
5.1 SMA historical background . . . 71
5.2 SMA properties . . . 71
5.3 Micromechanical interpretation of SMA properties . . . 73
5.4 SMA applications . . . 75
5.4.1 Couplings and fasteners . . . 76
5.4.2 Actuators . . . 77
5.4.3 Adaptive materials and hybrid composites . . . 78
5.4.4 Civil engineering applications . . . 78
5.4.5 Biomedical applications . . . 79
5.4.6 Other applications . . . 82

6 Literature review on SMA constitutive modeling 85
6.1 Constitutive modeling approaches for SMAs . . . 85
6.2 Phenomenological models for SMAs . . . 86
6.2.1 Models without internal variables . . . 87
6.2.2 Models with internal variables . . . 87
6.3 Review on some phenomenological models . . . 88
6.3.1 Model by Souza et al. (1998) . . . 89
6.3.2 Model by Auricchio et al. (2009) and Auricchio et al. (2011) . . . 90
6.3.3 Model by Boyd and Lagoudas (1996) and Lagoudas et al. (2012) . . . 90
6.3.4 Explicit integration scheme for the model by Boyd and Lagoudas (1996) and Lagoudas et al. (2012) . . . 92

7 A new 'flexible' approach for SMA modeling 95
7.1 Introduction and motivations . . . 95
7.2 A time-continuous model formulation . . . 99
7.2.1 A general model formulation . . . 99
7.2.2 A simplified model formulation . . . 104
7.3 Model calibration . . . 105
7.3.1 1D phase diagram . . . 107
7.3.2 Temperature-induced transformation . . . 109
7.3.3 Stress-induced transformation . . . 110
7.4 A time-discrete model formulation . . . 111
7.4.1 Numerical difficulties and adopted solutions . . . 113
7.5 Conclusions . . . 114

8 A numerical and experimental investigation of SMAs 115
8.1 'Flexible' model validation . . . 115
8.1.1 Uniaxial isothermal tensile tests . . . 116
8.1.2 Uniaxial thermal-cycling tests at constant applied stress . . . 117
8.1.3 Uniaxial thermo-mechanical recovering stress tests . . . 119
8.1.4 Isothermal combined tension-torsion tests . . . 119
8.1.5 Isothermal multiaxial non-proportional tests . . . 122
8.1.6 Simulations of a SMA-based real device . . . 123
8.2 A numerical/experimental investigation of NiTi actuator springs . . . 126
8.2.1 Introduction and motivations . . . 126
8.2.2 Experimental campaign conducted in SAES Getters . . . 128
8.2.3 Model parameter calibration . . . 129
8.2.4 Comparison with experiments on SMA helicoidal wires and springs . . . 132
8.2.5 Discussion on results . . . 134
8.3 Conclusions . . . 138

9 A theoretical, numerical, experimental investigation of SMPs 139
9.1 Introduction to SMP behavior and activities . . . 139
9.2 Motivations of the proposed work . . . 141
9.3 Experimental campaign conducted in Versalis (ENI) . . . 142
9.3.1 Orientation test . . . 144
9.3.2 Constrained thermal retraction test . . . 146
9.3.3 Free thermal retraction test . . . 147
9.3.4 Test above the melting temperature . . . 149
9.4 A new phenomenological model for SMPs . . . 149
9.4.1 A time-continuous model formulation . . . 149
9.4.2 Physical interpretation of model parameters . . . 154
9.4.3 A time-discrete model formulation . . . 156
9.5 Numerical investigation . . . 156
9.5.1 Orientation test . . . 157
9.5.2 Constrained thermal retraction test . . . 157
9.5.3 Free thermal retraction test . . . 159
9.6 Conclusions . . . 160

PART II: Fatigue modeling of elastoplastic and shape memory materials 161

10 Introduction to fatigue of metals 163
10.1 Definition of fatigue . . . 163
10.2 Review on fatigue notation . . . 164
10.3 Historical background . . . 165
10.4 Historical accidents . . . 166
10.5 Fatigue as a phenomenon in the material . . . 167
10.5.1 Fatigue-life phases . . . 168
10.6 The fatigue regimes . . . 168
10.7 Cyclic behavior of an elastoplastic structure . . . 169
10.8 The global computational approach . . . 171
10.9 General forms of fatigue criteria . . . 172

11 Polycyclic fatigue of metals 173
11.1 Empirical approach to fatigue . . . 173
11.1.1 Uniaxial fatigue criteria . . . 173
11.1.2 Multiaxial fatigue criteria . . . 175
11.2 Semi-empirical approach to fatigue . . . 177
11.2.1 Criterion by Findley (1957) . . . 177
11.2.2 Criterion by Crossland (1956) . . . 177
11.2.3 Criterion by Sines (1959) . . . 178
11.3 Multiscale approach to fatigue . . . 178
11.3.1 Meso-macro passage . . . 178
11.3.2 The criterion by Dang Van (1973) and Dang Van et al. (1989) . . . 179

12 Oligocyclic fatigue of metals 181
12.1 The global computational approach to fatigue . . . 181
12.2 Mechanical analysis . . . 181
12.2.1 Material constitutive behavior . . . 182
12.3 Fatigue analysis . . . 183

13 Fatigue of 316L notched microsize components 185
13.1 Introduction and motivations . . . 185
13.2 316L steel: material and fatigue experimental data . . . 188
13.2.1 Experimental tests by Wiersma et al. (2006); Wiersma and Taylor (2005) . . . 188
13.2.2 Experimental tests by Donnelly (2012) . . . 192
13.3 316L steel: constitutive law and mechanical analysis . . . 192
13.3.1 Modeling assumptions . . . 192
13.3.2 Constitutive law for 316L stainless steel . . . 194
13.3.3 Mechanical analysis . . . 195
13.3.4 Discussion on results . . . 197
13.4 316L steel: fatigue analysis . . . 199
13.4.1 Elastic shakedown: Dang Van criterion . . . 199
13.4.2 Plastic shakedown: fatigue crack initiation criteria . . . 201
13.5 Conclusions . . . 204

14 A computational approach for stent fatigue-life prediction 207
14.1 Introduction and motivations . . . 207
14.2 Mechanical analysis . . . 209
14.2.1 Stent: geometrical modeling and mesh . . . 209
14.2.2 Stent: constitutive modeling . . . 210
14.2.3 Vessel: geometrical modeling, mesh, constitutive modeling . . . 211
14.2.4 Analysis set-up . . . 211
14.2.5 Discussion on results . . . 213
14.3 Fatigue analysis . . . 218
14.3.1 Fatigue criterion . . . 218
14.3.2 Fatigue predictions . . . 219
14.4 Conclusions . . . 221

15 Introduction to fatigue of SMAs 223
15.1 SMAs and fatigue . . . 223
15.2 Mechanical fatigue of SMAs . . . 224
15.2.1 Metallurgical investigations . . . 224
15.2.2 Fatigue methodologies . . . 224
15.3 Thermal fatigue of SMAs . . . 226
15.4 SMA biomedical devices and fatigue . . . 227

Conclusions and future work 231

A Some elements of convex analysis 233
A.1 Convex sets . . . 233
A.2 Convex functions . . . 233
A.2.1 Examples of convex functions . . . 233
A.3 Linear spaces in duality . . . 234
A.3.1 Examples of linear spaces in duality . . . 234
A.4 Subgradients and subdifferential set of convex functions . . . 235
A.4.1 Properties of the subdifferential set . . . 235
A.4.2 Examples of subdifferential sets . . . 236
A.5 Dual functions . . . 236
A.5.1 Examples of dual functions . . . 236
A.5.2 Internal energy, potential and free enthalpy . . . 236
A.6 Concave functions . . . 237
A.6.1 Examples of concave functions . . . 237

B AceGen and AceFEM packages 239
B.1 Overview on traditional FE environments . . . 239
B.2 Introduction to AceGen and AceFEM packages . . . 240
B.2.1 AceGen package . . . 240
B.2.2 AceFEM package . . . 241

Bibliography 243

List of Tables

1.1 IBVP for isotropic linear elasticity. 21

2.1 IBVP for J_2 perfect elastoplasticity. 33

3.1 Return-mapping algorithm for J_2 rate-independent perfect plasticity. 52
3.2 Newton-Raphson algorithm to solve problem (3.4) in strain-space. 53
3.3 Newton-Raphson algorithm to solve problem (3.10) in stress-space. 54
3.4 Fixed-point iteration scheme for the discrete Augmented Lagrangian formulation (3.29) of the principle of maximum plastic dissipation. 56

4.1 J_2 elastoplastic model with linear isotropic kinematic hardening. Adopted parameters. . . 62
4.2 Biaxial butterfly-shaped loading history input. Comparison of computational efficiency between the RM and the FB algorithmic schemes in terms of average number of global Newton iterations and average computational time per time step increment. 64
4.3 Biaxial square-shaped loading history input. Comparison of computational efficiency between the RM and the FB algorithmic schemes in terms of average number of global Newton iterations and average computational time per time step increment. 64
4.4 3D perforated strip. Comparison of computational efficiency between the RM and the FB algorithmic schemes in terms of average number of global Newton iterations and average computational time per time step increment. 68
4.5 Helicoidal spring. Comparison of computational efficiency between the RM and the FB algorithmic schemes in terms of average number of global Newton iterations and average computational time per time step increment. 69

6.1 Explicit forward-Euler integration scheme for the model by Boyd and Lagoudas (1996) and Lagoudas et al. (2012). 93
6.2 Adopted parameters for the model by Boyd and Lagoudas (1996) and Lagoudas et al. (2012). 94

7.1 Time-continuous simplified 'flexible' model equations review. 106
7.2 Full algorithmic scheme for the proposed 'flexible' model. 114

8.1 'Flexible' model parameters used in all the numerical simulations. 116
8.2 Pseudoelastic test of a SMA spring actuator. Comparison of computational efficiency. . . . 125
8.3 Geometrical parameters of the first and second helicoidal spring actuators (Springs 1 and 2, respectively). 129
8.4 Summary of the performed tests in SAES Getters. 130
8.5 Calibrated material parameters for the three models. 131

9.1 Property values of the tested LDPE and HDPE polymers (Pachera, 2011; Talamazzi, 2012). 143

9.2 Model parameters calibrated on experimental orientation curves of materials A and E. . . . 157

13.1 Chemical composition ($wt\%$) of 316L austenitic stainless steel (Lê, 2013). 188
13.2 Thermo-mechanical properties of 316L austenitic stainless steel (Lê, 2013). 188
13.3 Summary of tests on macroscopic 316L specimens and of fatigue limits by Wiersma et al. (2006); Wiersma and Taylor (2005). 189
13.4 Summary of tests on μm-size 316L specimens and of fatigue limits by Wiersma et al. (2006); Wiersma and Taylor (2005). 190
13.5 Material properties from monotonic tensile tests by Wiersma et al. (2006). 191
13.6 Summary of tests on μm-size 316L specimens and of fatigue limits by Donnelly (2012). . 192
13.7 Summary of the adopted model parameters for 316L stainless steel (Lê, 2013). 195
13.8 Calibrated material parameters, a, b, and c, and obtained correlation coefficient, R^2. 202

14.1 Simulation outputs at different FE analysis steps. The following results are reported: diameter of the central section of the stent and maximum and minimum values, among all the elements of the stent model, of the von-Mises equivalent stresses (MISES), equivalent pressure stresses (PRESS), and equivalent plastic strains (PEEQ). 214

List of Figures

2.1 Fischer-Burmeister complementarity problem function. Effect of the replacement of the Kuhn-Tucker (KT) conditions by the smoothed Fischer-Burmeister (FB) function, Φ_δ, varying the smoothing parameter, δ. 42

2.2 Chen-Mangasarian smoothing procedure. Effect of the replacement of: (a) the max function, $\langle x \rangle$, by the p-function, $P = P(x, \alpha)$; (b) the Heaviside step function, $H = H(x)$, by the s-function, $S = S(x, \alpha)$; (c) the Kuhn-Tucker (KT) equation $\dot{\gamma} - \langle \dot{\gamma} + f \rangle = 0$ by the Chen-Mangasarian (CM) equation $\dot{\gamma} - P(\dot{\gamma} + f, \alpha) = 0$, varying the parameter, α. 44

2.3 Balakrishna-Biegler smoothing procedure. Effect of the replacement of: (a) the absolute value function, $|x|$, by hyperbole, $\sqrt{x^2 + \epsilon^2}$; (b) the maximum function, $\max[0, x]$, by hyperbole, $\left(\sqrt{x^2 + \epsilon^2} + x\right)/2$; (c) the Kuhn-Tucker (KT) equation $\dot{\gamma} - \langle \dot{\gamma} + f \rangle = 0$ by the Balakrishna-Biegler (BB) equation $(\dot{\gamma} - f)/2 - \sqrt{(\dot{\gamma} + f)^2 + \epsilon^2}/2 = 0$, varying the parameter, ϵ. 45

2.4 Complementarity problem functions. Comparison between the approaches based on the Fischer-Burmeister (FB) function, the Chen-Mangasarian (CM) smoothing procedure, and the Balakrishna-Biegler (BB) smoothing procedure. 46

3.1 One-dimensional setting for the discrete penalty formulation (3.33) of the principle of maximum plastic dissipation. Diagrams in terms of: (a) plastic strain, ε^p, and $\alpha = E\varepsilon - \sigma_y$; (b) stress, σ, and $\alpha = E\varepsilon - \sigma_y$; (c) stress, σ, and plastic strain, ε^p, varying the penalty parameter, c. 58

4.1 Mixed stress-strain loading histories. (a)-(b) Butterfly- and (c)-(d) square-shaped history inputs under strain control up to 4%. 63

4.2 Biaxial butterfly-shaped loading history input. Stress (left column) and strain (right column) relative error, E_n, for Δt of 0.5, 0.05 and 0.002 s for the RM and the FB algorithmic schemes. 65

4.3 Biaxial square-shaped loading history input. Stress (left column) and strain (right column) relative error, E_n, for Δt of 0.5, 0.05 and 0.002 s for the RM and the FB algorithmic schemes. 66

4.4 Biaxial butterfly-shaped loading history inputs. Stress (left) and strain (right) total error, E_T, vs. number of steps per second for the RM and the FB algorithmic schemes. 67

4.5 Biaxial square-shaped loading history inputs. Stress (left) and strain (right) total error, E_T, vs. number of steps per second for the RM and the FB algorithmic schemes. 67

4.6 3D perforated strip. Adopted mesh. 68

4.7 Helicoidal spring. Adopted mesh. 69

5.1 SMA material properties. (a) Shape memory effect and (b) pseudo-elasticity. 72

5.2 SMA material properties. (a) One-way and (b) two-way shape memory effect. 73

5.3 Formation of different martensitic variants in a single grain of polycrystalline CuZnAl alloy during uniaxial tensile loading, taken from (Patoor et al., 2006). 74
5.4 One-dimensional phase diagram in terms of stress, σ, and temperature, T. (a) Crystal structures for austenite, multi- and single-variant martensites and phase transformations (indicated by blue arrows); (b) shape memory effect and (c) pseudo-elastic loading paths. . 76
5.5 SMA devices. Clockwise from top left: memory card ejector mechanism for laptop computers; Cryofit® hydraulic pipe couplings; Cryocon® electrical connector; fire safety lid release for public garbage receptacles, taken from (Schwartz, 2002). 77
5.6 Orthodontic applications of SMAs. Examples of wires, taken from (Petrini and Migliavacca, 2011). 79
5.7 Orthodontic applications of SMAs. (a) Palatal arch, taken from (Petrini and Migliavacca, 2011); (b) orthodontic distracters, taken from (Idelsohn et al., 2004). 80
5.8 Orthodontic applications of SMAs. Endodontic file, taken from (Petrini and Migliavacca, 2011). 80
5.9 Orthopedic applications of SMAs. (a) Staple before and after distraction, taken from (Laster et al., 2001); (b) staple for fixing a frontozygomatic fracture, taken from (Laster et al., 2001); (c) NiTi plate for mandible fracture, taken from (Duerig et al., 1990); (d) spinal vertebrae spacer, taken from (Duerig et al., 1990). 81
5.10 Orthopedic applications of SMAs. Gloves with SMA wires: position at (a) low and (b) high temperatures, taken from (Machado and Savi, 2003). 82
5.11 General surgery of SMAs. Endoscopic tools, taken from (Duerig et al., 1999; Endosmart, 2013; Kourambas et al., 2000). 83
5.12 General surgery of SMAs. Examples of stents, taken from http://prashantborde123.blogspot.it/2013/02/biotechology-and-medicine.html. 83

6.1 Pseudoelastic uniaxial tensile test with displacement control and internal subloop at a constant temperature of 27 °C. Comparison between the implicit and explicit integration schemes for the models by Lagoudas et al. (2012) and Auricchio and Taylor (1997) (denoted, respectively, as TAMU and AAT). 94

7.1 1D phase diagrams generated by (a) the proposed 'flexible' model and (b) the Souza model, in terms of stress, σ, and temperature, T. 108
7.2 Identification of 'flexible' model parameters from a temperature-induced transformation. . 110
7.3 Identification of 'flexible' model parameters from a stress-induced transformation. 111

8.1 'Flexible' model calibration on a tensile test at a constant temperature of 10 °C. 116
8.2 Model response for isothermal tensile tests. 117
8.3 Model response for isothermal tensile tests with internal subloops. 118
8.4 Model response for thermal-cycling tests at constant tensile stresses. 119
8.5 Model response for thermo-mechanical recovering stress tests at upper plateau. 120
8.6 Model response for thermo-mechanical recovering stress tests at lower plateau. 121
8.7 Combined tension-torsion tests. Adopted mesh for the wire segment. 122
8.8 Model response for combined tension-torsion tests. 123
8.9 Model response for mixed stress-strain loading histories. (a) Butterfly- and (c)-(e) square-shaped history inputs under strain control; Obtained diagrams in terms of the non-zero stress components for the (b) butterfly- and (d)-(f) square-shaped history inputs (markers, large load increments; solid line, small increments). 124
8.10 SMA spring actuator. Adopted mesh. 125

8.11 Pseudoelastic test of a SMA spring actuator. (a) Spring initial geometry and scaled deformed geometry under the maximum force (color map indicates distribution of the single-variant martensite volume fraction, χ^S); (b) force vs. vertical displacement of the loaded end of the spring diagram (markers, large load increments; solid line, small increments). . 126

8.12 Thermal-cycling test at constant load of a SMA spring actuator. (a)-(c) Temperature and force loading histories during simulation; (b)-(d) vertical displacement of the loaded end of the spring vs. temperature diagrams. 127

8.13 Springs before and after testing. 130

8.14 1D phase diagrams generated by (a) the Souza-Auricchio model; (b) the modified Souza-Auricchio model and (c) the Auricchio-Bonetti model, in terms of stress, σ, and temperature, T. 132

8.15 Model parameter calibration on thermal-cycling tests on 1.5 mm SMA wires. Deformation, ε, vs. temperature, T, curves at constant tensile loads of 100 and 144 MPa. 133

8.16 Thermal-cycling test on 1.5 mm SMA wire. Deformation, ε, vs. temperature, T, curves at a constant tensile load of 55 MPa. 133

8.17 Adopted meshes. (a) Spring 1 of Table 8.3; (b) Spring 2 of Table 8.3. 134

8.18 Thermal-cycling tests on 1.5 mm wire springs. Spring relative elongation, $(L - L_0)/L_0$, vs. temperature, T, curves at constant loads of 3, 5 and 8 kg. 135

8.19 Thermal-cycling tests on 1.0 mm SMA wires. Deformation, ε, vs. temperature, T, curves at constant tensile loads of 15, 30, 50, 100 and 200 MPa. 136

8.20 Thermal-cycling tests on 1.0 mm wire springs. Spring relative elongation, $(L - L_0)/L_0$, vs. temperature, T, curves at constant loads of 1, 2, 5 and 7 N. 137

9.1 A closed flower (temporary shape), made of a SMP and fixed at a lower temperature, recovers its original shape (open flower) when the temperature is increased above its switch temperature, taken from (Hu and Chen, 2010). 140

9.2 Saspol press (left) and zoom of the plates (right) (Pachera, 2011; Talamazzi, 2012). 143

9.3 Dynamometer Instron series 4505 and temperature cell (Pachera, 2011; Talamazzi, 2012). . 144

9.4 Experimental orientation process on materials A and E. Curves in terms of stress, σ, and strain, ε, (a)-(c) at different temperatures of 26, 30, 45, 60, 75 and 90 °C and maximum imposed deformation of 600%; (b)-(d) at constant temperature of 60 °C and different imposed deformations of 10, 25, 50, 100, 200, 400 and 600%. 145

9.5 Experimental orientation process on materials B, C, and D. Curves in terms of stress, σ, and strain, ε, at a temperature of 60 °C and maximum imposed deformation of 600%. . . . 146

9.6 Rotational rheometer ARES LS II (left) and zoom of the temperature cell (right) (Pachera, 2011; Talamazzi, 2012). 147

9.7 Experimental constrained thermal retraction test on materials A and E. Curves in terms of stress, σ, and temperature, T, for specimens oriented (a)-(c) at temperatures of 26, 30, 60 and 90 °C and at maximum imposed deformation of 600%; (b) at a temperature of 60 °C and at imposed deformations of 200, 400 and 600%. 148

9.8 Experimental constrained thermal retraction test on materials B, C, and D. Curves in terms of stress, σ, and temperature, T, for specimens oriented at a temperature of 60 °C and at maximum imposed deformation of 600%. 149

9.9 Experimental free thermal retraction test on materials A and E. Curves in terms of shrinkage and temperature, T, for specimens oriented (a)-(c) at different temperatures of 26, 30, 60 and 90 °C and maximum imposed deformation of 600%; (b) at a temperature of 60 °C and at different imposed deformations of 200, 400 and 600%. 150

9.10 Experimental free thermal retraction test on materials B, C, and D. Curves in terms of shrinkage and temperature, T, for specimens oriented at a temperature of $60\,^{\circ}\mathrm{C}$ and at maximum imposed deformation of 600%. 151
9.11 Tests above the melting temperature, T_m, on materials B, C, and D. Curves (a) in terms of viscosity and strain rate; (b) in terms of stress, σ, and temperature, T, for specimens obtained through blown film processes. 151
9.12 Identification of model parameters from a 1D diagram in terms of stress, σ, and strain, ε. . 154
9.13 Model response for orientation tests. Comparisons with experimental data on materials A and E. 158
9.14 Qualitative model response for orientation tests at constant temperatures of 26 and $90\,^{\circ}\mathrm{C}$ and maximum imposed strain of 600%. 158
9.15 Constrained thermal retraction test. (a)-(b) Qualitative model response; (c)-(d) irreversibility of the retraction process during cooling. 159
9.16 Comparison between model response and experimental tests on materials A and E for (a) constrained and (b) free thermal retraction tests. 160
9.17 Free thermal retraction test. (a)-(b) Qualitative model response. 160

10.1 Review on fatigue notation for a structure subjected to an uniaxial stress cyclic loading. . . 164
10.2 Micrographs showing how surface fatigue cracks grow as material is further cycled, taken from (Ewing and Humfrey, 1903). 165
10.3 Development of cyclic slip bands and microcrack in a pure copper specimen, taken from (Bullen et al., 1953). (a) Visible slip lines; (b) Plastically strained opening a microcrack. . 167
10.4 Different phases of the fatigue-life (Schijve, 2009). 168
10.5 Representative elementary volume of material. Plasticity developed at the macroscopic scale in the LCF regime (left) and at the mesoscopic scale in the HCF regime (right), taken from (Charkaluk et al., 2009). 169
10.6 Schematic Wöhler curve and fatigue regimes. 170
10.7 Cyclic behavior of an elastoplastic structure. (a) Elastic shakedown; (b) plastic shakedown; and (c) ratchetting. 171

11.1 Fatigue test data on smooth specimens of a low alloy steel (SAE 4130) in the Wöhler diagram, taken from (Grover et al., 1951). 174
11.2 A comparison between uniaxial fatigue criteria in the Haigh diagram. 175
11.3 Macroscopic and local scales of material description, taken from (Dang Van et al., 2003). . 178
11.4 Calculation of the mesoscopic shear stress, τ, taken from (Dang Van, 1973). 180

12.1 Cyclic material behavior for isothermal LCF tests carried out by Skelton (1991, 1993). . . 182

13.1 Evolution of the cyclic stress at several temperatures for (a) $\Delta\epsilon_p/2 = \pm 2 \cdot 10^{-3}$; (b) $\Delta\epsilon_p/2 = \pm 6 \cdot 10^{-4}$ and (c) $\Delta\epsilon_p/2 = \pm 5 \cdot 10^{-3}$, taken from (Alain et al., 1997). 186
13.2 Fatigue hardening and softening curves for (a) 316L-VZ steel and (b) 316L-TH steel, taken from (Polak et al., 1994). 186
13.3 Scanning electron microscope of a 316L stainless steel stent strut, showing scale of strut dimensions and morphology of material microstructure, taken from (Murphy et al., 2003). 187
13.4 Geometries of the 316L μm-size notched specimens tested by Wiersma et al. (2006); Wiersma and Taylor (2005) (b is the net section; s the thickness; d the notch depth; R the fib-slot; H the hole radius; L the slot length). 189

13.5 Results from the experiments by Wiersma et al. (2006); Wiersma and Taylor (2005). (a) Stress vs. strain diagram from monotonic tensile tests. Net stress range vs. number of cycles to failure diagram from fatigue tensile tests on (b) smooth macroscopic and μm-size specimens; (c)-(d) notched μm-size specimens. 191
13.6 Results from the experiments by Donnelly (2012). (a) Stress vs. strain diagram from monotonic tensile tests; (b) stress amplitude vs. number of cycles to failure from fatigue tensile tests on μm-size specimens. 193
13.7 Schematic representation of the cyclic material behavior adopted in the present approach; see also (Skelton, 1991, 1993). 193
13.8 (a) Comparison between monotonic stress-strain tensile curves obtained by the adopted model and by Wiersma et al. (2006); Wiersma and Taylor (2005) and Donnelly (2012); (b) stabilized hysteresis curve generated by the adopted model compared to monotonic tensile curves by Wiersma et al. (2006); Wiersma and Taylor (2005) and Donnelly (2012). 195
13.9 Adopted meshes for the specimens of Figures 13.4(a)-(d). 2D quadratic plain stress elements for the (a) notch and (b) fib specimens; 3D quadratic brick elements for the (c) hole and (d) slot specimens. 196
13.10 Results of the mechanical analysis for the 50-notch specimen subjected to a net pressure range of 360 MPa. Distribution of the dissipated energy, W^p, in the specimen (left) and along the edge AB (right). 197
13.11 Results of the mechanical analysis for the 50-notch specimen subjected to a net pressure range of 360 MPa. Comparison between two mesh refinement in terms of the dissipated energy, W^p, along the edge AB. 198
13.12 Results of the mechanical analysis for the 50-fib subjected to a net pressure range of 320 MPa. Distribution of the dissipated energy, W^p, in the specimen (left) and along the edge AB (right). 198
13.13 Results of the mechanical analysis in terms of the dissipated energy, W^p, for the (a) 60-hole subjected to a net pressure range of 250 MPa; (b) 1500-slot subjected to a net pressure range of 115 MPa. 199
13.14 DV lines in the hydrostatic-mesoscopic stress plane and loading paths from the tensile experiments used for calibration (Donnelly, 2012; Wiersma et al., 2006; Wiersma and Taylor, 2005). 201
13.15 Hot-spot approach for the $\Phi_{\Delta\epsilon^p}$, Φ_{W^p}, and $\Phi_{W_{\sigma_h}}$ fatigue criteria. (a)-(c)-(e) Fatigue parameter vs. experimental number of cycles to failure; (b)-(d)-(f) estimated vs. experimental number of cycles to failure. 203
13.16 Volumetric approach for the Φ_{W^p} fatigue criterion. (a) Fatigue parameter vs. experimental number of cycles to failure; (b) estimated vs. experimental number of cycles to failure. . . 204
13.17 Dissipated energy, W^p, vs. maximal hydrostatic stress, σ_h^{max}, computed at the notch root. 204

14.1 Stent geometrical modeling and mesh: (a) primitive geometry; (b) mesh of the geometrical unit of the design; (c) creation of the stent model by replicating and mirroring the mesh of the geometrical unit along the plane; (d) final stent model. 210
14.2 Simulation of stent deployment: a) initial configuration; b) maximum balloon expansion (the contact between the balloon and the vessel is not activated); c) stent/vessel configuration after balloon deflation. 213
14.3 Contour plot of the von-Mises equivalent stress (MISES) distribution [MPa] along the stent strut. Three views of the stent strut (indicated, respectively, as *View 1*, *View 2*, and *View 3*) are reported at different steps of the stent FE simulation, i.e., at crimping, maximum balloon expansion, systole and diastole. 214

14.4 Contour plot of the equivalent pressure stress (PRESS) distribution [MPa] along the stent strut at different analysis steps: (a) at maximum balloon inflation; (b) at diastole peak. . . . 215

14.5 Histogram of the equivalent plastic strain (PEEQ) [%] at different analysis steps, i.e., at post crimping, maximum balloon inflation, systole, and diastole. The frequency is defined as the ratio between the number of elements, N_{el}, and the total number of elements of the mesh, N_{tot}. 216

14.6 Cyclic behavior of the metallic stent under consideration. Equivalent plastic strain vs. time diagram, proving the existence of a limit cycle in alternating elasticity, i.e., elastic shakedown in the HCF domain. Two curves are represented: the blue curve is related to the point where the maximum value of equivalent plastic strain is reached among all the mesh elements; the red curve is related to the point of the analyzed stent strut where the maximum value of equivalent plastic strain is reached. The locations of the two points in the stent model are shown. 216

14.7 Scanning electron microscope of a generic stent, taken from (Weldon, 2001), designed for laboratory testing based on the NIR stent: following (a) laser cutting and (c) deployment. Comparison with (b) the stent FE mesh and (d) the deformed stent FE geometry after deployment. 217

14.8 Application of the Dang Van (DV) criterion to the stent in the hydrostatic-mesoscopic stress plane. (a) The calibrated fatigue limit DV lines (in red), related to several micrometric widths, are represented as smooth lines; the loading paths (in blue), related to the integration points, are represented by markers. (b) Zoom of an integration point loading path (in blue). 219

14.9 Application of the Dang Van (DV) criterion to the stent strut (in red on the left). Isovalues of the DV parameter, C_{DV}, computed with respect to the DV line calibrated on 50 μm width specimens. Zoom of the region (on the right) where the critical points are located. . 220

15.1 Experimental fatigue tests on diamond stent subcomponents taken from Pelton (2011). (a) Strain amplitude vs. number of cycles to failure diagram; (b) constant-life diagram in terms of mean strain and strain amplitude. 227

15.2 Differential scanning calorimetry thermograms of heating and cooling cycles 1, 10, 20, 50, and 100 for annealed Ni50.5Ti49.5, taken from (Pelton, 2011). 228

15.3 (a) Stress-strain data for a NiTi stent, schematically illustrating the initial crimp stress, deployment and subsequent in vivo cycles; (b) Cordis NiTi SMART stent being deployed from a delivery catheter; the strain on the stent inside the catheter can be about 10%, taken from (Pelton et al., 2008; Robertson et al., 2012); (c) illustration of a 9 mm diameter Cordis NiTi SMART stent in a 6 mm diameter mock vessel, which simulates a constant in-vivo mean strain, taken from (Pelton et al., 2008; Robertson et al., 2012). 229

15.4 Experimental fatigue tests taken from Pelton et al. (2008). Stent pulsatile fracture data are overlaid on the diamond fatigue data from Figure 15.1(b). 230

A.1 (a) Indicator function, I, of segment $[0, 1]$. The subgradients at points 0 and 1 are the slopes of the lines which are under the curve representing the function and in contact with the curve at points 0 and 1; (b) subdifferential set, ∂I, of the indicator function, I, of segment $[0, 1]$ (Frémond, 2012). 234

A.2 The convex function, f, has generalized derivatives at point A. The slopes of the lines passing through A and under the curve representing f are the subgradients which constitute the subdifferential set (Frémond, 2012). 235

B.1 Structure of the HSN system AceGen for multi-language and multi-environment FE code generation, taken from (Korelc, 2002, 2009). 241
B.2 Structure of the AceFEM package, taken from (Korelc, 2002, 2009). 242

Thesis motivations and organization

Shape memory materials, which include shape memory alloys, shape memory ceramics and shape memory polymers, represent an important class of multi-phase smart materials that have the ability to return from a deformed state to their original shape. Such a property is typically induced by an external stimulus such as heat, electricity or magnetism.
Thanks to such a unique property, shape memory materials are utilized in a wide range of innovative commercial applications. As an example, shape memory alloys find the most successful applications in the biomedical, robotic as well as automotive areas, thanks to their properties known as pseudo-elasticity, one-way and two-way shape memory effects. On the contrary, shape memory polymers have a promising future for interesting applications as, e.g., MEMS, actuators, packaging, films with insulating properties, biomedical devices, and damping elements, thanks to their large elastic deformations, low energy consumption, cost and density, biocompatibility, biodegradability, and manufacturability.

The increasing number of shape memory material based applications and the consequent growing involvement of industrial players in the field have motivated researchers to formulate constitutive models able to catch the complex thermo-mechanical behavior of these materials and to develop robust computational tools for practical and advanced design purposes. However, such a research field is still under progress, especially in the prediction of shape memory polymer behavior as well as of several important effects characterizing shape memory alloy based applications.
Moreover, the frequent use of shape memory and metallic materials in biomedical devices, particularly in cardiovascular stents, which are permanently implanted in the human body and experience millions of in-vivo cycles induced by the pulsing blood pressure, clearly indicates the need for a deeper understanding of fatigue and fracture failure in microsize components. In particular, the development of a reliable stent design procedure against fatigue is still an open and debated subject in scientific literature.

Motivated by the described framework, the present thesis is dedicated to several research issues involving the advanced constitutive, numerical and fatigue modeling of elastoplastic and shape memory materials.

The thesis is divided into two main parts and an appendix. The first part addresses the constitutive and numerical modeling of elastoplastic and shape memory materials. The second part is dedicated to the fatigue modeling of elastoplastic and shape memory materials. An appendix gives a short introduction to convex analysis and to the numerical software used in the present thesis. In the following, we will shortly comment on the individual chapters.

PART I: Constitutive and numerical modeling of elastoplastic and shape memory materials

The first part of the thesis is organized as follows.

Chapter 1 is devoted to a brief summary of the fundamental concepts of Continuum Mechanics and Elasticity in order to prepare the framework for the study of non-linear inelastic material behavior.
Then, motivated by the similarities between the structures of equations representing shape memory and elastoplastic material behavior, Chapter 2 presents the fundamental concepts of the classical J_2 elastoplasticity theory and of the mathematical modeling of such phenomenon, in order to prepare the framework

for the analysis of several computational approaches relevant for the numerical solution of complex initial boundary-value problems. Chapter 3 presents a detailed and critical analysis of several computational approaches available from the literature for J_2 perfect plasticity in order to investigate possible solution algorithms to be then applied to shape memory material models. Chapter 4 is devoted to the numerical investigation of two integration algorithms for J_2 elastoplasticity with linear isotropic kinematic hardening, i.e., the return-mapping and the Fischer-Burmeister complementarity algorithms.

Chapter 5 presents an introduction to shape memory alloys by recalling the historical background, material properties, and applications. Then, Chapter 6 is devoted to a literature review on shape memory alloy constitutive modeling. The chapter concludes with the description of three well-known and widely accepted in practice phenomenological models, i.e., the models by Souza et al. (1998), Auricchio et al. (2009, 2011), and Boyd and Lagoudas (1996); Lagoudas et al. (2012). The explicit time-integration scheme for solving the constitutive equations of the model by Boyd and Lagoudas (1996); Lagoudas et al. (2012) is derived. Chapter 7 proposes to develop a refined, flexible and general three-dimensional phenomenological constitutive model for shape memory alloys. Such a 'flexible' model takes into account several physical phenomena and it is numerically treated through the effective and efficient procedure investigated in Chapter 4, consisting in the replacement of the classical set of Kuhn-Tucker inequality conditions by the Fischer-Burmeister function. Chapter 8 is devoted to a detailed numerical and experimental investigation of shape memory alloys to assess the reliability of the 'flexible' model as well as the effectiveness of its numerical counterpart. In particular, numerical predictions are compared to experimental data available from the literature and the finite element analysis of a real device is presented. Then, an experimental investigation of NiTi actuators springs, conducted in SAES Getters, is presented and the results are compared to numerical predictions.

Finally, Chapter 9 focuses on the experimental analysis, constitutive modeling and numerical simulation of shape memory polymers. In particular, the chapter presents an experimental campaign on semicrystalline shape memory polymers, conducted in the Basic Chemicals and Plastics Research Center of Versalis (ENI), and proposes to develop a new predictive one-dimensional phenomenological model associated to its numerical counterpart, based on the Fischer-Burmeister function.

PART II: Fatigue modeling of elastoplastic and shape memory materials

The second part of the thesis is organized as follows.

Chapter 10 starts with an overview of the fatigue problem in metals by recalling general concepts on the phenomenon, historical examples, and standard literature approaches. Then, Chapters 11 and 12 present an overview of the state of art in polycylic (or high-cycle) and oligocyclic (or low-cycle) fatigue of metals, in order to prepare the basis for the fatigue-life assessment of cardiovascular stents.

Chapter 13 provides an in-depth analysis of the fatigue-life assessment for microsize 316L stainless steel components, which find typical applications in the biomedical field, e.g., in cardiovascular stents. To this purpose, the chapter presents the analysis of some experimental data from the literature on 316L stainless steel smooth and notched microsize components by using a global computational approach. Several aspects are discussed as the choice of an appropriate constitutive law for cyclic material behavior, fatigue criteria based on shakedown concepts for finite and infinite lifetime, and gradient effects in relation with hot-spot as well as average or mean volume approaches for the lifetime estimation.

Then, Chapter 14 proposes the introduction of a reliable and general methodology for the numerical fatigue-life assessment of cardiovascular balloon-expandable stents. To this purpose, the main idea is to combine advanced computational methods and fatigue prediction techniques with the experimental fatigue data investigated in Chapter 13, in order to lay down the basis for a complete fatigue-life methodology for balloon-expandable stents.

Finally, Chapter 15 concludes by reviewing the actual knowledge on the fatigue of shape memory alloys, with a special focus on the fatigue of cardiovascular self-expanding stents.

Appendix

The appendix of the thesis is organized as follows.

Appendix A presents a brief introduction to convex analysis, particularly useful to understand the mathematical theory of elastoplasticity, presented in Chapter 2, within a convex-analytic context.

Appendix B presents a detailed introduction to the innovative Mathematica packages, called AceGen and AceFEM, developed by Joze Korelc, Professor at the Faculty of Civil and Geodetic Engineering of the University of Ljubljana, and recently released by Wolfram Research. Such packages, extensively used in the present thesis, bring to Mathematica a robust and optimized architecture for a rapid numerical prototyping and a finite element analysis.

PART I
Constitutive and numerical modeling of elastoplastic and shape memory materials

Chapter 1

Continuum Mechanics and Elasticity

This Chapter is devoted to a brief summary of the fundamental concepts of Continuum Mechanics and Elasticity in order to prepare the framework for the study of non-linear inelastic material behavior, that is the object of next chapters.

The Chapter is organized as follows. Section 1.1 presents a review on the notation used throughout the thesis. Section 1.2 focuses on the kinematics of a deformable material body. Then, Section 1.3 briefly presents the formulation of the static and dynamic equilibrium for a material body within the context of the three-dimensional infinitesimal theory. Section 1.4 reviews the constitutive equation for linear elastic isotropic materials. Section 1.5 focuses on the first and second laws of thermodynamics and, particularly, on the special case of linear elastic material bodies undergoing isothermal transformations. Finally, Section 1.6 presents the classical displacement local formulation of the initial boundary-value problem of equilibrium for a deformable body constituted of linear elastic material.
For a detailed discussion on the present topic, the reader is referred to, e.g., (Ciarlet, 1993; Gurtin et al., 2010; Lemaitre and Chaboche, 1994).

1.1 Review on notation

Vectors and tensors

The present thesis deals with different types of mathematical objects, namely with scalars, second-order tensors and fourth-order tensors as well as with generalized vector and matrix operators. In particular, we denote *scalars* with italic letters like a, α, A; *vectors*, *second-order tensors* and *generalized vector operators* with boldface letters like $\mathbf{a}$, $\boldsymbol{\alpha}$, $\mathbf{A}$, $\boldsymbol{\Sigma}$; *fourth-order tensors* and *generalized matrix operators* with uppercase bold blackboard letters like $\mathbb{A}$, $\mathbb{G}$.
In the following, we adopt the *summation* or *Einstein convention* for repeated indices[1].

We start by referring to a three-dimensional Euclidean space, $\Re^3$, and by making use of a Cartesian coordinate system equipped with an orthonormal basis, $(\mathbf{e}_1, \mathbf{e}_2, \mathbf{e}_3)$, to which components of vectors and tensors are systematically referred.

A vector, $\mathbf{a} \in \Re^3$, is identified by the ordered set $\{a_i\}^T$, for $i = 1, 2, 3$, which defines its coordinates with respect to the canonical basis, such that $\mathbf{a} = a_i \mathbf{e}_i$. We can adopt the following notations for vectors of $\Re^3$:

- Compact: $\mathbf{a}$

[1] The summation or Einstein convention requires that a repeated index in a multiplicative term implies the presence of a summation over the possible index range. Consistently, a non-repeated index in a multiplicative term implies that it may assume indifferently any value in the possible index range.

- Indicial: $a_i = \mathbf{a}|_i$
- Engineering: $\{\mathbf{a}\} = \{a_1, a_2, a_3\}^T$

The *scalar product* of two vectors $\mathbf{a}$ and $\mathbf{b}$ is defined by:

$$\mathbf{a} \cdot \mathbf{b} = a_i b_i \tag{1.1}$$

while the *Euclidean norm* of a vector $\mathbf{a}$ by:

$$\|\mathbf{a}\| = \sqrt{\mathbf{a} \cdot \mathbf{a}} \tag{1.2}$$

The three-dimensional Euclidean space, $\Re^3$, with the natural operations introduced above forms a vector space, indicated in the following as $\mathbf{l}in$.
The *cross product* or *vector product* of two vectors $\mathbf{a}$ and $\mathbf{b}$ is a vector $\mathbf{c}$, orthogonal to both $\mathbf{a}$ and $\mathbf{b}$, with length equal to the area of the parallelogram defined by the vectors $\mathbf{a}$ and $\mathbf{b}$ and direction defined according to the right-hand rule. The following expression results:

$$\mathbf{c} = \mathbf{a} \times \mathbf{b} = (a_i \mathbf{e}_i) \times (b_j \mathbf{e}_j) = a_i b_j \, (\mathbf{e}_i \times \mathbf{e}_j) \tag{1.3}$$

for $i, j = 1, 2, 3$.

Second-order tensors are objects defined to generalize such a property in the sense that they operate on a vector returning a vector. Thus, a second-order tensor, $\boldsymbol{\tau}$, is defined as a linear operator, mapping vectors into vectors. Clearly, dealing with a three-dimensional space, to completely define the action of a second-order tensor, it is necessary to consider at least the action on three independent vectors of $\mathbf{l}in$, such as the three basis vectors. Since the action of the second-order tensor on the three basis vectors is to return three new vectors, we may conclude that second-order tensors are in general identified through a set of nine scalar components.

The fundamental operation to construct the space of second-order tensors is the *tensor product* of two vectors $\mathbf{a}$ and $\mathbf{b}$, defined as:

$$(\mathbf{a} \otimes \mathbf{b}) \, \mathbf{c} = (\mathbf{b} \cdot \mathbf{c}) \, \mathbf{a} \qquad \forall \mathbf{a}, \mathbf{b}, \mathbf{c} \in \mathbf{l}in \tag{1.4}$$

The space of second-order tensors with the natural operation defined in Eq. (1.4) forms a vector space, indicated in the sequel as $\mathbf{L}in$.
We can adopt the following notations for second-order tensors of $\mathbf{L}in$:

- Compact: $\boldsymbol{\tau}$
- Indicial: $\tau_{ij} = \boldsymbol{\tau}|_{ij}$
- Engineering: $[\boldsymbol{\tau}] = \begin{bmatrix} \tau_{11} & \tau_{12} & \tau_{13} \\ \tau_{21} & \tau_{22} & \tau_{23} \\ \tau_{31} & \tau_{32} & \tau_{33} \end{bmatrix}$

The tensor products of the basis vectors of $\mathbf{l}in$, $(\mathbf{e}_i \otimes \mathbf{e}_j)$, are a set of second-order tensors, providing a suitable basis for expressing the components of second-order tensors of $\mathbf{L}in$. In particular, we define the ij-th component of a tensor $\boldsymbol{\tau}$ as $\tau_{ij} = \mathbf{e}_i \cdot \boldsymbol{\tau} \mathbf{e}_j$, which implies that the second-order tensor $\boldsymbol{\tau}$ can be expressed in component form as $\boldsymbol{\tau} = \tau_{ij} \, (\mathbf{e}_i \otimes \mathbf{e}_j)$.
The *transpose* of a second-order tensor $\boldsymbol{\tau}$ is defined by the following relation:

$$\boldsymbol{\tau}^T|_{ij} = \tau_{ji} \tag{1.5}$$

while the *trace* is a scalar-valued function defined as:

$$\text{tr}(\boldsymbol{\tau}) \; = \tau_{ii} \tag{1.6}$$

The *scalar product* or *double-dot product* of two second-order tensors $\boldsymbol{\sigma}$ and $\boldsymbol{\tau}$ is a scalar defined by:

$$\boldsymbol{\sigma} : \boldsymbol{\tau} = \text{ tr}(\boldsymbol{\tau}^T \boldsymbol{\sigma}) \ = \sigma_{ij}\tau_{ij} \tag{1.7}$$

The *Euclidean norm* of a second-order tensor $\boldsymbol{\tau}$, induced by the scalar product, is:

$$\|\boldsymbol{\tau}\| = \sqrt{\boldsymbol{\tau} : \boldsymbol{\tau}} \tag{1.8}$$

The *multiplication* or *combination* of two second-order tensors $\boldsymbol{\sigma}$ and $\boldsymbol{\tau}$ is a second-order tensor, defined as:

$$\boldsymbol{\eta} = \boldsymbol{\sigma}\boldsymbol{\tau} \qquad \text{such that} \qquad \eta_{ij} = \sigma_{ik}\tau_{kj} \tag{1.9}$$

A unique additive decomposition of any second-order tensor $\boldsymbol{\tau}$ is given by the sum of its *deviatoric part*, $\boldsymbol{\tau}_{dev}$, and its *volumetric* or *spherical part*, $\boldsymbol{\tau}_{vol}$, respectively defined as:

$$\begin{cases} \boldsymbol{\tau}_{vol} = \dfrac{1}{3} \text{ tr}(\boldsymbol{\tau}) \ \mathbf{I} \\ \boldsymbol{\tau}_{dev} = \boldsymbol{\tau} - \dfrac{1}{3} \text{ tr}(\boldsymbol{\tau}) \ \mathbf{I} \end{cases} \tag{1.10}$$

such that:

$$\boldsymbol{\tau} = \boldsymbol{\tau}_{vol} + \boldsymbol{\tau}_{dev} \tag{1.11}$$

where $\mathbf{I}$ is the second-order identity tensor, defined by the relation $\mathbf{I}\mathbf{a} = \mathbf{a} \ \ \forall \mathbf{a} \in \mathbf{l}in$.

A fourth-order tensor is defined as a linear operator mapping the space of second-order tensors, $\mathbf{L}in$, onto itself. To properly define the action of a fourth-order tensor, it is necessary to consider the action on a second-order tensor basis; since the action of a fourth-order tensor on a second-order tensor is to return a second-order tensor, we may conclude that fourth-order tensors are in general defined by a set of eighty-one scalar components.

The fundamental operation to construct the space of fourth-order tensors is the *dyadic product* of two second-order tensors $\boldsymbol{\tau}$ and $\boldsymbol{\sigma}$, defined as to return a fourth-order tensor $\mathbb{D}$:

$$\mathbb{D} = \boldsymbol{\tau} \otimes \boldsymbol{\sigma} \tag{1.12}$$

such that:

$$\mathbb{D}\boldsymbol{\eta} = (\boldsymbol{\tau} \otimes \boldsymbol{\sigma}) \, \boldsymbol{\eta} = (\boldsymbol{\sigma} : \boldsymbol{\eta}) \, \boldsymbol{\tau} = \text{ tr}(\boldsymbol{\eta}^T \boldsymbol{\sigma}) \ \boldsymbol{\tau} \quad \forall \boldsymbol{\eta} \in \mathbf{L}in \tag{1.13}$$

The space of fourth-order tensors with the natural operation introduced in Eq. (1.12) forms a vector space, indicated in the sequel by $\mathbb{L}in$.
We can adopt the following notations for fourth-order tensors of $\mathbb{L}in$:

- Compact: $\mathbb{D}$
- Indicial: $\mathbb{D}_{ijkl} = \mathbb{D}|_{ijkl}$

The *tensor products* between the second-order basis tensor provide a suitable basis for expressing the components of a fourth-order tensor of $\mathbb{L}in$. In particular, we define the $ijkl$-th component of a tensor $\mathbb{D}$, as follows:

$$\mathbb{D}_{ijkl} = (\mathbf{e}_i \otimes \mathbf{e}_j) : \mathbb{D} \, (\mathbf{e}_k \otimes \mathbf{e}_l) \tag{1.14}$$

such that the fourth-order tensor $\mathbb{D}$ can be expressed as:

$$\mathbb{D} = \mathbb{D}_{ijkl} \, (\mathbf{e}_i \otimes \mathbf{e}_j) \otimes (\mathbf{e}_k \otimes \mathbf{e}_l) \tag{1.15}$$

The *action* of a fourth-order tensor $\mathbb{D}$ on a second-order tensor $\boldsymbol{\tau}$ is denoted as follows:

$$\boldsymbol{\sigma} = \mathbb{D}\boldsymbol{\tau} \qquad \text{such that} \qquad \sigma_{ij} = \mathbb{D}_{abkl}\tau_{kl} \tag{1.16}$$

The fourth-order identity tensor, $\mathbb{I}$, is defined to satisfy the relation $\mathbb{I}\boldsymbol{\tau} = \boldsymbol{\tau} \ \ \forall\boldsymbol{\tau}$. A splitting into the volumetric and deviatoric parts of $\mathbb{I}$ in the form:

$$\mathbb{I} = \mathbb{I}_{vol} + \mathbb{I}_{dev} \tag{1.17}$$

is achievable by setting:

$$\begin{cases} \mathbb{I}_{vol} = \dfrac{1}{3}\,\mathbf{I}\otimes\mathbf{I} \\ \mathbb{I}_{dev} = \mathbb{I} - \dfrac{1}{3}\,\mathbf{I}\otimes\mathbf{I} \end{cases} \tag{1.18}$$

With the above positions, the volumetric and deviatoric part, $\boldsymbol{\tau}_{vol}$ and $\boldsymbol{\tau}_{dev}$, of any second-order tensor, $\boldsymbol{\tau}$, defined in Eq. (1.10), are respectively given by:

$$\begin{cases} \boldsymbol{\tau}_{vol} = \mathbb{I}_{vol}\ \boldsymbol{\tau} \\ \boldsymbol{\tau}_{dev} = \mathbb{I}_{dev}\ \boldsymbol{\tau} \end{cases} \tag{1.19}$$

In some cases, we make also use of *algebraic vectors* or m-tuples. For instance, the m-component algebraic vector, $\boldsymbol{\xi}$, can be equivalently indicated in compact or algebraic notation as $\boldsymbol{\xi} = (\boldsymbol{\xi}_k) = (\boldsymbol{\xi}_1, ..., \boldsymbol{\xi}_m)$. It is noted that components, $\boldsymbol{\xi}_k$, with $k = 1, ..., m$, may be objects of different type, namely scalars, vectors or tensors. Similarly, in some cases, we make also use of *algebraic* or *matrix operators*. Such matrix operators, generally represented in engineering notation as:

$$[\mathbb{G}] = \begin{bmatrix} \mathbb{G}_{11} & \mathbb{G}_{12} \\ \mathbb{G}_{21} & \mathbb{G}_{22} \end{bmatrix} \tag{1.20}$$

It is noted that components, $\mathbb{G}_{ij}$, may be objects of different type, namely scalars, second-order tensors or fourth-order tensors.
The use of algebraic vectors and matrix operators will be specified whenever needed in order to avoid confusion.

Invariants of second-order tensors

The algebraic problem of finding every scalar, λ, and every non-zero vector, $\mathbf{q}$, such that $\boldsymbol{\tau}\mathbf{q} = \lambda\mathbf{q}$ leads to the standard eigenvalue problem, which consists of solving the *characteristic equation*:

$$\det\left(\lambda\mathbf{I} - \boldsymbol{\tau}\right) = 0 \tag{1.21}$$

or equivalently:

$$\lambda^3 - I_1\lambda^2 + I_2\lambda - I_3 = 0 \tag{1.22}$$

Here, I_1, I_2, and I_3 are the *principal scalar invariants* of $\boldsymbol{\tau}$, defined as:

$$\begin{cases} I_1 = \ \mathrm{tr}(\boldsymbol{\tau}) \ = \lambda_1 + \lambda_2 + \lambda_3 \\ I_2 = \dfrac{1}{2}\left[\ \mathrm{tr}(\boldsymbol{\tau})^{\ 2} - \ \mathrm{tr}(\boldsymbol{\tau}^2)\ \right] = \lambda_1\lambda_2 + \lambda_2\lambda_3 + \lambda_1\lambda_3 \\ I_3 = \det\boldsymbol{\tau} = \lambda_1\lambda_2\lambda_3 \end{cases} \tag{1.23}$$

where the scalars, λ_1, λ_2, and λ_3, are the eigenvalues of $\boldsymbol{\tau}$ as well as the roots of the characteristic equation (1.21) (a multiple root is counted repeatedly according to its multiplicity). The eigenvalues of $\boldsymbol{\tau}$ are often referred to as the *principal components* of $\boldsymbol{\tau}$.
The *gradient* of a *scalar field*, $\phi = \phi\left(\mathbf{x}\right)$, defined on $\mathbb{l}in$, is defined as:

$$\nabla\phi = \frac{\partial\phi}{\partial x_i}\,\boldsymbol{\varepsilon}_i \tag{1.24}$$

The *divergence* and the *gradient* of a *vector field*, $\mathbf{u} = \mathbf{u}(\mathbf{x})$, defined on $\mathbf{l}in$, are respectively a scalar and a second-order tensor field, defined as:

$$\begin{cases} \text{div}\mathbf{u} = \dfrac{\partial u_i}{\partial x_i} \\ \nabla\mathbf{u} = \dfrac{\partial u_i}{\partial x_j}\, \mathbf{e}_i \otimes \mathbf{e}_j \end{cases} \tag{1.25}$$

The *divergence* of a *second-order tensor*, $\boldsymbol{\tau}$, defined on $\mathbf{l}in$, is a vector defined as:

$$\text{div}\boldsymbol{\tau} = \frac{\partial \tau_{ij}}{\partial x_j} \tag{1.26}$$

The derivative of a scalar-valued function, $f = f(\boldsymbol{\tau})$, defined on $\mathbf{L}in$, with respect to $\boldsymbol{\tau}$ is defined as a second-order tensor in the following form:

$$\frac{\partial f(\boldsymbol{\tau})}{\partial \boldsymbol{\tau}} = \frac{\partial f(\boldsymbol{\tau})}{\partial \tau_{ij}}\, \mathbf{e}_i \otimes \mathbf{e}_j \tag{1.27}$$

For a time-dependent quantity, z, we denote with $\dot{z}$ its partial derivative with respect to time, t.

1.2 Kinematics of a material body

Kinematical relations concern the description of the deformation and motion of a material body, the derivation of strain measures, as well as the time derivatives of kinematical quantities. All kinematical relations are needed within the constitutive equations and the weak formulation of balance laws.

Material body

We consider a body, B, that at the macroscopic level may be regarded as composed of material continuously distributed in space. We assume that at any time instant, t, the body, B, can be identified with a closed subset, $\Omega \subset \Re^3$, such that $B \equiv \Omega \subset \Re^3$. Accordingly, it is possible to associate any material point in the body, B, to a point $\mathbf{X} \in \Omega \subset \Re^3$. Such an identification procedure allows to treat the material body as a *continuum*.

In the present context, we start by addressing the kinematics of the body which is the common starting point to describe the behavior of general continuous media. As it is well known, such a framework remains independent of what acts on the body and of the constitution of the body itself.

Change of configuration

We consider two distinct time instants, t_0 and t, such that $t_0 < t$, referred to as initial and current time instant, respectively. At time t_0 the material body, B, can be identified with a subset $\Omega_0 \subset \Re^3$, indicated as *initial* or *reference configuration*, such that at the same time instant the generic material point in B can be identified with a corresponding point $\mathbf{X} \in \Omega_0$. At time t, the material body, B, can be identified with a subset $\Omega \subset \Re^3$, indicated as *current configuration*, such that at the same time instant the generic material point in B can be identified with a corresponding point $\mathbf{x} \in \Omega$[2].

It is possible to construct a map between the reference and the current configuration, indicated, in general, as *change of configuration* or *deformation map*, $\boldsymbol{\varphi} = \boldsymbol{\varphi}(\mathbf{X})$, expressed as:

$$\mathbf{x} = \boldsymbol{\varphi}(\mathbf{X}) \tag{1.28}$$

[2] The convention indicates the reference position vector, $\mathbf{X}$, with an upper case boldface letter and the current position vector, $\mathbf{x}$, with a lower case boldface letter. More generally, either using a compact or an indicial notation, quantities relative to the reference configuration are indicated with upper case letters and quantities relative to the current configuration are indicated with lower case letters.

The gradient of the deformation map, or *deformation gradient*, $\mathbf{F}$, is defined as:

$$\mathbf{F} = \nabla_{\mathbf{X}} \boldsymbol{\varphi} \tag{1.29}$$

Without distinguishing between the deformation map, $\boldsymbol{\varphi}$, and the current position, $\mathbf{x}$, the deformation gradient can be also written as:

$$\mathbf{F} = \nabla_{\mathbf{X}} \mathbf{x} \tag{1.30}$$

It can be shown that $\boldsymbol{\varphi}$ maps an infinitesimal vector, $d\mathbf{X}$, with origin in $\mathbf{X}$, into an infinitesimal vector, $d\mathbf{x}$, with origin in $\mathbf{x}$, as follows:

$$d\mathbf{x} = \mathbf{F} d\mathbf{X} \tag{1.31}$$

Accordingly, the deformation gradient is a two-point second-order tensor; in fact, it is a second-order tensor since it maps vectors into vectors, but it is two-point since one component is relative to the reference configuration and one component is relative to the current configuration. This is consistent with the fact that $\mathbf{F}$ operates on vectors defined in the reference configuration and it returns vectors defined in the current configuration. The deformation gradient, $\mathbf{F} = \mathbf{F}(\mathbf{X})$, is in general function of position, since the deformation map is in general non uniform as well. Likewise, $\boldsymbol{\varphi}$ is in general a non-linear map in space and $\mathbf{F}$ results as its pointwise linearization.

Strain tensor

It is possible to prove that the deformation gradient, $\mathbf{F}$, being a pointwise-defined second-order tensor, characterizes the strain status of the point $\mathbf{X}$ neighborhood. In particular, given $\mathbf{F}$, it is possible to compute the relative change in length of a generic fiber emanating from $\mathbf{X}$, as well as the change in angle between two fibers emanating from $\mathbf{X}$.

Consider an infinitesimal vector, $d\mathbf{S}$, with origin in $\mathbf{X}$ and expressed as $d\mathbf{S} = \mathbf{N} dS$, with $\mathbf{N}$ unit vector, and indicate with $d\mathbf{s}$ the vector with origin in $\mathbf{x}$, obtained from $d\mathbf{S}$ through the deformation map, $\boldsymbol{\varphi}$, i.e., $d\mathbf{s} = \mathbf{F} d\mathbf{S} = \mathbf{F}\mathbf{N} dS$.
After defining the *stretch* of the vector $d\mathbf{S}$ as the elongation of the vector through the deformation map, that is, as the ratio between the norm of the vector after and before the mapping:

$$\lambda = \frac{\|d\mathbf{s}\|}{\|d\mathbf{S}\|} \tag{1.32}$$

and recalling that $\|\mathbf{N}\| = 1$, it holds:

$$\lambda^2 = \mathbf{C}\mathbf{N} \cdot \mathbf{N} = \lambda^2(\mathbf{N}) \tag{1.33}$$

where $\mathbf{C}$ is the *right Cauchy-Green deformation tensor*, defined as:

$$\mathbf{C} = \mathbf{F}^T \mathbf{F} \tag{1.34}$$

Accordingly:

$$\lambda = \sqrt{\mathbf{C}\mathbf{N} \cdot \mathbf{N}} \tag{1.35}$$

i.e., given $\mathbf{F}$ and hence $\mathbf{C}$, we can compute the elongation of any fiber with origin in $\mathbf{X}$ and extremum in a sufficiently small neighborhood of $\mathbf{X}$. Such an elongation is a function of the direction $\mathbf{N}$.

Consider two infinitesimal vectors, $\mathbf{S}_1$ and $\mathbf{S}_2$, with origin in $\mathbf{X}$ and expressed as $\mathbf{S}_1 = \mathbf{N}_1 dS_1$ and $\mathbf{S}_2 = \mathbf{N}_2 dS_2$, respectively, with $\mathbf{N}_1$ and $\mathbf{N}_2$ unit vectors. Then, indicate with $\mathbf{s}_1$ and $\mathbf{s}_2$ the vectors with origin in $\mathbf{x}$, defined through the deformation map as $d\mathbf{s}_1 = \mathbf{F} d\mathbf{S}_1$ and $d\mathbf{s}_2 = \mathbf{F} d\mathbf{S}_2$, respectively. If θ_0 is

the angle between $d\mathbf{S}_1$ and $d\mathbf{S}_2$ and θ is the angle between $\mathbf{s}_1$ and $\mathbf{s}_2$, the difference $\gamma = \theta - \theta_0$ represents the angle variation. Also this quantity can be expressed in terms of $\mathbf{F}$ since:

$$\cos\theta = \frac{d\mathbf{s}_1 \cdot d\mathbf{s}_2}{\|d\mathbf{s}_1\| \, \|d\mathbf{s}_2\|} = \frac{\mathbf{F}\mathbf{N}_1 \cdot \mathbf{F}\mathbf{N}_2}{\|\mathbf{F}\mathbf{N}_1\| \, \|\mathbf{F}\mathbf{N}_2\|} \tag{1.36}$$

Despite the fact that $\mathbf{F}$ and $\mathbf{C}$ represent a correct tool to calculate the local state of strain, neither of them is an appropriate strain measure. In fact, in the undeformed configuration, we have $\mathbf{F} = \mathbf{C} = \mathbf{I}$, while we would expect a proper strain measure to be zero in the undeformed configuration. Such a lacking can be avoided by introducing the *Lagrangian* or *Green strain tensor*, $\mathbf{E}$, defined as:

$$\mathbf{E} = \frac{1}{2}\left(\mathbf{C} - \mathbf{I}\right) = \frac{1}{2}\left(\mathbf{F}^T\mathbf{F} - \mathbf{I}\right) \tag{1.37}$$

The second-order tensor, $\mathbf{e}$, called *Eulerian* or *Almansi strain tensor*, is defined as:

$$\mathbf{e} = \frac{1}{2}\left(\mathbf{I} - \mathbf{b}^{-1}\right) \tag{1.38}$$

where the second-order tensor, $\mathbf{b}$, is the *left Cauchy-Green* or *Finger deformation tensor*, defined as:

$$\mathbf{b} = \mathbf{F}\mathbf{F}^T \tag{1.39}$$

It is convenient to describe the change of configuration introducing the *displacement field*, $\mathbf{u} = \mathbf{u}(\mathbf{X})$, defined as the pointwise difference between the current and the reference vector position, i.e.,

$$\mathbf{u}(\mathbf{X}) = \mathbf{x}(\mathbf{X}) - \mathbf{X} \tag{1.40}$$

Then, the current position vector, $\mathbf{x}$, is given by the sum of the reference position and displacement vectors, as follows:

$$\mathbf{x} = \boldsymbol{\varphi}(\mathbf{X}) = \mathbf{X} + \mathbf{u}(\mathbf{X}) \tag{1.41}$$

The expression of the deformation map in terms of displacement gives rise to alternative expressions of the strain tensors introduced previously. For example, the deformation gradient, $\mathbf{F}$, becomes:

$$\mathbf{F} = \frac{\partial \mathbf{x}}{\partial \mathbf{X}} = \mathbf{I} + \nabla_{\mathbf{X}}\mathbf{u} = \mathbf{I} + \mathbf{H} \tag{1.42}$$

Moreover, we may write:

$$\begin{cases} \mathbf{C} = \mathbf{F}^T\mathbf{F} = \mathbf{I} + \mathbf{H} + \mathbf{H}^T + \mathbf{H}^T\mathbf{H} \\ \mathbf{E} = \dfrac{1}{2}\left(\mathbf{C} - \mathbf{I}\right) = \dfrac{1}{2}\left(\mathbf{H} + \mathbf{H}^T + \mathbf{H}^T\mathbf{H}\right) \end{cases} \tag{1.43}$$

The Lagrangian strain tensor, $\mathbf{E}$, defined in Eq. (1.37), admits the splitting:

$$\mathbf{E} = \mathbf{E}_1 + \mathbf{E}_2 = \boldsymbol{\varepsilon} + \mathbf{E}_2 \tag{1.44}$$

which identifies the linear and non-linear parts of $\mathbf{E}$, indicated respectively as $\mathbf{E}_1 = \left(\mathbf{H} + \mathbf{H}^T\right)/2$ and $\mathbf{E}_2 = \left(\mathbf{H}^T\mathbf{H}\right)/2$.

Small displacement gradient

In many structural engineering problems the deformations can be regarded as small in some sense. Such an assumption, which is rigorously formalized, obviously introduces an approximation in the treatment but, nevertheless, permits to simplify the problem formulation and thus remains of notable interest.

We consider the case of a motion with a small displacement gradient, $\nabla\mathbf{u}$, that is:

$$\|\nabla_{\mathbf{X}}\mathbf{u}\| = \varepsilon \quad \text{with } \varepsilon << 1 \tag{1.45}$$

Without entering into details (Gurtin et al., 2010), in such a case, we have:

- the non-linear term, introduced in Eq. (1.43), can be neglected;
- tensors $\mathbf{E}$ and $\boldsymbol{\varepsilon}$ coincide as well as $\mathbf{C}$ and $\mathbf{b}$;
- the displacement gradient corresponding to a rigid deformation is skew.

In the following chapters, we indicate a deformation map characterized by a small displacement gradient field as a small deformation map or simply we talk about *small deformations*, that is:

$$\text{Small deformations} \quad \Leftrightarrow \quad \begin{cases} \|\nabla_{\mathbf{X}}\mathbf{u}\| << 1 \\ \boldsymbol{\varepsilon} = \dfrac{1}{2}\left[\nabla_{\mathbf{X}}\mathbf{u} + (\nabla_{\mathbf{X}}\mathbf{u})^T\right] \end{cases} \tag{1.46}$$

Volume change

We are now interested in the evaluation of the unit volume variation produced in the change of configuration of the body by means of the deformation map, $\boldsymbol{\varphi}$.
The volume, $V = V(\mathbf{a}, \mathbf{b}, \mathbf{c})$, of a parallelepiped, defined by vectors $\mathbf{a}$, $\mathbf{b}$, and $\mathbf{c}$, is given by:

$$V = (\mathbf{a} \times \mathbf{b}) \cdot \mathbf{c} \tag{1.47}$$

Then, we consider a parallelepiped of material described by a triad of infinitesimal vectors, $\{d\mathbf{S}_1, d\mathbf{S}_2, d\mathbf{S}_3\}$, expressed respectively as a product of unit vectors, $\mathbf{N}_1, \mathbf{N}_2, \mathbf{N}_3$, and of infinitesimal lengths, dS_1, dS_2, dS_3. Accordingly, the infinitesimal volume, dV, of the parallelepiped is given by:

$$dV = [(\mathbf{N}_1 \times \mathbf{N}_2) \cdot \mathbf{N}_3]\, dS_1 dS_2 dS_3 \tag{1.48}$$

The deformed parallelepiped is described by vectors, $\{\mathbf{F}\mathbf{N}_1, \mathbf{F}\mathbf{N}_2, \mathbf{F}\mathbf{N}_3\}$, multiplied respectively by quantities, dS_1, dS_2, dS_3. Accordingly, the corresponding infinitesimal volume, dv, is given by:

$$dv = [(\mathbf{F}\mathbf{N}_1 \times \mathbf{F}\mathbf{N}_2) \cdot \mathbf{F}\mathbf{N}_3]\, dS_1 dS_2 dS_3 \tag{1.49}$$

Hence, we get:

$$\frac{dv}{dV} = \det \mathbf{F} = J \tag{1.50}$$

where the classical notation, $\det \mathbf{F} = J$, indicates the *Jacobian* of the deformation gradient.
The above formula can be specialized in the case of small deformations, as follows:

$$J = \det \mathbf{F} = \det \mathbf{I} + \nabla \mathbf{u} = 1 + \text{div}\mathbf{u} \tag{1.51}$$

A body transformation that produces no volume change is said to be *isochoric*, i.e.,

$$J = 1 \quad \forall \mathbf{x} \in \Omega \tag{1.52}$$

Accordingly, for an isochoric infinitesimal deformation process, the displacement field satisfies the condition:

$$\text{tr}(\boldsymbol{\varepsilon}(\mathbf{u}(\mathbf{x}))) = \text{div}\mathbf{u}(\mathbf{x}) \quad \forall \mathbf{x} \in \Omega \tag{1.53}$$

A material that cannot undergo any transformation that is accompanied by change in volume is called *incompressible*.

1.3 Equilibrium for a material body

1.3.1 Static equilibrium

This Section starts by investigating the conditions of *static equilibrium*.

Given a body, B, in a configuration, Ω, we postulate that the interaction between the external world and the body itself can be described through two force fields:

- a *surface* or *contact force field*, $\mathbf{t}$, with dimension of force per unit area and defined on a portion of the current boundary surface, $\partial\Omega^t$;
- a *volume* or *body force field*, $\mathbf{b}$, with dimension of force per unit volume and defined on the current configuration, Ω.

We also postulate that the interaction between any internal portion, $\Omega^{'}$, of the body in the current configuration, Ω, and the remaining part of the body, $\Omega/\Omega^{'}$, can be described through a surface force field, indicated also as *traction force field*, with dimension of force per unit area and defined on $\partial\Omega^{'}$. Such interaction forces are assumed to be functions of the local outward normal to $\Omega^{'}$ and, accordingly, we indicate such a field with $\mathbf{t_n}$, where subscript, $\mathbf{n}$, expresses the dependency on the normal, $\mathbf{n}$.
Then, we can define the force resultant, $\mathbf{r} = \mathbf{r}\left(\Omega^{'}\right)$, and the moment resultant, $\mathbf{m} = \mathbf{m}\left(\Omega^{'}\right)$, relative to $\Omega^{'} \subseteq \Omega$, as follows:

$$\begin{cases} \mathbf{r} = \int_{\Omega'} \mathbf{b} dv + \int_{\partial\Omega'} \mathbf{t_n} da \\ \mathbf{m} = \int_{\Omega'} (\mathbf{x} \times \mathbf{b})\, dv + \int_{\partial\Omega'} (\mathbf{x} \times \mathbf{t_n})\, da \end{cases} \tag{1.54}$$

where $\mathbf{x}$ is the current position vector and the resultant momentum is computed with respect to a generic origin, $\mathbf{o}$.
Now, we may state the following Axiom:

STATIC EQUILIBRIUM AXIOM. A deformable body is in equilibrium if and only if the force resultant, $\mathbf{r} = \mathbf{r}\left(\Omega^{'}\right)$, and the force momentum, $\mathbf{m} = \mathbf{m}\left(\Omega^{'}\right)$, on each portion, $\Omega^{'}$, of the body are zero, i.e., a body, B, in a configuration, Ω, is in equilibrium if and only if:

$$\begin{cases} \mathbf{r} = \mathbf{0} \quad \forall\Omega^{'} \subseteq \Omega \\ \mathbf{m} = \mathbf{0} \quad \forall\Omega^{'} \subseteq \Omega \end{cases} \tag{1.55}$$

Eqs. $(1.55)_1$ and $(1.55)_2$ are indicated as *linear momentum* and *angular momentum balance laws*, respectively.

We may note that the quantity $\mathbf{t_n}$, introduced in system (1.55) through system (1.54), is unknown. Thus, we need to investigate the actions that internal parts of the body mutually exchange. To this purpose, we introduce a surface, Σ, ideally dividing the body, Ω, in two parts. Assuming that the whole body is in equilibrium, by the static equilibrium axiom, we have that each single part of the body should be in equilibrium, hence, also the two parts. Without showing all the calculations (Gurtin et al., 2010), we have:

$$\int_{\Sigma} (\mathbf{t_n} + \mathbf{t_{-n}})\, da = \mathbf{0} \tag{1.56}$$

which, recalling the arbitrariness of the surface Σ, implies:

$$\mathbf{t_n} = -\mathbf{t_{-n}} \tag{1.57}$$

Eq. (1.57) is known as *action-reaction principle* or *Cauchy reciprocal principle* or *first Cauchy theorem*.

Stress tensor

Now, we introduce a right-angle tetrahedron, T, contained in the body, and a coordinate system with origin, $\mathbf{o}$, in the tetrahedron right-angle vertex and axes given by the tetrahedron edges, respectively with lengths along the coordinate axes equal to ε_1, ε_2, ε_3. Moreover, we indicate with $\mathbf{p}_i$ (with i = 1, 2, 3) the other tetrahedron vertices, with $\mathbf{e}_i$ the unit vector along the i-th coordinate axis, with v the volume, with a_i the area of the face with unit normal $-\mathbf{e}_i$, and with a_n the fourth area describing the tetrahedron, having normal $\mathbf{n}$.
We consider the tetrahedron equilibrium, taking into account the traction vector fields acting on the four sides and the body force field acting on the volume. The following integral force balance holds:

$$\int_v \mathbf{b} dv + \sum_{i=1}^{3} \int_{a_i} \mathbf{t}_{-\mathbf{e}_i} da + \int_{a_n} \mathbf{t}_{\mathbf{n}} da = \mathbf{0} \tag{1.58}$$

Omitting, for brevity, the mathematical manipulations and using the action-reaction principle, it is possible to state that the above equilibrium condition for the tetrahedron implies the following relation:

$$\mathbf{t}_{\mathbf{n}} = \boldsymbol{\sigma}\mathbf{n} \tag{1.59}$$

which is known as *second Cauchy theorem*, valid for any point internal to the body.
It is interesting to emphasize how, starting from the assumption that the traction vector $\mathbf{t}_{\mathbf{n}}$ depends on $\mathbf{n}$, this dependency is linear through a second-order tensor, $\boldsymbol{\sigma}$, known as *Cauchy stress tensor*. Accordingly, knowing $\boldsymbol{\sigma}$ in a point, it is possible to compute the stress vector, $\mathbf{t}_{\mathbf{n}}$, acting on any surface of normal $\mathbf{n}$, which is equivalent to say that $\boldsymbol{\sigma}$ contains all the information relative to the local state of stress.

Static equilibrium equations

Now, we transform the equilibrium requirements from the global integral format of system (1.55) to a local differential format.
To this purpose, we recall that, given any tensor field, $\mathbf{G}$, defined on a region, $\Omega^{'}$, with normal, $\mathbf{n}$, and boundary, $\partial\Omega^{'}$, the *divergence theorem* of a tensor field states:

$$\int_{\partial\Omega'} \mathbf{G}\mathbf{n}\, da = \int_{\Omega'} \mathrm{div}\mathbf{G}\, dv \tag{1.60}$$

Applying this equality to Eq. $(1.55)_1$, we get the corresponding *local form* of the *equilibrium equation* in the following form:

$$\mathrm{div}\boldsymbol{\sigma} + \mathbf{b} = \mathbf{0} \tag{1.61}$$

which corresponds to a set of three linear partial differential equations.
On the contrary, the corresponding *local form* of the *angular momentum balance* implies the symmetry of the Cauchy stress tensor, $\boldsymbol{\sigma}$, i.e., $\boldsymbol{\sigma} = \boldsymbol{\sigma}^T$; see, e.g., (Gurtin et al., 2010) for details.

In conclusion, the *local form* of the *balance equations* can be rewritten as follows:

$$\begin{cases} \mathrm{div}\boldsymbol{\sigma} + \mathbf{b} = \mathbf{0} \quad \text{in} \quad \Omega \\ \boldsymbol{\sigma} = \boldsymbol{\sigma}^T \quad \text{in} \quad \Omega \\ \mathbf{t} = \boldsymbol{\sigma}\mathbf{n} \quad \text{on} \quad \partial\Omega^t \end{cases} \tag{1.62}$$

1.3.2 Dynamic equilibrium

Without entering into details (Gurtin et al., 2010), we recall only that the *local form* of the *equation of motion* takes the form:

$$\mathrm{div}\boldsymbol{\sigma} + \mathbf{b} = \rho\ddot{\mathbf{u}} \tag{1.63}$$

where $\rho\ddot{\mathbf{u}}$ denotes the acceleration term. Again, the *local form* of the *angular momentum balance* implies the symmetry of the Cauchy stress tensor, $\boldsymbol{\sigma}$, i.e., $\boldsymbol{\sigma} = \boldsymbol{\sigma}^T$.

Remark 1.3.1. *All the equilibrium considerations presented so far are relative to the natural configuration where equilibrium should hold, hence they are all relative to the current configuration, Ω, and written in terms of geometrical quantities relative to the current configuration, Ω. However, thanks to the invertibility of the map, $\boldsymbol{\varphi}$, and relating the current configuration, Ω, to the reference configuration, Ω_0, we could also write:*

- *equilibrium equations relative to the current configuration, Ω, in term of geometrical quantities relative to the reference configuration, Ω_0;*
- *equilibrium equations relative to the reference configuration, Ω_0, in term of geometrical quantities relative to the reference configuration, Ω_0.*

In particular, when a small deformation regime is considered, the distinction between reference and current configuration may be ignored. In such a case, the alternative forms of equilibrium listed above coincide.

1.4 Constitutive equation

We have so far described the equations of motion and the strain-displacement relations within the framework of infinitesimal deformation. In component form, these equations are given by a set of nine partial differential equations: three from the balance law and six from the strain-displacement relation (admitting the symmetry of $\boldsymbol{\varepsilon}$). Correspondingly, we have a total of fifteen unknowns represented by the six independent components of the strain and of the stress and by the three displacement components. It is clear that six additional equations are needed in order to have a well-defined problem.
From physical considerations, we may infer that the missing equations should regard the behavior of the material constituting the body. This further set of equations are the *constitutive equations*.

In the present Section, we summarize the basic equations and properties related to linear elastic materials.

1.4.1 Linear elastic material body

A material body is said to be *elastic* if the stress tensor, $\boldsymbol{\sigma}$, is entirely determined by the current state of deformation. Assuming the strain tensor, $\boldsymbol{\varepsilon}$, as a measure of the local state of deformation, we have:

$$\boldsymbol{\sigma} = \boldsymbol{\sigma}(\boldsymbol{\varepsilon}) \tag{1.64}$$

Such a position implies that the stress cannot depend on the deformation history and, in particular, on the path followed to reach the actual state. However, introducing the *density of internal work* done in going from an initial strain, $\boldsymbol{\varepsilon}_i$, to a final strain, $\boldsymbol{\varepsilon}_f$, on a path, $\Gamma_{\boldsymbol{\varepsilon}}$, as:

$$W^{int}_{\Gamma_{\boldsymbol{\varepsilon}}} = \int_{\Gamma_{\boldsymbol{\varepsilon}}} \boldsymbol{\sigma} : d\boldsymbol{\varepsilon} \tag{1.65}$$

it is in general possible that $W^{int}_{\Gamma_{\boldsymbol{\varepsilon}}}$ may depend on the specific strain path, $\Gamma_{\boldsymbol{\varepsilon}}$.

In the absence of internal constraints and under proper mathematical conditions, Eq. (1.64) can be inverted, as follows:

$$\boldsymbol{\varepsilon} = \boldsymbol{\varepsilon}(\boldsymbol{\sigma}) \tag{1.66}$$

It is also interesting to consider an incremental format of Eq. (1.64), in the form:

$$\dot{\boldsymbol{\sigma}} = \mathbb{C}^{tg}\dot{\boldsymbol{\varepsilon}} \tag{1.67}$$

where $\mathbb{C}^{tg}$ is the *tangent elastic tensor*, defined as:

$$\mathbb{C}^{tg} = \frac{\partial \boldsymbol{\sigma}}{\partial \boldsymbol{\varepsilon}} \tag{1.68}$$

An elastic material is said to be *linear* if stress and strain are related through a (linear) relation of the type:

$$\boldsymbol{\sigma} = \mathbb{C}\boldsymbol{\varepsilon} \tag{1.69}$$

where the fourth-order tensor, $\mathbb{C}$, is called *elastic tensor* and presents the following properties:

- $\mathbb{C}$ possesses the so-called *minor symmetries* and thus presents, at most, twenty-one independent components, since, by definition, relates symmetric second-order tensors;
- $\mathbb{C}$ is said to be *positive definite* if:

$$\boldsymbol{\varepsilon} : \mathbb{C}\boldsymbol{\varepsilon} > 0 \quad \forall \boldsymbol{\varepsilon} \in \mathbf{L}in^{sym} \tag{1.70}$$

- $\mathbb{C}$ is said to be *strongly elliptic* if:

$$(\mathbf{a} \otimes \mathbf{b}) : \mathbb{C}\,(\mathbf{a} \otimes \mathbf{b}) > 0 \quad \forall \mathbf{a}, \mathbf{b} \in \mathbf{l}in \tag{1.71}$$

- $\mathbb{C}$ is said to be *pointwise stable* if there exists a constant $\alpha > 0$ such that:

$$\boldsymbol{\varepsilon} : \mathbb{C}\boldsymbol{\varepsilon} > \alpha \left\|\boldsymbol{\varepsilon}\right\|^2 \quad \forall \boldsymbol{\varepsilon} \in \mathbf{L}in^{sym} \tag{1.72}$$

  Clearly pointwise stability implies (but is not implied) strong ellipticity. Moreover, pointwise stability is equivalent to pointwise positive definiteness, under the assumption that $\mathbb{C}$ is continuous on $\overline{\Omega}$.

Inverting Eq. (1.69), we obtain:

$$\boldsymbol{\varepsilon} = \mathbb{A}\boldsymbol{\sigma} \tag{1.73}$$

where the fourth-order tensor, $\mathbb{A}$, is called *compliance tensor* and it is the inverse of $\mathbb{C}$.

1.4.2 Isotropic elastic material body

A material that has no preferred directions in a way that it resists to external agencies independently of its orientation is said to be *isotropic*. The property of isotropy for a linear elastic material reduces the twenty-one independent components of the elastic tensor, $\mathbb{C}$, to two and, from a mathematical standpoint, such a property amounts to say that the elastic tensor, $\mathbb{C}$, presents also the so-called *major symmetries*.
Such an hypothesis admits the following representation:

$$\mathbb{C} = \lambda\,(\mathbf{I} \otimes \mathbf{I}) + 2\mu\mathbb{I}^I \tag{1.74}$$

where constants λ and μ are called *Lamé moduli* and depend on the material.
Thus, Eq. (1.64) can be rewritten as follows:

$$\boldsymbol{\sigma} = \lambda\ \mathrm{tr}(\boldsymbol{\varepsilon})\ \mathbf{I} + 2\mu\boldsymbol{\varepsilon} \tag{1.75}$$

Bearing in mind the previous definition and recalling the volumetric/deviatoric splitting of the fourth-order identity tensor, presented in Eq. (1.17), we may perform the decoupling into volumetric and deviatoric parts of the elastic tensor, as well. Thus, the following relationship is derived:

$$\mathbb{C} = \lambda \left(\mathbf{I} \otimes \mathbf{I} \right) + 2\mu \mathbb{I}^I = 3K \mathbb{I}_{vol} \boldsymbol{\varepsilon} + 2\mu \mathbb{I}_{dev} \boldsymbol{\varepsilon} \tag{1.76}$$

with $3K = 3\lambda + 2\mu$.
Recalling the split of a second-order tensor into its volumetric and deviatoric components, introduced in Eq. (1.10), we may write:

$$\begin{cases} \boldsymbol{\sigma} = p\mathbf{I} + \mathbf{s} \quad \text{with} \quad p = \dfrac{1}{3} \operatorname{tr}(\boldsymbol{\sigma}) \\ \boldsymbol{\varepsilon} = \dfrac{1}{3} \theta \mathbf{I} + \mathbf{e} \quad \text{with} \quad \theta = \operatorname{tr}(\boldsymbol{\varepsilon}) \end{cases} \tag{1.77}$$

where p and θ are, respectively, the pressure and the volumetric deformation, while $\boldsymbol{\sigma}$ and $\mathbf{e}$ are, respectively, the stress and strain deviator.
The uncoupled volumetric and deviatoric constitutive equations, thus, read:

$$\begin{cases} p = K\theta \\ \mathbf{s} = 2\mu \mathbf{e} \end{cases} \tag{1.78}$$

The scalar coefficient, μ (denoted by G in the following), is referred to as the *shear modulus*, while the material coefficient, K, is called the *bulk modulus* and represents a measure of the ratio between the spherical stress and the change in volume.

With the above relation, it is possible to invert Eq. (1.75) and to obtain a useful expression of strain in terms of stress:

$$\boldsymbol{\varepsilon} = E^{-1} \left[(1+\nu) \boldsymbol{\sigma} - \nu \operatorname{tr}(\boldsymbol{\sigma}) \mathbf{I} \right] \lambda \operatorname{tr}(\boldsymbol{\varepsilon}) \mathbf{I} + 2\mu \boldsymbol{\varepsilon} \tag{1.79}$$

where E is the *Young's modulus* and ν the *Poisson's coefficient*. The above linear relationship between strain and stress, valid for isotropic media, is commonly referred to as *Hooke's law*.

1.5 Thermodynamic setting for Elasticity

A common procedure in Mechanics of Solids is to introduce a constitutive model as a set of relations that hold from a thermodynamic standpoint (Gurtin et al., 2010). Precisely, the most favorable context is within a *thermodynamic theory*. In the present Section, we present the linear elastic material behavior in such a framework.

Suppose that a material body, Ω, is subjected to a body force, $\mathbf{b}$, in its interior and to a surface traction, $\mathbf{t}$, upon its boundary. Analogously, the body is acted by thermal equivalents of the previous mechanical sources: a heat source, $\mathbf{r}$, per unit volume in the interior and a heat flux, $\mathbf{q}$, across its boundary unit area.

The *first law of thermodynamics*, which is an energy balance, indicates that for any part, $\Omega^{'}$, of the body, Ω, the rate of change of the total energy plus the kinetic energy equals the amount of work done on that part by the mechanical forces plus the heat supply. Mathematically, the law can be formulated as follows:

$$\frac{d}{dt} \int_{\Omega'} \left(e + \frac{1}{2} \rho \left\| \dot{\mathbf{u}} \right\|^2 \right) dv = \int_{\Omega'} \mathbf{b} \cdot \dot{\mathbf{u}} dv + \int_{\partial\Omega'} \mathbf{t}_{\mathbf{n}} \cdot \dot{\mathbf{u}} da + \int_{\Omega'} r dv - \int_{\partial\Omega'} \mathbf{q} \cdot \dot{\mathbf{n}} da \tag{1.80}$$

where e is the internal energy density, $\dot{\mathbf{u}}$ the velocity field, and $\partial\Omega^{'}$ the boundary of $\Omega^{'}$. The minus sign before the last integral in Eq. (1.80) appears, since the heat flux vector, $\mathbf{q}$, points outward the surface, $\Omega^{'}$,

as well as $\mathbf{n}$.
The preceding formulation can be simplified by applying the divergence theorem (1.60) to the term involving the surface traction which, invoking the symmetry of $\boldsymbol{\sigma}$, becomes:

$$\int_{\partial\Omega'} \mathbf{t}_{\mathbf{n}} \cdot \dot{\mathbf{u}} da = \int_{\Omega'} \boldsymbol{\sigma} : \dot{\boldsymbol{\varepsilon}} dv + \int_{\Omega'} \text{div}\boldsymbol{\sigma} \cdot \dot{\mathbf{u}} dv \tag{1.81}$$

Substituting Eq. (1.81) into Eq. (1.80) and recalling the equation of balance of linear momentum, the first law can be rewritten in the *local form*, as follows:

$$\dot{e} = \boldsymbol{\sigma} : \dot{\boldsymbol{\varepsilon}} + r - \text{div}\mathbf{q} \tag{1.82}$$

It is useful to introduce also the notions of *entropy* per unit volume or entropy density, η. This notion is given through the absolute temperature, $T > 0$. Accordingly, it is assumed that the *entropy flux* across the bounding surface, $\partial\Omega'$, into a material body, Ω', is given by:

$$\int_{\partial\Omega'} T^{-1}\mathbf{q} \cdot \mathbf{n} da \tag{1.83}$$

while the entropy supplied by the exterior is:

$$\int_{\Omega'} T^{-1} r dv \tag{1.84}$$

The *second law of thermodynamics* states that the rate of increase in entropy in the body is not less than the total entropy supplied to the body by the heat sources. The second law can be thus formalized as an integral inequality, as follows:

$$\frac{d}{dt}\int_{\Omega'} \eta dv \geq \int_{\Omega'} T^{-1} r dv - \int_{\partial\Omega'} T^{-1}\mathbf{q} \cdot \mathbf{n}\, da \tag{1.85}$$

As done for the first law, we can derive the *local form* of the second law, as follows:

$$\dot{\eta} \geq -\text{div}\left(T^{-1}\mathbf{q}\right) + T^{-1} r \tag{1.86}$$

Inequalities (1.85) and (1.86) are known as the *Clausius-Duhem form* of the second law of thermodynamics.

After introducing the *Helmholtz free-energy*, Ψ, defined by:

$$\Psi = e - \eta T \tag{1.87}$$

and recalling the local form of the first law (1.82), we rewrite Eq. (1.86) in the following form, known as *local dissipation inequality*:

$$\dot{\Psi} + \eta\dot{T} - \boldsymbol{\sigma} : \dot{\boldsymbol{\varepsilon}} + T^{-1}\mathbf{q} \cdot \nabla T \leq 0 \tag{1.88}$$

Since the arguments of the following Sections will always refer to *isothermal processes*, it is convenient to specialize the local dissipation inequality (1.88) to such a case. Assuming that the body temperature, T, is uniformly constant and that the reference material body does not experience any exterior heat supply, $\mathbf{q}$, the local dissipation inequality simplifies to:

$$\dot{\Psi} - \boldsymbol{\sigma} : \dot{\boldsymbol{\varepsilon}} \leq 0 \tag{1.89}$$

INITIAL BOUNDARY-VALUE PROBLEM for ISOTROPIC LINEAR ELASTICITY

Find the displacement field, $\mathbf{u}(\mathbf{x}, t)$, which, for any $\mathbf{x} \in \Omega$ and any $t \in [0, T]$, solves the following governing equations:

1. *equation of dynamic equilibrium*: $\text{div}\boldsymbol{\sigma} + \mathbf{b} = \rho\ddot{\mathbf{u}}$
2. *strain-displacement relation*: $\boldsymbol{\varepsilon} = \frac{1}{2}\left[\nabla\mathbf{u} + (\nabla\mathbf{u})^T\right]$
3. *constitutive relation*: $\boldsymbol{\sigma} = \mathbb{C}\boldsymbol{\varepsilon}$

and satisfies the:

1. *boundary conditions*: $\begin{cases} \mathbf{u} = \overline{\mathbf{u}} & \text{on } \overline{\Gamma}_D \\ \boldsymbol{\sigma}\mathbf{n} = \overline{\mathbf{t}} & \text{on } \overline{\Gamma}_S \end{cases}$
2. *initial conditions*: $\begin{cases} \mathbf{u}(\mathbf{x}, 0) = \mathbf{u}_0(\mathbf{x}) \\ \dot{\mathbf{u}}(\mathbf{x}, 0) = \dot{\mathbf{u}}_0(\mathbf{x}) \end{cases}$

Table 1.1: IBVP for isotropic linear elasticity.

1.5.1 Linear elastic material body

It is possible to give a characterization of the linear elastic material behavior in the thermodynamic framework. In such a sense, it is customary to define a linear elastic material as one for which the constitutive equations take the form:

$$\begin{cases} \Psi = \Psi(\boldsymbol{\varepsilon}) \\ \boldsymbol{\sigma} = \boldsymbol{\sigma}(\boldsymbol{\varepsilon}) \end{cases} \tag{1.90}$$

i.e., the Helmholtz free-energy, Ψ, and the stress, $\boldsymbol{\sigma}$, depending only on the strain, $\boldsymbol{\varepsilon}$. It is assumed that the functions appearing in system (1.90) are sufficiently regular with respect to their argument so that they can be differentiated as many times as required.

Substituting Eq. $(1.90)_1$ into the local dissipation inequality (1.89), we derive:

$$\left(\frac{\partial\Psi}{\partial\boldsymbol{\varepsilon}} - \boldsymbol{\sigma}\right) : \dot{\boldsymbol{\varepsilon}} \leq 0 \tag{1.91}$$

Hence, admitting that inequality (1.91) holds for all $\dot{\boldsymbol{\varepsilon}}$, the stress, $\boldsymbol{\sigma}$, is expressed through the Helmholtz free-energy, Ψ, as follows:

$$\boldsymbol{\sigma} = \frac{\partial\Psi}{\partial\boldsymbol{\varepsilon}} \tag{1.92}$$

The stress-strain relationship of Eq. (1.69), which is the characterizing feature of linear elastic materials, is obtained as a special case of Eq. (1.92), i.e., when the Helmholtz free-energy is a quadratic form of the strain, as follows:

$$\Psi = \frac{1}{2}\,\boldsymbol{\varepsilon} : \mathbb{C}\boldsymbol{\varepsilon} \tag{1.93}$$

Eq. (1.93) implies a relationship between $\mathbb{C}$ and Ψ of the following type:

$$\mathbb{C} = \frac{\partial^2\Psi}{\partial\boldsymbol{\varepsilon}^2} \tag{1.94}$$

which holds if the elastic tensor possesses the major symmetries, as already discussed.

1.6 Initial boundary-value problem of equilibrium in Elasticity

Following the previous arguments, it is possible to formulate the mathematical problem that describes the deformation and the stress state of an isotropic linear elastic material body under an assigned set of external actions. For simplicity, the treatment is limited to isothermal static processes in which the effects of temperature variations and of heat flux exchanges are neglected. Such a problem is modeled by a set of partial differential equations posed on the body domain, plus a set of boundary conditions, assigned on the boundary of the body, and a set of initial conditions.

Given a body with current configuration, $\Omega \subset \Re^3$, we indicate for compactness its boundary with $\partial\Omega$ such that $\Gamma = \overline{\Gamma}_D \cup \overline{\Gamma}_S$, with $\overline{\Gamma}_D \cap \overline{\Gamma}_S = \emptyset$. Suppose that, for $t \in [0, T] \subset \Re^+$, a body force, $\mathbf{b}(\mathbf{x}, t)$, is assigned in Ω, a displacement field, $\overline{\mathbf{u}}(\mathbf{x}, t)$, is assigned on $\overline{\Gamma}_D$ and a surface traction, $\overline{\mathbf{t}}(\mathbf{x}, t)$, is assigned on $\overline{\Gamma}_S$. Initial values for the displacement $\mathbf{u}(\mathbf{x}, 0) = \mathbf{u}_0(\mathbf{x})$ and the velocity field $\mathbf{v}(\mathbf{x}, 0) = \mathbf{v}_0(\mathbf{x})$ are known data as well.

With the above specifications, the formulation of the *initial boundary-value problem* (IBVP) for the isotropic linear elastic body under consideration is reported in Table 1.1. Taking the displacement as the primary unknown, the problem can be reduced to one singular partial differential equation, by solving successively for the stress and the strain. When the problem data are such that the acceleration term can be omitted, i.e., $\ddot{\mathbf{u}} = \mathbf{0}$, the problem is defined as *quasi-static*.

Chapter 2

Elastoplasticity theory

This Chapter is intended to present the fundamental concepts of the classical elastoplasticity theory and of the mathematical modeling of such phenomenon. The elastoplastic formulation is here critically revisited to prepare the framework for the analysis of several computational approaches relevant for the numerical solution of complex initial boundary-value problems, that is the object of Chapter 3.

The Chapter is organized as follows. Section 2.1 starts by addressing the three-dimensional infinitesimal elastoplastic modeling formulation within the thermodynamics with internal variables setting. Then, Section 2.2 presents the J_2 or von-Mises elastoplastic constitutive model with hardening mechanisms. Section 2.3 presents the initial boundary-value problem of equilibrium for a deformable body constituted of elastoplastic material. Section 2.4 recalls and revisits the principle of maximum plastic dissipation. Section 2.5 is dedicated to the recasting of the mathematical theory of elastoplasticity within a convex-analytic context, which is particularly useful when dealing with non-differentiable convex functions and multi-valued operators. The mathematical concepts used in this Section are supported by the definitions and fundamental results on convex analysis and sub-differential calculus (Rockafellar, 1970), which are briefly reported in Appendix A at the end of the thesis. Finally, Section 2.6 reformulates the elastoplastic constrained problem as an unconstrained problem, by introducing appropriate complementary functions.
For further reading on the physical background, detailed equations and generalizations, the reader is referred to (Besson et al., 2010; de Souza Neto et al., 2008; Lemaitre and Chaboche, 1994; Lubliner, 1990; Simo and Hughes, 1998), while on the mathematical theory to (Han and Reddy, 1999; Hill, 1950).

2.1 Thermodynamic setting for elastoplasticity

The continuum thermodynamic theory, presented in Section 1.5, is a suitable tool for the discussion of elasticity and thermo-elasticity, but the same does not hold true when complex mechanic phenomena are taken into consideration. In fact, it is often necessary to equip the thermodynamic models with a finite number of internal variables, intended to describe irreversible processes. In such a case, the theory is referred to as *thermodynamics with internal variables* and may be conveniently adopted as a plasticity theory[1].

2.1.1 Isothermal behavior

The theory of plasticity developed in the following assumes that all the transformations are *isothermal*, i.e., thermal effects as temperature variation or flux of heat are negligible.

[1] The first and second laws of thermodynamics remain valid, as well as the thermodynamic hypotheses of isothermal process with no heat flux nor change in temperature in the body.

2.1.2 Rate-independence

The theory of plasticity developed in the following refers to *quasi-static transformations* of a material body. In other words, the considered transformations take place sufficiently slow so that the inertial term appearing in the equation of motion (1.63) is negligible. Moreover, our discussion is here limited to the case of a body undergoing a sufficiently slow process such that the *rate-independent* material response can be taken as a good approximation of real behavior.

2.1.3 Internal variables

In order to apply the thermodynamic theory with internal variables to the context of elastoplasticity, we need to identify the variables describing material constitutive behavior.

In the classical rate-independent plasticity framework and from a phenomenological point of view, we regard plastic flow as an irreversible process in a material body (typically a metal), characterized in terms of the history of the total strain, $\boldsymbol{\varepsilon}$, and two additional variables: the *plastic strain*, $\boldsymbol{\varepsilon}^p$, and a set of *strain-like internal variables*, $\boldsymbol{\xi} = (\boldsymbol{\xi}_k) = (\boldsymbol{\xi}_1, ..., \boldsymbol{\xi}_m)$, describing internal kinematic irreversible phenomena such as, for instance, material hardening, and thus often referred to as hardening parameters. Such a set, $\boldsymbol{\xi}$, can be in general constituted of objects of different nature, namely second-order tensors and scalars[2].

Following thermodynamic arguments, the *stress-like primary* and *internal variables* are the thermodynamically conjugates to the kinematic variables. Thus, we assume as stress-like primary and internal variables, respectively, the stress, $\boldsymbol{\sigma}$, and the internal forces, $\boldsymbol{\chi} = (\boldsymbol{\chi}_k) = (\boldsymbol{\chi}_1, ..., \boldsymbol{\chi}_m)$.

In this context, the scalar product between the stress- and strain-like variables is defined as:

$$\boldsymbol{\sigma} : \dot{\boldsymbol{\varepsilon}}^p + \boldsymbol{\chi} \cdot \dot{\boldsymbol{\xi}} \tag{2.1}$$

and represents either a rate of work done or the dissipation taking place as a result of plastic deformation[3].

Accordingly, we could distinguish between a *strain-space* and a *stress-space formulation* of plasticity. In a strain-driven formulation, plastic flow is described in terms of the driving variables $\{\boldsymbol{\varepsilon}, \boldsymbol{\varepsilon}^p, \boldsymbol{\xi}\}$ and the stress tensor, $\boldsymbol{\sigma}$, is assumed as a dependent function of such variables. However, in classical plasticity, the response functions, i.e, the yield condition and the flow rule, are formulated in stress-space in terms of the variables $\{\boldsymbol{\sigma}, \boldsymbol{\chi}\}$, as discussed in next Sections.

In the following, we focus on the strain-driven formulation of plasticity and we formulate the response functions in stress-space. Nevertheless, implicitly we always regard $\{\boldsymbol{\varepsilon}, \boldsymbol{\varepsilon}^p, \boldsymbol{\xi}\}$ as the independent driving variables.

2.1.4 Thermodynamic assumptions

We assume that the Helmholtz free-energy, Ψ, and the stress, $\boldsymbol{\sigma}$, are functions of the strain, $\boldsymbol{\varepsilon}$, and of the strain-like internal variables, $\boldsymbol{\xi}$, as follows:

$$\begin{cases} \Psi = \Psi\left(\boldsymbol{\varepsilon}, \boldsymbol{\xi}\right) \\ \boldsymbol{\sigma} = \boldsymbol{\sigma}\left(\boldsymbol{\varepsilon}, \boldsymbol{\xi}\right) \end{cases} \tag{2.2}$$

[2]The choice of not grouping the plastic strain within the internal variables class turns out to be a consequence of the thermodynamic theory adopted, even if there are instances in which the specific model is so simple that $\boldsymbol{\varepsilon}^p$ can be identified as an internal variable, e.g., in the case of pure linear kinematic hardening behavior.

[3]In compact notation and generalizing the above definitions, we may refer to the kinematic variables representing irreversible internal phenomena with the ordered pair, $\mathbf{P} = (\boldsymbol{\varepsilon}^p, \boldsymbol{\xi})$, called *generalized plastic strain*. Similarly, the ordered pair, $\mathbf{S} = (\boldsymbol{\sigma}, \boldsymbol{\chi})$, is referred to as *generalized stress*. In this context, it is found that the scalar product between $\mathbf{S}$ and $\dot{\mathbf{P}}$ is defined as $\mathbf{S} \cdot \dot{\mathbf{P}}$. In this sense, we consider $\mathbf{S}$ and $\mathbf{P}$ thermodynamically conjugate variables of the model under consideration.

As a consequence of the second law of thermodynamics, the stress, $\boldsymbol{\sigma}$, is related to the Helmholtz free-energy function, Ψ, as follows:

$$\boldsymbol{\sigma} = \frac{\partial \Psi}{\partial \boldsymbol{\varepsilon}} \tag{2.3}$$

The internal forces, $\boldsymbol{\chi}$, are defined as conjugate quantities to the internal variables, $\boldsymbol{\xi}$, in the following sense:

$$\boldsymbol{\chi} = -\frac{\partial \Psi}{\partial \boldsymbol{\xi}} \tag{2.4}$$

The non-negative variation:

$$\boldsymbol{\chi} \cdot \dot{\boldsymbol{\xi}} = \boldsymbol{\chi}_k : \dot{\boldsymbol{\xi}}_k \tag{2.5}$$

is defined as *internal dissipation*.
Then, in order to account for non-linear irreversible effects, we consider an evolution law of the strain-like internal variables, $\boldsymbol{\xi}$, as follows:

$$\dot{\boldsymbol{\xi}} = \boldsymbol{\beta}\left(\boldsymbol{\varepsilon}, \boldsymbol{\xi}\right) \tag{2.6}$$

2.1.5 Additive decomposition of strain

The total strain, $\boldsymbol{\varepsilon}$, can be decomposed into two parts, the elastic strain, $\boldsymbol{\varepsilon}^e$, and the plastic strain, $\boldsymbol{\varepsilon}^p$, as a consequence of the thermodynamic framework herein adopted.

We introduce the *Gibbs free-energy*, $G = G\left(\boldsymbol{\sigma}, \boldsymbol{\xi}\right)$, defined through a Legendre transformation of the Helmholtz free-energy, Ψ, assuming the stress as independent variable:

$$G = \boldsymbol{\sigma} : \boldsymbol{\varepsilon} - \Psi \tag{2.7}$$

The relation conjugate to Eq. (2.3) is:

$$\boldsymbol{\varepsilon} = \frac{\partial G}{\partial \boldsymbol{\sigma}} \tag{2.8}$$

After defining the following fourth-order tensors:

$$\begin{cases} \mathbb{A} = \dfrac{\partial \boldsymbol{\varepsilon}}{\partial \boldsymbol{\sigma}} \\ \mathbb{B}_k = \dfrac{\partial \boldsymbol{\varepsilon}}{\partial \boldsymbol{\xi}_k} \end{cases} \tag{2.9}$$

for $k = 1, ..., m$, we compute the strain rate as:

$$\dot{\boldsymbol{\varepsilon}} = \mathbb{A}\dot{\boldsymbol{\sigma}} + \mathbb{B}_k \dot{\boldsymbol{\xi}}_k \tag{2.10}$$

It is known that for crystalline materials the elastic compliance matrix, $\mathbb{A}$, is independent of the irreversible processes and hence its dependence on the variables, $\boldsymbol{\xi}$, can be neglected. Thus, assuming $\mathbb{A} = \mathbb{A}\left(\boldsymbol{\sigma}\right)$, it follows that $\mathbb{B}_k = \mathbb{B}_k\left(\boldsymbol{\xi}\right)$, for $k = 1, ..., m$, since:

$$\mathbf{0} = \frac{\partial}{\partial \boldsymbol{\xi}_k} \frac{\partial \mathbb{B}_k}{\partial \boldsymbol{\sigma}} \tag{2.11}$$

It is then possible to decompose additively the strain tensor, $\boldsymbol{\varepsilon}$, in the form:

$$\boldsymbol{\varepsilon} = \boldsymbol{\varepsilon}^e + \boldsymbol{\varepsilon}^p \tag{2.12}$$

where the elastic strain, $\boldsymbol{\varepsilon}^e = \boldsymbol{\varepsilon}^e(\boldsymbol{\sigma})$, depends only on the stress, while the plastic strain, $\boldsymbol{\varepsilon}^p = \boldsymbol{\varepsilon}^p(\boldsymbol{\xi})$, on the internal variables.

In the case where $\mathbb{A}$ is independent of $\boldsymbol{\sigma}$, the elastic strain is given as a linear function of the stress by:

$$\boldsymbol{\varepsilon}^e = \mathbb{A}\boldsymbol{\sigma} \tag{2.13}$$

or

$$\boldsymbol{\sigma} = \mathbb{C}\boldsymbol{\varepsilon}^e \tag{2.14}$$

It is clear that the fourth-order *compliance tensor*, $\mathbb{A}$, is the inverse of the elastic tensor, $\mathbb{C}$.

2.1.6 Free-energy as a function of elastic strain and internal variables

Since Eqs. (2.3) and (2.12) imply that:

$$\frac{\partial \boldsymbol{\varepsilon}^e}{\partial \boldsymbol{\sigma}} = \frac{\partial \boldsymbol{\varepsilon}}{\partial \boldsymbol{\sigma}} = \frac{\partial \boldsymbol{\varepsilon}^T}{\partial \boldsymbol{\sigma}} = \frac{\partial \left(\boldsymbol{\varepsilon}^e\right)^T}{\partial \boldsymbol{\sigma}} \tag{2.15}$$

recalling a multivariable calculus theorem, we may assert the existence of a scalar potential, $G^e = G^e(\boldsymbol{\sigma})$, such that:

$$\boldsymbol{\varepsilon}^e = \frac{\partial G^e}{\partial \boldsymbol{\sigma}} \tag{2.16}$$

The above potential admits the Legendre transform, $\Psi^e = \Psi^e(\boldsymbol{\varepsilon}^e)$, defined by:

$$\Psi^e = \boldsymbol{\sigma} : \boldsymbol{\varepsilon}^e - G^e \tag{2.17}$$

which satisfies the following relation:

$$\boldsymbol{\sigma} = \frac{\partial \Psi^e}{\partial \boldsymbol{\varepsilon}^e} \tag{2.18}$$

Since Eq. (2.17) holds, we have the following representation of the Gibbs free-energy, $G = G(\boldsymbol{\sigma}, \boldsymbol{\xi})$:

$$G = \boldsymbol{\sigma} : (\boldsymbol{\varepsilon}^e + \boldsymbol{\varepsilon}^p) - \Psi = G^e + \boldsymbol{\sigma} : \boldsymbol{\varepsilon}^p - \Psi^p \tag{2.19}$$

by which the inelastic part of the Helmholtz free-energy, $\Psi^p = \Psi^p(\boldsymbol{\xi})$, results defined as:

$$\Psi^p = \Psi - \Psi^e \tag{2.20}$$

In conclusion, the Helmholtz free-energy, $\Psi = \Psi(\boldsymbol{\varepsilon}, \boldsymbol{\xi})$, and the Gibbs free-energy, $G = G(\boldsymbol{\sigma}, \boldsymbol{\xi})$, can be additively decomposed into elastic and plastic parts, respectively, as:

$$\begin{cases} \Psi = \Psi^e + \Psi^p \\ G = G^e + G^p \end{cases} \tag{2.21}$$

Recalling the second law of thermodynamics and using definition $(2.21)_1$, we obtain Eq. (2.18) which leads to the reduced dissipation inequality in the alternative form:

$$\boldsymbol{\sigma} : \dot{\boldsymbol{\varepsilon}}^p + \boldsymbol{\chi} \cdot \dot{\boldsymbol{\xi}} \geq 0 \tag{2.22}$$

2.1.7 Plastic incompressibility

Physical evidences have shown that, for metallic materials, volume changes occur almost exclusively as a consequence of elastic deformation. Hence, it is reasonable to assume that the plastic part of the deformation is only of deviatoric or shearing type, such that:

$$\mathrm{tr}(\boldsymbol{\varepsilon}^p) \ = 0 \tag{2.23}$$

which implies that $\boldsymbol{\varepsilon}^p = \mathbf{e}^p$.
Using the above arguments on the additive decomposition of strain and the assumption on plastic incompressibility, it is possible to generalize the linear elastic relations for the isotropic elastic material response, as follows:

$$\begin{cases} p = K\theta \\ \mathbf{s} = 2G\mathbf{e}^e = 2G\left(\mathbf{e} - \mathbf{e}^p\right) \end{cases} \tag{2.24}$$

where:

$$\begin{cases} \mathbf{e} = \mathbf{e}^e + \mathbf{e}^p \\ \theta = \theta^e \end{cases} \tag{2.25}$$

2.1.8 Yield surface

An yield function represents a constraint on the evolution of the stress and of the thermodynamic forces. In the three-dimensional case, this means that at all times the state, $(\boldsymbol{\sigma}, \boldsymbol{\chi})$, must lie in the closed connected set $E_{\boldsymbol{\sigma}}$, called *admissible region*. The interior of this set, $\mathrm{int}\,(E_{\boldsymbol{\sigma}})$, is called *elastic region*, while its boundary, $\partial E_{\boldsymbol{\sigma}}$, is known as *yield surface*. The complement of $E_{\boldsymbol{\sigma}}$ is not attainable. Whenever $(\boldsymbol{\sigma}, \boldsymbol{\chi})$ lies within the interior of $E_{\boldsymbol{\sigma}}$, purely elastic behavior takes place, while plastic loading may be observed only if $(\boldsymbol{\sigma}, \boldsymbol{\chi})$ evolves on the boundary of $E_{\boldsymbol{\sigma}}$.

A convenient way to represent the constrained evolution mechanism of $(\boldsymbol{\sigma}, \boldsymbol{\chi})$ is to introduce a convex scalar function, f, called *yield criterion*, such that the admissible region is defined as:

$$E_{\boldsymbol{\sigma}} := \{(\boldsymbol{\sigma}, \boldsymbol{\chi}) \ : \ f\,(\boldsymbol{\sigma}, \boldsymbol{\chi}) \leq 0\} \tag{2.26}$$

The elastic region is the interior of $E_{\boldsymbol{\sigma}}$ defined as:

$$\mathrm{int}\,(E_{\boldsymbol{\sigma}}) := \{(\boldsymbol{\sigma}, \boldsymbol{\chi}) \ : \ f\,(\boldsymbol{\sigma}, \boldsymbol{\chi}) < 0\} \tag{2.27}$$

while the yield surface is the boundary of $E_{\boldsymbol{\sigma}}$, defined as:

$$\partial E_{\boldsymbol{\sigma}} := \{(\boldsymbol{\sigma}, \boldsymbol{\chi}) \ : \ f\,(\boldsymbol{\sigma}, \boldsymbol{\chi}) = 0\} \tag{2.28}$$

As explained in next sections, plastic models differ from one another in the choice of the internal variable set and of the yield function.

2.1.9 Associative plasticity

When the yield surface is smooth, i.e., it presents a well-defined gradient at each point, recalling that $\left(\dot{\boldsymbol{\varepsilon}}^p, \dot{\boldsymbol{\xi}}\right)$ lies parallel to the normal to $\partial E_{\boldsymbol{\sigma}}$ at $(\boldsymbol{\sigma}, \boldsymbol{\chi})$, we may write the following important form of the *normality laws*:

$$\begin{cases} \dot{\boldsymbol{\varepsilon}}^p = \dot{\gamma}\,\dfrac{\partial f}{\partial \boldsymbol{\sigma}} = \dot{\gamma}\mathbf{n} \\ \dot{\boldsymbol{\xi}} = \dot{\gamma}\,\dfrac{\partial f}{\partial \boldsymbol{\chi}} = \dot{\gamma}\mathbf{h} \end{cases} \tag{2.29}$$

where $\dot{\gamma}$ is the non-negative *consistency parameter*. System of equations (2.29) states that f represents a *flow potential* for $\boldsymbol{\varepsilon}^p$ and $\boldsymbol{\xi}$. Flow rules $(2.29)_1$ and $(2.29)_2$ are said to be associated with the yield function in stress-space.
The following equation:

$$\boldsymbol{\chi} = -\frac{\partial \Psi^p}{\partial \boldsymbol{\xi}} \tag{2.30}$$

in rate form, reads:

$$\dot{\boldsymbol{\chi}} = -\frac{\partial^2 \Psi^p}{\partial \boldsymbol{\xi}^2}\dot{\boldsymbol{\xi}} \tag{2.31}$$

Introducing the evolutive equation $(2.29)_2$ into (2.31) and defining the fourth-order tensor:

$$\mathbb{D}_k = -\frac{\partial^2 \Psi^p}{\partial \boldsymbol{\xi}_k^2} \tag{2.32}$$

for $k = 1, ..., m$, we can recast the rate form of the hardening law (2.31) in the following form:

$$\dot{\boldsymbol{\chi}} = -\dot{\gamma}\, \mathbb{D}\, \frac{\partial f}{\partial \boldsymbol{\chi}} \tag{2.33}$$

where $\mathbb{D}$ is the (diagonal) generalized matrix operator containing the tensors $\mathbb{D}_k$. Eq. (2.33) can be regarded as a hardening law associated with the function, Ψ^p, which clearly reveals to be a hardening potential. Equivalently, Eq. (2.31) represents the rate form of the mentioned hardening law which, admitting the normality law, leads to the generalized associative hardening law (2.33) in stress-space.

A constitutive model characterized by the flow rule $(2.29)_1$ and by the two evolutive equations $(2.29)_2$ and (2.33), regarding the internal hardening variables, is then referred to as *associative plasticity*.

2.1.10 Kuhn-Tucker complementary inequality conditions

To complete the statement of our problem, we need to give the conditions on the plastic multiplier, $\dot{\gamma}$, and on the yield function, f.

Let $0 \leq \mathbf{x} \perp \mathbf{y} \geq 0$ be the *complementarity condition*, where $\mathbf{x}$ and $\mathbf{y}$ are vectors in $\Re^n$ and the symbol $\perp$ denotes orthogonality (Chen and Mangasarian, 1995). In particular for finite-dimensional real vector spaces this means that, if one has vectors $\mathbf{x}$ and $\mathbf{y}$ with non-negative components ($x_i \geq 0$ and $y_i \geq 0$ for all $i = 1, ..., n$), then for each pair of components x_i and y_i one of the pair must be zero, hence the name complementarity.

In classical plasticity, we could adopt this general definition by assuming that the consistency parameter, $\dot{\gamma}$, obeys the following *Kuhn-Tucker complementarity inequality conditions* (KT) (Karush, 1939; Kuhn and Tucker, 1951):

$$\dot{\gamma} \geq 0,\ f \leq 0,\ \dot{\gamma} f = 0 \tag{2.34}$$

In addition to conditions (2.34), $\dot{\gamma}$ satisfies the *consistency* (or persistency) *condition*:

$$\dot{\gamma}\dot{f} = 0 \tag{2.35}$$

which corresponds to the physical requirement that, for $\dot{\boldsymbol{\varepsilon}}^p$ and $\dot{\boldsymbol{\chi}}$ to be non-zero (i.e., $\dot{\gamma} > 0$), the state $(\boldsymbol{\sigma}, \boldsymbol{\chi})$ must persist on $\partial E_{\boldsymbol{\sigma}}$ so that $\dot{f} = 0$.
In the classical literature, conditions (2.34) and (2.35) go by the names loading/un-loading and consistency conditions, respectively.

Interpretation of the Kuhn-Tucker complementarity conditions

The following alternative situations occur:

1. First, consider the case in which $(\boldsymbol{\sigma}, \boldsymbol{\chi}) \in \text{int}\,(E_{\boldsymbol{\sigma}})$ so that $f < 0$. Therefore, from conditions (2.34) we conclude that:

$$\dot{\gamma} f = 0 \quad \text{and} \quad f < 0 \quad \Rightarrow \quad \dot{\gamma} = 0 \tag{2.36}$$

   Then, it follows that $\dot{\boldsymbol{\varepsilon}}^p = \mathbf{0}$ and $\dot{\boldsymbol{\chi}} = \mathbf{0}$; thus, $\dot{\boldsymbol{\varepsilon}} = \dot{\boldsymbol{\varepsilon}}^e$ and the rate form of Eq. (2.14) leads to:

$$\dot{\boldsymbol{\sigma}} = \mathbb{C}\,\dot{\boldsymbol{\varepsilon}} \equiv \mathbb{C}\,\dot{\boldsymbol{\varepsilon}}^e \tag{2.37}$$

   In view of Eq. (2.37), we call this type of response *instantaneously elastic*.

2. Now, suppose that $(\boldsymbol{\sigma}, \boldsymbol{\chi}) \in \partial E_{\boldsymbol{\sigma}}$ which implies that $f = 0$. Then, conditions (2.34) are automatically satisfied even if $\dot{\gamma} > 0$. Whether $\dot{\gamma}$ is actually positive or zero is concluded from condition (2.35). Two situations can arise:

   - First, if $\dot{f} < 0$, from condition (2.35) we conclude that:

$$\dot{\gamma} \dot{f} = 0 \quad \text{and} \quad \dot{f} < 0 \quad \Rightarrow \quad \dot{\gamma} = 0 \tag{2.38}$$

     Thus, from Eq. (2.29) it follows that $\dot{\boldsymbol{\varepsilon}}^p = \mathbf{0}$ and $\dot{\boldsymbol{\chi}} = \mathbf{0}$. Since Eq. (2.37) holds and $(\boldsymbol{\sigma}, \boldsymbol{\chi}) \in \partial E_{\boldsymbol{\sigma}}$, this type of response is called *unloading from a plastic state*.

   - Second, if $\dot{f} = 0$, condition (2.35) is automatically satisfied. If $\dot{\gamma} > 0$, then $\dot{\boldsymbol{\varepsilon}}^p \neq \mathbf{0}$ and $\dot{\boldsymbol{\chi}} \neq \mathbf{0}$ and the situation is called *plastic loading*; on the other hand, the case $\dot{\gamma} = 0$ (and $\dot{f} = 0$) is termed *neutral loading*.

Consistency condition and elastoplastic tangent moduli

Consider the case where $(\boldsymbol{\sigma}, \boldsymbol{\chi})\,(t) \in \partial E_{\boldsymbol{\sigma}} \;\Leftrightarrow\; f\,(t) = 0$ at time t. Then, it is easily shown that $\dot{f} \leq 0$, since should $\dot{f}$ be positive it would imply that $f\,(t + \Delta t) > 0$ for some $\Delta t > 0$, which violates the admissibility condition $f \leq 0$. Further, we specify that $\dot{\gamma} > 0$ only if $\dot{f} = 0$, and we set $\dot{\gamma} = 0$ if $\dot{f} < 0$, i.e.,

$$\begin{cases} \dot{\gamma} > 0 \;\; \Rightarrow \;\; \dot{f} = 0 \\ \dot{f} < 0 \;\; \Rightarrow \;\; \dot{\gamma} = 0 \end{cases} \tag{2.39}$$

Therefore, we have the additional condition (2.35) corresponding to the physical requirement that, for $\dot{\boldsymbol{\varepsilon}}^p$ and $\dot{\boldsymbol{\chi}}$ to be non-zero (i.e., $\dot{\gamma} > 0$), $(\boldsymbol{\sigma}, \boldsymbol{\chi})\,(t) \in \partial E_{\boldsymbol{\sigma}}$ must persists on $\partial E_{\boldsymbol{\sigma}}$ so that $\dot{f} = 0$.

To exploit condition (2.35), we start out by evaluating the time derivative of f at $(\boldsymbol{\sigma}, \boldsymbol{\chi}) \in E_{\boldsymbol{\sigma}}$. Using the chain rule, along with the rate forms of the stress-strain relationship (2.14), the flow rule and hardening laws (2.29), we find that:

$$\begin{aligned} \dot{f} &= \partial_{\boldsymbol{\sigma}} f : \dot{\boldsymbol{\sigma}} + \partial_{\boldsymbol{\chi}} f \cdot \dot{\boldsymbol{\chi}} = \partial_{\boldsymbol{\sigma}} f : \mathbb{C}\,(\dot{\boldsymbol{\varepsilon}} - \dot{\boldsymbol{\varepsilon}}^p) + \partial_{\boldsymbol{\chi}} f \cdot \dot{\boldsymbol{\chi}} \\ &\partial_{\boldsymbol{\sigma}} f : \mathbb{C}\,\dot{\boldsymbol{\varepsilon}} - \dot{\gamma}\,(\partial_{\boldsymbol{\sigma}} f : \mathbb{C}\,\mathbf{n} + \partial_{\boldsymbol{\chi}} f \cdot \mathbf{h}) \leq 0 \end{aligned} \tag{2.40}$$

To carry our analysis further, we need to make an additional assumption about the structure of the flow rule and hardening laws. Explicitly, we make the following hypothesis:

Assumption 2.1.1. *The flow rule, hardening law, and yield condition in stress-space are such that the following inequality holds:*

$$\partial_{\boldsymbol{\sigma}} f : \mathbb{C}\,\mathbf{n} + \partial_{\boldsymbol{\chi}} f \cdot \mathbf{h} > 0 \tag{2.41}$$

for all admissible states $(\boldsymbol{\sigma}, \boldsymbol{\chi}) \in \partial E_{\boldsymbol{\sigma}}$.

This assumption always holds for associative perfect plasticity. With such an assumption in hand, it follows from Eq. (2.35) that:

$$\dot{f} = 0 \;\;\Leftrightarrow\;\; \dot{\gamma} = \frac{\langle \partial_{\boldsymbol{\sigma}} f : \mathbb{C}\,\dot{\boldsymbol{\varepsilon}} \rangle}{\partial_{\boldsymbol{\sigma}} f : \mathbb{C}\,\mathbf{n} + \partial_{\boldsymbol{\chi}} f \cdot \mathbf{h}} \tag{2.42}$$

where $\langle\,\cdot\,\rangle$ denotes the maximum function. In view of Eqs. (2.41) and (2.42), we conclude that:

$$\text{for } \; f = 0 \;\text{ and }\; \dot{f} = 0, \;\; \dot{\gamma} \geq 0 \;\;\Leftrightarrow\;\; \partial_{\boldsymbol{\sigma}} f : \mathbb{C}\dot{\boldsymbol{\varepsilon}} \geq 0 \tag{2.43}$$

This relationship provides a useful geometric interpretation of the plastic and neutral loading conditions. Plastic or neutral loading takes place at a point $(\boldsymbol{\sigma}, \boldsymbol{\chi}) \in \partial E_{\boldsymbol{\sigma}}$ if the angle in the inner product defined by the elasticity tensor, $\mathbb{C}$, between the normal, $\partial_{\boldsymbol{\sigma}} f$, to $\partial E_{\boldsymbol{\sigma}}$ at $\boldsymbol{\sigma}$ and the strain rate, $\dot{\boldsymbol{\varepsilon}}$, is less or equal than $90\,^{\circ}\mathrm{C}$.
Finally, we have:

$$\dot{\boldsymbol{\sigma}} = \mathbb{C}\,(\dot{\boldsymbol{\varepsilon}} - \dot{\boldsymbol{\varepsilon}}^{p}) = \mathbb{C}\,(\dot{\boldsymbol{\varepsilon}} - \dot{\gamma}\mathbf{n}) \tag{2.44}$$

Then, substituting Eq. (2.42) into Eq. (2.44) yields the rate of change of $\boldsymbol{\sigma}$ in terms of the total strain rate, $\dot{\boldsymbol{\varepsilon}}$, as:

$$\dot{\boldsymbol{\sigma}} = \mathbb{C}^{ep}\dot{\boldsymbol{\varepsilon}} \tag{2.45}$$

where $\mathbb{C}^{ep}$ is the so-called *tangent elastoplastic moduli tensor* given by the following expression:

$$\mathbb{C}^{ep} = \begin{cases} \mathbb{C} & \text{if } \dot{\gamma} = 0 \\ \mathbb{C} - \dfrac{\mathbb{C}\,\mathbf{n} \otimes \mathbb{C}\,\partial_{\boldsymbol{\sigma}} f}{\partial_{\boldsymbol{\sigma}} f : \mathbb{C}\,\mathbf{n} + \partial_{\boldsymbol{\chi}} f \cdot \mathbf{h}} & \text{if } \dot{\gamma} > 0 \end{cases} \tag{2.46}$$

We remark that $\mathbb{C}^{ep}$ is generally non-symmetric for arbitrary $\mathbf{n}$, except in the case of associative flow rule.

2.2 von-Mises yield criterion

In this Section, we first introduce the definition of the *von-Mises yield function* for the simplest case of perfect plasticity. Then, we generalize the expression of the von-Mises yield criterion and of the relative flow and hardening laws to the case of hardening materials. The primary consideration that needs to be noted is that, regardless of the type of hardening, the von-Mises yield function is independent of the mean stress or pressure and it is an isotropic function.

Perfect plasticity

The von-Mises yield function, $f = f\,(\boldsymbol{\sigma})$, is defined by:

$$f = \|\mathbf{s}\| - \sigma_y \tag{2.47}$$

with $\sigma_y = \sigma_{y,0}$ the yield stress. Equivalently, denoting by J_2 the second scalar invariant of $\boldsymbol{\sigma}$, the von-Mises yield function may be expressed as:

$$f = \sqrt{2J_2} - \sigma_y \tag{2.48}$$

In view of the last expression, a perfect elastoplastic model with a von-Mises yield surface is usually referred to as J_2 *plasticity model*. We observe that the condition of plastic incompressibility can be satisfied if and only if the yield function depends on the stress only through its deviatoric part, $\mathbf{s}$.

The associated flow rule follows:

$$\dot{\boldsymbol{\varepsilon}}^p = \dot{\gamma}\,\frac{\partial f}{\partial \boldsymbol{\sigma}} = \dot{\gamma}\mathbf{n} \tag{2.49}$$

Linear isotropic hardening

Linear isotropic hardening is characterized by a single scalar strain-like internal variable, ξ, representing a measure of the accumulated plastic deformation, and by a single scalar thermodynamically conjugate force, χ. A typical choice for ξ is the accumulated plastic strain, defined as:

$$\overline{e}^p(t) = \int_0^t \|\dot{\boldsymbol{\varepsilon}}^p(\tau)\|\, d\tau \tag{2.50}$$

which represents the total plastic strain accumulated from the beginning of the loading history.
The von-Mises yield function becomes:

$$f = \|\mathbf{s}\| - \sigma_y \tag{2.51}$$

where $\sigma_y = \sigma_y(\chi)$ depends on the internal variable χ through a relation of the form:

$$\sigma_y = \sigma_{y,0} + G \tag{2.52}$$

where $\sigma_{y,0}$ is the uniaxial initial yield stress, while $G = G(\chi)$ is a monotonically increasing function satisfying $G(0) = 0$. Accordingly, isotropic hardening is viewable as the yield surface projection on the stress-space which expands retaining its original shape by an amount which is proportional to the accumulated plastic deformation through the function, G.
The expression of the Helmholtz free-energy, $\Psi = \Psi(\boldsymbol{\varepsilon}^e, \boldsymbol{\varepsilon}^p)$, is:

$$\Psi = \frac{1}{2}\,\boldsymbol{\varepsilon}^e : \mathbb{C}\,\boldsymbol{\varepsilon}^e + \frac{1}{2}H_{iso}\left(\overline{e}^p\right)^2 \tag{2.53}$$

where the material constant, H_{iso}, is the isotropic hardening modulus. We derive χ, as follows:

$$\chi = -\frac{\partial \Psi}{\partial \overline{e}^p} = -H_{iso}\overline{e}^p \tag{2.54}$$

Admitting, for simplicity, that $G = -\chi$, Eq. (2.52) becomes:

$$\sigma_y = \sigma_{y,0} + H_{iso}\overline{e}^p \tag{2.55}$$

The associated flow rule and hardening laws follow:

$$\begin{cases} \dot{\boldsymbol{\varepsilon}}^p = \dot{\gamma}\,\dfrac{\partial f}{\partial \boldsymbol{\sigma}} = \dot{\gamma}\mathbf{n} \\ \dot{\overline{e}}^p = \|\dot{\boldsymbol{\varepsilon}}^p\|\,\dot{\chi} = -H_{iso}\dot{\overline{e}}^p \end{cases} \tag{2.56}$$

Linear kinematic hardening

The kinematic hardening mechanism, differing from isotropic hardening which causes the yield domain to expand homogenously, produces a shifting of the initial yield surface in stress-space. The description of such a mechanism implies a single internal tensorial variable, $\boldsymbol{\xi}$, usually taken to be the plastic strain, $\boldsymbol{\varepsilon}^p$.
The Helmholtz free-energy, $\Psi = \Psi\left(\boldsymbol{\varepsilon}^e, \boldsymbol{\varepsilon}^p\right)$, is assumed in the form:

$$\Psi = \frac{1}{2}\boldsymbol{\varepsilon}^e : \mathbb{C}\boldsymbol{\varepsilon}^e + \frac{1}{2}\boldsymbol{\varepsilon}^p : \mathbb{D}\boldsymbol{\varepsilon}^p \tag{2.57}$$

where $\mathbb{D} = H_{kin}\mathbb{I}$, with H_{kin} the linear kinematic hardening modulus.
The conjugate force is defined as:

$$\boldsymbol{\chi} = -\frac{\partial \Psi}{\partial \boldsymbol{\varepsilon}^p} = -H_{kin}\boldsymbol{\varepsilon}^p \tag{2.58}$$

The yield condition, $f = f\left(\boldsymbol{\sigma}, \boldsymbol{\chi}\right)$, is obtained by introducing the thermodynamic force, $\boldsymbol{\chi}$:

$$f = \|\mathbf{s} + \boldsymbol{\chi}\| - \sigma_y \tag{2.59}$$

with $\sigma_y = \sigma_{y,0}$ the yield stress.
Introducing the new internal stress variable, $\boldsymbol{\alpha} = -\boldsymbol{\chi}$, which is a deviatoric tensor defined in the stress space, called *backstress*, the yield function, $f = f\left(\boldsymbol{\sigma}, \boldsymbol{\alpha}\right)$, becomes:

$$f = \|\mathbf{s} - \boldsymbol{\alpha}\| - \sigma_y \tag{2.60}$$

The backstress tensor represents the shifting of the center of the yield surface in the stress-space due to the kinematic hardening effects. The tensor, $\boldsymbol{\Sigma} = \mathbf{s} - \boldsymbol{\alpha}$, is called the relative stress and defines the generalized stress-space also referred to as the relative stress-space.
The associated flow rule and hardening laws are:

$$\begin{cases} \dot{\boldsymbol{\varepsilon}}^p = \dot{\gamma}\,\dfrac{\partial f}{\partial \boldsymbol{\sigma}} = \dot{\gamma}\mathbf{n} \\ \dot{\boldsymbol{\alpha}} = H_{kin}\dot{\boldsymbol{\varepsilon}}^p = H_{kin}\dot{\gamma}\mathbf{n} \end{cases} \tag{2.61}$$

Combined linear isotropic and kinematic hardening

To assemble the effects of both linear kinematic and linear isotropic hardening into a single model, it is necessary to sum up the hardening potential, in terms of internal variables, relative to each single mechanism.
The ensuing form of the Helmholtz free-energy, $\Psi = \Psi\left(\boldsymbol{\varepsilon}^e, \boldsymbol{\varepsilon}^p, \overline{e}^p\right)$, is given by:

$$\Psi = \frac{1}{2}\,\boldsymbol{\varepsilon}^e : \mathbb{C}\,\boldsymbol{\varepsilon}^e + \frac{1}{2}\,\boldsymbol{\varepsilon}^p : \mathbb{D}\,\boldsymbol{\varepsilon}^p + \frac{1}{2}H_{iso}\left(\overline{e}^p\right)^2 \tag{2.62}$$

The conjugate forces and laws are exactly the same ones found in the case of pure linear isotropic and kinematic hardening mechanisms.

2.3 Initial boundary-value problem of equilibrium in J_2 elastoplasticity

In this Section, we formulate the mathematical problem that describes the deformation and the stress state for an isotropic material body characterized by a J_2 elastoplastic model under an assigned set of external

actions. Such a problem is modeled by a set of partial differential equations posed on the body domain, plus a set of boundary conditions assigned on the boundary of the body and a set of initial conditions.

Given a body with current configuration, $\Omega \subset \Re^3$, we indicate for compactness its boundary with $\partial\Omega$ such that $\Gamma = \overline{\Gamma}_D \cup \overline{\Gamma}_S$, with $\overline{\Gamma}_D \cap \overline{\Gamma}_S = \emptyset$. Suppose that, for $t \in [0,T] \subset \Re^+$, a body force, $\mathbf{b}(\mathbf{x},t)$, is assigned in Ω, a displacement field, $\overline{\mathbf{u}}(\mathbf{x},t)$, is assigned on $\overline{\Gamma}_D$ and a surface traction, $\overline{\mathbf{t}}(\mathbf{x},t)$, is assigned on $\overline{\Gamma}_S$. Initial values for the displacement $\mathbf{u}(\mathbf{x},0) = \mathbf{u}_0(\mathbf{x})$ are known data as well.

Table 2.1 reports the formulation of the *initial boundary-value problem* (IBVP) for J_2 perfect plasticity. Such a problem results highly non-linear for two main reasons: (i) the time-integration of the rate constitutive equations requires careful consideration of the loading/unloading conditions relative to the choice of the correct tangent operator; (ii) the stress and the internal variables are constrained during their evolution by the yield limit. The object of next Chapters is mainly concerned with the numerical solution of the above stated problem.

INITIAL BOUNDARY-VALUE PROBLEM for J_2 ELASTOPLASTICITY

Find the displacement field, $\mathbf{u}(\mathbf{x},t)$, which, for any $\mathbf{x} \in \Omega$ and any $t \in [0,T]$, solves the following governing equations:

1. *equation of static equilibrium*: $\text{div}\boldsymbol{\sigma} + \mathbf{b} = \mathbf{0}$
2. *strain-displacement relation*: $\boldsymbol{\varepsilon}(\mathbf{u}) = \frac{1}{2}\left[\nabla\mathbf{u} + (\nabla\mathbf{u})^T\right]$
3. *elastoplastic constitutive laws*:
$$\begin{cases} p = K\theta \\ \mathbf{s} = 2G(\mathbf{e} - \mathbf{e}^p) \\ f = \|\mathbf{s}\| - \sigma_y \\ \dot{\boldsymbol{\varepsilon}}^p = \dot{\gamma}\mathbf{n} \\ \dot{\gamma} \geq 0,\ f \leq 0,\ \dot{\gamma}f = 0,\ \dot{\gamma}\dot{f} = 0 \end{cases}$$
together with $\dot{\boldsymbol{\sigma}} = \mathbb{C}^{ep}\dot{\boldsymbol{\varepsilon}}$

and satisfies the:

1. *boundary conditions*:
$$\begin{cases} \mathbf{u} = \overline{\mathbf{u}} & \text{on } \overline{\Gamma}_D \\ \boldsymbol{\sigma}\mathbf{n} = \overline{\mathbf{t}} & \text{on } \overline{\Gamma}_S \end{cases}$$
2. *initial conditions*: $\mathbf{u}(\mathbf{x},0) = \mathbf{u}_0(\mathbf{x})$

Table 2.1: IBVP for J_2 perfect elastoplasticity.

2.4 The principle of maximum plastic dissipation

This Section recalls and revisits the principle of maximum plastic dissipation, by limiting the discussion to the case of J_2 perfect plasticity.

We start by defining the *plastic dissipation*, $D^p = D^p(\boldsymbol{\tau}; \dot{\boldsymbol{\varepsilon}}^p)$, as:

$$D^p := \boldsymbol{\tau} : \dot{\boldsymbol{\varepsilon}}^p \tag{2.63}$$

where $\dot{\boldsymbol{\varepsilon}}^p$ is regarded as a fixed but otherwise arbitrary function and $\boldsymbol{\tau}$ as a possible stress satisfying the yield criterion.

The *principle of maximum plastic dissipation*, often credited to von-Mises (Hill, 1950), and subsequently considered by several authors (Lubliner, 1984, 1986; Mandel, 1964), plays a crucial role in the

variational formulation of plasticity. It states that, for given plastic strain, $\dot{\boldsymbol{\varepsilon}}^p$, among all possible stresses, $\boldsymbol{\tau}$, satisfying the yield criterion, the plastic dissipation, D^p, attains its maximum for the actual stress tensor $\boldsymbol{\sigma}$, i.e., $\boldsymbol{\sigma} \in E_{\boldsymbol{\sigma}}$ is the argument of the maximum principle:

$$\boldsymbol{\sigma} \in E_{\boldsymbol{\sigma}} \;\Leftrightarrow\; D^p(\boldsymbol{\sigma};\dot{\boldsymbol{\varepsilon}}^p) = \max_{\boldsymbol{\tau}\in E_{\boldsymbol{\sigma}}}[\boldsymbol{\tau} : \dot{\boldsymbol{\varepsilon}}^p] \tag{2.64}$$

Maximum plastic dissipation (2.64) implies:

- **i.** *associative flow rule in stress-space* $(2.29)_1$
- **ii.** *loading/un-loading conditions in Kuhn-Tucker complementarity form* (2.34)
- **iii.** *convexity of the elastic domain* $E_{\boldsymbol{\sigma}}$

Proof. To prove (**i**) and (**ii**), we use the classical method of Lagrange multipliers (Bertsekas, 1982), as follows. First, we transform the maximization principle into a minimization principle merely by changing the sign in Eq. (2.64) and considering $-D^p$ as objective function. Next, we transform the constraint minimization problem into an unconstrained problem by introducing the cone of Lagrange multipliers:

$$\mathbb{K}^p := \left\{\dot{\delta} \;:\; \dot{\delta} \geq 0\right\} \tag{2.65}$$

The Lagrangian functional, $\mathcal{L}_m$, follows:

$$\mathcal{L}_m\left(\boldsymbol{\tau}, \dot{\delta}; \dot{\boldsymbol{\varepsilon}}^p\right) := -D^p(\boldsymbol{\tau};\dot{\boldsymbol{\varepsilon}}^p) + \dot{\delta} f\left(\boldsymbol{\tau}\right) \tag{2.66}$$

where $\dot{\boldsymbol{\varepsilon}}^p$ is regarded as a fixed but otherwise arbitrary function.
Then, the solution to problem (2.64) is given by the point $(\boldsymbol{\sigma}, \dot{\gamma})$ satisfying the classical Kuhn-Tucker optimality conditions:

$$\begin{cases} \left.\dfrac{\partial \mathcal{L}_m}{\partial \boldsymbol{\tau}}\right|_{(\boldsymbol{\sigma},\dot{\gamma};\,\dot{\boldsymbol{\varepsilon}}^p)} \equiv -\dot{\boldsymbol{\varepsilon}}^p + \dot{\gamma}\nabla f\left(\boldsymbol{\sigma}\right) \\ \dot{\gamma} \geq 0,\; f\left(\boldsymbol{\sigma}\right) \leq 0,\; \dot{\gamma} f\left(\boldsymbol{\sigma}\right) = 0 \end{cases} \tag{2.67}$$

To see that the convexity condition (**iii**) on the elastic domain, $E_{\boldsymbol{\sigma}}$, also follows from the principle of maximum plastic dissipation, it suffices to show that the function f is convex. To this purpose, we observe that, in view of Eq. (2.64), the extremum point $\boldsymbol{\sigma} \in \partial E_{\boldsymbol{\sigma}}$ satisfies the condition:

$$D^p(\boldsymbol{\sigma}, \dot{\boldsymbol{\varepsilon}}^p) \geq D^p(\boldsymbol{\tau}, \dot{\boldsymbol{\varepsilon}}^p) \;\Leftrightarrow\; \boldsymbol{\sigma} : \dot{\boldsymbol{\varepsilon}}^p \geq \boldsymbol{\tau} : \dot{\boldsymbol{\varepsilon}}^p \;\; \forall \boldsymbol{\tau} \in E_{\boldsymbol{\sigma}} \tag{2.68}$$

Accordingly, we have the inequality:

$$[\boldsymbol{\tau} - \boldsymbol{\sigma}] : \dot{\boldsymbol{\varepsilon}}^p \leq 0 \;\; \forall \boldsymbol{\tau} \in E_{\boldsymbol{\sigma}} \tag{2.69}$$

which, in view of the Eq. $(2.67)_1$, reduces to:

$$[\boldsymbol{\tau} - \boldsymbol{\sigma}] : \dot{\boldsymbol{\varepsilon}}^p = \dot{\gamma}\,[\boldsymbol{\tau} - \boldsymbol{\sigma}] : \nabla f\left(\boldsymbol{\sigma}\right) \leq 0 \;\; \forall \boldsymbol{\tau} \in E_{\boldsymbol{\sigma}} \tag{2.70}$$

From the Kuhn-Tucker optimality condition, it follows that:

$$\dot{\gamma}\,[\boldsymbol{\tau} - \boldsymbol{\sigma}] : \nabla f\left(\boldsymbol{\sigma}\right) \leq \dot{\gamma} f\left(\boldsymbol{\tau}\right) \quad \text{for } \boldsymbol{\sigma} \in \partial E_{\boldsymbol{\sigma}} \text{ and } \forall \boldsymbol{\tau} \in E_{\boldsymbol{\sigma}} \tag{2.71}$$

If $\dot{\gamma} = 0$, the inequality is satisfied trivially. On the other hand, $\dot{\gamma} > 0$ and since $f\left(\boldsymbol{\sigma}\right) = 0$:

$$[\boldsymbol{\tau} - \boldsymbol{\sigma}] : \nabla f\left(\boldsymbol{\sigma}\right) \leq f\left(\boldsymbol{\tau}\right) - f\left(\boldsymbol{\sigma}\right) = f\left(\boldsymbol{\tau}\right) \leq 0 \;\; \forall \boldsymbol{\tau} \in E_{\boldsymbol{\sigma}} \tag{2.72}$$

which coincides with Eq. (2.71); hence, convexity follows. □

In the stated form, condition (2.64) is not suitable for numerical calculations. Therefore, in the following, we transform such an optimization problem into an evolution problem for the plastic deformation, $\boldsymbol{\varepsilon}^p$, i.e., yielding the flow rule with no more inequality constraints.

Lagrangian multiplier formulation

We transform the maximization principle into a minimization principle merely by changing the sign in Eq. (2.64) and considering $-D^p$ as objective function. Then, we transform the constraint minimization problem into an unconstrained problem by defining the following *Lagrangian multiplier functional*, $\mathcal{L}_m$:

$$\mathcal{L}_m\left(\boldsymbol{\tau}, \dot{\delta}; \dot{\boldsymbol{\varepsilon}}^p\right) := -D^p(\boldsymbol{\tau}; \dot{\boldsymbol{\varepsilon}}^p) + \dot{\delta} f\left(\boldsymbol{\tau}\right) - I_{\Re^+}\left(\dot{\delta}\right) \tag{2.73}$$

where $\dot{\boldsymbol{\varepsilon}}^p$ is regarded as a fixed but otherwise arbitrary function. Here, $\boldsymbol{\tau}$ and $\dot{\delta}$ are the generic stress and Lagrange multiplier, respectively; on the contrary, $\boldsymbol{\sigma}$ and $\dot{\gamma}$ denote the stress and Lagrange multiplier at the solution.

The function $I_{\Re^+}\left(\dot{\delta}\right)$ is the convex indicator function of the set of non-negative real numbers, $\Re^+$, defined as:

$$I_{\Re^+}\left(\dot{\delta}\right) = \begin{cases} 0 & \text{if } \dot{\delta} \geq 0 \\ +\infty & \text{otherwise} \end{cases} \tag{2.74}$$

The subdifferential set, $\partial I_{\Re^+}\left(\dot{\delta}\right)$, of the indicator function, $I_{\Re^+}\left(\dot{\delta}\right)$, is defined as:

$$\partial I_{\Re^+}\left(\dot{\delta}\right) = \begin{cases} \Re^- & \text{if } \dot{\delta} = 0 \\ 0 & \text{if } \dot{\delta} > 0 \end{cases} \tag{2.75}$$

Condition (2.64) is then enforced demanding stationarity of the Lagrangian functional (2.73) with respect to $\boldsymbol{\tau}$ and $\dot{\delta}$ (Bertsekas, 1982). Thus, the solution is given by the point $(\boldsymbol{\sigma}, \dot{\gamma})$ which satisfies the Kuhn-Tucker optimality conditions:

$$\begin{cases} 0 \in \partial_{\boldsymbol{\tau}} \mathcal{L}_m\left(\boldsymbol{\tau}, \dot{\delta}; \dot{\boldsymbol{\varepsilon}}^p\right)\big|_{(\boldsymbol{\sigma}, \dot{\gamma};\, \dot{\boldsymbol{\varepsilon}}^p)} & \Longleftrightarrow \quad \dot{\boldsymbol{\varepsilon}}^p \in \dot{\gamma} \partial_{\boldsymbol{\sigma}} f(\boldsymbol{\sigma}) \\ 0 \in \partial_{\dot{\delta}} \mathcal{L}_m\left(\boldsymbol{\tau}, \dot{\delta}; \dot{\boldsymbol{\varepsilon}}^p\right)\big|_{(\boldsymbol{\sigma}, \dot{\gamma};\, \dot{\boldsymbol{\varepsilon}}^p)} & \Longleftrightarrow \quad f(\boldsymbol{\sigma}) \in \partial I_{\Re^+}\left(\dot{\gamma}\right) \end{cases} \tag{2.76}$$

Condition $(2.76)_2$ may be written equivalently in the well-known form:

$$\dot{\gamma} \geq 0,\ f\left(\boldsymbol{\sigma}\right) \leq 0,\ \dot{\gamma} f\left(\boldsymbol{\sigma}\right) = 0 \tag{2.77}$$

Penalty formulation

Another approach is based on the elimination of constraints through a (standard quadratic) penalty formulation of problem (2.64) (Bertsekas, 1982).

We introduce the *penalty Lagrangian functional*, $\mathcal{L}_p$ (Schmidt-Baldassari, 2003):

$$\mathcal{L}_p\left(\boldsymbol{\tau}; \dot{\boldsymbol{\varepsilon}}^p\right) := -D^p(\boldsymbol{\tau}; \dot{\boldsymbol{\varepsilon}}^p) + \frac{1}{2}\left\{\max\left[0, cf\left(\boldsymbol{\tau}\right)\right]\right\}^2 \tag{2.78}$$

with an (arbitrary) positive penalty factor c (Luenberger, 1984). Here, $\boldsymbol{\tau}$ is the generic stress; on the other hand, $\boldsymbol{\sigma}$ denotes the stress at the solution.

Enforcing stationarity of the penalty Lagrangian functional (2.78) with respect to $\boldsymbol{\tau}$ yields:

$$\dot{\boldsymbol{\varepsilon}}^p = \max\left[0, cf\left(\boldsymbol{\sigma}\right)\right]\mathbf{n} \tag{2.79}$$

i.e., the flow rule with no further inequality constraints.

Augmented Lagrangian formulation

Another approach is based on elimination of constraints through an Augmented Lagrangian formulation of problem (2.64) (Bertsekas, 1982).

We convert the inequality constrained problem (2.64) into the following problem, involving exclusively equality constraints (Bertsekas, 1982):

$$D^p(\boldsymbol{\sigma};\dot{\boldsymbol{\varepsilon}}^p) = \max_{\boldsymbol{\tau}\in E^*_{\boldsymbol{\sigma}},\, z} [\boldsymbol{\tau} : \dot{\boldsymbol{\varepsilon}}^p] \tag{2.80}$$

where z is an additional variable and $E^*_{\boldsymbol{\sigma}}$ is defined as:

$$E^*_{\boldsymbol{\sigma}} := \left\{\boldsymbol{\sigma} \;:\; f^* = f + z^2 = 0\right\} \tag{2.81}$$

Then, we consider the following *Augmented Lagrangian functional*, $\mathcal{L}_a$:

$$\mathcal{L}_a\left(\boldsymbol{\tau}, \dot{\delta}, z; \dot{\boldsymbol{\varepsilon}}^p\right) := -D^p(\boldsymbol{\tau};\dot{\boldsymbol{\varepsilon}}^p) + \dot{\delta} f^*(\boldsymbol{\tau}) + \frac{1}{2}\, c f^*(\boldsymbol{\tau})^2 \tag{2.82}$$

where c is a positive parameter. Again, $\boldsymbol{\tau}$ and $\dot{\delta}$ are the generic stress and Lagrange multiplier, respectively; on the other hand, $\boldsymbol{\sigma}$ and $\dot{\gamma}$ denote the stress and Lagrange multiplier at the solution. The Augmented Lagrangian functional, $\mathcal{L}_a$, is a combination of the Lagrangian multiplier functional (2.73) and the penalty Lagrangian functional (2.78).

Demanding stationarity of $\mathcal{L}_a$ with respect to z allows to eliminate such a variable in advance. In fact, the minimization of $\mathcal{L}_a$ with respect to z can be carried out explicitly for fixed $\boldsymbol{\tau}$. In particular, we note that:

$$\min_z \mathcal{L}_a\left(\boldsymbol{\tau}, \dot{\delta}, z; \dot{\boldsymbol{\varepsilon}}^p\right) = -D^p(\boldsymbol{\tau};\dot{\boldsymbol{\varepsilon}}^p) + \min_z \left[\dot{\delta}\left[f(\boldsymbol{\tau}) + z^2\right] + \frac{1}{2}\, c\left[f(\boldsymbol{\tau}) + z^2\right]^2\right] \tag{2.83}$$

The minimization with respect to z is equivalent to the following minimization with respect to the variable $u \geq 0$:

$$\min_{u\geq 0} \left[\dot{\delta}\left[f(\boldsymbol{\tau}) + u\right] + \frac{1}{2}\, c\left[f(\boldsymbol{\tau}) + u\right]^2\right] \tag{2.84}$$

Since the function in Eq. (2.84) is quadratic in u, its unconstrained minimum is $\hat{u}$ at which the derivative is zero:

$$\dot{\delta} + c\left[f(\boldsymbol{\tau}) + \hat{u}\right] = 0 \tag{2.85}$$

Thus, the solution of problem (2.84) is:

$$u^* = \max\left[0, -\frac{\dot{\delta}}{c} - f(\boldsymbol{\tau})\right] \tag{2.86}$$

which can be rewritten as:

$$f(\boldsymbol{\tau}) + u^* = \max\left[f(\boldsymbol{\tau}), -\frac{\dot{\delta}}{c}\right] \tag{2.87}$$

The minimization problem (2.83) can be finally expressed as:

$$\min_z \mathcal{L}_a\left(\boldsymbol{\tau}, \dot{\delta}, z; \dot{\boldsymbol{\varepsilon}}^p\right) = -D^p(\boldsymbol{\tau};\dot{\boldsymbol{\varepsilon}}^p) + \dot{\delta}\max\left[f(\boldsymbol{\tau}), -\frac{\dot{\delta}}{c}\right] + \frac{c}{2}\left[\max\left[f(\boldsymbol{\tau}), -\frac{\dot{\delta}}{c}\right]\right]^2 \tag{2.88}$$

and the *reduced augmented Lagrangian functional*, $\mathcal{L}_a^r$, follows:

$$\mathcal{L}_a^r\left(\boldsymbol{\tau},\dot{\delta},z;\dot{\boldsymbol{\varepsilon}}^p\right)=-D^p(\boldsymbol{\tau};\dot{\boldsymbol{\varepsilon}}^p)+\dot{\delta}\max\left[f\left(\boldsymbol{\tau}\right),-\frac{\dot{\delta}}{c}\right]+\frac{c}{2}\left[\max\left[f\left(\boldsymbol{\tau}\right),-\frac{\dot{\delta}}{c}\right]\right]^2 \tag{2.89}$$

An alternative expression for the *reduced augmented Lagrangian functional*, $\mathcal{L}_a^r$, is:

$$\mathcal{L}_a^r\left(\boldsymbol{\tau},\dot{\delta};\dot{\boldsymbol{\varepsilon}}^p\right)=-D^p(\boldsymbol{\tau};\dot{\boldsymbol{\varepsilon}}^p)+\frac{1}{2c}\left[\max\left[0,\dot{\delta}+cf\left(\boldsymbol{\tau}\right)\right]^2-\dot{\delta}^2\right] \tag{2.90}$$

A straightforward calculation leads to the stationarity conditions for $\mathcal{L}_a^r$, as follows:

$$\begin{cases}\dot{\boldsymbol{\varepsilon}}^p=\max\left[0,\dot{\gamma}+cf\left(\boldsymbol{\sigma}\right)\right]\mathbf{n}\\ \dot{\gamma}=\max\left[0,\dot{\gamma}+cf\left(\boldsymbol{\sigma}\right)\right]\end{cases} \tag{2.91}$$

which result in an augmented flow rule and consistency condition with no further inequality constraints.

We can easily verify that system (2.91) with an arbitrary penalty factor, c, is equivalent to system of equations (2.76), expressing the flow rule and consistency conditions. Compared to the penalty Lagrangian functional, the penalty factor, c, is now a purely numerical regularization parameter with no influence on the exact fulfillment of the yield conditions and it may be chosen solely with respect to the argument of well-possessedness of the algorithm.

The attractive property of the Augmented Lagrangian methods is the ability to solve constrained optimization problems by combining the advantages of the Lagrange multiplier and penalty methods without inheriting the shortcomings. Namely, Augmented Lagrangian methods enforce the constraints with very high precision and, at the same time, the number of variables of the original problem is not increased by the presence of the multipliers. Finally, such methods are a very attractive alternative to Lagrangian algorithms, that present poor global convergence properties, in spite of their high (asymptotically quadratic) rate of convergence (Luenberger, 1984).

2.5 Elastoplasticity in a convex-analytic setting

It is possible to re-examine the elastoplastic thermodynamic theory studied hitherto by adopting the standpoint of convex analysis (Rockafellar, 1970). As a result, the yield surface constraint can be avoided, permitting to obtain a set of alternative forms of the plastic flow laws, which become of great importance for the analysis of the variational problem of elastoplasticity (Moreau, 1976; Nguyen and Halphen, 1975).

In the following, we focus on the classical J_2 perfect plasticity.

2.5.1 Pseudo-potential of dissipation for J_2 perfect plasticity

In the case of J_2 perfect plasticity, the internal variable is the plastic strain, $\boldsymbol{\varepsilon}^p$, and the corresponding associated variable is the Cauchy stress, $\boldsymbol{\sigma}$. Relations $(2.29)_1$ and (2.34) refer to the rate formulation of the plastic flow and are probably the most popular form of the flow rule.

An alternative form of the flow rule $(2.29)_1$ and of the complementarity relations (2.34) is given by the maximum plastic dissipation inequality, introduced in Section 2.4:

$$\boldsymbol{\sigma}\in E_{\boldsymbol{\sigma}}\quad\text{such that}\quad\dot{\boldsymbol{\varepsilon}}^p:(\boldsymbol{\sigma}-\boldsymbol{\tau})\geq 0\ \ \forall\boldsymbol{\tau}\in E_{\boldsymbol{\sigma}} \tag{2.92}$$

where $\boldsymbol{\tau}$ is any plastically admissible stress.

It can be shown through the use of the following Drucker's inequality:

$$\begin{cases}\dot{\boldsymbol{\sigma}}:\dot{\boldsymbol{\varepsilon}}^p\geq 0 & \text{for all states}\\ \dot{\boldsymbol{\sigma}}:\dot{\boldsymbol{\varepsilon}}^p=0 & \text{only if } \dot{\boldsymbol{\varepsilon}}^p=0\end{cases} \tag{2.93}$$

that the yield surface of a work-hardening or perfectly plastic material with an associated flow rule must be convex, so that any vector to a point on the surface from an interior point or from another point on the surface forms an acute (or at most a right) angle with the outward normal on the surface. Since the actual stress is necessarily plastically admissible, it follows that $\boldsymbol{\sigma} : \dot{\boldsymbol{\varepsilon}}^p = \sup_{\boldsymbol{\tau}} [\boldsymbol{\tau} : \dot{\boldsymbol{\varepsilon}}^p]$, where the maximum is taken over all currently possible stresses. Accordingly, we introduce the plastic dissipation, D^p:

$$D^p \left(\boldsymbol{\sigma}; \dot{\boldsymbol{\varepsilon}}^p\right) = \sup_{\boldsymbol{\tau}} \left[\boldsymbol{\tau} : \dot{\boldsymbol{\varepsilon}}^p\right] \tag{2.94}$$

Then, we can rewrite inequality (2.92), as follows:

$$D^p \left(\boldsymbol{\sigma}; \dot{\boldsymbol{\varepsilon}}^p\right) \geq \boldsymbol{\tau} : \dot{\boldsymbol{\varepsilon}}^p \tag{2.95}$$

known as postulate of maximum plastic dissipation and valid for all the elastoplastic materials with an associated flow rule and a convex yield surface. Conversely, the postulate of maximum plastic dissipation implies the associated flow rule and the convexity of the yield surface.

By transforming adequately inequality (2.92), we obtain the set-valued mapping relating the stress and the plastic strain rate (Moreau, 1976). The idea is to make use of the indicator function of the set $E_{\boldsymbol{\sigma}}$ to which stresses $\boldsymbol{\sigma}$ and $\boldsymbol{\tau}$ are required to belong and defined as:

$$I_{E_{\boldsymbol{\sigma}}}(\boldsymbol{\sigma}) = \begin{cases} 0 & \text{if } \boldsymbol{\sigma} \in E_{\boldsymbol{\sigma}} \\ +\infty & \text{otherwise} \end{cases} \tag{2.96}$$

The indicator function is not differentiable in the classical sense and it is convex if the set to which it refers is convex (see Appendix A). Having at hand this tool, a key step is to rewrite the variational inequality (2.92), in the following equivalent way:

$$\dot{\boldsymbol{\varepsilon}}^p : (\boldsymbol{\sigma} - \boldsymbol{\tau}) + I_{E_{\boldsymbol{\sigma}}}(\boldsymbol{\tau}) \geq I_{E_{\boldsymbol{\sigma}}}(\boldsymbol{\sigma}) \tag{2.97}$$

We remark that, if inequality (2.92) is satisfied, it follows that inequality (2.97) is also satisfied. Conversely, if inequality (2.97) holds, by taking $\boldsymbol{\tau} \in E_{\boldsymbol{\sigma}}$, we see that $I_{E_{\boldsymbol{\sigma}}}(\boldsymbol{\tau})$ has a finite value (zero) and $I_{E_{\boldsymbol{\sigma}}}(\boldsymbol{\sigma})$ must be equal to zero, i.e., $\boldsymbol{\sigma} \in E_{\boldsymbol{\sigma}}$ and therefore inequality (2.92) is fulfilled. Inequality (2.97) corresponds to the convexity inequality applied to a non-differentiable function. It means that $\dot{\boldsymbol{\varepsilon}}^p$ belongs to the subdifferential of $E_{\boldsymbol{\sigma}}(\boldsymbol{\sigma})$ at $\boldsymbol{\sigma}$ or, equivalently, $\dot{\boldsymbol{\varepsilon}}^p$ and $\boldsymbol{\sigma}$ are related by the differential inclusion:

$$\dot{\boldsymbol{\varepsilon}}^p \in \partial I_{E_{\boldsymbol{\sigma}}}(\boldsymbol{\sigma}) = \partial I_{[-\infty,0]}(f) \partial f\left(\boldsymbol{\sigma}\right) = \dot{\gamma} \partial f\left(\boldsymbol{\sigma}\right) \tag{2.98}$$

which is equivalent to the flow rule $(2.29)_1$ and the complementarity conditions (2.34).
Here, $I_{[-\infty,0]}(f)$ is the indicator function of the set of non-positive real values assumed by f, defined as:

$$I_{[-\infty,0]}(f) = \begin{cases} 0 & \text{if } f \leq 0 \\ +\infty & \text{otherwise} \end{cases} \tag{2.99}$$

which is called *complementary dissipation pseudo-potential* and it is denoted by $\phi^* = \phi^*(\boldsymbol{\sigma})$.
The term $\partial I_{[-\infty,0]}(f)$ represents the subdifferential of $I_{[-\infty,0]}(f)$ at $\boldsymbol{\sigma}$ and it corresponds to the set of all subgradients of $I_{[-\infty,0]}(f)$ at $\boldsymbol{\sigma}$ itself. In particular, for a differentiable function, the subdifferential is reduced to a singleton which corresponds to the classical gradient. The subdifferential is equal to a non-negative scalar, $\dot{\gamma}$, satisfying the Kuhn-Tucker conditions.
By recalling the definition of normal cone, N, to a convex set (Rockafellar, 1970) and by observing that the normal cone, $N_{E_{\boldsymbol{\sigma}}}$, to the convex domain, $E_{\boldsymbol{\sigma}}$, coincides with the subdifferential of the indicator function, $I_{E_{\boldsymbol{\sigma}}}(\boldsymbol{\sigma})$, of the convex set $E_{\boldsymbol{\sigma}}$, we have the following expression:

$$\dot{\boldsymbol{\varepsilon}}^p \in N_{E_{\boldsymbol{\sigma}}}(\boldsymbol{\sigma}) \tag{2.100}$$

which represents the normality law and ensures that the well-known property for the plastic strain rate to belong to the normal cone to the convex domain $E_{\boldsymbol{\sigma}}$ is satisfied.

Relationship (2.98) may be inverted by applying the Fenchel transform (Rockafellar, 1970):

$$\phi(\dot{\boldsymbol{\varepsilon}}^p) = \sup_{\boldsymbol{\sigma}}[\boldsymbol{\sigma} : \dot{\boldsymbol{\varepsilon}}^p - I_{E_{\boldsymbol{\sigma}}}(\boldsymbol{\sigma})] = \sup_{\boldsymbol{\sigma}\in E_{\boldsymbol{\sigma}}} [\boldsymbol{\sigma} : \dot{\boldsymbol{\varepsilon}}^p] \tag{2.101}$$

where $\phi = \phi(\dot{\boldsymbol{\varepsilon}}^p)$ is the *dissipation pseudo-potential*, which is convex by construction. The inverse flow rule is then:

$$\boldsymbol{\sigma} \in \partial\phi(\dot{\boldsymbol{\varepsilon}}^p) \tag{2.102}$$

which is equivalent to $\boldsymbol{\sigma} : \left(\dot{\boldsymbol{\varepsilon}}^p - \dot{\boldsymbol{\varepsilon}}^{p'}\right) + \phi\left(\dot{\boldsymbol{\varepsilon}}^{p'}\right) \geq \phi(\dot{\boldsymbol{\varepsilon}}^p)$.
Formulations (2.98) and (2.102) are particularly useful for associating dual extremum principles to IBVPs involving plastic materials with associated flow rules. The dissipated power is exactly equal to $\phi(\dot{\boldsymbol{\varepsilon}}^p)$; hence, in the present case, $\phi(\dot{\boldsymbol{\varepsilon}}^p)$ may be called the *dissipation function* of the material.

Now, we derive the expression of the dissipation pseudo-potential. The scalar product can be decomposed as:

$$\sup_{\boldsymbol{\sigma}\in E_{\boldsymbol{\sigma}}} [\boldsymbol{\sigma} : \dot{\boldsymbol{\varepsilon}}^p] = \sup_{\boldsymbol{\sigma}\in E_{\boldsymbol{\sigma}}} [\mathbf{s} : \dot{\mathbf{e}}^p + p\theta^p] \tag{2.103}$$

Since $\theta^p = 0$, i.e., $\boldsymbol{\varepsilon}^p = \mathbf{e}^p$, it is clear that the supremum is achieved for $\boldsymbol{\sigma}$ colinear to $\dot{\boldsymbol{\varepsilon}}^p$, i.e.,

$$\boldsymbol{\sigma} : \dot{\boldsymbol{\varepsilon}}^p \leq \|\boldsymbol{\sigma}\| \, \|\dot{\mathbf{e}}^p\| \tag{2.104}$$

To be able to use the yield criterion, we replace the Euclidean norm of $\boldsymbol{\sigma}$ by the von-Mises norm:

$$\boldsymbol{\sigma} : \dot{\boldsymbol{\varepsilon}}^p \leq \|\boldsymbol{\sigma}\|_{eq} \, \|\dot{\mathbf{e}}^p\|^*_{eq} \tag{2.105}$$

where $\|\dot{\mathbf{e}}^p\|^*_{eq} = \sqrt{2/3}\,\|\dot{\mathbf{e}}^p\|$. Taking into account that $\|\boldsymbol{\sigma}\|_{eq}$ is bounded by the yield stress, σ_y, we have:

$$\boldsymbol{\sigma} : \dot{\boldsymbol{\varepsilon}}^p \leq \sigma_y \, \|\dot{\mathbf{e}}^p\|^*_{eq} \tag{2.106}$$

Thus, the expression of the dissipation pseudo-potential is given by:

$$\phi(\dot{\boldsymbol{\varepsilon}}^p) = \sigma_y \, \|\dot{\mathbf{e}}^p\|^*_{eq} \tag{2.107}$$

As a consequence of the Fenchel transform property, the pseudo-potential of dissipation is convex. Moreover, it is a positive function, homogeneous of degree one which takes a zero value at the origin where the function is non-differentiable. The fact that the pseudo-potential is homogeneous of degree one implies a rate-independent behavior.

Functions $\phi(\dot{\boldsymbol{\varepsilon}}^p)$ and $\phi^*(\boldsymbol{\sigma})$ satisfy the following relation:

$$\phi\left(\dot{\boldsymbol{\varepsilon}}^{p'}\right) + \phi^*(\boldsymbol{\tau}) \geq \dot{\boldsymbol{\varepsilon}}^{p'} : \boldsymbol{\tau} \quad \forall \left(\dot{\boldsymbol{\varepsilon}}^{p'}, \boldsymbol{\tau}\right) \tag{2.108}$$

Equality is reached when a couple $(\dot{\boldsymbol{\varepsilon}}^p, \boldsymbol{\sigma})$ is linked by the evolution law. Finally, the evolution law can be expressed equivalently by:

$$\dot{\boldsymbol{\varepsilon}}^p \in \partial I_{E_{\boldsymbol{\sigma}}}(\boldsymbol{\sigma}) \;\Leftrightarrow\; \boldsymbol{\sigma} \in \partial\phi(\dot{\boldsymbol{\varepsilon}}^p) \;\Leftrightarrow\; \phi(\dot{\boldsymbol{\varepsilon}}^p) + \phi^*(\boldsymbol{\sigma}) = \dot{\boldsymbol{\varepsilon}}^p : \boldsymbol{\sigma} \tag{2.109}$$

Although the pseudo-potential was introduced here for the simple model of perfect plasticity, the previous approach can be easily extended to take into account hardening effects by providing additional internal variables. The elastic domain is then expressed in the generalized stress-space and the rate form of the evolution law takes the form of a generalized normality rule. This leads to the class of Generalized Standard Materials of (Nguyen and Halphen, 1975).

Remark 2.5.1. *In a one-dimensional setting, the expression of the dissipation pseudo-potential becomes:*

$$\phi(\dot{\mathbf{e}}^p) = \sigma_y \left|\dot{e}^p\right| \tag{2.110}$$

which is differentiable everywhere except at the origin. The subdifferential is given by:

$$\partial\phi(\dot{\mathbf{e}}^p) = \begin{cases} -\sigma_y & \text{if } \sigma \leq 0 \\ (-\sigma_y, -\sigma_y) & \text{if } \sigma = 0 \\ \sigma_y & \text{if } \sigma \geq 0 \end{cases} \tag{2.111}$$

which corresponds to the elastic domain at the origin. Again, the set-valued relation is related to the non-differentiability of the potential and the convexity of the potential is a consequence of the monotonic nature of the behavior.

Lagrangian multiplier formulation

The *Lagrangian multiplier functional*, $\mathcal{L}_m$, is defined as:

$$\mathcal{L}_m\left(\boldsymbol{\varepsilon}^{p'}, \dot{\delta}; \boldsymbol{\varepsilon}\right) := \Psi\left(\boldsymbol{\varepsilon}^{p'}; \boldsymbol{\varepsilon}\right) + \sigma_y \left\|\dot{\boldsymbol{\varepsilon}}^{p'}\right\|_{eq}^{*} + \dot{\delta}\ \mathrm{tr}(\boldsymbol{\varepsilon}^{p'}) \tag{2.112}$$

Here, $\boldsymbol{\varepsilon}^{p'}$ and $\dot{\delta}$ are the generic plastic strain and Lagrange multiplier, respectively; on the other hand, $\boldsymbol{\varepsilon}^{p}$ and $\dot{\gamma}$ denote the plastic strain and Lagrange multiplier at the solution.

2.6 Complementarity problem functions

In the literature, *complementarity problem* (CP) and *smoothing functions* have been extensively used to solve mathematical programs with equilibrium or complementarity constraints. Such problems play an important role, for example, in the design of transportation networks (Harker and Pang, 1990), economic modeling (Tobin, 1992), and shape optimization (Haslinger and Neittaanmäki, 1988).
The reader is referred to (Luo et al., 1996) for further material on mathematical programs with equilibrium constraints and their applications.

2.6.1 Fischer-Burmeister complementarity problem function

A CP function is a function, $\Phi : \Re^2 \to \Re$, such that:

$$\Phi(a, b) = 0 \ \Leftrightarrow \ a \geq 0,\ b \geq 0,\ ab = 0 \quad \forall a, b \in \Re \tag{2.113}$$

For classical plasticity we can adopt such a general definition by rewriting the complementarity inequality constraints (2.34) as an equality constraint, by replacing conditions (2.34) with an CP function.
Among all the possible choices (Leyffer, 2006), we apply to classical plasticity the *Fischer-Burmeister complementarity function* $\Phi = \Phi(f, \dot{\gamma})$ (FB) (Fischer, 1992):

$$\Phi = \sqrt{f^2 + \dot{\gamma}^2} + f - \dot{\gamma} \tag{2.114}$$

such that:

$$\Phi = 0 \ \Leftrightarrow \ f \leq 0,\ \dot{\gamma} \geq 0,\ f\dot{\gamma} = 0 \tag{2.115}$$

Proof. Start by proving: $\Phi = 0 \;\Rightarrow\; f \leq 0,\ \dot{\gamma} \geq 0,\ f\dot{\gamma} = 0$.
By imposing $\Phi = \sqrt{f^2 + \dot{\gamma}^2} + f - \dot{\gamma} = 0$, we have if $\dot{\gamma} \geq f$:

$$\sqrt{f^2 + \dot{\gamma}^2} = -f + \dot{\gamma} \tag{2.116}$$

Squaring both members:

$$f^2 + \dot{\gamma}^2 = f^2 + \dot{\gamma}^2 - 2f\dot{\gamma} \tag{2.117}$$

and simplifying, we obtain $f\dot{\gamma} = 0$. Thus, if $f \leq 0$, $\dot{\gamma} \geq 0$.

Now, we prove: $f \leq 0,\ \dot{\gamma} \geq 0,\ f\dot{\gamma} = 0 \;\Rightarrow\; \Phi = 0$.
Start by imposing the following equality $\sqrt{f^2 + \dot{\gamma}^2} = -f + \dot{\gamma}$ where $\dot{\gamma} \geq f$. We square both members:

$$f^2 + \dot{\gamma}^2 = f^2 + \dot{\gamma}^2 - 2f\dot{\gamma} \tag{2.118}$$

and simplifying, we obtain $f\dot{\gamma} = 0$ that is verified by hypothesis. Therefore, we have $\Phi = \sqrt{f^2 + \dot{\gamma}^2} + f - \dot{\gamma} = 0$. □

We may observe that the FB function, Φ, is non-differentiable at the origin, i.e., at $(f, \dot{\gamma}) = (0, 0)$, and its Hessian is unbounded at the origin. In fact, the first derivatives of Φ:

$$\begin{cases} \dfrac{\partial \Phi}{\partial f} = \dfrac{f}{\sqrt{f^2 + \dot{\gamma}^2}} + 1 \\ \dfrac{\partial \Phi}{\partial \dot{\gamma}} = \dfrac{\dot{\gamma}}{\sqrt{f^2 + \dot{\gamma}^2}} - 1 \end{cases} \tag{2.119}$$

are non-differentiable at $(f, \dot{\gamma}) = (0, 0)$.
The same considerations can be made for the second derivatives:

$$\begin{cases} \dfrac{\partial^2 \Phi}{\partial f^2} = \dfrac{1}{\sqrt{f^2 + \dot{\gamma}^2}} + \dfrac{2f^2}{(f^2 + \dot{\gamma}^2)^{3/2}} \\ \dfrac{\partial^2 \Phi}{\partial \dot{\gamma}^2} = \dfrac{1}{\sqrt{f^2 + \dot{\gamma}^2}} + \dfrac{2\dot{\gamma}^2}{(f^2 + \dot{\gamma}^2)^{3/2}} \\ \dfrac{\partial^2 \Phi}{\partial \dot{\gamma} \partial f} = \dfrac{\partial^2 \Phi}{\partial f \partial \dot{\gamma}} = \dfrac{2f\dot{\gamma}}{(f^2 + \dot{\gamma}^2)^{3/2}} \end{cases} \tag{2.120}$$

To circumvent such a numerical difficulty, we may use a smoothing technique, consisting in the introduction of the *smoothed Fischer-Burmeister function*, $\Phi = \Phi_\delta(f, \dot{\gamma}, \delta)$ (Kanzow, 1996):

$$\Phi_\delta = \sqrt{f^2 + \dot{\gamma}^2 + 2\delta} + f - \dot{\gamma} = 0 \tag{2.121}$$

where δ is a positive smoothing parameter.
Then, we have:

$$\Phi_\delta = 0 \;\Leftrightarrow\; f \leq 0,\ \dot{\gamma} \geq 0,\ f\dot{\gamma} = -\delta \tag{2.122}$$

Proof. Start by proving: $\Phi_\delta = 0 \;\Rightarrow\; f \leq 0,\ \dot{\gamma} \geq 0,\ f\dot{\gamma} = -\delta$.
By imposing $\Phi_\delta = \sqrt{f^2 + \dot{\gamma}^2 + 2\delta} + f - \dot{\gamma} = 0$, we have if $\dot{\gamma} > f$:

$$\sqrt{f^2 + \dot{\gamma}^2 + 2\delta} = -f + \dot{\gamma} \tag{2.123}$$

Squaring both members, we obtain:

$$f^2 + \dot{\gamma}^2 + 2\delta = f^2 + \dot{\gamma}^2 - 2f\dot{\gamma} \tag{2.124}$$

and simplifying, we have $f\dot{\gamma} = -\delta$. Thus, if $f \leq 0$, $\dot{\gamma} \geq 0$.

Now, we prove: $f \leq 0,\ \dot{\gamma} \geq 0,\ f\dot{\gamma} = -\delta \ \Rightarrow\ \Phi_\delta = 0$.
Start by imposing the following equality $\sqrt{f^2 + \dot{\gamma}^2} = -f + \dot{\gamma}$ where $\dot{\gamma} \geq f$. Squaring both members:

$$f^2 + \dot{\gamma}^2 + 2\delta = f^2 + \dot{\gamma}^2 - 2f\dot{\gamma} \tag{2.125}$$

and simplifying, we have $f\dot{\gamma} = -\delta$, that is verified by hypothesis. Thus, $\Phi_\delta = \sqrt{f^2 + \dot{\gamma}^2 + 2\delta} + f - \dot{\gamma} = 0$. □

Now, we may observe that for any $\delta > 0$, the function Φ_δ is smooth everywhere and its first derivatives are given by:

$$\begin{cases} \dfrac{\partial \Phi_\delta}{\partial f} = \dfrac{f}{\sqrt{f^2 + \dot{\gamma}^2 + 2\delta}} + 1 \\ \dfrac{\partial \Phi_\delta}{\partial \dot{\gamma}} = \dfrac{\dot{\gamma}}{\sqrt{f^2 + \dot{\gamma}^2 + 2\delta}} - 1 \end{cases} \tag{2.126}$$

The same considerations can be made for the second derivatives given by:

$$\begin{cases} \dfrac{\partial^2 \Phi_\delta}{\partial f^2} = \dfrac{1}{\sqrt{f^2 + \dot{\gamma}^2 + 2\delta}} + \dfrac{2f^2}{(f^2 + \dot{\gamma}^2 + 2\delta)^{3/2}} \\ \dfrac{\partial^2 \Phi_\delta}{\partial \dot{\gamma}^2} = \dfrac{1}{\sqrt{f^2 + \dot{\gamma}^2 + 2\delta}} + \dfrac{2\dot{\gamma}^2}{(f^2 + \dot{\gamma}^2 + 2\delta)^{3/2}} \\ \dfrac{\partial^2 \Phi_\delta}{\partial \dot{\gamma} \partial f} = \dfrac{\partial^2 \Phi_\delta(f, \dot{\gamma}, \delta)}{\partial f \partial \dot{\gamma}} = \dfrac{2f\dot{\gamma}}{(f^2 + \dot{\gamma}^2 + 2\delta)^{3/2}} \end{cases} \tag{2.127}$$

Figure 2.1 shows the effect of the replacement of the KT complementary conditions (2.34) by the smoothed FB function Φ_δ, varying the smoothing parameter, δ. As it can be observed, Φ_δ converges to the KT complementary conditions as δ decreases.

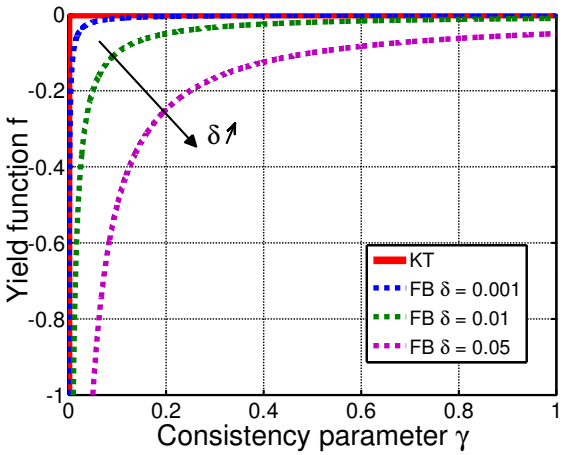

Figure 2.1: Fischer-Burmeister complementarity problem function. Effect of the replacement of the Kuhn-Tucker (KT) conditions by the smoothed Fischer-Burmeister (FB) function, Φ_δ, varying the smoothing parameter, δ.

2.6.2 A different form of complementarity problem function

Complementary inequality conditions (2.34) could also be rewritten in the following equivalent form:

$$\mu\dot{\gamma} - \langle \mu\dot{\gamma} + f \rangle = 0 \tag{2.128}$$

where μ is a positive constant used for dimensional consistency.
If Eq. (2.128) holds, only one of the two following cases occur for the yield surface, f, independently of the value of μ:

$$\begin{cases} \mu\dot{\gamma} + f \geq 0 \\ \mu\dot{\gamma} - \langle \mu\dot{\gamma} + f \rangle = 0 \end{cases} \Rightarrow \; f = 0, \; \dot{\gamma} \geq 0 \tag{2.129}$$

and

$$\begin{cases} \mu\dot{\gamma} + f < 0 \\ \mu\dot{\gamma} - \langle \mu\dot{\gamma} + f \rangle = 0 \end{cases} \Rightarrow \; \dot{\gamma} = 0, \; f < 0 \tag{2.130}$$

Since Eq. (2.128) is non-differentiable at the origin, i.e., at $(f, \dot{\gamma}) = (0, 0)$, several smoothing procedures have been proposed in the literature. In the following, we recall two approaches frequently used in the literature to overcome the problem.

Chen-Mangasarian smoothing procedure

The *Chen-Mangasarian smoothing procedure* (CM) (Chen and Mangasarian, 1995) consists in the introduction of the sigmoid function, known as s-function, $S = S(x, \alpha)$:

$$S := \frac{1}{1 + \exp^{-\alpha x}} \tag{2.131}$$

and of its integral, known as p-function, $P = P(x, \alpha)$:

$$P := \int_{-\infty}^{x} S(y, \alpha)\, dy = \int_{-\infty}^{x} \frac{1}{1 + \exp^{-\alpha y}}\, dy = x + \frac{1}{\alpha} \ln\left(1 + \exp^{-\alpha x}\right) \tag{2.132}$$

with α a positive parameter.
The p-function, P, is k-times continuously differentiable for any positive integer k and can be viewed as an approximation of the ramp or maximum function $\langle x \rangle = \max[0, x]$, as shown in Figure 2.2(a):

$$\langle x \rangle = \max[0, x] \approx P = x + \frac{1}{\alpha} \ln\left(1 + \exp^{-\alpha x}\right) \tag{2.133}$$

In particular, $P = P(x, \alpha)$ converges to $\langle x \rangle$ as α increases, since:

$$\lim_{\alpha \to +\infty} [P(x, \alpha) - \langle x \rangle] = 0 \tag{2.134}$$

Moreover, since the maximum function is the integral of the Heaviside or unit step function, $H = H(x)$:

$$H = \begin{cases} 0 & \text{if } x < 0 \\ 0.5 & \text{if } x = 0 \\ 1 & \text{if } x > 0 \end{cases} \tag{2.135}$$

the sigmoid function, S, can be treated as an approximation of H, as shown in Figure 2.2(b).

Thus, Eq. (2.128) can be rewritten, as follows (assuming $\mu = 1$):

$$\dot{\gamma} - P(\dot{\gamma} + f, \alpha) = \dot{\gamma} - \left[(\dot{\gamma} + f) + \frac{1}{\alpha} \ln\left[1 + \exp^{-\alpha(\dot{\gamma} + f)}\right]\right] = 0 \tag{2.136}$$

which, after some simple passages, becomes:

$$\exp^{-\alpha f}\left(1 - \exp^{-\alpha\dot{\gamma}}\right) = 1 \tag{2.137}$$

The KT conditions (2.34) are so converted into the smooth unconstrained minimization problem (2.137), the solution of which approximates the solution of the original problem to a high degree of accuracy for α sufficiently large (Areias et al., 2012). Figure 2.2(c) represents the effect of the replacement of Eq. (2.128) by Eq. (2.137), varying the parameter, α.

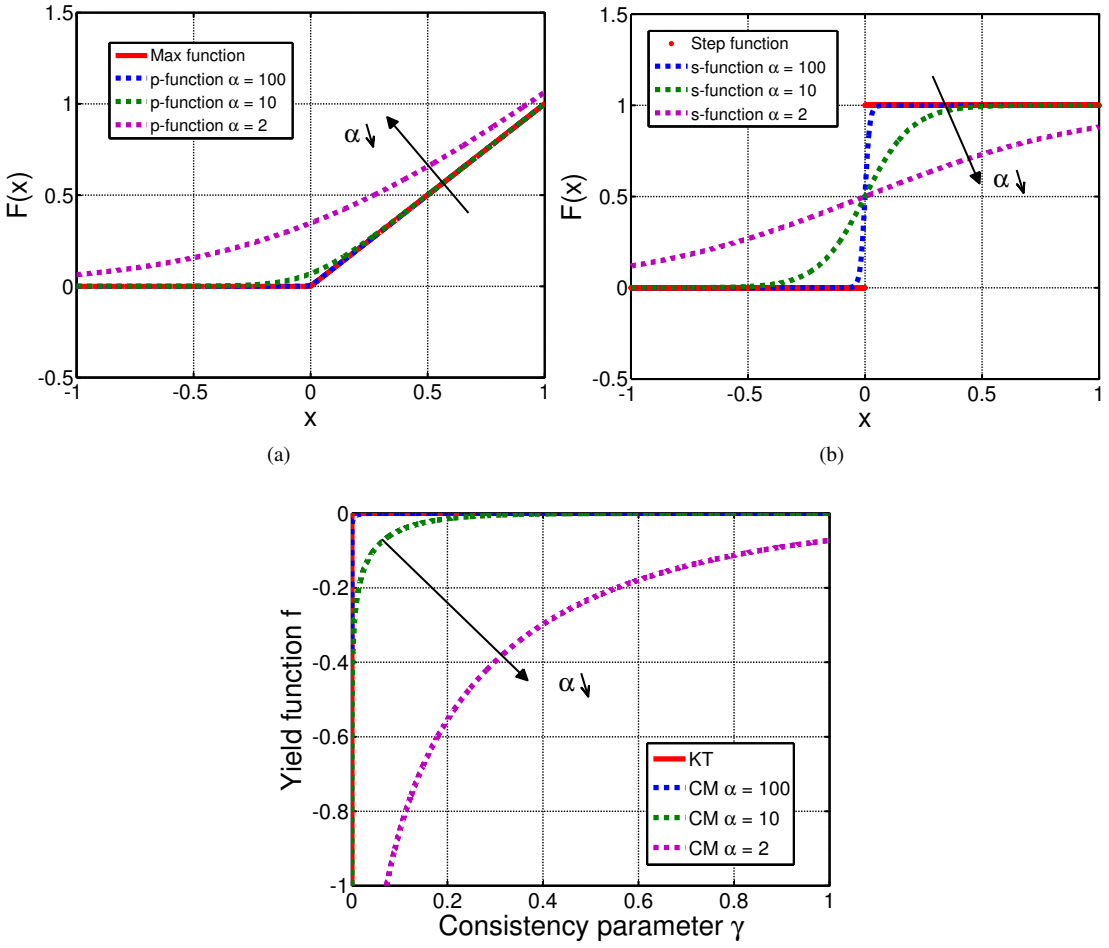

Figure 2.2: Chen-Mangasarian smoothing procedure. Effect of the replacement of: (a) the max function, $\langle x \rangle$, by the p-function, $P = P(x, \alpha)$; (b) the Heaviside step function, $H = H(x)$, by the s-function, $S = S(x, \alpha)$; (c) the Kuhn-Tucker (KT) equation $\dot{\gamma} - \langle \dot{\gamma} + f \rangle = 0$ by the Chen-Mangasarian (CM) equation $\dot{\gamma} - P(\dot{\gamma} + f, \alpha) = 0$, varying the parameter, α.

Balakrishna-Biegler smoothing procedure

The *Balakrishna-Biegler smoothing procedure* (BB) (Balakrishna and Biegler, 1992) consists in rewriting the maximum or ramp function, as follows:

$$\langle x \rangle = \max[0, x] = \frac{|x|}{2} + \frac{x}{2} \tag{2.138}$$

and in approximating the absolute value function, $|x|$, with an hyperbole, as shown in Figure 2.3(a):

$$|x| \approx \sqrt{x^2 + \epsilon^2} \tag{2.139}$$

The approximation of the maximum function (2.138) follows:

$$\langle x \rangle = \max[0, x] \approx \frac{\sqrt{x^2 + \epsilon^2}}{2} + \frac{x}{2} \tag{2.140}$$

with ϵ a positive smoothing parameter, as shown in Figure 2.3(b).

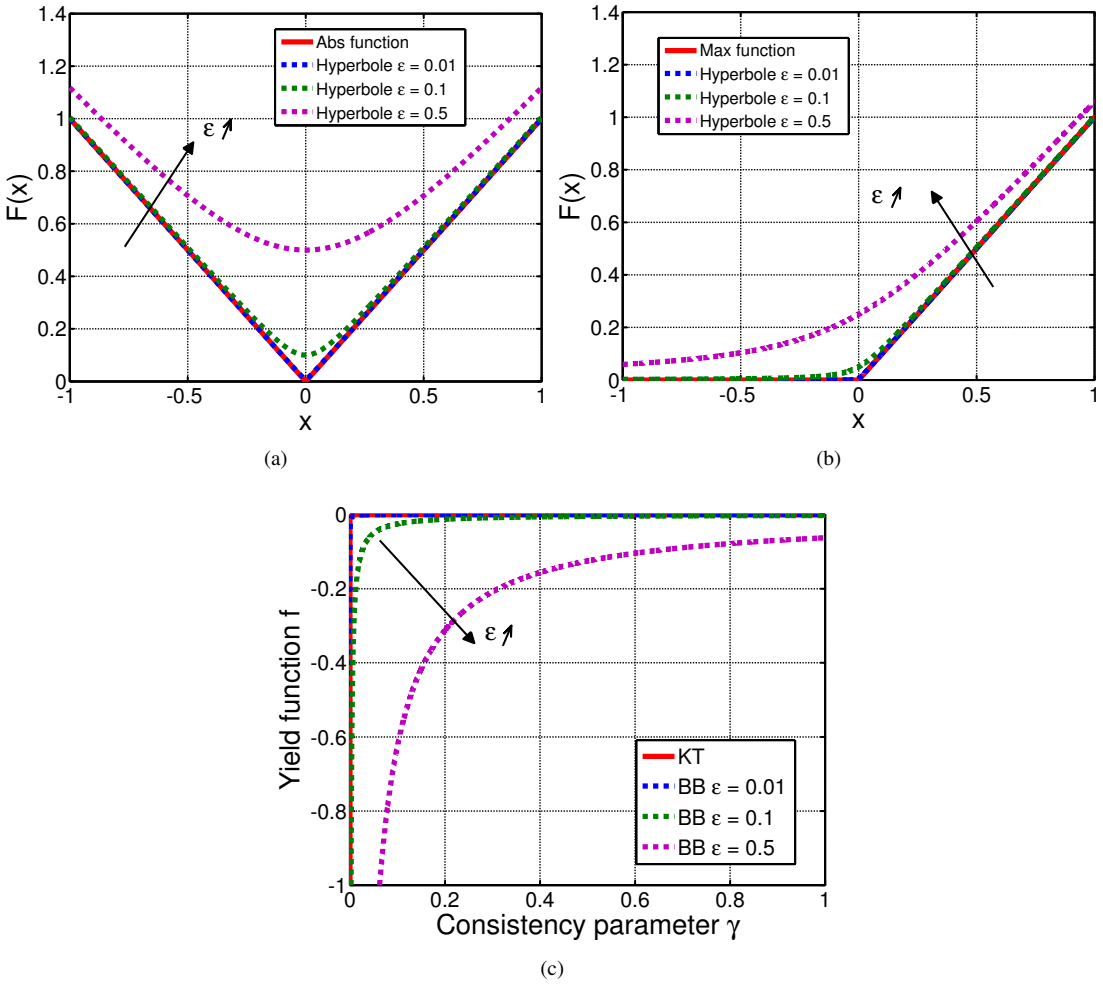

Figure 2.3: Balakrishna-Biegler smoothing procedure. Effect of the replacement of: (a) the absolute value function, $|x|$, by hyperbole, $\sqrt{x^2+\epsilon^2}$; (b) the maximum function, $\max[0,x]$, by hyperbole, $\left(\sqrt{x^2+\epsilon^2}+x\right)/2$; (c) the Kuhn-Tucker (KT) equation $\dot{\gamma}-\langle\dot{\gamma}+f\rangle=0$ by the Balakrishna-Biegler (BB) equation $(\dot{\gamma}-f)/2-\sqrt{(\dot{\gamma}+f)^2+\epsilon^2}/2=0$, varying the parameter, ϵ.

Therefore, Eq. (2.128) can be rewritten in the following form (assuming $\mu=1$):

$$\dot{\gamma}-\left[\frac{\dot{\gamma}+f}{2}+\frac{\sqrt{(\dot{\gamma}+f)^2+\epsilon^2}}{2}\right]=0 \tag{2.141}$$

and simplified, as follows:

$$\dot{\gamma}f=-\frac{\epsilon^2}{4} \tag{2.142}$$

Such an approximation is differentiable at the origin and its Hessian is bounded at the origin, i.e., at $(f,\dot{\gamma})=(0,0)$. Figure 2.3(c) represents the effect of the replacement of Eq. (2.128) by Eq. (2.141), varying the parameter, ϵ.

Comparisons

Figure 2.4 presents a comparison between the approaches based on the FB function, the CM smoothing procedure, and the BB smoothing procedure. The same value of the regularization parameters, δ, α, and ϵ, is assumed. As it can be observed, the FB function requires lower values of the parameter, δ, to better approximate the KT conditions.

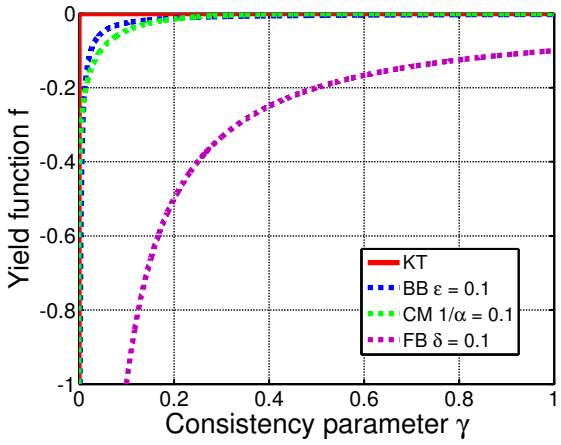

Figure 2.4: Complementarity problem functions. Comparison between the approaches based on the Fischer-Burmeister (FB) function, the Chen-Mangasarian (CM) smoothing procedure, and the Balakrishna-Biegler (BB) smoothing procedure.

Chapter 3

Integration algorithms for J_2 elastoplasticity

Due to the highly non-linearity of the governing equations for elastoplasticity, the solution to large scale problems rising from practical engineering area has to adopt robust and efficient computational methods. This Chapter presents a detailed analysis of several numerical approaches available from the literature and relevant to the olution of the initial boundary-value problem for J_2 perfect plasticity, presented in Section 2.3. The aim is to critically review a number of existing algorithmic schemes, starting from the classical and well-known return-map algorithm.

The Chapter is organized as follows. Section 3.1 presents an introduction to the problem and a detailed literature review on several numerical approaches. Section 3.2 presents the structure of the discrete problem for J_2 perfect plasticity, the fundamental role played by the discrete Kuhn-Tucker conditions, and the geometric interpretation of the solution as the closest point projection. Then, Section 3.3 focuses on the numerical treatment of the principle of maximum plastic dissipation presented in Section 2.4. Section 3.4 presents the derivation of the elastoplastic problem from the minimization of the total energy. Finally, Section 3.5 presents the discrete formulation of the complementary problem functions introduced in Section 2.6.
The reader is referred to, e.g., (Simo and Hughes, 1998), for a detailed analysis on the numerical solutions to elasto-plastic problems.

3.1 Literature review

The numerical solution of the initial boundary-value problem (IBVP), presented in Section 2.3, is based on an iterative solution of the discrete momentum balance equation. Typically, the following three steps are involved:

1. the discretized momentum equation generates incremental motions which, in turn, are used to calculate the incremental strain history by kinematic relationships;

2. for a given incremental strain history, new values of the variables, $\{\boldsymbol{\sigma}, \boldsymbol{\varepsilon}^p, \boldsymbol{\chi}\}$, are obtained by integrating the local constitutive equations with given initial conditions;

3. the discrete momentum balance equation is tested for the computed stresses and, if violated, the iteration process is continued by returning to step 1.

In most of the computational architectures currently in use, steps 1 and 3 are carried out at a global level by finite element (FE) or finite difference procedures. In the present Chapter, we are concerned with

the numerical integration of local constitutive equations (i.e., step 2), which is regarded as the central problem of computational plasticity as it corresponds to the main role played by constitutive equations in actual computations. Such an integration is carried out locally at each quadrature point in typical FE implementations. The crucial aspect is the fact that, from a computational standpoint, such a problem can always be regarded as strain-driven in the sense that variables, $\{\boldsymbol{\sigma}, \boldsymbol{\varepsilon}^p, \boldsymbol{\chi}\}$, are computed for a given deformation history. In particular, stresses and updated internal variables, characterizing material inelastic response, are sought for a given strain increment and previous values of the internal variables. Finding the solution of the discrete local constitutive equations of step 2 proves to be crucial for the successful solution of the global IBVP.

Nowadays, the use of return-mapping algorithms for the integration of the local plastic evolution equations has become widely used (Simo and Hughes, 1998). The main component in return-mapping algorithms is the enforcement of the plastic consistency condition defined by the yield function. A common feature is the use of an operator split strategy in the solution of such local equations. Briefly, final stresses and updated internal variables are obtained by imposing the consistency conditions after a trial state has detected the activation of the plastic evolution equations. Common to many approaches is the use of an elastic trial state in this process, leading then to a plastic corrector step approximating the plastic evolution equations. Of interest is the consideration of the so-called closest-point projection approximation for this plastic corrector step, perhaps the most commonly used strategy in practical applications, both in the infinitesimal and finite deformation ranges. This strategy involves an implicit approximation of the governing equations, leading to a non-linear system of algebraic equations in stresses and updated internal variables.

Except for very particular cases where a closed-form solution can be found (e.g., the J_2 theory with linear hardening), an iterative algorithm needs to be applied for the solution of the resulting non-linear system of local plastic algebraic equations. Generally, a Newton-Raphson scheme is applied thanks to its asymptotic quadratic rate of convergence and the availability of its linearization in closed form, leading to the algorithmic tangent employed in the solution of the global IBVP. However, the well-known limited local convergence properties of Newton-Raphson schemes (in the sense that actual convergence can only be assured for initial estimates close to the final solution) make this approach difficult when considering complex constitutive models required in many practical applications of interest.

Several strategies can be found in the literature to avoid such difficulties.
As an example, the consideration of alternative trial predictors initializing the iterative process can be found in (Bićanić and Pearce, 1996; de Souza Neto et al., 1994; Han and Reddy, 1999), which are however suitable for particular models. Iterative strategies involving line-search schemes can be found in, e.g., (Dutko et al., 1993). Similarly, the consideration of sub-stepping techniques has been proposed to alleviate convergence difficulties (Abbo and Sloan, 1996; Owen and Hinton, 1980; Pérez-Foguet et al., 2001; Sloan, 1987). The work by Artioli et al. (2007) considers four schemes based on the generalized midpoint rule and the return-map algorithm for the integration of the classical J_2 plasticity with linear hardening. Artioli et al. (2006) proposed a new exponential-based integration algorithm for associative J_2 plasticity with linear isotropic and kinematic hardening. The works by Armero and Pérez-Foguet (2002a,b) focus on a rich mathematical structure behind the closest-point projection equations characteristic of the local integration of elastoplastic models, including their viscoelastic extensions, in both the infinitesimal and finite deformation ranges, and address the formulation of robust numerical strategies for the solution of the resulting system of equations. Augmented Lagrangian extensions are also applied to the standard displacement approach, allowing a complete regularization of the problem in the constrained rate-independent limit.

Alternatively, we can find in the literature other approaches than abandon the original closest-point projection approximation. An early example is the so-called cutting plane algorithm, presented in (Ortiz and Simo, 1986), based on a steepest descent strategy which avoids an implicit treatment of the governing equations. The resulting scheme involves an explicit iterative process, thus exhibiting improved convergence properties. However, no expression exists for the algorithmic consistent linearization making the use of such techniques somehow limited in actual FE implementations employing a Newton-Raphson solu-

tion strategy. Furthermore, such schemes show poorer accuracy properties when compared to the original closest-point projection approximation (Simo, 1998).

Recently, the application of multi-step schemes (backward difference schemes) and alternative Runge-Kutta one-step methods can be found in (Papapadopulos and Taylor, 1994; Simo, 1998). Such approaches usually lead, however, to complex implicit non-linear systems of algebraic equations, exhibiting the same difficulties in their iterative solution.

An important class of numerical procedures developed on the basis of mathematical programming (MP) concepts (Luenberger, 1984) has been also proposed. For details on this class of methods, the reader is referred to (Comi et al., 1991; Maier, 1970; Martin et al., 1987; Reddy and Martin, 1991; Romano et al., 1993). Here, we recall that such procedures reduce the complete IBVP or only the elastoplastic evolution problem at the Gauss point level to an MP problem which can be solved by means of standard numerical algorithms, by exploiting the potential structure that characterizes many elastoplasticity models and concepts of convex analysis. Moreover, the MP approach can make the formulation and solution procedures of plasticity analysis separately. As a result, the MP developers do not have to take care of the details of plasticity theory and the computational plasticity researchers could release from the work of designing the solution algorithms. This is distinguished from the most currently used method in plasticity analysis, e.g., the return-mapping algorithms. Additionally, compared to the return-mapping algorithms, in which the set of active constraints (i.e., the set of Gauss points whose stress state changes) has to be identified artificially by a 'trial and error' process, the MP approach automatically chooses which inequalities satisfying as equations by a wealth of efficient and robust numerical algorithms.

Up to now, several approaches belonging to the MP class have been developed. The application of Augmented Lagrangian approaches to complementary formulations of plasticity has been introduced in the papers by Contrafatto and Ventura (2004); Cuomo and Contrafatto (2000), where the constitutive laws of elastoplasticity with internal variables are described through the definition of suitable dual potentials, including various hardening models. A family of variational principles for inelastic problems is so obtained using convex analysis tools and the structural problem is analyzed using the complementary energy functional. The present complementary formulation exhibits better convergence rate than classical displacement formulations (Armero and Pérez-Foguet, 2002a,b), reaching the same accuracy with a considerably smaller number of elements.

Other MP approaches are the parametric quadratic programming approaches (Zhang et al., 2004), the interior-point methods for general non-linear programming problems (Krabbenhoft et al., 2007), the solution methods based on linear (Zhu, 1995) or non-linear complementarity problems (Tin-Loi and Pang, 1993) (denoted as LCPs and NCPs, respectively), non-smooth Newton methods (Christensen, 2002), sequential quadratic programming methods (Wieners, 2008) and the so-called bi-potential formulation (Hjiaj et al., 2003). Recently, Bilotta et al. (2012) presented a new method for the incremental elastoplastic analysis of structures, where the elastoplastic step is solved through a sequential quadratic programming with equality constraints.

Semi-smooth Newton methods have been applied to small strain elastoplasticity with hardening by Gruber and Valdman (2009). The merit of semi-smooth Newton methods is their super-linear convergence at all levels of refinement and the independence of the number of iterations on the level of refinement.

In the context of LCPs and NCPs, the replacement of the Kuhn-Tucker conditions by equivalent complementary functions makes possible to omit an active set search, a fundamental advantage especially when dealing with many coupled evolution equations and constraints on internal variables. As an example, the effective and efficient procedure based on the Fischer-Burmeister complementarity function (Fischer, 1992), presented in Section 2.6, has been introduced by Schmidt-Baldassari (2003) in the context of crystal plasticity and applied to solve several engineering problems; see, e.g., Ahn (2007); Tin-Loi (1999).

Similar approaches consist in the Chen-Mangasarian (CM) (Chen and Mangasarian, 1995) and Balakrishna-Biegler (BB) (Balakrishna and Biegler, 1992) smoothing procedures, presented in Section 2.6. The CM procedure has been applied by Areias et al. (2012) to finite strain plasticity with elastic isotropy and ar-

bitrary flow rules; the BB procedure has been applied in several fields ranging from reactor networks to chemical processes and tray optimization (Balakrishna and Biegler, 1992; Gopal and Biegler, 1999; Lang and Biegler, 2002).

An amount of significant work has been dedicated to the so-called conic programming (CP) in the field of MP (Ben-Tal and Nemirovski, 2001). Based on the realization of the cone representation of some plasticity failure criterion (Bisbos and Pardalos, 2007; Krabbenhoft et al., 2007), the CP approach has been quickly applied to the formulation and solution of elastoplasticity problems. Compared to the classical non-linear programming method for plasticity, the CP method does not only provide elegant mathematical formulation for plasticity, but also holds as a computationally attractive aspect. Once a practical problem is formulated as a CP problem, a fruitful available specific software can be directly employed, developed by the MP community within the framework of interior point methods (Ben-Tal and Nemirovski, 2001) or non-interior point methods (Chen and Pan, 2012). As an important branch of conic optimization, the second-order cone complementarity problem, which can be regarded as the natural extension of LCP and just differs from LCP by permitting certain non-linear inequality constraints having the form of a convex cone, has received increasing attention from mathematical and algorithmic points of view (Hayashi, 2004; Zhang et al., 2013).

3.2 The notion of closest point projection

The non-linear evolution equations of classical J_2 perfect plasticity, as summarized in Table 2.1, define an *unilaterally constrained problem* of evolution. By applying an implicit backward-Euler difference scheme, such continuum problem is transformed into a discrete constrained optimization problem, governed by discrete Kuhn-Tucker (KT) conditions. Thus, computationally, the solution of the constrained problem of evolution collapses to the (iterative) solution of a convex mathematical programming problem. We will show below that such a problem reduces to the standard problem of finding the closest distance (in the energy norm) of a point (the trial state) to a convex set (the elastic domain).

3.2.1 Outline of the discrete equations for J_2 elastoplasticity

We now elaborate on the algorithmic treatment of the equations summarized in Table 2.1.
For the sake of notation simplicity, the convention establishes superscript n for all the variables evaluated at time t_n, while drops superscript $n+1$ for all the variables computed at time t_{n+1}. Knowing the strain, $\boldsymbol{\varepsilon}$, at time t_{n+1} and the solution at time t_n, represented by the ordered set $\{\boldsymbol{\sigma}_n, \boldsymbol{\varepsilon}_n, \boldsymbol{\varepsilon}_n^p\}$, we need to compute the solution at time t_{n+1}.

A backward-Euler discretization of flow rule $(2.29)_1$, together with the discrete form of the KT inequalities (2.34), yields:

$$\begin{cases} \boldsymbol{\varepsilon}^p = \boldsymbol{\varepsilon}_n^p + \Delta\gamma \partial_{\boldsymbol{\sigma}} f(\boldsymbol{\sigma}) \\ \Delta\gamma \geq 0,\ f(\boldsymbol{\sigma}) \leq 0,\ \Delta\gamma f(\boldsymbol{\sigma}) = 0 \end{cases} \tag{3.1}$$

where $\Delta\gamma = \int_{t_n}^{t_{n+1}} \dot{\gamma} dt$ is the time-integrated consistency parameter.
The evaluation of the stress-strain relationship (2.14) at time t_{n+1} yields:

$$\boldsymbol{\sigma} = \nabla\Psi(\boldsymbol{\varepsilon}^e) = \mathbb{C}(\boldsymbol{\varepsilon} - \boldsymbol{\varepsilon}^p) \tag{3.2}$$

As in the continuum case, the discrete KT conditions $(3.1)_2$ define the appropriate notion of loading-unloading and can be reformulated in a form directly amenable to computational implementations. We

introduce the following trial elastic state at time t_{n+1}, as follows:

$$\begin{cases} \boldsymbol{\varepsilon}^{p,trial} = \boldsymbol{\varepsilon}_n^p \\ \boldsymbol{\varepsilon}^{e,trial} = \boldsymbol{\varepsilon} - \boldsymbol{\varepsilon}^{p,trial} \\ \boldsymbol{\sigma}^{trial} = \nabla\Psi(\boldsymbol{\varepsilon}^{e,trial}) = \mathbb{C}\left(\boldsymbol{\varepsilon} - \boldsymbol{\varepsilon}^{p,trial}\right) \\ f^{trial} = f(\boldsymbol{\sigma}^{trial}) \end{cases} \tag{3.3}$$

which, from a physical standpoint, is obtained by freezing plastic flow during the time step. We will show below that such a trial state arises naturally in the context of an elastoplastic operator split.

3.2.2 Return-mapping algorithm

To deal with the non-linear discrete problem of Eqs. (3.1) and (3.2), we consider the so-called *return-map algorithm* (Simo and Hughes, 1998). Such a scheme belongs to a family of elastic-predictor plastic-corrector algorithms and, hence, is a two part procedure: (i) a purely elastic trial state is first computed, as reported in system (3.3); (ii) then, if the trial state violates the model constitutive equations, a plastic correction is computed using the trial state as an initial condition. Table 3.1 presents the numerical scheme for the return-mapping algorithm.

Such an algorithm possesses a fundamental interpretation which is the manifestation of a basic variational structure underlying classical rate-independent plasticity. We will show below that such algorithm is interpreted as the KT optimality conditions of a convex optimization problem which is, in fact, the discrete counterpart of the principle of maximum plastic dissipation (Simo and Hughes, 1998). The interpretation of such an algorithm as optimality conditions of a convex minimization problem is of fundamental significance in the three-dimensional theory, especially in the presence of complicated yield conditions, as often in practice. Such an interpretation opens the possibility of applying several algorithms developed in convex mathematical programming.

3.2.3 Geometric interpretation of closest point projection

Strain-space formulation

Now, we examine the geometric interpretation associated with the non-linear discrete problem of Eqs. (3.1) and (3.2) in strain-space.

The solution $\boldsymbol{\varepsilon}^e = \boldsymbol{\varepsilon} - \boldsymbol{\varepsilon}^p$ is the *closest point projection* in the energy norm of the trial state, $\boldsymbol{\varepsilon}^{e,trial}$, onto the yield surface, i.e.,

$$\boldsymbol{\varepsilon}^e = \arg\left[\min_{f\left(\nabla\Psi(\boldsymbol{\varepsilon}^{e'})\right)\leq 0} \frac{1}{2}\left\|\boldsymbol{\varepsilon}^{e,trial} - \boldsymbol{\varepsilon}^{e'}\right\|_{\mathbb{C}}^2\right] \tag{3.4}$$

where $\|\cdot\|_{\mathbb{C}} := \sqrt{\cdot : \mathbb{C} \cdot}$ is the energy norm.

Such a geometric interpretation follows by noting that the Lagrange multiplier functional, $\mathcal{L}_m$, associated with the constrained problem (3.4), is expressed as:

$$\mathcal{L}_m\left(\boldsymbol{\varepsilon}^{e'}, \Delta\delta\right) := \frac{1}{2}\left\|\boldsymbol{\varepsilon}^{e,trial} - \boldsymbol{\varepsilon}^{e'}\right\|_{\mathbb{C}}^2 + \Delta\delta f\left(\nabla\Psi(\boldsymbol{\varepsilon}^{e'})\right) \tag{3.5}$$

and the corresponding KT optimality conditions are:

$$\begin{cases} \left.\dfrac{\partial\mathcal{L}_m}{\partial\boldsymbol{\varepsilon}^e}\right|_{n+1} := \mathbb{C}\left[-\boldsymbol{\varepsilon}^{e,trial} + \boldsymbol{\varepsilon}^e + \Delta\gamma\left.\dfrac{\partial f}{\partial\boldsymbol{\sigma}}\right|_{n+1}\right] \\ \Delta\gamma \geq 0,\ f\left(\nabla\Psi(\boldsymbol{\varepsilon}^e)\right) \leq 0,\ \Delta\gamma f\left(\nabla\Psi(\boldsymbol{\varepsilon}^e)\right) = 0 \end{cases} \tag{3.6}$$

1. **Elastic Trial Step**
   We assume that no plastic deformation occurs in the interval $[t_n, t_{n+1}]$.
   We have as trial values:

$$\begin{cases} \boldsymbol{\varepsilon}^{p,trial} = \boldsymbol{\varepsilon}_n^p \\ \Delta\gamma = 0 \\ \boldsymbol{\sigma}^{trial} = \mathbb{C}\left(\boldsymbol{\varepsilon} - \boldsymbol{\varepsilon}^{p,trial}\right) \end{cases}$$

   If the elastic trial state is admissible, i.e., $f^{trial} = f\left(\boldsymbol{\sigma}^{trial}\right) \leq 0$, then it represents the new solution at t_{n+1} and step 2 is skipped.
   If the elastic trial state is not admissible, a plastic correction is performed.

2. **Plastic Corrector Step**
   We solve the following system:

$$\begin{cases} \boldsymbol{\varepsilon}^p = \boldsymbol{\varepsilon}_n^p + \Delta\gamma \partial_{\boldsymbol{\sigma}} f\left(\boldsymbol{\sigma}\right) \\ f\left(\boldsymbol{\sigma}\right) = 0 \end{cases}$$

   complemented with $\boldsymbol{\sigma} = \mathbb{C}\left(\boldsymbol{\varepsilon} - \boldsymbol{\varepsilon}^p\right)$.
   The plastic corrector stage consists in finding a solution $\{\boldsymbol{\varepsilon}^p, \Delta\gamma\}$, satisfying $\Delta\gamma > 0$.

Table 3.1: Return-mapping algorithm for J_2 rate-independent perfect plasticity.

which coincide with system of equations (3.1). Here, $\boldsymbol{\varepsilon}^{e'}$ and $\Delta\delta$ are the generic elastic strain and Lagrange multiplier, respectively; $\boldsymbol{\varepsilon}^e$ and $\Delta\gamma$ denote the elastic strain and the Lagrange multiplier at the solution.

We formulate on the algorithmic scheme for problem (3.4) as a minimization procedure. Then, we consider the Newton-Raphson algorithm reported in Table 3.2. Since $E_{\boldsymbol{\sigma}}$ is convex, the algorithm is unconditionally convergent, regardless of the initial starting point $\boldsymbol{\varepsilon}^{e,trial}$. Technically, step-size adjustment is needed (Luenberger, 1984).

The *penalty functional*, $\mathcal{L}_p$, associated with the constrained problem (3.4), is expressed as:

$$\mathcal{L}_p\left(\boldsymbol{\varepsilon}^{e'}\right) := \frac{1}{2}\left\|\boldsymbol{\varepsilon}^{e,trial} - \boldsymbol{\varepsilon}^{e'}\right\|_{\mathbb{C}}^2 + \frac{1}{2}\left\langle cf\left(\nabla\Psi(\boldsymbol{\varepsilon}^{e'})\right)\right\rangle^2 \tag{3.7}$$

where c is a positive penalty parameter.

The *Augmented Lagrangian functional*, $\mathcal{L}_a$, associated with the constrained problem (3.4), is expressed as:

$$\mathcal{L}_a\left(\boldsymbol{\varepsilon}^{e'}, \Delta\delta\right) := \frac{1}{2}\left\|\boldsymbol{\varepsilon}^{e,trial} - \boldsymbol{\varepsilon}^{e'}\right\|_{\mathbb{C}}^2 + \frac{1}{2c}\left(\left\langle \Delta\delta + cf\left(\nabla\Psi(\boldsymbol{\varepsilon}^{e'})\right)\right\rangle^2 - \Delta\delta^2\right) \tag{3.8}$$

Stress-space formulation

A similar interpretation holds in stress-space. From Eq. (3.2) we have:

$$\boldsymbol{\sigma} = \boldsymbol{\sigma}^{trial} - \Delta\gamma\, \mathbb{C}\, \nabla f\left(\boldsymbol{\sigma}\right) \tag{3.9}$$

where $\boldsymbol{\sigma}^{trial} = \mathbb{C}\left(\boldsymbol{\varepsilon} - \boldsymbol{\varepsilon}_n^p\right)$. It follows that, for an associative flow rule, $\boldsymbol{\sigma}$ is the *closest point projection* in the energy norm of the trial elastic stress $\boldsymbol{\sigma}^{trial}$ onto the yield surface, i.e.,

$$\boldsymbol{\sigma} = \arg\left[\min_{\boldsymbol{\tau}\in E_{\boldsymbol{\sigma}}} \frac{1}{2}\left\|\boldsymbol{\sigma}^{trial} - \boldsymbol{\tau}\right\|_{\mathbb{C}^{-1}}^2\right] \tag{3.10}$$

1. Define the residual at iteration (k) by:

$$\nabla \mathcal{L}_m^{(k)} := \left[\partial_{\boldsymbol{\varepsilon}^e} \mathcal{L}_m^{(k)} \;\; \partial_{\Delta\delta} \mathcal{L}_m^{(k)}\right]^T$$

2. Check whether convergence is attained. If $\left\|\nabla \mathcal{L}_m^{(k)}\right\| < tol$, then EXIT.

3. ELSE compute Hessian matrix $\nabla^2 \mathcal{L}_m^{(k)}$.

4. Solve the linearized system:

$$\nabla^2 \mathcal{L}_m^{(k)} \left[\Delta \boldsymbol{\varepsilon}^{e(k)} \;\; \Delta^2 \delta^{(k)}\right]^T = -\nabla \mathcal{L}_m^{(k)}$$

5. Update the solution, as follows:

$$\begin{cases} \Delta\delta^{(k+1)} = \Delta\delta^{(k)} + \Delta^2\delta^{(k)} \\ \boldsymbol{\varepsilon}^{e(k+1)} = \boldsymbol{\varepsilon}^{e(k)} + \Delta\boldsymbol{\varepsilon}^{e(k)} \end{cases}$$

6. Update $k = k + 1$.

7. GO to step 2.

Table 3.2: Newton-Raphson algorithm to solve problem (3.4) in strain-space.

where $\|\cdot\| := \sqrt{\cdot : \mathbb{C}^{-1} \cdot}$.

Such a geometric interpretation follows by noting that the Lagrangian multiplier functional, $\mathcal{L}_m$, associated with the constrained problem (3.10), is expressed as:

$$\mathcal{L}_m(\boldsymbol{\tau}, \Delta\delta) := \frac{1}{2} \left\|\boldsymbol{\sigma}^{trial} - \boldsymbol{\tau}\right\|^2_{\mathbb{C}^{-1}} + \Delta\delta f(\boldsymbol{\tau}) \tag{3.11}$$

The associated KT optimality conditions are given by:

$$\begin{cases} \left.\dfrac{\partial \mathcal{L}_m}{\partial \boldsymbol{\sigma}}\right|_{n+1} := \mathbb{C}^{-1}\left[-\boldsymbol{\sigma}^{trial} + \boldsymbol{\sigma}\right] + \Delta\gamma \left.\dfrac{\partial f}{\partial \boldsymbol{\sigma}}\right|_{n+1} \\ \Delta\gamma \geq 0,\; f(\boldsymbol{\sigma}) \leq 0,\; \Delta\gamma f(\boldsymbol{\sigma}) = 0 \end{cases} \tag{3.12}$$

which coincide with system of equations (3.1). Here, $\boldsymbol{\tau}$ and $\Delta\delta$ are the generic stress and Lagrange multiplier, respectively; $\boldsymbol{\varepsilon}^e$ and $\Delta\gamma$ denote the stress and the Lagrange multiplier at the solution, respectively.

Again, we formulate the algorithmic scheme for problem (3.10) as a minimization procedure. Then, we consider the Newton-Raphson algorithm reported in Table 3.3. Since $E_{\boldsymbol{\sigma}}$ is convex, the algorithm is unconditionally convergent, regardless of the initial starting point $\boldsymbol{\sigma}^{trial}$. Technically, step-size adjustment is needed, see, e.g., (Luenberger, 1984).

The *Augmented Lagrangian functional*, $\mathcal{L}_a$, associated to the constrained problem (3.10), is given by (Armero and Pérez-Foguet, 2002a):

$$\mathcal{L}_a(\boldsymbol{\tau}, \Delta\delta) := \frac{1}{2} \left\|\boldsymbol{\sigma}^{trial} - \boldsymbol{\tau}\right\|^2_{\mathbb{C}^{-1}} + \frac{c}{2}\left[\left\langle \frac{\Delta\delta}{c} + f(\boldsymbol{\tau})\right\rangle^2 - \left(\frac{\Delta\delta}{c}\right)^2\right] \tag{3.13}$$

for a general scalar variable $\Delta\delta$, not constrained to be non-negative as in the case for the plastic multiplier previously employed.

1. Define the residual at iteration (k) by:

$$\nabla \mathcal{L}_m^{(k)} := \left[\partial_{\boldsymbol{\sigma}} \mathcal{L}_m^{(k)} \;\; \partial_{\Delta\delta} \mathcal{L}_m^{(k)}\right]^T$$

2. Check whether convergence is attained. If $\left\|\nabla \mathcal{L}_m^{(k)}\right\| < tol$, then EXIT.

3. ELSE compute Hessian matrix $\nabla^2 \mathcal{L}_m^{(k)}$.

4. Solve the linearized system:

$$\nabla^2 \mathcal{L}_m^{(k)} \left[\Delta\boldsymbol{\sigma}^{(k)} \;\; \Delta^2\delta^{(k)}\right]^T = -\nabla \mathcal{L}_m^{(k)}$$

5. Update the solution, as follows:

$$\begin{cases} \Delta\delta^{(k+1)} = \Delta\delta^{(k)} + \Delta^2\delta^{(k)} \\ \boldsymbol{\sigma}^{(k+1)} = \boldsymbol{\sigma}^{(k)} + \Delta\boldsymbol{\sigma}^{(k)} \end{cases}$$

6. Update $k = k + 1$.

7. GO to step 2.

Table 3.3: Newton-Raphson algorithm to solve problem (3.10) in stress-space.

Setting the gradient of the Augmented Lagrangian functional (3.13) to zero and denoting the final solution by $(\boldsymbol{\sigma}, \Delta\gamma)$ leads to:

$$\begin{cases} \dfrac{\partial \mathcal{L}_a}{\partial \boldsymbol{\sigma}}\Big|_{(\boldsymbol{\sigma},\Delta\gamma)} = 0 \\ \dfrac{\partial \mathcal{L}_a}{\partial \Delta\delta}\Big|_{(\boldsymbol{\sigma},\Delta\gamma)} = 0 \end{cases} \tag{3.14}$$

where the solution coincides with the solution of the original closest-point projection equations for the case of associate plasticity. In particular, Eq. $(3.14)_2$ can be rewritten as:

$$\frac{\partial \mathcal{L}_a}{\partial \Delta\delta}\Big|_{(\boldsymbol{\sigma},\Delta\gamma)} = \frac{1}{c}\left[\langle \Delta\gamma + cf(\boldsymbol{\sigma})\rangle - \Delta\gamma\right] = 0 \tag{3.15}$$

from which we identify the relation:

$$\Delta\lambda = \langle \Delta\gamma + cf(\boldsymbol{\sigma})\rangle \tag{3.16}$$

The fact that solution, $(\boldsymbol{\sigma}, \Delta\gamma)$, of system of equations (3.14) corresponds to the solution of the closest-point projection equations, follows after noting that:

$$\Delta\gamma + cf(\boldsymbol{\sigma}) \leq 0 \quad \Rightarrow \quad \Delta\gamma = 0 \quad \Rightarrow \quad \Delta\lambda = 0 \tag{3.17}$$

and

$$\Delta\gamma + cf(\boldsymbol{\sigma}) > 0 \quad \Rightarrow \quad f(\boldsymbol{\sigma}) = 0 \Rightarrow \Delta\lambda = \langle \Delta\gamma\rangle > 0 \tag{3.18}$$

which recover the discrete Kuhn-Tucker conditions (2.34).
The Augmented Lagrangian functional can be written also in the form (Cuomo and Contrafatto, 2000):

$$\mathcal{L}_a(\boldsymbol{\tau}, \Delta\delta) := \frac{1}{2}\left\|\boldsymbol{\sigma}^{trial} - \boldsymbol{\tau}\right\|^2_{\mathbb{C}^{-1}} + \Delta\delta\, \overline{f}(\boldsymbol{\tau}) + \frac{1}{2}\, c\left|\overline{f}(\boldsymbol{\tau})\right|^2 \tag{3.19}$$

where c is a positive penalty parameter and the function $\overline{f}(\boldsymbol{\sigma})$:

$$\overline{f}(\boldsymbol{\sigma}) = \max\left[f(\boldsymbol{\sigma}), -\frac{\Delta\delta}{c}\right] \tag{3.20}$$

converts the inequality constraint $f(\boldsymbol{\sigma}) \leq 0$ into the equality one $\overline{f}(\boldsymbol{\sigma}) = 0$, removes the sign restriction on the Lagrangian multiplier and preserves the functional continuity in a neighbor of the solution.

For further details about the numerical treatment, the reader is referred to (Armero and Pérez-Foguet, 2002a).

Remark 3.2.1. *The normality law, in its subdifferential form, is equivalent to the inverse subdifferential relation:*

$$\boldsymbol{\sigma} \in \partial\phi(\dot{\boldsymbol{\varepsilon}}^p) \tag{3.21}$$

Moreover:

$$\partial I_{E_{\boldsymbol{\sigma}}}(\boldsymbol{\sigma}) \ni \dot{\boldsymbol{\varepsilon}}^p \tag{3.22}$$

and

$$\partial\phi^*(\boldsymbol{\sigma}) \ni \dot{\boldsymbol{\varepsilon}}^p \tag{3.23}$$

Since the elastic stress-strain relationship yields:

$$\boldsymbol{\sigma} = \mathbb{C}(\boldsymbol{\varepsilon} - \dot{\boldsymbol{\varepsilon}}^p) \tag{3.24}$$

we obtain:

$$\dot{\boldsymbol{\varepsilon}}^p = -\mathbb{C}^{-1}\dot{\boldsymbol{\sigma}} + \dot{\boldsymbol{\varepsilon}} \tag{3.25}$$

Substituting Eq. (3.22) *in Eq.* (3.25)*, we obtain:*

$$\mathbb{C}^{-1}\dot{\boldsymbol{\sigma}} + \partial I_{E_{\boldsymbol{\sigma}}}(\boldsymbol{\sigma}) \ni \dot{\boldsymbol{\varepsilon}} \tag{3.26}$$

In variational terms:

$$\mathbb{C}^{-1}\boldsymbol{\sigma} + \partial I_{E_{\boldsymbol{\sigma}}}(\boldsymbol{\sigma}) \ni \boldsymbol{\varepsilon} - \boldsymbol{\varepsilon}_n + \mathbb{C}^{-1}\boldsymbol{\sigma}_n \tag{3.27}$$

from which:

$$\boldsymbol{\sigma} = \left(\mathbb{C}^{-1} + \partial I_{E_{\boldsymbol{\sigma}}}(\boldsymbol{\sigma})\right)^{-1}\left(\boldsymbol{\varepsilon} - \boldsymbol{\varepsilon}_n + \mathbb{C}^{-1}\boldsymbol{\sigma}_n\right) \tag{3.28}$$

where $\left(\mathbb{C}^{-1} + \partial I_{E_{\boldsymbol{\sigma}}}(\boldsymbol{\sigma})\right)^{-1}$ *and* $\left(\boldsymbol{\varepsilon} - \boldsymbol{\varepsilon}_n + \mathbb{C}^{-1}\boldsymbol{\sigma}_n\right)$ *represent the projection onto* $E_{\boldsymbol{\sigma}}$ *and the elastic trial, respectively.*

3.3 The principle of maximum plastic dissipation

We now elaborate on the algorithmic treatment of Eqs. (2.91) and (2.79).
For the sake of notation simplicity, the convention establishes superscript n for all the variables evaluated at time t_n, while drops superscript $n+1$ for all the variables computed at time t_{n+1}. Knowing the strain, $\boldsymbol{\varepsilon}$, at time t_{n+1} and the solution at time t_n, represented by the ordered set $\{\boldsymbol{\sigma}_n, \boldsymbol{\varepsilon}_n, \boldsymbol{\varepsilon}_n^p\}$, we need to compute the solution at time t_{n+1}.

3.3.1 Augmented Lagrangian formulation

To achieve a stable time-integration, we apply a backward-Euler scheme to system (2.91) (Schmidt-Baldassari, 2003). We gain the following time-discrete formulation:

$$\begin{cases} \boldsymbol{\varepsilon}^p = \boldsymbol{\varepsilon}_n^p + \max\left[0, \Delta\gamma + \Delta t c f\left(\boldsymbol{\sigma}\right)\right] \partial_{\boldsymbol{\sigma}} f\left(\boldsymbol{\sigma}\right) \\ \Delta\gamma = \max\left[0, \Delta\gamma + \Delta t c f\left(\boldsymbol{\sigma}\right)\right] \end{cases} \tag{3.29}$$

where $\Delta\gamma = \int_{t_n}^{t_{n+1}} \dot{\gamma} dt$ is the time-integrated consistency parameter.

Now, a favorable algorithmic scheme can be developed by solving the discrete consistency condition $(3.29)_2$ with aid of a fixed-point iteration scheme:

$$\Delta\gamma^{(i+1)} = \max\left[0, \Delta\gamma^{(i)} + \Delta t c f\left(\boldsymbol{\sigma}^{(i)}\right)\right] \tag{3.30}$$

starting from $\Delta\gamma^{(1)} = 0$ and with $\boldsymbol{\sigma}^{(i)} = \mathbb{C}\left(\boldsymbol{\varepsilon} - \boldsymbol{\varepsilon}^{p(i)}\right)$. The intermediate states of the plastic strain is given implicitly via:

$$\boldsymbol{\varepsilon}^{p(i)} = \boldsymbol{\varepsilon}_n^p + \max\left[0, \Delta\gamma^{(i)} + \Delta t c f\left(\boldsymbol{\sigma}^{(i)}\right)\right] \partial_{\boldsymbol{\sigma}} f^{(i)} \tag{3.31}$$

The solution of (3.31) cannot be derived in closed form. The usage of a damped Newton-Raphson scheme, where the damping guarantees the convergence of the Newton-Raphson scheme on the non-smooth function, has been proposed (Allen and Isaacson, 1998). Within the fixed-point steps, the yield conditions can be fulfilled with arbitrary accuracy independent of the choice of c, but the number of iteration steps depends on c. Therefore, it seems to be convenient to replace c by a variable penalty factor $c^{(i)}$ and add the relation:

$$c^{(i+1)} = m c^{(i)}, \;\; c^{(1)} = c^0, \;\; m > 1 \tag{3.32}$$

Now, we are able to start the iterations using a substantially small penalty factor, which implies a rather smooth and well-conditioned problem. A rapid increase in c assures fast convergence of the fixed-point scheme.
The scheme is summarized in Table 3.4.

---

1. Start with $i = 1$.
2. Assume $\Delta\gamma^{(1)} = 0$ and $c^{(1)} = c^0$.
3. Solve (3.31).
4. Update (3.30).
5. If fixed-point reached, evaluate $\boldsymbol{\varepsilon}^p$ and EXIT.
6. Update $c^{(i+1)} = m c^{(i)}$.
7. GO to step 3.

Table 3.4: Fixed-point iteration scheme for the discrete Augmented Lagrangian formulation (3.29) of the principle of maximum plastic dissipation.

3.3.2 Penalty formulation

The time-integration of the penalty formulation (2.79) reduces simply to the first step during the fixed-point iteration in the implementation of the Augmented Lagrangian method as, for $i = 1$, Eq. (3.31) takes the

form (Schmidt-Baldassari, 2003):

$$\boldsymbol{\varepsilon}^{p(1)} = \boldsymbol{\varepsilon}_n^p + \max\left[0, \Delta t c f\left(\boldsymbol{\sigma}^{(1)}\right)\right] \partial_{\boldsymbol{\sigma}} f^{(1)} \tag{3.33}$$

This relation, together with $\boldsymbol{\varepsilon}^{p(1)} = \boldsymbol{\varepsilon}^p$, is exactly a backward-Euler step applied to the flow rule (2.79).

Numerical difficulties in the penalty formulation could be caused by the non-differentiable right-hand side of Eq. (2.79). Moreover, possible disadvantages could be due to slow convergence and ill-conditioning when minimizing Eq. (2.78) for large values of c (Bertsekas, 1982). In fact, the larger the penalty factor, c, the better is the approximation to a solution of the original problem (2.64).

Penalty formulation in a one-dimensional setting

Now, we reduce Eq. (2.79) to a one-dimensional setting.
The yield criterion f can be written as follows:

$$f(\sigma) = |\sigma| - \sigma_y = |E(\varepsilon - \varepsilon^p)| - \sigma_y \tag{3.34}$$

where σ_y and E are the yield stress and the elastic constant, respectively. Accordingly, Eq. (2.79) can be rewritten as follows:

$$\dot{\varepsilon^p} = \max[0, cf(\sigma)]\frac{\sigma}{|\sigma|} = \max[0, c(|E(\varepsilon - \varepsilon^p)| - \sigma_y)]\frac{\sigma}{|\sigma|} \tag{3.35}$$

Assume that during tensile loading ($\sigma > 0$) plastic deformation takes place. Eq. (3.35) becomes:

$$\dot{\varepsilon^p} = cE(\varepsilon - \varepsilon^p) - c\sigma_y \tag{3.36}$$

Now, we discretize in time, i.e., $\dot{\varepsilon^p} = (\varepsilon^p - \varepsilon_n^p)/\Delta t$, and we substitute in Eq. (3.36):

$$\frac{\varepsilon^p - \varepsilon_n^p}{\Delta t} = cE(\varepsilon - \varepsilon^p) - c\sigma_y \tag{3.37}$$

After some simplifications, we obtain:

$$\varepsilon^p = \frac{1}{\dfrac{1}{\Delta t} + cE}\left(c\alpha + \frac{\varepsilon_n^p}{\Delta t}\right) \tag{3.38}$$

where $\alpha = E\varepsilon - \sigma_y$. The expression for the stress σ can be rewritten in the form:

$$\sigma = E(\varepsilon - \varepsilon^p) = \alpha + \sigma_y - E\varepsilon^p \tag{3.39}$$

Consider a time interval $[0, 1]$ with a constant time-step $\Delta t = 0.1$ and assume $\sigma_y = 1$ MPa, $E = 1$ MPa and α increasing from 0 to 9. Figures 3.1(a), 3.1(b) and 3.1(c) represent diagrams in terms of plastic strain, $\alpha = E\varepsilon - \sigma_y$, and stress, varying the penalty parameter, c. We may observe that as c is increased, the diagrams plot the exact solution for perfect plasticity.

3.4 The energy minimization problem

This Section presents the J_2 perfect elastoplastic model within the incremental energy minimization framework (Petryk, 2003). In particular, the aim is to examine the applicability of the incremental energy minimization to time-independent dissipative solids when the increments of the internal variable are treated as independent unknown. Three constitutive functions are involved: the Helmholtz free-energy, the rate-independent dissipation, and the constraint function.

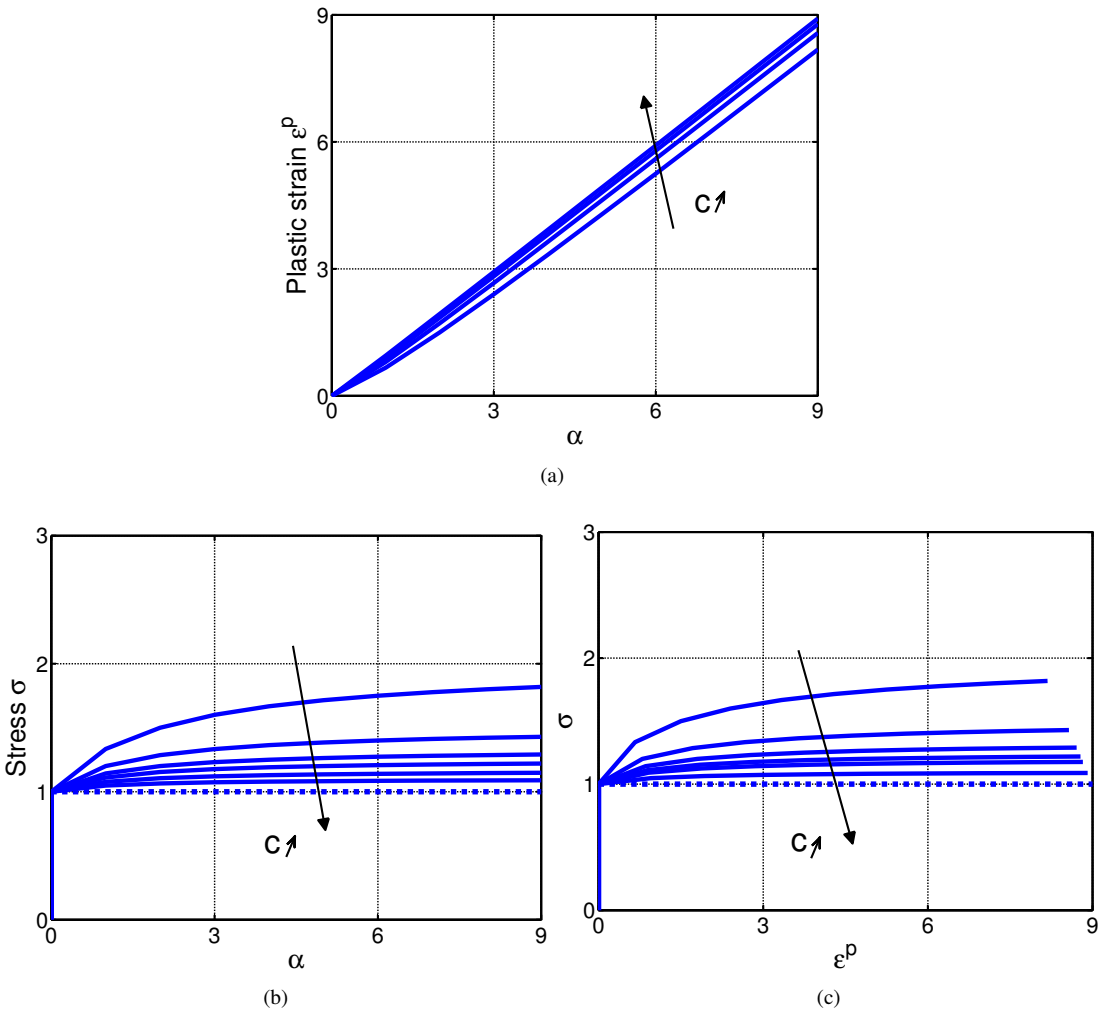

Figure 3.1: One-dimensional setting for the discrete penalty formulation (3.33) of the principle of maximum plastic dissipation. Diagrams in terms of: (a) plastic strain, ε^p, and $\alpha = E\varepsilon - \sigma_y$; (b) stress, σ, and $\alpha = E\varepsilon - \sigma_y$; (c) stress, σ, and plastic strain, ε^p, varying the penalty parameter, c.

Again, for the sake of notation simplicity, the convention establishes superscript n for all the variables evaluated at time t_n, while drops superscript $n+1$ for all the variables computed at time t_{n+1}. Knowing the strain, $\boldsymbol{\varepsilon}$, at time t_{n+1} and the solution at time t_n, represented by the ordered set $\{\boldsymbol{\sigma}_n, \boldsymbol{\varepsilon}_n, \boldsymbol{\varepsilon}_n^p\}$, we need to compute the solution at time t_{n+1}.

Starting from the definition of the Helmholtz free-energy function, $\Psi = \Psi(\boldsymbol{\varepsilon}, \boldsymbol{\varepsilon}^p)$:

$$\Psi := \frac{1}{2}(\boldsymbol{\varepsilon} - \boldsymbol{\varepsilon}^p) : \mathbb{C}(\boldsymbol{\varepsilon} - \boldsymbol{\varepsilon}^p) \tag{3.40}$$

and of the plastic dissipation function, $D^p = D^p(\boldsymbol{\sigma}; \dot{\boldsymbol{\varepsilon}}^p)$:

$$D^p := \boldsymbol{\sigma} : \dot{\boldsymbol{\varepsilon}}^p \tag{3.41}$$

we recover the elastic stress-strain relationship:

$$\boldsymbol{\sigma} = -\partial_{\boldsymbol{\varepsilon}^p}\Psi = \mathbb{C}(\boldsymbol{\varepsilon} - \boldsymbol{\varepsilon}^p) \tag{3.42}$$

as wee as the normality law, in its subdifferential form, which is equivalent to the inverse subdifferential relation:

$$\boldsymbol{\sigma} \in \partial D^p(\dot{\boldsymbol{\varepsilon}}^p) \tag{3.43}$$

From Eqs. (3.43) and (3.42) we have:

$$\partial_{\boldsymbol{\varepsilon}^p} \Psi\left(\boldsymbol{\varepsilon}^p; \boldsymbol{\varepsilon}\right) + \partial D^p(\dot{\boldsymbol{\varepsilon}}^p) = 0 \tag{3.44}$$

Substituting $\dot{\boldsymbol{\varepsilon}}^p$ by its incremental form $(\boldsymbol{\varepsilon}^p - \boldsymbol{\varepsilon}_n^p)$ (time step Δt can be neglected), Eq. (3.44) becomes:

$$\partial_{\boldsymbol{\varepsilon}^p} \Psi\left(\boldsymbol{\varepsilon}^p; \boldsymbol{\varepsilon}\right) + \partial D^p(\boldsymbol{\varepsilon}^p - \boldsymbol{\varepsilon}_n^p) = 0 \tag{3.45}$$

Now, we introduce the total energy in the incremental form:

$$\Delta e = \Delta\Psi + \Delta D^p \tag{3.46}$$

where:

$$\Delta\Psi = \Psi\left(\boldsymbol{\varepsilon}^p; \boldsymbol{\varepsilon}\right) - \Psi\left(\boldsymbol{\varepsilon}_n^p; \boldsymbol{\varepsilon}_n\right) \tag{3.47}$$

and ΔD^p represents the energy dissipation related to jumps from one energy well to another:

$$\Delta D^p = \boldsymbol{\sigma} : (\boldsymbol{\varepsilon}^p - \boldsymbol{\varepsilon}_n^p) \tag{3.48}$$

It is assumed that the increment, symbolized by Δ, is sufficiently small to treat all changes within the increment as monotonic. The increments can be arbitrarily small, so that the formulation covers both the time-discrete form and the time-continuous rate form in the limit. Note that the incremental dissipation, ΔD^p, does not vanish with reducing the rate of change of $\boldsymbol{\varepsilon}^p$ with respect to a natural time to zero as it is independent of that rate.

With the rate-independence property of ΔD^p used, the material response is postulated to be governed by the incremental energy minimization principle (Petryk, 2003).

$$\text{Find } \boldsymbol{\varepsilon}_{n+1}^p : \min_{f \le 0} \Delta e \;\; (\text{for given } \boldsymbol{\varepsilon}) \tag{3.49}$$

The solution can be shown to be unique if Ψ is strictly convex (Petryk, 2003).

Lagrangian multiplier formulation

The *Lagrangian multiplier functional*, $\mathcal{L}_m$, associated with the constrained problem (3.49), is expressed as:

$$\mathcal{L}_m\left(\boldsymbol{\varepsilon}^{p'}, \Delta\delta\right) := \Psi\left(\boldsymbol{\varepsilon}^{p'}; \boldsymbol{\varepsilon}\right) + \Delta D^p\left(\boldsymbol{\varepsilon}^{p'} - \boldsymbol{\varepsilon}_n^p\right) - \Delta\delta f\left(-\nabla\Psi(\boldsymbol{\varepsilon}^{p'})\right) \tag{3.50}$$

and the corresponding KuhnTucker optimality conditions are:

$$\begin{cases} \left.\dfrac{\partial \mathcal{L}_m}{\partial \boldsymbol{\varepsilon}^p}\right|_{(\boldsymbol{\varepsilon}^p, \Delta\gamma)} := \mathbb{C}\left[\boldsymbol{\varepsilon}^p - \boldsymbol{\varepsilon}_n^p - \Delta\gamma \left.\dfrac{\partial f}{\partial \boldsymbol{\sigma}}\right|_{n+1}\right] \\ \Delta\gamma \ge 0,\; f\left(-\nabla\Psi(\boldsymbol{\varepsilon}^p)\right) \le 0,\; \Delta\gamma f\left(-\nabla\Psi(\boldsymbol{\varepsilon}^p)\right) = 0 \end{cases} \tag{3.51}$$

We note that, for the minimum, the parts of Eq. (3.49) which depend only on the previous time step are of no interest.

Penalty formulation

The *penalty functional*, $\mathcal{L}_p$, associated with the constrained problem (3.49), is expressed as:

$$\mathcal{L}_p\left(\boldsymbol{\varepsilon}^{p'}\right) := \Psi\left(\boldsymbol{\varepsilon}^{p'};\boldsymbol{\varepsilon}\right) + \Delta D^p\left(\boldsymbol{\varepsilon}^{p'} - \boldsymbol{\varepsilon}_n^p\right) - \frac{1}{2}\left\langle cf\left(-\nabla\Psi(\boldsymbol{\varepsilon}^{p'})\right)\right\rangle^2 \tag{3.52}$$

Augmented Lagrangian formulation

The *Augmented Lagrangian functional*, $\mathcal{L}_a$, associated with the constrained problem (3.49), is expressed as:

$$\mathcal{L}_a\left(\boldsymbol{\varepsilon}^{p'};\Delta\delta\right) := \Psi\left(\boldsymbol{\varepsilon}^{p'};\boldsymbol{\varepsilon}\right) + \Delta D^p\left(\boldsymbol{\varepsilon}^{p'} - \boldsymbol{\varepsilon}_n^p\right) - \frac{1}{2c}\left(\left\langle\Delta\delta + cf\left(-\nabla\Psi(\boldsymbol{\varepsilon}^{p'})\right)\right\rangle^2 - \Delta\delta^2\right) \tag{3.53}$$

3.5 Complementarity problem functions

We now elaborate on the algorithmic treatment of the complementary problem functions, presented in Section 2.6. Again, for the sake of notation simplicity, the convention establishes superscript n for all the variables evaluated at time t_n, while drops superscript $n+1$ for all the variables computed at time t_{n+1}. Knowing the strain, $\boldsymbol{\varepsilon}$, at time t_{n+1} and the solution at time t_n, represented by the ordered set $\{\boldsymbol{\sigma}_n, \boldsymbol{\varepsilon}_n, \boldsymbol{\varepsilon}_n^p\}$, we need to compute the solution at time t_{n+1}.

3.5.1 Fischer-Burmeister complementarity problem function

The discrete Kuhn-Tucker conditions $(3.1)_2$ are substituted by the following discrete Fischer-Burmeister (FB) function in the time-discrete frame:

$$\sqrt{f^2 + \Delta\gamma^2 + 2\delta} + f - \Delta\gamma = 0 \tag{3.54}$$

As we will note in next Chapter, possible numerical difficulties, especially for complex model problems, can be linked to the numerical sensitiveness of the FB scheme (due to the presence of the regularization parameter δ) and to the proper choice of Newton-Raphson initial guess to guarantee a fast and correct convergence. To overcome potential difficulties it is possible to apply a line search strategy.

3.5.2 A different form of complementarity problem function

Chen-Mangasarian smoothing procedure

The discrete Kuhn-Tucker conditions $(3.1)_2$ can be substituted by the following Chen-Mangasarian (CM) function in the time-discrete frame, which is the discrete form of Eq. (2.136):

$$-f - \frac{1}{\alpha}\ln\left[1 + \exp^{-\alpha(\Delta\gamma+f)}\right] = 0 \tag{3.55}$$

Balakrishna-Biegler smoothing procedure

The discrete Kuhn-Tucker conditions $(3.1)_2$ can be substituted by the following Balakrishna-Biegler (BB) function in the time-discrete frame, which is the discrete form of Eq. (2.141):

$$\frac{\Delta\gamma - f}{2} - \frac{\sqrt{(\Delta\gamma + f)^2 + \epsilon^2}}{2} = 0 \tag{3.56}$$

Chapter 4

Numerical tests for J_2 elastoplasticity

This Chapter is devoted to the numerical investigation of two integration algorithms for J_2 elastoplasticity with linear isotropic kinematic hardening, presented in Chapter 2, i.e., the return-mapping and the Fischer-Burmeister algorithms. The proposed numerical analysis is intended to provide a comparison in terms of precision and efficiency and it is carried out through several kinds of numerical tests, ranging from mixed stress-strain loading histories to initial boundary-value problems on three-dimensional material bodies.

The Chapter is organized as follows. Section 4.1 briefly presents the governing equations for J_2 elastoplasticity with linear isotropic kinematic hardening, in both time-continuous and time-discrete frameworks. Then, Section 4.2 concerns with the setup of the numerical tests and the investigation of the two numerical schemes.

4.1 Outline of the governing equations for J_2 elastoplasticity

We recall the following system of time-continuous equations for J_2 elastoplasticity with linear isotropic kinematic hardening, already introduced in Section 2.2:

$$\begin{cases} p = K\theta \\ \mathbf{s} = 2G\left(\mathbf{e} - \mathbf{e}^p\right) \\ \boldsymbol{\Sigma} = \mathbf{s} - \boldsymbol{\alpha} \\ f = \|\boldsymbol{\Sigma}\| - \sigma_y \\ \dot{\boldsymbol{\varepsilon}}^p = \dot{\gamma}\mathbf{n} \\ \sigma_y = \sigma_{y,0} - H_{iso}\overline{e}^p \\ \dot{\boldsymbol{\alpha}} = H_{kin}\dot{\gamma}\mathbf{n} \\ \dot{\gamma} \geq 0,\ f \leq 0,\ \dot{\gamma}f = 0,\ \dot{\gamma}\dot{f} = 0 \end{cases} \tag{4.1}$$

where $\dot{\overline{e}}^p = \|\dot{\boldsymbol{\varepsilon}}^p\| = \dot{\gamma}$ and $\boldsymbol{\varepsilon}^p = \mathbf{e}^p$.

We now elaborate on the algorithmic treatment of system of equations (4.1). For the sake of notation simplicity, the convention establishes superscript n for all the variables evaluated at time t_n, while drops superscript $n+1$ for all the variables computed at time t_{n+1}. Thus, the corresponding system of time-

discrete equations follows:

$$\begin{cases} p = K\theta \\ \mathbf{s} = 2G\left(\mathbf{e} - \mathbf{e}^p\right) \\ \boldsymbol{\Sigma} = \mathbf{s} - \boldsymbol{\alpha} \\ f = \|\boldsymbol{\Sigma}\| - \sigma_y \\ \boldsymbol{\varepsilon}^p - \boldsymbol{\varepsilon}_n^p - \Delta\gamma\mathbf{n} = 0 \\ \sigma_y = \sigma_{y,0} - H_{iso}\overline{e}^p \\ \boldsymbol{\alpha} - \boldsymbol{\alpha}_n - H_{kin}\Delta\gamma\mathbf{n} = 0 \\ \Delta\gamma \geq 0,\ f \leq 0,\ \Delta\gamma f = 0 \end{cases} \tag{4.2}$$

where $\Delta\gamma = \int_{t_n}^{t_{n+1}} \dot{\gamma} dt$ is the time-integrated consistency parameter and $\overline{e}^p = \overline{e}_n^p + \Delta\gamma$.
The Kuhn-Tucker conditions of system of equations (4.2) can be equivalently rewritten as follows:

$$\sqrt{f^2 + \Delta\gamma^2} + f - \Delta\gamma = 0 \tag{4.3}$$

In the following, we focus on two algorithmic schemes, i.e., the return-mapping and Fischer-Burmeister based algorithms, already presented in Chapter 2. The FE implementation of model equations and of all the numerical examples presented in the next Section is carried out using the symbolic code generation system AceGen/AceFEM (Korelc, 2009). This system extends the symbolic capabilities of Mathematica (Wolfram, 2013a) with the automatic differentiation technique, simultaneous optimization of expressions, and automatic generation of program code. Accordingly, we do not provide explicit expressions resulting from differentiation as these are obtained automatically using the automatic differentiation technique implemented in AceGen (Korelc, 2009). Application of these automation tools leads to exact linearization of the non-linear FE equations (consistent tangent matrix). This guarantees quadratic convergence rate of the global Newton method and results in a robust and efficient FE implementation of the model. The reader is referred to Appendix B for further details about the AceGen and AceFEM packages.

Parameter	**Value**	**Unit**
E	21000	MPa
ν	0.3	-
$\sigma_{y,0}$	24	MPa
H_{iso}	100	MPa
H_{kin}	1	MPa

Table 4.1: J_2 elastoplastic model with linear isotropic kinematic hardening. Adopted parameters.

4.2 Numerical test setup

The present Section is devoted to the setup of several numerical tests in order to investigate two algorithmic schemes presented in Sections 3.2.2 and 3.5, i.e., the return-mapping and the Fischer-Burmeister based algorithms (denoted, respectively, as *RM* and *FB*). We carry out a detailed comparison of the presented methods in terms of accuracy, robustness, efficiency as well as of specific properties shown by each method. First, we consider mixed stress-strain loading histories for a material point in order to study both the accuracy and efficiency granted by the numerical methods with respect to the computation of the stress-strain asset. Then, we present two classical initial boundary-value problems (IBVPs), which we study to

analyze the algorithms reliability and efficiency on practical engineering problems. In the following, we first present the conducted tests; then, we discuss the obtained results. Table 4.1 lists the model parameters adopted in all the numerical tests.

4.2.1 Mixed stress-strain loading histories

We consider biaxial non-proportional stress-strain loading histories. Such histories are obtained assuming to control two strain components and four stress components, particularly, $\{\epsilon_{11}, \epsilon_{22}, \sigma_{33}, \sigma_{12}, \sigma_{13}, \sigma_{23}\}$. For each loading history we require that all the controlled stress components are identically equal to zero, while the strains are varied according to a chosen history. In particular, we investigate two types of loading histories, defined on the reference time interval $[0, T]$, with T equal to 8 and 10 s, respectively. The histories consist of an hourglass- and a square-shaped strain history input, respectively, where the strain components, ϵ_{11} and ϵ_{22}, vary in the range $\pm 4\%$, as shown in Figures 4.1(a)-(d).

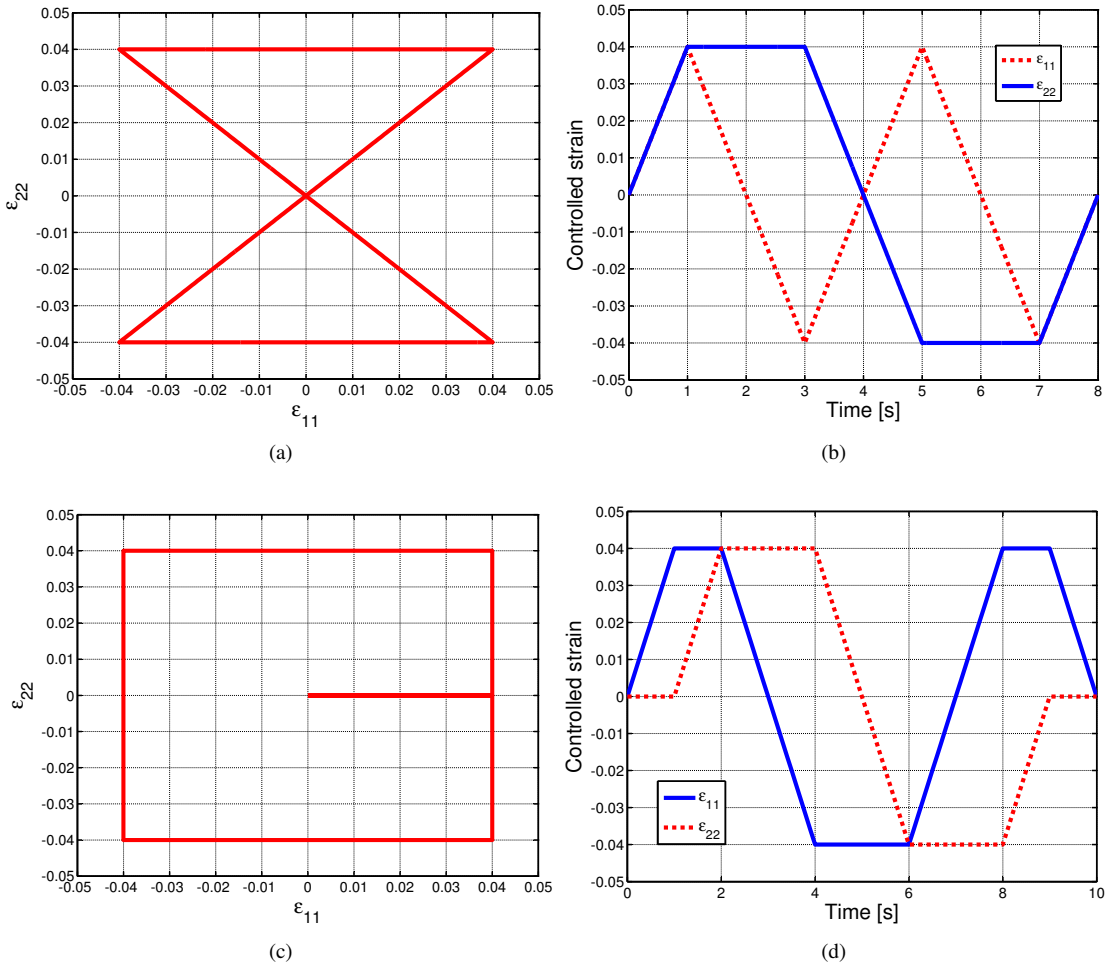

Figure 4.1: Mixed stress-strain loading histories. (a)-(b) Butterfly- and (c)-(d) square-shaped history inputs under strain control up to 4%.

Algorithm	**Steps/second**	**Aver. Newton iteration number/step**	**Aver. comput. time/step** [s]
RM	2	4.875	0.1148
	20	3.9063	0.0457
	500	3.3293	0.0426
FB	2	5.0625	0.1194
	20	4.2688	0.0489
	500	3.8818	0.0499

Table 4.2: Biaxial butterfly-shaped loading history input. Comparison of computational efficiency between the RM and the FB algorithmic schemes in terms of average number of global Newton iterations and average computational time per time step increment.

Iterations and computational time

The biaxial non-proportional tests are performed using time step increments, Δt, of 0.5, 0.05 and 0.002 s, corresponding to 2, 20 and 500 steps per second. To assess the computational efficiency of the RM and FB algorithms, Tables 4.2 and 4.3 report the average number of global Newton iterations and the average computational time per time step increment for the butterfly- and square-shaped histories, respectively.

Algorithm	**Steps/second**	**Aver. Newton iteration number/step**	**Aver. comput. time/step** [s]
RM	2	6	0.1189
	20	5.97	0.0982
	500	5.2872	0.0611
FB	2	6	0.2544
	20	5.98	0.0722
	500	4.9816	0.0594

Table 4.3: Biaxial square-shaped loading history input. Comparison of computational efficiency between the RM and the FB algorithmic schemes in terms of average number of global Newton iterations and average computational time per time step increment.

Instantaneous error

Lacking the analytical solutions of the two loading histories under investigation, we compute the 'exact' solutions using a reference scheme, i.e., the RM algorithm with a very fine time discretization, corresponding to 10000 steps per second (i.e., $\Delta t = 0.0001$ s). Then, we compare the 'exact' solutions to the 'numerical' ones, computed respectively with 2, 20 and 500 steps per second (i.e., Δt of 0.5, 0.05 and 0.002 s).

The error is evaluated separately for stresses and strains; for stresses we introduce the following relative norm:

$$E_n = \frac{\|\mathbf{v}_n^{ex} - \mathbf{v}_n^{num}\|_2}{R_n} \tag{4.4}$$

where R_n is the yield surface radius at time t_n and $\mathbf{v}_n^{ex}$ and $\mathbf{v}_n^{num}$ are vectors containing, respectively, the 'exact' and the 'numerical' solution at time t_n. For strains we use the same relative norm scaled by $2G$. Figures 4.2 and 4.3 show the stress and strain relative error, E_n, related to Δt of 0.5, 0.05 and 0.002 s for the butterfly- and square-shaped histories, respectively.

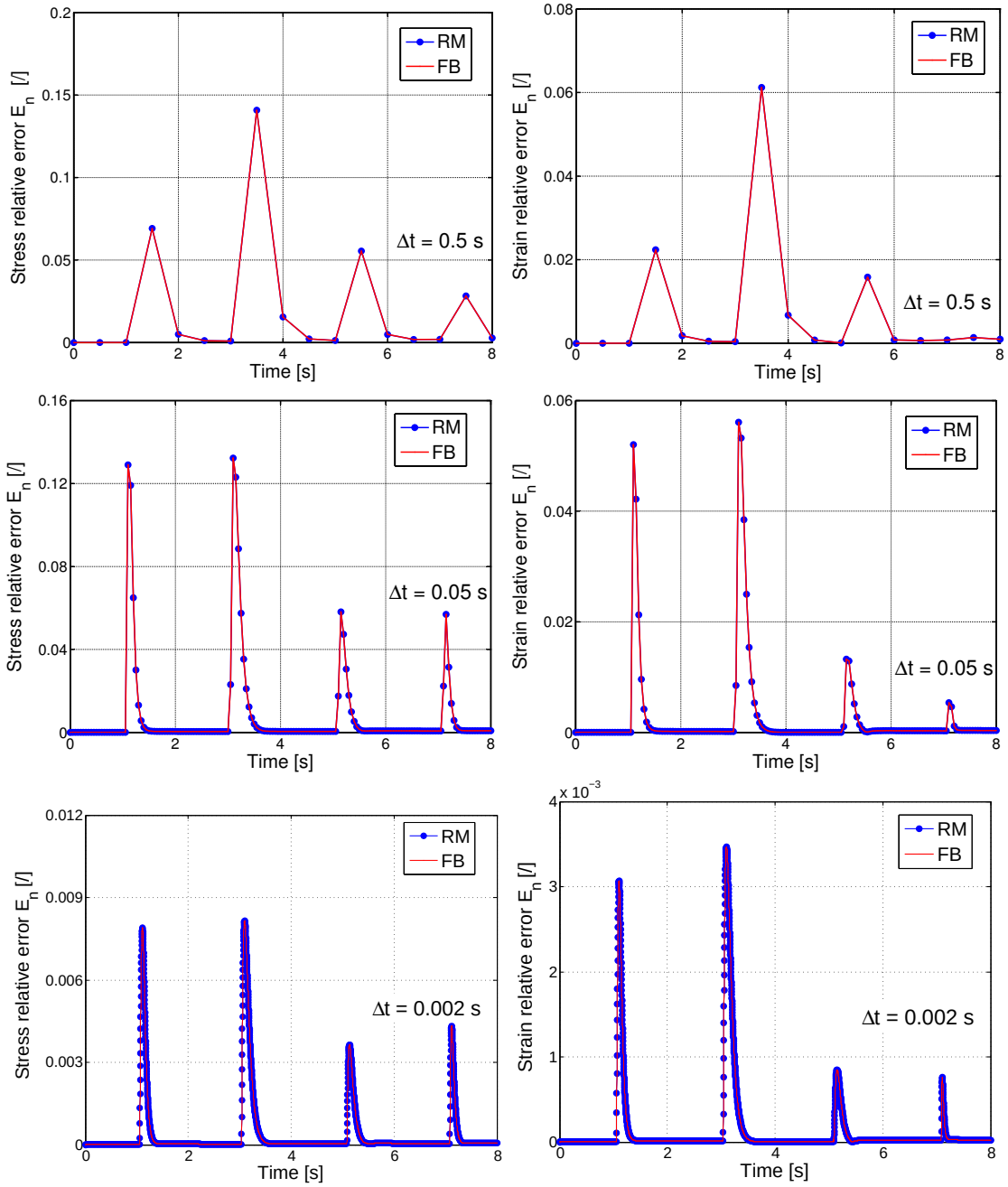

Figure 4.2: Biaxial butterfly-shaped loading history input. Stress (left column) and strain (right column) relative error, E_n, for Δt of 0.5, 0.05 and 0.002 s for the RM and the FB algorithmic schemes.

Total error

In order to further investigate the rate of convergence of the compared methods, we introduce the total error, defined as follows:

$$E_T = \sum_{n=1}^{N} \Delta t \left\| \mathbf{v}_n^{ex} - \mathbf{v}_n^{num} \right\|_1 \tag{4.5}$$

Figures 4.4(a)-(b) and 4.5(a)-(b) present the stress and strain total error, E_T, versus the number of steps per second for the butterfly- and square-shaped histories, respectively.

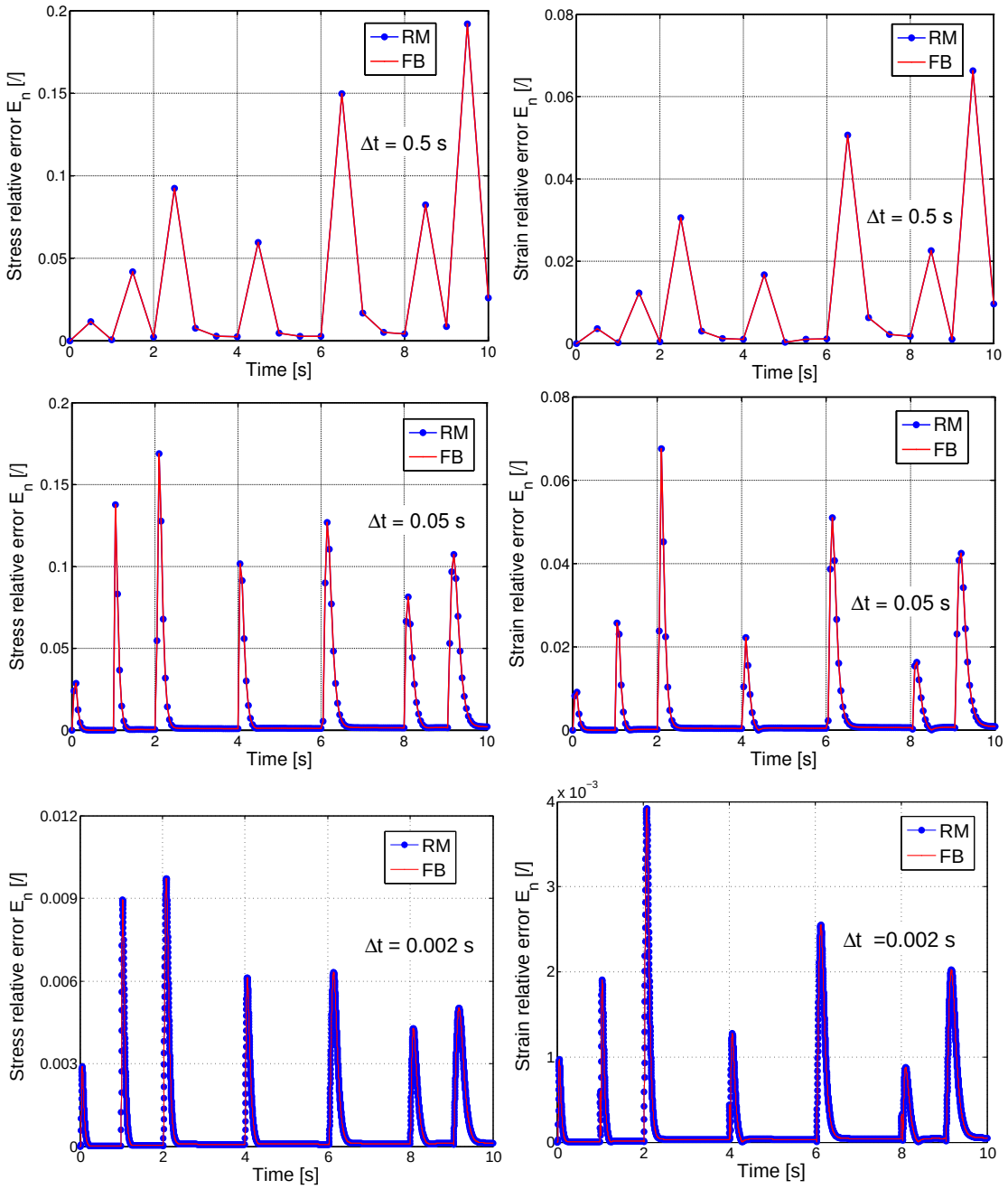

Figure 4.3: Biaxial square-shaped loading history input. Stress (left column) and strain (right column) relative error, E_n, for Δt of 0.5, 0.05 and 0.002 s for the RM and the FB algorithmic schemes.

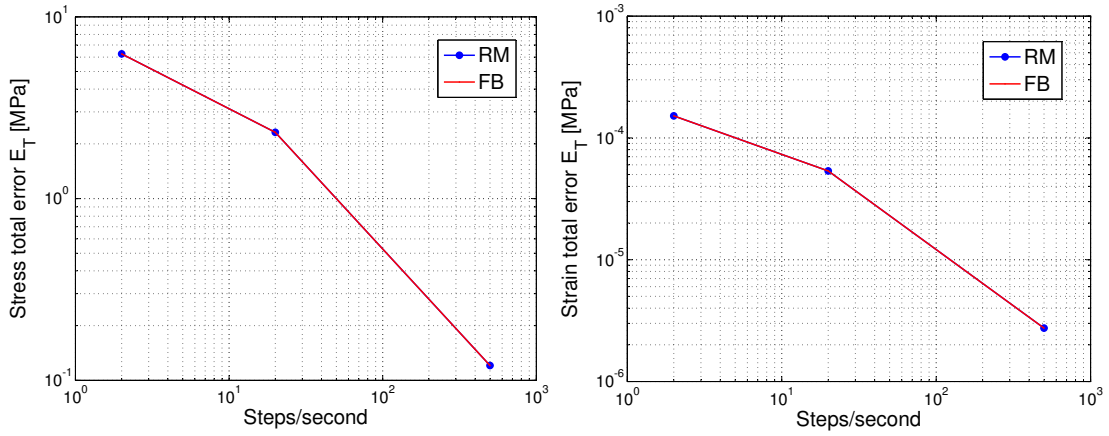

(a) (b)

Figure 4.4: Biaxial butterfly-shaped loading history inputs. Stress (left) and strain (right) total error, E_T, vs. number of steps per second for the RM and the FB algorithmic schemes.

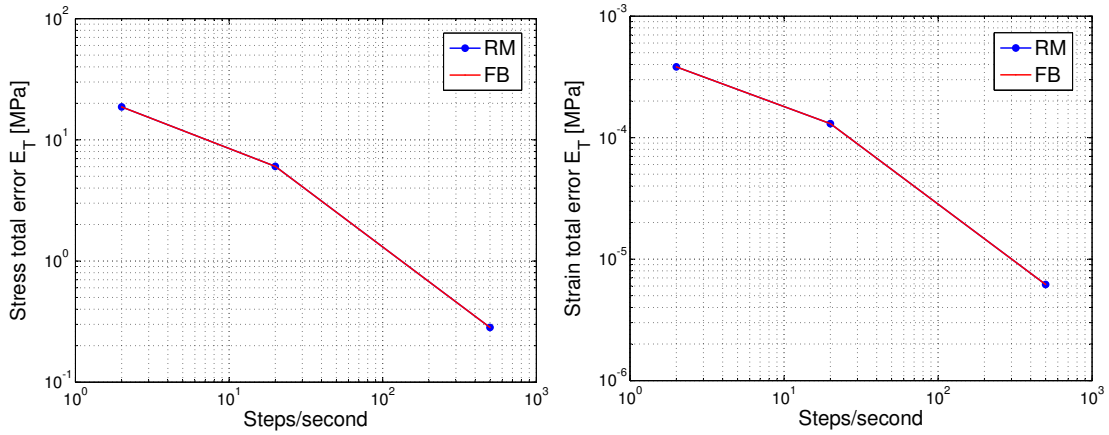

(a) (b)

Figure 4.5: Biaxial square-shaped loading history inputs. Stress (left) and strain (right) total error, E_T, vs. number of steps per second for the RM and the FB algorithmic schemes.

4.2.2 Initial boundary-value problems

Three-dimensional perforated strip

We consider a three-dimensional perforated square strip, subjected to uniaxial displacement-control extension. The strip has an edge length of 50 mm and a thickness of 10 mm; moreover, the strip has a central circular hole of radius 10 mm. According to the symmetry of the problem, we model only one quarter of the domain for the strip by applying appropriate boundary conditions. The mesh is composed of 3080 8-node brick elements and 4002 nodes (see Figure 4.6).

Initially the strip results undeformed and unstressed. The loading history is composed of a first phase, in which, the strip is stretched up to a maximum vertical displacement of 0.1 mm at top side, and a second phase in which the imposed displacement is set back to zero. Tests are performed using time step increments, Δt, of 0.1 and 0.01 s, corresponding to 10 and 100 steps per second. To assess the computational

efficiency of the RM and FB algorithms, Table 4.4 reports the average number of global Newton iterations and the average computational time per time step increment.

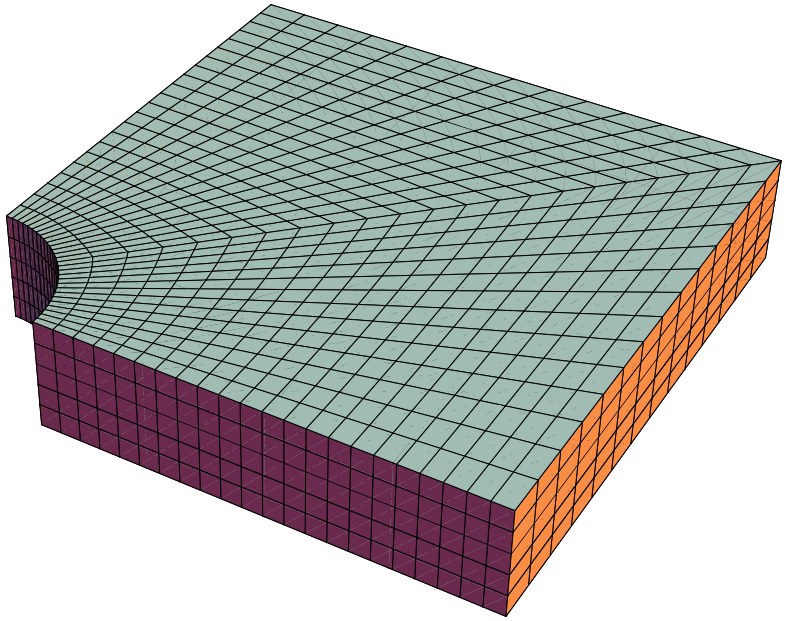

Figure 4.6: 3D perforated strip. Adopted mesh.

Algorithm	**Steps/second**	**Aver. Newton iteration number/step**	**Aver. comput. time/step** [s]
RM	10	5.55	1.8315
	100	4.77	1.36
FB	10	5.55	2.1271
	100	4.735	1.63911

Table 4.4: 3D perforated strip. Comparison of computational efficiency between the RM and the FB algorithmic schemes in terms of average number of global Newton iterations and average computational time per time step increment.

Helicoidal spring

To test the algorithms on a more complex three-dimensional case, we consider a helicoidal spring. The spring consists of 3.5 free coils of initial length of 24.59 mm, a wire diameter of 1.5 mm, a spring external diameter of 13.3 mm, a spring internal diameter of 10.3 mm and a pitch size of 6.4 mm. Figure (4.7) reports the adopted mesh, consisting of 6912 8-node brick elements and 7497 nodes.

The spring is fixed at one end and at the other hand a force is applied. The force is increased to a maximum value of 3 N and then unloaded back to zero. Tests are performed using time step increments, Δt, of 0.1 and 0.01 s, corresponding to 10 and 100 steps per second. Table 4.5 reports the average number of global Newton iterations and the average evaluation time per time step increment for the RM and FB algorithmic schemes.

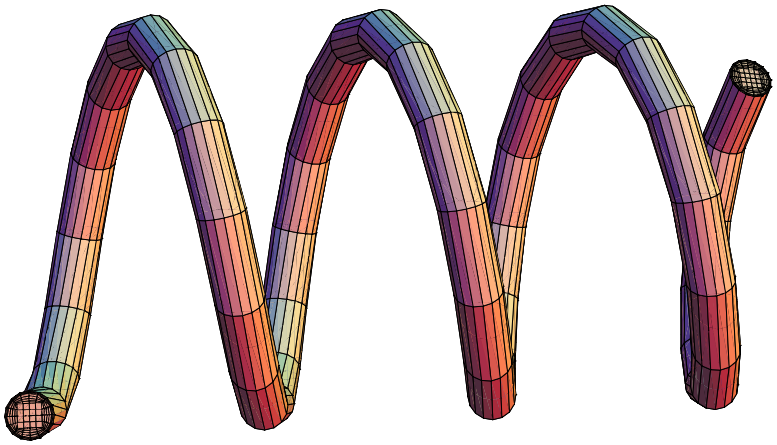

Figure 4.7: Helicoidal spring. Adopted mesh.

Algorithm	**Steps/second**	**Aver. Newton iteration number/step**	**Aver. comput. time/step** [s]
RM	10	5.65	11.6661
	100	5.035	7.9420
FB	10	5.7	8.4455
	100	4.7	7.8232

Table 4.5: Helicoidal spring. Comparison of computational efficiency between the RM and the FB algorithmic schemes in terms of average number of global Newton iterations and average computational time per time step increment.

4.2.3 Discussion on results

As it can be observed from all the numerical tests, the obtained results reveal that the RM and FB algorithms can be equally used for numerical simulations of elastoplastic bodies with linear isotropic kinematic hardening. In particular, the number of global Newton iterations and the computational time is quite similar for the two algorithms (see Tables 4.2, 4.3, 4.4, and 4.5) and decrease as the number of steps per second increases. Also, the stress and strain total and relative errors, E_n and E_T, present identical values, as shown in Figures 4.2, 4.3, 4.4(a)-(b), and 4.5(a)-(b). We remark that possible difficulties in the FB scheme could be linked to the numerical sensitiveness of such scheme (due to the presence of the regularization parameter) and to the proper choice of the Newton-Raphson initial guess to guarantee a fast and correct convergence. In fact, a potential disadvantage of this method is that when the initial point is far from a solution, the method might not converge or may converge very slowly. To resolve these shortcomings, we could apply a line-search strategy. In the present case, however, the presence of the regularization parameter in the FB algorithm does not affect the convergence.
Therefore, the obtained results encourage a further investigation of the FB scheme and of its application to more complex constitutive models, e.g., involving non-linear kinematic hardening or describing the behavior of smart materials, as shape memory materials. In the following Chapters, we will make use of the FB algorithm for the numerically treatment of several computational problems involving shape memory alloys and polymers. The FB scheme will demonstrate its suitability to treat numerically constitutive equations involving several constraints on internal variables and Kuhn-Tucker conditions.

Chapter 5

Introduction to shape memory alloys

This Chapter presents an introduction to shape memory alloys which, among the different types of smart materials, play an important role in various innovative applications.

The Chapter is organized as follows. Starting from the role of intelligent materials in the technological progress, Section 5.1 describes shape memory alloy historical background. To briefly explain the reasons of the great success of shape memory alloys, Section 5.2 focuses on physical material properties, particularly on pseudo-elasticity and shape memory effects. Then, Section 5.3 reinterprets material properties in terms of micromechanical configuration. Finally, Section 5.4 presents a quick overview on the large variety of shape memory alloy-based applications.

5.1 Shape memory alloy historical background

Shape memory alloy discovery dates back to the 1960s, when Buehler et al. (1963) developed a series of nickel-titanium alloys (NiTi), composed of 53 to 57% nickel by weight and exhibiting an unusual effect: severely deformed specimens of the alloys, with residual strain of 8-15%, regained their original shape after a thermal cycle. This effect became known as the *shape memory effect* and the alloys exhibiting it were named *shape memory alloys* (SMAs). It was later found that, at sufficiently high temperatures, such materials also possess the property of *pseudoelasticity*, i.e., the ability of recovering large deformations during mechanical loading-unloading cycles performed at constant temperature. The term NiTiNOL was coined for the NiTi material in honor of its discovery at the Naval Ordinance Laboratory (NOL).

The discovery of NiTi alloys spearheaded active research interest into SMAs and allowed the development of many commercial applications. The first commercial SMA applications, known as Cryofit, were pipe couplings in F-14 fighter aircraft (Wayman and Harrison, 1989). During the 1970s, several uses of NiTi alloys in biomedical applications appeared, but it was not until the 1990s that NiTi stents made their commercial breakthrough. By this time, SMAs had found additional applications in air conditioning vents, electronic cable connectors, valves, and other products (Duerig et al., 1990; Lagoudas, 2008).

Various other materials are known to display shape memory properties, such as ternary NiTi alloys (e.g., NiTi-Cu, NiTi-Fe) and copper-based alloys (e.g., Cu-Zn, Cu-Al-Ni). However, the NiTi alloy is still the most common commercially available SMA.

5.2 Shape memory alloy properties

As one of the most important branches of smart materials, shape memory alloys (SMAs) provide a huge variety of fascinating properties, known as *pseudo-elasticity* (PE), *one-way* and *two-way shape memory*

effects (SMEs) (Duerig et al., 1990; Otsuka and Wayman, 1998). If the material is deformed at low temperature, upon unloading it retains an apparently plastic deformation, which can be recovered by heating it above a characteristic temperature (*thermal recovery*, known as the SME). At high temperature, on the contrary, large deformations can be recovered by simply removing the applied load (*mechanical recovery*, known as PE).

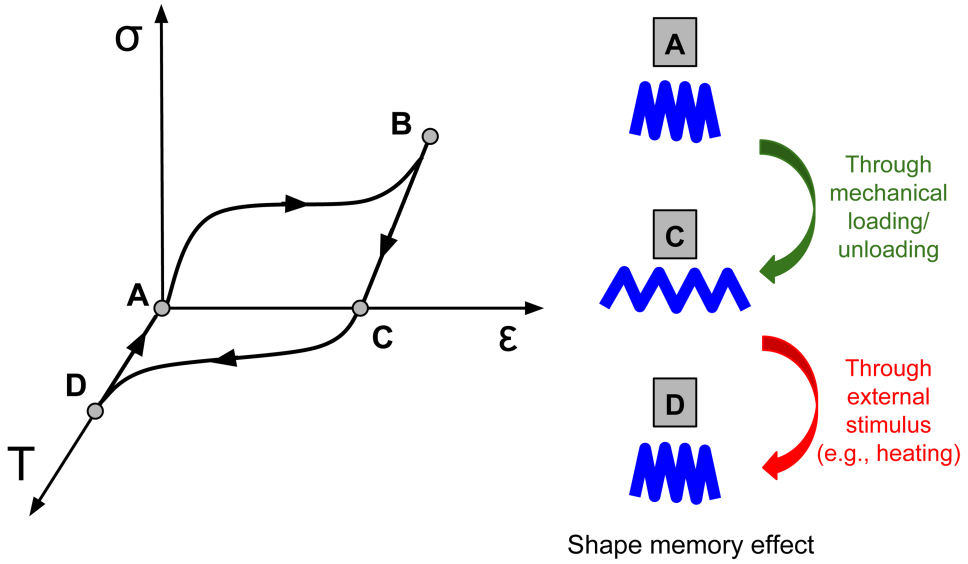

(a)

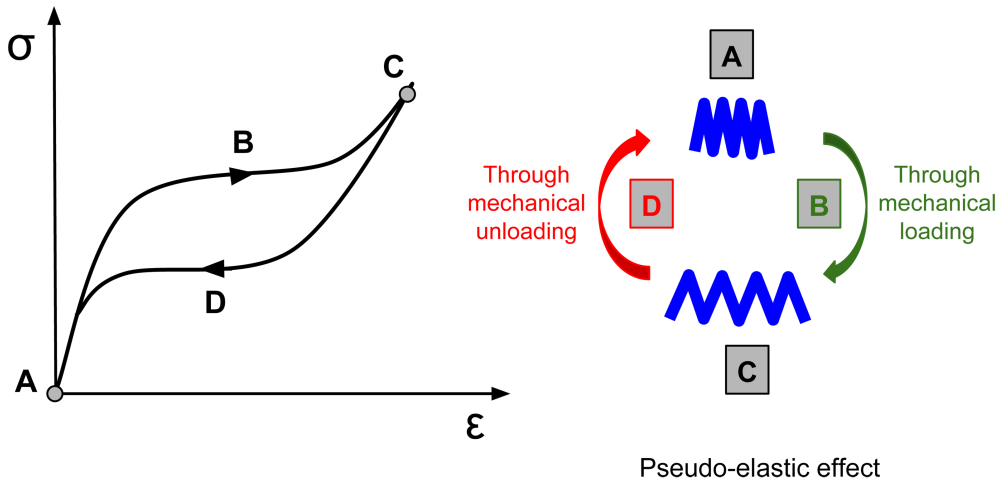

(b)

Figure 5.1: SMA material properties. (a) Shape memory effect and (b) pseudo-elasticity.

Figure 5.1(a) presents the SME property in a one-dimensional diagram, in terms of stress, σ, strain, ϵ, and temperature, T. The material starts from the reference configuration at a given low temperature and zero stress (point A). If a load is applied and increased, material behavior is at first linearly elastic; then apparently plastic deformations start to develop at nearly constant stress. Unlike plastic deformation, however, SMA deformation reaches saturation at a certain level of the load and an additional increase of the load leads to a new linear elastic branch until the final point B. Upon unloading, a residual deformation

is present (point C), which can be recovered by heating the material above a characteristic temperature under no applied load (from point C to point D). Finally, if the material is cooled down to the starting reference temperature (from point D to point A), the initial material state (point A) is completely recovered and no change in shape occurs. The described property is also known as one-way SME, as only the high-temperature shape is memorized by the material.

The two-way SME, on the contrary, is related to the ability of the material to remember two different shapes at low and high temperatures. Such a property allows to move between the two shapes by simply changing the temperature, with no need of an applied load. Figures 5.2(a) and 5.2(b) schematically represent the one-way and two-way SMEs, respectively. It should be noted that, while the one-way SME is an intrinsic characteristic of SMAs, the two-way SME needs to be induced by particular treatments, such as training[1].

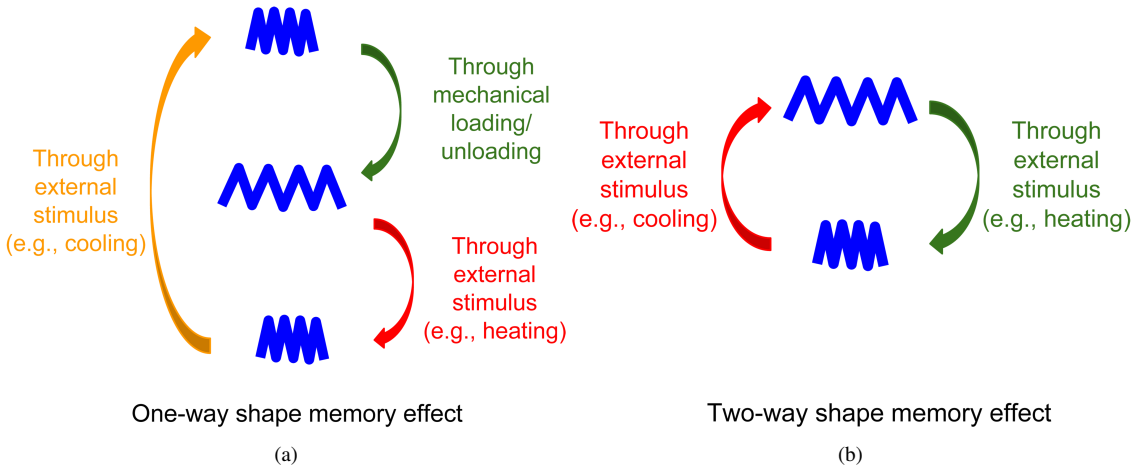

Figure 5.2: SMA material properties. (a) One-way and (b) two-way shape memory effect.

Figure 5.1(b) presents the PE property in a one-dimensional diagram, in terms of stress, σ, and strain, ϵ. The material starts from the reference configuration at a given high temperature and zero stress (point A). The loading branch is similar to that described for the SME (from point A to points C through B), whereas a stress plateau is present upon unloading (point D), leading to no residual deformation at zero stress (point A).

The apparently unrelated properties of SME and PE, can be observed in the same material if it is tested at different temperatures. Indeed, the characteristic temperature that separates SME and PE temperature ranges depends upon the type and the chemical composition of the alloy; thus, it is possible to find alloys which show either of the effects at room temperature.

5.3 Micromechanical interpretation of shape memory alloy properties

The macroscopic behavior of SMAs depends upon the presence of two solid phases with different degrees of symmetry (Duerig et al., 1990). The parent phase, called *austenite*, has a high symmetry crystal structure (typically body-centered cubic) and it is stable at high temperature and low levels of stress; the other phase, called *martensite*, has lower symmetry (typically rhombohedral or monoclinic) and it can appear in a

[1]Training consists in repeatedly cycling the material in different ways. It is also useful to stabilize SMA properties.

number of cristallographically equivalent variants, which differ in their orientation with respect to material axes[2]. The different martensitic variants, formed in a single grain of polycrystalline SMA, are shown in Figure 5.3.

The transformation from one phase to the other (known as *martensitic transformation*) occurs by a shear lattice distortion, without volume change (Lagoudas, 2008; Otsuka and Wayman, 1998). Indeed, the phase transformation (PT) between the two phases is displacive; thus, it requires only small movements of the atoms within the crystal lattice and its evolution is time-independent[3].

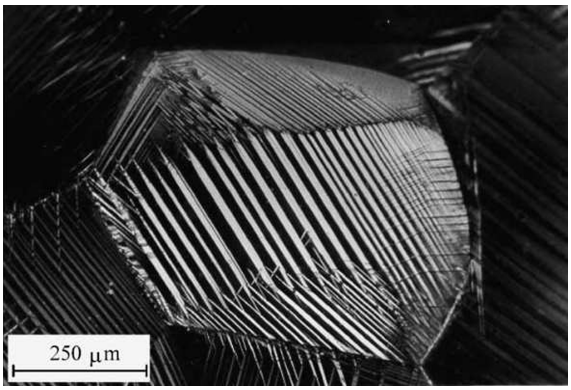

Figure 5.3: Formation of different martensitic variants in a single grain of polycrystalline CuZnAl alloy during uniaxial tensile loading, taken from (Patoor et al., 2006).

A PT can be induced by controlling material temperature and/or stress conditions. In thermal-induced transformations under zero stress, multi-direction martensite variants compensate each other and arrange themselves in a self accommodating manner through twinning, with no observable macroscopic shape change (Duerig et al., 1990). In stress-induced transformations, starting from a martensitic specimen, the application of a loading induces martensite reorientation, resulting into a detwinning process of martensitic variants and leading to the presence of a single-variant; upon unloading, a large residual strain remains, which can be recovered by heating (Duerig et al., 1990). This phenomenon, introduced in Section 5.2, is referred to as SME. On the contrary, when a stress is applied to an austenitic specimen, at high temperature, the growth of some martensite variants (up to 24 for NiTi) is favoured and a transformation from austenite to single-variant martensite occurs; upon unloading, the strain attained during loading is recovered. This process, introduced in Section 5.2, is referred to as PE (Otsuka and Wayman, 1998).
We remark, also, that some NiTi alloys display a two-step PT (Sadjadpour and Bhattacharya, 2007). Upon cooling, austenite transforms first into a trigonal structure known as the R-phase, which in turn changes into martensite as the temperature continues to decrease. The austenite to R-phase transition has a very small hysteresis and it is associated to a limited recoverable shape change (about 1% elongation versus the 10% elongation associated to martensite) and to a significant change in electrical resistivity.

Figure 5.4(a) represents a schematic one-dimensional diagram, in terms of stress, σ, and temperature, T, which illustrates the different crystal structures of a given SMA with fixed composition, i.e., austenite, multi-variant and single-variant martensites, along with the PT regions[4]. The construction of such a

[2]Martensite can be present in different but crystallographically equivalent forms (*variants*). If there is no preferred direction along which the martensite variants tend to align, then *multiple-variants* are formed. If, instead, there is a preferred direction for the formation of martensite, just one (*single*) *variant* is formed.

[3]Diffusive phase transitions, on the other hand, require breaking of the crystal lattice and long distance atom movements, thus their evolution depends upon the time of reaction.

[4]Another unique SMA material feature is the possibility to modify and adjust the PT regions and the thermo-mechanical characteristic parameters through variations in the alloy composition and/or through proper thermo-mechanical treatments (Coda et al., 2006; Norwich, 2011). As an example, the material can remember a desired manufactured shape, which can be set to be different from the original shape, through a process referred to as *shape training* (Barras and Myers, 2010).

diagram, called *phase diagram*, involves the interpretation of SMA material response to various thermo-mechanical loading paths. In Figure 5.4(a) the PTs from austenite to multi- and single-variant martensites (termed *forward transformations*), from multi-variant to single-variant martensite, and from multi- and single-variant martensites to austenite (termed *reverse transformations*) are indicated by blue arrows.

Accordingly, the properties of SMA materials, i.e., SME and PE, described in Section 5.2, can be represented in the phase diagram. Figures 5.4(b) and 5.4(c) show the loading paths associated to the SME and PE, respectively.
As it can be seen in Figure 5.4(b), material microstructure is initially composed of multi-variant martensite at low temperature. Upon loading, the stress reaches the critical value for detwinning and martensite reorientation starts, leading to single-variant martensite and to macroscopic deformation. At the end of the PT, martensite is completely detwinned and further loading only causes elastic deformation of the new microstructure. Upon unloading, the macroscopic deformation is retained as all variants of martensite are equally stable. When the material is heated above a characteristic temperature, the transformation from martensite to austenite starts, allowing to recover the macroscopic deformation. During cooling, the austenite to martensite PT occurs under no load, thus no macroscopic change can be observed.

As it can be seen in Figure 5.4(c), material microstructure is initially austenitic at high temperature. During loading, the critical stress for PT is reached and the material transforms directly into single-variant martensite. Once PT is complete, further loading only causes elastic deformation of multi-variant martensite. Since austenite is the only stable phase at high temperature and no stress, during unloading the critical stress for the reverse PT is reached and the macroscopic deformation is recovered.

5.4 Shape memory alloy applications

Thanks to their unique properties, SMAs represents an attractive choice for a huge variety of innovative applications. SMA applications can be divided into the following categories (Van Humbeeck, 2010):

1. *free-recovery applications*, exploiting the one-way and two-way SMEs, e.g., applications in which the single function of the SMA element is to cause motion or shape changes, without any biasing stress;

2. *clamping devices*, exploiting the generation of recovery stresses, e.g., SMA couplings and connectors, ranging from very small (< 1 mm) to very large (> 1 m) diameters;

3. *actuation applications*, exploiting the work production capacity of SMAs;

4. *biomedical applications*, exploiting the PE property of SMAs;

5. *damping applications*, exploiting the high damping capacity of SMAs. In particular, the high damping capacity of martensite is interesting for passive damping, while the PE hysteresis for earthquake damping and isolation purposes.

At present, more than 90% of SMA applications are based on NiTi or ternary NiTi-Cu and NiTi-Nb alloys (Van Humbeeck, 2010). Other SMAs are close to market introduction (Fe-Mn-Si), while still others have interesting potentials, but are difficult to produce or suffer from brittleness, such as alloys envisaged for applications at high temperatures (Firstov et al., 2006). Although NiTi-based SMAs are more expensive and more difficult to machine than Cu-based SMAs, there are several reasons why almost only NiTi-based SMAs are used in new developments. In particular, NiTi-based SMAs are stronger and more ductile, show a higher stability in cyclic applications, and have a higher electrical resistivity which makes electrical activation simpler. The biocompatibility requirement for medical applications also eliminates Cu-based alloys. Mainly Ni, but also Ti, can be partially (a few percent) replaced by elements as Cu, Co,

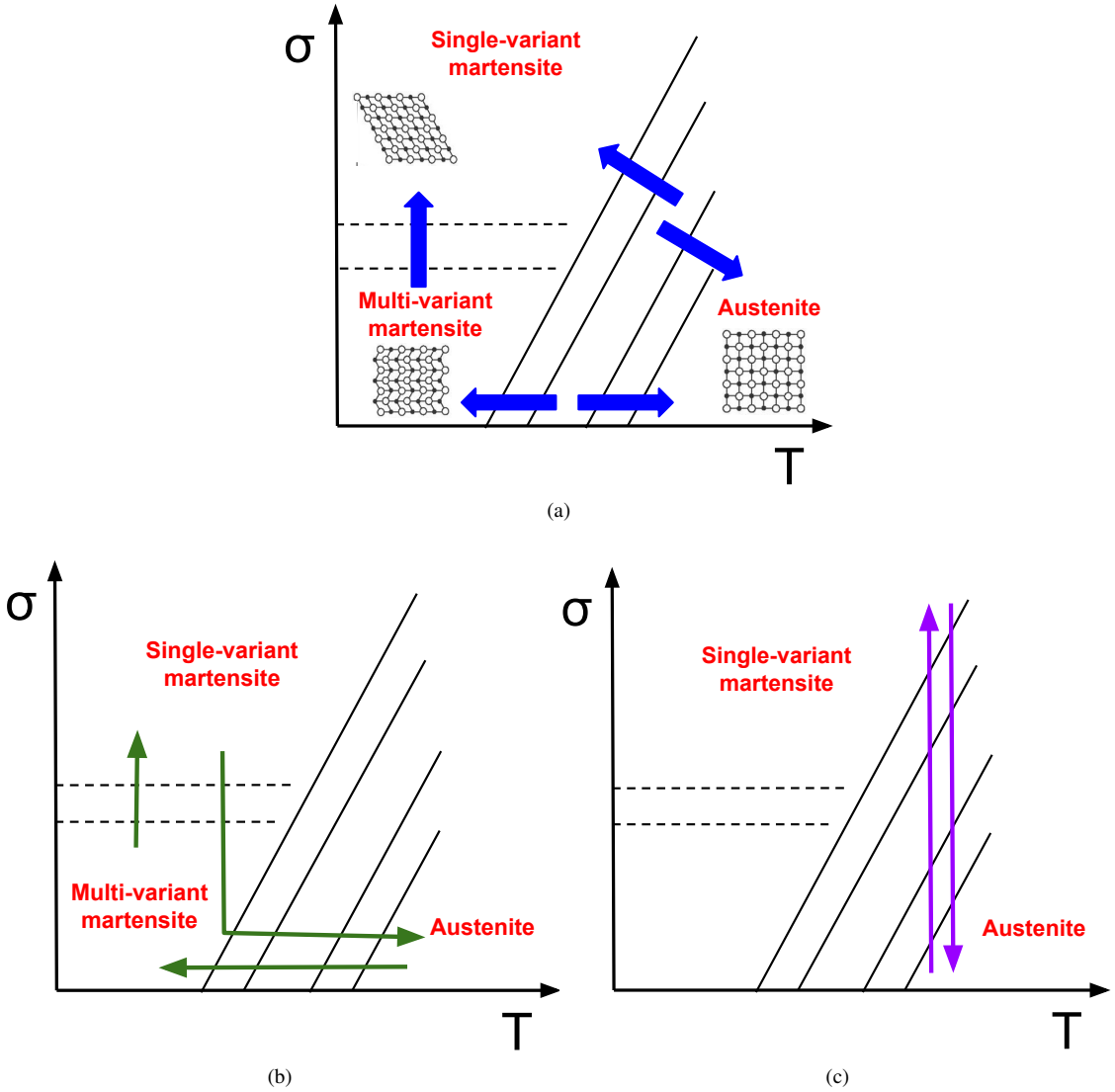

Figure 5.4: One-dimensional phase diagram in terms of stress, σ, and temperature, T. (a) Crystal structures for austenite, multi- and single-variant martensites and phase transformations (indicated by blue arrows); (b) shape memory effect and (c) pseudo-elastic loading paths.

Fe, Nb, or Mo, that can improve, for instance, stress and/or temperature hysteresis, corrosion, resistance, transformation temperatures or fatigue behavior.

In the following, we mention some famous SMA-based applications.

5.4.1 Couplings and fasteners

Couplings and fasteners exploit the force created by a deformed SMA element during constrained recovery.

The first large-scale application of SMAs, consisting in a coupling to connect titanium hydraulic tubing in the Grumman F-14 aircraft, was developed by Raychem in 1971 (Otsuka and Wayman, 1998). The original alloy was a NiTi-Fe, where Fe was alloyed to obtain a low transformation temperature down to $-55\,^{\circ}\mathrm{C}$ and to possibly prevent the transformation into martensite at lower temperatures, and thus the leakage. The mounting procedure was, however, quite complicated: expansion of the ring in liquid nitrogen,

storing (also during transport) in liquid nitrogen until mounting by just bringing it to room temperature. Later, the problem of liquid nitrogen storage was solved by the stabilization of martensite, either thermal (in Cu-based alloys) or mechanical (in NiTi-Nb alloys). The development of NiTi-Nb alloys was a real breakthrough for the coupling business, but also Fe-Mn-Si alloys received quite a lot of attention in spite of their low recoverable strain (Duerig et al., 1990).
Dedicated applications were specifically named as Crocon and Crofit®(hydraulic couplings), Crolive®(more complicated tool to couple), Tinel®lock and Unilock®rings, and Betaflex™and Crotact™electrical connectors for Zero Insertion Force connectors (Van Humbeeck, 2010). Figure 5.5 shows some commercially available SMA devices.

Figure 5.5: SMA devices. Clockwise from top left: memory card ejector mechanism for laptop computers; Cryofit® hydraulic pipe couplings; Cryocon® electrical connector; fire safety lid release for public garbage receptacles, taken from (Schwartz, 2002).

The main advantages of all the listed systems are their lightweight, easy installation even in difficult to access areas, proven reliability, good shock, vibration and thermal cycling properties providing a hermetic seal (Otsuka and Wayman, 1998); possible disadvantages are the high costs, limited operational temperature range (from $-20\,^{\circ}\mathrm{C}$ to $200\,^{\circ}\mathrm{C}$), and limited memory amount of motion available.

5.4.2 Actuators

A thermal actuator is a constrained SMA element able to generate a recovery force that can be used to perform work. Indeed, thermal energy is directly converted into mechanical energy. Important reasons to select SMA as an actuation mechanism are its simplicity, the creation of clean, silent, spark-free and zero gravity working conditions, as well as high power/weight (or power/volume) ratios (Van Humbeeck, 2010). However, some drawbacks have to be considered, e.g., low energy efficiency, limited bandwidth due to heating and cooling restrictions, degradation, and fatigue.

Apart from some specific on/off applications, such as an air damper for a multifunction electric oven or an SMA generated fog lamp protective louver, designers have shown a special interest in such a type of applications, namely in robotic applications. Three important items distinguish robotic applications: the type of deformation used for the active memory element (bending, torsion, or pure tension), the position feedback that enables free-positioning of the actuator, the way of heating (cooling) the active element (mainly resistive heating, induction heating, immersion heating).

Space applications offer other arguments in favor of SMA actuators, e.g., almost zero-gravity action in contrast to most electrical engines, high power/volume (mass) density, and simple mechanism, no dust

particles created, and no leakage of fluids (Van Humbeeck, 2010).

SMA actuators are also considered for repeated actions such as grippers and positioners, where the low thermal energy is compensated by the ease of mechanism which includes a high gain on weight, high work/volume density, and almost zero gravity accelerations.

5.4.3 Adaptive materials and hybrid composites

Smart materials involve three functions, i.e., sensor, actuator and control, generally combined by using different materials connected with a control unit. The combination of several materials leads to structural elements called hybrid composites that, if connected with a control unit, can then be used eventually as a smart structure.

The most envisaged applications can be summarized as follows:

- *active strain energy tuning*: restrained wires are embedded in the matrix. If such composite plate vibrates at resonance, the wires can be heated to develop a recovery stress at the composite matrix wire interface and thus to produce a change in energy balance;
- *active modal modification*: unstrained wires are embedded in the matrix. To change the modal response, the wires are heated resulting in a large increase of the elastic modulus of wires during martensitic transformation;
- *active shape control*: SME is used to change the shape of the composite matrix;
- *active fatigue-life* and *impact resistance improvement* (self-repairing or self-healing): PE embedded deformed wires create compressive stresses inhibiting crack growth and even promoting crack closure. Embedded strained martensitic wires can also be activated by heating;
- *active stress-relaxation*: stress- or strain-induced martensite can relax imposed stresses due to specific loading, differences in thermal expansion coefficients or thermal chocks. Depending on the type of application, SMAs can be embedded as thin wires, fibers, particles, thin films, while the matrix can be a metallic material, a ceramic, a polymer or a composite.

5.4.4 Civil engineering applications

SMA applications in civil engineering are still significantly limited due to the high cost and small size of components (Janke et al., 2005).

The significant damping capacity of SMAs, related to the hysteresis present in both superelastic and shape memory stress-strain curves, can be used in earthquake engineering to develop passive control devices which reduce the response of a structural system during dynamic excitation (Casciati et al., 1998). The cost issue can be partially overcome by using copper-based SMAs (Casciati and Faravelli, 2004).

Another idea is to use SMA devices to prevent two classical damage mechanisms of masonry buildings, i.e., out of plane collapse and diagonal cracks. The first mechanism can be prevented by improving the connections between the walls placed in different directions. This is usually done with steel connections, whose linear elastic behavior might end up exerting excessive forces and damaging historical masonry. Superelastic devices, on the contrary, can limit the forces applied on the masonry by tuning the upper and lower transformation plateau. This concept has been applied to the restoration of Assisi Upper Basilica, damaged during the earthquake of September 26th and 27th, 1997. The second damage mechanism can be prevented by pre-compressing the masonry walls. With respect to traditional steel devices, superelastic elements exert only a limited pre-compression force and dissipate part of the seismic action due to their damping capacity. This concept has been applied to the seismic retrofitting of the San Giorgio in Trignano bell tower in San Martino in Rio (Reggio Emilia), damaged during the earthquake of October 15th, 1996.

Recently, several applications exploit the SME property to create self-erecting structures. Another recent idea is to use SMA bars as concrete reinforcement; this idea falls within the topic of SMA composites, thus it is not discussed here (Daghia et al., 2011, 2008, 2010; Faiella et al., 2011).

5.4.5 Biomedical applications

Nowadays, the largest commercial successes of SMAs are linked to biomedical applications, thanks to material good workability in the martensite phase, good strength and ductility, good resistance to corrosion and fatigue, Food and Drug Administration approval, excellent biocompatibility, good compatibility with magnetic resonance imaging and computer tomography scanning (Duerig et al., 1999; Petrini and Migliavacca, 2011). Especially, the PE property results in a unique combination of high strength, high stiffness and high pliability and the temperature-dependent character of the PE property is of less importance in the biomedical field because of the stable temperature in the human body (Van Humbeeck, 2010). Also, the concept of a metallic material with an extreme elasticity and with nearly constant stress levels over a large strain area is something that can be tackled easier by designers.

In the following, we describe only some of the numerous medical applications for SMAs, ranging from orthodontics, orthopedics, and otoryngology to neurosurgery, ophthalmology, physiotherapy, active prostheses, and robot-assisted surgery.

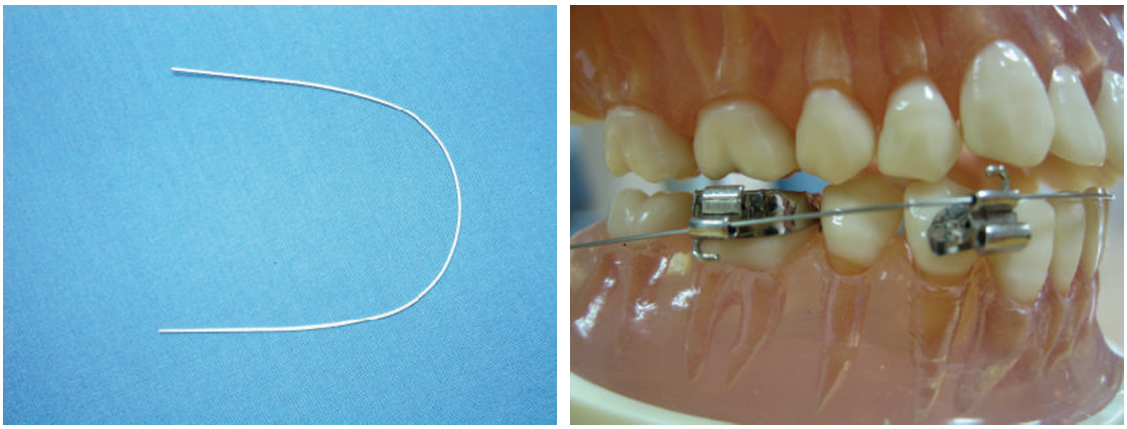

Figure 5.6: Orthodontic applications of SMAs. Examples of wires, taken from (Petrini and Migliavacca, 2011).

Orthodontic applications

The first medical use of NiTi-based alloys was in the orthodontic field in 1971, when Andreasen and Hilleman (1971) introduced NiTi orthodontic archwires, observing that NiTi was able to produce constant and lighter forces. Nowadays, even if SMAs are more difficult and expensive to manufacture than conventional materials, they are among the most common materials used for orthodontic devices.

The properties of SMAs have been successfully implemented in a variety of dental applications. Currently, archwires of Figure 5.6 and palatal expanders of Figure 5.7(a) are the most important SMA orthodontic applications, taking advantage of PE features. The motivation for such a successful exploitation is connected to the material ability to apply to the teeth almost constant forces over a large range of deformations. Material PE behavior is also exploited for producing orthodontic distractors, as in Figure 5.7(b), which are used for solving the problem of teeth overcrowding in the mandible district (Idelsohn et al., 2004). Another example is represented by dental drills for root canal procedures (see Figure 5.8)

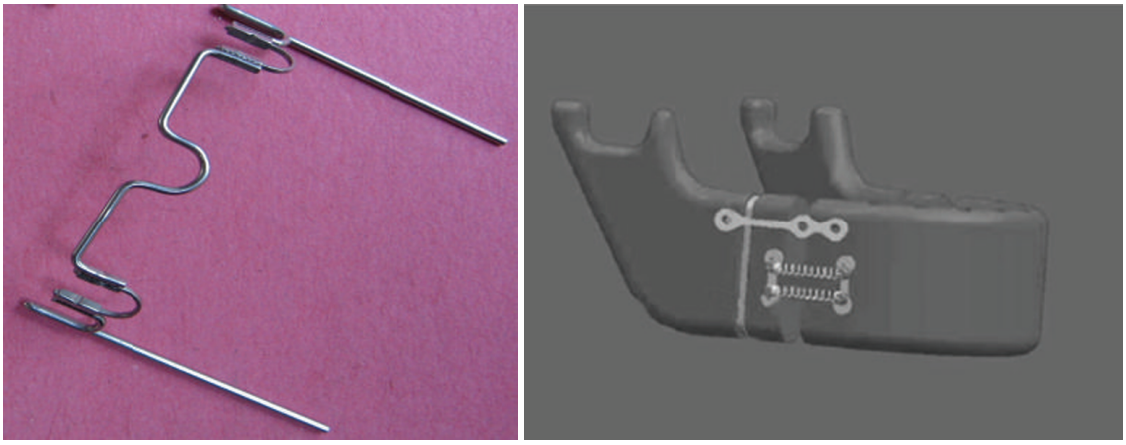

(a) (b)

Figure 5.7: Orthodontic applications of SMAs. (a) Palatal arch, taken from (Petrini and Migliavacca, 2011); (b) orthodontic distracters, taken from (Idelsohn et al., 2004).

(Lagoudas, 2008; Montenegro-Santillan et al., 2013), which exploit NiTi performance at high strains in strain-controlled environments (Pelton et al., 2000).

Figure 5.8: Orthodontic applications of SMAs. Endodontic file, taken from (Petrini and Migliavacca, 2011).

Orthopedic applications

To obtain an effective soldering or union between two disjoint bone segments, essential aspects are a stable fixation and a proper compression action between the two segments. Accordingly, fractured bones are treated with a fixation device, which should strengthen the bone and keep the correct alignment during healing, being sufficiently stable at the same time; moreover, the fixation should be minimally invasive, biocompatible, and induce a biologically-appropriate compression to enhance optimal fracture healing (Tarnita et al., 2011). SMAs can provide all these requirements in a very efficient way.

The simplest fixation device is the SMA staple, shown in Figure 5.9(a). At room temperature, the material being in martensitic phase, the staple can be easily shaped to facilitate insertion; when installed and maintained at body temperature, the staple tends to close and compress the two disjoint bones (i.e., inducing a constrained shape recovery), taking advantage from the material transformation into austenite, hence from the presence of an unloading stress-strain plateau (Dai et al., 1993). In particular, the device simplicity allows a reduction in operation time with apparent advantage also from the clinical perspective.

Similar conceptual devices are exploited in SMA plates, shown in Figures 5.9(b) and 5.9(c), fixed with screws to maintain bone alignment and placed on fractured regions where external cast cannot be easily performed (e.g., facial area, nose, jaws).

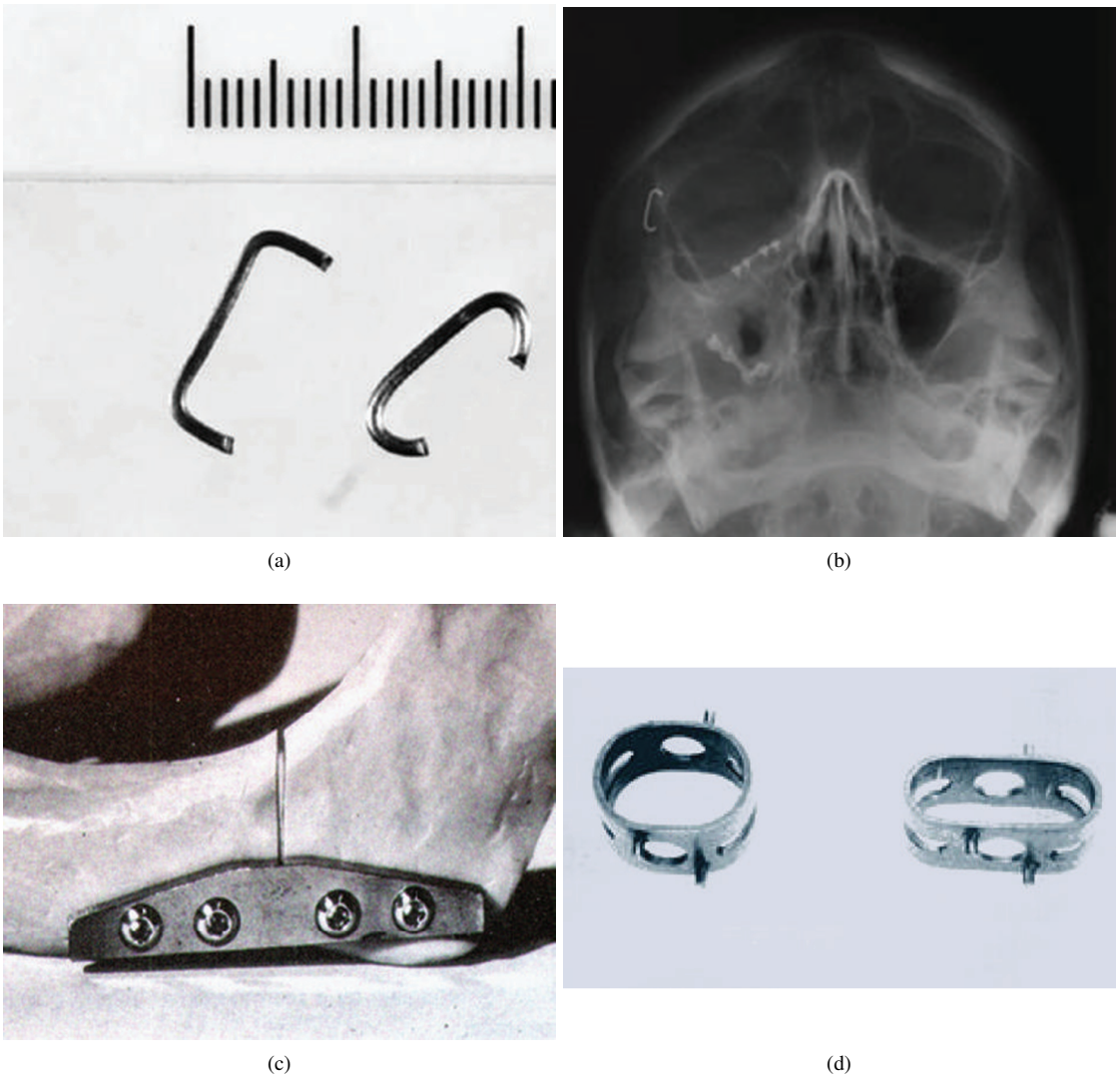

(a) (b)

(c) (d)

Figure 5.9: Orthopedic applications of SMAs. (a) Staple before and after distraction, taken from (Laster et al., 2001); (b) staple for fixing a frontozygomatic fracture, taken from (Laster et al., 2001); (c) NiTi plate for mandible fracture, taken from (Duerig et al., 1990); (d) spinal vertebrae spacer, taken from (Duerig et al., 1990).

Special NiTi devices have also been designed for the treatment of spine damage or deformities. As an example, the spinal vertebrae spacer of Figure 5.9(d) is a device for the treatment of scoliosis. Material PE response allows the application of a constant load regardless of the patient position, patient who preserves some degree of motion (Machado and Savi, 2003).

In orthopedics treatments, SMA properties are also exploited during the physiotherapy of partially atrophied muscles (Machado and Savi, 2003). As an example, gloves for promoting the movements of hands are developed by positioning SMA wires in correspondence of the fingers. In such an application the two-way SME is exploited: by heating or cooling, the wires contract or stretch and, accordingly, the hand is closed or opened, as shown in Figures 5.10(a) and 5.10(b).

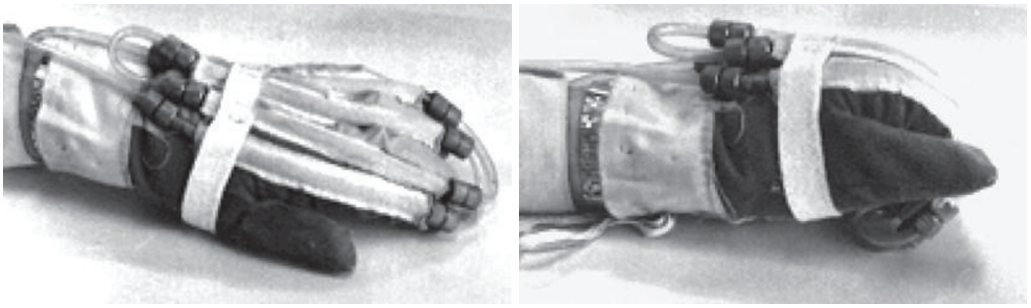

(a) (b)

Figure 5.10: Orthopedic applications of SMAs. Gloves with SMA wires: position at (a) low and (b) high temperatures, taken from (Machado and Savi, 2003).

General surgery applications

Another field taking significant advantage of SMA features is endoscopic surgery, which is a modern surgical technique where diagnosis and disease treatment are performed through small incisions or natural body openings. As easily inferable, endoscopic surgery, also called minimally invasive surgery, provide patients with several benefits such as less post-operational complications, reduced pain, faster recovery, reduction of infection risk (Kianzad et al., 2011).

However, surgical endoscopic procedures require devices able to access and operate into intricate regions. In this respect, a great advantage of SMAs with respect to stainless steel and other conventional materials is that lower size of the components is needed, since PE and SME provide higher flexibility, improving effectiveness in narrow cavities. Furthermore, PE provides high strain recovery and a wide constant stress plateau over a large range of strains. Such unique SMA characteristics have led to the design and manufacturing of novel optimized instruments, especially suited for endoscopic surgery, e.g., ablation devices, tongs, suture passers, grippers, deflectable graspers, scissors (see Figure 5.11).

Among the first applications of SMA devices in endoscopic surgery, we can cite, for example, various NiTi tools for laparoscopy, retrieval baskets used to remove stones from bile ducts and kidneys, the RITA radio frequency tissue ablation device, forceps for laparoscopy, active bending electric endoscopes, self-closing clips for suturing tissues, and guide wires (Cuschieri, 1991).

The most celebrated medical applications of NiTi are probably the self-expandable stents (Petrini and Migliavacca, 2011), consisting of a tubular NiTi mesh, possibly coated, which can be introduced in body conduits to treat dangerous obstructions (see Figure 5.12). NiTi stents find their major application in cardiovascular surgery to treat atherosclerotic lesions in the coronary, carotid, and pheriperal arteries, but they are also successfully used for the treatment of obstructions in various body canals, such as biliary, intestinal and esophageal conduits.

5.4.6 Other applications

There are many other fields and applications incorporating SMAs. The oil industry has shown extensive interest to use SMA actuation capabilities in release devices and protection systems for down hole drilling equipment. The high-temperature operating conditions have also opened the avenue for the use of high-temperature SMAs in these devices (Lagoudas, 2008). Flexible metallic eyeglasses and headphones, that can be bent without breaking, are other applications that employ the PE behavior. SMAs have also been used in sporting goods like golf clubs where SMAs, embedded in the club, absorb the impact of the strike.

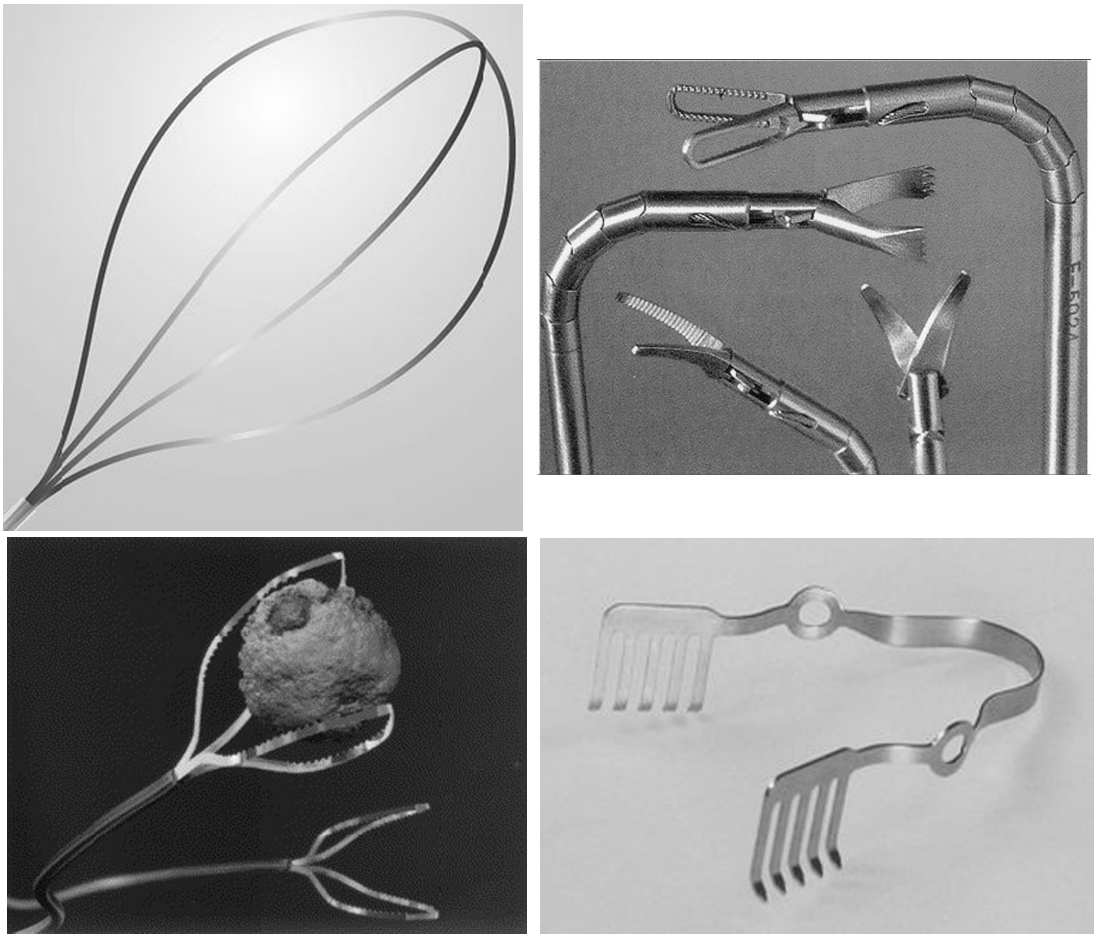

Figure 5.11: General surgery of SMAs. Endoscopic tools, taken from (Duerig et al., 1999; Endosmart, 2013; Kourambas et al., 2000).

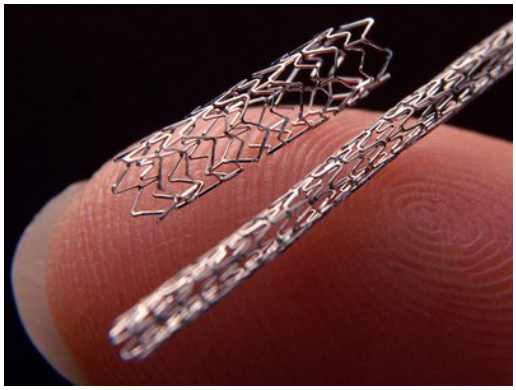

Figure 5.12: General surgery of SMAs. Examples of stents, taken from http://prashantborde123.blogspot.it/2013/02/biotechology-and-medicine.html.

Chapter 6

Literature review on shape memory alloy constitutive modeling

This Chapter is first devoted to a literature review on shape memory alloy constitutive modeling. Then, it focuses on the description of three well-known and widely accepted in practice phenomenological models, i.e., the models by Souza et al. (1998), Auricchio et al. (2009, 2011), and Boyd and Lagoudas (1996); Lagoudas et al. (2012). The explicit integration scheme for solving the constitutive equations of the model by Boyd and Lagoudas (1996); Lagoudas et al. (2012) is derived.

The Chapter is organized as follows. Section 6.1 starts with the description of the approaches generally adopted to model shape memory alloy behavior. Then, Section 6.2 focuses on the phenomenological modeling approach by presenting some contributions available from the literature. Finally, Section 6.3 concludes with the description of three cited models and with the derivation of the explicit integration scheme for the model by Boyd and Lagoudas (1996); Lagoudas et al. (2012).
The reader is referred to, e.g., (Khandelwal and Buravalla, 2009; Lagoudas et al., 2006; Patoor et al., 2006), for an overview on shape memory alloy modeling.

6.1 Constitutive modeling approaches for shape memory alloys

From 1980 up to now, constitutive modeling of shape memory alloys (SMAs) has been a topic of great interest. Several approaches have been exploited by researchers in order to propose one-dimensional and three-dimensional models, able to describe the complex thermo-mechanical behavior of SMAs.

The main characteristics, which characterize SMA behavior, are the pseudo-elastic and shape memory properties under a general three-dimensional multiaxial loading (i.e., variant reorientation is also important), while other characteristics are of secondary importance. We may thus categorize SMA characteristics into two groups, as follows:

- *primary effects*, which include pseudo-elasticity, shape memory effect, as well as variant reorientation. It is expected that a SMA constitutive model can capture, at least, such effects;
- *secondary effects*, which cover other effects which may turn out to be relevant in some practical cases, e.g., tension-compression asymmetry (Orgeas and Favier, 1998; Thamburaja and Anand, 2001), different elastic properties for austenite and martensite (Auricchio et al., 2009; Cernoch et al., 2004), progressive strain under cyclic loadings (Feng and Sun, 2007; Sittner et al., 1995; Tanaka et al., 1995), internal loops (Dolce and Cardone, 2001), thermo-mechanical coupling (Grabe and Bruhns, 2008; Shaw and Kyriakides, 1995; Tobushi et al., 1998).

The resulting models can be classified into three major categories:

1. *macroscopic phenomenological models*, built on phenomenological thermodynamics and/or directly on curves fitting experimental data. These models are generally suitable for engineering applications due to their simplicity and fast computations, but they can only describe the global mechanical response and ignore all the microscopic details. Moreover, since these models are generally based on standard phase diagrams determined experimentally, the models are also quite accurate. However, several three-dimensional macroscopic phenomenological models based on continuum thermodynamics with internal variables have been successfully proposed in the literature, as described in the following;

2. *microscopic thermodynamics models*, focused on the description of micro-scale features, e.g., nucleation, interface motion, and twin growth (Abeyaratne and Knowles, 1990; Ball and James, 1987). Such models are extremely helpful to understand the fundamental phenomena rather than the quantitative description of macroscopic behavior, but are often difficult to apply to engineering applications. Details can be found in, e.g., (Ball and James, 1987; Falk, 1980, 1983);

3. *micro-mechanics based macroscopic models*, based on the modeling of a single grain and further averaging the results over a representative volume element to obtain a polycrystalline response of the SMA. Such models use thermodynamics laws to describe phase transformations and utilize micro-mechanics to estimate the interaction energy due to material transformation (Fischer and Tanaka, 1992; Gao et al., 2000; Huang et al., 2000; Lexcellent et al., 1996; Sun and Hwang, 1993a). As an example, Patoor et al. (1996) modeled the behavior of a polycrystalline SMA by using a single crystal model and the self-consistent averaging method to account for the interactions between the grains. Sun and Hwang (1993a,b) presented a micro-mechanical model able to capture different effects of SMA behavior such as pseudo-elasticity and shape memory effect. Micro-mechanics based macroscopic models appear to have good predictive capabilities and moreover, in some cases, they are also able to successfully reproduce reorientation and detwinning of martensite variants (Gao and Brinson, 2002; Marketz and Fischer, 1996; Thamburaja, 2005). However, such models employ a large number of internal variables which makes computations time intensive, resulting in a difficult application for engineering purposes.

6.2 Phenomenological models for shape memory alloys

The present thesis focuses on the macroscopic or phenomenological modeling approach, since well-suited for practical engineering purposes.

In the phenomenological framework, the thermodynamic state of a material at a given point and instant is completely described by a set of *state variables* at that instant, which depends only upon the considered point. Therefore, different material behaviors can be described by choosing an appropriate set of state variables, whose evolution in time constitutes a thermodynamic process. As an example, we recall the elastoplastic modeling based on continuum thermodynamics with internal variables, presented in Chapter 2. State variables can be divided into *observable variables* (typically the total strain and temperature), which are the only ones involved in non-dissipative phenomena, and *internal variables*, introduced to keep track of material history and influencing material current behavior in dissipative phenomena. Some examples of internal variables often introduced in SMA models are the martensite volume fraction and the total transformation strain.

Generally, the macroscopic or phenomenological modeling approach can be categorized in two groups of models, depending on the presence or not of internal variables in the formulation, as explained in the following.

6.2.1 Models without internal variables

Such models describe material behavior by strain, stress, temperature, and entropy without the introduction of internal variables representing phase mixture.

Polynomial potential models

Such models provide constitutive information by introducing a polynomial free-energy function from which constitutive equations for strain (or stress) and entropy are derived (Daghia et al., 2010; Falk, 1980, 1983; Falk and Konopka, 1990). The main advantage of such models is their simple form, but they are not able to model complex material behaviors as well as to describe accurately the evolutive nature of the processes.

Hysteresis models

Hysteresis models seek to reproduce experimental curves that involve high non-linearity and complex looping and have been widely used in several fields, in particular for magnetic materials. In such an approach, constitutive equations are proposed directly on the basis of their mathematical properties, often without explicit focus on their link with the underlying physical phenomena of interest (Huo, 1989; Ivshin and Pence, 1994; Likhacev and Koval, 1992; Ortin, 1992).

6.2.2 Models with internal variables

Such models introduce appropriate internal variables describing material internal structure. A general thermodynamical consistent approach then allows to derive evolution equations for the internal variables. The first application of such an approach to SMAs seems to be due to Tanaka and Nagaki (1982) who employed internal variables to describe the development of the underlying phase mixture.
Models based on internal variables can be categorized into two groups, as described in the following.

Models with assumed phase transformation kinetics

Models with assumed phase transformation kinetics consider the martensitic volumetric fraction as an internal variable. Several authors propose different functions to describe the volumetric fraction evolution. The model firstly developed by Lin et al. (1994); Tanaka and Iwasaki (1985); Tanaka et al. (1995) was originally conceived to describe three-dimensional problems involving SMAs, but nevertheless, its implementation was restricted to the one-dimensional context. Boyd and Lagoudas (1994) rewrote the Tanaka original model in a three-dimensional framework. Liang and Rogers (1990) presented an alternative evolution law for the volumetric fraction and developed a three-dimensional model. Brinson (1993) offered an alternative approach to the phase transformation kinetics, in which the author splitted the martensite fraction into two distinct quantities, the temperature-induced and the stress-induced martensites.

Models with internal variable evolution equations

Such models are developed within a more rigorous thermodynamical continuum approach. The theory is in fact composed of physical laws, i.e., constitutive equations characterizing material features, and material behavior requirements ensuring thermo-dynamical process restrictions. Constitutive information are specified by two kinds of relations:

- *state equations* for the entities conjugated to control variables, directly formulated or obtained as partial derivatives of a suitable free-energy function after enforcing the Clausius-Duhem inequality for every process. If heat conduction is included, then a constitutive equation relating temperature gradient and heat flux (usually the Fourier equation) is also required;

- *kinetic equations* for the internal variables. In view of phase transformation hysteresis, these equations generally depend on material past history. Standard practice is to specify such a dependence through equations relating the rates of the internal variables to the current state and its time derivatives. The internal state then follows from the solution of differential equations in time.

Micro-plane method

The micro-plane modeling approach originated from the work by Taylor (1938), who studied the constitutive behavior of polycrystalline metals by developing relations between stress and strain vectors on generic planes of arbitrary orientations in the material and by determining the macroscopic stress or strain tensors as a resultant of all these vectors. Such concept is commonly known as *slip theory* of plasticity. As slip is not the source of inelastic response for all types of materials, Bazant (1984) introduced a neutral term called the *micro-plane theory*. In such an approach, a one-dimensional constitutive law for one stress component and the associated strain component on each micro-plane is sufficient to generate a macroscopic three-dimensional model by considering either of two main formulations in micro-plane theory, named static and kinematic constraint. In the static constraint formulation, it is assumed that the stress vector acting on each micro-plane is the projection of the macroscopic stress; in the kinematic constraint formulation, the strain vector on any micro-plane is considered as the projection of the macroscopic strain. Moreover, there are some particular material laws where both static and kinematic constraints coexist. Brocca et al. (2002) presented a model based on micro-plane theory, able to describe both pseudo-elasticity and shape memory effect. Kadkhodaei et al. (2007) proposed a micro-plane constitutive model for polycrystalline SMA by first deriving a one-dimensional model and then generalizing it to a three-dimensional case.

Frémond model

Frémond (2002) developed a three-dimensional model, able to reproduce both the pseudo-elasticity and shape memory effect, with the aid of three internal variables that should obey internal constraints related to the coexistence of the different phases. The model takes into account phenomena as linear hardening plasticity, plastic-phase transformation coupling, phase transformation due to temperature variation, internal subloops due to incomplete phase transformation, tension-compression asymmetry, and transformation-induced plasticity. Successively, Paiva et al. (2005); Savi and Braga (1993) published several works based on the model by Frémond (2002).

6.3 Review on some phenomenological models

In the present thesis we employ the continuum thermodynamics with internal variables which is, in our opinion, the most suited approach for the development of reliable three-dimensional SMA constitutive equations, able to describe material response under complex multiaxial thermo-mechanical loadings, as discussed in Chapter 7.
This Section briefly reviews the principal features of the three-dimensional phenomenological constitutive models investigated in the following Chapters, i.e., the models by Souza et al. (1998), Auricchio et al. (2009, 2011), and Boyd and Lagoudas (1996); Lagoudas et al. (2012). The explicit integration scheme for solving the constitutive equations of the model by Lagoudas et al. (2012) is also derived. For a detailed model presentation, the reader is referred to the works (Auricchio et al., 2009, 2011; Auricchio and Petrini, 2004a; Boyd and Lagoudas, 1996; Lagoudas et al., 2012; Souza et al., 1998).

6.3.1 Model by Souza et al. (1998)

The first investigated model has been originally presented by Souza et al. (1998) and then investigated by Auricchio and Petrini (2004a). The model has been recognized as very effective in capturing main SMA macroscopic features, especially in consideration of the limited number of involved parameters. The model is in fact able to describe both pseudo-elasticity and shape memory effect by assuming the total strain, $\boldsymbol{\varepsilon}$, and the absolute temperature, T, as control variables, and the transformation strain, $\mathbf{e}^{tr}$, associated to transformations between austenite and single-variant martensite, as internal one.

Assuming a small strain regime, the free-energy function, $\Psi = \Psi\left(\boldsymbol{\varepsilon}, T, \mathbf{e}^{tr}\right)$, is defined as:

$$\Psi = \Psi^{el} + \Psi^{tr} + \Psi^{ch} + \Psi^{v} \tag{6.1}$$

where:

$$\begin{cases} \Psi^{el} = \dfrac{1}{2} K\theta^2 + G\|\mathbf{e} - \mathbf{e}^{tr}\|^2 \\ \Psi^{tr} = \dfrac{1}{2} h\|\mathbf{e}^{tr}\|^2 \\ \Psi^{ch} = \tau_m\left(T\right)\|\mathbf{e}^{tr}\| \end{cases} \tag{6.2}$$

Here K and G are, respectively, the bulk and the shear modulus, depending on the Young's modulus, and on the Poisson's ratio; h is a positive parameter related to material hardening during phase transformation; $\tau_m = \beta\left\langle T - T_0\right\rangle$ with β a positive material parameter related to the dependence of the critical stress on temperature and T_0 the temperature below which only martensite phase is stable.

The term $\Psi^v = I_{\varepsilon_L}(\|\mathbf{e}^{tr}\|)$ is an indicator function introduced to satisfy the constraint on the norm of $\mathbf{e}^{tr}$, as follows:

$$I_{\varepsilon_L}(\|\mathbf{e}^{tr}\|) = \begin{cases} 0 & \text{if } \|\mathbf{e}^{tr}\| \leq \varepsilon_L \\ +\infty & \text{otherwise} \end{cases} \tag{6.3}$$

where ε_L is a parameter related to the maximum transformation strain reached at the end of the transformation during an uniaxial test.

Following standard arguments (Gurtin et al., 2010), the constitutive equations are derived:

$$\begin{cases} p = \dfrac{\partial \Psi}{\partial \theta} = K\theta \\ \mathbf{s} = \dfrac{\partial \Psi}{\partial \mathbf{e}} = 2G(\mathbf{e} - \mathbf{e}^{tr}) \\ \mathbf{X} = -\dfrac{\partial \Psi}{\partial \mathbf{e}^{tr}} = \mathbf{s} - \tau_m \dfrac{\mathbf{e}^{tr}}{\|\mathbf{e}^{tr}\|} - h\mathbf{e}^{tr} - \gamma \dfrac{\mathbf{e}^{tr}}{\|\mathbf{e}^{tr}\|} \end{cases} \tag{6.4}$$

The quantities $p = \text{tr}(\boldsymbol{\sigma})/3$ and $\mathbf{s}$ are, respectively, the volumetric and the deviatoric part of the stress, $\boldsymbol{\sigma}$; the quantity, $\mathbf{X}$, is the thermodynamic force associated to the transformation strain, $\mathbf{e}^{tr}$; the variable, γ, results from the indicator function subdifferential, $\partial I_{\varepsilon_L}(\|\mathbf{e}^{tr}\|)$.

To describe phase transformation and inelasticity evolution, the limit function, $F = F\left(\mathbf{X}\right)$, is defined as follows:

$$F = \|\mathbf{X}\| - R \tag{6.5}$$

while the flow rule for $\mathbf{e}^{tr}$ as:

$$\dot{\mathbf{e}}^{tr} = \dot{\zeta}\frac{\mathbf{X}}{\|\mathbf{X}\|} \tag{6.6}$$

where R is the positive radius of the elastic domain and $\dot{\zeta}$ a non-negative consistency parameter.

The model is finally completed by the classical Kuhn-Tucker conditions:

$$\dot{\zeta} \geq 0,\ F \leq 0,\ \dot{\zeta} F = 0,\ \dot{\zeta} \dot{F} = 0 \tag{6.7}$$

The model has been numerically treated by Auricchio and Petrini (2004a). The solution algorithm is simple and robust as it is based on a plasticity-like return map procedure and makes the model suitable for implementation within FE codes, allowing the simulation of complex SMA devices.

6.3.2 Model by Auricchio et al. (2009) and Auricchio et al. (2011)

The model by Auricchio and Petrini (2004a); Souza et al. (1998) presents some limitations, e.g., in properly capture low stress phase transformations, as often required by industrial applications (Auricchio et al., 2009).
The model can be extended as done by Auricchio et al. (2009, 2011), through the introduction of a linear dependence of the elastic radius, R, on temperature, T, to improve model capability to catch the transition phase for low stress phase transformations. The radius, R, introduced in Eq. (6.5), is thus assumed to control the width of the hysteresis loops, i.e., $R = R(T)$, through the introduction of two radii, R_0 and R_1, corresponding to the elastic domain radii at low and high temperatures, respectively.
The same numerical treatment of the model by Souza et al. (1998) has been adopted for the model by Auricchio et al. (2009, 2011).

6.3.3 Model by Boyd and Lagoudas (1996) and Lagoudas et al. (2012)

The last investigated model has been originally presented by Boyd and Lagoudas (1996) and then generalized by Lagoudas et al. (2012). The improved model is able to take into account the description of smooth transitions in the thermo-mechanical response at the beginning and the end of phase transformation, the variation of transformation strain magnitude with applied stress level, and the variation of the transformation hysteresis area with applied stress level due to the stress-dependent critical thermodynamic force for transformation.

The model assumes the stress, $\boldsymbol{\sigma}$, and the absolute temperature, T, as control variables, and the transformation strain, $\boldsymbol{\varepsilon}^t$, the total martensitic volume fraction, ξ, and the transformation hardening energy, g^t, as internal ones. The total martensitic volume fraction, ξ, is bounded by $0 \leq \xi \leq 1$.

Assuming a small strain regime, the Gibbs free-energy function, $G = G\left(\boldsymbol{\sigma}, T, \boldsymbol{\varepsilon}^t, \xi, g^t\right)$, is defined as:

$$G = (1 - \xi)\, G^A + \xi G^M + G^{mix} \tag{6.8}$$

where $G^i = G^i\left(\boldsymbol{\sigma}, T\right)$ is defined as follows:

$$G^i = -\frac{1}{2\rho}\, \boldsymbol{\sigma} : \mathbf{S}^i \boldsymbol{\sigma} - \frac{1}{\rho}\, \boldsymbol{\sigma} : \boldsymbol{\alpha}\,(T - T_0) + c^i \left[T - T_0 - T \ln\left(\frac{T}{T_0}\right)\right] - s_0^i T + u_0^i \tag{6.9}$$

for $i = A, M$.
The energy of mixing, $G^{mix} = G^{mix}\left(\boldsymbol{\sigma}, \boldsymbol{\varepsilon}^t, \xi, g^t\right)$, is defined as:

$$G^{mix} = -\frac{1}{\rho} \boldsymbol{\sigma} : \boldsymbol{\varepsilon}^t + \frac{1}{\rho} g^t \tag{6.10}$$

Model parameters, $\mathbf{S}$, c, s_0, and u_0, denoting the compliance tensor, specific heat, specific entropy at the reference state, and specific internal energy at the reference state, respectively, are assumed to be different for each phase; parameters, ρ and $\boldsymbol{\alpha}$, denoting the density and the thermal expansion tensor, respectively, are assumed to be the same regardless of phase. The effective values of the phase-dependent parameters,

$\mathbf{S}$, c, s_0, and u_0, are evaluated in terms of the martensitic volume fraction, ξ, by the rule of mixtures, as follows:

$$\begin{cases} \mathbf{S} = \mathbf{S}^A + \xi\left(\mathbf{S}^M - \mathbf{S}^A\right) \\ c = c^A + \xi\left(c^M - c^A\right) \\ s_0 = s_0^A + \xi\left(s_0^M - s_0^A\right) \\ u_0 = u_0^A + \xi\left(u_0^M - u_0^A\right) \end{cases} \tag{6.11}$$

The evolution equation for the transformation strain, $\boldsymbol{\varepsilon}^t$, is defined as follows:

$$\dot{\boldsymbol{\varepsilon}}^t = \dot{\xi}\boldsymbol{\Lambda}^t \tag{6.12}$$

where:

$$\boldsymbol{\Lambda}^t = \begin{cases} \boldsymbol{\Lambda}_{fwd}^t = \dfrac{3}{2}H^{cur}\dfrac{\mathbf{s}}{\overline{\sigma}} & \text{if } \dot{\xi} > 0 \\ \boldsymbol{\Lambda}_{rev}^t = \dfrac{\boldsymbol{\varepsilon}^{t-r}}{\xi^r} & \text{if } \dot{\xi} < 0 \end{cases} \tag{6.13}$$

with $\overline{\sigma} = \sqrt{3/2\,\mathbf{s} : \mathbf{s}}$.
In the above definition, $\boldsymbol{\Lambda}_{fwd}^t$ and $\boldsymbol{\Lambda}_{rev}^t$ are the transformation direction tensors during forward and reverse transformation, respectively, while $\boldsymbol{\varepsilon}^{t-r}$ and ξ^r are the macroscopic transformation strain and the martensite volume fraction at the reverse transformation, respectively. The uniaxial transformation strain magnitude for full transformation, $H^{cur} = H^{cur}\left(\overline{\sigma}\right)$, is defined as:

$$H^{cur} = \begin{cases} H_{min} & \text{if } \overline{\sigma} \leq \overline{\sigma}_{crit} \\ H_{min} + \left(H_{sat} - H_{min}\right)\left(1 - \exp^{-k\left(\overline{\sigma} - \overline{\sigma}_{crit}\right)}\right) & \text{if } \overline{\sigma} > \overline{\sigma}_{crit} \end{cases} \tag{6.14}$$

Here, H_{min} corresponds to the observable uniaxial two-way shape memory effect; the parameter, H_{sat}, describes the ultimate transformation strain given in an uniaxial loading, i.e., the maximum recoverable transformation strain generated such that increases in stress magnitude do not increase the transformation strain. Additionally, $\overline{\sigma}_{crit}$ denotes the critical Mises equivalent stress below which $H^{cur} = H_{min}$. The parameter, k, controls the rate at which H^{cur} exponentially evolves from H_{min} to H_{sat}.

The evolution equation for the transformation hardening energy, g^t, is defined as follows:

$$\dot{g}^t = f^t\dot{\xi} \tag{6.15}$$

where the hardening function, $f^t = f^t\left(\xi\right)$, is defined as:

$$f^t = \begin{cases} f_{fwd}^t & \text{if } \dot{\xi} > 0 \\ f_{rev}^t & \text{if } \dot{\xi} < 0 \end{cases} \tag{6.16}$$

such that $\int_0^1 f_{fwd}^t d\xi + \int_1^0 f_{rev}^t d\xi = 0$. The two terms for forward and reverse transformation, f_{fwd}^t and f_{rev}^t, are defined to take into account a smooth transition from elastic to transformation response, as follows:

$$f^t = \begin{cases} f_{fwd}^t = \dfrac{1}{2}a_1\left(1 + \xi^{n_1} - \left(1 - \xi\right)^{n_2}\right) + a_3 \\ f_{rev}^t = \dfrac{1}{2}a_2\left(1 + \xi^{n_3} - \left(1 - \xi\right)^{n_4}\right) - a_3 \end{cases} \tag{6.17}$$

where a_1, a_2, a_3 are positive material parameters and the exponents n_1, n_2, n_3 and n_4 assume real number values in the interval $(0, 1]$.

Following standard arguments (Gurtin et al., 2010), the following constitutive equations are derived:

$$\begin{cases} \boldsymbol{\varepsilon} = -\rho \dfrac{\partial G}{\partial \boldsymbol{\sigma}} = \mathbf{S}\boldsymbol{\sigma} + \boldsymbol{\alpha}\left(T - T_0\right) + \boldsymbol{\varepsilon}^t \\ s = -\dfrac{\partial G}{\partial T} = \dfrac{1}{\rho}\boldsymbol{\alpha} : \boldsymbol{\sigma} + c \ln\left(\dfrac{T}{T_0}\right) + s_0 \end{cases} \tag{6.18}$$

The total thermodynamic force, π^t, conjugate to ξ, is then derived:

$$\pi^t = \boldsymbol{\sigma} : \boldsymbol{\Lambda}^t + p - f^t \tag{6.19}$$

where $p = -\rho \partial G / \partial \xi$.
The transformation function, ϕ^t, is denoted as follows:

$$\phi^t = \begin{cases} \phi^t_{fwd} = \pi^t_{fwd} - Y^t_{fwd} & \text{if } \dot{\xi} > 0 \\ -\phi^t_{rev} = -\pi^t_{rev} - Y^t_{rev} & \text{if } \dot{\xi} < 0 \end{cases} \tag{6.20}$$

where the critical thermodynamic driving force, $Y^t = Y^t\left(\boldsymbol{\sigma}\right)$, is:

$$Y^t = \begin{cases} Y^t_{fwd} = Y^t_0 + D\boldsymbol{\sigma} : \boldsymbol{\Lambda}^t_{fwd} & \text{if } \dot{\xi} > 0 \\ Y^t_{rev} = Y^t_0 + D\boldsymbol{\sigma} : \boldsymbol{\Lambda}^t_{rev} & \text{if } \dot{\xi} < 0 \end{cases} \tag{6.21}$$

Here Y^t_0 is a positive constant and D is an additional positive model parameter that captures the stress dependency of the critical thermodynamic force.

The model is finally completed by the classical Kuhn-Tucker conditions:

$$\begin{cases} \dot{\xi} \geq 0,\ \phi^t_{fwd} \leq 0,\ \dot{\xi}\phi^t_{fwd} = 0 \\ \dot{\xi} \leq 0,\ \phi^t_{rev} \leq 0,\ \dot{\xi}\phi^t_{rev} = 0 \end{cases} \tag{6.22}$$

6.3.4 Explicit integration scheme for the model by Boyd and Lagoudas (1996) and Lagoudas et al. (2012)

We now elaborate on the algorithmic treatment of the governing equations of the model by Boyd and Lagoudas (1996); Lagoudas et al. (2012). For the sake of notation simplicity, the convention establishes superscript n for all the variables evaluated at time t_n, while drops superscript $n+1$ for all the variables computed at time t_{n+1}.

In order to discretize Eq. (6.12) in time, we can use the general trapezoidal rule, as follows (Hartl, 2009):

$$\boldsymbol{\varepsilon}^t = \boldsymbol{\varepsilon}^t_n + \left(\xi - \xi_n\right)\left[\left(1-\alpha\right)\boldsymbol{\Lambda}^t_n + \alpha\boldsymbol{\Lambda}^t_{n+1}\right] \tag{6.23}$$

where α is an algorithmic parameter that ranges from 0 to 1. Infinitely many options exist for the value of α, which is often chosen and then held constant during the analysis. In particular, the case $\alpha = 0$ leads to the well-known *forward-Euler integration*, while the case $\alpha = 1$ leads to the well-known *backward-Euler integration*. For a detailed investigation, the reader is referred to (Hartl, 2009; Lagoudas et al., 2012; Ortiz and Simo, 1986; Qidwai and Lagoudas, 2000a).

In this Section, we consider only the case $\alpha = 0$ (Hartl, 2009). Therefore, forward integration is performed by setting $\alpha = 0$ in Eq. (6.23), which gives:

$$\boldsymbol{\varepsilon}^t = \boldsymbol{\varepsilon}^t_n + \left(\xi - \xi_n\right)\boldsymbol{\Lambda}^t_n \tag{6.24}$$

where a purely explicit forward integration depends on the ability to approximate both $\boldsymbol{\varepsilon}^t$ and $\boldsymbol{\Lambda}^t$ directly from the solution at the previous time step. While the transformation strain direction tensor, $\boldsymbol{\Lambda}^t$, has a

known functional form thanks to Eq. (6.13), i.e., $\mathbf{\Lambda}^t = \mathbf{\Lambda}^t(\boldsymbol{\sigma}_n)$, a similar form for calculating ξ is not immediately evident. We can derive such a relation by using the transformation consistency conditions (6.22).

Enforcing the consistency condition in the current time step, we have:

$$\phi^t(T, \xi, \boldsymbol{\sigma}) = 0 \tag{6.25}$$

In some cases, i.e., when $n_1 = n_2 = n_3 = n_4 = 1$ in Eq. (6.17), it is possible to invert Eq. (6.25) and to find $\xi = \widehat{\xi}(\boldsymbol{\sigma}, T)$. Using the forward-Euler explicit methodology and recalling that T is provided by the global solver, we then assume that for small increments $\xi \approx \widehat{\xi}(\boldsymbol{\sigma}_n, T)$.

Thus, we can write the explicit forward-Euler integration of the transformation strain evolution equation as:

$$\boldsymbol{\varepsilon}^t = \boldsymbol{\varepsilon}_n^t + \left(\widehat{\xi}(\boldsymbol{\sigma}_n, T) - \xi_n\right) \mathbf{\Lambda}_n^t \tag{6.26}$$

This allows for simplified coding and rapid calculation, but very small time steps are required to achieve accuracy. This reduces the overall efficiency of the scheme. Further, the integration algorithm can become unstable and thus may not converge to the correct solution (Hartl, 2009; Lagoudas et al., 2012; Ortiz and Simo, 1986; Qidwai and Lagoudas, 2000a).

Table 6.1 provides a summary of the full explicit algorithm needed to integrate the constitutive relations in a FE framework. Such a scheme has been implemented within the Abaqus/Explicit user material subroutine, VUMAT (SIMULIA, 2012).

---

1. Initialize: $\xi^{(0)} = \xi_n$, $\boldsymbol{\varepsilon}^{t(0)} = \boldsymbol{\varepsilon}_n^t$, $\mathbf{S}^{(0)} = \mathbf{S}_n$, $\boldsymbol{\alpha}^{(0)} = \boldsymbol{\alpha}_n$
2. Elastic prediction:
   - $\boldsymbol{\sigma}^{(0)} = \mathbf{C}^{(0)}\left[\boldsymbol{\varepsilon} - \boldsymbol{\alpha}^{(0)}(T - T_0) - \boldsymbol{\varepsilon}^{t(0)}\right]$
   - $\mathbf{\Lambda}^{t(0)} = \mathbf{\Lambda}^t\left(\boldsymbol{\sigma}^{(0)}\right)$
   - Evaluate $\phi^{t(0)}$
   - If $\phi^{t(0)} \leq 0$ then EXIT (elastic response)
3. Transformation correction:
   - else if $\phi^{t(0)} > 0$ CONTINUE
   - find $\xi = \widehat{\xi}\left(\boldsymbol{\sigma}^{(0)}, T\right)$
   - if $0 \leq \xi \leq 1$ then CONTINUE, ELSE set ξ to violated bound
   - update $\boldsymbol{\varepsilon}^t = \boldsymbol{\varepsilon}_n^t + (\xi - \xi_n)\,\mathbf{\Lambda}^{t(0)}$
   - update $\mathbf{S} = \mathbf{S}(\xi)$, $\boldsymbol{\alpha} = \boldsymbol{\alpha}(\xi)$
   - update $\boldsymbol{\sigma} = \mathbf{C}\left[\boldsymbol{\varepsilon} - \boldsymbol{\alpha}(T - T_0) - \boldsymbol{\varepsilon}^t\right]$
   - update $\mathbf{\Lambda}^t = \mathbf{\Lambda}^t(\boldsymbol{\sigma})$
   - EXIT

Table 6.1: Explicit forward-Euler integration scheme for the model by Boyd and Lagoudas (1996) and Lagoudas et al. (2012).

Numerical test for the model by Boyd and Lagoudas (1996) and Lagoudas et al. (2012)

We now test the proposed VUMAT on an uniaxial tensile test at constant temperature, simulated as simple uniaxial tension test with displacement control and prescribed homogeneous constant temperature field.

In the numerical test we adopt the material parameters reported in Table 6.2. We consider a constant temperature of $27\,^{\circ}\mathrm{C}$ for the tensile test with internal subloop. Accordingly, Figure 6.1 reports the stress-strain diagram with the curves obtained with both the implicit and explicit integration schemes for the models by Boyd and Lagoudas (1996); Lagoudas et al. (2012) and by Auricchio and Taylor (1997)[1] (denoted as TAMU and AAT, respectively). The reported curves are exactly matching and encourage further investigations of the developed VUMAT for more complex quasi-static and dynamic analyses.

Parameter	**Value**	**Unit**
E^A	55	GPa
E^M	46	GPa
$\nu^A = \nu^M$	0.33	-
α	0	$1/\,^{\circ}\mathrm{C}$
M_s	-28	$^{\circ}\mathrm{C}$
M_f	-43	$^{\circ}\mathrm{C}$
A_s	-3	$^{\circ}\mathrm{C}$
A_f	7	$^{\circ}\mathrm{C}$
$\left(C^M = C^A\right)_{\bar{\sigma}=300\,MPa}$	7.4	$\mathrm{MPa}/\,^{\circ}\mathrm{C}$
$H^{cur}\left(\bar{\sigma}\right) = H$	0.056	-

Table 6.2: Adopted parameters for the model by Boyd and Lagoudas (1996) and Lagoudas et al. (2012).

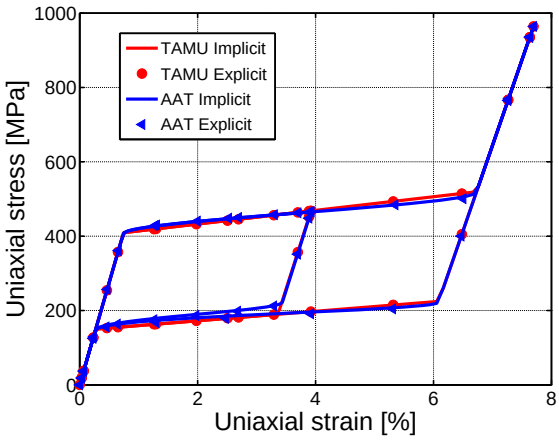

Figure 6.1: Pseudoelastic uniaxial tensile test with displacement control and internal subloop at a constant temperature of $27\,^{\circ}\mathrm{C}$. Comparison between the implicit and explicit integration schemes for the models by Lagoudas et al. (2012) and Auricchio and Taylor (1997) (denoted, respectively, as TAMU and AAT).

[1]The model by Auricchio and Taylor (1997) is currently provided as a standard component of all recent Abaqus installations.

Chapter 7

A new 'flexible' approach for shape memory alloy modeling

This Chapter proposes to develop a refined, flexible and general three-dimensional phenomenological constitutive model for shape memory alloys, along the lines of what recently proposed by Auricchio and Bonetti (2013) in a more theoretical context. Such a 'flexible' model takes into account several physical phenomena, as martensite reorientation and different kinetics between forward/reverse phase transformations, including also smooth thermo-mechanical response, low-stress phase transformations as well as transformation-dependent elastic properties. The model is then treated numerically through the effective and efficient procedure based on the Fischer-Burmeister complementarity function, already investigated in Chapter 4 for J_2 elastoplasticity.

The Chapter is organized as follows. Section 7.1 presents an introduction to the work and explains the motivations of the proposed approach. Then, Section 7.2 presents the new 'flexible' model. Section 7.3 presents the one-dimensional phase diagram and model calibration based on a simple physical interpretation. Section 7.4 describes the numerical implementation of model equations and the full solution algorithm. Finally, conclusions are given in Section 7.5.

7.1 Introduction and motivations

The unique functional properties of shape memory alloys (SMAs), described in Section 5.2, motivate researchers to formulate constitutive models able to catch the interesting behavior of these alloys and to develop robust computational tools for practical purposes.
In the following, we focus on both the constitutive and numerical modeling of SMAs by briefly reviewing the actual state of art and by carefully describing the improvements of the proposed 'flexible' approach.

Constitutive modeling: state of art

In the past three decades SMAs have been deeply investigated from the point of view of modeling, analysis, and computation with the focus on a variety of aspects, e.g., stress- and temperature-induced transformations, martensite reorientation, or cyclic effects.

In terms of modeling, there have been several attempts to properly reproduce SMA features and the resulting models can be categorized as either micro, micro-macro or macro, as extensively discussed in Chapter 6. In the following, we focus on phenomenological macro-modeling approaches which appear to be a powerful tool for the direct simulation of SMA applications, thanks to their simple numerical implementation and reduced time-consuming calculations, compared to micro-mechanical approaches. In

particular, the research presented in this Chapter is devoted to the aim of finding a flexible and accurate three-dimensional phenomenological model for a reliable description of SMA-based real devices behavior.

In the phenomenological framework, an appropriate set of internal variables has to be chosen to represent at least a scalar and a directional information (Luig and Bruhns, 2008). Physical motivations usually lead to the introduction of a martensite volume fraction and of a tensorial variable describing martensitic inelastic deformation processes (Arghavani et al., 2010; Luig and Bruhns, 2008; Peultier et al., 2006; Saleeb et al., 2011). Such a simplified description is motivated by the aim to obtain fast and efficient models with a low number of fitting parameters.

A set of only scalar variables is, in fact, not adequate due to the loss of explicit directional information. For instance, the model by Frémond (2002) describes SMA behavior in terms of austenite and two martensite variants and assumes the transformation strain direction to be known, although experimental studies showed that variant reorientation can be considered as a main phenomenon in SMA non-proportional loadings (Bouvet et al., 2002; Grabe and Bruhns, 2009; Helm and Haupt, 2003; Lim and McDowell, 1999; Sittner et al., 1995; Sun and Li, 2002).

On the other hand, models with only tensorial internal variables, by including directional information, seem to be more successful, but present some limitations since scalar and directional informations are tightly interconnected, possibly leading to limited or constrained modeling approaches. As an example, the model by Souza et al. (1998), then investigated by (Auricchio and Petrini, 2004a,b), introduces the transformation strain tensor as an internal variable and presents a simple and robust algorithm (see Section 6.3.1 for details). On the contrary, it is not able to capture phase transformations (PTs) for low levels of stress and does not include some secondary effects that may turn out to be relevant in practical cases (Auricchio et al., 2009; Thamburaja and Anand, 2001).

Numerous analyses of existing models and their comparison to experimental results have shown that current SMA constitutive models have reached a high level of sophistication. Several authors extended, in fact, such simplified phenomenological descriptions by using additional variables as volume fraction of twinned/detwinned martensites (Lexcellent et al., 2000; Panico and Brinson, 2007; Popov and Lagoudas, 2007), plastic strain (Auricchio et al., 2007; Hartl et al., 2010; Peng et al., 2012; Saint-Sulpice et al., 2009; Zaki et al., 2010), twins accommodation strain (Chemisky et al., 2011), viscoplasticity (Chemisky et al., 2014), or thermo-mechanical coupling (Morin et al., 2011a,b; Zaki and Moumni, 2007a,b). The recent and innovative work by Sedlák et al. (2012) formulates a new dissipation function to simulate non-proportional loadings and includes anisotropic behavior of textured SMAs as well as the thermo-mechanical response due to austenite-R-phase transformation. However, the most capable models usually achieve accuracy at the cost of complexity, since they consider multiple and simultaneous processes (Chemisky et al., 2011; Popov and Lagoudas, 2007) or require costly calibrations of a high number of model parameters (Saleeb et al., 2013, 2011).

Constitutive modeling: proposed improvements

Starting from the reviewed literature about constitutive modeling, the work proposed in the present Chapter is motivated by the necessity of developing constitutive models that can predict the complex thermo-mechanical behavior of SMAs and that can also be implemented numerically. Such models have to accurately capture material response not only during classical pseudo-elastic (PE) and shape memory effect (SME) loading paths, but also during loading paths involving the co-existence of all the three material phases, i.e., austenite, multiple- and single-variant martensite. Moreover, model material parameters have to be derived from a simple physical interpretation, which is important for the calibration process. Indeed, the goal of the present work is to introduce a refined, flexible and general three-dimensional phenomenological constitutive model for SMAs, along the lines of the recent theoretical work by Auricchio and Bonetti (2013), limiting the discussion to the small deformation regime.

The model by Auricchio and Bonetti (2013) addresses a general flexible theoretical framework for the

development of constitutive models able to describe multiple phase transformations (PTs), which may or may not interact. The model is investigated from a purely mathematical point of view, by proposing some general considerations on requirements to be satisfied to make the model thermo-dynamically consistent. In particular, the cited reference does not cover the following fundamental details:

1. as concerns the constitutive modeling, the cited work gives only some very general indications on the effective modeling of SMA materials and, as a matter of fact, it reports only a very simple one-dimensional qualitative hand-computed response of the model. In fact, the cited reference does not apply in details the model to the case of SMAs and, at the same time, it does not give any indication on the possibility of effectively and robustly solving the complex set of possible PTs occurring in real SMAs, which represents the essential starting point into SMA modeling;

2. as concerns the model parameters' physical interpretation and identification, the cited reference does not address the important issue related to the physical interpretation of model parameters, as a clear and effective parameter identification procedure is an important key for the employment of a constitutive model by engineers in real-life simulations. In particular, model parameters are defined as general constants or general functions of temperature and volume fractions;

3. as concerns the numerical modeling, the cited model does not address any numerical solution algorithm to model formulation.

In this context, the present work aims to do a step-forward with respect to the work by Auricchio and Bonetti (2013) by deepening all the listed lacking aspects and to possibly offer a new contribution to the existing modeling solutions. The purpose is to formulate a general, complete and flexible theoretical framework that can predict the complex behavior of SMAs and is based on a physical interpretation of material parameters as well as to offer a robust numerical framework to be then used for the simulation of real devices.

From the modeling point of view, the proposed model combines the main features of the approaches by Frémond (2002) and Souza et al. (1998) and describes secondary effects in PTs as well as directional information for the transformation strain. Volume proportions of different configurations of crystal lattice (i.e., austenite, single- and multiple-variant martensites) are used as scalar internal variables and the direction of single-variant martensite as tensorial internal variable. From the physical point of view, material parameters are then derived from a simple physical interpretation, and thus, are no more represented as general constants or general functions of temperature and volume fractions.

With respect to the model by Frémond (2002), the present model considers the transformation strain direction unknown, by assuming the direction of single-variant martensite as tensorial internal variable. Compared to the model by Souza et al. (1998), the proposed theoretical framework allows for a completely independent description of the different PTs, leading to a very flexible frame in terms of model features and allowing to capture PTs at low levels of stress. Compared to the model by Auricchio and Bonetti (2013), the proposed model naturally presents similarities in terms of theoretical aspects and governing equations. In the present work, however, we propose an enriched generalization, able to describe several phenomena such as martensite reorientation, different kinetics between forward/reverse phase transformations, smooth thermo-mechanical response, low stress phase transformations, transformation-dependent elastic properties. We remark, moreover, that the proposed modeling approach presents similarities with some three-dimensional phenomenological models presented in the literature, in terms of capturing the reorientation process in martensite. Among the others, we can cite the interesting works by Arghavani et al. (2010) and Chemisky et al. (2011). Compared to the cited references, the proposed approach is very flexible since it can capture loading paths involving the co-existence of three material phases.

Numerical modeling: state of art

The proposed work focuses on another important aspect of SMA modeling, i.e., the development of an appropriate model implementation into numerical softwares (such as FE packages) to guarantee a robust computational tool, which could be effectively utilized for practical purposes. From a numerical point of view, robust and efficient integration algorithms for the zero-dimensional problem (e.g., constitutive equations at the Gauss point level in a FE scheme) need to be proposed in order to then solve complex boundary-value problems and to simulate SMA real devices behavior within FE codes. Some examples of SMA models are available in the literature in a suitable form to conduct three-dimensional thermo-mechanical simulations (Arghavani et al., 2011; Auricchio and Petrini, 2004a; Gao et al., 2007; Hartl et al., 2010; Hartl and Lagoudas, 2009; Helm, 2007; Lagoudas et al., 2012; Peultier et al., 2008; Popov and Lagoudas, 2007; Sedlák et al., 2012; Stupkiewicz and Petryk, 2012; Zaki, 2012a,b).

Generally, SMA macroscopic models are solved by return-map algorithms, either through norm regularization schemes at the cost of inaccuracy due to the corresponding approximation (Auricchio and Petrini, 2004a,b; Auricchio and Stefanelli, 2004) or nucleation-completion conditions (Arghavani et al., 2011). The recent work by Sedlák et al. (2012) applies the Nelder-Mead minimization algorithm to solve the derived energy minimization problem and introduces a regularization energy to assure the fulfillment of constraints on internal variables. Stupkiewicz and Petryk (2012) presented a PE model within the incremental energy minimization framework and proposed an unified augmented Lagrangian treatment of both constitutive constraints and non-smooth dissipation function. The recent works by Peigney and Seguin (2013); Peigney et al. (2011) propose a new numerical approach for a micro-mechanical material model, based on the reformulation of the incremental problem as a linear complementarity problem (LCP), which can be solved using well established algorithms such as interior-point methods. Solving the obtained LCP allows to fully take the constraints on the internal variable into account and leads to an efficient numerical algorithm. The work by Popov and Lagoudas (2007) applies an extension of the closest point projection algorithm to describe a SMA model incorporating single- and multi-variant martensites. The work by Hartl and Lagoudas (2009) proposes a three-dimensional constitutive model capturing conventional SMA functional properties and thermal strain recovery, and additionally considering the initiation and evolution of plastic strains. The model is numerically implemented in a FE framework using a return mapping algorithm to solve the constitutive equations at each material point.

However, algorithm schemes still need robustness investigations, aiming also at the development of flexible, effective and efficient procedures, applicable to models as the one introduced in the present work. In fact, the numerical application of standard predictor-corrector methods is not suitable for the proposed approach, because an elaborate active set search has to be carried out. Compared to the work by Hartl and Lagoudas (2009), for instance, the proposed model deals with multiple scalar and tensorial internal variables, whose evolution is strongly coupled, and involving several constitutive constraints imposed on internal variables, which introduce additional complexity in the incremental schemes used in FE computations and, consequently, decrease algorithmic efficiency.

Numerical modeling: proposed improvements

For the reasons explained above, different approaches need to be explored for the proposed modeling framework. Recalling the above discussion, the model by Auricchio and Bonetti (2013) does not address any numerical solution algorithm to model formulation.

The purpose of the present work to integrate the proposed constitutive equations is to reduce the complexity, and thus increase the efficiency, of the algorithmic treatment. This is achieved by eliminating the need for a predictor-corrector-type scheme and by automatically constraining the range of the variant volume fractions. Consequently, we conduct the numerical investigation of the proposed model through the effective and efficient procedure, based on the Fischer-Burmeister complementarity function, already

investigated in Chapter 4 for J_2 elastoplasticity. It allows to omit an active set search, a fundamental advantage when dealing with several phase fractions and many coupled evolution equations.

Besides the contributions by Bartel and Hackl (2009, 2010); Bartel et al. (2011) in the context of SMA micro-mechanical modeling, the work by Kiefer et al. (2012) presents two alternative algorithms for the integration of the coupled, non-linear and inelastic constitutive equations for magnetic SMAs, i.e., the classical predictor-corrector return-mapping scheme and the Fischer-Burmeister based algorithm. The work shows the greater numerical efficiency of the second algorithm that is however tested for simple loading cases and not for three-dimensional analyses. Therefore, the research of the present Chapter aims to a detailed investigation of the Fischer-Burmeister based algorithm, applied to the case of SMAs, to test its robustness and efficiency.

7.2 A time-continuous model formulation

This Section addresses a general three-dimensional phenomenological model for SMAs along the lines of the recent theoretical work by Auricchio and Bonetti (2013) and then, it proposes a simplified formulation based on physically motivated considerations.
In the following, we adopt superscripts A, M, and S to indicate austenite, multi-variant and single-variant martensites, respectively.

7.2.1 A general model formulation

In the framework of macroscopic modeling and of small strain continuum mechanics, we assume the total strain, $\boldsymbol{\varepsilon}$, and temperature, T, as state variables. A general assumption of additive strain decomposition is adopted in the form:

$$\boldsymbol{\varepsilon} = \boldsymbol{\varepsilon}^e + \boldsymbol{\varepsilon}^{ie} + \boldsymbol{\varepsilon}^{th} \tag{7.1}$$

where $\boldsymbol{\varepsilon}^e$, $\boldsymbol{\varepsilon}^{ie}$ and $\boldsymbol{\varepsilon}^{th}$ denote the elastic, inelastic and thermal strain, respectively. The inelastic strain, $\boldsymbol{\varepsilon}^{ie}$, should include the description of several physical phenomena, ranging from permanent plasticity and PTs, up to void generation and fracture. In the following, all inelastic phenomena are neglected except for reversible martensitic PTs which are considered in combination with martensite reorientation.

Recalling the discussion reported in Section 7.1, the model introduces scalar and tensorial internal variables taking into account different PTs between austenite, multiple- and single-variant martensites as well as directional information for the transformation strain. The model decouples the pure reorientation from the pure transformation mechanism, but additionally, takes into account for temperature-induced transformation. Consequently, similarly to (Arghavani et al., 2010; Chemisky et al., 2011), we do not treat the inelastic strain, $\boldsymbol{\varepsilon}^{ie}$, as a unique tensor variable, but we clearly distinguish between its norm and direction with the aim of getting more modeling freedom. In the following, we choose a measure of the amount of single-variant martensite as scalar internal variable, being related to the amount of inelastic strain due to stress-induced PT, while the average direction of different variants (or preferred direction of variants) as tensorial internal variable, representing the inelastic strain direction. Consequently, we may clearly interpret these two internal variables as PT and variant reorientation in order to hopefully describe transformation and reorientation with more flexibility. Moreover, we choose a measure of the amount of multiple-variant martensite as scalar internal variable, being related to the amount of martensite due to thermal-induced PT.

According to the previous discussion, volume proportions of different configurations of crystal lattice (austenite and martensite variants) are assumed as scalar internal variables and are represented by three phase parameters, χ^A, χ^M, χ^S, standing, respectively, for austenite, multiple-variant and single-variant martensite, such that $\chi^A, \chi^M, \chi^S \in [0,1]$ and $\chi^A + \chi^M + \chi^S = 1$. Thanks to this last constraint, the

model restricts itself just to two independent phase variables, χ^M and χ^S, letting $\chi^A = 1 - \chi^M - \chi^S$. Then, the following restrictions need to be fulfilled:

$$0 \leq \chi^M, \chi^S \leq 1, \quad \chi^M + \chi^S \leq 1 \tag{7.2}$$

Consequently, the inelastic strain is given by:

$$\boldsymbol{\varepsilon}^{ie} = \varepsilon_L \chi^S \mathbf{d}^{tr} \tag{7.3}$$

where ε_L is a material parameter related to the maximum transformation strain reached at the end of the transformation during an uniaxial test (Otsuka and Ren, 2005), while $\mathbf{d}^{tr}$ is the direction of single-variant martensite, assumed as tensorial internal variable with the following constraint:

$$\|\mathbf{d}^{tr}\| = 1 \tag{7.4}$$

We remark, again, that the choice of dealing with a tensorial variable, $\mathbf{d}^{tr}$, and two scalar variables, χ^M and χ^S, allows to distinguish between a phase to which no macroscopic strain is associated and a phase to which a homogenized macroscopic strain is associated, as well as to consider thermal-induced transformations when no stress is applied. Moreover, the model is able to distinguish between the norm and the direction of the inelastic strain, $\boldsymbol{\varepsilon}^{ie}$, similarly to other effective modeling approaches as the one proposed in Arghavani et al. (2010); Chemisky et al. (2011), but allowing to get a richer model compared, for instance, to the works by Auricchio and Petrini (2004a,b); Frémond (2002); Souza et al. (1998).

Helmholtz free-energy function

The Helmholtz free-energy function, $\Psi = \Psi\left(\boldsymbol{\varepsilon}, T, \chi^M, \chi^S, \mathbf{d}^{tr}\right)$, is assumed in the following form:

$$\Psi = \Psi^{el} + \Psi^{ch} + \Psi^{int} + \Psi^{v} \tag{7.5}$$

where Ψ^{el} is the elastic energy, Ψ^{ch} the chemical energy related to entropic changes due to PTs, Ψ^{int} the interaction or interfacial energy, often derived from micro-mechanical or metallurgical considerations (Chemisky et al., 2011; Moumni et al., 2008; Peultier et al., 2006), and Ψ^{v} the energy due to internal constraints.

For the first two components of the Helmholtz free-energy function, i.e., $\Psi^{el} = \Psi^{el}\left(\boldsymbol{\varepsilon}, \chi^M, \chi^S, \mathbf{d}^{tr}\right)$ and $\Psi^{ch} = \Psi^{ch}\left(T, \chi^M, \chi^S\right)$, presented in Eq. (7.5), we employ the rule of mixtures (Lagoudas et al., 2006), considering that each of them is a combination of austenite, multiple-variant and single-variant martensites. In particular, we set:

$$\begin{cases} \Psi^{el} = \left(1 - \chi^M - \chi^S\right) \Psi^{el,A} + \chi^M \Psi^{el,M} + \chi^S \Psi^{el,S} \\ \Psi^{ch} = \left(1 - \chi^M - \chi^S\right) \Psi^{ch,A} + \chi^M \Psi^{ch,M} + \chi^S \Psi^{ch,S} \end{cases} \tag{7.6}$$

To treat the elastic energy of Eq. $(7.6)_1$, Ψ^{el}, we develop the aspect of phase mixture following the model of Reuss, by assuming the material as elastically isotropic with a homogeneous distribution of stresses in austenite, multiple-variant and single-variant martensites. The elastic energy term, Ψ^{el}, follows:

$$\Psi^{el} = \frac{1}{2} K \theta^2 + G \|\mathbf{e} - \varepsilon_L \chi^S \mathbf{d}^{tr}\|^2 - 3\alpha K \theta \left(T - T_0\right) \tag{7.7}$$

where T_0 is the equilibrium temperature. The bulk modulus, K, is assumed equal for all phases and the total shear modulus, $G = G\left(\chi^M, \chi^S\right)$, is determined from the Reuss model (Wagner and Windl, 2008), i.e.:

$$\begin{cases} K = K^A = K^M = K^S \\ \dfrac{1}{G} = \left(1 - \chi^M - \chi^S\right) \dfrac{1}{G^A} + \chi^M \dfrac{1}{G^M} + \chi^S \dfrac{1}{G^S} \end{cases} \tag{7.8}$$

The last right-side term of Eq. (7.7) derives from the assumption that $\boldsymbol{\varepsilon}^{th} = \boldsymbol{\alpha}\,(T - T_0)$, $\boldsymbol{\alpha} = \alpha\mathbf{I}$ being the thermal expansion coefficient tensor.

To treat the chemical energy of Eq. $(7.6)_2$, Ψ^{ch}, we define the free-energies of pure phases at stress-free conditions, $\Psi^{ch,i} = \Psi^{ch,i}\,(T)$, as:

$$\Psi^{ch,i} = u_0^i - s_0^i T + c^i \left[(T - T_0) - T\log\frac{T}{T_0}\right] \tag{7.9}$$

for $i \in A, M, S$. Here u_0^i and s_0^i are the internal energy and entropy of the i-phase at a fixed equilibrium temperature, T_0; c^i is the constant heat capacity of the i-phase (Leclercq and Lexcellent, 1996; Lexcellent et al., 2006; Panico and Brinson, 2007).

The free-energy component, $\Psi^{int} = \Psi^{int}\left(\chi^M, \chi^S\right)$, presented in Eq. (7.5), represents the interactions that appear between the phases, typically the incompatibilities between deformations (Leclercq and Lexcellent, 1996; Raniecki et al., 1992). One of the characteristics of this energy is that it must disappear when only one phase is present inside the material. Moreover, in the case of three phases coexisting, this term must take into account interactions between one phase and the two remaining ones, separately (one interface separates two phases and not three). Indeed, we assume the following expression for the configurational energy (this expression has the great advantage to become fairly simple):

$$\Psi^{int} = \left(1 - \chi^M - \chi^S\right)\left(\overline{\Psi}^{AM}\chi^M + \overline{\Psi}^{AS}\chi^S + \overline{\Psi}^{AMS}\chi^M\chi^S\right) + \overline{\Psi}^{MS}\chi^M\chi^S \tag{7.10}$$

$\overline{\Psi}^{AM}$, $\overline{\Psi}^{AS}$, $\overline{\Psi}^{MS}$, and $\overline{\Psi}^{AMS}$ being material constants indicating interaction energies between phases A and M, A and S, M and S, A, M and S, respectively (Leclercq and Lexcellent, 1996; Raniecki et al., 1992).

To satisfy constraints (7.2) and (7.4) on internal variables, we define the free-energy contribution, Ψ^v, presented in Eq. (7.5), as:

$$\Psi^v = I_{[0,1]}\left(\chi^M, \chi^S\right) + I_1\left(\|\mathbf{d}^{tr}\|\right) \tag{7.11}$$

where the indicator function, $I_{[0,1]}\left(\chi^M, \chi^S\right)$, is set to enforce inequality constraints (7.2) on χ^M and χ^S as (Rockafellar, 1970):

$$I_{[0,1]}\left(\chi^M, \chi^S\right) = \begin{cases} 0 & \text{if } 0 \le \chi^M, \chi^S \le 1,\ \chi^M + \chi^S \le 1 \\ +\infty & \text{otherwise} \end{cases} \tag{7.12}$$

and the indicator function, $I_1\left(\|\mathbf{d}^{tr}\|\right)$, is defined to enforce equality constraint (7.4) on $\mathbf{d}^{tr}$ as:

$$I_1\left(\|\mathbf{d}^{tr}\|\right) = \begin{cases} 0 & \text{if } \|\mathbf{d}^{tr}\| = 1 \\ +\infty & \text{otherwise} \end{cases} \tag{7.13}$$

In conclusion, the energy term, Ψ, reads as:

$$\begin{aligned} \Psi = {} & \frac{1}{2}K\theta^2 + G\|\mathbf{e} - \varepsilon_L\chi^S\mathbf{d}^{tr}\|^2 - 3\alpha K\theta\,(T - T_0) \\ & + u_0^A - s_0^A T + c^A\left[(T - T_0) - T\log\frac{T}{T_0}\right] \\ & - \left(\Delta u^{AM}\chi^M + \Delta u^{AS}\chi^S\right) + \left(\Delta s^{AM}\chi^M + \Delta s^{AS}\chi^S\right)T \\ & - \left(\Delta c^{AM}\chi^M + \Delta c^{AS}\chi^S\right)\left[(T - T_0) - T\log\frac{T}{T_0}\right] \\ & + \left(1 - \chi^M - \chi^S\right)\left(\overline{\Psi}^{AM}\chi^M + \overline{\Psi}^{AS}\chi^S + \overline{\Psi}^{AMS}\chi^M\chi^S\right) \\ & + \overline{\Psi}^{MS}\chi^M\chi^S + I_{[0,1]}\left(\chi^M, \chi^S\right) + I_1\left(\|\mathbf{d}^{tr}\|\right) \end{aligned} \tag{7.14}$$

where:

$$\begin{cases}\Delta u^{AM} = u_0^A - u_0^M \\ \Delta u^{AS} = u_0^A - u_0^S\end{cases} \quad \begin{cases}\Delta s^{AM} = s_0^A - s_0^M \\ \Delta s^{AS} = s_0^A - s_0^S\end{cases} \quad \begin{cases}\Delta c^{AM} = c^A - c^M \\ \Delta c^{AS} = c^A - c^S\end{cases} \tag{7.15}$$

Constitutive equations

Starting from the adopted free-energy, Ψ, presented in Eq. (7.14), and following standard arguments (Gurtin et al., 2010), we derive the volumetric and the deviatoric part of the stress tensor, $\boldsymbol{\sigma}$, denoted, respectively, with p and $\mathbf{s}$, and the entropy, η:

$$\begin{cases} p = \dfrac{\partial \Psi}{\partial \theta} = K\theta - 3\alpha K\left(T - T_0\right) \\ \mathbf{s} = \dfrac{\partial \Psi}{\partial \mathbf{e}} = 2G\left(\mathbf{e} - \varepsilon_L \chi^S \mathbf{d}^{tr}\right) \\ \eta = -\dfrac{\partial \Psi}{\partial T} = s_0^A - \left(\Delta s^{AM}\chi^M + \Delta s^{AS}\chi^S\right) \\ \qquad\qquad + \left(c^A - \Delta c^{AM}\chi^M - \Delta c^{AS}\chi^S\right)\log\dfrac{T}{T_0} + 3\alpha K\theta \end{cases} \tag{7.16}$$

as well as the thermodynamic forces, B^M, B^S and $\mathbf{B}^d$, associated to χ^M, χ^S and $\mathbf{d}^{tr}$, respectively:

$$\begin{cases} B^M = -\dfrac{\partial \Psi}{\partial \chi^M} = -\dfrac{\partial G}{\partial \chi^M}\|\mathbf{e} - \varepsilon_L\chi^S\mathbf{d}^{tr}\|^2 + \Delta u^{AM} - \Delta s^{AM}T \\ \qquad\qquad +\Delta c^{AM}\left[(T - T_0) - T\log\dfrac{T}{T_0}\right] \\ \qquad\qquad -\left(\overline{\Psi}^{AM} + \overline{\Psi}^{AMS}\chi^S\right)\left(1 - 2\chi^M - \chi^S\right) \\ \qquad\qquad +\left(\overline{\Psi}^{AS} - \overline{\Psi}^{MS}\right)\chi^S - \gamma^M \\ B^S = -\dfrac{\partial \Psi}{\partial \chi^S} = 2G\varepsilon_L\left(\mathbf{e} - \varepsilon_L\chi^S\mathbf{d}^{tr}\right) : \mathbf{d}^{tr} - \dfrac{\partial G}{\partial \chi^S}\|\mathbf{e} - \varepsilon_L\chi^S\mathbf{d}^{tr}\|^2 \\ \qquad\qquad +\Delta u^{AS} - \Delta s^{AS}T + \Delta c^{AS}\left[(T - T_0) - T\log\dfrac{T}{T_0}\right] \\ \qquad\qquad -\left(\overline{\Psi}^{AM} + \overline{\Psi}^{AMS}\chi^M\right)\left(1 - \chi^M - 2\chi^S\right) \\ \qquad\qquad +\left(\overline{\Psi}^{AS} - \overline{\Psi}^{MS}\right)\chi^M - \gamma^S \\ \mathbf{B}^d = -\dfrac{\partial \Psi}{\partial \mathbf{d}^{tr}} = 2G\varepsilon_L\chi^S\left(\mathbf{e} - \varepsilon_L\chi^S\mathbf{d}^{tr}\right) - \gamma^d\mathbf{d}^{tr} \end{cases} \tag{7.17}$$

Variables γ^M and γ^S are defined as:

$$\gamma^M = \partial I_{[0,1]}\left(\chi^M, \chi^S\right) = \begin{cases}\gamma^{M0} \le 0 & \text{if } \chi^M = 0 \\ 0 & \text{if } 0 < \chi^M < 1 \\ \gamma^{MS} \ge 0 & \text{if } \chi^M + \chi^S = 1\end{cases} \tag{7.18}$$

and

$$\gamma^S = \partial I_{[0,1]}\left(\chi^M, \chi^S\right) = \begin{cases}\gamma^{S0} \le 0 & \text{if } \chi^S = 0 \\ 0 & \text{if } 0 < \chi^S < 1 \\ \gamma^{MS} \ge 0 & \text{if } \chi^M + \chi^S = 1\end{cases} \tag{7.19}$$

while

$$\gamma^d = \partial I_1\left(\|\mathbf{d}^{tr}\|\right) \neq \emptyset \text{ if } \|\mathbf{d}^{tr}\| = 1 \tag{7.20}$$

We can rewrite Eqs. (7.18)-(7.19) in terms of the classical Kuhn-Tucker complementarity conditions:

$$\begin{cases} \chi^M \geq 0,\ \gamma^{M0} \leq 0,\ \gamma^{M0}\chi^M = 0 \\ \chi^S \geq 0,\ \gamma^{S0} \leq 0,\ \gamma^{S0}\chi^S = 0 \\ \left(\chi^M + \chi^S - 1\right) \leq 0,\ \gamma^{MS} \geq 0,\ \gamma^{MS}\left(\chi^M + \chi^S - 1\right) = 0 \end{cases} \tag{7.21}$$

Moreover, we may observe that, in the case of proportional loading, i.e., neglecting the reorientation process, by definition, the preferred variant direction, $\mathbf{d}^{tr}$, coincides with the deviatoric stress direction, $\mathbf{s}$. Under this assumption, we may simplify model equations by setting $\mathbf{d}^{tr} = \mathbf{s}/\|\mathbf{s}\|$.

Evolution equations and limit functions

As traditionally done in the context of associative evolution, we assume the evolution equations of internal variables as follows:

$$\begin{cases} \dot{\chi}^M = \dot{\zeta}^M \dfrac{B^M}{|B^M|} \\ \dot{\chi}^S = \dot{\zeta}^S \dfrac{B^S}{|B^S|} \\ \dot{\mathbf{d}}^{tr} = \dot{\zeta}^d \dfrac{\mathbf{B}^d}{\|\mathbf{B}^d\|} \end{cases} \tag{7.22}$$

where $\dot{\zeta}^M$, $\dot{\zeta}^S$ and $\dot{\zeta}^d$ are non-negative consistency parameters.

Then, we define three limit functions, i.e., $F^M = F^M\left(B^M\right)$, $F^S = F^S\left(B^S, \chi^S, T\right)$ and $F^d = F^d\left(\mathbf{B}^d, \chi^S\right)$, playing the role of yield functions (Lubliner, 1990), to describe PTs and reorientation evolutions, in the following form:

$$\begin{cases} F^M = |B^M| - R^M \\ F^S = |B^S| - R^S \\ F^d = \|\mathbf{B}^d\| - R^d \end{cases} \tag{7.23}$$

where R^M and $R^S = R^S\left(B^S, \chi^S, T\right)$ represent the positive radii of elastic domains to activate temperature and pure transformations, respectively, while $R^d = R^d\left(\chi^S\right)$ represents a positive threshold value for the component of stress in the direction normal to the preferred direction of variants to activate variant reorientation. We observe that the proposed limit functions depend on the three thermodynamic forces, B^M, B^S, and $\mathbf{B}^d$, and on the radii, R^M, R^S, and R^d, whose adopted forms determine the specific dependencies of each limit function.

The model is finally completed by the classical Kuhn-Tucker and consistency conditions, as follows:

$$\begin{cases} \dot{\zeta}^M \geq 0,\ F^M \leq 0,\ \dot{\zeta}^M F^M = 0,\ \dot{\zeta}^M \dot{F}^M = 0 \\ \dot{\zeta}^S \geq 0,\ F^S \leq 0,\ \dot{\zeta}^S F^S = 0,\ \dot{\zeta}^S \dot{F}^S = 0 \\ \dot{\zeta}^d \geq 0,\ F^d \leq 0,\ \dot{\zeta}^d F^d = 0,\ \dot{\zeta}^d \dot{F}^d = 0 \end{cases} \tag{7.24}$$

A significant flexibility is assigned to the model in terms of ability to reproduce experimental evidences by introducing a very special form for R^S. In particular, through a proper choice of R^S we can guarantee the following features:

- asymmetric behavior between forward and reverse PTs, also modeled, for instance, in the works by Bouvet et al. (2004); Lagoudas et al. (2012);

- hardening effects, also modeled, for instance, in the work by Bouvet et al. (2004);
- increasing hysteresis width for low applied stresses in thermal-cycling tests at constant load, as experimentally demonstrated by Shaw and Kyriakides (1995); Stachowiak and McCormick (1987, 1988) and also modeled, for instance, in the works by Brinson (1993); Chemisky et al. (2011); Lagoudas et al. (2012); Panico and Brinson (2007); Peultier et al. (2008); Popov and Lagoudas (2007);
- width of the hysteresis loop in superelasticity (i.e., difference between upper and lower plateau stress) decreasing with increasing temperature, as experimentally demonstrated by Sittner et al. (2009) and also modeled, for instance, in the work by Sedlák et al. (2012);
- smooth thermo-mechanical response, as experimentally demonstrated by Hartl et al. (2010); Lagoudas et al. (2006) and also modeled, for instance, in the work by Lagoudas et al. (1996).

To take into account all these aspects we introduce the following very specific form for R^S:

$$R^S = \begin{cases} R^S_{f^0} + h^S_f \chi^S + a^S_{f^0} \left(\chi^S\right)^n + a^S_{f^1} \left(1-\chi^S\right)^n & \text{if } B^S \geq 0 \\ R^S_{r^0} - h^S_r \chi^S - c^S_T \left(T - T_0\right) + a^S_{r^0} \left(\chi^S\right)^n + a^S_{r^1} \left(1-\chi^S\right)^n & \text{if } B^S < 0 \end{cases} \tag{7.25}$$

$R^S_{f^0}$, $R^S_{r^0}$, h^S_f, h^S_r, c^S_T, $a^S_{f^0}$, $a^S_{r^0}$, $a^S_{f^1}$, $a^S_{r^1}$, and $n \in [0,1]$ being positive material parameters, discussed in Section 7.3 (subscripts f and r stand for forward and reverse PT).

We remark that we derive such an expression by starting from some modeling contributions presented in the literature and cited in the above list. In particular, we distinguish between the positive and negative sign of B^S to model the asymmetric behavior between forward and reverse PTs. Then, we introduce the following terms: (i) $h^S_f \chi^S$ and $h^S_r \chi^S$ to classically describe hardening effects due to single-variant martensite; (ii) $a^S_{f^0} \left(\chi^S\right)^n$, $a^S_{f^1} \left(1-\chi^S\right)^n$, $a^S_{r^0} \left(\chi^S\right)^n$, and $a^S_{r^1} \left(1-\chi^S\right)^n$ to describe hardening effects as well as smooth thermo-mechanical response always due to single-variant martensite; and (iii) $c^S_T \left(T - T_0\right)$ to model increasing hysteresis width for low applied stresses in thermal-cycling tests at constant load as well as the width of the hysteresis loop in superelasticity decreasing with increasing temperature. This last choice manifests itself as two different slopes of the phase diagram boundaries for forward and reverse transformations, known as stress influence coefficients (Liang and Rogers, 1992) or stress rates (Duerig et al., 1990; Otsuka and Wayman, 1998), as presented in Section 7.3.

Dissipation function

Although the proposed model relies on an yield surface-based formulation, we complete the description by recalling that the yield surface conditions can be equivalently converted in a pseudo-potential of dissipation, $\phi = \phi\left(\dot{\chi}^M, \dot{\chi}^S, \dot{\mathbf{d}}^{tr}\right)$, which is a positive convex functional depending on dissipative variables, vanishing for vanishing dissipation, in particular in the form:

$$\phi = R^M |\dot{\chi}^M| + R^S |\dot{\chi}^S| + R^d \|\dot{\mathbf{d}}^{tr}\| \tag{7.26}$$

The introduced pseudo-potential of dissipation, ϕ, captures forward and reverse austenite to multiple-variant martensite and austenite to single-variant martensite transformations as well as the reorientation process of single-variant martensite. The pseudo-potential of dissipation, ϕ, may also depend on state and internal variables through the particular forms chosen for R^M, R^S, and R^d. This choice assigns a significant flexibility to the model.

7.2.2 A simplified model formulation

Based on physically motivated considerations, the present Section introduces a simplified model formulation, still able to capture fundamentals SMA feature effects.

We start by making the following assumptions:

1. regarding single- and multiple-variant martensites, we reasonably assume:

   - equal internal energies and entropies between single- and multi-variant martensites, implying $\Delta u^{AMS} = \Delta u^{AM} = \Delta u^{AS}$ and also $\Delta s^{AMS} = \Delta s^{AM} = \Delta s^{AS}$;
   - equal interaction energies between single- and multiple-variant martensites with austenite, i.e., $\overline{\Psi}^{in} = \overline{\Psi}^{AM} = \overline{\Psi}^{AS}$ and $\overline{\Psi}^{AMS} = \overline{\Psi}^{MS} = 0$;
   - equal shear moduli between single- and multiple-variant martensites, i.e., $G^{MS} = G^{M} = G^{S}$;

2. since many calorimetry experiments showed that the heat capacities of austenite and single-variant martensite are almost equal, we assume $\Delta c^{AS} = 0$ (Qidwai and Lagoudas, 2000b). We make the same reasonable assumption for multiple-variant martensite, i.e., $\Delta c^{AM} = 0$;

3. since T_0 denotes the equilibrium temperature at which phases energy is equal, we choose T_0 such that $\Psi^{ch,A}(T_0) = \Psi^{ch,S}(T_0)$, i.e., we obtain $T_0 = \Delta u^{AS}/\Delta s^{AS}$ (Sedlák et al., 2012). Since $\Delta u^{AMS} = \Delta u^{AM} = \Delta u^{AS}$ and $\Delta s^{AMS} = \Delta s^{AM} = \Delta s^{AS}$, it follows $\Delta u^{AMS} = \Delta s^{AMS} T_0$.

4. since thermal expansion is a secondary effect compared to martensite production, we set the thermal expansion material coefficient, α, equal to zero.

Then, by applying such assumptions to Eq. (7.14), we derive the free-energy function, $\Psi^{simpl} = \Psi^{simpl}\left(\boldsymbol{\varepsilon}, T, \chi^M, \chi^S, \mathbf{d}^{tr}\right)$ (superscript $simpl$ stands for simplified):

$$\begin{aligned}\Psi^{simpl} = &\frac{1}{2}K\theta^2 + G\|\mathbf{e} - \varepsilon_L \chi^S \mathbf{d}^{tr}\|^2 \\ &+ u_0^A - s_0^A T + c^A\left[(T - T_0) - T\log\frac{T}{T_0}\right] \\ &+ \Delta s^{AMS}\left(\chi^M + \chi^S\right)(T - T_0) + \overline{\Psi}^{in}(1 - \chi^M - \chi^S)(\chi^M + \chi^S) \\ &+ I_{[0,1]}\left(\chi^M, \chi^S\right) + I_1\left(\|\mathbf{d}^{tr}\|\right)\end{aligned} \tag{7.27}$$

We remark that the introduced free-energy function, Ψ^{simpl}, does not include full thermo-mechanical coupling since temperature is considered as a prescribed parameter.

A review of the model equations derived from the simplified free-energy (7.27) is reported in Table 7.1.

7.3 Model calibration

This Section is dedicated to the calibration of the proposed model. To properly calibrate most of the model parameters it is sufficient to focus on one-dimensional stress states, condition which reduces the model to the following simplified form:

$$\begin{aligned}\Psi^{1D} = &\frac{1}{2}\frac{\sigma^2}{E} + u_0^A - s_0^A T + c^A\left[(T - T_0) - T\log\frac{T}{T_0}\right] + \Delta s^{AMS}\left(\chi^M + \chi^S\right) \\ &(T - T_0) + \overline{\Psi}^{in}\left(1 - \chi^M - \chi^S\right)\left(\chi^M + \chi^S\right) + I_{[0,1]}\left(\chi^M, \chi^S\right)\end{aligned} \tag{7.28}$$

where σ is the uniaxial state of stress and E is the Young's modulus defined in terms of the elastic modulus of austenite, E^A, and of the elastic modulus of martensite, E^{MS}, as follows:

$$\frac{1}{E} = \left(1 - \chi^M - \chi^S\right)\frac{1}{E^A} + \left(\chi^M + \chi^S\right)\frac{1}{E^{MS}} \tag{7.29}$$

In the following, for the sake of calculus simplicity, we assume $E = E^A = E^{MS}$.

TIME-CONTINUOUS SIMPLIFIED 'FLEXIBLE' MODEL FORMULATION

State variables: $\boldsymbol{\varepsilon}$, T

Internal variables: χ^M, χ^S, $\mathbf{d}^{tr}$

Constraints on internal variables:

$$0 \leq \chi^M, \chi^S \leq 1, \quad \chi^M + \chi^S \leq 1, \quad \|\mathbf{d}^{tr}\| = 1$$

Constitutive equations:

$$\begin{cases} p = K\theta \\ \mathbf{s} = 2G(\mathbf{e} - \varepsilon_L \chi^S \mathbf{d}^{tr}) \\ \eta = s_0^A - \Delta s^{AMS}(\chi^M + \chi^S) + c^A \log \dfrac{T}{T_0} \end{cases}$$

$$\begin{cases} B^M = -\dfrac{\partial G}{\partial \chi^M}\|\mathbf{e} - \varepsilon_L \chi^S \mathbf{d}^{tr}\|^2 - \Delta s^{AMS}(T - T_0) \\ \qquad\quad -\overline{\Psi}^{in}(1 - 2\chi^M - 2\chi^S) - \gamma^M \\ B^S = 2G\varepsilon_L(\mathbf{e} - \varepsilon_L \chi^S \mathbf{d}^{tr}) : \mathbf{d}^{tr} - \dfrac{\partial G}{\partial \chi^S}\|\mathbf{e} - \varepsilon_L \chi^S \mathbf{d}^{tr}\|^2 \\ \qquad\quad -\Delta s^{AMS}(T - T_0) - \overline{\Psi}^{in}(1 - 2\chi^M - 2\chi^S) - \gamma^S \\ \mathbf{B}^d = 2G\varepsilon_L \chi^S(\mathbf{e} - \varepsilon_L \chi^S \mathbf{d}^{tr}) - \gamma^d \mathbf{d}^{tr} \end{cases}$$

Evolution equations:

$$\dot{\chi}^M = \dot{\zeta}^M \frac{B^M}{|B^M|}, \quad \dot{\chi}^S = \dot{\zeta}^S \frac{B^S}{|B^S|}, \quad \dot{\mathbf{d}}^{tr} = \dot{\zeta}^d \frac{\mathbf{B}^d}{\|\mathbf{B}^d\|}$$

Limit functions:

$$F^M = |B^M| - R^M, \quad F^S = |B^S| - R^S, \quad F^d = \|\mathbf{B}^d\| - R^d$$

Radii of elastic domains:

$$R^M = \text{const.}$$

$$R^S = \begin{cases} R^S_{f^0} + h^S_f \chi^S + a^S_{f^0}\left(\chi^S\right)^n + a^S_{f^1}\left(1 - \chi^S\right)^n & \text{if } B^S \geq 0 \\ R^S_{r^0} - h^S_r \chi^S - c^S_T(T - T_0) + a^S_{r^0}\left(\chi^S\right)^n + a^S_{r^1}\left(1 - \chi^S\right)^n & \text{if } B^S < 0 \end{cases}$$

$$R^d = \chi^S$$

Kuhn-Tucker conditions:

$$\begin{cases} \dot{\zeta}^M \geq 0,\ F^M \leq 0,\ \dot{\zeta}^M F^M = 0,\ \dot{\zeta}^M \dot{F}^M = 0 \\ \dot{\zeta}^S \geq 0,\ F^S \leq 0,\ \dot{\zeta}^S F^S = 0,\ \dot{\zeta}^S \dot{F}^S = 0 \\ \dot{\zeta}^d \geq 0,\ F^d \leq 0,\ \dot{\zeta}^d F^d = 0,\ \dot{\zeta}^d \dot{F}^d = 0 \end{cases}$$

Table 7.1: Time-continuous simplified 'flexible' model equations review.

Then, we can derive the thermodynamic forces, B^M and B^S, as follows:

$$\begin{cases} B^M = -\Delta s^{AMS}(T - T_0) - \overline{\Psi}^{in}\left(1 - 2\chi^M - 2\chi^S\right) - \gamma^M \\ B^S = \varepsilon_L \sigma - \Delta s^{AMS}(T - T_0) - \overline{\Psi}^{in}\left(1 - 2\chi^M - 2\chi^S\right) - \gamma^S \end{cases} \tag{7.30}$$

Moreover, we recall the adopted expression for R^S:

$$R^S = \begin{cases} R^S_{f^0} + h^S_f \chi^S + a^S_{f^0}\left(\chi^S\right)^n + a^S_{f^1}\left(1 - \chi^S\right)^n & \text{if } B^S \geq 0 \\ R^S_{r^0} - h^S_r \chi^S - c^S_T(T - T_0) + a^S_{r^0}\left(\chi^S\right)^n + a^S_{r^1}\left(1 - \chi^S\right)^n & \text{if } B^S < 0 \end{cases} \tag{7.31}$$

In the following, we firstly present the one-dimensional stress-temperature phase diagram related to the proposed model. Then, we list the model parameters to be calibrated, we indicate possible calibration

techniques and we also comment, whenever possible, on their physical interpretation. In particular, we observe that:

- the elastic moduli (E^A and E^{MS}, with the corresponding three-dimensional quantities, G^A, G^{MS}, and K) and the maximum amount of single-variant martensite, ε_L, can be determined directly from experimental uniaxial stress-strain curves at constant temperature;
- the difference of entropy between the austenitic and single-variant martensitic phases, Δs^{AMS}, can be determined from the slope of the forward phase transformation curve in a stress-temperature space, usually obtained from experimental tensile tests (Qidwai and Lagoudas, 2000b; Sedlák et al., 2012). Its determination is deepened in Section 7.3.3;
- the material parameter, c_T^S, describes the change of the hysteresis loop width in superelasticity (i.e., the difference between upper and lower plateau stress), which decreases with increasing temperature, as experimentally demonstrated by Sittner et al. (2009) and also modeled, for instance, in the work by Sedlák et al. (2012). Its determination from the slope of the reverse phase transformation curve in a stress-temperature space, usually obtained from experimental tensile tests, is reported in Section 7.3.3;
- the material constant indicating interaction energies between phases, $\overline{\Psi}^{in}$, the equilibrium temperature, T_0, and the parameters related to the transformation radii, i.e., R^M, $R^S_{f^*}$, $R^S_{r^*}$, h^S_f, h^S_r, can be easily calibrated by considering a temperature-induced transformation under zero stress and a stress-induced transformation at high temperature;
- the parameters $a^S_{f^0}$, $a^S_{r^0}$, $a^S_{f^1}$, $a^S_{r^1}$, and exponent, n, of Eq. (7.25) or (7.31), do not have an associated material property and are directly chosen to best fit the four corners of the transformation hysteresis plots.

In the following, we consider only the governing equations of the two transformations necessary to model calibration, i.e., a temperature-induced transformation under zero stress and a stress-induced transformation at high temperature. Moreover, for the sake of calculus simplicity, we assume R^S as follows:

$$R^S = \begin{cases} R^S_{f^0} + h^S_f \chi^S & \text{if } B^S \geq 0 \\ R^S_{r^0} - h^S_r \chi^S - c^S_T \left(T - T_0\right) & \text{if } B^S < 0 \end{cases} \tag{7.32}$$

7.3.1 One-dimensional phase diagram

This Section presents the one-dimensional stress-temperature phase diagram related to the proposed model and shown in Figure 7.1(a).

To simplify the presentation, the three phases are denoted by A, M and S, standing for austenite, multi- and single-variant martensites, respectively. The five possible PTs, indicated in Figure 7.1(a), are denoted by $A \to M$, $A \to S$, $M \to A$, $S \to A$, and $M \to S$ for austenite to multi-variant martensite, austenite to single-variant martensite, multi-variant martensite to austenite, single-variant martensite to austenite and multi- to single-variant martensite, respectively.

The critical start and finish transformation temperatures at zero stress level are denoted as follows: M_s and M_f for the $A \to M$ transformation, A^M_s and A^M_f for the $M \to A$ transformation, S_s and S_f for the $A \to S$ transformation, and A^S_s and A^S_f for the $S \to A$ transformation. A^S_s and A^S_f are assumed as different from A^M_s and A^M_f in agreement with experiments provided by Popov and Lagoudas (2007). All the temperatures are indicated in Figure 7.1(a), except for S_s and S_f.

The critical uniaxial start and finish stresses required for detwinning of twinned martensite, i.e., transformation $M \to S$, are denoted by σ_s and σ_f, respectively.

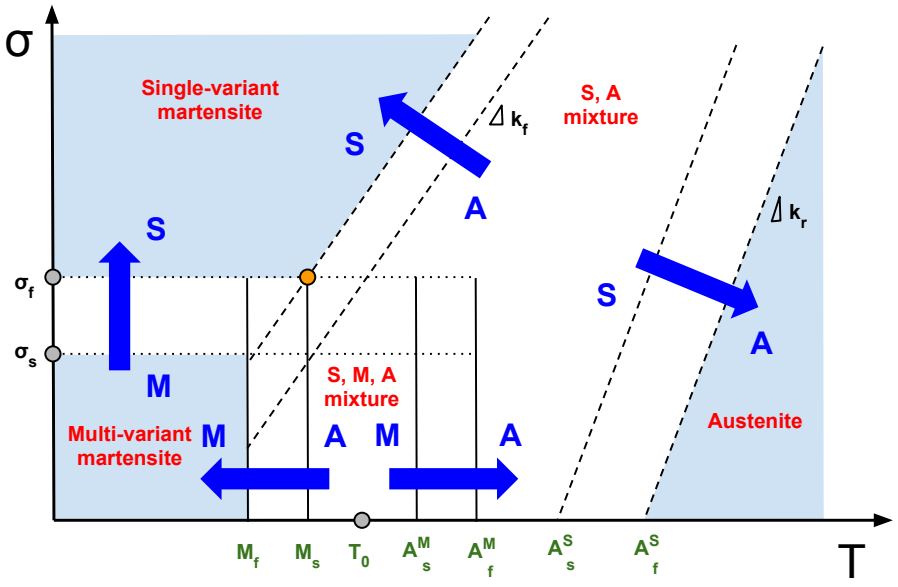

(a)

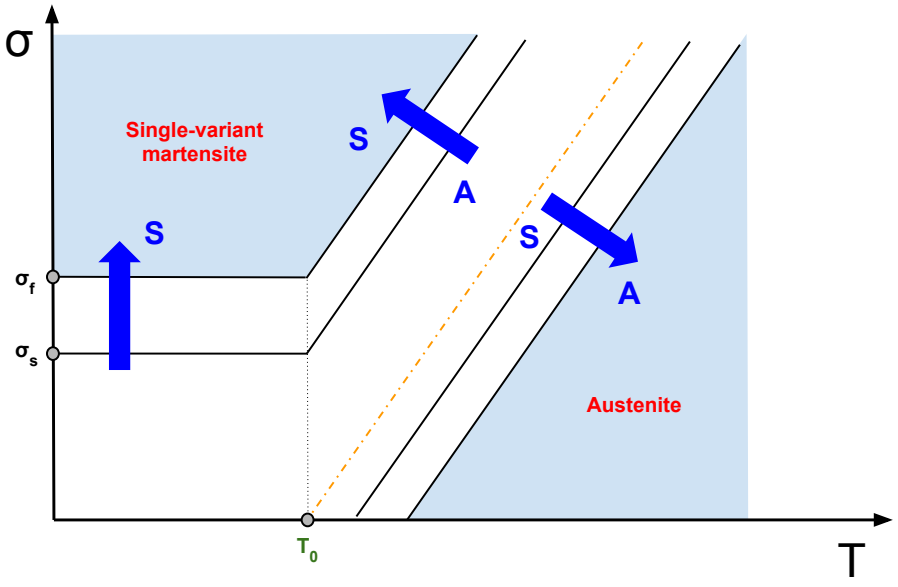

(b)

Figure 7.1: 1D phase diagrams generated by (a) the proposed 'flexible' model and (b) the Souza model, in terms of stress, σ, and temperature, T.

The phase diagram of Figure 7.1(a) follows the established literature in assuming three regions where only the pure phases A, M and S can exists (light-blue shaded regions of Figure 7.1(a)). The three regions are separated by transformation strips which are labeled according to the transformations which take place. Note that some of these strips overlap and in an overlap region multiple transformations are possible. In the non-shaded region of the phase diagram various mixtures can exist (white regions of Figure 7.1(a)).

Due to the lack of inelastic strain associated with the $A \leftrightarrow M$ transformation, we assume the start and finish lines for the forward and reverse transformations $A \leftrightarrow M$ vertical and passing through the critical temperatures M_s, M_f, A_s^M and A_f^M, respectively (Leclercq and Lexcellent, 1996; Popov and Lagoudas,

2007). This assumption has been adopted in several models taking into account the separate development of single- and multiple-variant martensites, e.g., for instance, (Leclercq and Lexcellent, 1996; Popov and Lagoudas, 2007). Clearly, the two strips are bounded by the critical stress, σ_f.

The start and finish lines for the forward strip $A \to S$ pass through the critical temperatures S_s and S_f and exhibits a temperature dependence, defined by the positive slope, k_f, in Figure 7.1(a). Equivalently, the start and finish lines for the reverse strip $S \to A$ pass through the critical temperatures A_s^S and A_f^S and exhibits a temperature dependence, defined by the positive slope, k_r. Moreover, the two strips present different widths. These features are due to the fact that the present flexible model takes into account for: (i) different kinetics between forward and reverse PTs; (ii) the increasing hysteresis width for low applied stresses in thermal-cycling tests at constant load; and (iii) the width of the hysteresis loop in superelasticity decreasing with increasing temperature.

Since Popov and Lagoudas (2007) demonstrated that if the finish line for the $A \to S$ strip passes above the intersection point (M_s, σ_f) then one can find a particular isobaric cooling path which leads to jump discontinuities in the strain as the temperature is lowered, we assume the finish line for the $A \to S$ strip passing through or below the point (M_s, σ_f) (in Figure 7.1(a) the extreme case is represented by an orange dot). Furthermore, two approaches are available from the literature for the definition of the $A \to S$ strip at low stresses ($\sigma < \sigma_s$) and temperatures ($T < M_s$): some authors have extended it to zero-stress level (Bekker and Brinson, 1997); others (Lagoudas and Shu, 1999) suggest that in the region $T < M_s$ the dependence on temperature disappears and there is a critical stress below which $A \to S$ does not occur. In our case, we assume the first choice reasonable.

Now, we consider the simple phase diagram related to the model by Souza et al. (1998) and shown in Figure 7.1(b), which classically describes the behavior of SMAs material in a one-dimensional setting. The model considers the presence of only two possible phase fractions, i.e., austenite and single-variant martensite, as shown in Figure 7.1(b). As clearly explained in Section 7.1, the model is unable to catch SMA behavior for work conditions where the material is considered as linear elastic and where the model is particularly sensitive to its numerical implementation. Such a work condition includes stress values lower than σ_f at $T < T_0$, as it can be observed in Figure 7.1(b). Contrarily, the proposed model allows for a more flexible approach taking into account the presence of multiple PTs and PTs at low levels of stress.

7.3.2 Temperature-induced transformation

We start considering a temperature-induced transformation under zero stress. To this purpose, Figure 7.2 focuses only on the $A \leftrightarrow M$ transformation, by highlighting the two related vertical strips (orange regions). Accordingly, exploiting the definition $(7.30)_1$ for the driving force B^M, we can detect start and finish of forward and reverse PT through the following conditions:

- Start forward PT: $F^M\big|_{T=M_s} = -\Delta s^{AMS}(M_s - T_0) - \overline{\Psi}^{in} - R^M = 0$
- Finish forward PT: $F^M\big|_{T=M_f} = -\Delta s^{AMS}(M_f - T_0) + \overline{\Psi}^{in} - R^M = 0$
- Start reverse PT: $F^M\big|_{T=A_s^M} = -\Delta s^{AMS}(A_s^M - T_0) + \overline{\Psi}^{in} + R^M = 0$
- Finish reverse PT: $F^M\big|_{T=A_f^M} = -\Delta s^{AMS}(A_f^M - T_0) - \overline{\Psi}^{in} + R^M = 0$

where M_s, M_f, A_s^M and A_f^M can be easily determined by differential scanning calorimetry tests (Popov and Lagoudas, 2007; Qidwai and Lagoudas, 2000b). We assume $T_0 = \left(M_f + A_f^M\right)/2$, i.e., we treat T_0 as equilibrium temperature. Accordingly, since forward and reverse PTs are perfectly symmetric, we derive

R^M and $\overline{\Psi}^{in}$ by considering only the two equations related to forward PT:

$$\begin{cases} \overline{\Psi}^{in} = -\dfrac{\Delta T^{AM} \Delta s^{AMS}}{2} \\ R^M = \Delta s^{AMS} \left(\Delta T_0 + \dfrac{\Delta T^{AM}}{2} \right) \end{cases} \tag{7.33}$$

where $\Delta T^{AM} = M_s - M_f = A_f^M - A_s^M$ and $\Delta T_0 = T_0 - M_s = A_s^M - T_0$ (see Figure 7.2).

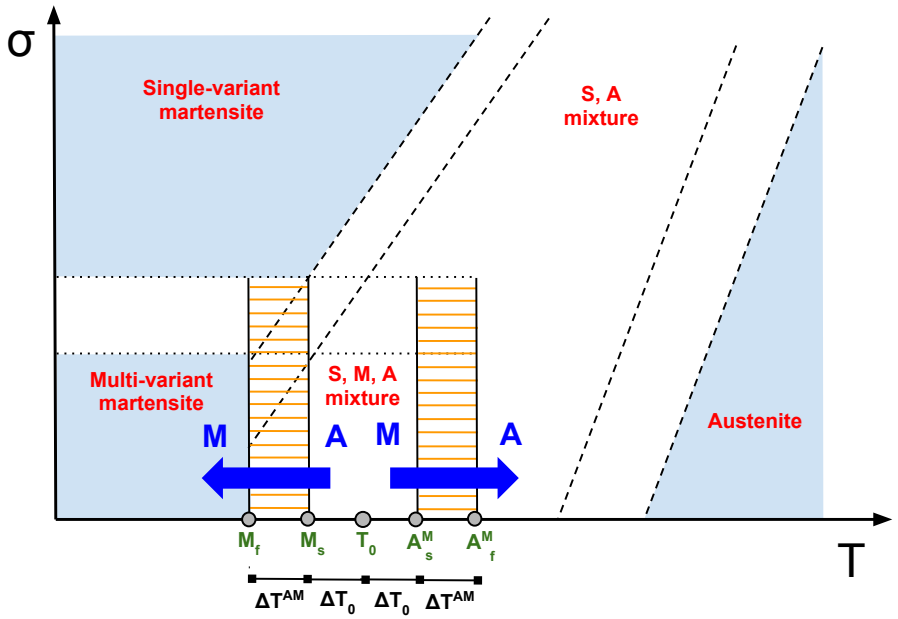

Figure 7.2: Identification of 'flexible' model parameters from a temperature-induced transformation.

7.3.3 Stress-induced transformation

We now consider a stress-induced transformation at constant high temperature, T^*. To this purpose, Figure 7.3 focuses only on $A \leftrightarrow S$ transformation, by highlighting the related strips (orange regions). The loading path is represented in Figure 7.3 by a vertical violet line passing through T^*.

Accordingly, exploiting the definition $(7.30)_2$ for the driving force B^S, we can detect start and finish of forward and reverse PT through the following conditions:

- Start forward PT: $F^S\big|_{\sigma=\sigma_s^S} = \varepsilon_L \sigma_s^S - \Delta s^{AMS}(T^* - T_0) - \overline{\Psi}^{in} - R_{f0}^S = 0$
- Finish forward PT: $F^S\big|_{\sigma=\sigma_f^S} = \varepsilon_L \sigma_f^S - \Delta s^{AMS}(T^* - T_0) + \overline{\Psi}^{in} - R_{f0}^S - h_f^S = 0$
- Start reverse PT: $F^S\big|_{\sigma=\sigma_s^A} = \varepsilon_L \sigma_s^A - \Delta s^{AMS}(T^* - T_0) + \overline{\Psi}^{in} + R_{r0}^S - h_r^S - c_T^S (T^* - T_0) = 0$
- Finish reverse PT: $F^S\big|_{\sigma=\sigma_f^A} = \varepsilon_L \sigma_f^A - \Delta s^{AMS}(T^* - T_0) - \overline{\Psi}^{in} + R_{r0}^S - c_T^S (T^* - T_0) = 0$

where σ_s^S, σ_f^S, σ_s^A and σ_f^A are the martensitic and austenitic start and finish stresses, respectively. The transformation lines for forward and reverse transformations are linear with slopes $k_f = \Delta s^{AMS}/\varepsilon_L$ and $k_r = \left(\Delta s^{AMS} + c_T^S\right)/\varepsilon_L$, respectively (see Figure 7.3). Once k_f and k_r are experimentally determined, we can calibrate both Δs^{AMS} and c_T^S.

Finally, we deduce the remaining model parameters by considering the four equations, as follows:

$$\begin{cases} h_f^S = \varepsilon_L \Delta\sigma^S + 2\overline{\Psi}^{in} \\ h_r^S = \varepsilon_L \Delta\sigma^A + 2\overline{\Psi}^{in} \\ R_{f0}^S = \varepsilon_L \sigma_s^S - \overline{\Psi}^{in} - \Delta s^{AMS}(T^* - T_0) \\ R_{r0}^S = (\Delta s^{AMS} + c_T^S)(T^* - T_0) + \overline{\Psi}^{in} - \varepsilon_L \sigma_f^A \end{cases} \tag{7.34}$$

where $\Delta\sigma^S = \sigma_f^S - \sigma_s^S$ and $\Delta\sigma^A = \sigma_s^A - \sigma_f^A$ (see Figure 7.3).

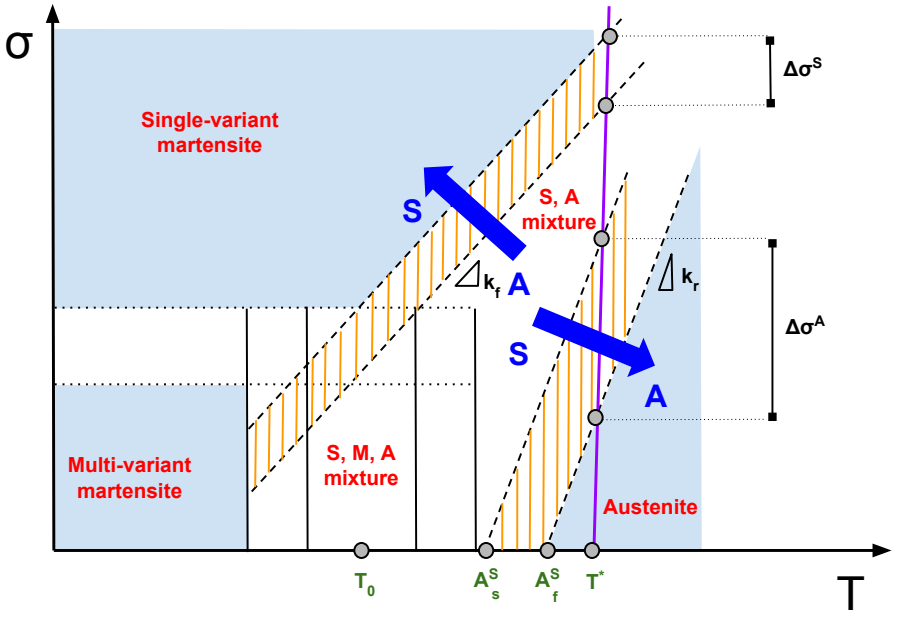

Figure 7.3: Identification of 'flexible' model parameters from a stress-induced transformation.

7.4 A time-discrete model formulation

The present Section aims to a detailed investigation of the Fischer-Burmeister based algorithm, applied to the case of SMAs, to test its robustness and efficiency.

We start by elaborating on the algorithmic treatment of the model equations summarized in Table 7.1. For the sake of notation simplicity, the convention establishes superscript n for all the variables evaluated at time t_n, while drops superscript $n+1$ for all the variables computed at time t_{n+1}.

We make use of a classical backward-Euler integration algorithm for the evolution equations (7.22), as follows:

$$\begin{cases} \chi^M - \chi_n^M - \Delta\zeta^M \dfrac{B^M}{|B^M|} = 0 \\ \chi^S - \chi_n^S - \Delta\zeta^S \dfrac{B^S}{|B^S|} = 0 \\ \mathbf{d}^{tr} - \mathbf{d}_n^{tr} - \Delta\zeta^d \dfrac{\mathbf{B}^d}{\|\mathbf{B}^d\|} = 0 \end{cases} \tag{7.35}$$

where $\Delta\zeta^M = \int_{t_n}^{t_{n+1}} \dot{\zeta}^M$, $\Delta\zeta^S = \int_{t_n}^{t_{n+1}} \dot{\zeta}^S$ and $\Delta\zeta^d = \int_{t_n}^{t_{n+1}} \dot{\zeta}^d$ are the time-integrated consistency parameters.

Then, according to the Fischer-Burmeister based algorithm investigated in Chapter 4 for J_2 elastoplasticity, we substitute the discrete Kuhn-Tucker conditions deriving from system (7.24) by the following set of functions in the time-discrete frame:

$$\begin{cases} \sqrt{(F^M)^2 + (\Delta\zeta^M)^2} + F^M - \Delta\zeta^M = 0 \\ \sqrt{(F^S)^2 + (\Delta\zeta^S)^2} + F^S - \Delta\zeta^S = 0 \\ \sqrt{(F^d)^2 + (\Delta\zeta^d)^2} + F^d - \Delta\zeta^d = 0 \end{cases} \tag{7.36}$$

We employ the same strategy to treat the set of inequalities given by constraint (7.2). In fact, the additional Kuhn-Tucker conditions (7.21) can be substituted by the equivalent equalities:

$$\begin{cases} \sqrt{(\gamma^{M0})^2 + (\chi^M)^2} + \gamma^{M0} - \chi^M = 0 \\ \sqrt{(\gamma^{S0})^2 + (\chi^S)^2} + \gamma^{S0} - \chi^S = 0 \\ \sqrt{(\gamma^{MS})^2 + (\chi^M + \chi^S - 1)^2} - \gamma^{MS} + (\chi^M + \chi^S - 1) = 0 \end{cases} \tag{7.37}$$

The time-discrete problem, $\mathbf{Q} = \mathbf{Q}(\boldsymbol{\varepsilon}, \mathbf{h})$, evaluated at time t_{n+1}, takes the specific form:

$$\mathbf{Q} = \begin{bmatrix} \chi^M - \chi_n^M - \Delta\zeta^M \dfrac{B^M}{|B^M|} = 0 \\ \sqrt{(F^M)^2 + (\Delta\zeta^M)^2} + F^M - \Delta\zeta^M = 0 \\ \sqrt{(\gamma^{M0})^2 + (\chi^M)^2} + \gamma^{M0} - \chi^M = 0 \\ \chi^S - \chi_n^S - \Delta\zeta^S \dfrac{B^S}{|B^S|} = 0 \\ \sqrt{(F^S)^2 + (\Delta\zeta^S)^2} + F^S - \Delta\zeta^S = 0 \\ \sqrt{(\gamma^{S0})^2 + (\chi^M)^2} + \gamma^{S0} - \chi^S = 0 \\ \sqrt{(\gamma^{MS})^2 + (\chi^M + \chi^S - 1)^2} - \gamma^{MS} + (\chi^M + \chi^S - 1) = 0 \\ \mathbf{d}^{tr} - \mathbf{d}_n^{tr} - \Delta\zeta^d \dfrac{\mathbf{B}^d}{\|\mathbf{B}^d\|} = 0 \\ \sqrt{(F^d)^2 + (\Delta\zeta^d)^2} + F^d - \Delta\zeta^d = 0 \\ \|\mathbf{d}^{tr}\| - 1 = 0 \end{bmatrix} = \mathbf{0} \tag{7.38}$$

with $\mathbf{h} = \left\{\chi^M, \Delta\zeta^M, \gamma^{M0}, \chi^S, \Delta\zeta^S, \gamma^{S0}, \gamma^{MS}, \mathbf{d}^{tr}, \Delta\zeta^d, \gamma^d\right\}$. The active set can now be determined via the solution of the non-linear system of equations (7.38), using a classical Newton-Raphson method, which results in the standard update relation at iteration (k), as follows:

$$\mathbf{h}^{(k+1)} = \mathbf{h}^{(k)} + \Delta\mathbf{h}^{(k)} \tag{7.39}$$

where:

$$\Delta\mathbf{h}^{(k)} = -\left(\frac{\partial\mathbf{Q}}{\partial\mathbf{h}}\right)^{-1} \mathbf{Q}\left(\boldsymbol{\varepsilon}, \mathbf{h}^{(k)}\right) \tag{7.40}$$

The FE implementation of model equations and of all the numerical examples presented in Chapter 8 is carried out using the symbolic code generation system AceGen/AceFEM (Korelc, 2009); the reader is referred to the Appendix B for further details about AceGen/AceFEM. Accordingly, we do not provide explicit expressions resulting from differentiation as these are obtained automatically using the automatic differentiation technique implemented in AceGen (Korelc, 2009). Application of these automation tools leads to exact linearization of the non-linear FE equations (consistent tangent matrix). This guarantees

quadratic convergence rate of the global Newton method and results in a robust and efficient FE implementation of the model, as illustrated by the numerical examples of Chapter 8. We remark that, in cases where no analytically evaluation of the Jacobian matrix is possible, the most known approximation is through a finite difference scheme (Quarteroni et al., 2007).

Moreover, we observe that in the case of proportional loading, we may simplify model equations by setting $\mathbf{d}^{tr} = \mathbf{s}/\|\mathbf{s}\|$, as presented in Section 7.2.1. In such a case, system (7.38) is composed of only scalar-valued, rather than tensorial, equations by consequently increasing efficiency.

7.4.1 Numerical difficulties and adopted solutions

Since the Fischer-Burmeister complementary function is non-differentiable at $(0, 0)$, we make use of the smoothed Fischer-Burmeister function, presented in Eq. (2.121), by assuming δ as a positive regularization parameter (Kanzow, 1996). This aspect characterizes especially the initiation of PTs, when both a and b are equal to zero.

Therefore, as already discussed in Chapter 4 for J_2 plasticity, possible difficulties could be linked to the numerical sensitiveness of these schemes (due to the presence of δ) and to the proper choice of the Newton-Raphson initial guess to guarantee a fast and correct convergence. In fact, a potential disadvantage of this method is that when the initial point is far from a solution, the method might not converge or may converge very slowly. In the present case, to resolve these shortcomings, we apply a line-search strategy (Dennis and Schnabel, 1983; Nocedal and Wright, 1999). Such a choice is suggested by practical experience which reveals that it is not necessary to solve accurately for Eq. (7.40) to devise efficient methods (Quarteroni et al., 2007), rather, it is crucial to enforce some limitations on the step length such that:

$$\mathbf{h}^{(k+1)} = \mathbf{h}^{(k)} + \alpha^{(j)} \Delta \mathbf{h}^{(k)} \tag{7.41}$$

where $\alpha^{(j)}$ represents the admissible coefficient at iteration (j) of the line-search procedure. Without introducing any limitation, a reasonable request on the choice of $\alpha^{(j)}$ would seem be that satisfying the following condition:

$$\left\| \mathbf{Q}\left(\boldsymbol{\varepsilon}, \mathbf{h}^{(k+1)}\right) \right\| < \left\| \mathbf{Q}\left(\boldsymbol{\varepsilon}, \mathbf{h}^{(k)}\right) \right\| \tag{7.42}$$

for which the new iterate, $\mathbf{h}^{(k+1)}$, satisfies the inequality when $\mathbf{h}^{(k)}$ and $\Delta \mathbf{h}^{(k)}$ have been fixed. To this purpose, a simple procedure, that starts from a sufficiently large value of the step length, $\alpha^{(j)}$, and halves this value until condition (7.42) is fulfilled, can be used even if not always satisfactory (Dennis and Schnabel, 1983). In fact, more stringent criteria than condition (7.42) have to be adopted in the choice of possible values for $\alpha^{(j)}$ to avoid a slow descent rate of the sequence and the use of small step sizes. Among the most up-to-date strategies, we adopt here the back-tracking line-search technique for which the following condition needs to be satisfied (Quarteroni et al., 2007):

$$\left\| \mathbf{Q}\left(\boldsymbol{\varepsilon}, \mathbf{h}^{(k+1)}\right) \right\| < \left\| \mathbf{Q}\left(\boldsymbol{\varepsilon}, \mathbf{h}^{(k)}\right) \right\| + \lambda \alpha^{(j)} \frac{\partial \mathbf{Q}}{\partial \mathbf{h}} \Delta \mathbf{h}^{(k)} \tag{7.43}$$

with $\lambda \in (0, 0.5)$. In our case, the procedure, that starts from a sufficiently large value of the step length, $\alpha^{(j)}$, and halves this value until condition (7.43) is fulfilled, has been demonstrated effective and efficacy. Clearly, other strategies can be used for the choice of $\alpha^{(j)}$ and theoretical results can be found in the well-known book by Dennis and Schnabel (1983).

The application of the Fischer-Burmeister algorithm to the proposed problem leads to a well-behaved and robust algorithmic scheme as demonstrated by examples described in Chapter 8. Table 7.2 provides a summary of the full algorithm needed to integrate the constitutive relations in a FE framework, also detailing the algorithmic scheme for the adopted line-search strategy, where we assume $\lambda = 10^{-4}$ and $\rho = 0.5$.

1. **Initialize**
   i. Set $k = 0$, $\mathbf{h}^{(0)} = \left(\chi_n^M; \Delta\zeta_n^M; \gamma_n^{M0}; \chi_n^S; \Delta\zeta_n^S; \gamma_n^{S0}; \gamma_n^{MS}; \mathbf{d}_n^{tr}; \Delta\zeta_n^d; \gamma_n^d\right)$ at time t_{n+1}
2. **Determination of the solution**
   Repeat:
   i. Compute $B^{S(k)} = B^S(\boldsymbol{\varepsilon}, T, \mathbf{h}^{(k)})$ at time t_{n+1}
   ii. Compute $R^{S(k)} = R^S(B^{S(k)}, \mathbf{h}^{(k)}, T)$ at time t_{n+1}
   iii. Find $\Delta\mathbf{h}^{(k)}$ solving system (7.38) via Newton-Raphson scheme through Eq. (7.40)
   iv. Evaluate $\mathbf{h}^{(k+1)}$ by applying a line-search strategy, as follows:
      a. Choose $\lambda \in (0, 0.5)$ and $\rho \in (0, 1)$
      b. Set $j = 0$, $\alpha^{(0)} = 1$
      c. Compute $\mathbf{h}^{(k+1)} = \mathbf{h}^{(k)} + \alpha^{(0)}\Delta\mathbf{h}^{(k)}$
      d. While $\left\|\mathbf{Q}\left(\boldsymbol{\varepsilon}, \mathbf{h}^{(k+1)}\right)\right\| > \left\|\mathbf{Q}\left(\boldsymbol{\varepsilon}, \mathbf{h}^{(k)}\right)\right\| + \lambda\alpha^{(j)}\dfrac{\partial\mathbf{Q}}{\partial\mathbf{h}}\Delta\mathbf{h}^{(k)}$ do
         - $\alpha^{(j+1)} = \rho\alpha^{(j)}$
         - $\mathbf{h}^{(k+1)} = \mathbf{h}^{(k)} + \alpha^{(j+1)}\Delta\mathbf{h}^{(k)}$
         - $j = j + 1$
      e. End
   v. Set $k = k + 1$

   until $\left\|\mathbf{Q}\left(\boldsymbol{\varepsilon}, \mathbf{h}^{(k)}\right)\right\| < tol$

Table 7.2: Full algorithmic scheme for the proposed 'flexible' model.

Moreover, in Eq. (7.25) we choose R^S such that its derivatives become infinite as χ^S approaches 0 or 1 to ensure a smooth transition in stress-strain or strain-temperature response predicted at initiation and completion of transformation. While this condition is essentially an analytical one, the numerical evaluation of these derivatives at $\chi^S = 0$ and $\chi^S = 1$ may cause computational difficulties. To avoid this problem, we introduce a modification of R^S as follows:

$$R^S = \begin{cases} R_{f^0}^S + h_f^S\chi^S + a_{f^0}^S\left(\chi^S + \epsilon\right)^n + a_{f^1}^S\left(1 - \chi^S + \epsilon\right)^n & \text{if } B^S \geq 0 \\ R_{r^0}^S - h_r^S\chi^S - c_T^S\left(T - T_0\right) + a_{r^0}^S\left(\chi^S + \epsilon\right)^n + a_{r^1}^S\left(1 - \chi^S + \epsilon\right)^n & \text{if } B^S < 0 \end{cases} \tag{7.44}$$

ϵ being a positive regularization parameter. For small values of ϵ (e.g., $\epsilon = 10^{-8}$), Eq. (7.44) produces results similar to those provided by Eq. (7.25).

7.5 Conclusions

This Chapter has developed a refined, general and flexible three-dimensional phenomenological constitutive model for SMAs, taking into account several physical phenomena, and has proposed the numerical implementation of the new model, through the effective and efficient procedure, based on the Fischer-Burmeister function. The great advantage of such a numerical algorithm is that no active set search is required, allowing an efficient procedure for complex models. Possible numerical difficulties and the adopted solutions have been described. In the following Chapter, numerical robustness and efficiency as well as model reliability will be carefully investigated through several extensive numerical tests.

Chapter 8

A numerical and experimental investigation of shape memory alloys

This Chapter is first devoted to a detailed numerical investigation of the 'flexible' model, presented in Chapter 7, in order to assess its reliability as well as the effectiveness of its numerical counterpart. In particular, we conduct several numerical finite element simulations, ranging from simple uniaxial tests to more complex three-dimensional analyses of a real-life device, and we give details about computational times, number of steps and iterations. The conducted finite element analyses allow to qualitatively show and emphasize all the 'flexible' model features, while the comparison between numerical predictions and experimental data available from the literaure allows to quantitatively validate the proposed model and to demonstrate its reliability. Then, the present Chapter is dedicated to a numerical and experimental investigation of NiTi actuators springs, in order to discuss several aspects characterizing shape memory alloy behavior as well as prediction capabilities of shape memory alloy models.

The Chapter is organized as follows. Section 8.1 compares numerical predictions to several experimental data available from the literature and presents the finite element analysis of a real device. Then, Section 8.2 presents the experimental investigation of NiTi actuators springs, conducted in SAES Getters. The results of the experimental campaign are then compared to the numerical predictions of the proposed 'flexible' model and of the models by Souza et al. (1998) and Auricchio et al. (2009, 2011), presented in Section 6.3.

8.1 'Flexible' model validation

In this Section we test the validity of the 'flexible' model as well as its algorithm efficiency through several numerical simulations and comparisons with experimental results on thin superelastic NiTi wires, reported by Sittner et al. (2009). Then, we approach a complex three-dimensional finite element (FE) analysis of a real shape memory alloy (SMA) based device, i.e., an helical spring actuator.

In all the numerical tests we adopt the material parameters reported in Table 8.1 and calibrated as described in Section 7.3, by referring to the material properties characterizing NiTi wires and provided by Pilch et al. (2009); Sittner et al. (2009); in particular, the material parameters are extracted from an experimental curve, i.e., a tensile test at a constant temperature of $10\,^{\circ}\mathrm{C}$ (see Figure 8.1).

It is important to notice that all the parameters are calibrated using only uniaxial data. The reduced number of experimental data for the calibration certainly reduces the model accuracy, but the purpose is to emphasize model prediction capabilities, based on a simple calibration method, through a quantitative validation with experimental data, as well as the robustness and efficiency of the adopted numerical procedure, through a more complex three-dimensional analysis of a real SMA-based device. In all the simulations, to

Parameter	Value	Unit	Parameter	Value	Unit
G^A	21890	MPa	R^M	1	MPa
G^{MS}	9016	MPa	R^S_{f0}	1	MPa
K	31125	MPa	R^S_{r0}	17	MPa
ε_L	6.15	%	h^S_f	1	MPa
T_0	-48.15	°C	h^S_r	1	MPa
Δs^{AMS}	0.31	MPa/ °C	a^S_{f0}	2	MPa
$\overline{\Psi}^{in}$	-0.1	MPa	a^S_{f1}	0.5	MPa
c^S_T	0.2	MPa/ °C	a^S_{r0}	0.01	MPa
n	0.1	-	a^S_{r1}	9	MPa

Table 8.1: 'Flexible' model parameters used in all the numerical simulations.

emphasize the improvements of the new modeling framework, we compare the proposed model with the model by Souza et al. (1998), presented in Section 6.3, whose parameters are reported in (Auricchio et al., 2009).

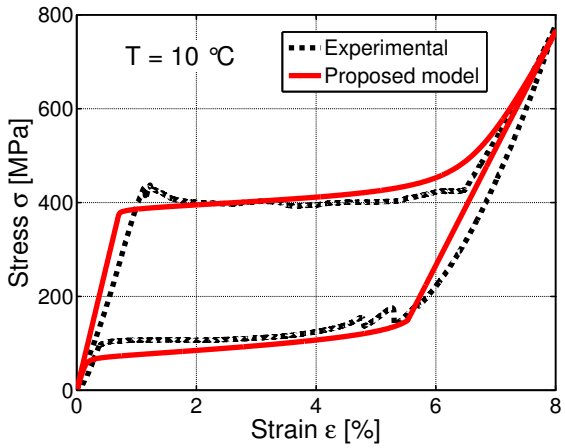

Figure 8.1: 'Flexible' model calibration on a tensile test at a constant temperature of $10\,^\circ$C.

8.1.1 Uniaxial isothermal tensile tests

We start considering uniaxial tensile tests at constant temperature, simulated as simple uniaxial tension tests, with displacement control and prescribed homogeneous constant temperature field. We consider five constant temperatures of 60, 40, 20, -10 and $-20\,^\circ$C for the tensile tests and five constant temperatures of 60, 40, 20, 10 and $-20\,^\circ$C for the tensile tests with internal subloops. Accordingly, Figures 8.2 and 8.3 report stress-strain diagrams. Compared to the model by Souza et al. (1998), the proposed model allows for an accurate description of material behavior by reproducing experimental hysteresis loops decreasing with increasing temperature, transformation-dependent elastic properties as well as phase transformations (PTs) smoothness.

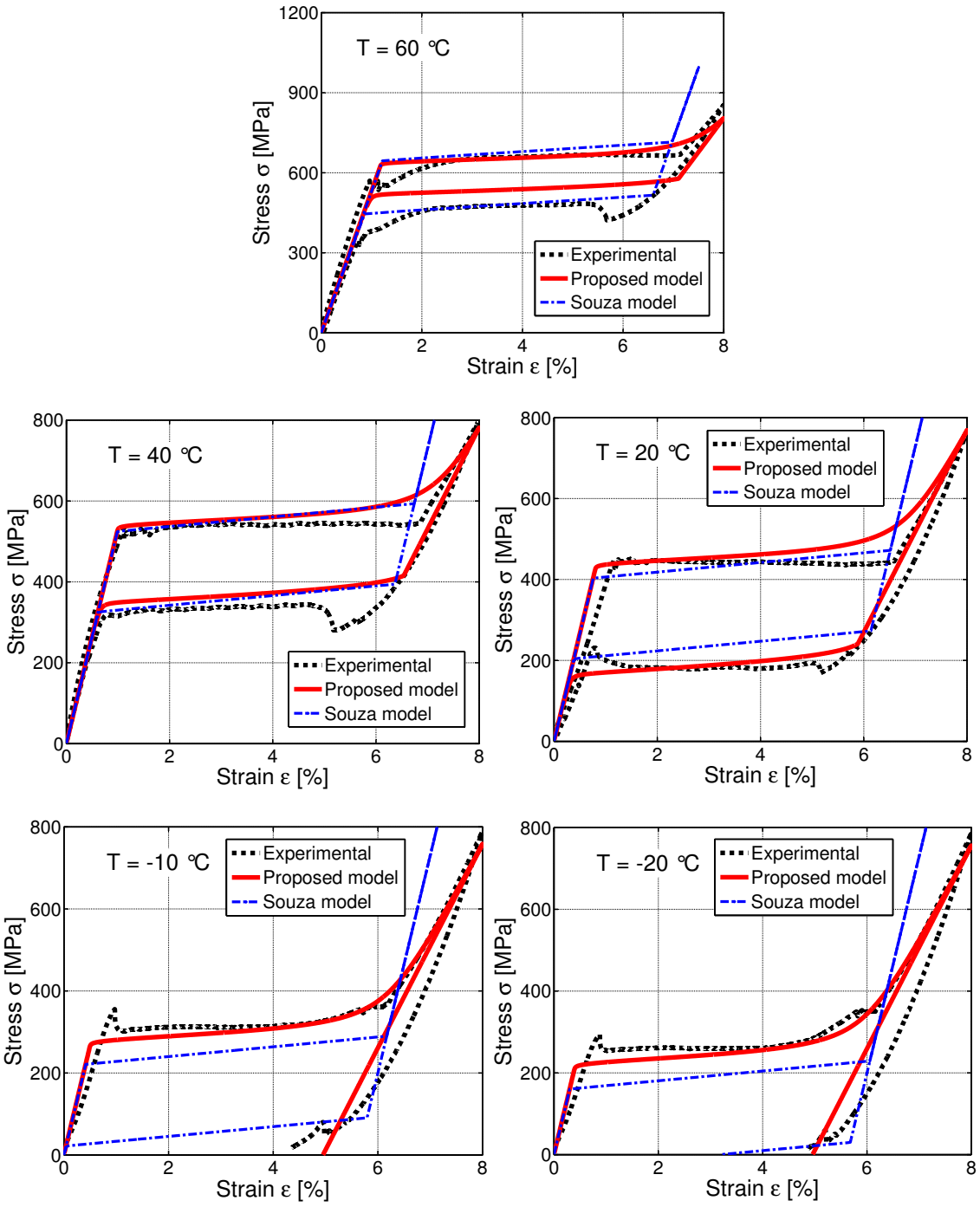

Figure 8.2: Model response for isothermal tensile tests.

8.1.2 Uniaxial thermal-cycling tests at constant applied stress

We now present thermal-cycling tests at constant stress, simulated as uniaxial tension tests with load control and prescribed homogeneous varying temperature field. We consider four constant stresses of 300, 400, 450 and 500 MPa. Accordingly, Figure 8.4 reports strain-temperature diagrams. The experimental curves are successfully predicted by both models for $\sigma = 400$, $\sigma = 450$, and $\sigma = 500$ MPa, while both models fail for

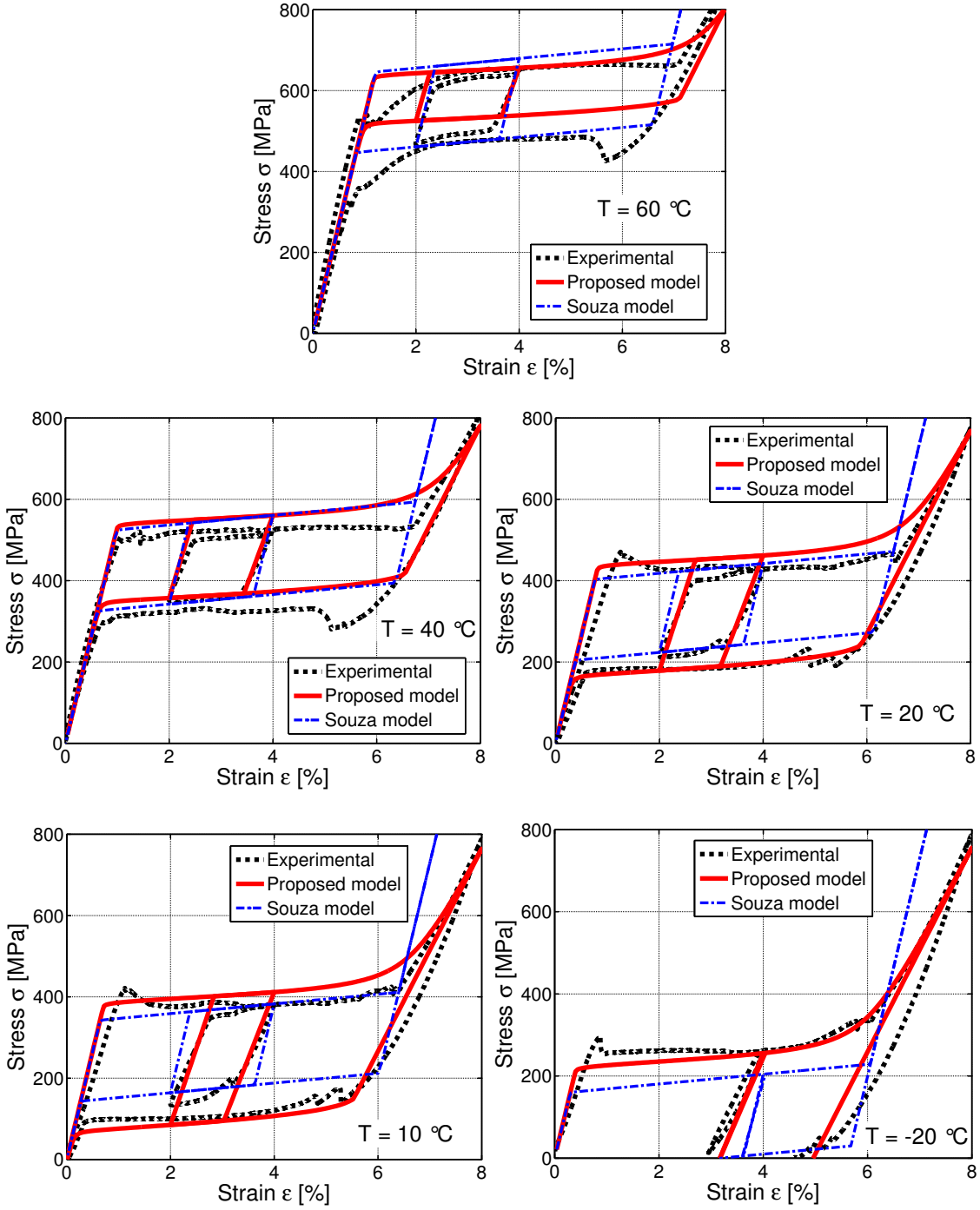

Figure 8.3: Model response for isothermal tensile tests with internal subloops.

$\sigma = 300$ MPa since an experimental weak inelastic strain is obtained for low stress levels. Although there is no clear experimental evidence, these small actuation strains can be attributed to a R-phase transformation (Sittner et al., 2009), not taken into account by both models. Another clear feature of the proposed model is the decrease of temperature hysteresis width with increasing stress.

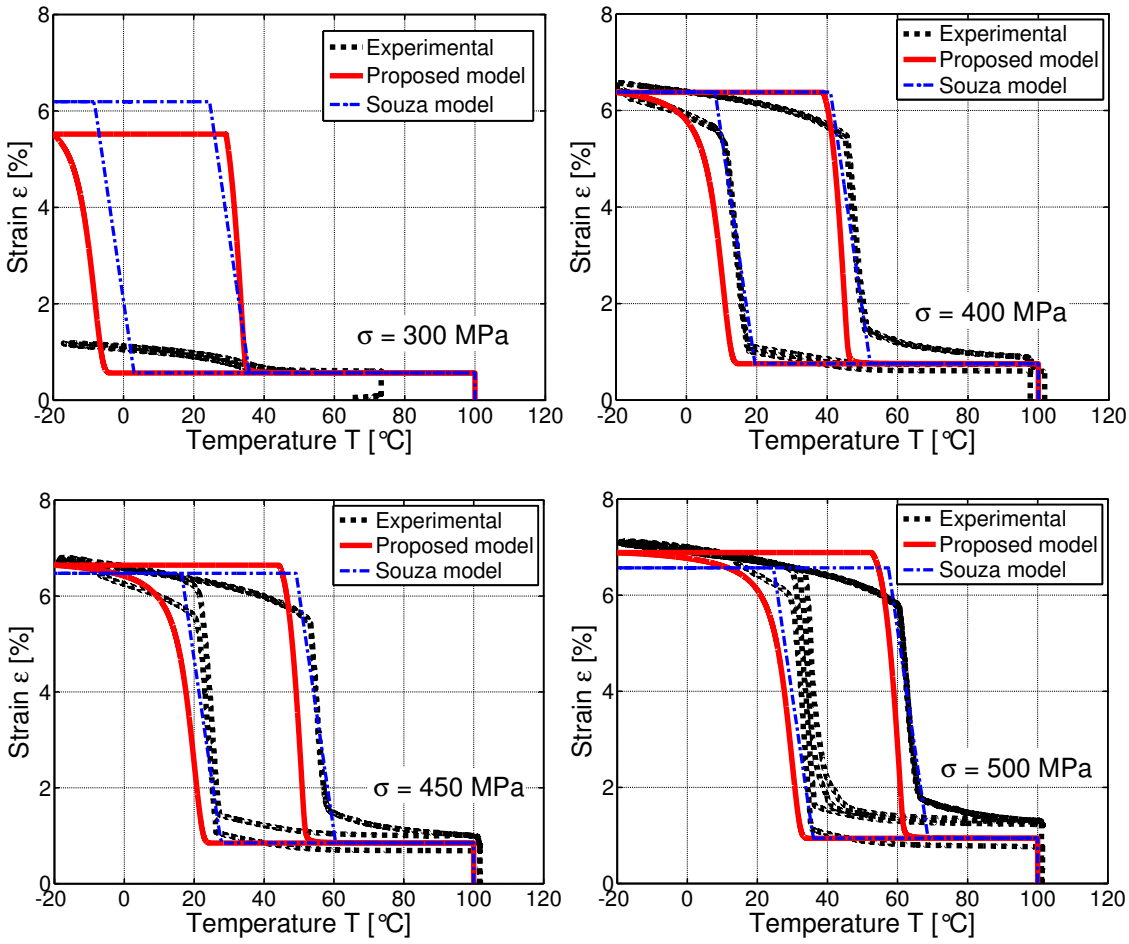

Figure 8.4: Model response for thermal-cycling tests at constant tensile stresses.

8.1.3 Uniaxial thermo-mechanical recovering stress tests

We now present thermo-mechanical recovering stress tests carried out on a wire strained in tension at room temperature, up to a certain level of prestrain, at upper and lower plateau, respectively, followed by thermal-cycling at constant prestrain and final unloading at room temperature. Again, the present tests are simulated as uniaxial tension tests. We consider a room temperature of $24\,^{\circ}\mathrm{C}$ and three levels of prestrain of 2%, 3.5% and 5%. Accordingly, Figures 8.5 and 8.6 represent stress-strain (left) and stress-temperature (right) diagrams at both upper and lower plateau. The transformation slopes as well as the achieved magnitude of the recovery stress at maximum temperature predicted by the proposed model are in good agreement with experiments also if both models do not capture the absence of hysteresis in the stress-temperature plot.

8.1.4 Isothermal combined tension-torsion tests

We present results of combined tension-torsion tests consisting of isothermal loading paths with applied angular displacement at constant axial stress. The numerical prediction are obtained considering a 1 mm wire segment, modeled using 8-node brick FE discretization consisting in one element through the wire thickness and 320 elements in the cross-section (see Figure 8.7). Accordingly, Figure 8.8 represents torque-angular displacement (left) and axial strain-angular displacement (right) diagrams. Tests in the first row of Figure 8.8 are performed at a constant tensile stress of 70 MPa and at a constant temperature of $30\,^{\circ}\mathrm{C}$;

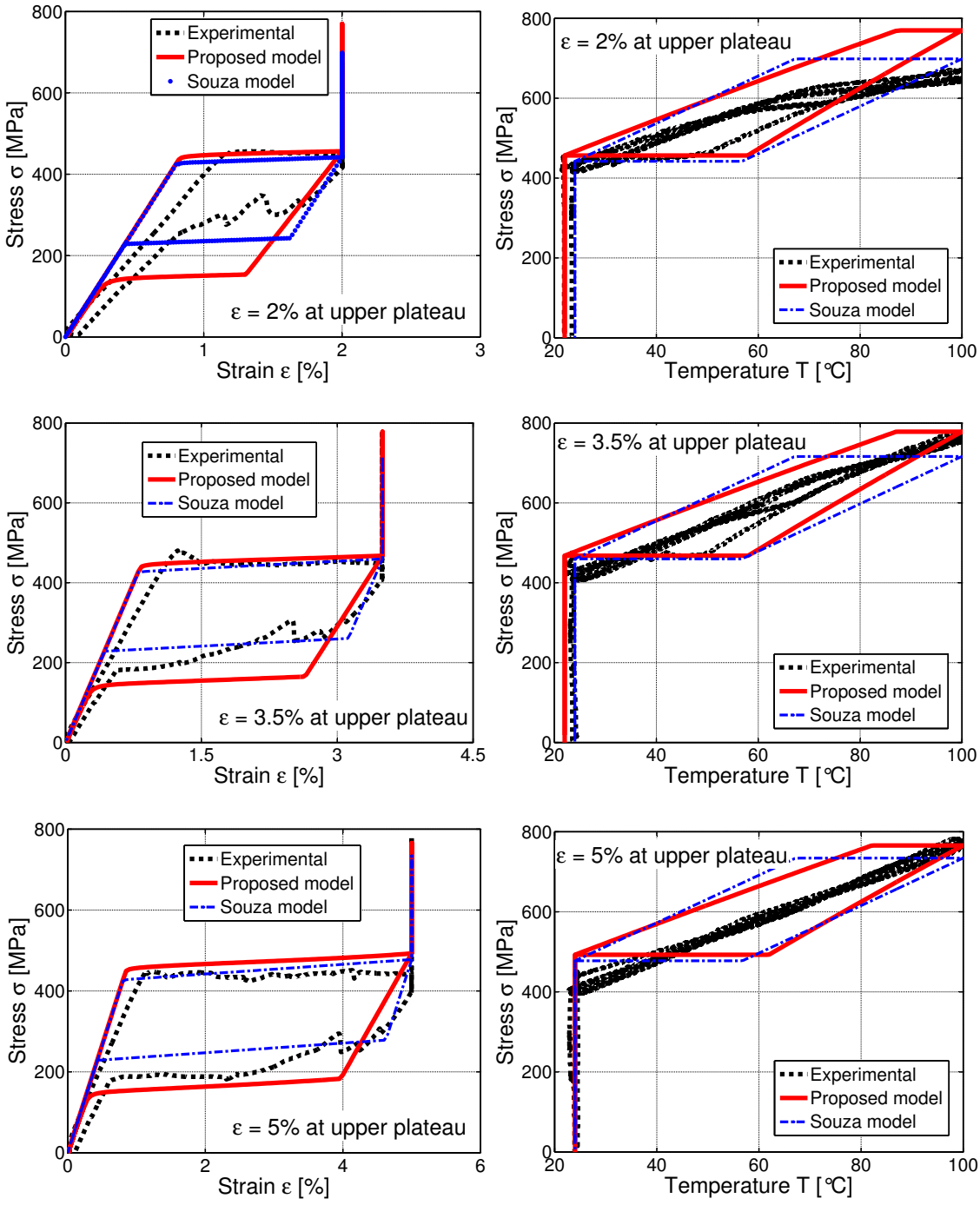

Figure 8.5: Model response for thermo-mechanical recovering stress tests at upper plateau.

curves in the second row are plotted for a constant tensile stress of 194 MPa and at a constant temperature of 40 °C; curves in the third row are plotted for a constant tensile stress of 379 MPa and at a constant temperature of 40 °C.

Both models underpredict the resulting torque moment and overestimate the maximum amount of transformation strain reached at the end of the transformation. However, discrepancies are not surprising since

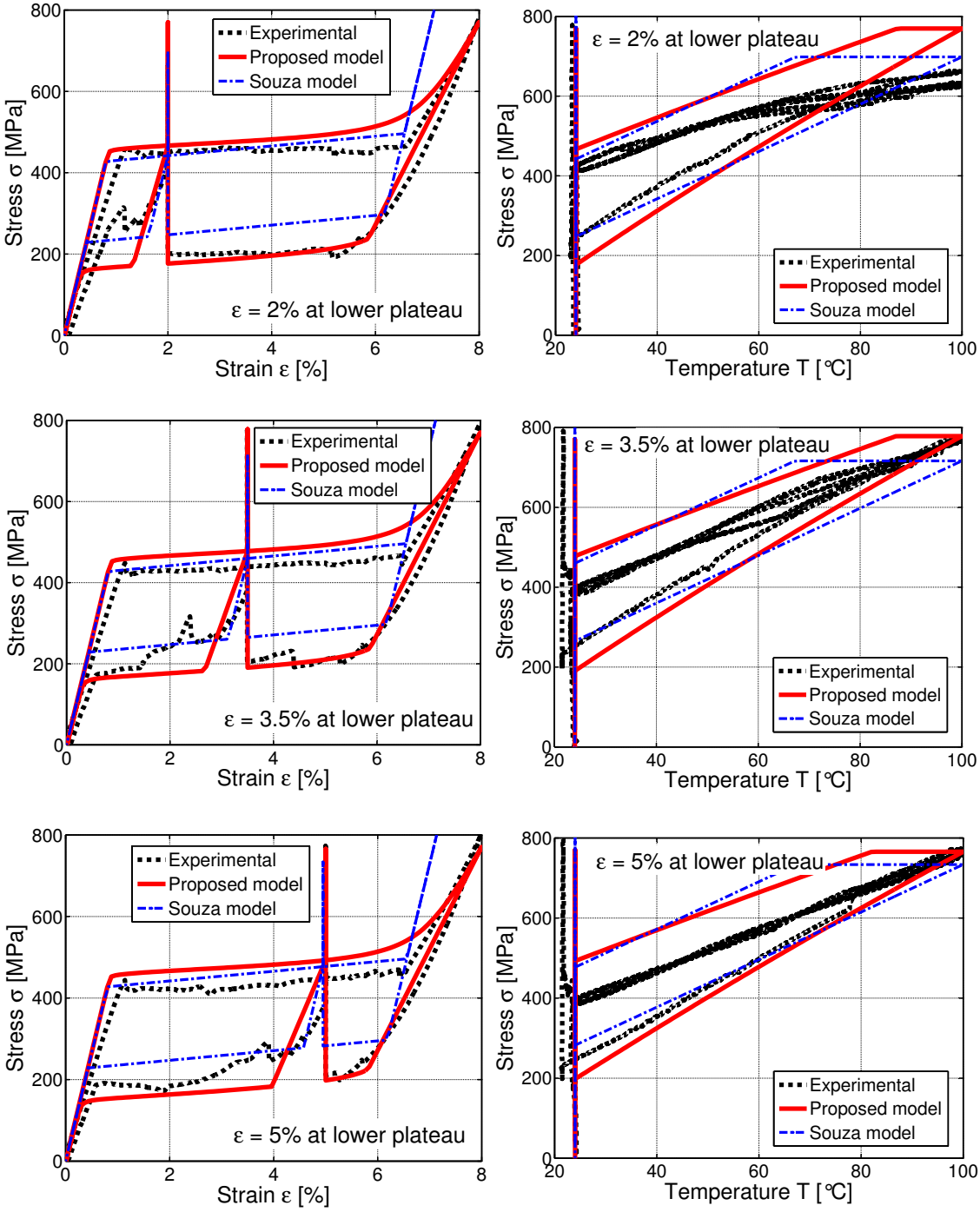

Figure 8.6: Model response for thermo-mechanical recovering stress tests at lower plateau.

all the material parameters are calibrated using uniaxial tests. In fact, thin wires loaded in tension often exhibit a localization of transformation, which produces more well stress-oriented variants, resulting in an important transformation strain in tension. In torsion test, due to the stress gradient through the radius, no localization is expected and, consequently, a reduced transformation strain is expected. As the models consider the transformation in an average way, this kind of effects is not captured. Moreover, there

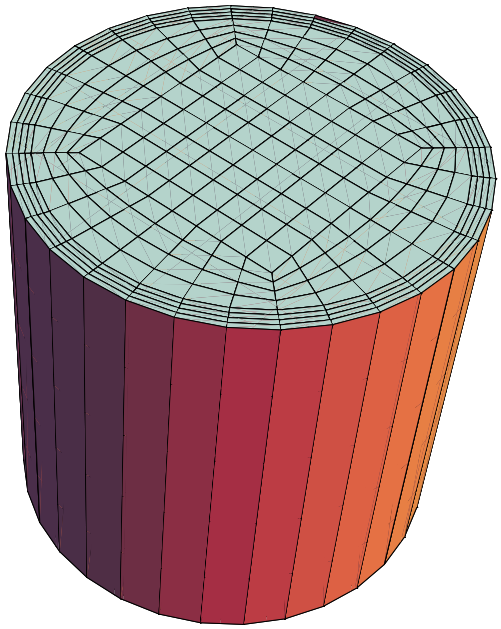

Figure 8.7: Combined tension-torsion tests. Adopted mesh for the wire segment.

are discrepancies in terms of axial strains, due to the effect of strong material texture and anisotropy, not accounted by isotropic models, which influences yield transformation surfaces and transformation strains (Sittner et al., 2009). In fact, tension/compression asymmetry, which is accounted for in the model by Souza et al. (1998), originates from the transformation anisotropy associated with NiTi cubic to monoclinic martensitic transformation (Sittner et al., 2009). The model by Souza et al. (1998) nevertheless remains isotropic and hence the tension/compression asymmetry does not solve the problem of the length of the plateau in angular displacements in torsion. Beside these discrepancies, the global behavior of the proposed model is generally in good agreement with experiments.

8.1.5 Isothermal multiaxial non-proportional tests

We now present the results of three biaxial non-proportional stress-strain loading histories. Such histories are obtained assuming to control two strain components and four stress components, particularly, $\{\epsilon_{11}, \epsilon_{22}, \sigma_{33}, \sigma_{12}, \sigma_{13}, \sigma_{23}\}$ and $\{\epsilon_{11}, \epsilon_{12}, \sigma_{22}, \sigma_{33}, \sigma_{13}, \sigma_{23}\}$. For each loading history we require that all the controlled stress components are identically equal to zero, while the strains are varied according to a chosen history. In particular, we investigate two types of loading histories, consisting of an hourglass- and a square-shaped strain history input, respectively, as shown in Figures 8.9(a), 8.9(c), and 8.9(e). We consider a constant temperature of $60\,^{\circ}\mathrm{C}$.
Accordingly, Figures 8.9(b), 8.9(d), and 8.9(f) represent diagrams in terms of the non-zero stress components. The aim is to emphasize qualitative aspects of the model response, which are similar to that observed experimentally. Moreover, the results illustrate also the robustness of the present formulation and implementation. The markers indicate the solution obtained using large load increments (automatic step size control[1]), whereas the solid line corresponds to fixed small load increments. As it can be seen, the former solution follows exactly the latter.

[1] All computations are performed using an automatic step size control procedure in which the desired number of Newton iterations is prescribed (here, equal to 8), and the current load increment is increased (decreased) when the number of iterations at the previous increment is smaller (larger) then the desired number.

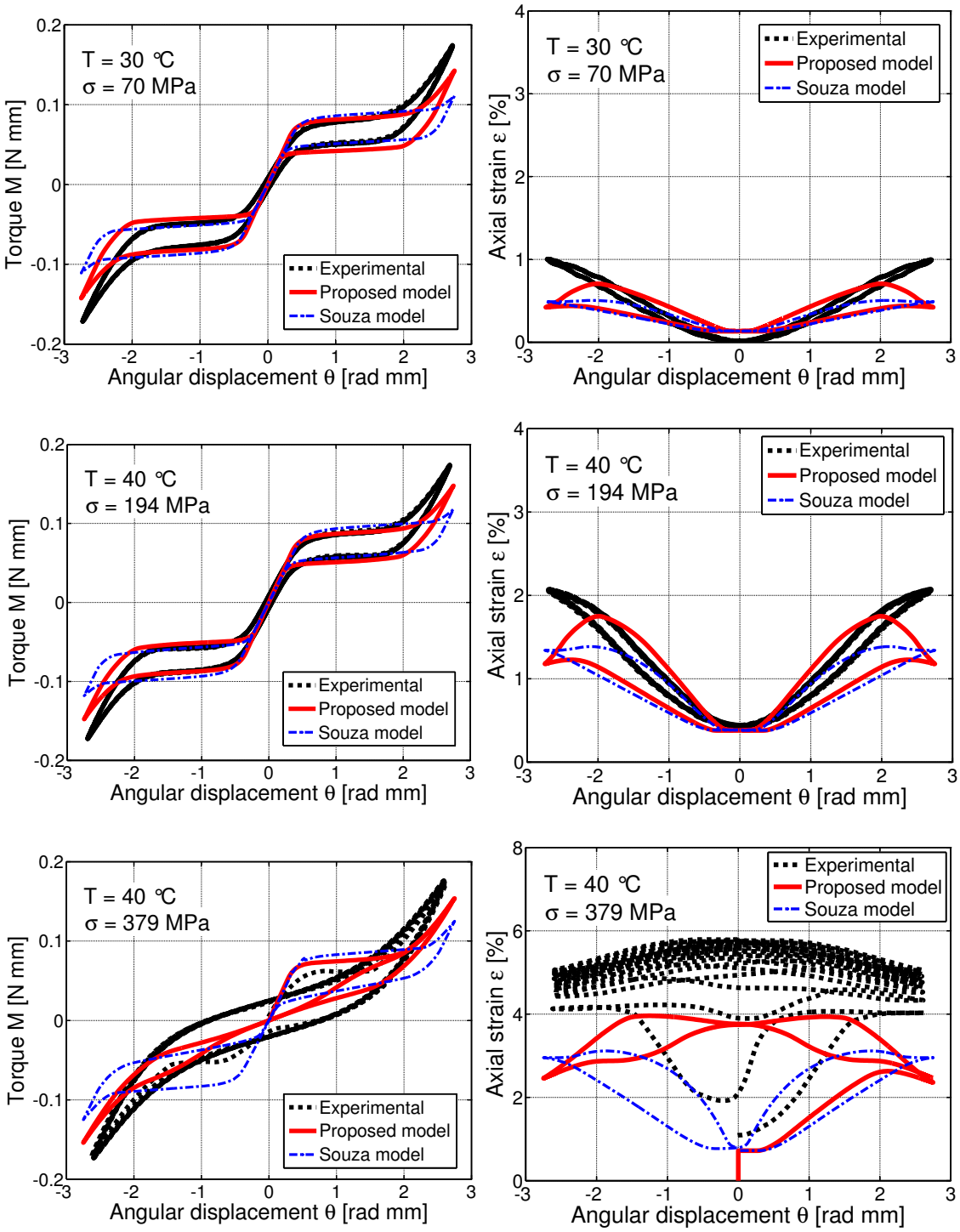

Figure 8.8: Model response for combined tension-torsion tests.

8.1.6 Simulations of a shape memory alloy based real device

We conclude this Section by considering a real SMA-based device, i.e., an SMA helical spring actuator. The device consists of 3.5 free coils of initial length of 24.59 mm, a wire diameter of 1.5 mm, a spring

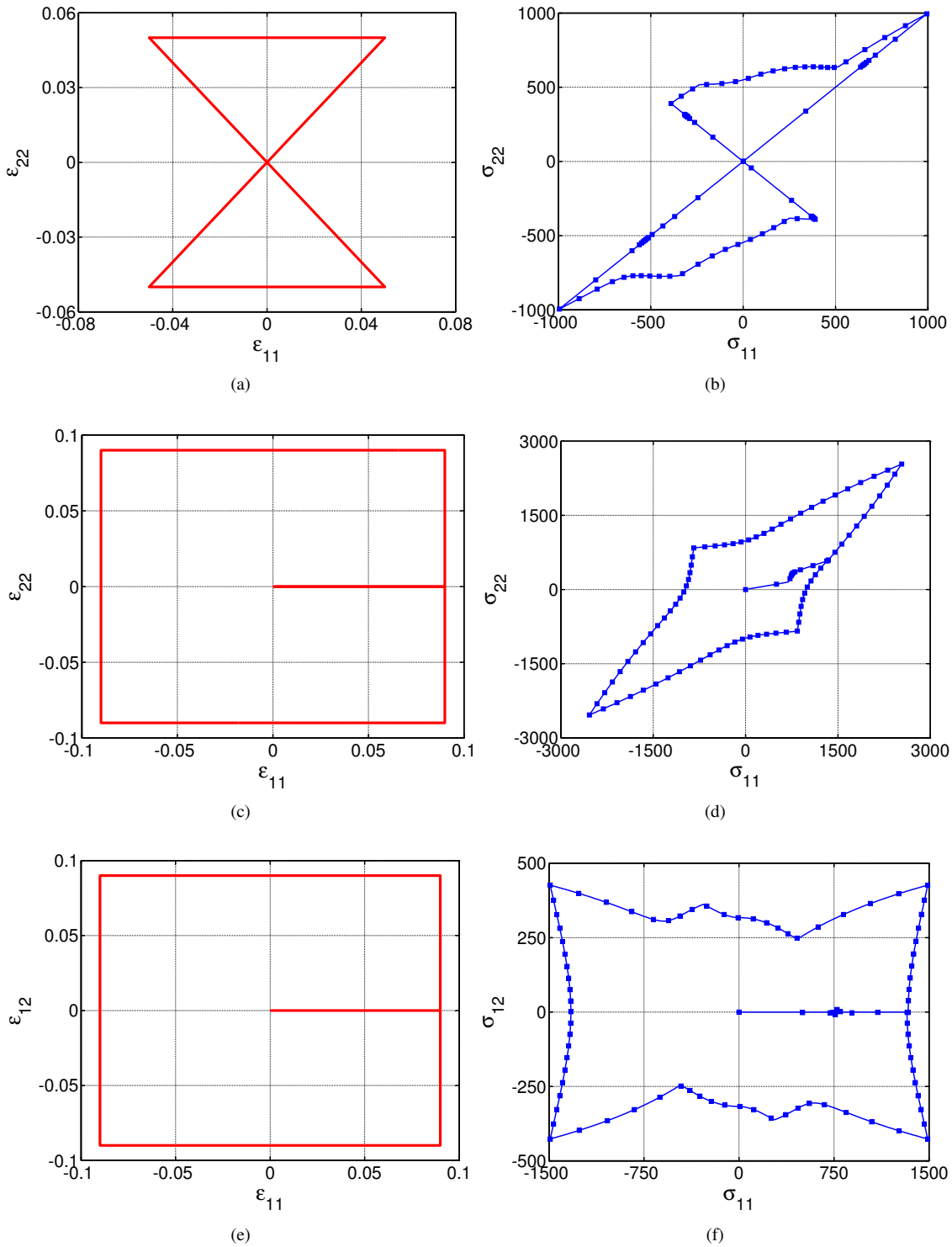

Figure 8.9: Model response for mixed stress-strain loading histories. (a) Butterfly- and (c)-(e) square-shaped history inputs under strain control; Obtained diagrams in terms of the non-zero stress components for the (b) butterfly- and (d)-(f) square-shaped history inputs (markers, large load increments; solid line, small increments).

external diameter of 13.3 mm, a spring internal diameter of 10.3 mm and a pitch size of 6.4 mm. Figure (8.10) reports the adopted mesh, consisting of 6912 8-node brick elements and 7497 nodes, and the initial geometry.

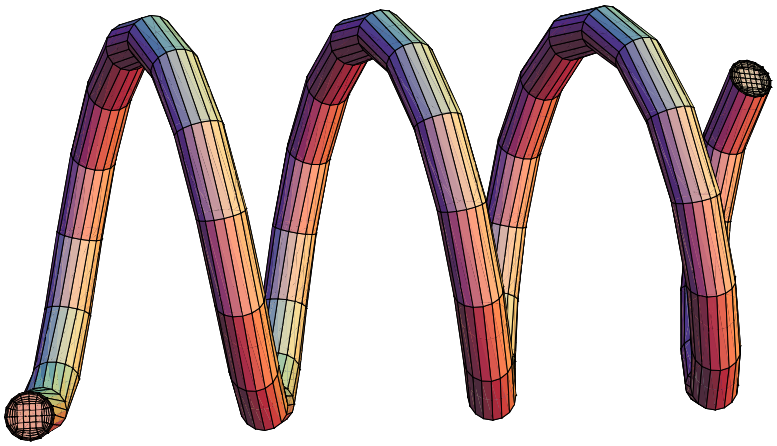

Figure 8.10: SMA spring actuator. Adopted mesh.

First, we simulate a helical spring at a constant temperature of $40\,^{\circ}\mathrm{C}$. We apply an axial force at the bottom end of the helical spring while the top end is completely fixed. We increase the force from zero to its maximum value and then, we unload the force back to zero. We remark that all the nodes on the bottom section are constrained against the two translations in the directions orthogonal to the axial one (thus ensuring that the bottom section is restrained against twist rotation). Figure 8.11(a) shows the deformed shape under the maximum force, compared to the initial geometry of the spring. After unloading, the spring recovers its original shape as expected in the pseudo-elastic (PE) regime. Figure 8.11(b) shows the force-vertical displacement (of the loaded end) diagram. The results presented in Figure 8.11(b) illustrate also the robustness of the present formulation and implementation. The markers indicate the solution obtained using large load increments (automatic step size control), whereas the solid line corresponds to fixed small load increments. As it can be seen, the former solution follows exactly the latter. To assess computational efficiency of the present model and its FE implementation, Table 8.2 provides the total number of steps, the total number of global Newton iterations and the total computation time for both small and large load increments.

Load increments	**Number of steps**	**Number of iterations**	**Total time** [s]
Large	52	401	909.046
Fine	204	1023	2134.75

Table 8.2: Pseudoelastic test of a SMA spring actuator. Comparison of computational efficiency.

Then, to qualitatively compare the behavior of the proposed model to that by Souza et al. (1998) for low-stress PTs, we consider the spring fixed at the top end, initially loaded by a vertical force at the bottom end and subjected to temperature cycle while keeping constant the load. We consider two constant loads of 5 and 15 N. Figures 8.12(a) and 8.12(c) show the two loading histories during the simulations, while Figures 8.12(b) and 8.12(d) show the vertical displacement-temperature diagrams. As it can be observed from Figures 8.12(b) and 8.12(d), compared to the model by Souza et al. (1998), the proposed model is

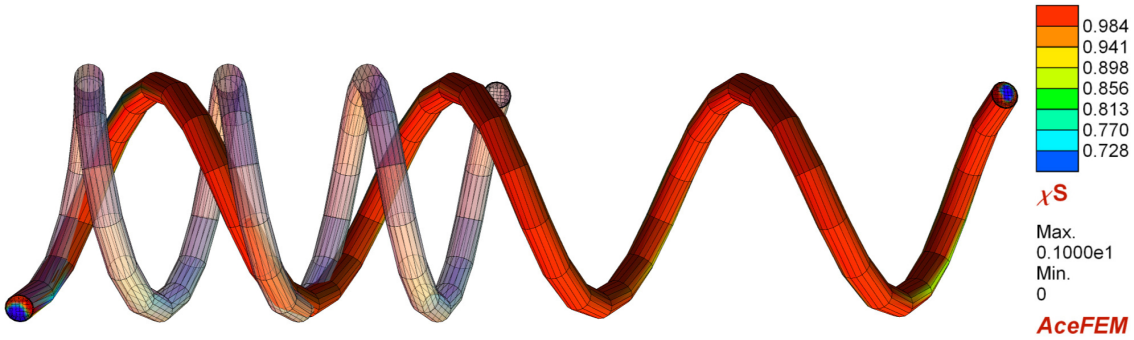

(a)

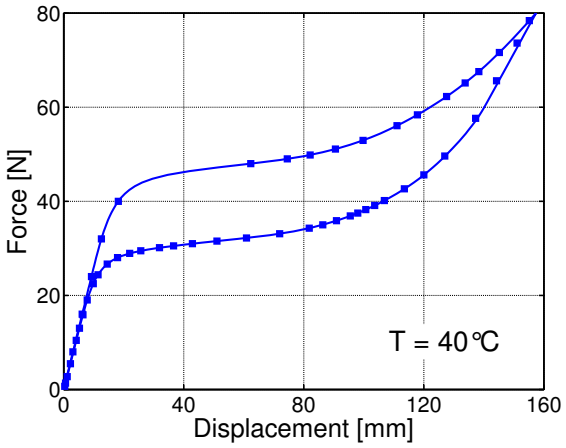

(b)

Figure 8.11: Pseudoelastic test of a SMA spring actuator. (a) Spring initial geometry and scaled deformed geometry under the maximum force (color map indicates distribution of the single-variant martensite volume fraction, χ^S); (b) force vs. vertical displacement of the loaded end of the spring diagram (markers, large load increments; solid line, small increments).

able to capture low-stress PTs and to predict the decrease of temperature hysteresis width with increasing stress.

8.2 A numerical/experimental investigation of NiTi actuator springs

The present Section deals with the numerical modeling, simulation and experimental analysis of SMA helicoidal springs. An experimental campaign is conducted in SAES Getters and the obtained experimental results are used to investigate three phenomenological constitutive models, i.e., the models by Souza et al. (1998) and Auricchio et al. (2009, 2011), and the proposed 'flexible' model.

8.2.1 Introduction and motivations

NiTi-based SMAs are exploited in a variety of interesting applications. Solid PTs, induced either by stress or temperature, are behind the remarkable functional properties of SMAs, promoting the concept of innovative smart actuators. SMA helicoidal springs are devices that combine an actuator, a sensor (typically a temperature sensor), and a displacement amplifier. A single component is indeed a system able to accomplish complex functions, as reacting to a temperature variation with an actuation. Despite the apparent

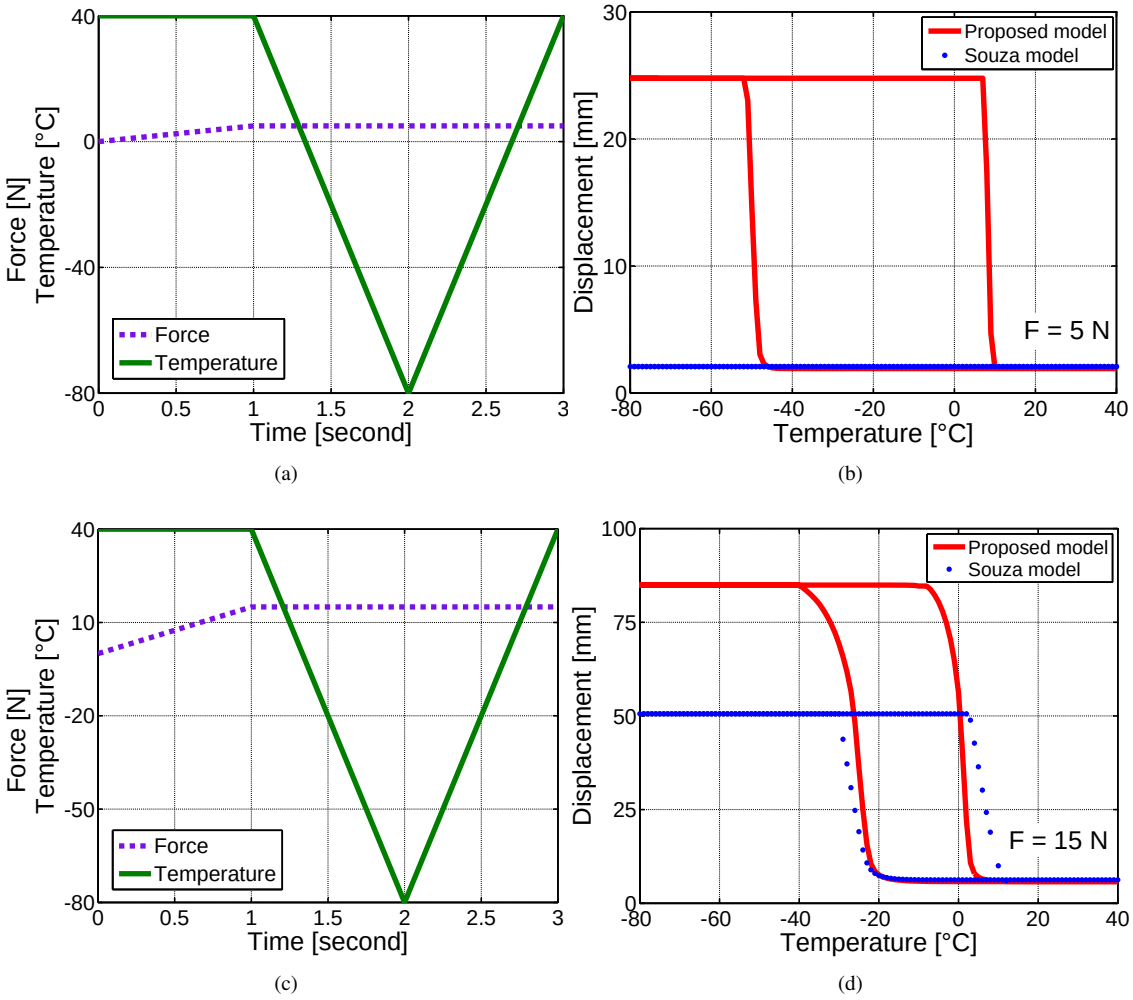

Figure 8.12: Thermal-cycling test at constant load of a SMA spring actuator. (a)-(c) Temperature and force loading histories during simulation; (b)-(d) vertical displacement of the loaded end of the spring vs. temperature diagrams.

simplicity, the behavior of SMA helicoidal springs is rather complex due to SMA thermo-mechanical properties. Consequently, the development process of such devices is a difficult task and their design may possibly take advantage of numerical simulations.

The literature presents numerous efforts for the modeling, design, simulation and control of SMA actuator systems (Bundhoo et al., 2009; Khidir et al., 2008). Among them, some works present different spring modeling approaches and calibration techniques to model the thermo-mechanical behavior of SMA helicoidal springs (Attanasi et al., 2011; de Aguiar et al., 2013, 2010; Dhakal et al., 2013; Dumont and Kuhl, 2005; Savi and Braga, 1993; Toi et al., 2004). For instance, the paper by Attanasi et al. (2011) investigates SMA spring superelastic mechanical behavior in tension and compression through some experimental and numerical analyses. Springs are modeled using two-node simple beam elements and material properties are computed through a trial and error fitting process on several experimental data related to a spring specimen. The paper by Dumont and Kuhl (2005) proposes a FE model of the Euler-Bernoulli beam and a material parameters identification on experimental data related to SMA wires. de Aguiar et al. (2010) assume a one-dimensional constitutive model to describe SMA thermo-mechanical shear behavior and a

classical approach for linear-elastic springs. Toi et al. (2004) extend Brinson's one-dimensional constitutive modeling to consider the asymmetric tensile and compressive behavior as well as the torsional behavior of superelastic, large deformation analysis of SMA springs. The authors formulate the FE method using linear Timoshenko beam elements. The work by Dhakal et al. (2013) focuses on the characterization of the cyclic behavior of 55NiTi using a new modeling framework and its three-dimensional FE implementation applied to springs. Model calibration is based on a single thermal-cycling test at constant load on a SMA wire.

However, computational methods have not yet been well established for the analysis of SMA springs (Toi et al., 2002a,b), particularly, in relation to the aim of finding an accurate FE modelization of spring devices, an appropriate SMA constitutive model as well as a simple calibration technique.

Motivated by these considerations, the work presented in this Section focuses on the investigation of SMA helicoidal spring actuator behavior, by combining the results of an experimental campaign conducted in SAES Getters with a thorough understanding of SMA experimental behavior and the selection of appropriate constitutive models. More specifically, the purpose is to investigate reliable and exhaustive SMA three-dimensional constitutive models which could be used by engineers needing to perform accurate simulations for the design and study of the response of SMA structures or components, in particular of SMA helicoidal springs. To reach this goal, the considered models have to be interfaced with commercial analysis programs; accordingly, good models should also be robust and flexible, possibly including both superelasticity and shape-memory effect, without increasing modeling complexity. Also, the problem of the physical interpretation of the model parameters is an important issue, as a clear and effective parameter identification procedure is the key for the employment of a constitutive model by engineers in real-life simulations.

Among the several models available in the recent literature, the present work focuses on three different SMA macroscopic constitutive models; in particular, on (i) the model by Souza et al. (1998) and then investigated by Auricchio and Petrini (2004a,b); (ii) the model by Auricchio et al. (2009, 2011); and (iii) the proposed 'flexible' model.

The investigation of the three models is based on a comparison between numerical predictions and experimental data. Such data are obtained by an experimental campaign conducted in SAES Getters on both SMA straight wires and helicoidal springs that experienced the same annealing process and presenting different geometries. The conducted tests consist of two experimental temperature loops at different constant tensile loads, carried out on wires and springs. Accordingly, the main goal of the present work is to calibrate constitutive model parameters on some experimental results related to SMA wires and then to test the resulting models with experimental data on helicoidal springs. The comparison between numerical predictions and experimental results allows to make considerations on the models reliability and design aspects as well as to discuss some features of SMA material behavior, highlighted by the experimental campaign. In the following, we describe the calibration process of constitutive model parameters and we compare numerical predictions to experimental data on helicoidal springs. Finally, we conclude by discussing and commenting the obtained results.

8.2.2 Experimental campaign conducted in SAES Getters

This Section presents the experimental campaign conducted in SAES Getters. Experiments consisted in thermal cycling at constant tensile load and were performed on the following samples:

- 1.5 mm diameter straight annealed wires;
- 1.0 mm diameter straight annealed wires;
- helicoidal springs manufactured by shape setting of either 1.5 mm and 1.0 mm diameter cold drawn wires.

All samples material nominal composition was Ti-49Ni at%. The geometrical parameters of the two spring configurations are reported in Table 8.3.

Geometrical parameters	**Spring** 1	**Spring** 2
Wire diameter	1.5 mm	1.0 mm
External coil diameter	13.3 mm	7.5 mm
Pitch	6.4 mm	3.0 mm
Free coils	3.5	6
Initial length	24.59 mm	18.0 mm

Table 8.3: Geometrical parameters of the first and second helicoidal spring actuators (Springs 1 and 2, respectively).

The shape setting processes of both spring versions were conducted with identical process parameters. Wires heat treatment were performed so that the wire experienced the same temperature time evolution of the corresponding spring. All thermal cycling tests were carried out on a self-constructed measuring system, already described in (Urbano and SMAq, 2006). The system was recently provided with a thermostatic chamber featuring a temperature range from less than $-100\,^{\circ}\mathrm{C}$ to more than $350\,^{\circ}\mathrm{C}$. The chamber is made of an inner brass chamber. Inside its walls holes for Nitrogen flow and resistive heaters are drilled. The brass chamber is contained is a two layers thermal insulation case, the inner layer having high temperature stability, the outer layer good structural capability. Temperature inside the thermostatic chamber is monitored by means of three thermocouples, one of which, placed more or less in the center of the free volume and very close to the sample, is utilized for feedback control. A fan inside the chamber contributes to homogenize the temperature profile. Temperature and displacement were registered during the tests. The displacement was measured by means of the encoder of the linear motor exerting the load, properly corrected to compensate for thermal dilatation and elastic elongation of the loading chain. Thermal cycling was run on each SMA sample, either wire or spring, with increasing load. Two thermal cycles, starting from the high temperature, were performed for each load. Figure 8.13 shows the springs before and after testing and Table 8.4 summarizes all the performed tests.

8.2.3 Model parameter calibration

This Section is dedicated to the calibration of the investigated models. Ideally, the calibration procedure of a comprehensive material model with an extensive amount of experimental data on SMA springs should be automated using sophisticated optimization techniques. In the present work, however, the identification of all the material parameters is based on two experimental thermal-cycling tests at constant load conducted on a SMA wire. We consider these kind of experimental results, instead of classical stress-strain curves, because the strain-temperature response is very significant for SMA producers, being one of the most important characteristic of SMA for actuators. In particular, the calibration technique is achieved through a comparison between the two experimental curves in a one-dimensional setting, as already done for the Souza model by Auricchio et al. (2009). Consequently, we easily calibrate the following parameters of the model by Souza et al. (1998): (i) the elastic properties (E and ν), (ii) the maximum amount for single-variant martensite (ε_L), and (iii) four additional parameters (R, h, β and T_0) characteristic of martensitic transformations. We remark that, since the performed tests are under tensile load, we take a typical approximate value of the Poisson's ratio from literature (Lagoudas, 2008).
Then, we adopt the same values for the parameters of the model by Auricchio et al. (2009, 2011), except for R_1, assumed equal to R, and for the radius, R_0, calibrated to catch material behavior for low stress conditions. Finally, we adopt the same elastic properties (E and ν) and the same maximum amount for

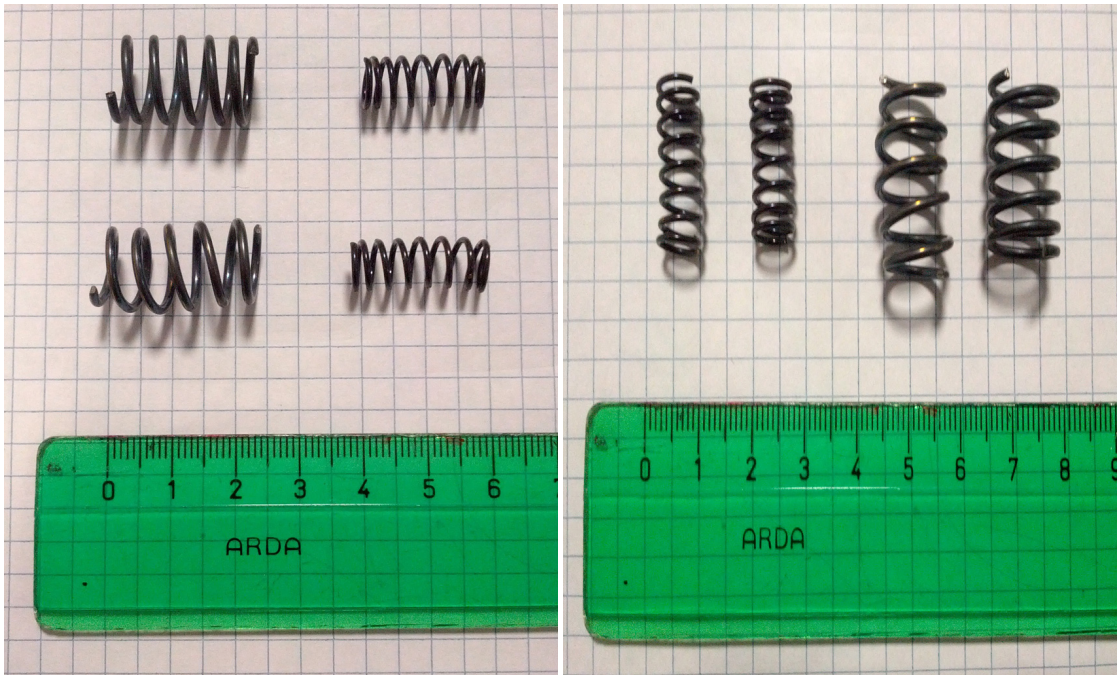

Figure 8.13: Springs before and after testing.

Component	Load	Thermal Cycles for each load
1.0 mm diameter wire	15 MPa 30 MPa 50 MPa 100 MPa 200 MPa	2
1.5 mm diameter wire	55 MPa 100 MPa 144 MPa	2
Spring 1	3 N 5 N 8 N	2
Spring 2	1 N 2 N 5 N 7 N	2

Table 8.4: Summary of the performed tests in SAES Getters.

single-variant martensite (ε_L) for the 'flexible' model and we calibrate the remaining parameters (i.e., Ψ^{in}, Δs^{ASM}, R^M, R^S_f, R^S_r, h^M_f, h^S_f, h^S_r and T_0), through a comparison between the two experimental curves in a one-dimensional setting as described in Section 7.3. In the following, we refer to the three models as the *Souza-Auricchio model*, the *modified Souza-Auricchio model*, and the *Auricchio-Bonetti model*.

We remark that the above calibration process is based on the results of tensile tests under the hypothesis

of isotropic material response and tension-compression symmetry, since we are interested in catching the global material behavior. Thus, we do not capture important features for drawn NiTi wires as the effects of tension-compression asymmetry and of material texture which may strongly influence the yield transformation surfaces and the transformation strains. In such a case, a multiaxial characterization of NiTi wires would be appropriate, although difficult.

For the identification procedure, we use the 100 and 144 MPa curves related to the 1.5 mm wire. Table 8.5 lists the values of the parameters adopted in all the numerical simulations (already reported to a three-dimensional setting) and Figures 8.14(a)-(c) present the one-dimensional phase diagrams for the three models in terms of stress, σ, and temperature, T.

Souza-Auricchio model	**Mod. Souza-Auricchio model**	**Auricchio-Bonetti model**
E = 45000 MPa	E = 45000 MPa	E = 45000 MPa
ν = 0.3	ν = 0.3	ν = 0.3
ε_L = 0.049	ε_L = 0.049	ε_L = 0.049
T_0 = 343 K	T_0 = 343 K	T_0 = 325 K
R = 110 MPa	R_1 = 110 MPa	R^M = 1 MPa
h = 1000 MPa	R_0 = 10 MPa	R_f^S = 2.4 MPa
β = 4.49 MPa/K	h = 1000 MPa	R_r^S = 8 MPa
	β = 4.49 MPa/K	h_f^S = 1.3 MPa
		h_r^S = 2.0 MPa
		Ψ^{in} = 0.25 MPa
		Δs^{ASM} = 0.2 MPa/K

Table 8.5: Calibrated material parameters for the three models.

As it can be observed from Figures 8.14(a) and 8.14(b), the Souza-Auricchio and the modified Souza-Auricchio models consider the coexistence of only two phases, i.e., austenite and single-variant martensite, and differ from each other for material behavior at low temperatures, i.e., at $T < T_0$, where T_0 is assumed equal to $70\,^{\circ}\mathrm{C}$. In particular, the modified Souza-Auricchio model considers a lower value of the elastic radius than the Souza-Auricchio model, i.e., $R_0 = 10$ MPa, which allows to take into account temperature transformations at low levels of stress. The Auricchio-Bonetti model considers also the presence of multi-variant martensite, consequently taking into account thermal-induced transformations at zero stress (indicated by vertical red dot lines in Figure 8.14(c)).

With the calibrated parameters of Table 8.5, we produce the numerical curves for the 100 and 144 MPa cases, to compare with the experimental curves from which the parameters have been identified. Such numerical curves have been obtained in two Mathematica FE packages, AceGen and AceFEM (Korelc, 2009), by simulating the experimental thermal-cycling tests at constant load as uniaxial tension tests with load control and prescribed homogeneous varying temperature field (see Appendix B for further details about AceGen/AceFEM). Figures 8.15(a) and 8.15(b) report the comparison between the experimental and the calibrated curves in terms of strain, ε, and temperature, T, for the two levels of load. In this and in the following figures, we refer to the Souza-Auricchio model as **SA**, to the modified Souza-Auricchio model as **mod. SA**, and to the Auricchio-Bonetti model as **AB**.

In particular, Figures 8.15(a) and 8.15(b) show the inability of the Souza-Auricchio model to catch SMA behavior for work conditions where the material is considered as linear elastic and where the model is particularly sensitive to its numerical implementation. Given the assessed material coefficient set, such a work condition includes stress values approximately lower than 150 MPa at $T < T_0$, as it can be observed in Figure 8.15(a). The applied experimental loads belong exactly to such a stress range, causing the inefficiency of the Souza-Auricchio model. Contrarily, the modified Souza-Auricchio and Auricchio-Bonetti

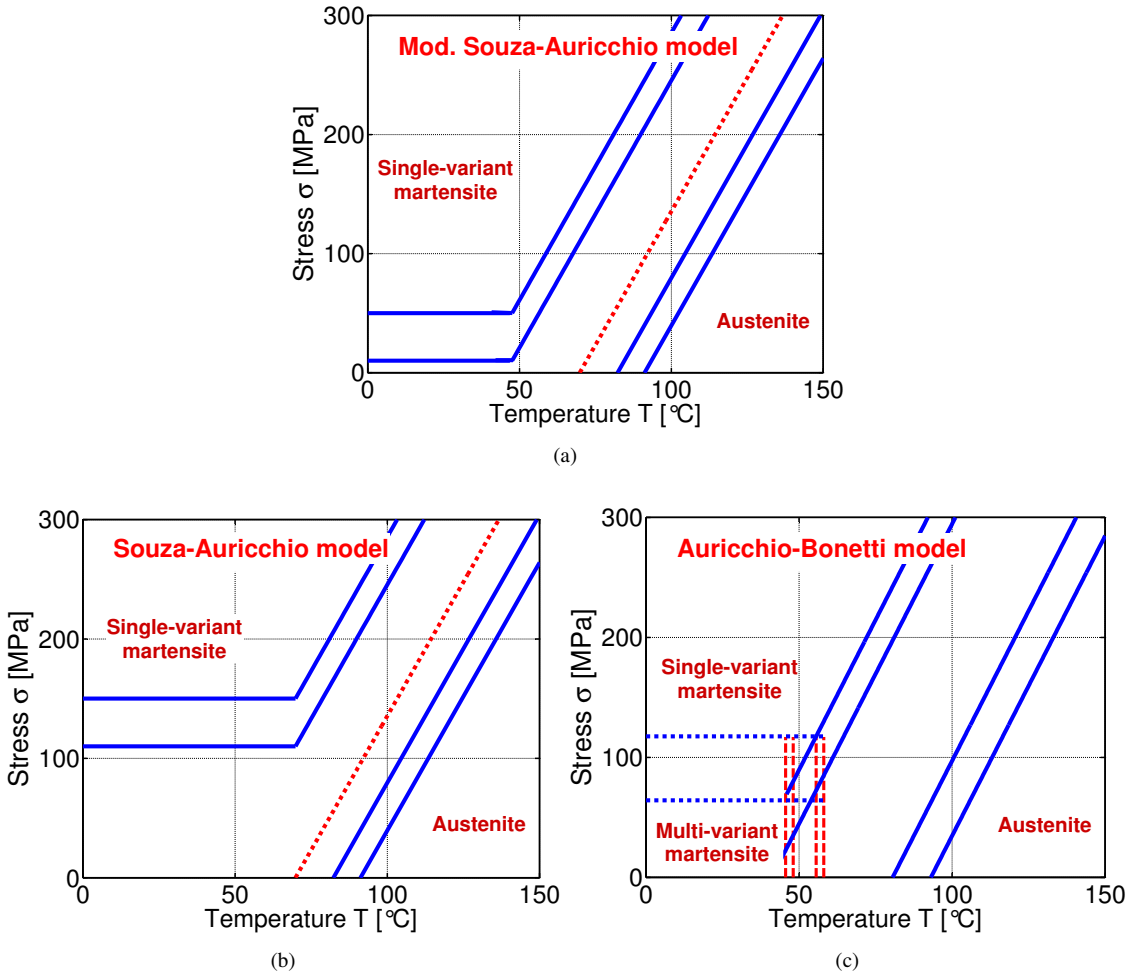

Figure 8.14: 1D phase diagrams generated by (a) the Souza-Auricchio model; (b) the modified Souza-Auricchio model and (c) the Auricchio-Bonetti model, in terms of stress, σ, and temperature, T.

models demonstrate their efficiency in capturing real material response.

8.2.4 Comparison with experiments on SMA helicoidal wires and springs

This Section presents the comparison between experimental data and numerical predictions on SMA helicoidal wires and springs presenting different geometries.
Experimental tests have been carried out in SAES Getters, as described in Section 8.2.2. Numerical results are obtained by conducting three-dimensional FE analyses of SMA helicoidal springs subjected to temperature cycling at constant load with the material parameters presented in Table 8.5.
We remark that the aim is to show as the three models catch SMA experimental behavior with a simple calibration process. Consequently, all the studied experimental data-sets are simulated with a unique choice of material parameters, obtained with the calibration procedure described in Section 8.2.3. The material parameters calibrated on 1.5 mm wires are so employed in the analysis of 1.0 mm wires.
In the following, we present the results of FE analyses on 1.5 and 1.0 mm wire springs and, then, we report some considerations about model results and SMA experimental behavior.

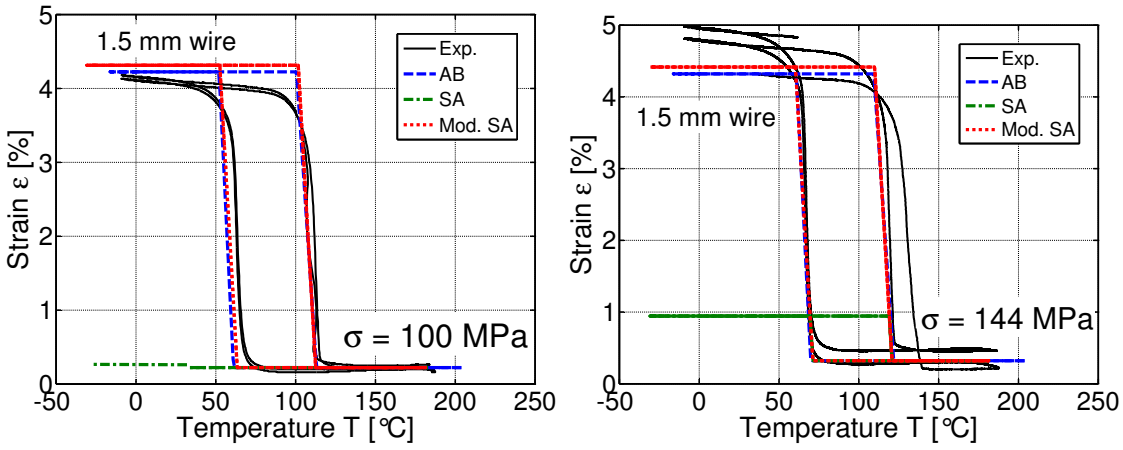

(a) (b)

Figure 8.15: Model parameter calibration on thermal-cycling tests on 1.5 mm SMA wires. Deformation, ε, vs. temperature, T, curves at constant tensile loads of 100 and 144 MPa.

Results for 1.5 mm wires and 1.5 mm wire springs

First, we present thermal-cycling tests at constant load on a 1.5 mm wire, simulated as uniaxial tension tests with load control and prescribed homogeneous varying temperature field. Figure 8.16 reports the comparison between experimental and numerical curves in terms of deformation, ε, and temperature, T, for a tensile load of 55 MPa.

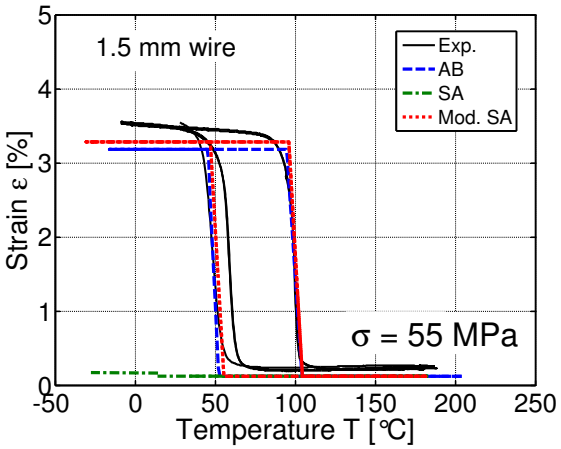

Figure 8.16: Thermal-cycling test on 1.5 mm SMA wire. Deformation, ε, vs. temperature, T, curves at a constant tensile load of 55 MPa.

Then, we consider the FE analysis of a SMA helicoidal spring actuator (Spring 1 of Table 8.3). The adopted mesh consists of 6912 8-node brick elements and 7497 nodes, as shown in Figure 8.17(a).

We consider the spring fixed at the top end, initially loaded by an axial force at the bottom end and then, keeping constant the load, subjected to temperature cycle. We apply three forces of 3, 5, and 8 N. We remark that all the nodes on the bottom section are constrained against the two translations in the directions orthogonal to the axial one (thus ensuring that the bottom section is restrained against twist rotation). Moreover, we observe that the magnitudes of the three forces produce average values of approximately

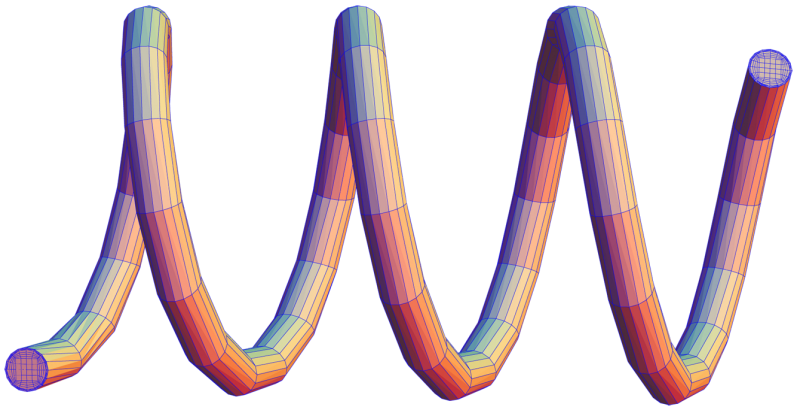

(a)

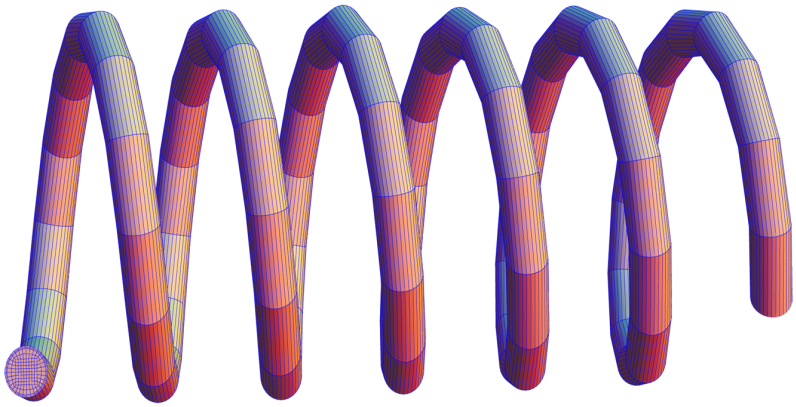

(b)

Figure 8.17: Adopted meshes. (a) Spring 1 of Table 8.3; (b) Spring 2 of Table 8.3.

33, 55, and 88 MPa for the distribution of effective stresses ($\sqrt{3/2\,\mathbf{s} : \mathbf{s}}$, where $\mathbf{s}$ is the stress deviator tensor) in SMA coils. This provides a comparable stress level to that utilized in the experiments used for characterization and calibration described in Section 8.2.3. Figures 8.18(a)-(c) show the spring relative elongation, $(L - L_0)/L_0$, versus temperature, T, diagrams, where L_0 is the initial length of the spring.

Results for 1.0 mm wires and 1.0 mm wire springs

First, we present thermal-cycling tests at constant load on a 1.0 mm wire. We consider simulations of thermal-cycling tests at constant loads of 15, 30, 50, 100, and 200 MPa. Figures 8.19(a)-(e) report ε-T diagrams for the five levels of loads.

Then, we consider the FE analysis of a SMA helicoidal spring actuator (Spring 2 of Table 8.3). The adopted mesh consists of 14976 8-node brick elements and 16511 nodes, as shown in Figure 8.17(b). In this case, we consider four force values of 1, 2, 5, and 7 N, whose magnitudes produce average values of approximately 23, 46, 115, and 161 MPa for the distribution of effective stresses in SMA coils. Figures 8.20(a)-(d) show spring relative elongation, $(L - L_0)/L_0$, versus temperature, T, diagrams.

8.2.5 Discussion on results

Numerical simulations show that the results of both the Auricchio-Bonetti and modified Souza-Auricchio models are almost the same and in close agreement with experimental data, revealing that the considered

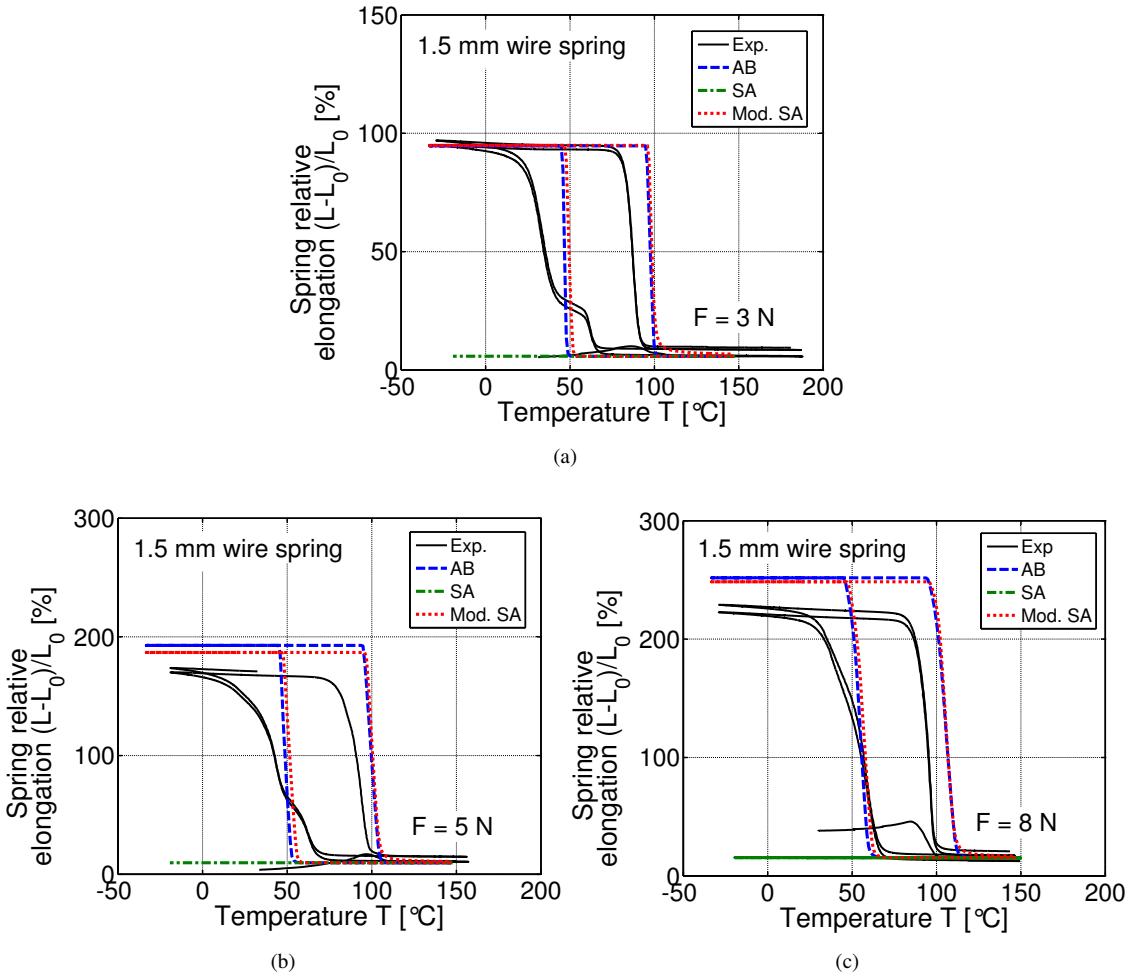

Figure 8.18: Thermal-cycling tests on 1.5 mm wire springs. Spring relative elongation, $(L - L_0)/L_0$, vs. temperature, T, curves at constant loads of 3, 5 and 8 kg.

models capture the general thermo-mechanical behavior of SMA springs, notwithstanding the simple calibration process.
Starting from Figures 8.15(a)-(b), 8.16 and 8.18(a)-(c), referring to 1.5 mm wires and 1.5 mm wire springs, both the models catch successfully the experimental curves.

The effect of the variation of spring geometrical properties (e.g., diameter, number of coils, etc.) is then investigated by focusing on 1.0 mm wires and 1.0 mm wire springs. Numerical predictions related to 1.0 mm wires do not present satisfactory results, as shown in Figures 8.19(a)-(e). Experimental curves reveal, in fact, a significative influence of the variation of the diameter on SMA wire behavior, which is not taken into account by the uniaxial FE simulations. This can be observed by comparing, for instance, the experimental curves related to the applied load of 100 MPa for both the 1.5 mm and 1.0 mm wires (see Figures 8.15(a) and 8.19(d), respectively). Numerical curves are almost matching, while experimental ones differ for the values of the stroke and of the transformation temperatures. Despite the poor matching for 1.0 mm wires, the results related to 1.0 mm wire springs are satisfactory in terms of the hysteresis loops, as reported in Figures 8.20(a)-(d), especially for the loads of 5 and 7 N, both generating high values of the effective stress. In fact, the two models capture successfully the hysteresis loops, while don't match exactly the transformation temperatures. This issue could be related to the fact that material parameters

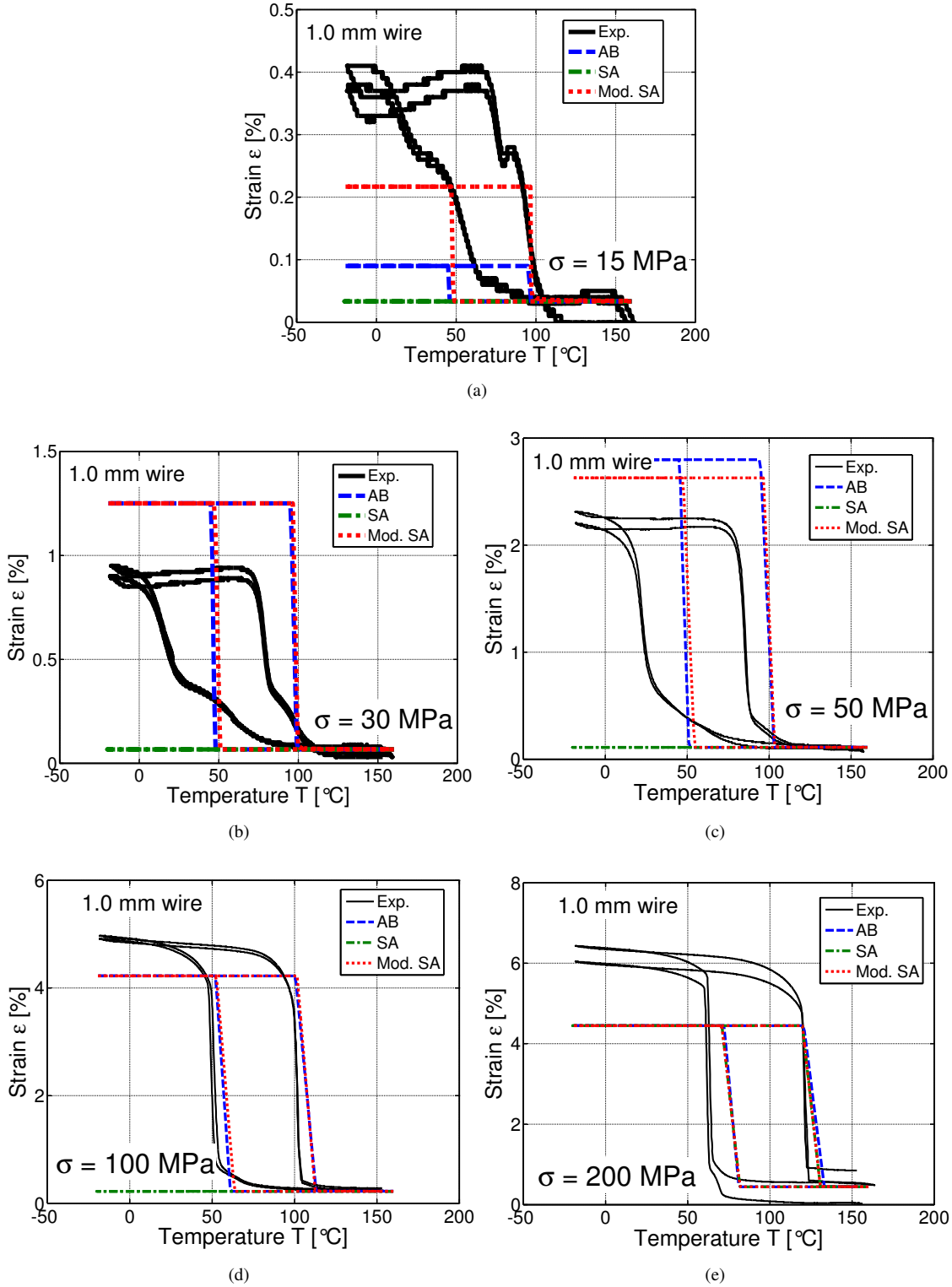

Figure 8.19: Thermal-cycling tests on 1.0 mm SMA wires. Deformation, ε, vs. temperature, T, curves at constant tensile loads of 15, 30, 50, 100 and 200 MPa.

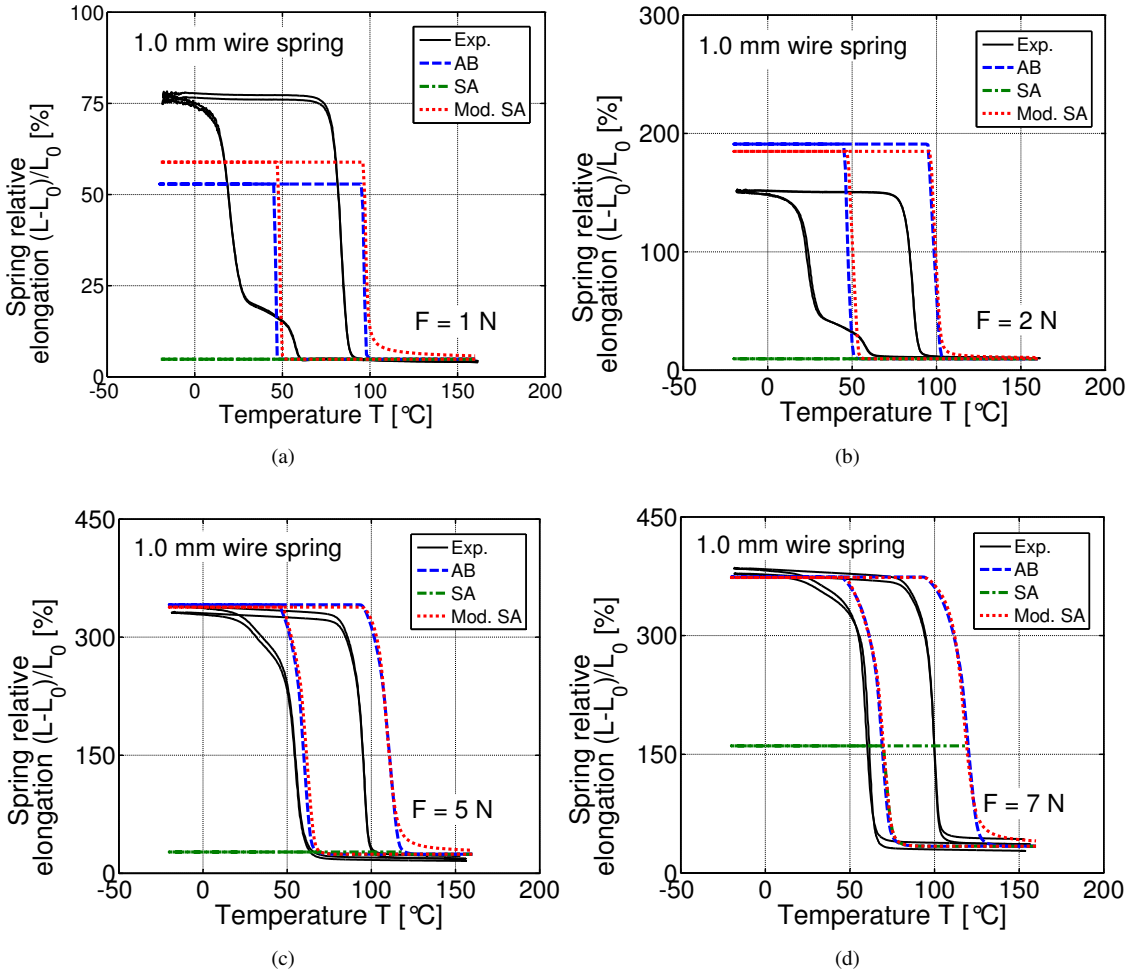

Figure 8.20: Thermal-cycling tests on 1.0 mm wire springs. Spring relative elongation, $(L - L_0)/L_0$, vs. temperature, T, curves at constant loads of 1, 2, 5 and 7 N.

have been calibrated on 1.5 mm wires and, in fact, experimental curves related to 1.5 mm wire springs are well described (see Figures 8.18(a)-(c)).

Compared to the modified Souza-Auricchio model, the Auricchio-Bonetti model presents a more flexible approach, but also an increasing modeling complexity and a high number of material parameters. Moreover, the modified Souza-Auricchio model solves, with a low number of material parameters, the problem highlighted for the Souza-Auricchio model whose behavior depends on the numerical implementation. As anticipated in Section 8.2.3, the Souza-Auricchio model does not catch successfully the experimental curves. This issue is related to the low values of the applied loads in experimental tests. In fact, starting from Figures 8.15(a) and (b), 8.16 and 8.18(a)-(c), referring to 1.5 mm wires and 1.5 mm wire springs, we observe the inability of the Souza-Auricchio model to catch SMA behavior for low work conditions. The results of the Souza-Auricchio model for 1.0 mm wires and 1.0 mm wire springs are not satisfactory too, as reported in Figures 8.19(a)-(e) and 8.20(a)-(d). In Figures 8.19(a)-(e), in fact, we observe that the only caught curve is that related to an applied load of 200 MPa. In Figures 8.20(a)-(d), the Souza-Auricchio model does not match the curve related to the load of 7 N, generating an approximate effective high stress of 161 MPa. This issue could be related to the numerical sensitiveness of the algorithm in the range of stresses lower or around 150 MPa and, in fact, the Souza-Auricchio model shows a starting transformation

producing an uncompleted hysteresis loop.

Moreover, experimental curves highlight some characteristic features of SMA real behavior. As it can be observed in Figures 8.18(a)-(c), 8.19(a)-(e) and 8.20(a)-(d), the 1.5 mm wire springs, 1.0 mm wires and 1.0 mm wire springs reveal a double transformation transition due to the presence of the R-phase, particularly evident for low levels of stress. In Figures 8.19(a)-(e), related to 1.0 mm wires, such a transition takes place in the range of temperatures between 40 and $60\,^{\circ}\mathrm{C}$. Contrarily, the 1.5 mm wires do not show any effect due to the R-phase, since their characterization involves high values of the load. Additionally, all the figures show irreversible strains.

8.3 Conclusions

Section 8.1 has presented extensive numerical tests in order to carefully investigate the robustness as well as efficiency of the integration algorithm for the proposed 'flexible' model, introduced in Chapter 7. The quantitative validation of the proposed model with several experimental data available from the literature has been addressed to confirm the reliability of the 'flexible' model.

Then, Section 8.2 has presented the numerical and experimental investigation of NiTi actuator springs. Comparison between numerical and experimental results has shown the inability of Souza-Auricchio model to catch SMA behavior for low levels of stress, while the modified Souza-Auricchio and Auricchio-Bonetti models have revealed good predictions of global SMA behavior, by allowing to take advantage of these preliminary results for future design purposes. Moreover, experimental curves have revealed the presence of some aspects characterizing SMA material behavior, as R-phase, plasticity, as well as training effects, which are not accounted by the models.

We remark, however, that the calibration process, adopted in the present study, requires the availability of experimental data on SMA wires for the identification of model parameters to be then used for spring simulations. Thus, in order to make the calibration as easy as possible and to avoid a calibration process for each type of available wire, we have calibrated model parameters only on 1.5 mm wires. Moreover, the calibration on data related to wires with specific geometries and material treatments are not well representative of all SMA wire springs. Despite this, the calibration is very simple compared to more sophisticated optimization techniques requiring large amount of experimental data and calculation time.

The present work will be used as a starting point for an ongoing detailed investigation about the calibration technique, the study of the effect of the variation of geometry properties and material treatment as well as of the application of compression loads.

Chapter 9

A theoretical, numerical and experimental investigation of shape memory polymers

This Chapter focuses on the experimental analysis, constitutive modeling and numerical simulation of shape memory polymers, which nowadays represent a new and challenging field of research.

The Chapter is organized as follows. Sections 9.1 and 9.2 present an introduction to material behavior and modeling and to the motivations of the proposed work. Then, Section 9.3 focuses on an experimental uniaxial campaign on semi-crystalline shape memory polymers conducted in the Basic Chemicals and Plastics Research Center of Versalis (ENI). Section 9.4 present a new predictive one-dimensional phenomenological model and its numerical counterpart, based on the Fischer-Burmeister function, already tested for J_2 elastoplasticity in Chapter 4 and for shape memory alloys in Chapter 7. Finally, Section 9.5 qualitatively and quantitatively investigates the proposed model and compares numerical predictions to experimental results.

9.1 Introduction to shape memory polymer behavior and activities

Shape memory materials represent an important class of multi-phase smart materials that have the ability to return from a deformed state to their original shape. Such a property, known as *shape memory recovery*, is typically induced by an external stimulus such as heat, electricity or magnetism (Wei et al., 1998a,b).

Among the others, *shape memory polymers*[1] (SMPs) possess the advantages of large elastic deformations, low energy consumption for shape programming, low cost and density, potential biocompatibility, biodegradability, and excellent manufacturability (El Feninat et al., 2002; Hu et al., 2012). As an example, SMPs can recover an elongation as large as 150%, which is significantly larger than the largest shape recovery observed in shape memory alloys, which is about 8% (Lendlein and Kelch, 2002). Moreover, SMPs are less expensive than shape memory alloys and they need a cheaper process for the production of different shapes and sizing. Figure 9.1 shows a closed flower (temporary shape), made of a SMP and fixed at a low temperature, which recovers its original shape (open flower) when the temperature is increased (Hu and Chen, 2010).

Thanks to such characteristics, SMPs have attracted a great deal of interest for their potential applications and have a promising future for applications as, e.g., micro electro-mechanical system devices,

[1] A *polymer* is a large molecule composed of many repeated subunits, known as monomers. The most common way of classifying polymers is to separate them into three groups: thermo-plastics, thermo-sets, and elastomers.

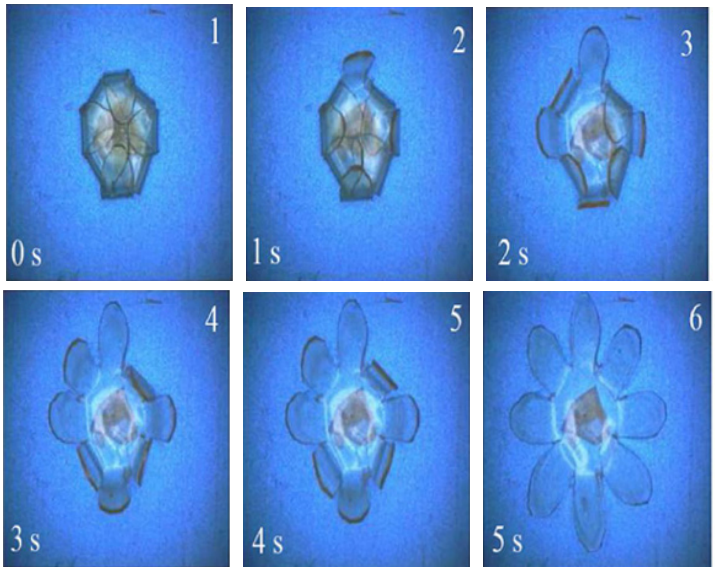

Figure 9.1: A closed flower (temporary shape), made of a SMP and fixed at a lower temperature, recovers its original shape (open flower) when the temperature is increased above its switch temperature, taken from (Hu and Chen, 2010).

actuators, temperature sensors, packaging, fibers and films with insulating properties, digital storage, biomedical devices, and damping elements (Monkman, 2000; Poilane et al., 2000; Sai, 2010; Tey et al., 2001).

The mechanism responsible for shape memory in polymers is not related to a single material property of a specific polymer; rather, it results from the combination of polymer structure and morphology[2], together with the applied processing and heat treatment[3]. In fact, shape memory behavior can be observed for several polymers that may differ significantly in their chemical composition.
Despite the increasing interests, only a few SMPs are described in the literature. As an example, various studies are devoted to polymers mainly based on polyurethanes (Kim et al., 1998, 1996; Yang et al., 2006) or focus on systems as ethylene/vinyl acetate copolymers, poly(ϵ-caprolactone), semi-crystalline polymers and related blends (Pandini et al., 2012; Zhu et al., 2003, 2006, 2005).

Several experimental investigations have been conducted to characterize the behavior of SMPs (Abrahamson et al., 2003; Atli et al., 2009; Baer et al., 2007; Gall et al., 2002; Kim et al., 2010; Kolesov et al., 2009; Lagoudas et al., 2010; Lendlein and Kelch, 2002; Liu et al., 2006, 2004; Tobushi et al., 1997, 1998; Volk et al., 2010). Many of the initial studies focused on the SMP response under small deformations, i.e., under extensions less than 10% (Liu et al., 2006; Tobushi et al., 1997, 1998); recently, experimental efforts have investigated the response under finite deformations, i.e., under extensions greater than 10% (Atli et al., 2009; Baer et al., 2007; Lagoudas et al., 2010; Voit et al., 2010; Volk et al., 2010; Ware et al., 2010; Wilson et al., 2007).

In addition to experimental efforts, the ever increasing applications of SMPs have motivated a considerable part of the research, focused on the prediction and description of SMP behavior, through the development of appropriate and reliable constitutive models. However, such research field is still under

[2]Polymer morphology is the overall form of the polymer structure, including, e.g., crystallinity, branching, molecular weight, cross-linking. Polymers can be crystalline (molecules are arranged in a regular order), amorphous (totally lacking positional order on the molecular scale), or semi-crystalline (containing both crystalline and amorphous regions in the same sample).

[3]A cross-link is a bond that links one polymer chain to another. Cross-linking is used in both synthetic polymer chemistry and in the biological sciences. When the term 'cross-linking' is used in the synthetic polymer science field, it usually refers to the use of cross-links to promote a difference in the polymer physical properties. When cross-linking is used in the biological field, it refers to the use of a probe to link proteins together to check for protein-protein interactions, as well as other creative cross-linking methodologies.

progress, due to the complex behavior of SMPs. In particular, there is a lack of modeling of shape memory effect in polymers, in spite of the fact that polymers represent a good and promising alternative to, e.g., shape memory alloys which have been widely studied from the point of view of both theoretical and numerical aspects (Arghavani et al., 2010; Auricchio and Bonetti, 2013; Auricchio and Petrini, 2004a; Lagoudas et al., 2012).

Several macroscopic or phenomenological constitutive models, e.g., (Baghani et al., 2012; Chen and Lagoudas, 2008a,b; Kim et al., 2010; Liu et al., 2006; Qi et al., 2008; Reese et al., 2010; Xu and Li, 2010) as well as microscopic or physical-based models (Barot et al., 2008; Nguyen et al., 2008; Srivastava et al., 2010) have been proposed in both the small and finite deformation regimes.

In the following, we focus on phenomenological macro-modeling approaches which appear to be a powerful tool for the direct simulation of SMP applications, thanks to their simple numerical implementation and reduced time-consuming calculations, compared to micromechanical approaches.

Most of the earlier modeling efforts have adopted rheological models consisting of spring, dashpot, and frictional elements in one-dimensional models, in order to quantitatively describe the shrinkage behavior in amorphous polymers (Abrahamson et al., 2003; Bhattacharyya and Tobushi, 2000; Khonakdar et al., 2007; Pakula and Trznadel, 1985; Tobushi et al., 1997, 2001; Trznadel and Kryszewski, 1988). However, while such models seem to be simple, they have limitations in certain classes of constitutive relations and usually lead to predictions that agree only qualitatively with experiments.

Liu et al. (2006) developed a one-dimensional constitutive model where the SMP consists of two phases, a rubbery and a glassy phase, and the memory effect is achieved by defining a storage deformation. Based on Liu's phase concept and storage deformation, Chen and Lagoudas (2008a,b) extended the model to a three-dimensional framework. Recently, Qi et al. (2008) developed a three-dimensional finite deformation model for thermo-mechanical behavior of SMPs, based on the evolution of the deformation energy from an entropy dominated state to an enthalpy dominated state. Barot and Rao (2006); Barot et al. (2008) applied a similar concept to crystallizable polymers.

Approaches involving the viscosity change in the material when the temperature traverses the glass transition temperature are particularly suited for amorphous polymers. As an example, the work by Nguyen et al. (2008) considers visco-elasticity in a finite deformation framework and the works by Reese et al. (2010); Srivastava et al. (2010) include thermo-mechanical coupling in models that have been implemented in finite element (FE) analysis packages.

On the contrary, the phase evolution approach represents the physical phenomena at work during deformation in semi-crystalline polymers. Recently, Long et al. (2009) have showed that such a modeling scheme can also be applied to other active polymers, like photo-activated polymers. The paper by Westbrook et al. (2010) presents a one-dimensional model based on the concept of phase evolution to quantitatively capture both one-way and two-way SMEs in semi-crystalline polymers exhibiting stretch-induced crystallization. Volk et al. (2011) performed tensile tests and one-dimensional modeling on a high recovery force polyurethane SMP for biomedical applications. Recently, Baghani et al. (2012) have presented a three-dimensional phenomenological model under time-dependent multiaxial thermo-mechanical loadings in the small strain regime.

9.2 Motivations of the proposed work

The work proposed in the present Chapter focuses on *semi-crystalline polymers*, particularly, both on *low-density* (LDPE) and *high-density* (HDPE) *polyethylene-based polymers*[4].

In semi-crystalline polymeric materials, the shape memory behavior manifests itself through *thermal retraction* on heating when the molecular structure has been oriented by mechanical loads. Such an effect may be considered as a shape memory property since, after a permanent deformation by mechanical loads,

[4]The difference between LDPE and HDPE is due to the range of density which is of 0.910-0.935 and 0.935-0.965, respectively.

polymers may recover their original shape just by thermal actions. In particular, the deformation remains fixed by lowering the temperature, while a retraction occurs (or a residual stress) by heating. In PE-based polymers, thermal retraction finds important industrial applications, e.g., in packaging of goods. For example, while LDPE is very flexible and used for packaging and production of home products, HDPE finds applications in blow molding and it is used to produce tubes, film, bottles.

The objectives of the present Chapter are two-fold and aim to experimentally investigate LDPE and HDPE polymers with known compositions, that are being considered for packaging applications, and to introduce and numerically assess a new one-dimensional macroscopic model, limiting the discussion to the small deformation regime.

Specifically, the first objective of the proposed work is to evaluate the behavior and the characteristics of PE-based SMPs through an experimental campaign conducted at the Basic Chemicals and Plastics Research Center in Versalis (ENI) by Pachera (2011); Talamazzi (2012). Such experimental effort characterizes the orientation process as well as the free and constrained thermal retraction properties, which are of fundamental importance in the design of SMP devices for packaging applications. Specifically, to achieve the requested shape change, the material and/or the thermo-mechanical load paths have to be appropriately selected. We investigate both HDPE and LDPE polymers to study the effect of density on material behavior. Moreover, some of the tested LDPE polymers differ in terms of molecular weights to evaluate the effect of weight variation.

The second objective of the present work is to introduce and numerically investigate a new one-dimensional macroscopic model, describing the thermo-mechanical behavior of semi-crystalline polymers. The idea is to extend to SMPs modeling and numerical features already introduced and widely accepted for shape memory alloys. The proposed model is thus based on the so-called phase transition approach which describes both phase transformation and phase separation dynamics, as well as non-smooth internal constraints on the variables (Frémond, 2002, 2012). Thanks to such an approach, we are able to include in our model the typical phenomenon of crystallization in semi-crystalline polymers, which represents a microscopic configuration change taking place at certain temperatures and which can be described as a phase transformation. The main idea is that material properties depend on the microscopic structure which is represented by a suitable scalar parameter, the so-called phase parameter, denoting which kind of microstructure is present. As shape memory in polymers strongly depends on the orientation of the polymers chains, we associate an order parameter to the non-oriented microstructure and we also define a set of parameters capable of describing the mechanical behavior of the material at different temperatures. Hence, by using general thermo-mechanical laws, we recover a system of constitutive relations coming from energy and dissipation functionals, chosen on the basis of the experimental obtained evidences. Moreover, we assume that no viscosity appears and that phase evolution is rate-independent. We conduct the numerical investigation of the proposed model through an effective and efficient computational procedure, introduced in the framework of crystal plasticity by Schmidt-Baldassari (2003) and of shape memory alloys by Bartel and Hackl (2009, 2010); Bartel et al. (2011); Kiefer et al. (2012) and in Chapter 7. It consists in replacing the Kuhn-Tucker complementarity inequality conditions by the equivalent Fischer-Burmeister complementarity function (Fischer, 1992) and in making possible to omit an active set search, a fundamental advantage when dealing with several variable constraints as in our model. Additionally, the proposed work presents several numerical results for uniaxial tests and a comparison between numerical predictions and experimental results, to show the capability of the model to qualitatively and quantitatively reproduce basic effects such as the orientation process, free and constrained thermal retraction.

9.3 Experimental campaign conducted in Versalis (ENI)

The present Section describes an experimental campaign conducted at the Basic Chemicals and Plastics Research Center - Versalis (ENI), on commercial LDPE and HDPE polymers by Pachera (2011); Talamazzi

(2012).

Table 9.1 lists the property values of the tested materials, which differ in terms of density and molecular weight. In particular, we conduct some experimental tests on one type of LDPE (Mat. A) and one type of HDPE (Mat. E) to evaluate the effect of density variation on material behavior; then, we conduct some tests on three types of LDPE (Mat. B, C and D) to consider the effect of molecular weight variation on material behavior.

Property	**Mat. A**	**Mat. B**	**Mat. C**	**Mat. D**	**Mat. E**
Melt flow index (MFI) ($190\,^{\circ}\mathrm{C}, 2.16$ Kg) [g/10 min]	0.79	0.80	2.20	0.25	0.15
Density [g/cm^3]	0.9221	0.9230	0.9230	0.922	0.939
Cristallinity [%]	50.00	47.47	47.30	47.54	70.00
Melting point (T_m) [$^{\circ}\mathrm{C}$]	110.1	113.0	113.0	112.0	129.0
Weight Average Molecular Weight (Mw) [KDa]	-	170	145	220	-

Table 9.1: Property values of the tested LDPE and HDPE polymers (Pachera, 2011; Talamazzi, 2012).

All the specimens are obtained from isotropic sheets created through a Saspol press (see Figure 9.2). For the realization of the isotropic material, the technique of compression molding, consisting in both combining and compacting the material, is used. Starting from a reel of polymeric film, 100×100 mm material portions are obtained and subsequently placed in the center of a square mold of 200×0.0002 mm. The mold is placed between the plates of the press, previously heated up to a temperature of $170\,^{\circ}\mathrm{C}$ (see Figure 9.2). After ten minutes, the mold is first pressed for two minutes at a pressure of 15 bar, then further three minutes at 50 bar. Finally, the mold is cooled without applying any external force, which is the ideal situation to ensure a state of isotropy. Consequently, polymeric sheets of dimension $200 \times 200 \times 0.2$ mm are obtained. The tested specimens, obtained from these sheets, take the form of 100×9 mm rectangular bars.

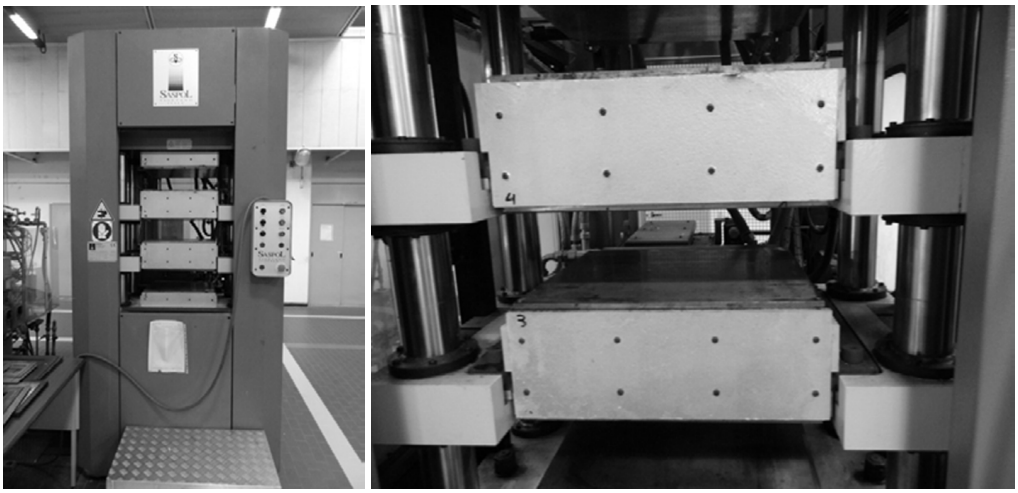

Figure 9.2: Saspol press (left) and zoom of the plates (right) (Pachera, 2011; Talamazzi, 2012).

9.3.1 Orientation test

Material orientation under isothermal conditions (at temperatures below the melting temperature[5], T_m) is realized by using a dynamometer Instron series 4505 equipped with a cell temperature (see Figure 9.3), in which it is possible to set the following variables:

- gage length (fixed at 15 mm);
- maximum imposed elongation;
- testing temperature;
- crosshead speed (fixed at 9 mm/min).

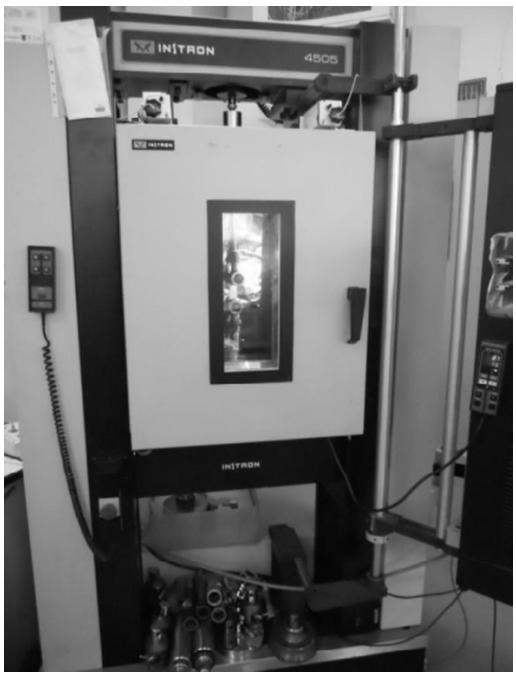

Figure 9.3: Dynamometer Instron series 4505 and temperature cell (Pachera, 2011; Talamazzi, 2012).

The orientation test consists of the following steps:

1. the crosshead moves at a fixed speed until the maximum imposed elongation is reached;
2. after reaching the required elongation, the crosshead moves in the opposite direction at the same speed, thus allowing the specimen to recover a partial deformation until it reaches a stable thermodynamic state at zero stress.

Figures 9.4(a) and 9.4(c) present the orientation curves in terms of stress, σ, and strain, ε, at temperatures of 26, 30, 45, 60, 75 and $90\,^{\circ}\mathrm{C}$ and maximum imposed deformation of 600%, for materials A and E, respectively. Figures 9.4(b) and 9.4(d) show the orientation curves in terms of stress, σ, and strain, ε, at a constant temperature of $60\,^{\circ}\mathrm{C}$ and maximum imposed deformations of 10, 25, 50, 100, 200, 400 and 600% for materials A and E, respectively.

[5]The term *melting point*, when applied to polymers, suggests a transition from a crystalline or semi-crystalline phase to a solid amorphous phase. Though abbreviated as simply T_m, the property in question is more properly called the crystalline melting temperature. Another parameter of particular interest is the *glass transition temperature* (T_g), at which amorphous polymers undergo a transition from a rubbery, viscous liquid, to a brittle, glassy amorphous solid on cooling.

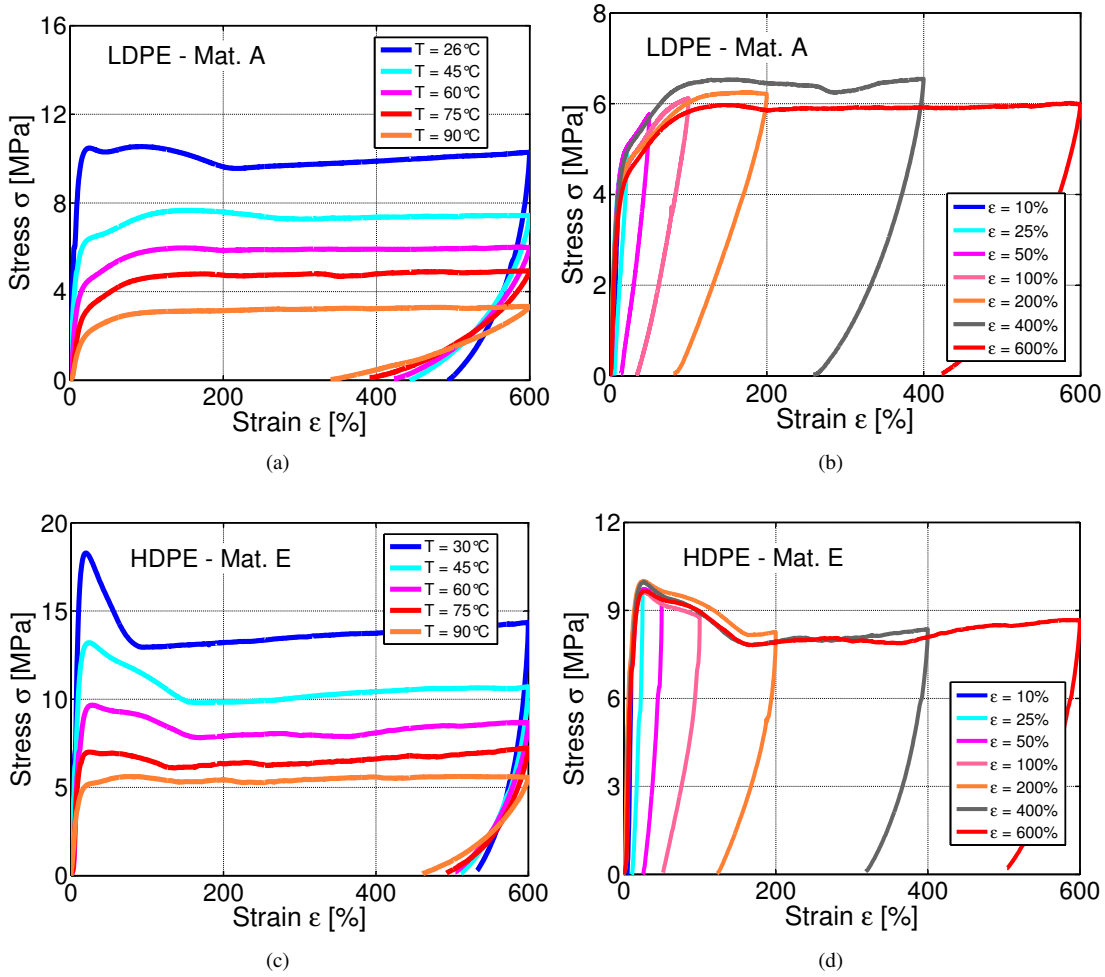

Figure 9.4: Experimental orientation process on materials A and E. Curves in terms of stress, σ, and strain, ε, (a)-(c) at different temperatures of 26, 30, 45, 60, 75 and 90 °C and maximum imposed deformation of 600%; (b)-(d) at constant temperature of 60 °C and different imposed deformations of 10, 25, 50, 100, 200, 400 and 600%.

As it can be observed from Figures 9.4(a) and 9.4(c), the material is first deformed in the elastic region, characterized by increasing slope and yield stress and by decreasing yield strain with decreasing temperature. At high temperatures, in fact, the macromolecular chains have more freedom to move; thus, the deformation of the elastic phase increases with increasing temperature, while the slope decreases. Similarly, at high temperatures material toughness and yield stress decrease. Then, after reaching the yield stress, the orientation process of the amorphous chains starts. Upon unloading, the material reaches a residual strain at zero stress, as equilibrium thermodynamic state for a given temperature. The slope of the curve upon unloading and the residual strain increase with decreasing temperature.

As it can be observed from Figures 9.4(b) and 9.4(d), the slope of the curve upon unloading decreases with increasing imposed deformation, while the residual deformation increases. We already remark that, if temperature is increased after unloading, the material is no more in an equilibrium state due to the presence of a reduced number of oriented chains and thermal retraction effect is manifested.

Materials A (LDPE) and E (HDPE) present a similar trend, but also some differences:

- the slope in the elastic region is higher in material E which presents a lower amorphous part than material A;
- material E presents a higher yield stress and a transition zone around the yield stress from a maximum stress to a lower stress before reaching a plateau. This aspect is explained by the phenomenon of necking, not manifesting in material A which shows a gradual transition from the elastic to the plastic zone;
- upon unloading, the recovered strain is higher in material A than material E, consequence of the fact that material E has a lower elastic part to recover.

Figure 9.5 shows the orientation curves in terms of stress, σ, and strain, ε, at a constant temperature of $60\,^{\circ}\mathrm{C}$ and maximum imposed deformation of 600% for materials B, C and D. As it can be observed, material behavior is equivalent.

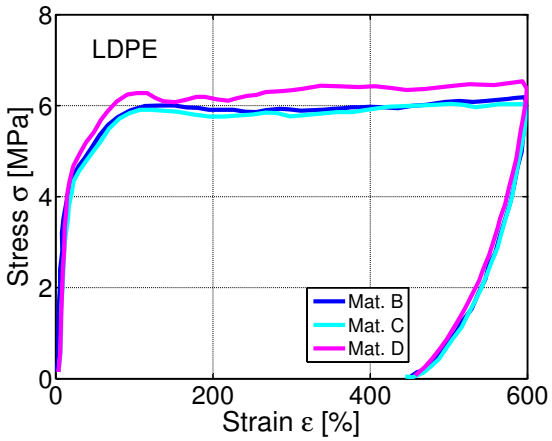

Figure 9.5: Experimental orientation process on materials B, C, and D. Curves in terms of stress, σ, and strain, ε, at a temperature of $60\,^{\circ}\mathrm{C}$ and maximum imposed deformation of 600%.

9.3.2 Constrained thermal retraction test

All the specimens, oriented as described in Section 9.3.1, are subjected to a constrained thermal retraction test. The test is carried out by using a rheometer ARES LS II (see Figure 9.6), equipped with a temperature cell, able to measure the force generated by the specimen when subjected to heating at constrained deformation.

The constrained thermal retraction test consists of the following steps:

1. the specimen is oriented at a predefinite temperature and imposed deformation;
2. the specimen is placed inside the temperature cell on grips at a predefined distance, which remains unchanged during the whole test. After few minutes at an initial temperature of $30\,^{\circ}\mathrm{C}$, a small force is applied to fully relax the specimen;
3. the temperature is increased from the initial temperature to a value above the melting temperature, T_m, at a rate of $2\,^{\circ}\mathrm{C}/\mathrm{min}$. As temperature increases, the specimen tries to shrink in order to reach a thermodynamic equilibrium state. Due to the constraint, the specimen generates a force of entropic nature and consequence of the tendency of the oriented macromolecular chains to reach a state of thermodynamic equilibrium.

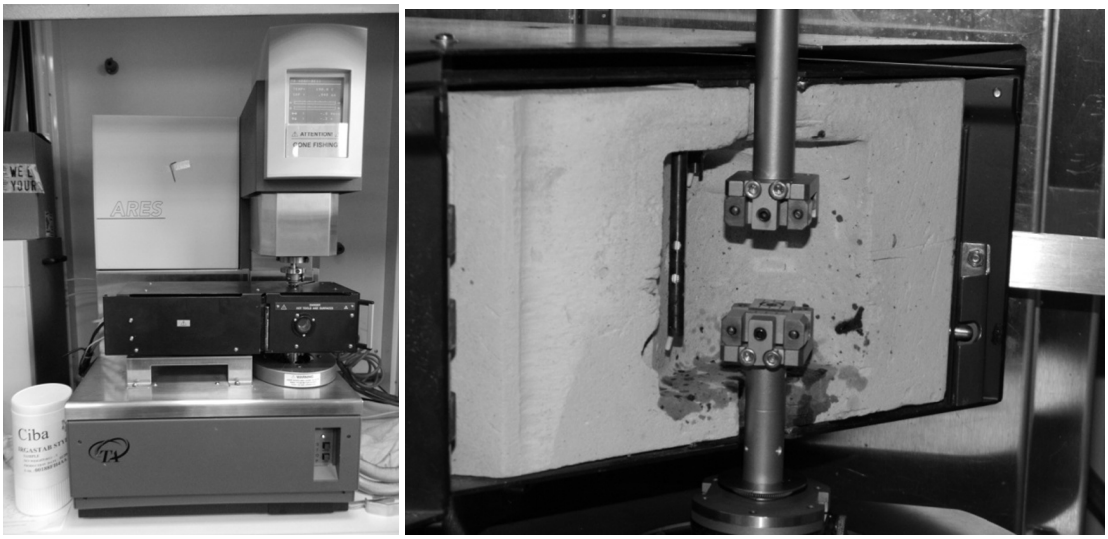

Figure 9.6: Rotational rheometer ARES LS II (left) and zoom of the temperature cell (right) (Pachera, 2011; Talamazzi, 2012).

Figures 9.7(a) and 9.7(c) present the constrained thermal retraction curves in terms of stress, σ, and temperature, T, for materials A and E, oriented at temperatures of 26, 30, 60 and 90 °C and at maximum imposed deformation of 600%, respectively. Figure 9.7(b) shows the constrained thermal retraction curves in terms of stress, σ, and temperature, T, for material A oriented at a temperature of 60 °C and at three imposed deformations of 200, 400 and 600%.

As it can be observed from Figures 9.7(a) and 9.7(c), the stress increases until a maximum value and then decreases until a zero value at the melting temperature, T_m, where material loses its original shape. In particular, the slope of the curve increases until the orientation temperature is reached and the maximum value of the stress increases with decreasing orientation temperature. From Figure 9.7(b), we observe that firstly the maximum value of the stress increases with increasing imposed strain and then it decreases with increasing imposed strain.

Again, materials A (LDPE) and E (HDPE) present a similar trend, but however material E exerts higher stresses than material A .

Figure 9.8 shows the comparison between the experimental curves in terms of stress, σ, and temperature, T, for materials B, C and D oriented at a temperature of 60 °C and at maximum imposed deformation of 600%. As it can be observed, material behavior is again equivalent.

9.3.3 Free thermal retraction test

All the specimens, oriented as described in Section 9.3.1, are also subjected to a free thermal retraction test. The test is carried out by using a rheometer ARES LS II (see Figure 9.6), equipped with a temperature cell.

The free thermal retraction test consists of the following steps:

1. the specimen is oriented at a predefinite temperature and imposed deformation;
2. the specimen is placed inside the temperature cell on grips at a predefined distance and initial temperature of 30 °C;
3. the temperature is increased from the initial temperature to a value above the melting temperature, T_m, at a rate of 2 °C/min. The specimen is free to move.

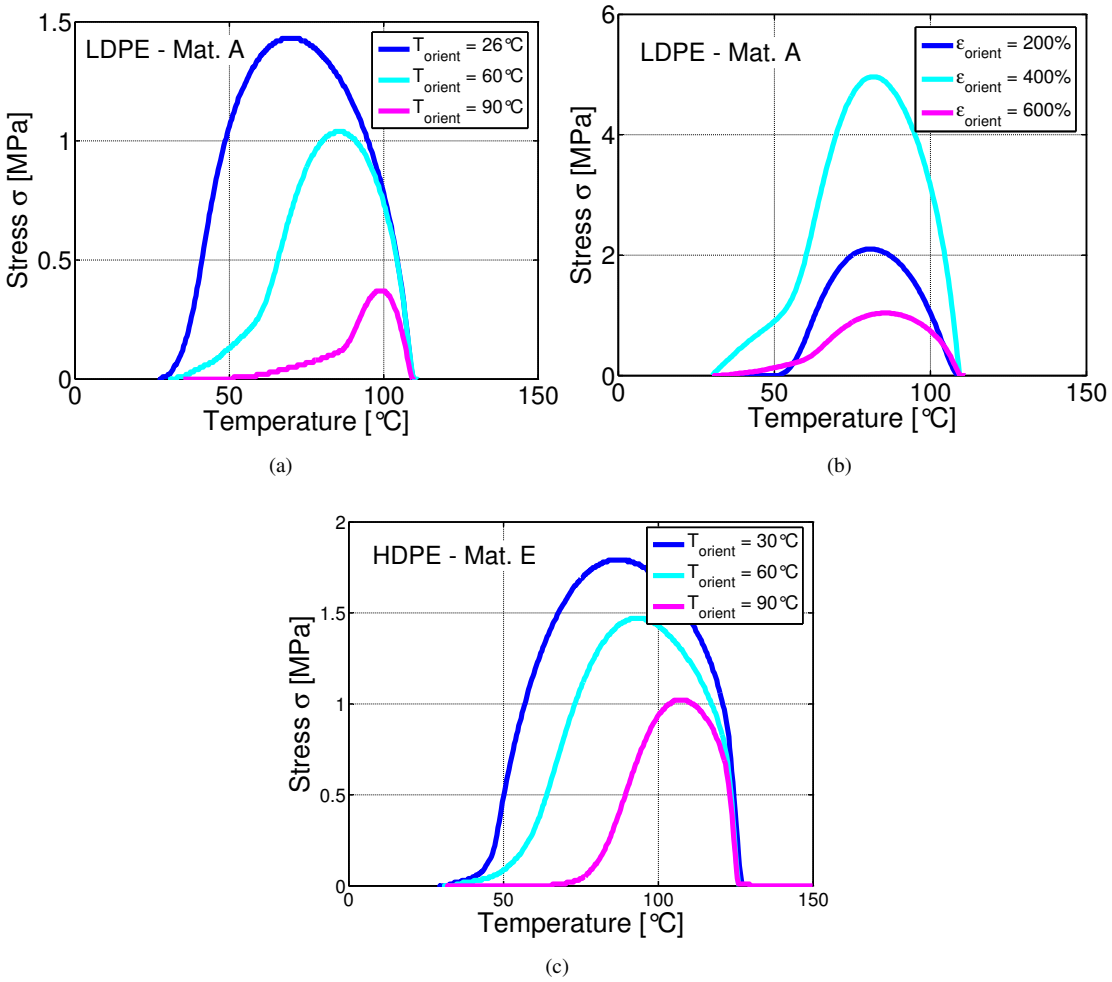

Figure 9.7: Experimental constrained thermal retraction test on materials A and E. Curves in terms of stress, σ, and temperature, T, for specimens oriented (a)-(c) at temperatures of 26, 30, 60 and 90 °C and at maximum imposed deformation of 600%; (b) at a temperature of 60 °C and at imposed deformations of 200, 400 and 600%.

Figures 9.9(a) and 9.9(c) present the free thermal retraction curves in terms of shrinkage, and temperature, T, for materials A and E oriented at temperatures of 26, 30, 60 and 90 °C and at maximum imposed deformation of 600%, respectively. Figure 9.9(b) shows the free thermal retraction curves in terms of shrinkage and temperature, T, for materials A oriented at a temperature of 60 °C and at three imposed deformations of 200, 400 and 600%.

As it can be observed from Figures 9.9(a) and 9.9(c), the retraction process begins at the orientation temperature and the maximum value of the shrinkage is reached at the melting temperature, T_m. Moreover, as shown in Figure 9.9(b), the maximum value of the shrinkage increases with increasing imposed strain. In such a test, the curve related to material E (HDPE) at low temperatures is below the curve of material A (LDPE), while, around T_m, the slope of the curve increases and reaches a maximum value of shrinkage which is greater for material E.

Figure 9.10 shows the comparison between the experimental curves in terms of shrinkage and temperature, T, for materials B, C and D oriented at a temperature of 60 °C and at maximum imposed deformation of 600%. Again, material behavior is equivalent.

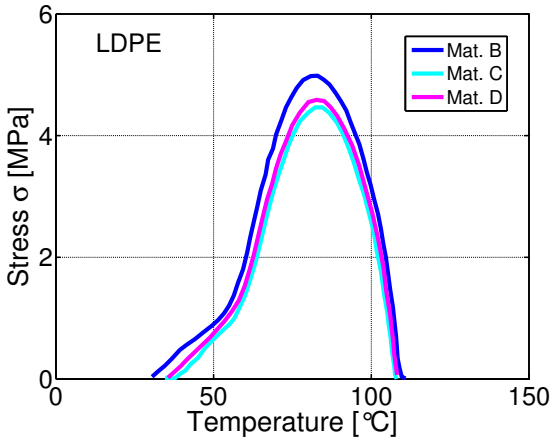

Figure 9.8: Experimental constrained thermal retraction test on materials B, C, and D. Curves in terms of stress, σ, and temperature, T, for specimens oriented at a temperature of $60\,^{\circ}\mathrm{C}$ and at maximum imposed deformation of 600%.

9.3.4 Test above the melting temperature

From the results related to materials B, C, and D (see Figures 9.5, 9.8 and 9.10), it is clear that the molecular weight has no influence on material behavior at temperatures below the melting temperature, T_m. Consequently, we investigate the behavior of such materials at the molten state (Talamazzi, 2012).

The material is placed in a tank at a temperature of $190\,^{\circ}\mathrm{C}$, and then melted. Through the movement of a piston, a force increasing in time is then applied, thus leading to an increase of the internal pressure in the tank and to an exiting flow. A capillary rheometer measures material viscosity with increasing force and flow. Figure 9.11(a) shows the flow curves in terms of viscosity and strain rate. As it can be observed, materials B, C, and D present a different degree of fluidity.

Then, the constrained thermal retraction test is realized on polymeric films created through blown film processes. Figure 9.11(b) shows the comparison between the experimental curves in terms of stress, σ, and temperature, T. As it can be observed, stress is zero until temperatures around the melting temperature, T_m, it reaches its maximum value at T_m, and finally, it comes back to zero. An important result is the fact that stresses obtained by orienting the specimens below T_m are higher than those obtained by orienting above T_m, as shown in Figures 9.8 and 9.11(b).

9.4 A new phenomenological model for shape memory polymers

This Section addresses a new one-dimensional phenomenological model for SMPs, based on the so-called phase transition approach. In the following, we present the model formulation in both time-continuous and time-discrete framework and we propose a physical interpretation of model parameters.

9.4.1 A time-continuous model formulation

In the framework of macroscopic modeling and of small strain continuum mechanics, we assume the total strain, ε, representing the total deformation of the material, and temperature, T, as state variables. A general assumption of additive strain decomposition is adopted in the form:

$$\varepsilon = \varepsilon^e + \varepsilon^{ie} \tag{9.1}$$

where ε^e and ε^{ie} denote the elastic and inelastic strain, respectively.

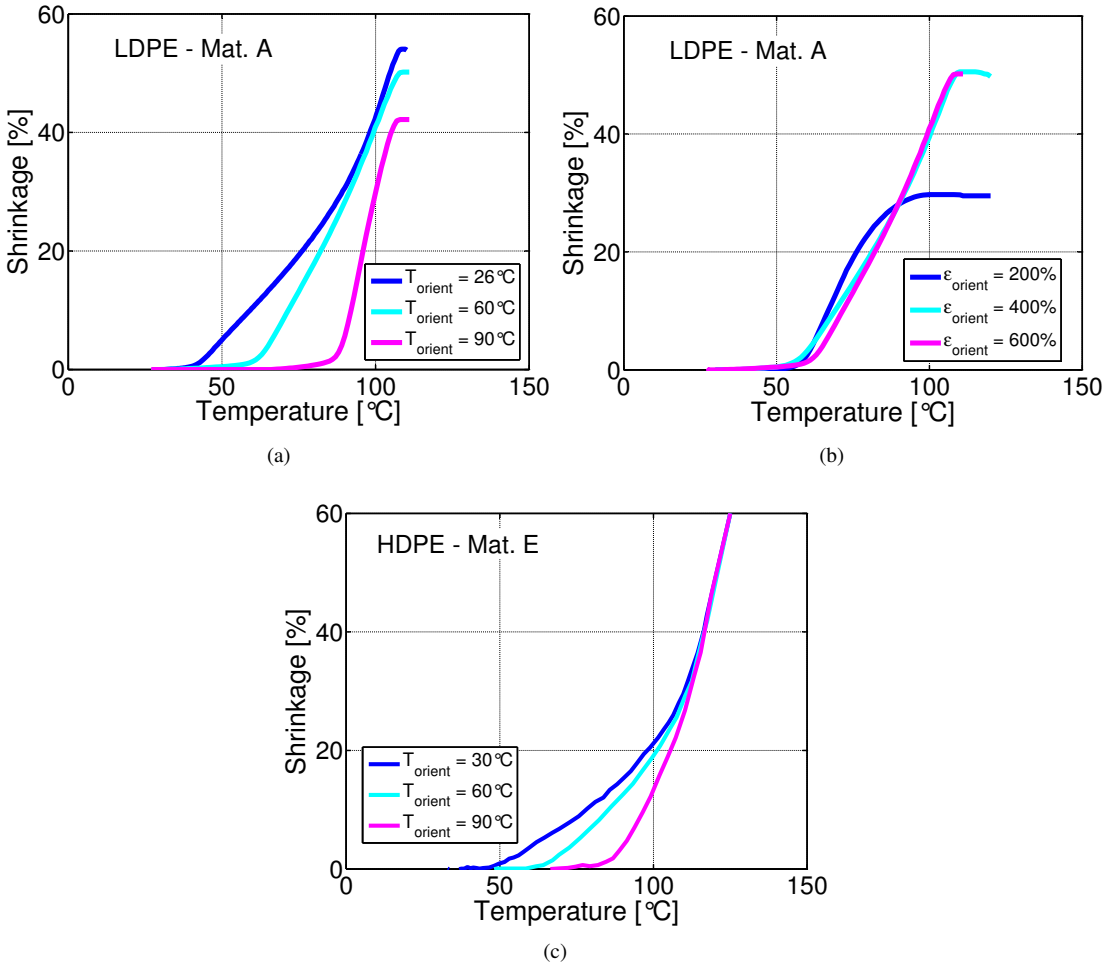

Figure 9.9: Experimental free thermal retraction test on materials A and E. Curves in terms of shrinkage and temperature, T, for specimens oriented (a)-(c) at different temperatures of 26, 30, 60 and 90 °C and maximum imposed deformation of 600%; (b) at a temperature of 60 °C and at different imposed deformations of 200, 400 and 600%.

Recalling the discussion of Section 9.1, the phenomenon of thermal retraction in PE-based polymers is a shape memory property and it is strongly connected with molecules orientation under mechanical and thermal loads. Thus, in the phase transition framework, the main idea is that the microscopic structure of the polymer can be represented by a suitable scalar parameter, the so called phase-parameter, denoting which kind of microstructure is present. As shape memory strongly depends on the orientation of the polymer chains, we associate to the non-oriented microstructure a phase parameter, χ, related to the local proportion of non-oriented phase with respect to oriented phase. Due to its physical meaning, the phase parameter has to be between 0 and 1, i.e., $\chi \in [0, 1]$. In particular, the case $\chi = 1$ corresponds to the presence of completely non-oriented chains, while the case $\chi = 0$ stands for complete ordered phase.

The inelastic strain, $\varepsilon^{ie} = \varepsilon^{ie}(T, \chi)$, is assumed as follows:

$$\varepsilon^{ie} = C_\alpha \exp\left[\frac{\alpha}{T - T_0}\right](1 - \chi) \tag{9.2}$$

where α and C_α are positive material parameters and T_0 a reference temperature.

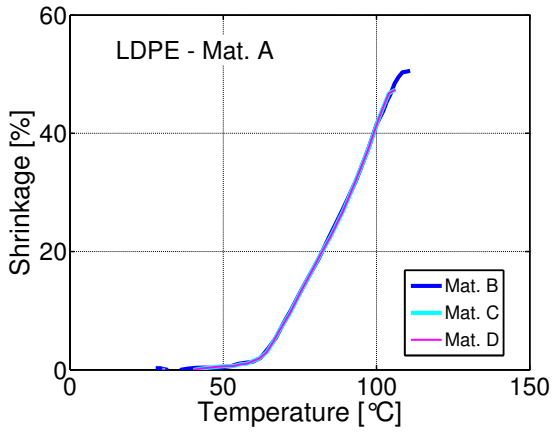

Figure 9.10: Experimental free thermal retraction test on materials B, C, and D. Curves in terms of shrinkage and temperature, T, for specimens oriented at a temperature of $60\,^{\circ}\mathrm{C}$ and at maximum imposed deformation of 600%.

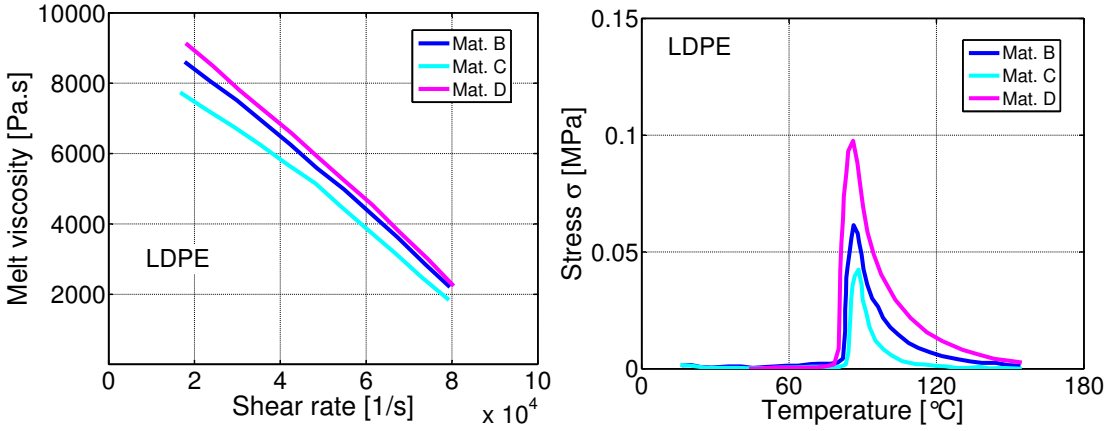

(a) (b)

Figure 9.11: Tests above the melting temperature, T_m, on materials B, C, and D. Curves (a) in terms of viscosity and strain rate; (b) in terms of stress, σ, and temperature, T, for specimens obtained through blown film processes.

Helmholtz free-energy function

The Helmholtz free-energy function, $\Psi = \Psi\left(\varepsilon, T, \chi\right)$, is assumed in the following classical form:

$$\Psi = \frac{1}{2} E \left(\varepsilon^{e}\right)^{2} - c_s T \ln T + I_{[0,1]}\left(\chi\right) \tag{9.3}$$

which, after introducing Eq. (9.1), becomes:

$$\Psi = \frac{1}{2} E \left(\varepsilon - \varepsilon^{ie}\right)^{2} - c_s T \ln T + I_{[0,1]}\left(\chi\right) \tag{9.4}$$

where $c_s > 0$ is the specific heat and $I_{[0,1]}\left(\chi\right)$ is the indicator function forcing to fulfill the constraints on χ, defined as:

$$I_{[0,1]}(\chi) = \begin{cases} 0 & \text{if } 0 \leq \chi \leq 1 \\ +\infty & \text{otherwise} \end{cases} \tag{9.5}$$

The function $E = E(T, \chi)$ represents the Young's modulus, which, according to experimental evidences of Figures 9.4(a)-(d), we assume to strongly depend on the temperature, T, and on the phase, χ, as follows:

$$E(T, \chi) = E_T(T) E_\chi(\chi) \tag{9.6}$$

In particular, we assume that at constant temperature, T, the Young's modulus depends on the phase, χ, following the model of Reuss, while at constant phase, χ, the Young's modulus depends exponentially on temperature, T, as shown in Figures 9.4(a)-(d). Thus, we assume the following expression for $E = E(T, \chi)$:

$$E = \exp\left[\frac{\beta}{T - T_0}\right] \frac{1}{\dfrac{\chi}{E_1} + \dfrac{1-\chi}{E_0}} \tag{9.7}$$

E_1 and E_0 being positive parameters due to material rigidity for the two cases $\chi = 1$ and $\chi = 0$, respectively (with $E_1 > E_0$), and β a positive material parameter. Such an expression has been demonstrated to be the only function of χ such that $d\sigma/d\varepsilon = 0$ when no hardening is assumed, i.e., we have a flat plateau in the stress, σ, versus strain, ε, diagram during phase transformation (Auricchio et al., 2009).

Constitutive equations

Starting from the free-energy, Ψ, presented in Eq. (9.4), and following standard arguments (Gurtin et al., 2010), we derive the stress, σ:

$$\begin{aligned} \sigma = \frac{\partial \Psi}{\partial \varepsilon} &= E\left(\varepsilon - \varepsilon^{ie}\right) \\ &= \exp\left[\frac{\beta}{T - T_0}\right] \frac{1}{\dfrac{\chi}{E_1} + \dfrac{1-\chi}{E_0}} \left(\varepsilon - C_\alpha \exp\left[\frac{\alpha}{T - T_0}\right](1 - \chi)\right) \end{aligned} \tag{9.8}$$

as well as the thermodynamic force, X^{nd}, governing the evolution of χ:

$$\begin{aligned} X^{nd} = -\frac{\partial \Psi}{\partial \chi} &= -\frac{1}{2}\frac{\partial E}{\partial \chi}\left(\varepsilon - \varepsilon^{ie}\right)^2 + E\left(\varepsilon - \varepsilon^{ie}\right)\frac{\partial \varepsilon^{ie}}{\partial \chi} - \gamma \\ &= -\frac{1}{2}\frac{\partial E}{\partial \chi}\frac{\sigma^2}{E^2} + \frac{\partial \varepsilon^{ie}}{\partial \chi}\sigma - \gamma \\ &= -\frac{1}{2}\exp\left[\frac{\beta}{T - T_0}\right] \frac{(E_1 - E_0) E_1 E_0}{\left(E_0 \chi + E_1 (1 - \chi)\right)^2} \left(\varepsilon - C_\alpha \exp\left[\frac{\alpha}{T - T_0}\right](1 - \chi)\right)^2 \\ &\quad - C_\alpha \exp\left[\frac{\alpha + \beta}{T - T_0}\right] \frac{1}{\dfrac{\chi}{E_1} + \dfrac{1-\chi}{E_0}} \left(\varepsilon - C_\alpha \exp\left[\frac{\alpha}{T - T_0}\right](1 - \chi)\right) - \gamma \end{aligned} \tag{9.9}$$

where $\gamma \in \partial I_{[0,1]}(\chi)$, with $\partial I_{[0,1]}(\chi)$ the subdifferential of the indicator function $I_{[0,1]}(\chi)$, taken in the sense of convex analysisis (Brézis, 1973):

$$\partial I_{[0,1]}(\chi) = \begin{cases} \gamma^0 \leq 0 & \text{if } \chi = 0 \\ 0 & \text{if } 0 < \chi < 1 \\ \gamma^1 \geq 0 & \text{if } \chi = 1 \end{cases} \tag{9.10}$$

We can associate to Eq. (9.10) the classical Kuhn-Tucker complementarity conditions, as follows:

$$\begin{cases} \chi \geq 0,\ \gamma^0 \leq 0,\ \gamma^0 \chi = 0 \\ (\chi - 1) \leq 0,\ \gamma^1 \geq 0,\ \gamma^1 (\chi - 1) = 0 \end{cases} \tag{9.11}$$

Evolution equations and limit functions

We define a limit function, $F = F\left(X^{nd}, T\right)$, playing the role of yield function (Lubliner, 1990), in the following form:

$$F = \left|X^{nd} + \frac{\eta}{2}\right| - \frac{\eta}{2} \tag{9.12}$$

where $\eta = \eta\left(T\right)$ is a sufficiently smooth function, governing the yield level of stress activating the phase transition, i.e., the orientation process:

$$\eta = C_\eta \exp\left[\frac{E_\eta}{T - T_0}\right] \tag{9.13}$$

being C_η and E_η positive material parameters.

Then, as traditionally done in the context of associative evolution, we assume the evolution equation of the internal variable, χ, as follows:

$$\dot{\chi} = \dot{\zeta}\frac{X^{nd} + \frac{\eta}{2}}{\left|X^{nd} + \frac{\eta}{2}\right|} \tag{9.14}$$

where $\dot{\zeta}$ is a non-negative consistency parameter.

The model is finally completed by the classical Kuhn-Tucker conditions, as follows:

$$\dot{\zeta} \geq 0;\ F \leq 0;\ \dot{\zeta}F = 0 \tag{9.15}$$

Dissipation function

Although the proposed model relies on an yield surface-based formulation, we complete the description by recalling that the yield surface condition can be equivalently converted in a pseudo-potential of dissipation, $\phi = \phi\left(\dot{\chi}, T\right)$, which is a positive convex functional depending on dissipative variables, vanishing for vanishing dissipation, in particular in the form:

$$\phi = \begin{cases} -\eta\dot{\chi} & \text{if } \ \dot{\chi} \leq 0 \\ 0 & \text{if } \ \dot{\chi} > 0 \end{cases} \tag{9.16}$$

We remark that, once defined the pseudo-potential of dissipation, ϕ, we can prescribe the constitutive relation for the internal force, X, responsible for the phase transition, as follows (Frémond, 2002, 2012; Gurtin et al., 2010):

$$X = X^{nd} + X^d = -\frac{\partial\Psi}{\partial\chi} - \frac{\partial\phi}{\partial\dot{\chi}} \tag{9.17}$$

Such a force is splitted into two contributions, i.e., a non-dissipative term, X^{nd}, and a dissipative term, X^d. The constitutive relation for the internal non-dissipative force, X^{nd}, is given in Eq. (9.9), while the constitutive relation for the dissipative force, X^d, is:

$$X^d = -\frac{\partial\phi}{\partial\dot{\chi}} = \begin{cases} -\eta & \text{if } \ \dot{\chi} \leq 0 \\ 0 & \text{if } \ \dot{\chi} > 0 \end{cases} \tag{9.18}$$

From the definition of X we can then derive the limit function introduced in Eq. (9.12). We note that such an approach, similar to that employed in shape memory alloy modeling, considers a translation of X^{nd} to allow phase transformation in the thermal retraction case, for which $X = 0$, i.e., $\sigma = 0$.

Therefore, the evolution of the phase, χ, depends on the internal force, X, which is included in the energy balance of the system. We get the following balance equation:

$$X = X^{nd} + X^{d} = 0 \tag{9.19}$$

after assuming that no micro-forces are applied to activate the orientation of polymer chains. From Eq. (9.19) we can derive the evolution equation (9.14) of the internal variable, χ.

9.4.2 Physical interpretation of model parameters

To introduce a physical interpretation of the model parameters, we consider the one-dimensional diagram of Figure 9.12, in terms of stress, σ, and strain, ε, where all the quantities of interests are reported.
In the following, we derive all the general equations and then we simplify such equations by assuming an unique Young's modulus, $E^* = E_1 = E_0$, to give a simple and practical interpretation of all the parameters. We recall, moreover, that model parameters are discussed by taking into account that the aim of the model is to reproduce experimental evidences.

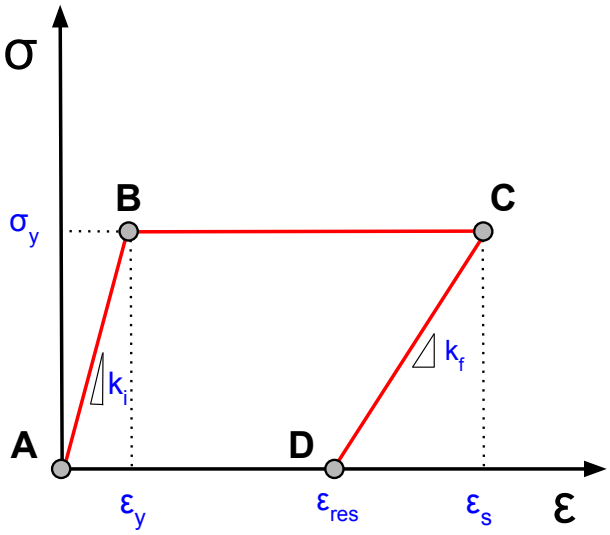

Figure 9.12: Identification of model parameters from a 1D diagram in terms of stress, σ, and strain, ε.

The material starts from the reference configuration at a given temperature and zero stress in the amorphous state, i.e., $\chi = 1$ (point A).

If a load is applied and then increased, material behavior is at first linearly elastic with slope, k_i, which increases with decreasing temperature, T, as follows:

$$k_i = \exp\left[\frac{\beta}{T - T_0}\right] E_1 \tag{9.20}$$

According to Eq. (9.12), the material stays in equilibrium for $\dot{\chi} = 0$ till $X^{nd} = -\eta$. Thus, with increasing load, when $X^{nd} = -\eta$, the strain reaches an yield value, ε_y (point B). After substituting Eq. (9.9) into Eq. (9.12), the yield strain, ε_y, is solution of the following equation:

$$\exp\left[\frac{\beta}{T - T_0}\right] \frac{(E_1 - E_0)\, E_1}{2E_0} \varepsilon_y^2 + C_\alpha \exp\left[\frac{\alpha + \beta}{T - T_0}\right] E_1 \varepsilon_y = C_\eta \exp\left[\frac{E_\eta}{T - T_0}\right] \tag{9.21}$$

The yield stress, σ_y, follows:

$$\sigma_y = E\varepsilon_y = \exp\left[\frac{\beta}{T - T_0}\right] E_1 \varepsilon_y \tag{9.22}$$

If we assume an unique Young's modulus E^*, the yield strain and stress result:

$$\begin{cases} \varepsilon_y = \dfrac{C_\eta}{C_\alpha}\dfrac{1}{E_1}\exp\left[\dfrac{E_\eta - \alpha - \beta}{T - T_0}\right] \\ \sigma_y = \dfrac{C_\eta}{C_\alpha}\exp\left[\dfrac{E_\eta - \alpha - \beta}{T - T_0}\right] \end{cases} \tag{9.23}$$

Since experimental evidences of Figures 9.4(a)-(d) show that the yield strain decreases with decreasing temperature and the yield stress increases with decreasing temperature, we derive the following constraints on model parameters from system of equations (9.23):

$$\begin{cases} E_\eta < \alpha + \beta \\ E_\eta > E_\alpha \end{cases} \tag{9.24}$$

If the load further increases, inelastic deformations start to develop at constant yield stress (no hardening is assumed) and the orientation process starts. Once reached the imposed level of load, the orientation process reaches a certain level of orientation (point C), where $\chi = \widehat{\chi}$ and $\varepsilon = \varepsilon_s$. In such a case, if the orientation process is completed, i.e., $\chi = \widehat{\chi} = 0$, the maximum transformation strain, ε_{max}, is reached at $\sigma = \sigma_y$ for $\chi = 0$, as follows:

$$\exp\left[\frac{\beta}{T - T_0}\right] E_1 \varepsilon_y = \exp\left[\frac{\beta}{T - T_0}\right] E_0 \left(\varepsilon_{max} - C_\alpha \exp\left[\frac{\alpha}{T - T_0}\right]\right) \tag{9.25}$$

If we assume an unique Young's modulus E^*, the maximum transformation strain, ε_{max}, becomes:

$$\varepsilon_{max} = \frac{C_\eta}{C_\alpha}\frac{1}{E_0}\exp\left[\frac{E_\eta - \alpha - \beta}{T - T_0}\right] + C_\alpha \exp\left[\frac{\alpha}{T - T_0}\right] \tag{9.26}$$

and increases with decreasing temperature, T, thus reproducing experimental evidences of Figures 9.4(a)-(d).

If we start to unload, we evolve in the region $\dot{\chi} = 0$. The slope upon unloading, k_f, follows:

$$k_f = \exp\left[\frac{\alpha}{T - T_0}\right] \frac{1}{\dfrac{\widehat{\chi}}{E_1} + \dfrac{1 - \widehat{\chi}}{E_0}} \tag{9.27}$$

and increases with decreasing temperature, T, and with increasing χ, as experimentally observed in Figures 9.4(a)-(d).

Upon unloading, i.e., when $\sigma = 0$ and thus $X^{nd} = 0$, a residual strain, ε_{res}, is present (point D), in the following form:

$$\varepsilon_{res} = C_\alpha \exp\left[\frac{\alpha}{T - T_0}\right](1 - \widehat{\chi}) \tag{9.28}$$

and increases with decreasing temperature, T, and χ. At such a point, we have $\dot{\chi} > 0$. This last remark justifies irreversibility of the retraction process at $\sigma = 0$.

If we start increasing temperature, at fixed $\varepsilon = \varepsilon_{res}$, we obtain, after assuming an unique Young's modulus E^*,:

$$\begin{cases} \sigma = E^* \exp\left[\dfrac{\beta}{T - T_0}\right]\left(\varepsilon_{res} - C_\alpha \exp\left[\dfrac{\alpha}{T - T_0}\right](1 - \widehat{\chi})\right) \\ X = -C_\alpha \exp\left[\dfrac{\alpha}{T - T_0}\right]\sigma \end{cases} \tag{9.29}$$

On the other hand, if we start increasing temperature at $\sigma = 0$ and no constraints on the material, the residual strain, ε_{res}, can be partially recovered. The two described cases are known as constrained and free thermal retraction tests, respectively.

9.4.3 A time-discrete model formulation

We now elaborate on a possible algorithmic treatment of model equations. For the sake of notation simplicity, the convention establishes superscript n for all the variables evaluated at time t_n, while drops superscript $n+1$ for all the variables computed at time t_{n+1}.

We start making use of a classical backward-Euler integration algorithm for the evolution equation (9.14). In this sense, the time-discretized evolution equation is given by:

$$\chi - \chi_n - \Delta\zeta \frac{X^{nd} + \dfrac{\eta}{2}}{\left| X^{nd} + \dfrac{\eta}{2} \right|} = 0 \tag{9.30}$$

where $\Delta\zeta = \int_{t_n}^{t_{n+1}} \dot{\zeta}$ is the time-integrated consistency parameter.

In the resulting model, since we deal with one phase fraction involving constraints, we adopt the approach based on the Fischer-Burmeister complementarity function, already applied to J_2 elastoplasticity in Chapter 4 and to shape memory alloys in Chapter 7. The discrete Kuhn-Tucker conditions deriving from Eq. (9.15) are so substituted by the following set of functions in the time-discrete frame:

$$\sqrt{F^2 + \Delta\zeta^2} + F - \Delta\zeta = 0 \tag{9.31}$$

The same strategy can be employed to treat the set of inequalities given by the constraint on χ. In fact, the additional Kuhn-Tucker conditions (9.11) can be substituted by the equivalent equalities:

$$\begin{cases} \sqrt{\chi^2 + (\gamma^0)^2} + \gamma^0 - \chi = 0 \\ \sqrt{(\chi - 1)^2 + (\gamma^1)^2} + (\chi - 1) - \gamma^1 = 0 \end{cases} \tag{9.32}$$

The time-discrete problem, $\mathbf{Q} = \mathbf{Q}(\varepsilon, \mathbf{h})$, evaluated at time t_{n+1}, takes the specific form:

$$\mathbf{Q} = \begin{bmatrix} \chi - \chi_n - \Delta\zeta \dfrac{X^{nd} + \dfrac{\eta}{2}}{\left| X^{nd} + \dfrac{\eta}{2} \right|} = 0 \\ \sqrt{F^2 + \Delta\zeta^2} + F - \Delta\zeta = 0 \\ \sqrt{\chi^2 + (\gamma^0)^2} + \gamma^0 - \chi = 0 \\ \sqrt{(\chi - 1)^2 + (\gamma^1)^2} + (\chi - 1) - \gamma^1 = 0 \end{bmatrix} = \mathbf{0} \tag{9.33}$$

with $\mathbf{h} = \left\{ \chi, \Delta\zeta, \gamma^0, \gamma^1 \right\}$. The active set can now be determined via the solution of the non-linear system of equations (9.33), using a classical Newton-Raphson method.

The FE implementation of model equations and of all the numerical examples presented in Section 9.5 is carried out using the symbolic code generation system AceGen/AceFEM (Korelc, 2009). The reader is referred to the Appendix B for further details about AceGen/AceFEM. Similarly to the 'flexible' model algorithm presented in Chapter 7, since the Fischer-Burmeister function is non-differentiable at $(0, 0)$, we make use of its smoothed countepart, by introducing δ as a positive regularization parameter (Kanzow, 1996).

9.5 Numerical investigation

In this Section we test the validity of the proposed model as well as its algorithm through some numerical simulations and comparisons with experimental results described in Section 9.3. The purpose is to emphasize model prediction capabilities through a qualitative and then quantitative validation with experimental data.

In all the numerical tests we adopt the material parameters reported in Table 9.2. Parameters are calibrated through a trial and error procedure on some experimental orientation curves of Figures 9.4(a) and 9.4(c), related to materials A and E, by starting from the physical interpretation given in Section 9.4.2.

Parameter	Unit	LDPE	HDPE
E_1	MPa	1.6	1.6
E_0	MPa	0.02	0.03
α	K	195	195
β	K	390	390
E_η	K	385	385
C_η	MPa	5.24117	15.72351
C_α	MPa	4	9.8
T_0	K	216	216

Table 9.2: Model parameters calibrated on experimental orientation curves of materials A and E.

9.5.1 Orientation test

We start by simulating the orientation tests on materials A and E, shown in Figures 9.4(a)-(d), as simple uniaxial tension tests, with displacement control and prescribed homogeneous constant temperature field. We first consider constant temperatures of 26, 30, 45, 60, 75 and 90 °C and maximum imposed deformation of 600%; then, we consider a constant temperature of 60 °C and imposed deformations of 10, 25, 50, 100, 200, 400 and 600%.
Figures 9.13(a)-(d) shows the comparison between predicted and experimental curves, in terms of stress, σ, and strain, ε. As it can be observed the model successfully predicts the experimental curves for both LDPE and HDPE polymers, thus demonstrating its flexibility in capturing the behavior of PE-based polymers with different densities. As expected, model quantities, k_i, k_f, σ_y, and ε_{res}, increase with decreasing temperature, while ε_y decreases (see Figure 9.14).

9.5.2 Constrained thermal retraction test

Due to evident difficulties in the simulation of the experimental constrained thermal retraction test, we make a qualitative interpretation of such a test for numerical purposes. In particular, we simulate the test as simple uniaxial tension test, with displacement control and prescribed homogeneous constant temperature field. Upon unloading, at zero stress, we fix the residual strain and we start increasing the temperature until a value above the melting temperature, T_m. Figures 9.15(a) and 9.15(b) show the qualitative model response for a specimen orientated at a temperature of 26 °C and maximum deformation of 600%. As shown in Figure 9.15(b), the stress starts from a zero value at 26 °C, reaches its maximum value and then decreases. As expected from Eq. (9.8), the stress stabilizes around an asymptotic value at temperatures above T_m.
To verify the irreversibility of the retraction process, we simulate a simple uniaxial tension test, with displacement control and prescribed homogeneous constant temperature field. Upon unloading, at zero stress, we fix the residual strain and we start lowering the temperature. Figures 9.15(c) and 9.15(d) show the results predicted by the model. In such a case, the specimen does not change its state.

Following this line, we simulate the experimental constrained thermal retraction tests on materials A and E for specimens oriented at a temperature of 30 °C and maximum deformation of 600%. Figure 9.16(a) shows the comparison between numerical and experimental results. As it can be observed, the predicted stress reaches its maximum value at a lower temperature than the experimental stress and then decreases.

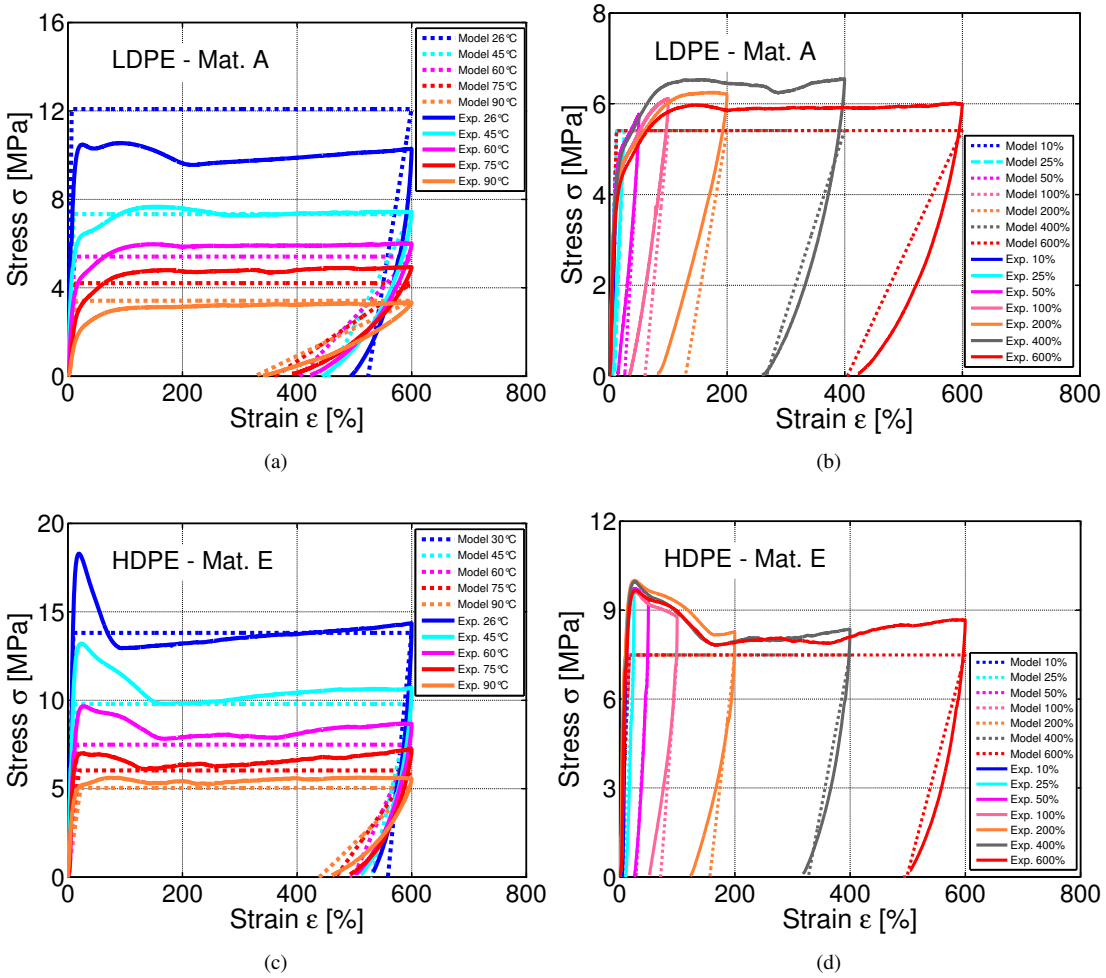

Figure 9.13: Model response for orientation tests. Comparisons with experimental data on materials A and E.

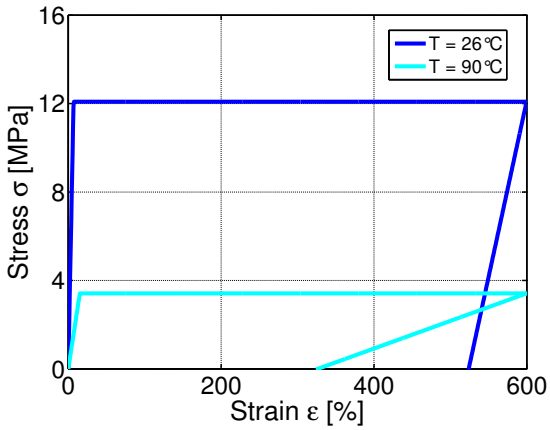

Figure 9.14: Qualitative model response for orientation tests at constant temperatures of 26 and 90 °C and maximum imposed strain of 600%.

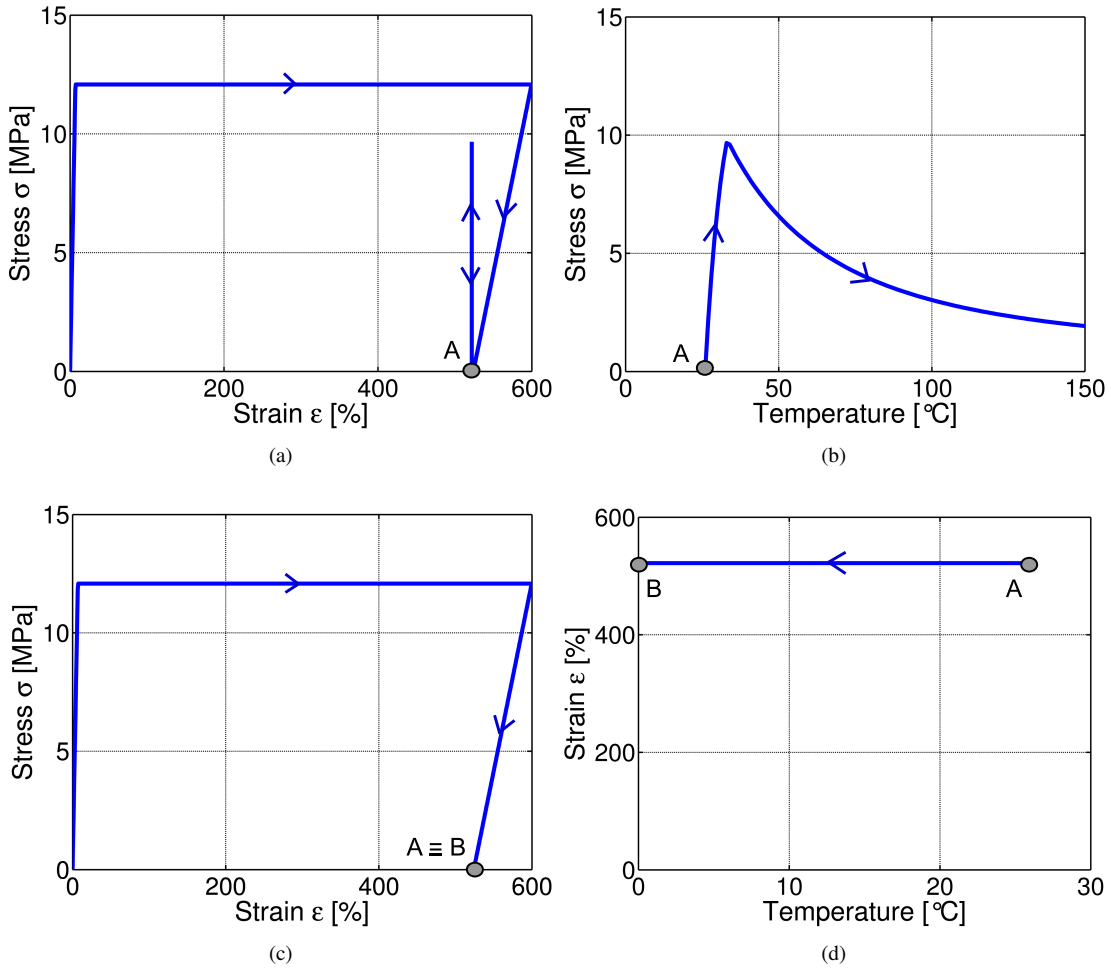

Figure 9.15: Constrained thermal retraction test. (a)-(b) Qualitative model response; (c)-(d) irreversibility of the retraction process during cooling.

The poor matching is due to the evident difficulties into simulating the experimental tests and to the use of true stresses in experimental curves. Moreover, discrepancies could be also attributed to the fact that no viscous effects are accounted by the proposed model.

9.5.3 Free thermal retraction test

Also in such a case, we make a similar qualitative interpretation of the test. We simulate such a test as simple uniaxial tension test, with displacement control and prescribed homogeneous constant temperature field. Upon unloading, at zero stress, we fix the stress and we start increasing the temperature until a value above the melting temperature, T_m. Figures 9.17(a)-(b) show the qualitative model response for a specimen orientated at a temperature of $26\,^{\circ}\mathrm{C}$ and maximum deformation of 600%. As shown in Figure 9.17(b), the strain starts from a residual value at $26\,^{\circ}\mathrm{C}$ and then decreases, i.e, a shape recovery takes place by heating.

Following this line, we simulate the experimental tests on materials A and E for specimens oriented at a temperature of $30\,^{\circ}\mathrm{C}$ and maximum deformation of 600%. Figure 9.16(b) shows the comparison. As it can be observed, the maximum value of the shrinkage is well predicted. However, the two curves present different concavities, due to the fact that no viscous effects are accounted by the proposed model.

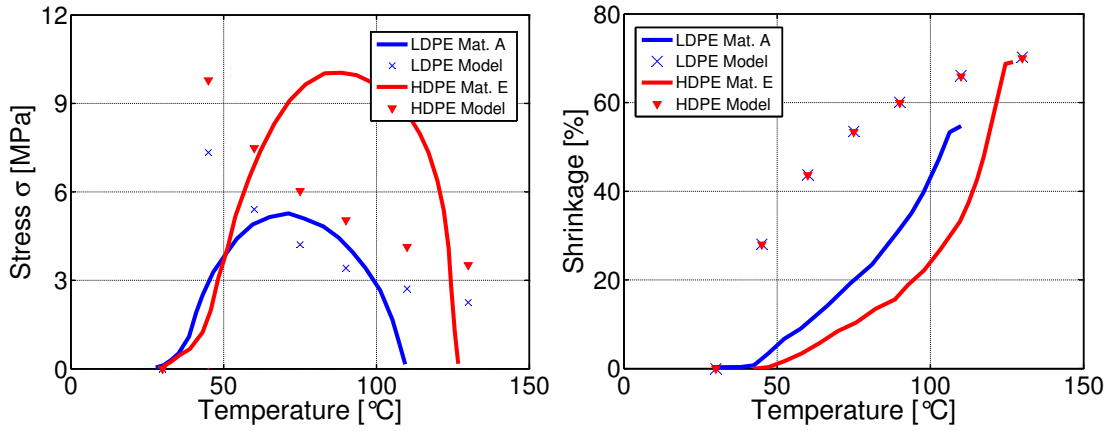

(a) (b)

Figure 9.16: Comparison between model response and experimental tests on materials A and E for (a) constrained and (b) free thermal retraction tests.

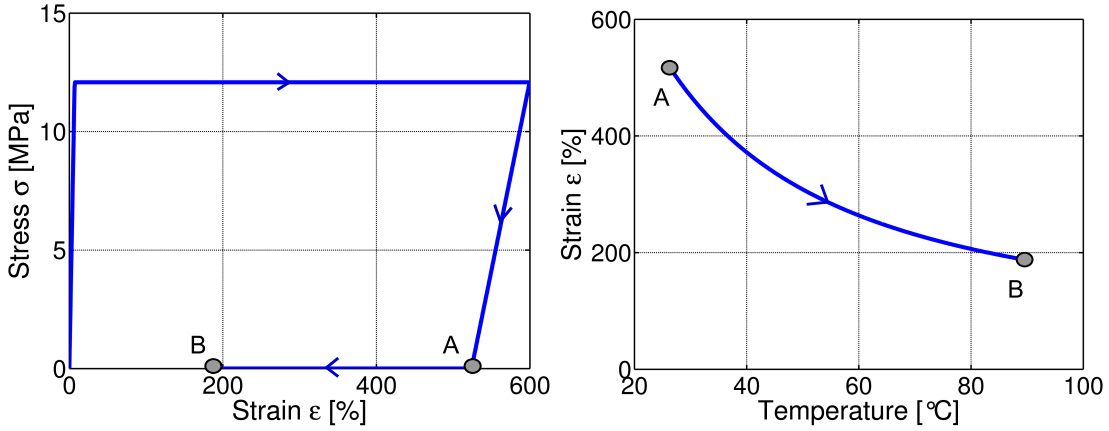

(a) (b)

Figure 9.17: Free thermal retraction test. (a)-(b) Qualitative model response.

9.6 Conclusions

The present Chapter has first presented the results of an experimental investigation on semi-crystalline SMPs by Pachera (2011); Talamazzi (2012). Experimental data have been analyzed to show the main features of material behavior, in particular related to material orientation and thermal retraction. Then, a simple new one-dimensional model has been introduced to predict the behavior of LDPE and HDPE polymers at temperatures below the melting temperature. The model has been demonstrated to be able to describe qualitative aspects of material behavior, involving both orientation and thermal retraction, as well as to predict experimental orientation processes for semi-crystalline PE-based polymers with different densities. In future works, the model can be extended to include viscous effects as well as material orientation at temperatures above the melting temperature and it can be expanded to a three-dimensional and finite strain framework to possibly simulate important industrial processes, e.g., packaging.

PART II
Fatigue modeling of elastoplastic and shape memory materials

Chapter 10

Introduction to fatigue of metals

Fatigue has been a problem for engineers since the earliest days of industrial revolution. This Chapter presents an overview on the fatigue problem in metals by recalling general concepts on the phenomenon, historical examples, and standard literature approaches.

The Chapter is organized as follows. Section 10.1 starts with the definition of fatigue. Section 10.2 presents a review on fatigue notation. Then, Sections 10.3 and 10.4 report the description of the historical background and of some historical accidents. Section 10.5 discusses the fatigue phenomenon as a mechanism occurring in metallic materials, first on a microscopic scale and later on a macroscopic scale. Then, Section 10.6 presents the standard classification of fatigue regimes, depending on the number of cycles to failure. Section 10.7 describes the shakedown concept at the macroscopic scale and Section 10.8 presents the global computational approach methodology usually adopted in the literature to treat fatigue problems. Finally, Section 10.9 concludes by recalling the fatigue criteria forms, usually adopted in the literature to evaluate the fatigue lifetime of a structure.

10.1 Definition of fatigue

The phenomenon of fatigue occurs when a material is subjected to cyclic loading and manifests itself as a localized and progressive degradation of the mechanical material properties, often leading to cracking or final breaking. Initially, fatigue is in fact a phenomenon localized at the scale of a material volume, for which the load-induced stresses are less than the ultimate tensile strength and often lower than the yield strength of the material.

Over the years, fatigue has been a widely accepted term in engineering field to describe damage and failure of materials under cyclic loading. In general, several common types of fatigue can be distinguished: mechanical, creep, thermo-mechanical, sliding, rolling, fretting, and corrosion fatigue (Schijve, 2009; Suresh, 1998). Fluctuations in applied stresses or strains result in *mechanical fatigue*; cyclic loading associated to high temperatures results in *creep fatigue*; combinations of cyclic loading and thermal high-low temperature fluctuations cause *thermo-mechanical fatigue*; repeated applications of load in conjunction with sliding and rolling contact between material surfaces produce *sliding* and *rolling contact fatigue*, respectively; pulsating stresses along with oscillatory relative motion and frictional sliding between surfaces result in *fretting fatigue*; fluctuating loads in the presence of corrosive environments cause *corrosion fatigue*.

10.2 Review on fatigue notation

This Section presents a brief review on fatigue notation.
Consider a structure subjected to an uniaxial stress cyclic loading with constant amplitude, as shown in Figure 10.1. We define the following parameters to characterize a given cyclic loading history:

- *stress range*, $\Delta\sigma$:

$$\Delta\sigma = \sigma_{max} - \sigma_{min} \tag{10.1}$$

- *stress amplitude*, σ_a:

$$\sigma_a = \frac{\Delta\sigma}{2} = \frac{\sigma_{max} - \sigma_{min}}{2} \tag{10.2}$$

- *mean stress*, σ_m:

$$\sigma_m = \frac{\sigma_{max} + \sigma_{min}}{2} \tag{10.3}$$

- *loading ratio*, R:

$$R = \frac{\sigma_{min}}{\sigma_{max}} \tag{10.4}$$

Therefore, we can distinguish between:

- *fluctuating loads*: both stresses, σ_{max} and σ_{min}, are strictly different from zero and have the same sign;
- *repeated loads*: one of the two stresses, σ_{max} or σ_{min}, is zero;
- *alternating loads*: both stresses, σ_{max} and σ_{min}, have different signs.

The listed notation is also valid in case of strain cyclic loading with constant amplitude.

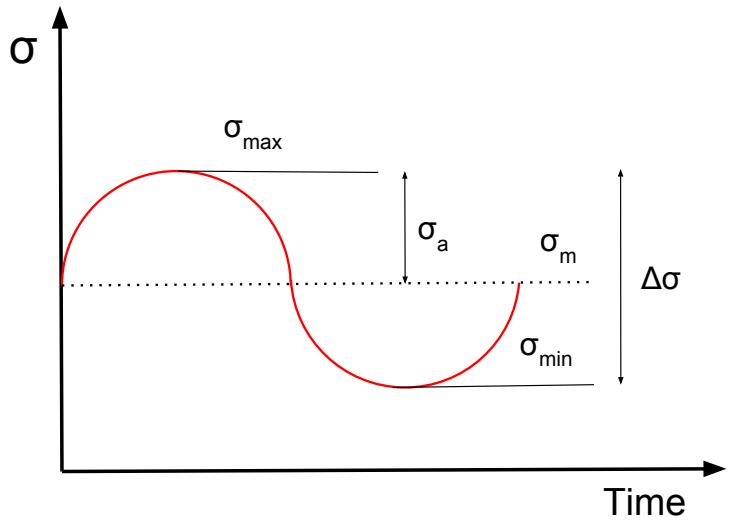

Figure 10.1: Review on fatigue notation for a structure subjected to an uniaxial stress cyclic loading.

10.3 Historical background

Fatigue has been a problem for engineers since the earliest days of industrial revolution.
The first study of metal fatigue was conducted by a German mining engineer, W.A.J. Albert, who performed repeated proof load tests on iron mine-hoist chains around 1829.

Since then, significant progress has been made in the study of fatigue (Schijve, 2009; Suresh, 1998). The first detailed research into fatigue was initiated in 1842, following the Versailles railway accident in France (Suresh, 1998). An early explanation for fatigue has been the crystallization theory, which postulates that the cause of fatigue failure in materials results from microstructural crystallization due to the very fine and smooth appearance of fatigue crack. This theory remained unchallenged for several decades until the work of Ewing and Humfrey (1903) showed the development of slip bands and subsequent fatigue cracks in polycrystalline materials (see Figure 10.2).

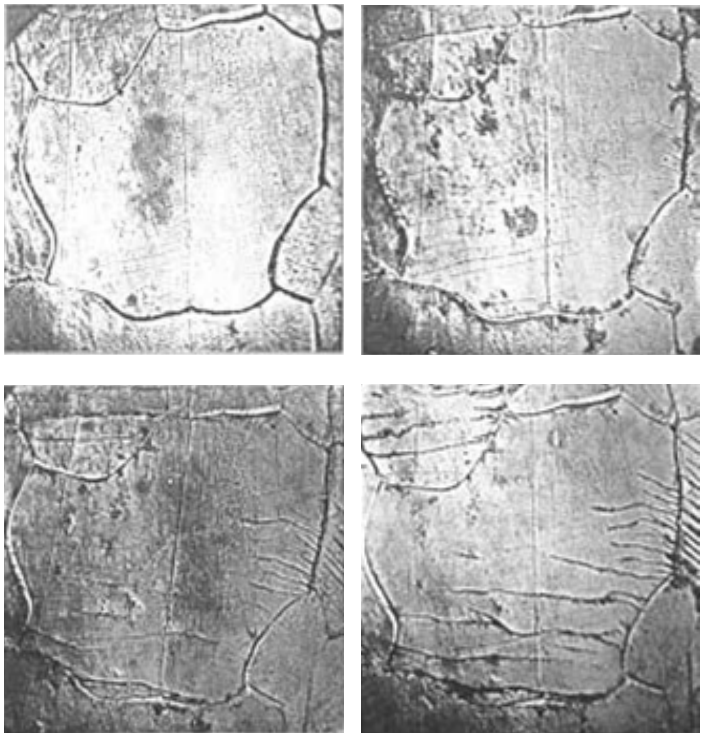

Figure 10.2: Micrographs showing how surface fatigue cracks grow as material is further cycled, taken from (Ewing and Humfrey, 1903).

Successive workers, e.g., (Thompson et al., 1956), used ductile polycrystals and sophisticated metallographic techniques and added details which, in general, confirmed the sequence of events described by Ewing and Humfrey (1903).

One of the earliest systematic investigations of fatigue failure, worked by Wöhler (1870) from 1852 to 1869, was a full scale fatigue testing in torsion, bend and axial loading of railway axles. Such a work contributed to the characterization of fatigue behavior in terms of stress amplitude-life curves (the so-called S-N curves) and also to the introduction of the concept of fatigue endurance limit. Some engineers in the second half of the nineteenth century, such as Gerber (1874) and Goodman (1899), began developing methods for fatigue design and formulated ways to account for mean stresses. Bauschinger (1886) first observed the differences in the elastic limit for materials subjected to reverse loading, and later, Bairstow (1910) investigated the changes in the stress-strain response during cycling and, subsequently, identified

cyclic softening and hardening behavior in metals.

Basquin (1910) first proposed equations for the characterization of S-N curves, later refined by Coffin (1953) for strain-based characterization of fatigue. Palmgren (1924) and Miner (1945) performed investigations into damage accumulation models for fatigue. Neuber (1946) studied the effects of notches on monotonic and cyclic deformation, while Langer (1937) pioneered the work in variable amplitude fatigue.

Paris et al. (1961) proposed a power law, known as *Paris law*, which characterized the crack propagation rate in terms of stress intensity factor amplitude. The next important contribution came when Elber (1970) showed that fatigue cracks could remain closed even when subjected to cyclic tensile loads (the so-called *crack closure effect*). Today, crack closure and its associated effects form the basis for any mechanistic study of fatigue crack propagation (Suresh, 1998).

Recently, significant interest in fatigue research has centered on short or small fatigue crack propagation. This problem was first identified by Pearson (1975), who observed that crack propagation rates for short cracks are higher than those observed for long cracks at the same stress intensity range. Crack propagation, even at stress intensity ranges below the threshold for long cracks has also been detected. Such anomalous behavior contradicts conventional linear elastic fracture mechanics theory and thus far, significant progress has been made in characterizing the types of short cracks and explaining this unique behavior (Suresh, 1998).

The past decade witnessed a confluence of high performance computing, advanced experimental methods for in-situ and ex-situ measurement of evolving microstructure at various length scales under cyclic loading, and substantial advances in understanding deformation mechanisms, material degradation, and relevant modeling concepts in fatigue. Together, these various elements introduced new possibilities to consider the role of the microstructure on the initiation and propagation of small cracks in fatigue. Microstructure-sensitive computational methods for fatigue crack formation in polycrystalline microstructures over the past few decades were developed rapidly (Barbe et al., 2001; Devincre et al., 2006; Forest et al., 2001; McDowell and Dunne, 2010; Saai et al., 2010; Schwartz et al., 2010). Such approaches can be pursued to explore effects of microstructure attributes that give rise to extreme value fatigue responses which are associated with the tails of probability distributions of potential surface and subsurface fatigue crack formation sites, including transitions between modes of crack formation, surface to subsurface transitions, and so forth.

10.4 Historical accidents

The phenomenon of fatigue strongly affects several industrial fields. In the following, we recall some noticeable accidents in both the mechanical and nuclear fields.

Versailles rail accident in 1842

The Versailles rail accident occurred on 8th May 1842 and was probably the starting point dedicated to the phenomenon of fatigue studies. During King Louis Philippe I's celebrations at the Palace of Versailles, a train returning to Paris derailed at Meudon, due to the rupture of an axle in the leading locomotive, and the carriages piled into it and caught fire. The French government appointed a commission to investigate such an accident, that recommended to test several axles to determine their service life and to monitor their usage so that they could be replaced after traveling a safe distance. Metal fatigue was poorly understood at the time and, consequently, the accident is linked to the beginnings of systematic research into the problem.

Comet aircraft accident in 1954

Around 1950, several Comet aircraft manufactured by Havilland failed at high altitude and crashed. To understand the origin of these failures attributed to the cabin, several tests were carried out on the ground

by pressurizing the cabin and by applying cyclic bending on the wings of the plane. After applying tests equivalent to 9000 hours of flight, the pressure inside the cabin dropped quickly and caused the propagation of cracks in the corner of a square window.

Nuclear Civaux accident in 1998

Rail and aviation are not the only industries affected by the phenomenon of fatigue. In May 1998, a leak of 30 m^3 per hour was detected in the stop circuit of the nuclear power plant at Civaux, at a mixing tee realized in 304L austenitic stainless steel. The leak was attributed to a crack caused by thermal fatigue phenomenon.

10.5 Fatigue as a phenomenon in the material

When a structure is subjected to a cyclic loading, a fatigue crack nucleus can be initiated on a microscopically small scale, followed by crack growth to a macroscopic size, and finally by the failure of the structure in the last cycle of the fatigue-life (Schijve, 2009). Thus, in the phenomenon of fatigue three different scales can be considered:

1. the *microscopic scale* of atoms, crystals and dislocations;

2. the *mesoscopic scale* of grains;

3. the *macroscopic scale* of the structure.

The present Section discusses the fatigue phenomenon as a mechanism occurring in metallic materials, first on a microscopic scale and later on a macroscopic scale. Understanding of the fatigue mechanism is essential for considering various technical conditions which affect fatigue-life and crack growth, such as the material surface quality, residual stress, and environmental influence, and, consequently, for the analysis of fatigue properties of an engineering structure.

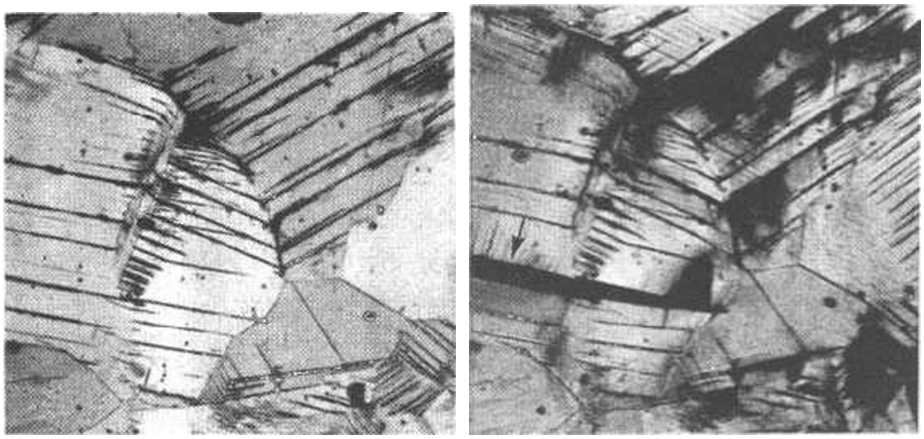

(a) (b)

Figure 10.3: Development of cyclic slip bands and microcrack in a pure copper specimen, taken from (Bullen et al., 1953). (a) Visible slip lines; (b) Plastically strained opening a microcrack.

10.5.1 Fatigue-life phases

Microscopic investigations in the beginning of the twentieth century showed that fatigue crack nuclei start as invisible microcracks in slip bands (Ewing and Humfrey, 1903), as shown in Figures 10.3(a) and 10.3(b). After more microscopic information on the growth of small cracks became available, it turned out that nucleation of microcracks generally occurs very early in the fatigue-life and that it may take place almost immediately if a cyclic stress above the fatigue limit is applied[1]. In spite of the early crack nucleation, microcracks remain invisible for a considerable part of the total fatigue-life, due to effects of the microstructure, e.g., grain boundaries. This micro-plasticity can occur more easily in grains at the material surface, that are less constrained than subsurface grains, because the surrounding material is present at one side only. However, after some micro-crack growth has occurred away from the nucleation site, a more regular growth is observed. This is the beginning of the real crack growth period. Once cracks become visible, the remaining fatigue-life of a laboratory specimen is usually a small percentage of the total life. The latter percentage may be much larger for real structures such as ships and aircraft (Schijve, 2009).

Figure 10.4 shows the various steps in the fatigue-life. In particular, the fatigue-life until failure consists of two periods: the *crack initiation period* and the *crack growth period*. Differentiating between the two periods is of great importance because several surface conditions affect the initiation period, but have a negligible influence on the crack growth period, e.g., surface roughness and corrosive environments. We can already note here that fatigue prediction methods are different for the two periods.

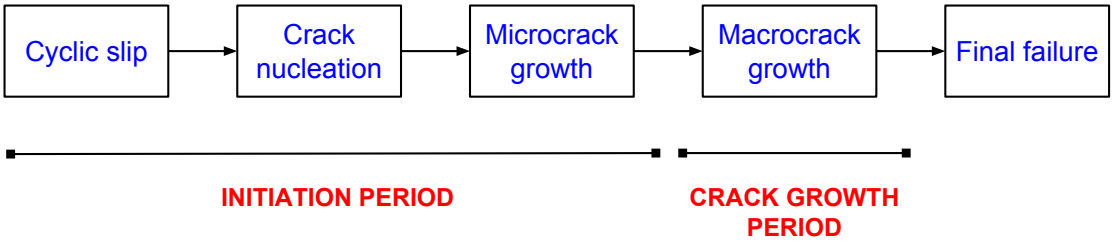

Figure 10.4: Different phases of the fatigue-life (Schijve, 2009).

The fatigue mechanism and design

By summarizing, the failure of a structure subjected to a cyclic loading is composed of the following steps: (i) initiation of microcracks and voids, i.e., micro-defects; (ii) propagation and coalescence of micro-defects; (iii) initiation of a macroscopic crack; (iv) propagation of the macroscopic crack; (v) failure of the structure.

From the structural point of view, we are essentially interested in the macroscopic initiation and propagation of cracks; from the design point of view, we often consider that the lifetime of the structure is defined by the initiation of a macroscopic crack. However, in cases where inspections occur during the functioning of the structure (e.g., aero-engines or electrical plants), we can also accept the existence of cracks in the structures, provided they do not propagate to a critical length in the period between inspections.

10.6 The fatigue regimes

The general terminology distinguishes between the two following fatigue regimes as depending on the applied loading level, i.e., on the number of cycles to failure:

[1] The fatigue limit is the cyclic stress level below which a fatigue failure does not occur.

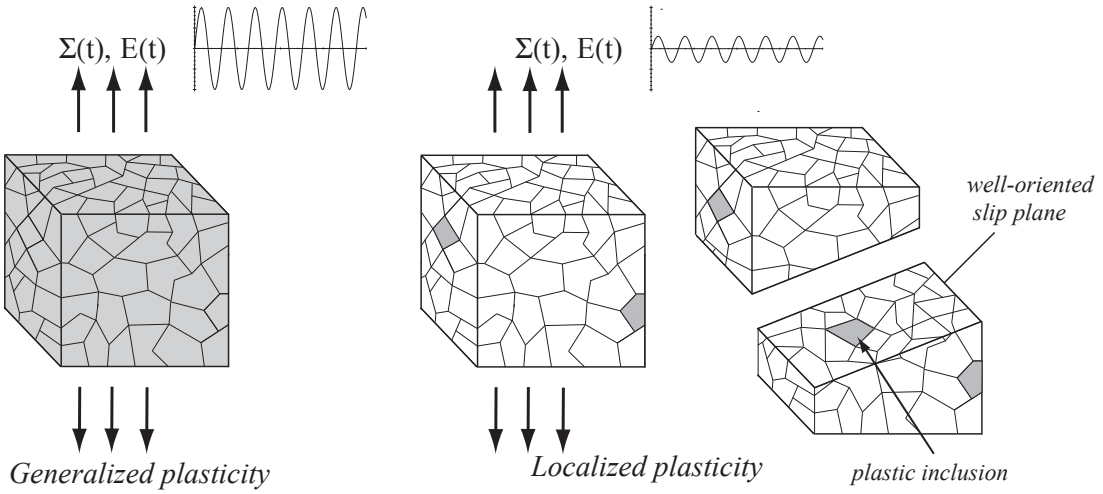

Figure 10.5: Representative elementary volume of material. Plasticity developed at the macroscopic scale in the LCF regime (left) and at the mesoscopic scale in the HCF regime (right), taken from (Charkaluk et al., 2009).

1. the *high-cycle fatigue* (HCF) or *polycyclic fatigue* regime, which is defined by a number of cycles to failure greater than 10^4. In general no irreversible deformation (plastic or viscous) is detected at the macroscopic level. Material behavior seems to be purely elastic, meaning that stresses and strains are related through linear relations. However, at a mesoscopic level, irreversible strains occur in a certain number of grains and generate a heterogeneous plastic strain field. Only misoriented crystals undergo plastic slip corresponding to a heterogeneous distribution of microcracks (see Figure 10.5 on the right). Within the HCF region, we can distinguish between two subdomains: the *infinite endurance* domain (HCF-IE) at small loads, where lifetime seems to be infinite, and the *finite endurance* domain (HCF-FE) at slightly higher loads, where lifetime is finite;

2. the *low-cycle fatigue* (LCF) or *oligocyclic fatigue* regime, which is defined by a number of cycles to failure less than 10^4. Significant macroscopic deformations conducting to irreversible deformations are detected. Stress and strain fields are generally related through highly non-linear differential equations. At the mesoscopic level, metal grains are subjected to plastic deformation in a more homogeneous manner than in the HCF regime (see Figure 10.5 on the left). The first cracks at a mesoscopic level appear in the persistent slip bands quite early in the lifetime of the structure. Within this region we generally distinguish three domains with increasing load: the *alternating plasticity* domain (LCF-P), the *ratchetting* domain (LCF-R) where failure occurs due to accumulation of plastic strain, and the *unrestricted plastic strain* domain (LCF-U).

Figure 10.6 shows the diagram in terms of the stress amplitude, σ_a, and the number of cycles to failure, N_f, where the Wöhler's or S-N curve is represented along with the listed fatigue regimes.

10.7 Cyclic behavior of an elastoplastic structure

Depending on the loading level, we can classify the asymptotic response of an elastoplastic structure subjected to cyclic mechanical loading, as follows:

- existence of a limit cycle in alternating elasticity (i.e., *elastic shakedown* in the HCF-IE and HCF-FE domains) or in alternating plasticity (i.e., *plastic shakedown* in the HCF-FE and LCF-P domains), as

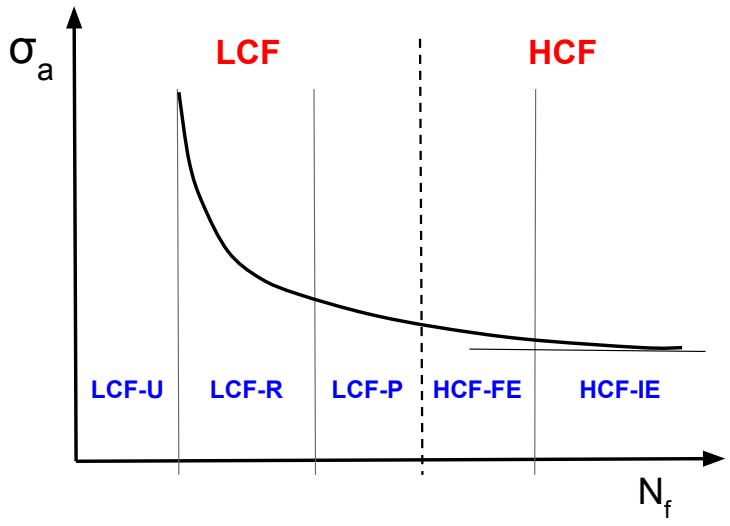

Figure 10.6: Schematic Wöhler curve and fatigue regimes.

shown in Figures 10.7(a) and 10.7(b);

- no limit cycle described generally as *ratchetting* (i.e., accumulation of plastic strain over all cycles in the LCF-R domain) or unrestricted plastic yield in the LCF-U domain, as shown in Figure 10.7(c).

Different theoretical studies have been performed to define the conditions for the occurrence of an asymptotic state in an elastoplastic structure subjected to cyclic mechanical loading. The works by Koiter (1960); Mandel et al. (1977); Melan (1936) give a theorem with sufficient conditions for the elastic shake-down of a perfect plastic material. Such conditions are path-independent and do not depend on the initial state of the structure. This work has been extended to other elastoplastic constitutive laws (Nguyen, 2003).

In addition to theoretical results, the asymptotic response of a structure subjected to cyclic loading can be also determined after a complete computation of a large number of cycles. However, the time required to determine the stabilized response of a structure subjected to cyclic mechanical loading can be prohibitive, due to the tens of cycles that have to be computed to reach the asymptotic state. The reduction of this computation time is of prime importance for industrial applications. To this aim, different approaches have been proposed in literature, mainly for elastoplastic constitutive laws.
The different methods proposed to reduce computation time aim at determining the asymptotic material state directly, without going through the whole loading history. Among these approaches, Peigney and Stolz (2003) proposed a method based on the optimal control theory. The asymptotic state is calculated as the solution of a minimization problem and the minimized function represents the elastic energy of a generalized stress field associated to the distance to periodicity (the function is equal to zero when the solution is periodic). Zarka et al. (1998) proposed a simplified method, which allows a direct computation of the stabilized cycle based on the introduction of a transformed parameter linked to both the local behavior and to the structural coupling. A direct cyclic method was developed by Maitournam et al. (2002), based on a method proposed by Akel and Nguyen (1989) and on the large time increment method developed by Boisse et al. (1990). Masud and Xia (2006) developed a variational multiscale method, which has been applied to shape memory alloys and leads to interesting gain of computation time. Another finite element method have been developed for elastoplasticity by Commend et al. (2004) employing the Petrov-Galerkin method.

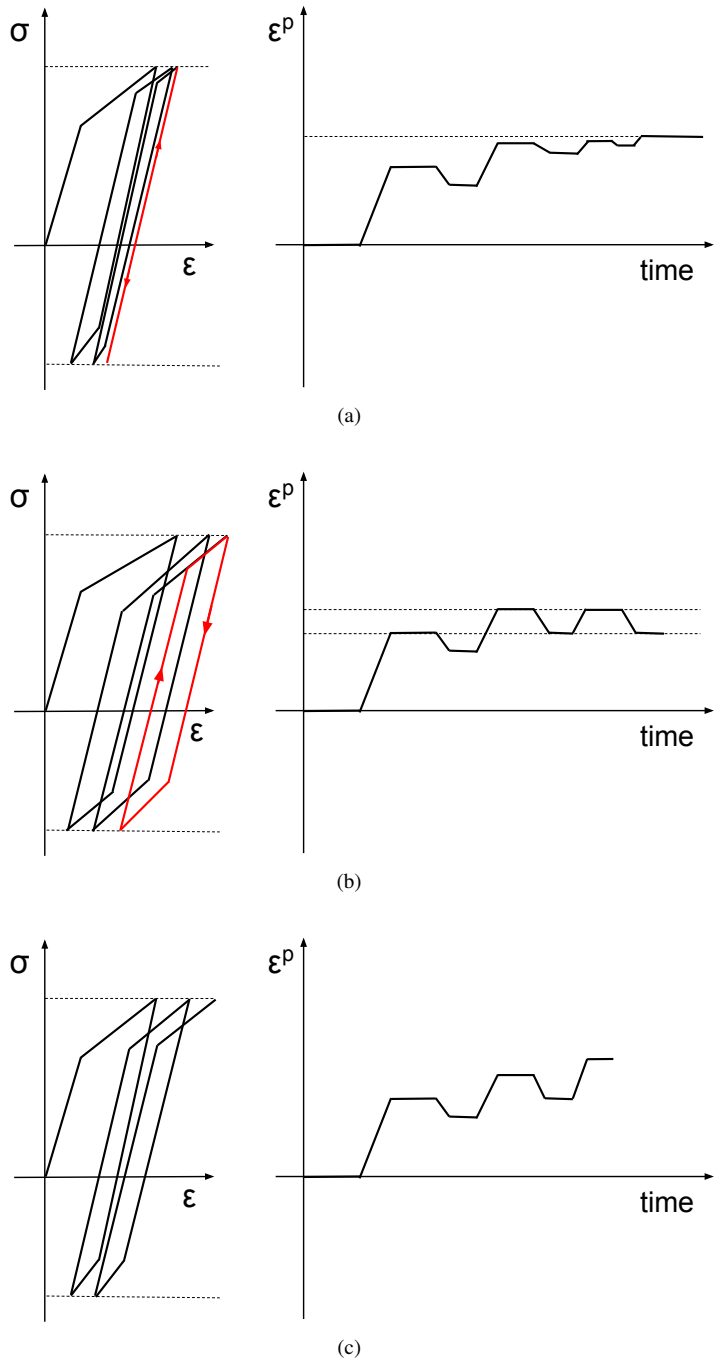

Figure 10.7: Cyclic behavior of an elastoplastic structure. (a) Elastic shakedown; (b) plastic shakedown; and (c) ratchetting.

10.8 The global computational approach

The methodology generally adopted in the literature to treat fatigue problems is based on the general philosophy of the *global computational approach*, consisting of the following two steps (Constantinescu et al., 2003):

i. a *mechanical analysis* to calculate the shakedown or stabilized mechanical state, by assuming the geometry of the structure, loading, and material constitutive law known. Such an analysis can be performed with different tools, such as the finite element method (Amiable et al., 2006) or analytical and semi-analytical solutions (Ferjani et al., 2011a,b). The mechanical behavior can be described by microscopic or macroscopic models. To keep the final objective of a global simple representation of material behavior at the structure scale, we restrict our choice to phenomenological macroscopic models, in the following;

ii. a *fatigue analysis* to compute the number of cycles before failure, e.g., the macroscopic crack initiation, through the introduction of appropriate fatigue criteria (see Section 10.9). Such an analysis assumes the existence of a stabilized cycle, i.e., elastic or plastic shakedown, and the possibility of computing such a cycle through the mechanical analysis. Fatigue damage parameters are in fact evaluated at this cycle.

We remark that the main assumption of the global computational approach is the uncoupling between material behavior and damage. This is a consequence of the assumption on cyclic material behavior, which is considered stabilized for most of the lifetime; therefore, the evolution of damage parameters can be neglected in the constitutive law and consequently in the structural computation. On the contrary, Lemaitre and Chaboche (1994) proposed interesting constitutive laws coupled with damage for continuum mechanics. In the following, we accept such the uncoupling hypothesis to be able to compute three-dimensional structures in a reasonable amount of time.

10.9 General forms of fatigue criteria

The lifetime of a structure can be generally evaluated through the following two forms of fatigue criteria:

1. a *parametric form*, with the classical fatigue criteria expressed as:

$$\Phi\left(\boldsymbol{\varepsilon}, \boldsymbol{\varepsilon}^p, \boldsymbol{\sigma}, ...\right) = N_f \tag{10.5}$$

   where Φ denotes the criterion function depending on both the mechanical state of the point under consideration and material parameters, and the set $(\boldsymbol{\varepsilon}, \boldsymbol{\varepsilon}^p, \boldsymbol{\sigma}, ...)$ represents the values of the mechanical field during a complete stabilized cycle. In the case of infinite lifetime, the form becomes:

$$\Phi\left(\boldsymbol{\varepsilon}, \boldsymbol{\varepsilon}^p, \boldsymbol{\sigma}, ...\right) \leq 0 \tag{10.6}$$

   We remark that an underlying hypothesis is the existence of a stabilized cycle and that the life estimation is done on such a limit cycle. Within this framework, stress-, strain-, and energy-based approaches can be used (Schijve, 2009). We can cite, for instance, for the LCF regime, the works by Coffin (1953); Ellyin (1989); Manson (1953) and, for the HCF regime, by Crossland (1956); Dang Van (1999); Papadopoulos (2001); Sines (1959);

2. an *evolutionary form* to track the complete evolution of damage. The evolution of the damage parameter set, $\mathbf{d}$, is described as a system of ordinary differential equations, as follows:

$$\dot{\mathbf{d}} = \Phi\left(\mathbf{d}, \boldsymbol{\varepsilon}, \boldsymbol{\varepsilon}^p, \boldsymbol{\sigma}\right) \tag{10.7}$$

   Such an approach stems from the pioneering works of Kachanov (1986); Rabothov (1969) and it has been later developed by Lemaitre and Desmorat (2005).

Compared to the parametric approach, the evolutionary form of fatigue criteria hides a series of difficulties related to the definition of the damage parameters, which is correlated with micromechanical mechanism and conducts to a large number of variables, to the necessity of a complex function, Φ, as well as to a large number of parameters. For such reasons, the present thesis focuses on the parametric form of the fatigue criteria for the design of structures.

Chapter 11

Polycyclic fatigue of metals

This Chapter presents an overview on the state of art in polycylic or high-cycle fatigue of metals, which can be defined by a number of cycles to failure greater than 10^4. Such an overview allows to prepare the framework for the treatment of the fatigue-life assessment of cardiovascular stents treated in next Chapters.

The Chapter is organized as follows. Sections 11.1 and 11.2 focus on both the empirical and semi-empirical approaches to fatigue by recalling some uniaxial and multiaxial criteria. Then, Section 11.3 concludes with the description of the multiscale approach to fatigue, by focusing on the criterion by Dang Van (1973).

11.1 Empirical approach to fatigue

The empirical approach to fatigue is based on simple conventional tests, e.g., uniaxial tests at room temperature. Such a classical approach allows to define different phases of the fatigue-life of the tested material. This Section presents some well-known uniaxial and multiaxial stress-based criteria, particularly suited in the high-cycle fatigue regime.

11.1.1 Uniaxial fatigue criteria

Uniaxial stress loading paths are commonly used in simple experiments and are therefore easily explored. Standard proportional stress loading paths are expressed in the following form:

$$\boldsymbol{\sigma}(t) = \begin{pmatrix} \sigma_m + \sigma_a \sin(t) & 0 & 0 \\ 0 & 0 & 0 \\ 0 & 0 & 0 \end{pmatrix} \tag{11.1}$$

$$\boldsymbol{\sigma}(t) = \begin{pmatrix} 0 & \tau_m + \tau_a \sin(t) & 0 \\ \tau_m + \tau_a \sin(t) & 0 & 0 \\ 0 & 0 & 0 \end{pmatrix} \tag{11.2}$$

In the following, we list some classical uniaxial fatigue criteria developed from traction-compression fatigue experiments. We remark that such criteria are very restrictive, since obtained from uniaxial traction-compression tests.

The diagram by Wöhler (1870)

As we have already stated in Chapter 10, the work by Wöhler (1870) represents the result of the first systematic studies on the phenomenon of fatigue. Wöhler recognized, in fact, that a single load application,

below the static strength of a structure, does not damage the structure itself; however, if the same load is repeated many times, it could induce a complete failure of the structure.

Starting from such considerations, we consider a structure submitted to a cyclic loading with stress amplitude, σ_a, and we record the lifetime as the number of cycles to failure, N_f, for each loading amplitude. The experimental points can be represented in a stress amplitude versus number of cycles to failure diagram and the obtained curve is known as *Wöhler* or *S-N curve* (see Figure 11.1).

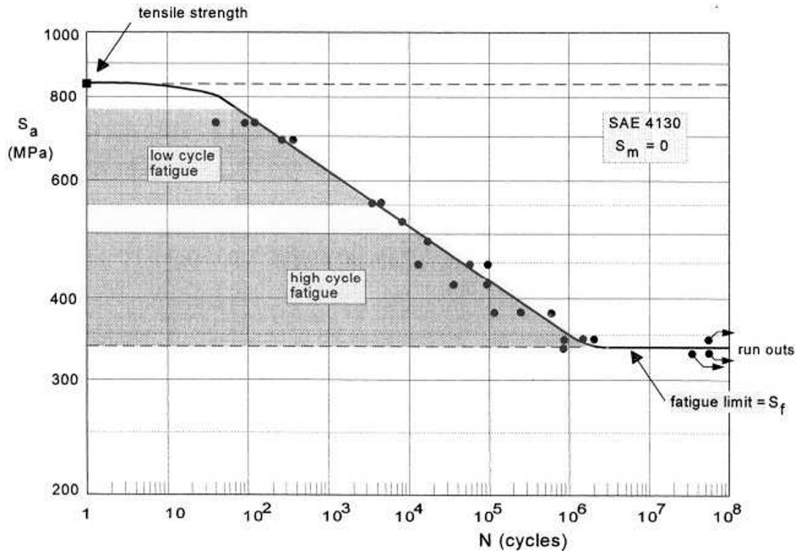

Figure 11.1: Fatigue test data on smooth specimens of a low alloy steel (SAE 4130) in the Wöhler diagram, taken from (Grover et al., 1951).

To connect the stress amplitude, σ_a, to the number of cycles to failure, N_f, several functions have been proposed. As an example, we may mention the relation by Basquin (1910), expressed in the following form:

$$\sigma_a = \sigma_f^{'} \left(2N_f\right)^b \tag{11.3}$$

where $\sigma_f^{'}$ is the fatigue strength coefficient and b the fatigue strength or Basquin's exponent.

The diagram by Haigh (1917)

Another common way to represent experimental points is to plot the stress amplitude, σ_a, versus the mean stress, σ_m, as shown in Figure 11.2. The obtained diagram is known as *Haigh* or *constant-life diagram* (Haigh, 1917).

Several fatigue criteria have been proposed to be plotted in such a diagram. Among the others, we can cite the following criteria, whose representations are shown in Figure 11.2:

- *Goodman line (1899)*:

$$\frac{\sigma_a}{\sigma_{-1}} + \frac{\sigma_m}{\sigma_u} \leq 1 \tag{11.4}$$

  where σ_u is the ultimate tensile stress and σ_{-1} the fatigue limit for fully reversed loading.

- *Soderberg line (1939)*:

$$\frac{\sigma_a}{\sigma_{-1}} + \frac{\sigma_m}{\sigma_y} \leq 1 \tag{11.5}$$

  where σ_y is the yield stress.

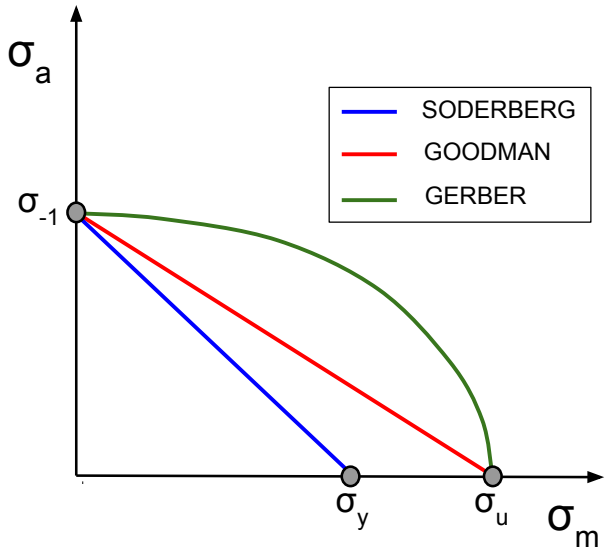

Figure 11.2: A comparison between uniaxial fatigue criteria in the Haigh diagram.

- *Gerber parabola (1874)*:

$$\frac{\sigma_a}{\sigma_{-1}} + \left(\frac{\sigma_m}{\sigma_u}\right)^2 \leq 1 \tag{11.6}$$

From Figure 11.2 we note that the lines by Goodman (1899) and Soderberg (1939) strongly reduce the fatigue domain compared to the parabola by Gerber (1874). The relationship by Gerber (1874) is interesting in the case of positive mean stresses, i.e., in traction; however, it does not reflect material behavior in the case of negative mean stresses, i.e., in compression.

11.1.2 Multiaxial fatigue criteria

Complex multiaxial stress loading paths have also been explored and analyzed in the literature. However, such paths involve a large number of parameters, thus implying that a large number of experiments have to be explored to asses the fatigue laws.
In the following, we shortly present some criteria established in the literature. It is important to notice that the range of validity includes only loading systems similar to the tested ones.

Formula by Hohenemser and Prager (1933)

Hohenemser and Prager (1933) studied the influence of a static traction state superposed on an alternated traction. The stress path is expressed in the following form:

$$\boldsymbol{\sigma}(t) = \begin{pmatrix} \sigma_m & 0 & 0 \\ 0 & 0 & 0 \\ 0 & 0 & 0 \end{pmatrix} + \begin{pmatrix} 0 & \tau_a & 0 \\ \tau_a & 0 & 0 \\ 0 & 0 & 0 \end{pmatrix} \sin(t) \tag{11.7}$$

For the studied metal, the authors noticed an important influence of the value of the static traction test on the endurance limit of the metal. They concluded by proposing the following criterion:

$$\frac{\tau_a^2}{\tau_{-1}^2} + \frac{\sigma_m}{\sigma_u} \leq 1 \tag{11.8}$$

where τ_{-1} is the endurance limit in alternated torsion.

Criterion by Gough and Pollard (1935)

The criterion by Gough and Pollard (1935) is the first systematic analysis of fatigue tests in order to construct a fatigue criterion. Their work covers a large database of alternating bending-torsion stress paths, expressed in the following form:

$$\boldsymbol{\sigma}(t) = \begin{pmatrix} \sigma_a & \tau_a & 0 \\ \tau_a & 0 & 0 \\ 0 & 0 & 0 \end{pmatrix} \sin(t) \tag{11.9}$$

Gough and Pollard (1935) tested several metals, splitted in two different classes, i.e., ductile and brittle metals; then, for each class, the authors proposed a different infinite endurance curve.

Later, the authors completed the initial work in collaboration with Gough et al. (1951), with stress paths in the following form:

$$\boldsymbol{\sigma}(t) = \begin{pmatrix} \sigma_m & \tau_m & 0 \\ \tau_m & 0 & 0 \\ 0 & 0 & 0 \end{pmatrix} + \begin{pmatrix} \sigma_a & \tau_a & 0 \\ \tau_a & 0 & 0 \\ 0 & 0 & 0 \end{pmatrix} \sin(t) \tag{11.10}$$

such that $\sigma_m/\sigma_a = \tau_m/\tau_a$.

For ductile metals, the authors described the infinite endurance curve as follows:

$$\frac{\tau_a^2}{\tau_{-1}^2} + \frac{\sigma_a^2}{\sigma_{-1}^2} \leq 1 \tag{11.11}$$

while for brittle metals as:

$$\frac{\tau_a^2}{\tau_{-1}^2} + \left(\frac{\sigma_{-1}}{\tau_{-1}} - 1\right)\frac{\sigma_a^2}{\sigma_{-1}^2} + \left(2 - \frac{\sigma_{-1}}{\tau_{-1}}\right)\frac{\sigma_a}{\sigma_{-1}} \leq 1 \tag{11.12}$$

Formula by Davies (1935)

Davies (1935) tested a relative small number of specimens in combined bending-torsion experiments, precisely, in an alternating bending stress state superimposed on a static torsion state. The non-proportional stress path can be expressed as follows:

$$\boldsymbol{\sigma}(t) = \begin{pmatrix} 0 & \tau_m & 0 \\ \tau_m & 0 & 0 \\ 0 & 0 & 0 \end{pmatrix} + \begin{pmatrix} \sigma_a & 0 & 0 \\ 0 & 0 & 0 \\ 0 & 0 & 0 \end{pmatrix} \sin(t) \tag{11.13}$$

Then, Davies (1935) proposed the following relation as endurance limit:

$$\frac{\sigma_a^2}{\sigma_{-1}^2} + \frac{\tau_m}{\tau_u} \leq 1 \tag{11.14}$$

where τ_u is the ultimate stress in a monotonic torsion test. We remark that the conclusions by Davies (1935) are in contradiction with the formulas proposed by Gough and Pollard (1935).

Criterion by Nishihara and Kawamoto (1945)

After exploring the endurance limit on nine different steels, Nishihara and Kawamoto (1945) proposed two empirical fatigue criteria, depending on the value of the ratio (σ_{-1}/τ_{-1}):

- for $(\sigma_{-1}/\tau_{-1}) \geq \sqrt{3}$, the authors recovered the ellipse proposed by Gough and Pollard (1935);
- for $(\sigma_{-1}/\tau_{-1}) \leq \sqrt{3}$, the authors proposed the criterion:

$$\frac{\tau_a^2}{\tau_{-1}^2} + \frac{1}{2}\left(3 - \frac{\sigma_{-1}^2}{\tau_{-1}^2}\right)\frac{\sigma_a}{\sigma_{-1}} + \frac{1}{2}\left(1 - \frac{\sigma_{-1}^2}{\tau_{-1}^2}\right)\frac{\sigma_a^2}{\sigma_{-1}^2} \leq 1 \tag{11.15}$$

11.2 Semi-empirical approach to fatigue

Since it was difficult to experimentally explore all the possible stress loading paths, it appeared the necessity to assume a basic physical phenomenon associated to fatigue, in order to successfully formulate a series of criteria for a large number of stress paths and materials.

Most of such criteria are based on physical observations of the first propagation stage of a fatigue crack[1]. Since in the first propagation stage the crack evolves in a slip plane, many authors naturally concluded that the mechanical parameter governing crack initiation is the shear stress on the corresponding slip plane and they accepted that the normal stress has also influence on the crack initiation stage, since such a stress component has a crack opening or closing role. As a consequence, the parameter determining the endurance limit was assumed to be a combination between the shear and normal stress components on a given slip plane. The fatigue criterion can be expressed as follows:

$$\Phi\left(\mathbf{n}, C, N\right) \leq 0 \tag{11.16}$$

where C and N are the shear and normal stress components on the slip plane of unit normal, $\mathbf{n}$, respectively.

Several criteria have been proposed along this line, which differentiate in the definition of the stress measure (e.g., in terms of stress components, C and N, or in terms of equivalent shear, C_{eq}, and hydrostatic pressure, P) and in the choice of the critical plane of unit normal, $\mathbf{n}$, representing the plane of the fatigue crack propagation in the first stage[2].
In the following, we mention some of the most famous criteria.

11.2.1 Criterion by Findley (1957)

After exploring a large number of testing configurations, Findley (1957) proposed the following criterion:

$$C_a\left(\mathbf{n}^*\right) + aN_{max}\left(\mathbf{n}^*\right) \leq b \tag{11.17}$$

where a and b denote material parameters. The critical plane, Π^*, with unit normal, $\mathbf{n}^*$, is defined by the following minimum:

$$\mathbf{n}^* = \text{argmin}_{\mathbf{n}}\left[C_a\left(\mathbf{n}\right) + aN_{max}\left(\mathbf{n}\right)\right] \tag{11.18}$$

Such a formula is the best compromise between a simple theoretical concept and experimental results from bending-torsion tests and it can be applied for all the loading paths. However, due to its computation complexity, Findley himself only applied the criterion to radial bending-torsion loading paths.

11.2.2 Criterion by Crossland (1956)

Crossland (1956) derived a criterion from an important series of experiments on En25T steel (in british denomination). In particular, Crossland (1956) proposed a linear combination between the amplitude of equivalent shear, T_a, and the maximal hydrostatic pressure, P_{max}, during the cycle, as fatigue parameter:

$$T_a + aP_{max} \leq b \tag{11.19}$$

where material constants, a and b, can be identified from reversed torsion and bending experiments. The criterion matches well the general trends of the observations in a large range of materials and it is a good compromise between criteria complexity and experimental results.

[1] The first propagation stage of a fatigue crack is defined as the initial propagation of a crack in a polycrystalline metal on a slip plane in the interior of a metal grain (Schijve, 2009).

[2] The critical slip plane is in general different from the plane of maximal equivalent shear strain or stress.

11.2.3 Criterion by Sines (1959)

The criterion proposed by Sines (1959) is one of the most used fatigue criteria for practical purposes. The fatigue parameter is similar to that proposed by Crossland (1956), but the maximal hydrostatic pressure is replaced by the mean hydrostatic pressure, P_m, as follows:

$$T_a + aP_m \leq b \tag{11.20}$$

where material constants, a and b, can be identified from reversed torsion and bending experiments. However, Sines discouraged the application of his fatigue criterion to brittle materials.

11.3 Multiscale approach to fatigue

All the above high-cycle fatigue criteria define the endurance limit as a function of macroscopic quantities, i.e., quantities computed at the structure scale. Consequently, such criteria do not take into account physical phenomena inducing fatigue, as observed at the grain scale. In order to represent such phenomena, it is necessary to adopt a *multiscale approach* to fatigue. The first application of such a passage to fatigue is attributed to Dang Van (1973). Later, such a proposal has been extended by Dang Van et al. (1989) and Papadopoulos (1987, 2001), who proposed a similar criterion using quantities which are more easily computed.

11.3.1 Meso-macro passage

The multiscale approach to fatigue considers two scales: (i) a *macroscopic scale*, characterized by an arbitrary elementary volume surrounding the point where fatigue analysis is made and representing, for instance, an element of the finite element mesh (the usual scale considered by engineers); (ii) a *mesoscopic scale*, corresponding to a subdivision of the previous volume (see Figure 11.3).

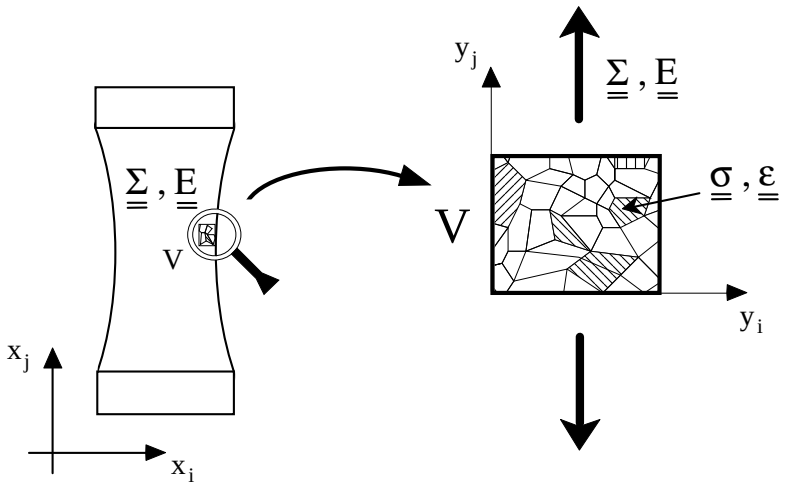

Figure 11.3: Macroscopic and local scales of material description, taken from (Dang Van et al., 2003).

The dependence of the mesoscopic quantities (e.g., stress $\boldsymbol{\sigma}$, strain $\boldsymbol{\varepsilon}$, plastic strain $\boldsymbol{\varepsilon}^p$) on the macroscopic ones (e.g., stress $\boldsymbol{\Sigma}$, strain $\boldsymbol{E}$, plastic strain $\boldsymbol{E}^p$) is complex and exact relations can be found, for instance, in (Bui et al., 1981); intuitively macroscopic quantities are approximately the mean value of the mesoscopic ones. Therefore, the macroscopic field is supposed constant in a small volume, surrounding the point under consideration. In the theories of polycrystalline aggregates, such a volume is called representative volume element (RVE).

As an example, the mesoscopic stress, $\boldsymbol{\sigma}$, and the macroscopic stress, $\boldsymbol{\Sigma}$, are related by the following (exact) formula:

$$\boldsymbol{\sigma} = \mathbf{A}\boldsymbol{\Sigma} + \boldsymbol{\rho} \tag{11.21}$$

where $\boldsymbol{\rho}$ is the local residual stress and $\mathbf{A}$ is the elastic stress localization tensor, corresponding to the identity tensor if the local and the macroscopic elastic moduli are similar. All the variables of Eq. (11.21) depend of time, t, except when the asymptotic cyclic state is purely elastic. In order to derive a unified theory of fatigue, Dang Van (1973) supposed that elastic shakedown occurs at the microstructure level as well as at the macroscopic one, as explained in the following.

Relation (11.21) shows that $\boldsymbol{\Sigma}$ is not adequate for characterizing phenomena which occur at the grain scale since the local stress, $\boldsymbol{\sigma}$, in the grain is not proportional to $\boldsymbol{\Sigma}$. The additive term, $\boldsymbol{\rho}$, function of the plastic strain, is closely related to the loading path. Therefore, fatigue criteria using maximum stress (or some combination of maximum stress) are only valid for the loading paths for which they are derived by correlating experimental results. They should be extended to take account of multiaxial loadings, and as a consequence their use for practical design is difficult, and sometime non-conservative. However, this way to proceed is very often used even if not theoretically valid.

To illustrate relation (11.21), we consider the Lin-Taylor model which supposes that the total macroscopic and mesoscopic strains are equal, i.e., $\boldsymbol{E} = \boldsymbol{\varepsilon}$ (Lin, 1957). Thus, $\boldsymbol{E}^p + \boldsymbol{E}^e = \boldsymbol{\varepsilon}^p + \boldsymbol{\varepsilon}^e$. If $\mathbf{l}$ and $\mathbf{L}$ are respectively the mesoscopic and the macroscopic compliance tensors of the material, we obtain:

$$\boldsymbol{\sigma} = \mathbf{l}\mathbf{L}^{-1}\boldsymbol{\Sigma} + \mathbf{l}\left(\boldsymbol{E}^p - \boldsymbol{\varepsilon}^p\right) \tag{11.22}$$

where $\mathbf{l}\mathbf{L}^{-1}$ corresponds to the localization tensor, $\mathbf{A}$, which is equal to the identity tensor if $\mathbf{l} = \mathbf{L}$, as assumed in the following. The term, $\mathbf{l}\left(\boldsymbol{E}^p - \boldsymbol{\varepsilon}^p\right)$, corresponds to the local residual stress, $\boldsymbol{\rho}$, characterizing the difference between the local stress, $\boldsymbol{\sigma}$, and the mean stress, $\boldsymbol{\Sigma}$, in the REV. Thus, $\boldsymbol{\rho}$ is due to the heterogeneity of plastic strain, difference between the local plastic strain, $\boldsymbol{\varepsilon}^p$, and its mean value, $\boldsymbol{E}^p$. In particular, $\boldsymbol{\rho}$ decreases if this difference diminishes and the gap between mesoscopic and macroscopic parameters vanishes, i.e., in situations when plastic deformation is important.

The evaluation of the local mesoscopic fields from the macroscopic ones is in general a difficult task, because the material is locally heterogeneous and has to be considered as a structure when submitted to complex loading histories. Depending on the loading characteristics, we can accept reasonable simplifying assumptions which will permit a solution to the problem.

11.3.2 The criterion by Dang Van (1973) and Dang Van et al. (1989)

The classical Dang Van criterion allows to define the limit of the imposed external loads under which the structure will have an infinite life. To this purpose, Dang Van adopted a multiscale approach which assumes that elastic shakedown happens at both macroscopic and mesoscopic scales before crack initiation.

As a first step, Dang Van evaluated the stabilized mesoscopic stresses. Thanks to the shakedown assumption at the mesoscopic scale, it is possible to estimate the mesoscopic stress cycle from the macroscopic stress cycle through Eq. (11.21), as follows:

$$\boldsymbol{\sigma}\left(t\right) = \boldsymbol{\Sigma}\left(t\right) + \boldsymbol{\rho}^* \tag{11.23}$$

where $\boldsymbol{\rho}^*$ is a time-independent stress field.

Then, Dang Van defined his fatigue criterion in the following form:

$$\forall \mathbf{n},\ \forall t \quad \tau\left(\mathbf{n}, t\right) + a\sigma_h\left(t\right) \leq b \tag{11.24}$$

Here, σ_h and τ are the instantaneous hydrostatic and shear stresses, associated to the stabilized mesoscopic stress, $\boldsymbol{\sigma}$, respectively; material parameters, a and b, are usually deduced from two Wöhler curves related to smooth specimens, giving the fatigue limit in alternated torsion and in fully reversed bending.

To express the criterion in terms of macroscopic stresses, Dang Van (1973) made the following considerations. Firstly, the mesoscopic hydrostatic stress, σ_h, is equal to the macroscopic one, Σ_h. Then, to evaluate the mesoscopic shear stress, τ, Dang Van suggested the following method, shown in Figure 11.4: on a material surface with a normal vector, $\mathbf{n}$, the macroscopic shear, $\mathbf{C}(\mathbf{n}, t)$, describes a closed curve, $\phi(\mathbf{n})$ (smooth curve in Figure 11.4); the residual shear stress, $\boldsymbol{\tau}^*(\mathbf{n}) = \boldsymbol{\rho}^*.\mathbf{n}$ is given by the vector RO, where R is the center of the smallest circle circumscribing the curve, $\phi(\mathbf{n})$.

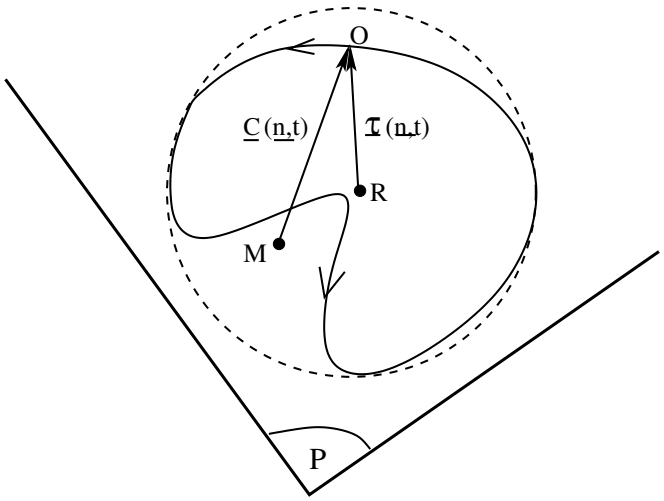

Figure 11.4: Calculation of the mesoscopic shear stress, τ, taken from (Dang Van, 1973).

Consequently, the criterion can be rewritten in the following form:

$$\max_{\mathbf{n}} \left\{ \max_{t} \left[\tau(\mathbf{n}, t) + a\sigma_h(t) \right] \right\} \leq b \tag{11.25}$$

and allows to state that the lifetime is infinite if the mesoscopic shear stress, τ, and the hydrostatic stress, σ_h, satisfy inequality 11.25 in all the points of the structure.

Later, Dang Van et al. (1989) proposed another way to evaluate the mesoscopic stress. In particular, by knowing that the mesoscopic deviator stress, $\mathbf{s}(t)$, is given by:

$$\mathbf{s}(t) = \mathbf{S}(t) + \boldsymbol{\rho}^* \tag{11.26}$$

Dang Van defined $-\boldsymbol{\rho}^*$ as the center of the smallest hypersphere circumscribing the loading path, $\mathbf{S}(t)$. The maximum mesoscopic shear over all the material plane passing by a given point is thus given by:

$$\tau(t) = \frac{\Sigma_I(t) - \Sigma_{III}(t)}{2} \tag{11.27}$$

where $\Sigma_I(t)$ and $\Sigma_{III}(t)$ are respectively the greatest and the smallest principal macroscopic stresses; principal stresses of the mesoscopic stress can also be used.
The Dang Van criterion is then rewritten as:

$$\max_{t} \left[\tau(t) + a\sigma_h(t) \right] \leq b \tag{11.28}$$

Chapter 12

Oligocyclic fatigue of metals

This Chapter presents an overview on the state of art in oligocyclic or low-cycle fatigue of metals, which is defined by a number of cycles to failure less than 10^4. Such an overview allows to prepare the framework for the fatigue-life assessment of cardiovascular stents treated in next Chapters. In particular, the application of the global computational approach, described in Chapter 10, to the low-cycle fatigue regime is treated in detail.

The Chapter is organized as follows. Section 12.1 describes the main features of the global computational approach. Section 12.2 presents the first step of the global computational approach, i.e., the mechanical analysis, by concentrating on material constitutive behavior. Then, Section 12.3 focuses on the second step of the global computational approach, i.e., the fatigue analysis, by presenting some strain- and energy-based fatigue criteria usually adopted in the literature.

12.1 The global computational approach to fatigue

The question of *oligocyclic* or *low-cycle fatigue* (LCF), defined by a number of cycles to failure less than 10^4, arised in the middle of the twentieth century, when the engineering needs demanded lifetime predictions for aeronautical and nuclear plants.
The main difference when compared to the high-cycle fatigue domain, treated in Chapter 11, is the presence of plasticity and/or viscosity at the macroscopic scale of the structure and therefore the modeling needs the application of non-linear constitutive laws. Moreover, in the LCF domain, an energy dissipation takes place through a series of mechanisms, and therefore the structure does not attain an infinite lifetime. Consequently, the classical stress-life approaches, described in Chapter 11, are no more appropriate, since suitable for situations involving primarily elastic deformations and components expected to have a long lifetime. Thus, energy- and strain-based fatigue life approaches are usually adopted in the literature to treat LCF and the generally applied methodology is based on the philosophy of the *global computational approach* (Constantinescu et al., 2003), introduced in Section 10.8 and consisting of a mechanical and a fatigue analysis. In the following sections, we discuss in details the main aspects characterizing these two steps.

12.2 Mechanical analysis

The mechanical analysis assumes the geometry of the structure, loading, and material constitutive law known and can be performed with different tools, such as the finite element method (Amiable et al., 2006) or analytical and semi-analytical solutions (Ferjani et al., 2011a,b). Material behavior can be described by microscopic or macroscopic models. To keep the final objective of a global simple representation of

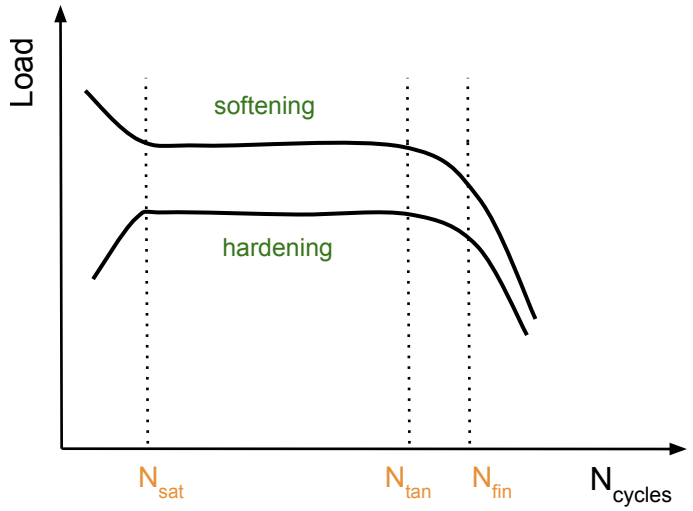

Figure 12.1: Cyclic material behavior for isothermal LCF tests carried out by Skelton (1991, 1993).

material behavior at the scale of the structure, we restrict our choice to phenomenological macroscopic models, in the following.

12.2.1 Material constitutive behavior

Monotonic versus cyclic material behavior

Monotonic stress-strain curves are usually used to obtain design parameters for limiting stresses on structures subjected to static loading. In the description of material constitutive behavior, we generally suppose that material behavior can be identified from a series of traction-compression or torsion tests also combined with dwell, relaxation and creep periods (Lemaitre and Chaboche, 1994).

By analogy, cyclic stress-strain curves may be used to evaluate the durability of structures subjected to cyclic loading. When a metal is subjected to cyclic loading, characteristic stress-strain response curves are observed depending on material type, initial condition (annealed or work hardened) and loading conditions (e.g., stress- or strain-controlled, loading amplitude). With continued cyclic loading, a quasi-steady state of stress-strain cycle (i.e., cyclic saturation) is usually reached within half-life fatigue loading. As a result, the calculation of fatigue parameters is generally based on mid-life hysteresis loop data (Schijve, 2009; Stephens et al., 2000).

To better understand the underlying phenomena, we recall the interpretation of material cyclic behavior in the LCF regime by Skelton (1991, 1993), who described the cyclic material behavior, i.e., the recorded stress level under applied strain amplitude, by proposing the identification of three different phases defined by the saturation, tangent, and final points, as shown in Figure 13.7: the *hardening/softening phase* $[0\text{-}N_{sat}]$ corresponding to the stabilization of the plastic material properties; (ii) the *stabilized phase* $[N_{sat}\text{-}N_{tan}]$ represented by a flat plateau with small property variations; (iii) a final *failure phase* $[N_{tan}\text{-}N_{fin}]$ characterized by a fast drop of the measured stress (as we impose the displacements/strains). Conventionally, N_{fin} is defined by a 5% or 10% load drop. Reaching the saturation of the plastic cyclic behavior implies a stabilized cyclic behavior of the structure.

Skelton (1991, 1993) showed that the accumulated dissipated energy until stabilization can be considered constant for a given material. These results also suggested that the accumulated dissipated energy up to the hardening or softening stabilization point is reached can be used as a crack initiation criterion in LCF. Such a view has been successfully applied to LCF lifetime predictions in (Amiable et al., 2006, 2009a,b; Constantinescu et al., 2003).

Identification of material behavior

It is well accepted that the choice of the constitutive law, the identification of material parameters, and the numerical integration algorithm are key issues of every structural computation. It is generally recommend a simple constitutive law, with a small number of parameters, capable of modeling the phenomena of interest. As an example, structures evolving at high temperature need to consider elasto-visco-plastic constitutive laws, whether in a low temperature range one can restrain to elastoplastic constitutive laws (Lemaitre and Chaboche, 1994).

The parameters of the adopted constitutive law can be identified through the following two methods:

- *direct method*, which directly estimates material parameters, e.g., tangent slope at the origin for the Young's modulus, tangent slope at high strain level for the hardening parameters, apparent stress level after relaxation for the yield limit;
- *inverse method*, which uses an optimization tool and tries to minimize a cost functional measuring the distance between computed and measured strain or stress predictions with respect to the parameters of the constitutive law (Constantinescu and Verger, 2002).

12.3 Fatigue analysis

The fatigue analysis assumes the existence of a stabilized cycle, i.e., elastic or plastic shakedown, and the possibility of computing such a cycle through the mechanical analysis, in order to evaluate fatigue damage parameters at such a cycle.

Depending on the stabilized state obtained from the mechanical analysis, different damage states can occur and appropriate predictive criteria can be applied during the fatigue analysis.

A fatigue crack initiation criterion is classically defined as a local relation (i.e., in each spatial point of the structure, $x \in \Omega$), between the values of the mechanical fields, $(\boldsymbol{\varepsilon}, \boldsymbol{\varepsilon}^p, \boldsymbol{\sigma}..)$, computed for the stabilized cycle, and the number of cycles to failure, N_f, of the structure:

$$\max_{x \in \Omega} \left[f\left(\boldsymbol{\varepsilon}, \boldsymbol{\varepsilon}^p, \boldsymbol{\sigma}\right) \right] = c N_f^b \tag{12.1}$$

where b and c are material parameters and f represents the fatigue damage parameter that is characteristic of each criterion. Within the LCF framework, strain- and energy-based approaches can be used (Schijve, 2009).
In the present Section, we focus on some multiaxial criteria for LCF, that we will use in the following Chapters.

The fatigue criterion by Coffin (1953) and Manson (1953)

The fatigue criterion by Coffin (1953) and Manson (1953) is defined as follows:

$$\Delta\epsilon^p = c N_f^b \tag{12.2}$$

where $f = \Delta\epsilon^p$ is the amplitude of the plastic strain in the uniaxial case. If the considered experiments are multiaxial, we can extend the amplitude, $\Delta\epsilon^p$, to this case as follows:

$$\Delta\epsilon^p = \max_{t_1} \max_{t_2} \sqrt{\frac{2}{3} \left[\epsilon^p\left(t_1\right) - \epsilon^p\left(t_2\right)\right] : \left[\epsilon^p\left(t_1\right) - \epsilon^p\left(t_2\right)\right]} \tag{12.3}$$

where t_1 and t_2 represent different time instants of the stabilized cycle. The present extension measures the diameter of the plastic strain path.

The dissipated energy per cycle criterion and modified version

The criterion based on the dissipated energy per cycle is defined as follows (Charkaluk and Constantinescu, 2009; Korsunsky et al., 2007):

$$W^p = cN_f^b \tag{12.4}$$

where $f = W^p$ is the dissipated energy per cycle, integrated in each point of the structure over the complete stabilized cycle, as follows:

$$W^p = \int_{cycle} \boldsymbol{\sigma} : \dot{\boldsymbol{\varepsilon}}^p dt \tag{12.5}$$

The use of the dissipated energy as fatigue damage parameter allows a continuous approach from LCF to high-cycle fatigue and it is generally preferable in case of complex fatigue problems (e.g., for instance, multiaxial or thermo-mechanical fatigue) (Bentachfine et al., 1999). As an example, such a criterion has been successfully used in a series of fatigue analyses on specimens (Dowling, 1972; Feltner and Morrow, 1961; Morrow, 1965) and structures (Charkaluk et al., 2002; Constantinescu et al., 2004; Tabibian et al., 2013) and presents the advantage of a direct relation of the fatigue properties with the plastic shakedown strain-stress loop.

The definition of a fatigue parameter depending only on the dissipated energy implies that this quantity is the only driving force of the damage. However, the effect of mean stress on fatigue is a well-known phenomenon. The modification proposed by Amiable et al. (2006, 2009a,b) consists in the addition of a maximal hydrostatic stress term.

The modified dissipated energy criterion takes the following form:

$$(W^p + a\sigma_h^{max}) = cN_f^b \tag{12.6}$$

where $f = (W^p + a\sigma_h^{max})$ is the sum of the dissipated energy, W^p, and the maximal hydrostatic stress attended during the stabilized cycle, $\sigma_h^{max} = \max_t \sigma_h(t)$, with $\sigma_h = 1/3\ \mathrm{tr}(\boldsymbol{\sigma})$, while a is an additional material parameter.

Chapter 13

Fatigue of 316L stainless steel notched microsize components

This Chapter provides an in-depth analysis of the fatigue-life assessment for microsize 316L stainless steel components, which find typical applications in the biomedical field, e.g., in cardiovascular stents. To this purpose, the present Chapter presents the analysis of some experimental data from the literature, related to 316L stainless steel smooth and notched microsize components, by using the global computational approach described in Chapter 10. Several aspects are discussed, as the choice of an appropriate constitutive law for cyclic material behavior, fatigue criteria for finite and infinite lifetime, and gradient effects in relation with hot-spot as well as average or mean volume approaches for the lifetime estimation.

The Chapter is organized as follows. Section 13.1 presents an introduction to the problem and the motivations of the proposed work. Section 13.2 revisits the two experimental campaigns. Then, in the framework of the global computational approach, Sections 13.3 and 13.4 present the performed mechanical and fatigue analyses. Conclusions and summary are finally given in Section 13.5.

13.1 Introduction and motivations

In the past fifty years, austenitic stainless steels have been widely and extensively used in several fields, ranging from nuclear or aerospace industries to chemistry or food and beverage processing (Baddoo, 2008). In particular, type 316L stainless steel has been largely appreciated for its high ductility and strength under complex thermo-mechanical loadings, i.e., such a material can reach considerable plastic strains of 0.5-1% at millions of cycles. However, materials like the 316L or 304L stainless steels present a complex material behavior characterized by primal and secondary hardening (Alain et al., 1997; Gerland and Violan, 1986; Pham et al., 2011; Polak et al., 1994), as shown in Figures 13.1(a)-(c) and 13.2(a)-(b), which make the design of structures a difficult task. Nowadays, in spite of a large database of models and experimental data (Lemaitre and Chaboche, 1994), both experimental (Huang et al., 2006; Mohammad et al., 2013; Puchi-Cabrera et al., 2008) and modeling campaigns (Amiable et al., 2006, 2009a,b; Laamouri et al., 2013; Le Pécheur et al., 2012) are still continuing in order to improve both safety and performance of the designed structures.

In the recent decades, type 316L stainless steel has gained a privileged position among the materials employed in biomedical devices, e.g., stents, vena cava filters, guide-wires for catheters and pacemaker leads (Bombac et al., 2007; Winters and Nutt, 2003). The attractive properties of such a material, e.g., well adapted mechanical characteristics (great ductility, high tensile strength, and a raised elastic limit), biocompatibility, resistance to corrosion as well as fatigue performances, assure the long-term service required by biomedical devices. However, the biomedical field is imposing two specific constraints in the

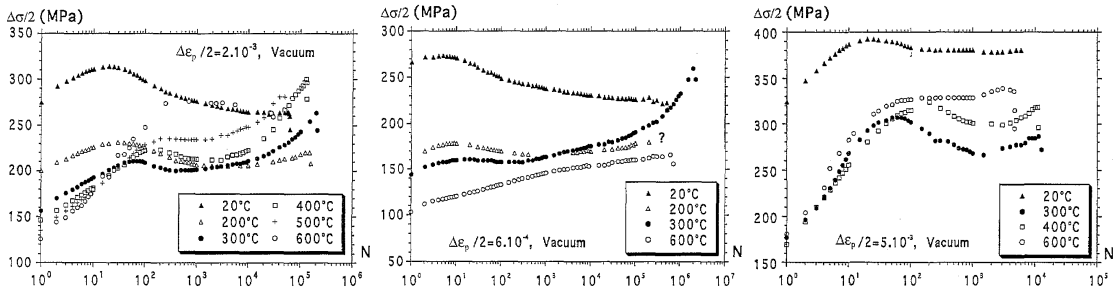

(a) (b) (c)

Figure 13.1: Evolution of the cyclic stress at several temperatures for (a) $\Delta\epsilon_p/2 = \pm 2 \cdot 10^{-3}$; (b) $\Delta\epsilon_p/2 = \pm 6 \cdot 10^{-4}$ and (c) $\Delta\epsilon_p/2 = \pm 5 \cdot 10^{-3}$, taken from (Alain et al., 1997).

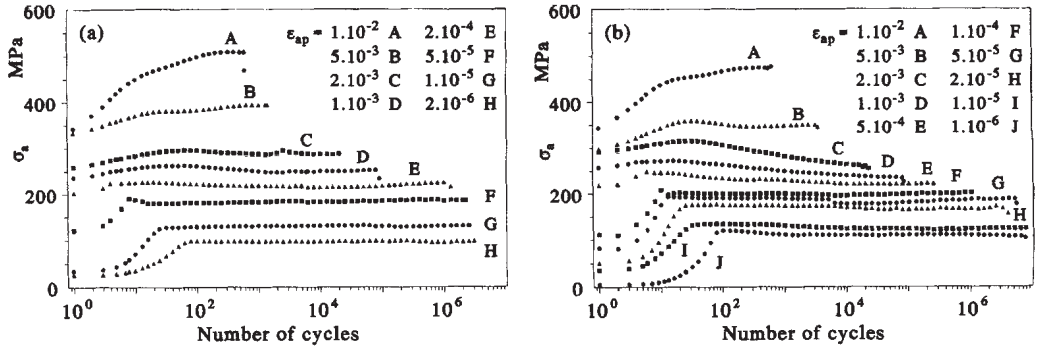

(a) (b)

Figure 13.2: Fatigue hardening and softening curves for (a) 316L-VZ steel and (b) 316L-TH steel, taken from (Polak et al., 1994).

design of 316L stainless steel devices: (i) the interest in the very high-cycle fatigue domain (i.e., 10^7-10^8 cycles) and (ii) the use of mm- and μm-size components.

As an example, cardiovascular 316L stainless steel stents have to withstand both their initial deployment within the artery, which involves large amounts of plastic deformation, and the long-term service loading induced by the pulsing blood pressure (Dumoulin and Cochelin, 2000). In particular, such devices must withstand at least 10 years service without failure (US Food and Drug Administration, 2010). Such a constraint translates into 400 million (i.e., $4 \cdot 10^8$) cycles during stent lifetime, since 70 artery pulses per minute impose 40 million cycles per year.

Moreover, stents are manufactured either through welding of microscopic wires or through laser cutting from thin-walled tubes, both leading to a final truss-type structure composed of struts connected by hinges, with thicknesses in the range of 50-150 μm (Harewood and McHugh, 2007; Murphy et al., 2006, 2003; You et al., 2006). Stents manufactured through both processes will finally present small radius and thus will be subjected to stress concentrations (Wiersma et al., 2006). Also, μm-size components like stents have length scale in the order of magnitude of the length of grains characterizing their microstructure, i.e., the ratio between the length scales of the mesoscopic structure of grains and of the macroscopic structure of the device, characterized by approximately 10-20 grains across the section, makes the application of standard bulk models inadequate (Connolley et al., 2005; Harewood and McHugh, 2007; Murphy et al., 2006, 2003; You et al., 2006). As an example, Figure 13.3 illustrates the scanning electron microscope image of a 316L steel stent strut, where only 6-10 grains are visible accross the width.

Additionally, in spite of the importance of such applications, insufficient (only few) data sets are available in the literature (Donnelly, 2012; Wiersma et al., 2006; Wiersma and Taylor, 2005), due to practical difficulties of testing very small specimens. Standard mechanical test equipment is in fact not suitable for testing micrometric components due to the operating range and resolution of load and displacement transducers and the design of gripping members.

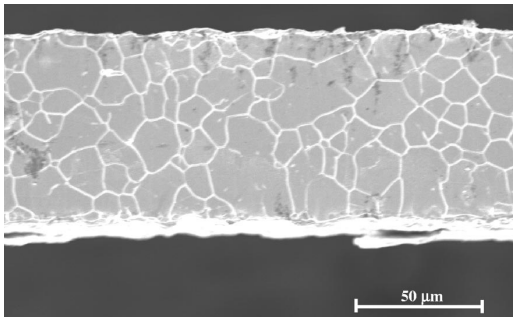

Figure 13.3: Scanning electron microscope of a 316L stainless steel stent strut, showing scale of strut dimensions and morphology of material microstructure, taken from (Murphy et al., 2003).

Thus, the design for reliability of cardiovascular stents is very complex, since it has to take into account high and very high-cycle fatigue loading, material and device specificities, manufacturing-induced features as well as corrosive environment.

In order to bridge the gap between the existing experiments and the fatigue design of such components, several numerically-based attempts have recently been proposed to assess the lifetime of these microscopic structures; see, e.g (Auricchio, 2001; Azaouzi et al., 2012b; Barrera et al., 2012; dos Santos et al., 2012; McGarry et al., 2004; Sweeney et al., 2012). Numerical simulations minimize the number of design cycles and structural experiments and prevent failure. However, the use of an appropriate constitutive law and the application of standard fatigue prediction criteria to biomedical devices have to be carefully investigated, since they could potentially produce non-conservative estimates of safe working loads in case of size effects and stress gradients, and thus they could result in in-vivo fractures of devices. Moreover, most of the available numerical approaches for the fatigue-life assessment of stents do not dispose of adequate criteria, i.e., identified on appropriate experimental data in terms of size and notch effects.

Accordingly, the aim of the present work is to provide an in-depth analysis of the fatigue-life assessment of microsize components for the design of stents manufactured by laser cutting. This is realized by revisiting the shakedown concepts and by taking into account several aspects characterizing stents, as the complex material behavior, size effects, and stress concentration features.

The practical difficulties of testing microsize specimens and the inadequacy of fatigue data related to macroscopic specimens lead us to critically investigate and analyze two experimental campaigns available from the literature by Wiersma et al. (2006); Wiersma and Taylor (2005) and Donnelly (2012), on 316L stainless steel microscopic smooth and notched components, produced with the standard procedure applied in the stent manufacturing industry.

We complete the reported data by using the *global computational approach* described in Chapter 10. In particular, in the fatigue analysis, in case of elastic shakedown, we focus on the fatigue criterion by Dang Van (1999) and, in case of plastic shakedown, on fatigue crack initiation criteria associated with hot-spot as well as mean or volume element approaches, i.e., the Manson-Coffin criterion (Coffin, 1953; Manson, 1953), the dissipated energy per cycle criterion (Charkaluk and Constantinescu, 2009; Korsunsky et al., 2007), and a modified version of the dissipated energy criterion (Amiable et al., 2006, 2009a,b).

The discussion of the shakedown state, resulting from the elastoplastic mechanical analysis, allows to investigate several fatigue criteria for infinite and finite lifetime, in particular distinguishing between high-cycle, very high-cycle, and low-cycle fatigue regimes (denoted, respectively, as HCF, VHCF and LCF).

We calibrate such criteria on the cited experimental data and therefore, we are able to provide a set of criteria that can be used to numerically predict the fatigue-life of cardiovascular 316L stainless steel stents. The obtained results assess the suitability of standard prediction methods, normally used for macroscopic components, for μm-size components and give a new insight into the treatment of fatigue issues in μm-size components.

13.2 316L steel: material and fatigue experimental data

The present Chapter focuses on 316L austenitic stainless steel with chemical composition and thermo-mechanical properties given in Tables 13.1 and 13.2; see (Lê, 2013) for details.
Before entering into the details of the global computational approach adopted in the present work, this Section describes the main results of the two extensive experimental campaigns conducted on 316L specimens of micrometric size by Wiersma et al. (2006); Wiersma and Taylor (2005) and Donnelly (2012).

Element	C	Mn	Si	S	P	Ni	Cr	Mo	Cu	N
Mass content [%]	0.024	1.86	0.36	0.0045	0.026	11.6	17.2	2.55	-	-

Table 13.1: Chemical composition ($wt\%$) of 316L austenitic stainless steel (Lê, 2013).

Property	**Unit**	**Values**							
T	$^\circ$C	20	50	100	150	200	250	300	350
ν	$-$	0.3	0.3	0.3	0.3	0.3	0.3	0.3	0.3
E	10^3 MPa	197	195	191.5	187.5	184	180	176.5	172
α	$10^{-6}/^\circ$C	15.54	16.0	16.49	16.98	17.47	17.97	18.46	18.95
$\frac{\lambda}{\rho C}$	10^{-6}m^{2}s^{-1}	3.89	3.89	3.89	3.94	3.99	4.06	4.17	4.26
λ	W/m$^\circ$C	14.0	15.2	15.4	15.8	16.6	17.3	17.9	18.6

Table 13.2: Thermo-mechanical properties of 316L austenitic stainless steel (Lê, 2013).

13.2.1 Experimental tests by Wiersma et al. (2006); Wiersma and Taylor (2005)

Wiersma et al. (2006); Wiersma and Taylor (2005) carried out a complete experimental campaign on 316L stainless steel specimens taking the form of smooth and notched round/rectangular bars (see Figures 13.4(a)-(d) and Tables 13.3 and 13.4).
Specimens were produced with the standard procedure applied in the stent manufacturing industry: (i) laser cutting; (ii) vacuum anneal treatment or not; (iii) electro-polishing. The size of the tested specimens was approximately 0.1 mm, thus comparable to that characterizing industrially produced stents. Moreover, the cross-section of the tested specimens contained around 10 grains.

Monotonic tensile test results are represented in terms of stress-strain curves in Figure 13.5(a) and mechanical properties are reported in Table 13.5. The grain size and hardness values provided in Table 13.5 are identical for the macroscopic and microscopic specimens, confirming that the material itself is identical. The stress-strain curves show that μm-size annealed specimens, when compared to macroscopic specimens, display lower values of yield and ultimate tensile strengths and strain to failure, as well as larger

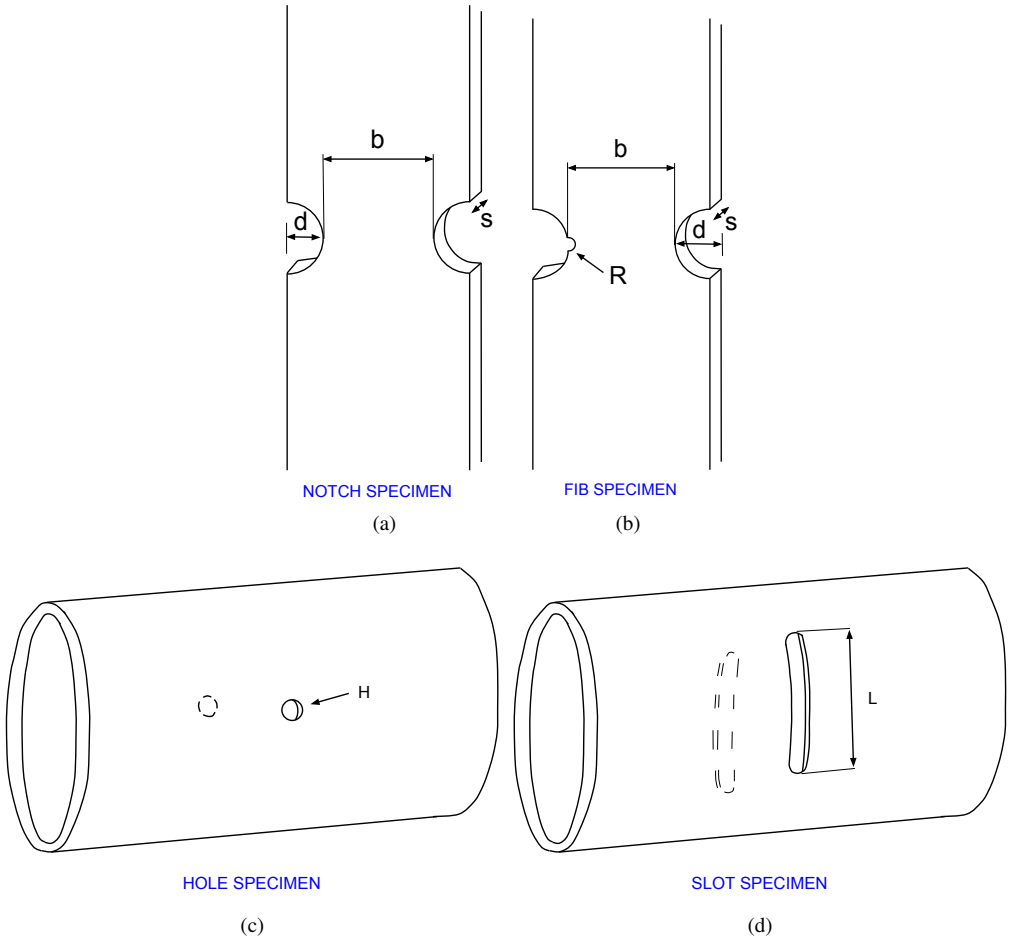

Figure 13.4: Geometries of the 316L μm-size notched specimens tested by Wiersma et al. (2006); Wiersma and Taylor (2005) (b is the net section; s the thickness; d the notch depth; R the fib-slot; H the hole radius; L the slot length).

Specimen	**Features**	**Fatigue ratio** (R)	**Experimental fatigue limit** [MPa]
MACRO			
Smooth	Round bar ($D = 7.5$ mm, gauge length 25 mm)	0.1	420
Notched	Round bar ($D = 12$ mm, circumf. V-shaped notch of depth 1 mm, root radius 0.08 mm)	0.1 0.8	150

Table 13.3: Summary of tests on macroscopic 316L specimens and of fatigue limits by Wiersma et al. (2006); Wiersma and Taylor (2005).

Specimen	**Features**	**Fatigue ratio** (R)	**Experimental fatigue limit** [MPa]
MICRO			
Smooth	Rectangular bar (width 0.1 mm, thickness 0.09 mm)	0.1	420
50-notch	Rectangular bar (net section of 0.11 mm, thickness 0.09 mm, notch depth 0.05 mm)	0.1	360
100-notch	Rectangular bar (net section of 0.11 mm, thickness 0.09 mm, notch depth 0.1 mm)	0.1	355
145-notch	Rectangular bar (net section of 0.11 mm, thickness 0.09 mm, notch depth 0.145 mm)	0.1	350
50-fib	Rectangular bar (net section of 0.11 mm, thickness 0.09 mm, notch depth 0.05 mm, slot of 0.001 mm)	0.1	320
60-hole	Thin-walled tube (outer diameter 1.7 mm, wall thickness 0.09 mm, hole radius 0.06 mm)	0.1	250
400-slot	Thin-walled tube (outer diameter 1.7 mm, wall thickness 0.09 mm, slot length 0.4 mm)	0.1	120
1500-slot	Thin-walled tube (outer diameter 1.7 mm, wall thickness 0.09 mm, slot length 1.5 mm)	0.1	115

Table 13.4: Summary of tests on μm-size 316L specimens and of fatigue limits by Wiersma et al. (2006); Wiersma and Taylor (2005).

values of reduction in area before failure, thus demonstrating a size effect. Therefore, one can conclude that for annealed material decreasing specimen size reduces strength but increases ductility. On the contrary, unannealed specimens show a higher strength and lower ductility.

Fatigue tensile tests were carried out using a sinusoidal loading cycle with R ratios varying from 0.1 to 0.8 and are summarized in Tables 13.3 and 13.4. Figures 13.5(b)-(d) show fatigue tensile test results in terms of the applied stress range and the number of cycles to failure. The reported applied stress level for specimens with stress concentrations (notches or slots) is a mean stress level computed as the ratio between the applied force and the net area. Tables 13.3 and 13.4 summarize the obtained fatigue limits, defined as the values of the stress range for which the average number of cycles to failure is $2 \cdot 10^6$.

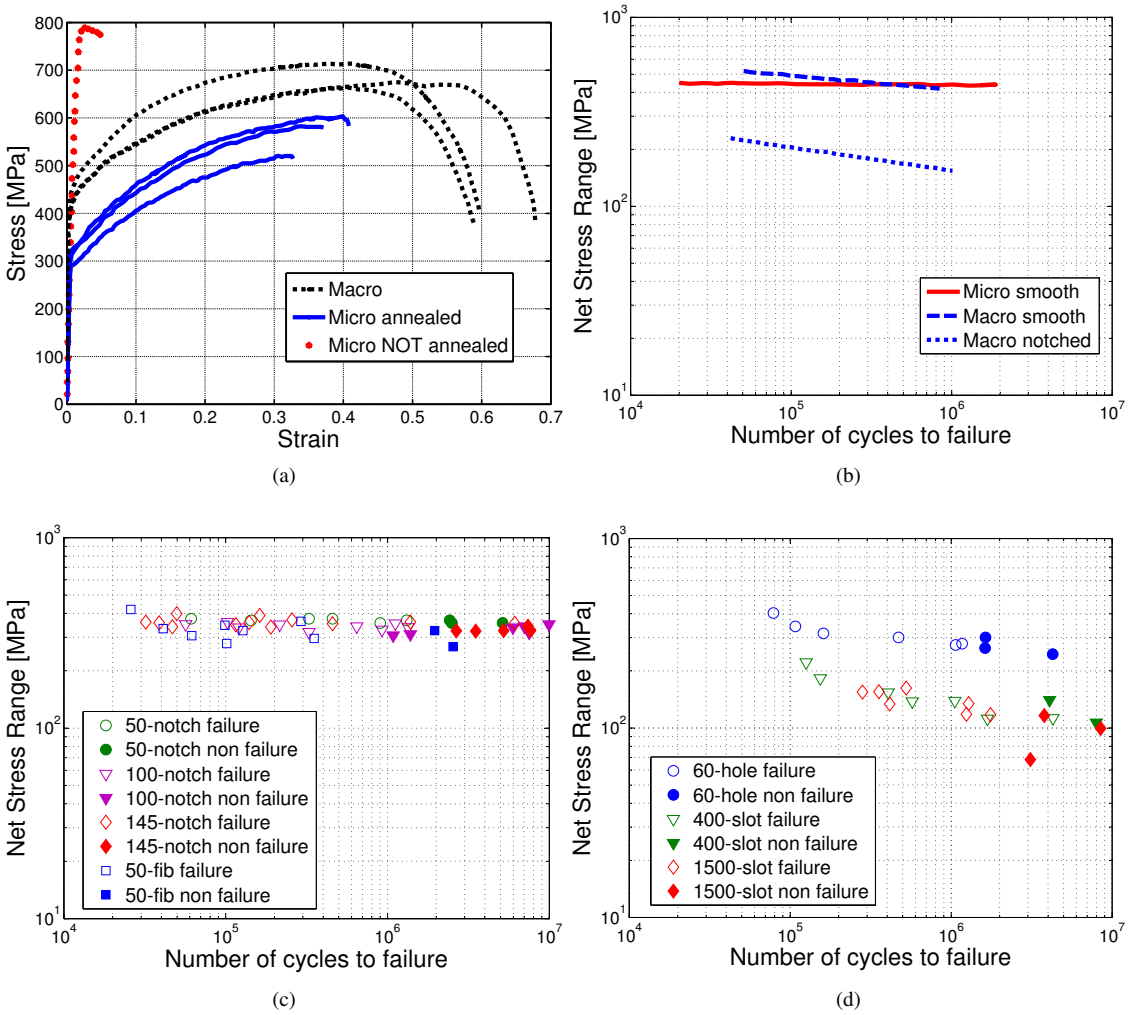

Figure 13.5: Results from the experiments by Wiersma et al. (2006); Wiersma and Taylor (2005). (a) Stress vs. strain diagram from monotonic tensile tests. Net stress range vs. number of cycles to failure diagram from fatigue tensile tests on (b) smooth macroscopic and μm-size specimens; (c)-(d) notched μm-size specimens.

Specimen	**Grain size** [mm]	**Yield strength** (0.2% proof) [MPa]	**Ultimate tensile strength** [MPa]	**Hardness** [Vickers]	**Strain to failure**	**Reduction in area** [%]
MACRO	0.0115	396	754	186	0.60	73
MICRO	0.0105	315	580	170	0.37	87
MICRO (unannealed)	-	680	780	312	0.05	-

Table 13.5: Material properties from monotonic tensile tests by Wiersma et al. (2006).

13.2.2 Experimental tests by Donnelly (2012)

Donnelly (2012) carried out a complete experimental campaign on 316L stainless steel specimens taking the form of smooth rectangular bars (see Table 13.6).
Again, specimens were produced with the standard procedure applied in the stent manufacturing industry: (i) laser cutting; (ii) vacuum anneal treatment; (iii) seamless tubing; (iv) electro-polishing. The size of the tested specimens ranged from 0.05 to 0.15 mm, thus comparable to that characterizing industrially produced stents. The number of grains per cross-section ranged from 5 to 15.

Fatigue tensile tests were carried out using a push-pull traction cycle with R ratio of 0.5 and are summarized in Table 13.6. Figures 13.6(a) and (b) show the results of the monotonic and fatigue tensile tests, where the fatigue limit is defined as the value of the stress amplitude for which the average number of cycles to failure is 10^7. The fatigue limit decreases for the 50 μm specimen, which can be associated to a size effect.

Specimen	**Features**	**Fatigue ratio** (R)	**Experimental fatigue limit** [MPa]
MICRO			
Smooth 50 μm	Rectangular bar (width 0.05 mm, thickness 0.06 mm)	0.5	120
Smooth 75 μm	Rectangular bar (width 0.075 mm, thickness 0.06 mm)	0.5	150
Smooth 100 μm	Rectangular bar (width 0.1 mm, thickness 0.06 mm)	0.5	150
Smooth 150 μm	Rectangular bar (width 0.15 mm, thickness 0.06 mm)	0.5	150

Table 13.6: Summary of tests on μm-size 316L specimens and of fatigue limits by Donnelly (2012).

13.3 316L steel: constitutive law and mechanical analysis

In order to critically investigate the described experimental campaigns, this Section presents the first step of the adopted global computational approach, that is, a mechanical analysis to calculate the shakedown or stabilized mechanical state. In particular, we describe first our modeling assumptions and the adopted constitutive law; then, we present the mechanical analysis performed with the finite element (FE) method. Models and analyses are realized using the object-oriented FE program, Cast3M; see, e.g., (Cast3M, 2013).

13.3.1 Modeling assumptions

The cyclic behavior of 316L stainless steel shows exceptional ductility and a complex evolution which can be described by using a series of superposed hardening laws, see, e.g., (Alain et al., 1997; Gerland and Violan, 1986; Pham et al., 2011; Polak et al., 1994).

In the following, we adopt the simplifying view, shown in Figure 13.7, as proposed initially by Skelton (1991, 1993) and described in Section 12.2.1. During the saturation phase we assume that the structure has

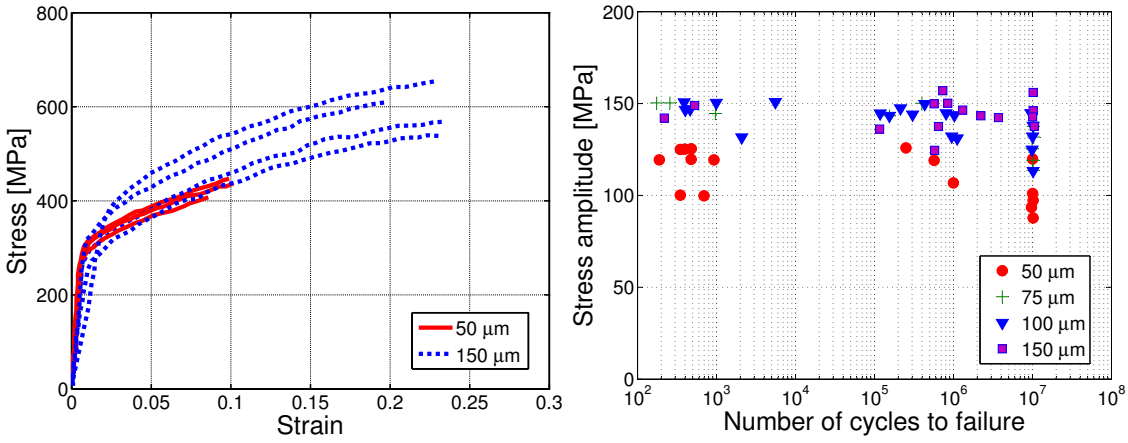

Figure 13.6: Results from the experiments by Donnelly (2012). (a) Stress vs. strain diagram from monotonic tensile tests; (b) stress amplitude vs. number of cycles to failure from fatigue tensile tests on μm-size specimens.

reached an asymptotic limit cyclic (plastic shakedown) which is described by the constitutive law and can be computed numerically on the structure under scrutinity.
Moreover, we reasonably admit that the mechanical response at $N_f = N_{fin}/2$ lies within the stabilized period and corresponds to material behavior identified for our computational needs (see Figure 13.7). This is compatible with the fatigue analysis where characteristics used in the interpretation are equally taken after $N_{fin}/2$ cycles.
Such an approach neglects the fine description of real material behavior (Alain et al., 1997; Gerland and Violan, 1986; Pham et al., 2011; Polak et al., 1994) and leads to an approximate error of about 5% in the computed stress level, which is of the order of magnitude of other uncertainties in the modeling. Similar assumptions have already been successfully used for thermo-mechanical fatigue predictions of 304L steel behavior (Amiable et al., 2006, 2009a,b) or other steels (Skelton, 1991, 1993).

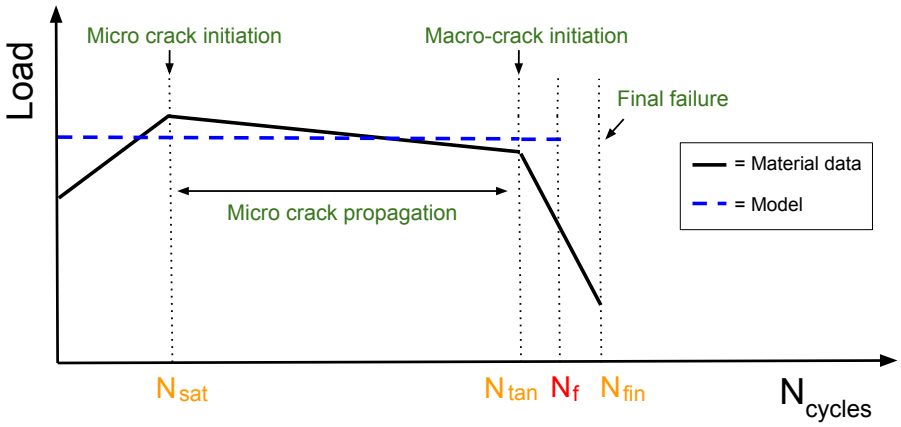

Figure 13.7: Schematic representation of the cyclic material behavior adopted in the present approach; see also (Skelton, 1991, 1993).

Another modeling assumption concerns size effects and the application of a continuous model to a structure with sizes close to the grain size. We assume that the present analysis will provide a typical

'mean' answer of the structure and that the inherent variability of the properties of the microstructure will provide the spread of the fatigue lifetime. However, such an aspect is not treated here and will be the object of future work.
Moreover, since an important feature of cardiovascular stent applications is given by their small size, where the size of the structure is close to that of the representative volume element, one could reasonably suggest that an appropriate model should include crystal plasticity. However, this would further imply that the microstructure is precisely known, or that a Monte Carlo method need to be employed to estimate the solution for different grain orientations (Morhácová, 1995). Here, we consider a homogenized macroscopic approach and we further assume that size effects are taken into account through the fatigue-life estimations based on μm-size experiments.

13.3.2 Constitutive law for 316L stainless steel

The elastoplastic constitutive model has a J_2 yield function and non-linear isotropic and kinematic hardening (with one kinematic center) (Benallal and Marquis, 1987; Chaboche et al., 1979; Krempl and Khan, 2003; Lemaitre and Chaboche, 1994). On the one side, isotropic hardening controls the rate at which the stabilized response is achieved, by allowing yield surface expansion and thus, by defining the evolution of stress magnitudes reached in a cyclic stress-strain response; on the other side, kinematic hardening influences the shape of the stabilized hysteresis curve, by allowing yield surface displacement and thus, by introducing a back stress into the cyclic stress-strain response, which reduces yield stress upon reversal of loading.

The multiaxial equation for the back stress tensor, $\mathbf{X}$, is defined by:

$$\dot{\mathbf{X}} = \frac{2}{3} C\left(p\right) \dot{\boldsymbol{\varepsilon}}^p - \gamma \mathbf{X} \dot{p} \tag{13.1}$$

with $C\left(p\right) = C_\infty \left(1 + \left(\psi - 1\right) \exp^{-\omega p}\right)$ and $\dot{p} = \sqrt{2/3\, \dot{\boldsymbol{\varepsilon}}^p : \dot{\boldsymbol{\varepsilon}}^p}$, where $\boldsymbol{\varepsilon}^p$ is the plastic strain tensor, p is the accumulated plastic strain, and C_∞, ψ, γ, and ω are kinematic constants. The isotropic hardening function, $R = R\left(p\right)$, is given by the following relation:

$$\dot{R} = b\left(R_\infty - R\right) \dot{p} \tag{13.2}$$

where R_∞ is the saturated value of isotropic hardening and b the rate of decay for isotropic hardening. The yield surface, $f = f(\boldsymbol{\sigma}, \mathbf{X}, p)$, is defined by the classical function:

$$f = \sqrt{\frac{3}{2} \left(\mathbf{s} - \mathbf{X}\right) : \left(\mathbf{s} - \mathbf{X}\right)} - R_0 - R \tag{13.3}$$

where $\mathbf{s}$ is the deviatoric tensor for stress and R_0 the initial yield stress. The evolution law for the plastic strain, $\boldsymbol{\varepsilon}^p$, takes the form:

$$\dot{\boldsymbol{\varepsilon}}^p = \frac{3}{2} \dot{\xi} \, \frac{\mathbf{s} - \mathbf{X}}{\sqrt{\frac{3}{2} \left(\mathbf{s} - \mathbf{X}\right) : \left(\mathbf{s} - \mathbf{X}\right)}} \tag{13.4}$$

In the absence of direct cyclic measurements on the fatigue experiments, we identify model parameters on the experiments by Lê (2013), consisting of uniaxial strain controlled tension tests with variable amplitude loading on cylindrical specimens. Table 13.7 lists the adopted constitutive model parameters.
Figures 13.8(a) and 13.8(b) present the monotonic and stabilized stress-strain curves generated by the model with parameters of Table 13.7. The order of magnitude of the numerical stresses and strains with respect to the experimental ones is illustrated in Figures 13.8(a) and 13.8(b) through a comparison with the monotonic experimental curves obtained by Wiersma et al. (2006); Wiersma and Taylor (2005) and Donnelly (2012). As it can be observed, the numerical monotonic and stabilized curves lie within the experimental stress range.

Parameter	Description	Value	Unit
E	Young modulus	196000	MPa
ν	Poisson ratio	0.3	-
R_0	Initial yield stress	211	MPa
R_∞	Saturated value of isotropic hardening	231	MPa
b	Decay rate for isotropic hardening	6.69	-
C_∞	Kinematic constant	67050	MPa
γ	Kinematic constant	218	-
ψ	Kinematic constant	0.73	-
ω	Kinematic constant	0.91	-

Table 13.7: Summary of the adopted model parameters for 316L stainless steel (Lê, 2013).

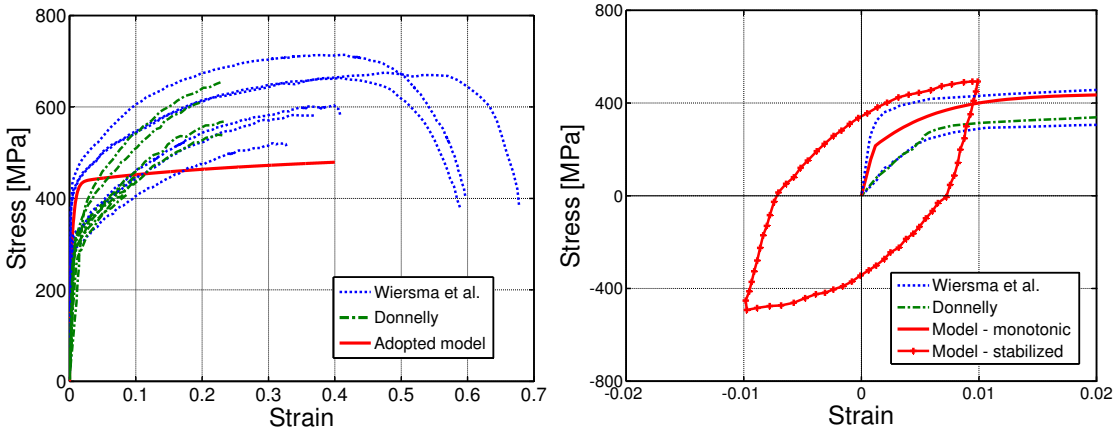

(a) (b)

Figure 13.8: (a) Comparison between monotonic stress-strain tensile curves obtained by the adopted model and by Wiersma et al. (2006); Wiersma and Taylor (2005) and Donnelly (2012); (b) stabilized hysteresis curve generated by the adopted model compared to monotonic tensile curves by Wiersma et al. (2006); Wiersma and Taylor (2005) and Donnelly (2012).

13.3.3 Mechanical analysis

A complete series of elastoplastic FE analyses is performed on each specimen in accordance to the loading cycle of experiments (Donnelly, 2012; Wiersma et al., 2006; Wiersma and Taylor, 2005). In the case of notched specimens, a preliminary analysis is accomplished in order to asses the accuracy of the solution at the notch tip. The mesh refinement is stopped when the elastic solution converges and, therefore, correctly represents the solution.

We consider the notched specimens of Figures 13.4(a)-(d) and we generate all the meshes for the specimens taking the form of rectangular bars (i.e., the 50-notch, 100-notch, 145-notch, and 50-fib specimens) using two-dimensional 6-node quadratic plain stress elements, due to the lack of constraint in the thickness direction of these specimens. Then, we generate the meshes of the specimens taking the form of tubes (i.e., the 60-hole, 400-slot, and 1500-slot specimens) using three-dimensional 20-node quadratic brick elements.

According to the symmetry of the problem, we model only one quarter of each specimen, except for the 50-fib specimen for which we model only one half, as shown in Figures 13.9(a)-(d). The finest zone of the mesh corresponds to the notched zone of the specimen and the elements in this part of the mesh are refined

depending on the dimension of the notch radius and of the grain size. In particular, specimens are meshed using 4662 elements for the 50-notch, 6582 for the 100-notch, 9068 for the 145-notch, 75000 for the 50-fib, 61624 for the 60-hole, 23346 for the 400-slot, and 25473 for the 1500-slot, as shown in Figures 13.9(a)-(d). Compared to the grain size, we assume approximately 5 elements per grain size. Consequently, the smallest element size at the root of the notch is characterized by an element size/notch radius ratio ranging between 0.0013 and 0.04. To estimate possible errors due to large spatial gradients, we test finer meshes and we can report that refining mesh above the present limit causes an important increase of computing time without a noticeable improvement of the results (see Section 13.3.4 for details).

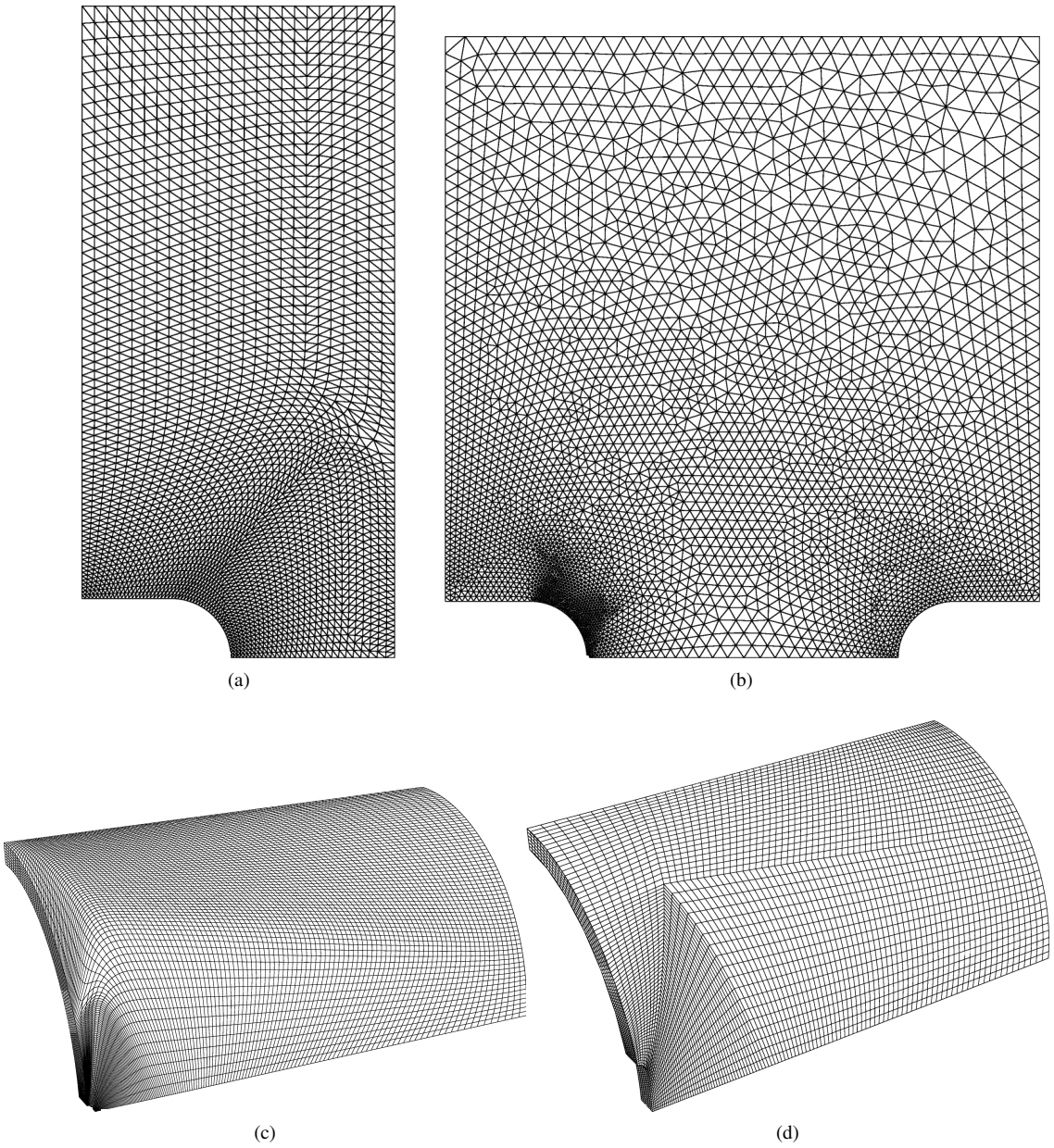

Figure 13.9: Adopted meshes for the specimens of Figures 13.4(a)-(d). 2D quadratic plain stress elements for the (a) notch and (b) fib specimens; 3D quadratic brick elements for the (c) hole and (d) slot specimens.

13.3.4 Discussion on results

As a result of the conducted elastoplastic FE analyses, we obtain elastic shakedown for the experiments on smooth specimens by Wiersma et al. (2006); Wiersma and Taylor (2005) and Donnelly (2012) and plastic shakedown for the experiments on notched specimens by Wiersma et al. (2006); Wiersma and Taylor (2005).

In order to avoid possible material failures, we first compare the computed strains to the experimental strains to failure (see Table 13.5) and to the strains of the monotonic curves of Figures 13.8(a) and 13.8(b). The computed strains lie in the range 0.01-0.1 for all the specimens and loading conditions, thus avoiding possible premature failures.

Figure 13.10 shows the distribution of the dissipated energy, W^p, at the stabilized cycle, defined as follows:

$$W^p = \int_{cycle} \boldsymbol{\sigma} : \dot{\boldsymbol{\varepsilon}}^p dt \tag{13.5}$$

for the 50-notch specimen of Figure 13.4(a), subjected to a net pressure range of 360 MPa (see Figure 13.5(c)). As it can be observed, plasticity is localized in a very small region of about 0.01 mm (grain size) around the notch, where W^p assumes a maximum value of about 1 MPa; the remaining part of the specimen presents an elastic shakedown state and no W^p is manifested. The dissipated energy, W^p, is also plotted along the edge AB in Figure 13.10. Moreover, Figure 13.11 shows how mesh refinement does not allow noticeable improvements of the results in terms of dissipated energy.
The 100-notch and 145-notch specimens present similar results since they have the same net section.

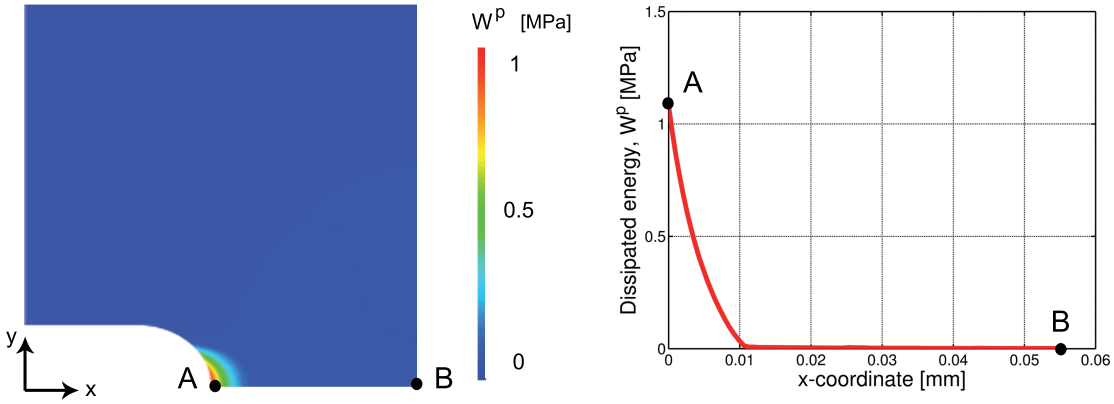

Figure 13.10: Results of the mechanical analysis for the 50-notch specimen subjected to a net pressure range of 360 MPa. Distribution of the dissipated energy, W^p, in the specimen (left) and along the edge AB (right).

Figure 13.12 shows the distribution of the dissipated energy, W^p, in the 50-fib specimen of Figure 13.4(b), subjected to a net pressure range of 320 MPa (see Figure 13.5(c)). In such a case, plastic effects are distributed in a very small zone of only 0.001 mm (1/10 grain size) around the smaller notch (point A), where W^p assumes a maximum value of 6 MPa, evidencing elevated gradient effects. Plastic effects are also visible around the bigger notch (point B) where, however, W^p assumes a maximum value of about 0.5 MPa, comparable to the one obtained for the 50-notch specimen. The dissipated energy, W^p, is also plotted along the edge AB in Figure 13.12.

The reported observations for the notch specimens are confirmed by the results of a linear elastic analysis conducted on each notched specimen to evaluate the stress concentration factor, K_t, defined as the ratio between the peak stress, σ_{peak}, at the root of the notch and the nominal stress, σ_{nom}, which would be

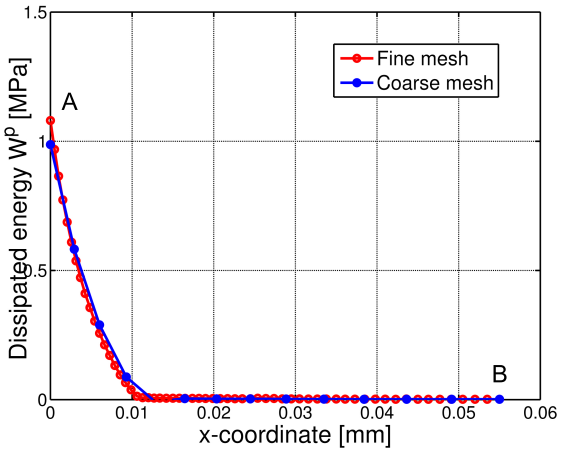

Figure 13.11: Results of the mechanical analysis for the 50-notch specimen subjected to a net pressure range of 360 MPa. Comparison between two mesh refinement in terms of the dissipated energy, W^p, along the edge AB.

present if a stress concentration did not occur (Pilkey and Pilkey, 2008):

$$K_t = \frac{\sigma_{peak}}{\sigma_{nom}} \tag{13.6}$$

In particular, we obtain a value of approximately 2.4 for the 50-notch, 100-notch, and 145-notch specimens (in accordance with the values provided in (Pilkey and Pilkey, 2008)) and of 6 for the 50-fib specimen.

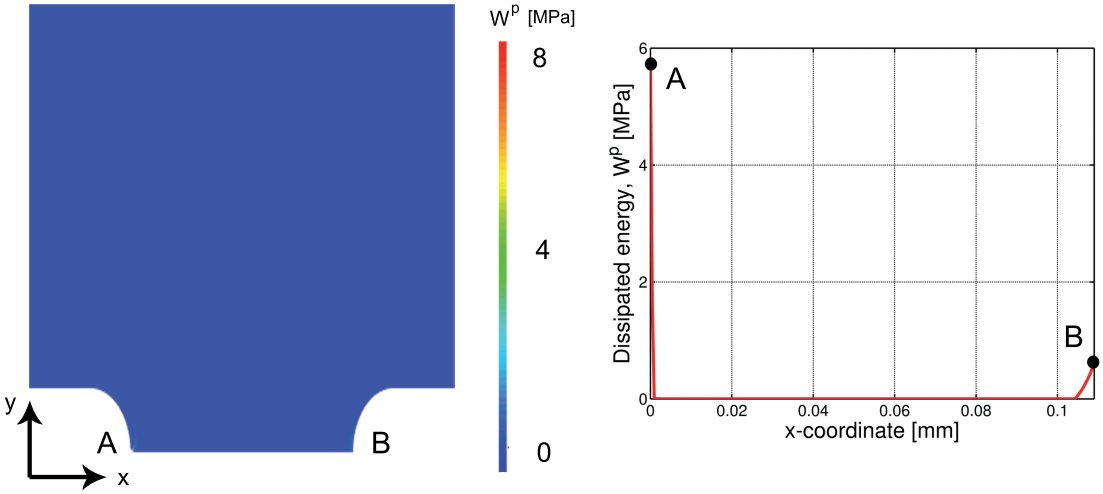

Figure 13.12: Results of the mechanical analysis for the 50-fib subjected to a net pressure range of 320 MPa. Distribution of the dissipated energy, W^p, in the specimen (left) and along the edge AB (right).

Figure 13.13(a) shows the distribution of the dissipated energy, W^p in the 60-hole and 1500-slot specimens of Figures 13.4(c)-(d), subjected to a net pressure range of 250 and 115 MPa, respectively (see Figure 13.5(d)). The values assumed by the dissipated energy are higher for the 1500-slot specimen, notwithstanding the lower load, and additionally, are distributed in a very small zone. In this case, the stress concentration factor, K_t, assumes a value of approximately 3 for the 60-hole, 6 for the 400-slot, and 10 for the 1500-slot specimen.

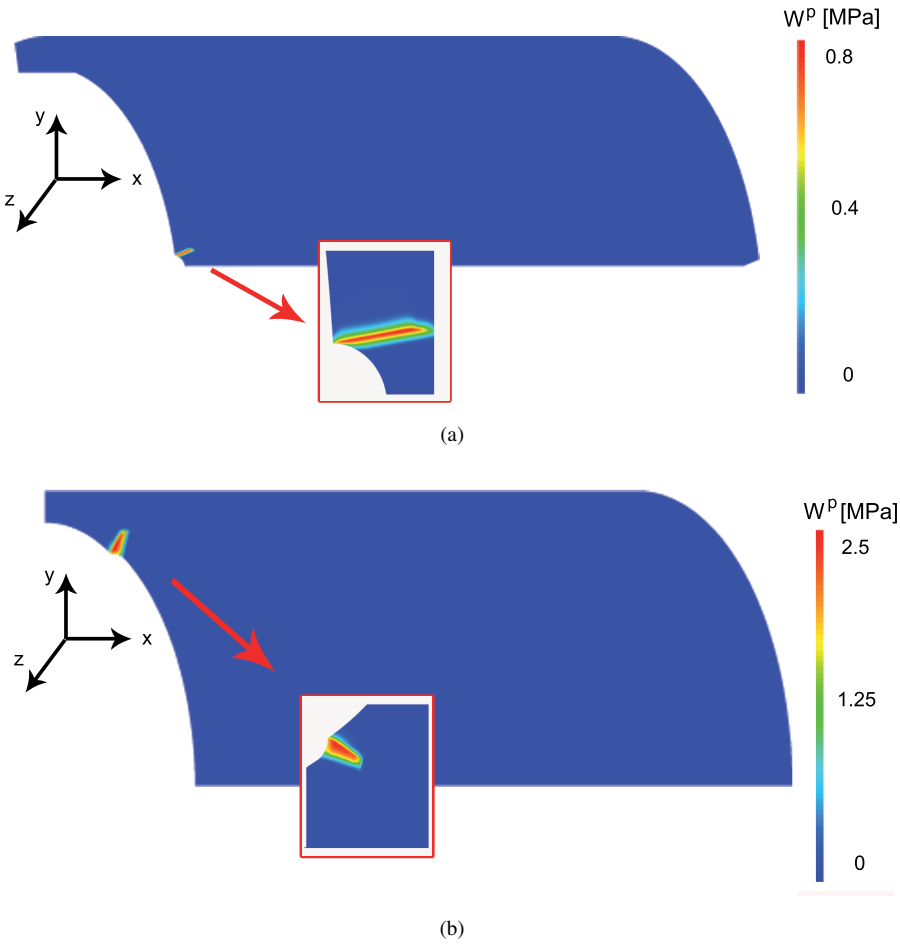

Figure 13.13: Results of the mechanical analysis in terms of the dissipated energy, W^p, for the (a) 60-hole subjected to a net pressure range of 250 MPa; (b) 1500-slot subjected to a net pressure range of 115 MPa.

13.4 316L steel: fatigue analysis

This Section presents the second step of the adopted global computational approach, i.e., the fatigue analysis to compute the number of cycles before failure. Such an analysis is based on the investigation of the stabilized cycle obtained within the mechanical analysis described in Section 13.3.3. In particular, depending on the nature of the shakedown cycle, i.e., elastic or plastic, we use a Dang Van (1999) or LCF crack initiation (Amiable et al., 2006, 2009a,b; Charkaluk and Constantinescu, 2009; Korsunsky et al., 2007) criterion, respectively. All the criteria are calibrated on the described experimental campaigns in order to provide a set of criteria that can be used to numerically predict the fatigue-life of cardiovascular 316L stainless steel stents.

13.4.1 Elastic shakedown: Dang Van criterion

The classical Dang Van (DV) criterion (Dang Van, 1999) has been described in Section 11.3.2. Without entering into details (see Section 11.3.2), a simple passages between the macroscopic and the mesoscopic scale allow to state that the lifetime is infinite if the mesoscopic shear stress, $\tau_\mu(t)$, and the hydrostatic stress, $\sigma_h(t)$, satisfy the following inequality in all the points of the structure (subscript μ stands for

mesoscopic variables):

$$\max_t \tau_\mu(t) + \alpha_\infty \sigma_h(t) \leq \beta_\infty \tag{13.7}$$

where α_∞ and β_∞ are material parameters (subscript ∞ stands for infinite lifetime). Such parameters are usually deduced from two Wöhler curves related to smooth specimens, giving the fatigue limit in alternated torsion and fully reversed bending. In general, the Wöhler curves are not defined for an infinite number of cycles but rather for 10^6-10^7 cycles. Thus, in the following, we indicate these coefficients as α_N and β_N, where subscript N stands for finite lifetime (Ferjani et al., 2011a,b; Wackers et al., 2010).

Material parameters, α_N and β_N, can be also calibrated by considering two uniaxial cyclic loadings with respective ratios R_1 and R_2 and fatigue limits f_{R_1} and f_{R_2}. In the simple case of a cyclic uniaxial bending loading of R ratio, expressed in the classical form $\sigma_{xx}(t) = \sigma_a \sin \omega t + \sigma_m$, we derive the following equation:

$$\frac{\sigma_a}{2} + \alpha_N \frac{\sigma_a}{3}\left(1 + \frac{1+R}{1-R}\right) = \beta_N \quad \forall R \tag{13.8}$$

which can be generalized for two different loadings of ratios R_1 and R_2, as follows:

$$\frac{f_{R_i}}{2} + \alpha_N \frac{f_{R_i}}{3}\left(1 + \frac{1+R_i}{1-R_i}\right) = \beta_N \quad \text{for } i = 1,2 \tag{13.9}$$

The following expressions for α_N and β_N are then obtained:

$$\begin{cases} \alpha_N = \dfrac{3}{4} \dfrac{f_{R_2} - f_{R_1}}{\dfrac{f_{R_1}}{1-R_1} - \dfrac{f_{R_2}}{1-R_2}} \\ \beta_N = \dfrac{f_{R_1} f_{R_2}}{\dfrac{f_{R_1}}{1-R_1} - \dfrac{f_{R_2}}{1-R_2}} \dfrac{R_1 - R_2}{2(1-R_1)(1-R_2)} \end{cases} \tag{13.10}$$

The DV parameters, α_N and β_N, are calibrated by using the experimental data on the smooth rectangular bars of 75, 100, and 150 μm widths, resulting in an elastic shakedown state (see Tables 13.4-13.6). The calibrated DV parameters refer to 10^7 cycles (i.e., $N = 10^7$) or to an equivalent stent implant period of approximately 8 months, instead of the requested 10^8 cycles (US Food and Drug Administration, 2010). We however remark that 10^7 cycles have already been considered as an infinite lifetime as, for example, in (Pelton et al., 2008; Subash, 1998), coherently with the definition given in (Donnelly, 2012; Wiersma et al., 2006; Wiersma and Taylor, 2005). Although specimens tested by Wiersma et al. (2006); Wiersma and Taylor (2005) and Donnelly (2012) refer to a fatigue-life of $2 \cdot 10^6$ and 10^7 cycles, respectively, we could set $N = 10^7$ for the specimens used for the calibration, since the slope of the fatigue curves of Figure 13.5(b) is almost horizontal (Wiersma et al., 2006; Wiersma and Taylor, 2005). For safety reasons, we assume a reduced fatigue limit of 400 MPa for the specimens tested by Wiersma et al. (2006); Wiersma and Taylor (2005) (see Table 13.4).
The calibrated DV parameters follow:

$$\begin{cases} \alpha_N = 0.4821 \\ \beta_N = 171.4286 \text{ MPa} \end{cases} \tag{13.11}$$

Figure 13.14 represents the diagram in terms of the mesoscopic shear stress, τ_μ, and the hydrostatic stress, σ_h, where the calibrated DV line (red smooth line) and the loading paths generated by the simulations of the experimental specimens of 75, 100, and 150 μm widths are represented. The maximum values for the hydrostatic stress are generated by the specimens tested by Donnelly Donnelly (2012) since presenting high values of mean stress, while the highest mesoscopic shear stresses are generated by the

specimen tested by Wiersma et al. (2006); Wiersma and Taylor (2005), presenting a higher load amplitude. Additionally, Figure 13.14 shows the calibrated DV line (red dot line) related to the specimen of 50 μm width, which presents a lower value of the fatigue-life due to size effects (Donnelly, 2012). As additional data for another R ratio are absent in this case, we construct such a DV line assuming the same slope as in the 75-150 μm width case.

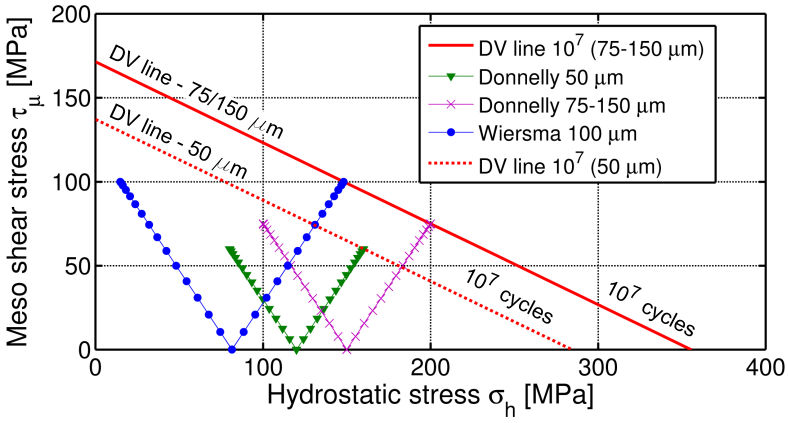

Figure 13.14: DV lines in the hydrostatic-mesoscopic stress plane and loading paths from the tensile experiments used for calibration (Donnelly, 2012; Wiersma et al., 2006; Wiersma and Taylor, 2005).

13.4.2 Plastic shakedown: fatigue crack initiation criteria

In the present Section, we focus on the following fatigue crack initiation criteria: (i) the Manson-Coffin criterion (Coffin, 1953; Manson, 1953); (ii) the dissipated energy per cycle criterion (Charkaluk and Constantinescu, 2009; Korsunsky et al., 2007); and (iii) a modified version of the dissipated energy criterion (Amiable et al., 2006, 2009a,b). Such criteria have been described in Section 12.3 and are denoted, respectively, as $\Phi_{\Delta\epsilon^p}$, Φ_{W^p}, and $\Phi_{W_{\sigma_h}}$, in the following. Moreover, in order to tackle the difficulties related to the high gradients of the fields close to the notched regions, we adopt a volumetric approach in the dissipated energy per cycle criterion. In the following, we compare the obtained results.

Discussion on results

The identification of material parameters, a, b and c, introduced in Eqs. (12.2), (12.4) and (12.6), is a regression problem which can be easily solved using existing solvers (e.g., the fitting tools, *cfootl* and *sftool*, in Matlab).
Such parameters are identified by postprocessing the values of the fatigue damage parameters, $\Delta\epsilon^p$, W^p, and $(W^p + a\sigma_h^{max})$, computed at the root of the notch (hot-spot approach) or around the notch (volumetric approach). In particular, the volumetric approach consists in considering a process volume for fatigue mechanisms (Dang Van et al., 2009; Maitournam et al., 2009) and in assuming such a volume to be a cylinder for the three-dimensional specimens (slot tubes) and a circle for the two-dimensional specimens (notch bars) with the center corresponding to the root of the notch. We evaluate the radius of the cylinder/circle by minimizing the differences between the experimental and predicted numbers of cycles.
We apply such an approach to the dissipated energy criterion, Φ_{W^p}, since averaging the dissipated energy inside a process volume can be seen as a distribution of plastic localization around the notch. The size of the radius which minimizes the differences between the experimental and predicted numbers of cycles results of 0.01 mm (grain size).

Criterion	**Approach**	a	b	c	R^2
$\Phi_{\Delta\epsilon^p}$	Hot-spot	-	-0.4214	0.6199	0.75
Φ_{W^p}	Hot-spot	-	-0.4687	431.4 MPa	0.74
Φ_{W^p}	Volume element	-	-0.6187	907.8 MPa	0.86
$\Phi_{W_{\sigma_h}}$	Hot-spot	0.00203	-0.3641	137.1 MPa	0.76

Table 13.8: Calibrated material parameters, a, b, and c, and obtained correlation coefficient, R^2.

Table 13.8 lists the calibrated parameters, a, b and c, for the considered criteria.
Figures 13.15(a)-(c)-(e) and 13.16(a) present the diagram in terms of the fatigue parameter and the experimental number of cycles to failure, while Figures 13.15(b)-(d)-(f) and 13.16(b) present the comparison between the experimental and the estimated number of cycles to failure for both the hot-spot and volumetric approaches. The results can be placed in a scattered band with a factor of ± 3 on the number of cycles to failure, corresponding to the standard deviation.

As a first observation, the lifetimes predicted with the hot-spot approach are not well predicted by all the criteria, while the volumetric approach gives very good results as the points are inside the ± 3 factor on the lifetimes. However, all the hot-spot criteria predict safely lower numbers of cycles to failure.

As it can be observed from Figures 13.15(b)-(d)-(f), the hot-spot approach fails into predicting the fatigue limits of the 50-fib and 1500-slot specimens due to their high stress gradients and plastic strain localization at a distance of only few microns near the notch (see Section 13.3).
This aspect has been also treated by Wiersma et al. (2006); Wiersma and Taylor (2005) who observed that the three notched bar specimens (i.e., the 50-notch, 100-notch, and 145-notch bars) have the same fatigue behavior in terms of net stress range (a fact which might be anticipated from basic notch theory, since the stress field of these notches is almost identical as well), as reported in Table 13.4. On the contrary, the fatigue limit of the 50-fib specimen is slightly lower. This has important consequences for the design of microscopic components, because it implies that very small root radii can be used in components such as stents, without compromising their fatigue behavior (Wiersma et al., 2006). Slotted tube specimens (i.e., the 60-hole, 400-slot, and 1500-slot tubes) show a decreasing fatigue limit with increasing slot length (see Table 13.4).

Moreover, we observe that the dissipated energy criterion and its modified version present almost the same results. This can be due to the fact that both these criteria based on values computed at the root of the notch fail in case of high stress gradients. To this purpose, Figure 13.17 presents the diagram in terms of the dissipated energy, W^p, and the maximal hydrostatic stress, σ_h^{max}, for all the specimens and shows very high values of the hydrostatic terms for the 50-fib and 1500-slot specimens. We observe also that there is a linear correlation between the dissipated energy and the maximal hydrostatic stress.

To compare accurately the prediction capabilities of the different criteria, we propose to use the correlation coefficient, R^2, corresponding to the linear association between experimental and computed fatigue lifetimes. R^2 is defined as in standard statistical textbooks (Di Bucchianico, 2008), as follows:

$$R^2 = 1 - \frac{\sum_j \left(N_j^{exp} - N_j^{comp}\right)^2}{\sum_j \left(N_j^{exp} - \overline{N}\right)^2} \tag{13.12}$$

where N_j is the number of cycles related to experiment j (subscripts exp and $comp$ stand for the experimental and the computed values of the number of cycles, respectively), and $\overline{N}$ is the mean of the experimental data.
Table 13.8 lists the computed correlation coefficients for each criterion. The obtained values lie in a reasonable range of reliability for the criteria (see, e.g., (Tabibian et al., 2013) for comparison). However, the results related to the hot-spot approach show relative low values of $R^2 \approx 0.74$-0.76, while the volumetric

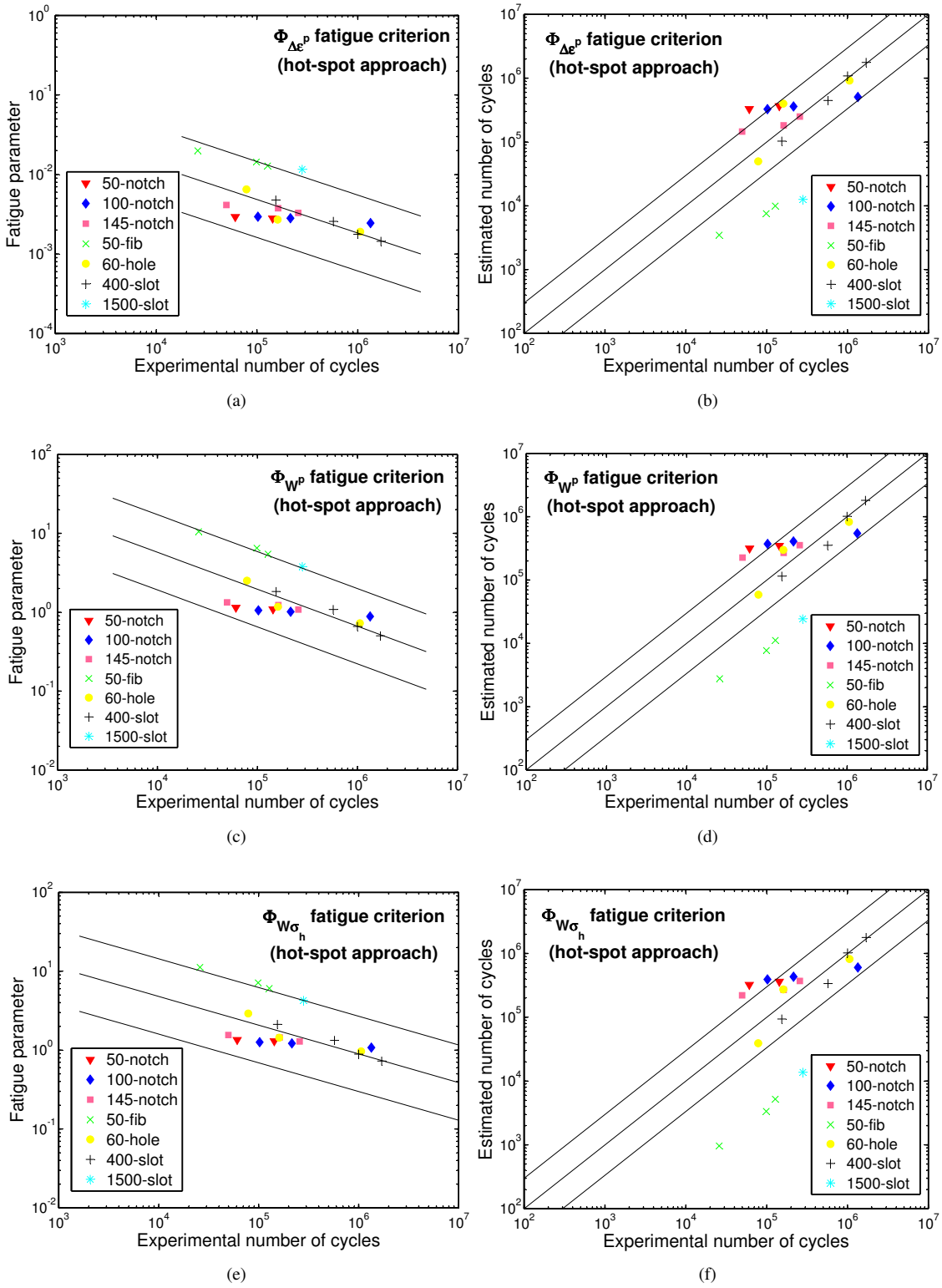

Figure 13.15: Hot-spot approach for the $\Phi_{\Delta\epsilon^p}$, Φ_{W^p}, and $\Phi_{W_{\sigma_h}}$ fatigue criteria. (a)-(c)-(e) Fatigue parameter vs. experimental number of cycles to failure; (b)-(d)-(f) estimated vs. experimental number of cycles to failure.

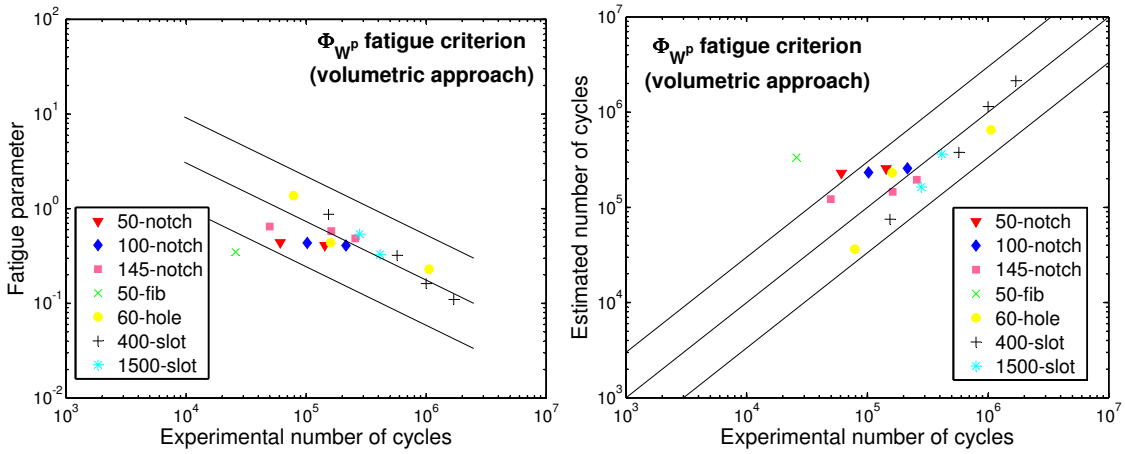

Figure 13.16: Volumetric approach for the Φ_{W^p} fatigue criterion. (a) Fatigue parameter vs. experimental number of cycles to failure; (b) estimated vs. experimental number of cycles to failure.

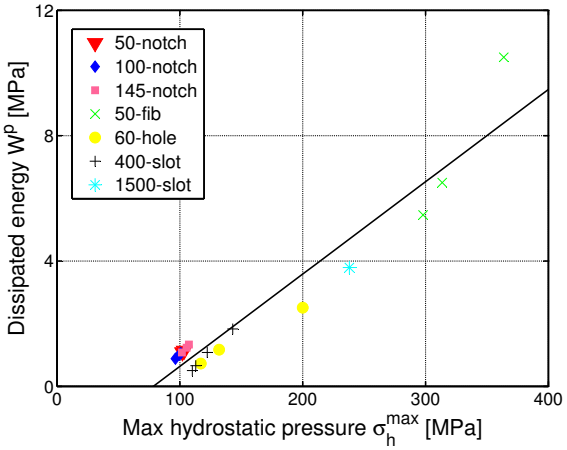

Figure 13.17: Dissipated energy, W^p, vs. maximal hydrostatic stress, σ_h^{max}, computed at the notch root.

approach $R^2 = 0.86$. Consequently, all the hot-spot approach criteria are relatively equivalent for the lifetime prediction, while the volumetric approach demonstrates its capability in lifetime prediction of notched μm-size specimens.

13.5 Conclusions

The present Chapter has explored the fatigue of stainless steel microsize components by analyzing experimental data from the literature. The specimens were either smooth or notched and presented features similar to those characterizing cardiovascular stents. In fact, 316L stainless steel for biomedical devices is subjected to conditions (e.g., HCF or VHCF loading and corrosive environment) completely different from those characterizing standard applications as nuclear components, and additionally, it is employed in structures of very small sizes (of the order of grain size).

The proposed work has investigated several fatigue criteria for infinite and finite lifetime, i.e., the fatigue criteria by Dang Van and Manson-Coffin as well as the dissipated energy per cycle criterion and its modified

version, associated with hot-spot as well as volume element approaches. The results have demonstrated that the volume element approach is efficient in the presence of high stress gradients and size effects. The provided criteria, calibrated on suitable experimental data, can be used in the numerical fatigue-life assessment of cardiovascular 316L stainless steel stents.
In order to effectively demonstrate the reliability of the proposed criteria, next Chapter will focus on the introduction of a computational approach which combines advanced numerical methods with fatigue-life prediction methodologies and available material fatigue data to lay down the basis for the prediction of fatigue-controlled service life of biomedical stents. The idea of introducing material variability as a probability density function will be the object of future work.

Chapter 14

A computational approach for the fatigue-life prediction of cardiovascular balloon-expandable stents

This Chapter proposes the introduction of a reliable and general methodology for the numerical fatigue-life assessment of cardiovascular balloon-expandable stents. To this purpose, the main idea is to combine advanced computational methods and fatigue prediction techniques with available material fatigue data in order to lay down the basis for a complete fatigue-life methodology for balloon-expandable stents. In particular, the present Chapter investigates the fatigue behavior of a classical 316L stainless steel coronary stent design (i.e., the Medinol/Boston Scientific NIR™stent) through a global computational approach composed of a mechanical finite element analysis, followed by a fatigue analysis. After assuming an appropriate material constitutive model and computing the loading of the stent during the implant, the fatigue analysis is conducted through the application of the multiaxial high-cycle fatigue criterion by Dang Van. Such a criterion is calibrated on experimental data on 316L stainless steel μm-size components, used during industrial stent manufacturing, as reported in Chapter 13.

The Chapter is organized as follows. Section 14.1 starts with an introduction to the problem and explains the motivations of the proposed work. Section 14.2 presents the mechanical analysis. Then, Section 14.3 describes the fatigue analysis. Conclusions are finally given in Section 14.4.

14.1 Introduction and motivations

Cardiovascular disease has become a major global health care problem in the last decade. The advantage of stenting intervention with respect to the classical bypass surgery has been largely demonstrated in the treatment of heart disease (AHA, 2010).

Stents are small tube-like medical devices used to restore patency of blood vessels where the lumen area is reduced due to atherosclerosis, a degenerative disease of the vessel wall. The stent acts as a mechanical scaffold for the vessel and its implant is performed by a minimally invasive procedure inserting a catheter through a small incision in the femoral artery.

Several materials, as the 316L austenitic stainless steel, the cobalt-chromium alloy or the NiTi-based shape memory alloy, have been imposed as standard materials for cardiovascular stents (Bombac et al., 2007; Disegi et al., 1999; Petrini and Migliavacca, 2011; Winters and Nutt, 2003). As an example, the 316L stainleess steel is used for the PalmazSchatz (Cordis) or the Medinol/Boston Scientific NIR™balloon-expandable stents, thanks to its good properties in the fully annealed condition, e.g., well adapted mecha-

nical characteristics (i.e., great ductility, high tensile strength, and a raised elastic limit), biocompatibility, resistance to corrosion as well as fatigue performances (Winters and Nutt, 2003).

Although stent design is considered a relatively mature topic, recently, fatigue failure has emerged as one of the main cause of stent drawback (Hibbert and O'Brien, 2011; Morlacchi et al., 2014; Shaikh et al., 2008; Sianos et al., 2004). This indicates the need for a deeper understanding of fatigue and fracture failure in microsize components and for a reliable fatigue design procedure.
In particular, stent fatigue investigation represents a complex task since these devices have to withstand both their initial deployment within the artery, which involves large amounts of plastic strains, and the long-term service loading induced by the pulsing blood pressure (Aziz et al., 2007; Dumoulin and Cochelin, 2000). Moreover, stents should survive at least for 10 years without exhibiting failure (US Food and Drug Administration, 2010). This constraint translates into 400 million cycles during stent lifetime, since 70 artery pulses per minute impose 40 million cycles per year. Therefore, the design lies within the high- and very high-cycle fatigue regime (denoted, respectively, as HCF and VHCF) (Schijve, 2009; Suresh, 1998).

The reliability or fatigue design of stents is, however, a complex task due to a series of conditions: small-size of the devices, manufacturing-induced features, complex material behavior, corrosive environment. Stents are in fact manufactured either through welding of microscopic wires or through laser cutting from thin-walled tubes, both leading to a final truss-type structure composed of struts connected by hinges, whose small thicknesses generally belong to the range of 50-150 μm (Harewood and McHugh, 2007; Murphy et al., 2006, 2003; You et al., 2006). Both these manufacturing processes induce the presence of stress concentration features, in particular, of small radius connections affecting stent fatigue behavior (Wiersma et al., 2006). We also remark that μm-size components like stents have the same order of magnitude as microstructure of steel alloys, i.e., the specific ratio between the length scales of the mesoscopic structure of grains and of the macroscopic structure of the device, characterized by approximately 10-20 grains in the section, makes the application of standard bulk models inadequate (Connolley et al., 2005; Harewood and McHugh, 2007; Murphy et al., 2006, 2003; You et al., 2006). Moreover, despite the importance of such applications and the associated difficulty, the literature dispose of few experimental data sets (Donnelly, 2012; Glenn and Lee, 1997; Szymczak et al., 2009; Weiss and Meissner, 2006; Weiss et al., 2009; Wiersma et al., 2006; Wiersma and Taylor, 2005).

In order to bridge the gap between the existing experiments and the fatigue design of such components, several computational tools, as finite element (FE) analysis, have already proved extensively their usefulness for stent design, e.g., (Auricchio, 2001; Cao et al., 2009; De Beule et al., 2008; Grogan et al., 2013; Ju et al., 2008; Martin and Boyle, 2013; Wang et al., 2009). Among the others, only a few works deal with the numerical fatigue-life assessment of stents, e.g., (Azaouzi et al., 2012b; Barrera et al., 2012; dos Santos et al., 2012; Harewood and McHugh, 2007; Li et al., 2010; Marrey et al., 2006; McGarry et al., 2004; Perry et al., 2002; Schievano et al., 2010; Sweeney et al., 2012), which however are not calibrated from real precise experiments on stents. As an example, the interesting work by Sweeney et al. (2012) introduces a refined FE 316L stent fatigue methodology based on crystal plasticity theory and some simple criteria calibrated on experiments related to macroscopic specimens (Lemaitre and Chaboche, 1994). Additionally, many computational modeling works on stents directly apply bulk material properties to the structure (Auricchio, 2001; Azaouzi et al., 2012b; Barrera et al., 2012; dos Santos et al., 2012; Li et al., 2010; Marrey et al., 2006; Schievano et al., 2010). Among these works, the recent work by dos Santos et al. (2012) presents a numerical lifetime procedure for the analysis of balloon-expandable stainless steel stents by incorporating a two-scale plasticity-damage model (Lemaitre et al., 1999). Such an approach, however, requires the calibration of several parameters, which has been done by referring to experimental data on macroscopic specimens. The work by Barrera et al. (2012) applies the multiaxial HCF criterion by Dang Van (1999) to cardiovascular stents. Such a criterion, based on a micro-macro approach, successfully meets the need of microstructural representation in crack initiation predictions. However, the work by Barrera et al. (2012) does not investigate the experimental data used for the criterion calibration (Wiersma et al., 2006; Wiersma and Taylor, 2005) and assumes the same fatigue limits in bending and torsion. The

work by Azaouzi et al. (2012b) predicts the fatigue-life of 316L stainless steel stents through the well-known Goodman diagram and the theory of critical distance based on the results provided by Wiersma et al. (2006); Wiersma and Taylor (2005). The Goodman parameters are again calibrated on experimental data by Wiersma et al. (2006); Wiersma and Taylor (2005) without a detailed investigation.

The aim of the present Chapter is the introduction of a computational approach for the lifetime assessment of a classical coronary stent design (i.e., the Medinol/Boston Scientific NIR™stent). The main idea is to adapt and interpret classical notions, models, and techniques as well as to consider suitable experimental data for the calibration of stent fatigue criteria, in order to obtain a reliable, general and coherent fatigue prediction methodology for biomedical balloon-expandable stents.

The proposed methodology is based on the introduction of a global computational approach, composed of a three-dimensional mechanical FE analysis, followed by a fatigue analysis. The mechanical FE analysis calculates the shakedown or stabilized mechanical state of the stent under investigation, by assuming the structure, loading, and material behavior known. The fatigue analysis is then based on the investigation of the stabilized state obtained within the mechanical analysis and it is conducted by using the results presented in Chapter 13, where we proposed several fatigue criteria for the fatigue-life assessment of 316L stainless steel stents, calibrated on the experimental data (Donnelly, 2012; Wiersma et al., 2006; Wiersma and Taylor, 2005) on smooth and notched μm-size components, produced with the standard procedure applied in the stent manufacturing industry. In particular, we investigated the criterion by Dang Van (1999) and several LCF crack initiation criteria (Amiable et al., 2006; Charkaluk and Constantinescu, 2009; Coffin, 1953; Korsunsky et al., 2007; Manson, 1953).
Since the investigated stent results in an elastic shakedown state from the performed mechanical FE analysis, we conduct the fatigue analysis through the application of the multiaxial HCF criterion by Dang Van (1999). Such a criterion takes into account the micrometric size of biomedical components as well as material monotonic and cyclic behavior.
The results from both the mechanical and fatigue analyses are compared to several results available from the literature in order to assess the validity and reliability of the proposed methodology.

Consequently, the present work combines advanced computational methods with fatigue-life prediction methodologies and available material fatigue data to lay down the basis for the prediction of fatigue-controlled service life of biomedical balloon-expandable stents.

14.2 Mechanical analysis

In this Section we illustrate the mechanical analysis performed with the FE method to compute the loading and the stabilized state of the stent during and after the implant.
In particular, we adopt a stent model resembling the design of the Medinol/Boston Scientific NIR™stent, which is nowadays a classical coronary stent design. However, it is worth noting that the present study aims at proposing a general numerical framework addressing the fatigue behavior of a generic stent design, independently of the chosen shape or material of the stent.

14.2.1 Stent: geometrical modeling and mesh

The geometry of the adopted stent model is based on the information reported by Sweeney et al. (2012). The generation of such a model is defined by a series of steps, detailed in the following.
We firstly create a planar computer aided design representation of the stent, using the software Rhinoceros v.4.0 (McNeel & associates, Seattle, WA, USA). The unfolded geometry of the device can be constructed by mirroring and replicating a primitive geometry, shown in Figure 14.1(a). The FE mesh is obtained by meshing the primitive geometry as reported in Figure 14.1(b) and similarly by mirroring and replicating it, as shown in Figure 14.1(c). The software used for this operation is Abaqus v.6.11 (Simulia, Dassault Systems, Providence, RI, USA). The final mesh of the stent is presented in Figure 14.1(d).

The whole stent model has an outer diameter of 0.876 mm and a length of 8.049 mm. As depicted in Figure 14.1(a), both strut thickness and width are approximately 0.10 mm. We remark that the characteristic dimensions of the stent geometry are comparable to the dimensions (ranging from 0.05 to 0.15 mm) of the specimens (Donnelly, 2012; Wiersma et al., 2006; Wiersma and Taylor, 2005), on which the considered fatigue criteria have been calibrated (for details, see Chapter 13).
The mesh is defined by 89760 nodes and 57600 three-dimensional brick elements (C3D8) available in the element library of the software Abaqus v.6.11, used as finite element analysis (FEA) solver. Taking into account the grain size given in (Donnelly, 2012; Wiersma et al., 2006; Wiersma and Taylor, 2005), the actual mesh has about 2 elements per grain.

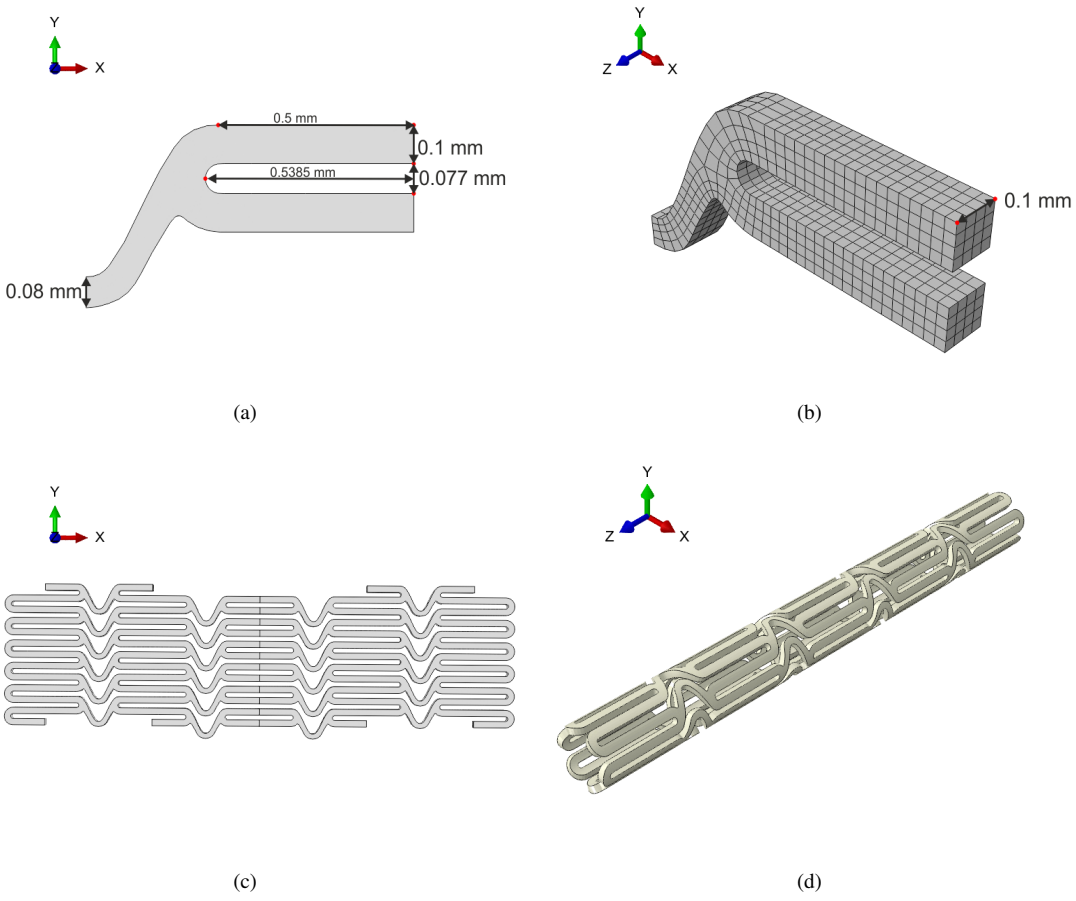

Figure 14.1: Stent geometrical modeling and mesh: (a) primitive geometry; (b) mesh of the geometrical unit of the design; (c) creation of the stent model by replicating and mirroring the mesh of the geometrical unit along the plane; (d) final stent model.

14.2.2 Stent: constitutive modeling

The stent is assumed to be made of a 316L stainless steel. Since stent lifetime is affected by the initial deformation due to the crimp and deployment processes and by systolic-diastolic cyclic loading, the adopted material model has to simulate both monotonic and cyclic behaviors of 316L stainless steel. In particular, we adopt a J_2 elastoplastic constitutive model with non-linear isotropic and kinematic hardening (with one kinematic center), which facilitates computational studies of both monotonic and cyclic behaviors of 316L

stainless steel.

The J2 continuum constitutive model has been described in Section 13.3.2 and it is already implemented within the material library of the FEA software Abaqus v.6.11 and labeled by the keyword **Plastic, hardening=COMBINED, number backstresses=1*.

It is worth noting that we adopt a constitutive model calibrated on experimental data related to both monotonic and cyclic behavior of 316L stainless steel. However, we make a simplifying assumption concerning size effects and the application of a continuous model to a structure with sizes close to the grain size, explained as follows. Since an important feature of cardiovascular stent applications is given by their small size, where the size of the structure is close to that of the representative volume element, one could reasonably suggest that an appropriate model should include crystal plasticity. This would further imply that the microstructure is precisely known or that a Monte Carlo method is needed to estimate the solution for different grain orientations (Morhácová, 1995). Therefore, in our work, we simply assume to consider a homogenized macroscopic approach and that the size effect is taken into account through the fatigue-life estimations based on μm-size experiments.

14.2.3 Vessel: geometrical modeling, mesh, constitutive modeling

The coronary artery is modeled as an idealized vessel represented by a thick-walled pipe with an initial inner diameter of 2 mm, wall thickness 0.5 mm and length 14 mm.
The mesh model consists in 19552 nodes and 14508 hybrid three-dimensional brick elements (C3D8H) available in the Abaqus v.6.11 element library.

The mechanical response of the artery wall is modeled using polynomial hyperelastic model, suitable for incompressible isotropic materials and available in the software material library as **Hyperelastic*; see (SIMULIA, 2012). The adopted material parameters stem from the work by Lally et al. (2005, 2006), who performed FEA of coronary stenting to investigate the impact of stent design on vessel tissue solicitation.

14.2.4 Analysis set-up

The device is first mounted onto an angioplasty balloon, through a radial crimping in order to ensure the necessary grip between the device and the delivery system. Subsequently, the balloon/stent system is driven to the target vascular region and, once in place, the balloon is inflated forcing the stent deployment. After the acute elastic recoil, the stent acts as a scaffold of the vessel ensuring the lumen patency.

Although comprehensive simulation of stenting would embed all the previously described procedural steps, i.e., crimping, delivery and deployment (Mortier et al., 2010), in the present study we neglect the delivery stage for three specific reasons. From the mechanical point of view, the solicitations experienced by the stent during crimping and deployment are more predominant when compared to those imposed by the stent delivery. Furthermore, given the study aim, our main interest regards the pulsatile solicitation experienced by the stent after its implant. Nevertheless, such a choice reduces significantly the computational cost of the analysis.
For such reasons, we split the stenting simulation in two analyses: the first one accounts for the stent crimping, while the second one addresses the simulation of stent deployment and the subsequent physiological loading within the artery (i.e., fatigue loading).

Stent crimping

The FE model of this analysis accounts for two parts: the stent and a rigid cylinder, which is aimed at imposing the reduction of the stent outer diameter; the rigid surface is discretized by 1280 4-node quadrilateral surface elements (SFM3D4) and 1312 nodes.
The analysis is divided in two steps. In the first step the outer diameter of the rigid surface is reduced from 0.9 mm to 0.72 mm through a displacement-driven strategy. At the same time, a surface-to-surface

contact is activated between the outer surface of the stent and the inner surface of the rigid cylinder. In particular, we adopt a frictionless contact characterized by hard contact pressure-overclosure relationship for the normal component, enforced by linear penalty method (with 0.001 as a scale factor for the default linear penalty stiffness). In the second step, the rigid cylinder is re-enlarged allowing the elastic recoil of the stent, which however keeps partially crimped. At the end of the analysis the outer stent profile is reduced from 0.876 mm to 0.758 mm. Appropriate boundary conditions are applied to some stent nodes to avoid rigid motion.

Stent deployment and physiological loading

This second stage of the analysis has the final increment of the previous analysis as starting point, i.e., see Figure 14.2(a). In fact, the loaded and deformed configuration of the crimped stent is imported in the simulation environment, which now consists of three model parts: i) the stent itself, ii) the vessel, and iii) the balloon. The vessel and the balloon are modeled as previously discussed (see Section 14.2.3). The balloon inflation is consequently modeled through a displacement-driven analysis where an uniform radial displacement is imposed to the cylindrical rigid surface imposing the corresponding stent enlargement through the contact with the inner stent surface.
The analysis is divided into the following steps:

1. *vessel inflation*: the arterial model is pressurized through the application of an internal pressure of 120 mmHg. Assuming a cylindrical coordinate system, axial and circumferential displacements of the vessel ends are fixed, allowing only the radial displacement.

2. *stent expansion*: the balloon model is radially enlarged, allowing the stent expansion to the target outer diameter of 3 mm, as shown in Figure 14.2(b). In this step two contact pairs are activated: the first between the inner surface of the stent (slave surface) and the outer surface of the balloon model (master surface) and the second between the inner surface of the vessel (slave surface) and the outer surface of the stent (master surface). The contact settings are similar to those adopted for the crimping analysis.

3. *vessel deflation* (diastole): in this step the contact between the balloon and the stent is deactivated and the inner pressure reduced to 80 mmHg, thus mimicking the diastolic conditions and allowing the stent/vessel system to reach the equilibrium after elastic recoil; see Figure 14.2(c).

4. *vessel inflation* (systole): the internal pressure of artery is again increased to 120 mmHg, thus simulating the systolic condition, closing a loading cycle.

The analysis is then completed by ten loading cycles.

Considerations

It is worth noting that, as the first main goal of the present study is to propose a fatigue-life numerical method for the analysis of balloon-expandable coronary stents, and not an accurate simulation of the stent implant, the adopted modeling procedure does not take into account the actual in-vivo behavior of the stent. More realistic simulations should account for patient-specific vessel geometry and anisotropy of the vessel tissue (Mortier et al., 2010). Also regarding this point, although the inclusion of the balloon can provide a more realistic representation of the transient deformation during the deployment (De Beule et al., 2008; Gervaso et al., 2008), the balloon is herein modeled as an expanding cylinder. Further developments of the present work will focus on the impact evaluation of these aspects on the computation of the stent stress state and the related fatigue-life assessment.
As for the loading conditions, systolic-diastolic pulsatile pressure is not the only clinical force/deformation mode that must be addressed in bench testing or analysis. Other cyclic deformation modes, such as arterial

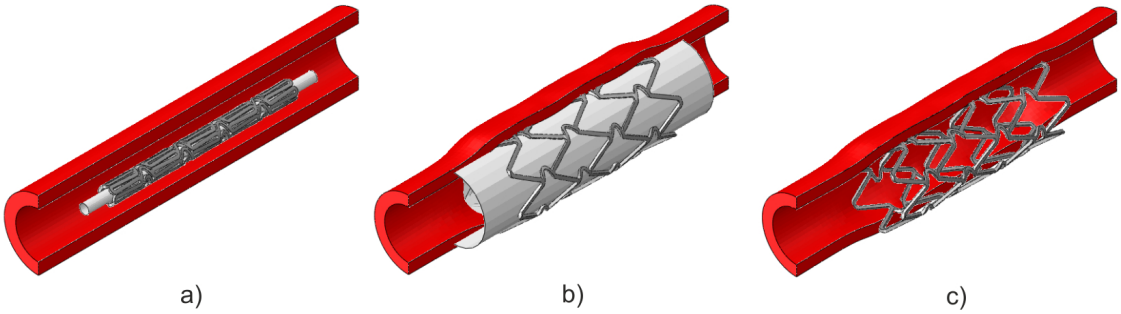

Figure 14.2: Simulation of stent deployment: a) initial configuration; b) maximum balloon expansion (the contact between the balloon and the vessel is not activated); c) stent/vessel configuration after balloon deflation.

bending, crushing, axial tension or compression, and torsion, can occur at various frequencies and phases, appearing due to the different physiological forcing functions (e.g., cardiac, respiratory, locomotion), as well as the physiological environment, in particular humidity and corrosion conditions, should also be accounted for.

14.2.5 Discussion on results

Table 14.1 reports several outputs at different steps of the performed FE simulation, i.e., at crimping, maximum balloon expansion, systole and diastole. In particular, we report the diameter of the central section of the stent as well as the maximum and minimum values, among all the elements of the stent model, of the von-Mises equivalent stress (MISES), equivalent pressure stress (PRESS), and equivalent plastic strain (PEEQ).
As expected, the diameter of the stent increases from a value of 0.737 mm during crimping to a value of 3.022 mm at maximum balloon inflation. The passage from systole to diastole results in a very low diameter change of 0.002 mm. The von-Mises equivalent stress ranges between a minimum value of 0.898 MPa during crimping and a maximum value of 442.067 MPa at maximum balloon inflation. Similarly, the equivalent pressure stress reaches its (absolute) maximum values at maximum balloon inflation and presents almost constant values during systole and diastole. The presented results highlight very high values of the equivalent plastic strain, especially at maximum balloon inflation, which slightly increase during systole and remain constant during diastole. Such values evidence how both the initial deployment of the stent within the artery and the long-term service loading induced by the pulsing blood pressure are important steps which need to be accounted for during stent design and simulation.

In order to further investigate the results presented in Table 14.1, we focus on the distribution of the variables of interest in a stent strut composed of two axialsymmetric units; the single unit is shown in Figure 14.1(b).

Residual stresses introduced in the described analysis steps can be clearly seen in the von-Mises equivalent stress (MISES) distributions along the stent strut of Figure 14.3. In particular, we report three views of the stent strut (indicated, respectively, as *View 1*, *View 2*, and *View 3*) at different steps of the FE simulation, i.e., at crimping, maximum balloon expansion, systole and diastole.
After the elastic recoil, the von-Mises stress distribution remains mainly at the inner regions of the curved stent strut sections (see *View 1* and *View 2* for *crimping*) and it is particularly concentrated along the thickness of the strut with the lowest curvature radius (see *View 3* for *crimping*). The highest stresses are generated in the same regions at maximum balloon inflation (see *View 1*, *View 2*, and *View 3* for *max expansion*). The von-Mises stress distribution during fatigue loading at systole and diastole peaks is almost

Step	**Diameter** [mm]	**MISES** [MPa]		**PRESS** [MPa]		**PEEQ** [%]	
		Max	*Min*	*Max*	*Min*	*Max*	*Min*
Crimping	0.737	249.745	0.898	138.640	-126.074	5.500	0
Max balloon expansion	3.022	442.067	2.515	482.840	-475.611	95.800	0
Systole	2.760	421.852	3.386	252.984	-271.799	99.700	0
Diastole	2.758	441.905	3.806	252.071	-271.702	99.700	0

Table 14.1: Simulation outputs at different FE analysis steps. The following results are reported: diameter of the central section of the stent and maximum and minimum values, among all the elements of the stent model, of the von-Mises equivalent stresses (MISES), equivalent pressure stresses (PRESS), and equivalent plastic strains (PEEQ).

the same and again shows the highest values at the inner regions of the curved stent strut sections (see *View 1*, *View 2* and *View 3* for *systole* and *diastole*).

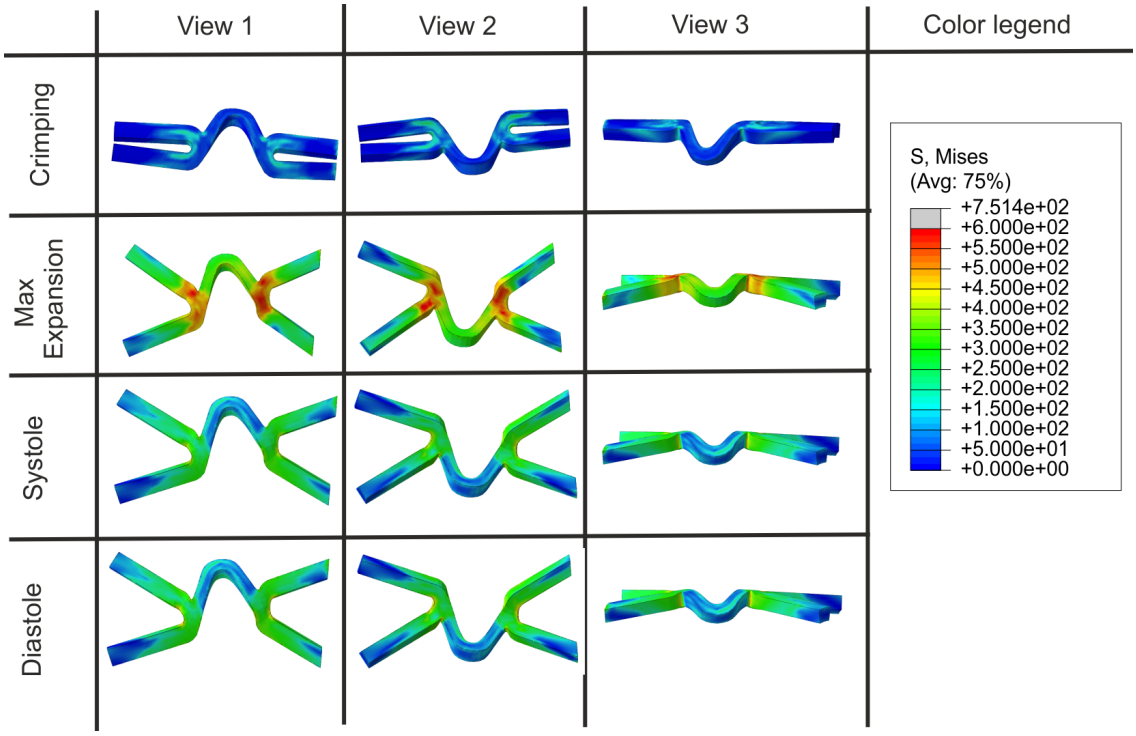

Figure 14.3: Contour plot of the von-Mises equivalent stress (MISES) distribution [MPa] along the stent strut. Three views of the stent strut (indicated, respectively, as *View 1*, *View 2*, and *View 3*) are reported at different steps of the stent FE simulation, i.e., at crimping, maximum balloon expansion, systole and diastole.

Contour plots of the equivalent pressure stress (PRESS) are presented in Figures 14.4(a) and 14.4(b) at different analysis steps. The maximum values are again reached at maximum balloon inflation, as shown in Figure 14.4(a), while decrease at diastole peak, as reported in Figure 14.4(b). Similarly to the von-Mises stress distribution, the pressure distribution remains mainly at the inner regions of the curved stent strut

sections and along the thickness. Such a concentrated distribution of both the von-Mises and pressure stresses will affect the fatigue-life of these regions, as explained in the following Section.

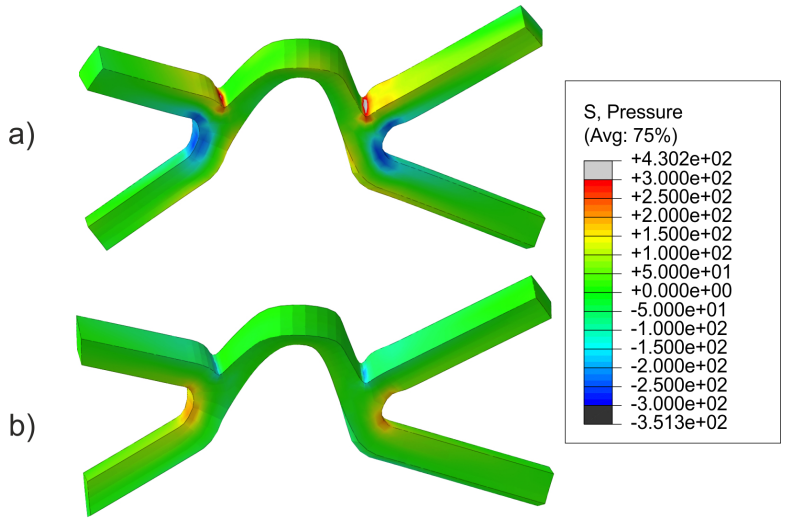

Figure 14.4: Contour plot of the equivalent pressure stress (PRESS) distribution [MPa] along the stent strut at different analysis steps: (a) at maximum balloon inflation; (b) at diastole peak.

As already mentioned above, high values of the equivalent plastic strain (PEEQ) are reached at the maximum balloon expansion (see Table 14.1). This could imply a failure of material during initial deployment of the stent rather than during fatigue loading. To this purpose, we propose to investigate also the distribution of the equivalent plastic strain along the entire stent during the analysis steps. We remark, moreover, that many works from the literature, dealing with stent fatigue, have mainly focused on variable evolution during fatigue loading without analyzing a possible failure during deployment.
Figure 14.5 shows the histogram of the equivalent plastic strain at different analysis steps, i.e., at post crimping, maximum balloon inflation, systole, and diastole. The frequency is defined as the ratio between the number of elements, N_{el}, and the total number of elements of the mesh, N_{tot}. The values assumed by the equivalent plastic strain during the analysis are divided into five intervals ranging from 0 to 100%. As it can be observed, the major percentage of elements (about 90-95$\%$) presents low equivalent plastic strain values ranging from 0 to 20% at all the analysis steps. In particular, 93% of elements at post crimping, 67% of elements at maximum balloon inflation, and 65% of elements at diastole and systole present values between 0 and 1%. Only few elements (0.0885% at max balloon inflation and 0.1163% at diastole and systole), mainly located at the inner regions of the curved stent strut sections, show values of the equivalent plastic strain in the range 80-100$\%$.

Recalling the discussion of Section 14.1, the mechanical FE analysis allows to calculate the variables of interest at the shakedown or stabilized mechanical state reached by the stent under investigation, to be then used for the fatigue analysis. As a result of the mechanical FE analysis, we obtain a stabilized cycle under elastic shakedown. This is particularly clear by recalling the results provided in Table 14.1 and Figure 14.5, which show a constant value of the equivalent plastic strain during diastole and systole. To this purpose, Figure 14.6 shows the equivalent plastic strain versus time diagram. Two curves are represented: the blue curve is related to the point where the maximum value of equivalent plastic strain is reached among all the mesh elements; the red curve is related to the point of the analyzed stent strut where the maximum value of equivalent plastic strain is reached. In both cases, the equivalent plastic strain stabilizes on a limit value, thus demonstrating the existence of a stabilized cycle for the stent, i.e., the occurrence of elastic shakedown.

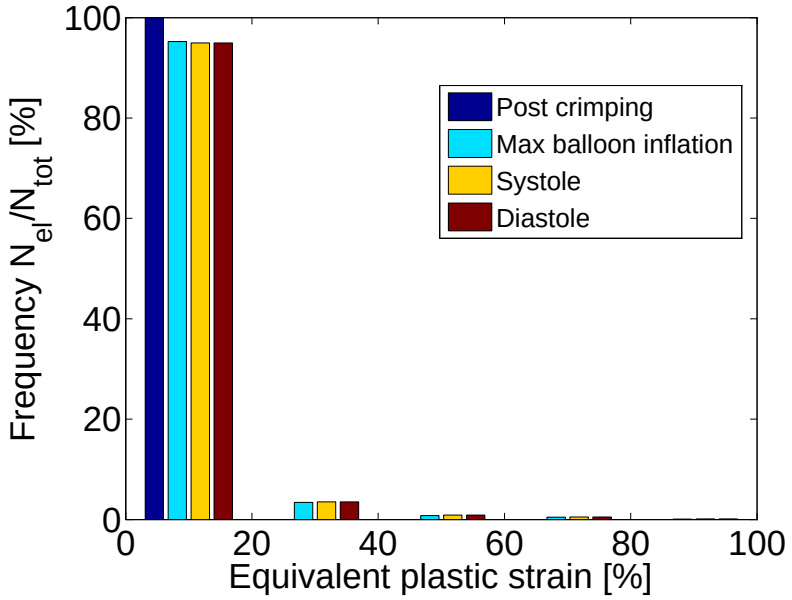

Figure 14.5: Histogram of the equivalent plastic strain (PEEQ) [%] at different analysis steps, i.e., at post crimping, maximum balloon inflation, systole, and diastole. The frequency is defined as the ratio between the number of elements, N_{el}, and the total number of elements of the mesh, N_{tot}.

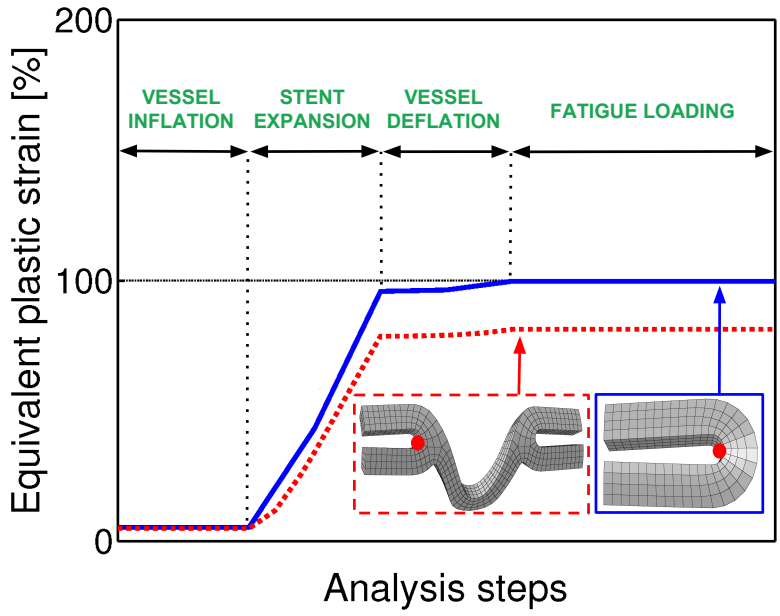

Figure 14.6: Cyclic behavior of the metallic stent under consideration. Equivalent plastic strain vs. time diagram, proving the existence of a limit cycle in alternating elasticity, i.e., elastic shakedown in the HCF domain. Two curves are represented: the blue curve is related to the point where the maximum value of equivalent plastic strain is reached among all the mesh elements; the red curve is related to the point of the analyzed stent strut where the maximum value of equivalent plastic strain is reached. The locations of the two points in the stent model are shown.

Comparison with results from the literature

In order to assess the reliability of the obtained FEA results, we compare our results to those available from the literature. In particular, Figures 14.7(a)-(d) compare the initial and deformed stent geometry from the conducted FE simulations to the scanning electron microscope of a generic stent, designed for laboratory testing based on the NIR™stent following laser cutting and deployment (Weldon, 2001). As it can be observed, the proposed geometry successfully matches the available data.
The, we compare our results to those provided by McGarry et al. (2004); Sweeney et al. (2012), who investigated the same stent design. In particular, the predicted values of the von-Mises stress are in accordance with those by Sweeney et al. (2012), ranging between 0 and 250 MPa after post crimp recoil and between 0 and 700 MPa after post deployment recoil (see Table 14.1). Additionally, the equivalent pressure stress values reported by McGarry et al. (2004) are comparable to our values (see Table 14.1), although very high peaks (about 4000 MPa) are highlighted in some localized regions (McGarry et al., 2004). Similarly to our results (see Table 14.1), the accumulated plastic slip by McGarry et al. (2004); Sweeney et al. (2012) ranges between 0 and 100%. Also, the distribution of the reported variables is similar and shows the highest values along the curved regions of the stent strut.

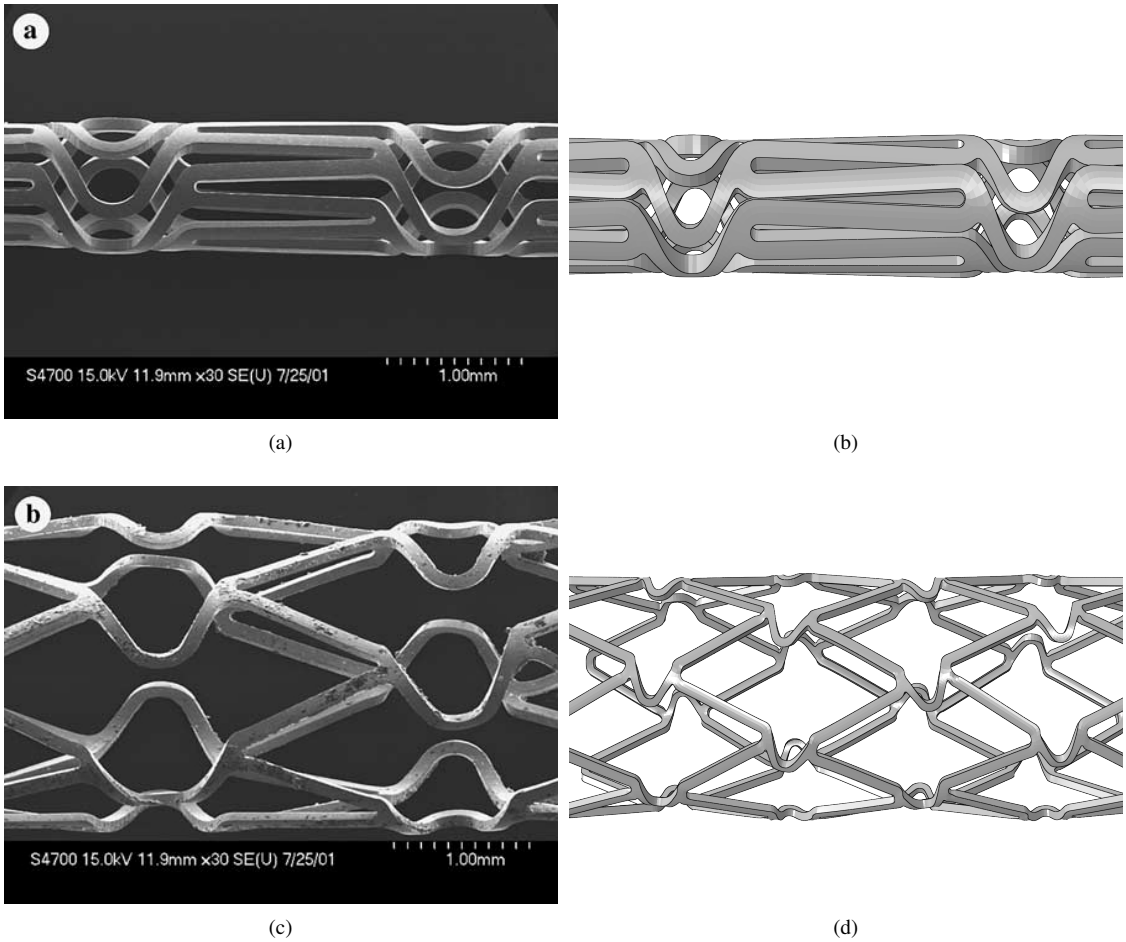

(a) (b)

(c) (d)

Figure 14.7: Scanning electron microscope of a generic stent, taken from (Weldon, 2001), designed for laboratory testing based on the NIR stent: following (a) laser cutting and (c) deployment. Comparison with (b) the stent FE mesh and (d) the deformed stent FE geometry after deployment.

14.3 Fatigue analysis

This Section presents the fatigue analysis based on the investigation of the shakedown or stabilized mechanical cycle of the stent, obtained after crimping, deployment and ten cycles of physiological loading.

14.3.1 Fatigue criterion

Once the mechanical fields are obtained, the major challenge is to determine a fatigue criterion to be used. The proposed criterion need to predict crack initiation, and not fatigue rupture. To predict the total life of the stent up to final failure, the analysis should also take into account crack propagation effects and proceed with the fatigue analysis using, for instance, a fracture mechanics approach up to final failure (Schijve, 2009). Despite this, we remind that, in the HCF regime, the crack initiation stage may cover a large percentage of the fatigue-life and, thus, a fracture mechanics approach up to final failure is out of the present scope.

Since the stabilized cycle results under elastic shakedown (see Section 14.2.5), then we propose to use a Dang Van (DV) based approach (Dang Van, 1999), already described in Section 11.3.2. Without entering into details (see Section 11.3.2), a passage between the macroscopic and the mesoscopic scale (Dang Van et al., 1989) allows to state that the lifetime is infinite if the mesoscopic shear stress, $\tau_\mu(t)$, and the hydrostatic stress, $\sigma_h(t)$, satisfy the following inequality in all the points of the structure (subscript μ stands for mesoscopic variables):

$$\max_t \left[\tau_\mu(t) + \alpha_N \sigma_h(t)\right] \leq \beta_N \tag{14.1}$$

where α_N and β_N are material parameters, calibrated as presented in Chapter 13. The reader is referred to Chapter 13 for details about the fatigue criterion and its calibration on experimental data related to μm-size components (Donnelly, 2012; Wiersma et al., 2006; Wiersma and Taylor, 2005). We remark that the calibrated DV parameters refer to 10^7 cycles (i.e., $N = 10^7$) or to an equivalent stent implant period of approximately 8 months, instead of the requested 10^8 cycles (US Food and Drug Administration, 2010). We however highlight that 10^7 cycles have already been considered as an infinite lifetime as, for example, in (Pelton et al., 2008; Subash, 1998), coherently with the definition given in (Donnelly, 2012; Wiersma et al., 2006; Wiersma and Taylor, 2005).

Considerations

It is worth noting that the adopted multiaxial HCF criterion by Dang Van (1999), based on a micro-macro approach, successfully meets the need of microstructural representation in crack initiation predictions. Obviously, inhomogeneity effects observed in explicit modeling of random crystalline microstructures cannot be captured by the DV approach. However, we have already mentioned that, in our work, the size effect is taken into account through the fatigue-life estimations based on μm-size experiments.
It is worth to emphasize, also, that such a criterion has been calibrated on experimental data related to micrometric specimens, produced with the standard procedure applied in the stent manufacturing industry. We remark here that such fatigue data have been obtained by testing the specimens in air. However, the fatigue results in terms of numbers of cycle to failure are comparable to those provided by the experimental tests by Glenn and Lee (1997), who tested thirty IsoStent NiTi stents and ten real 316L stainless steel Palmaz-ShatzTM stents (15 mm long stents from Johnson and Johnson Corporation) in a saline solution at $37\,^\circ\mathrm{C}$ to simulate real (in-vivo) physiological conditions. In particular, as regards 316L stainless steel stents, results show that, although 2 out of 2 tested stents have survived to $1 \cdot 10^6$ cyclic loadings, 0 out of 2 stents have survived to $10 \cdot 10^6$ cycles, only 1 out of 2 stents have survived to $40 \cdot 10^6$ cycles. The experimental results also indicate that 0 out of 4 stents have survived to $100 \cdot 10^6$ cycles.

14.3.2 Fatigue predictions

The mechanical fields have been obtained by the FE simulation described in Section 14.2 and the DV criterion is computed as post-processing in all the Gauss integration points of the stent model. The post-process is performed with the Matlab implementation of the optimization code SDPT3 (Tütüncü et al., 2003).

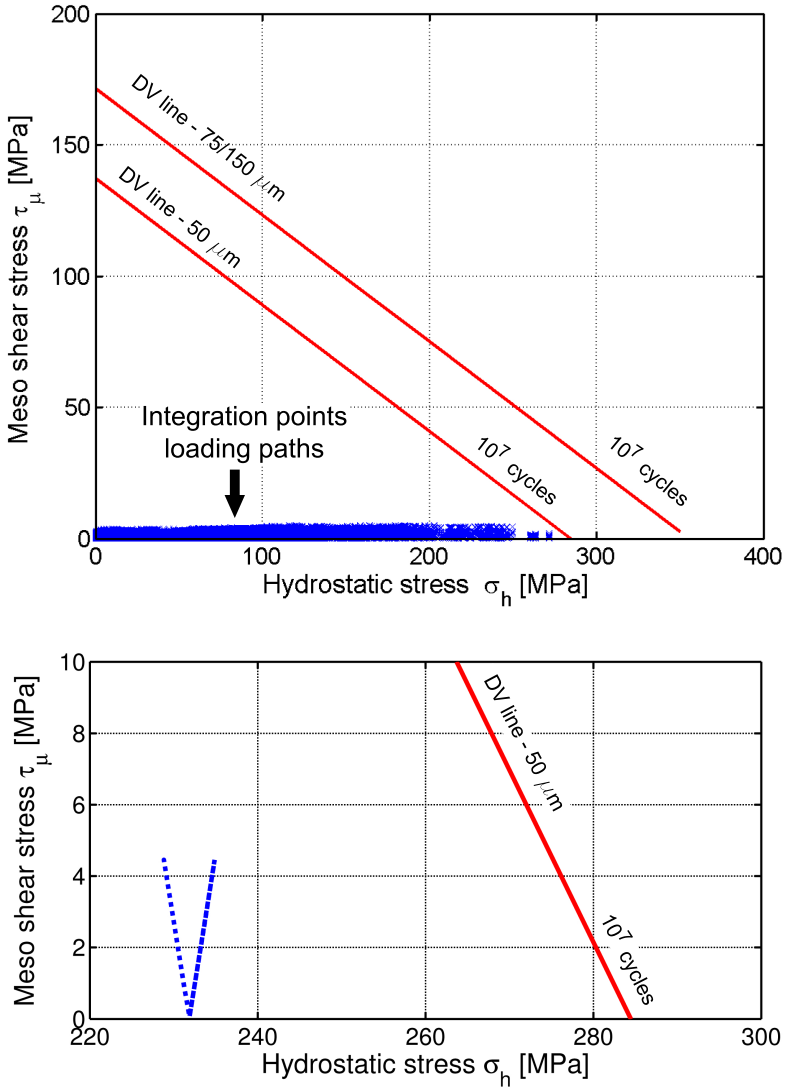

Figure 14.8: Application of the Dang Van (DV) criterion to the stent in the hydrostatic-mesoscopic stress plane. (a) The calibrated fatigue limit DV lines (in red), related to several micrometric widths, are represented as smooth lines; the loading paths (in blue), related to the integration points, are represented by markers. (b) Zoom of an integration point loading path (in blue).

Figure 14.8(a) represents the diagram in terms of the mesoscopic shear stress, τ_μ, and the hydrostatic stress, σ_h. The set of calibrated DV lines, related to several micrometric widths of the tested specimens (Donnelly, 2012; Wiersma et al., 2006; Wiersma and Taylor, 2005), are represented as red smooth lines (see Chapter 13); the loading paths related to all the Gauss integration points of the stent model are represented by blue markers. Compared to the DV lines, both strut thickness and width are approximately 0.10 mm and the diameter of the stent unit cell is 0.077 mm, as depicted in Figure 14.1(a). Figure 14.8(b) shows a

zoom of a generic loading path (in blue).
As it can be observed from Figure 14.8(a), all the markers lie under the DV lines, thus indicating that the considered stent has an endurance limit of 10^7 cycles. In particular, data from stent FEA reveal high values of the hydrostatic stress, σ_h and low values of mesoscopic shear, τ_μ. The stress paths in terms of hydrostatic versus shear stress at the mesoscopic grain level (see, e.g., the one reported in Figure 14.8(b)) present a very interesting feature, as they are almost allineated with the hydrostatic stress axes. This emphasizes the important role of stress concentrations in stents, due to the existence of small radii and high stress gradients. The von-Mises stress values of Figure 14.3 shows, in fact, a variation of around 200 MPa along the stent strut at the same istant, while the pressure stress values of Figure 14.4 a variation of 200-300 MPa. Moreover, the high values assumed by the pressure stress play a fundamental role in fatigue predictions of stents and need to be accounted for.

In order to highlight the most solicited parts of the stent strut, we compute the following DV fatigue damage parameter:

$$C_{DV} = \max_t \frac{\tau_\mu(t) + \alpha_N \sigma_h(t) - \beta_N}{\beta_N} \tag{14.2}$$

Positive values of the DV parameter, C_{DV}, indicate failure, while negative values indicate no failure.
Figure 14.9 shows the isovalues of the DV parameter, C_{DV}, calibrated with respect to the 50 μm DV line, along the stent strut. As it can be observed, the distribution of C_{DV} is almost uniform in the stent strut. The critical points (see the zoom on the right of Figure 14.9) are located along the thickness in the region with the lowest curvature radius, where a value of -0.14 is reached.

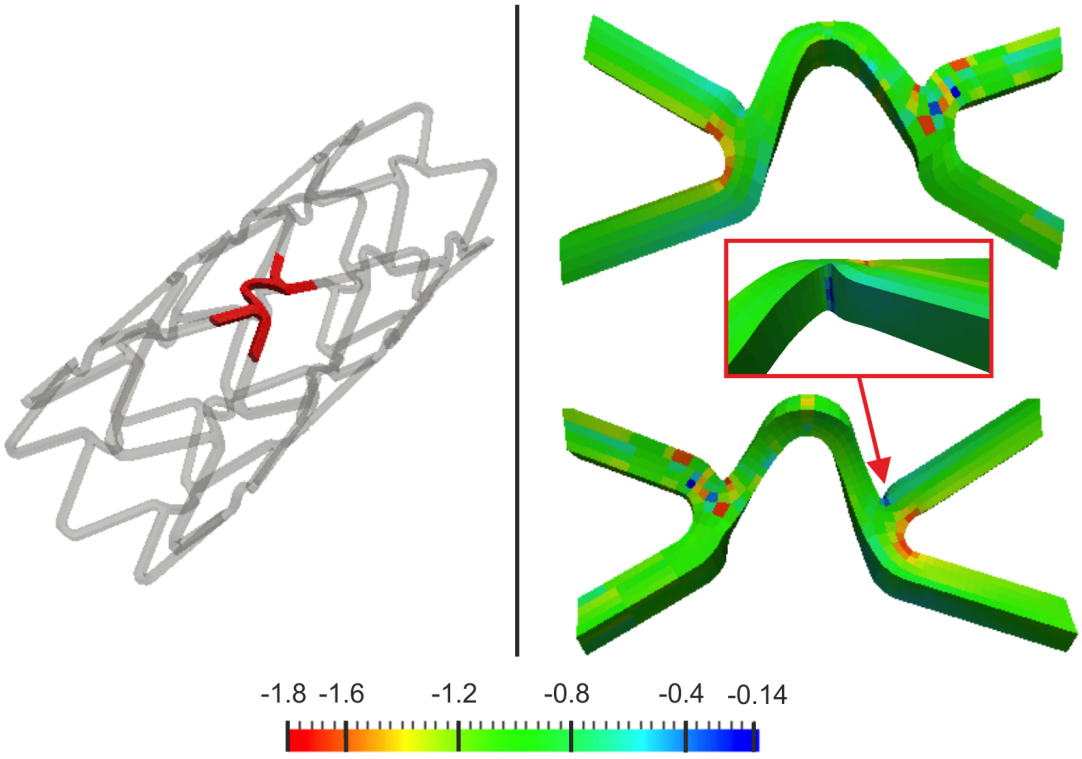

Figure 14.9: Application of the Dang Van (DV) criterion to the stent strut (in red on the left). Isovalues of the DV parameter, C_{DV}, computed with respect to the DV line calibrated on 50 μm width specimens. Zoom of the region (on the right) where the critical points are located.

Comparison with results from the literature

The presented fatigue predictions are in accordance with the results provided by McGarry et al. (2004); Sweeney et al. (2012). It is worth to highlight that the conducted three-dimensional analysis allows to take into account variable distributions and gradients along the stent thickness and thus to localize possible critical points along the stent thickness for the fatigue-life assessment.

14.4 Conclusions

This Chapter paper has presented the numerical fatigue-life assessment of balloon-expandable stents. To this purpose, the present work has investigated the fatigue behavior of a classical 316L stainless steel coronary stent design through a structural FEA, followed by a fatigue analysis. The fatigue analysis has been conducted through the application of the multiaxial HCF criterion by Dang Van, calibrated on experimental data on 316L stainless steel μm-size components. The advantages and limitations of the proposed method have been highlighted, and possible research directions for the development of numerical approaches for the fatigue-life assessment of cardiovascular balloon-expandable stents have been briefly discussed. The results of the mechanical and fatigue analyses have been verified to be in accordance with numerical and experimental results available from the literature.
The obtained results provide useful information either to be used for product improvement or for clinicians to make life-saving decisions and encourage further investigation of such an approach for future research developments in the framework of the numerical fatigue-life assessment of stents. This approach is in fact not limited to 316L stainless steel: further applications could concern other metallic materials as, e.g., cobalt-chromium alloys. Moreover, the idea of introducing the material variability as a probability density function will be the object of future work.

Chapter 15

Introduction to fatigue of shape memory alloys

Since their discovery in 1960, shape memory alloys have been used for couplings and actuators as well as for biomedical applications. Most of the biomedical applications are permanently implanted in the human body and experience millions of in-vivo cycles, and thus require a fully understand of material fatigue and fracture resistance. However, descriptions of shape memory alloy fatigue remain incomplete even today, due to the uncertain role of the transformation under cyclically varying deformations and the complexity of the various phases. This Chapter is intended to review the actual knowledge on the fatigue of shape memory alloys, with a special focus on the fatigue of cardiovascular stents.

The Chapter is organized as follows. Section 15.1 presents a general introduction to the phenomenon of fatigue in shape memory alloys. Then, Sections 15.2 and 15.3 focus on the mechanical and thermal fatigue of shape memory alloys, respectively. Section 15.4 concludes with a review on the fatigue concepts in the biomedical field.
For a recent comprehensive review, the reader is referred to (Robertson et al., 2012).

15.1 Shape memory alloys and fatigue

Literature usually distinguish between two kinds of fatigue for shape memory alloys (SMAs) (Eggeler et al., 2004; Lagoudas et al., 2009; Pelton, 2011; Van Humbeeck, 1991; Wagner et al., 2004):

1. *mechanical fatigue*, which occurs in a structure subjected to cyclic mechanical loading at imposed strain or stress amplitude under constant external temperature. The material may be either martensitic, austenitic or undergo phase change during the loading cycle. Classically, the phenomena associated with mechanical fatigue are a cyclic hardening of the stress-strain plateaus, the appearance of persistent slip bands, the initiation and propagation of cracks, ultimately leading to the failure of the structure;

2. *thermal fatigue* or *amnesia*, which occurs in a structure subjected to thermal or thermo-mechanical cycling. This kind of fatigue causes the degradation of the physical, mechanical or functional properties of the material, such as the transformation temperatures, the size of the hysteresis loop, the degradation of the two-way shape memory effect.

During the past fifty years, many investigations have focused on both the mechanical and thermal fatigue behavior of SMAs, especially of NiTi-based alloys (Robertson et al., 2012), but most of them suffer from several problems. First, NiTi-based SMAs are difficult to melt and requires tight controls on the

absolute purity and on the reproducibility of melt compositions; therefore, the results of the earlier studies have to be used with caution if they are included to provide predictions about devices fatigue. Second, many of the early investigations reflect the state of art of those years, since focusing on materials tested in the fully annealed condition or with high temperature and long duration thermal treatments; again, such results may lead to generalizations that may not pertain to modern thermo-mechanically processed materials used in NiTi implants. Third, there is the question of how the early studies evaluated the fatigue properties of NiTi-based SMAs (Robertson et al., 2012).

Nevertheless, taken as a whole, such fatigue studies fail to provide a comprehensive approach to the fatigue design of SMA-based components, with appropriate test methods, life prediction strategies and mechanistic understanding. However, such a dearth of understanding is not unexpected. Such an alloy exhibits, in fact, unusual fracture and fatigue responses, if compared with common engineering metals, due to its stress-induced and/or thermally-induced microstructural evolution. As a consequence, well-known theoretical models and standard testing procedures cannot be applied to NiTi-based SMAs. Moreover, NiTi-based SMAs are currently employed in the shape of wires, tubes or sheets and their functional and mechanical properties are significantly affected by the thermo-mechanical processes. Furthermore, such a situation is completed by the fact that experimental fatigue data of NiTi devices are not largely available.

15.2 Mechanical fatigue of shape memory alloys

The available research on the mechanical fatigue behavior of SMAs can be classified into the following groups:

- *metallurgical investigations*, which aim at explaining the cyclic stabilization of the thermo-mechanical properties of SMAs by, e.g., the creation of defects, the presence of residual martensite, the creation of persistent slip bands;

- *development of fatigue methodologies*, which involves tests on specimens presenting different geometries and chemical compositions and subjected to different loading cases.

15.2.1 Metallurgical investigations

In conventional materials as well as in SMAs, surface quality has a detrimental effect on fatigue resistance, by the presence of inclusions and grain size. For SMAs, phase change also participates to the creation of defects.
Melton and Mercier (1979) were early pioneers in the field of the mechanical fatigue of NiTi-based SMAs. They performed tensile tests on NiTi cylindrical specimens and showed that the martensite start temperature does not impact the rate of crack growth in martensite. Miyazaki et al. (1986, 1988) studied the influence of inclusions on crack initiation, which generate geometric incompatibilities and stress concentrations. They showed that it is important to avoid inclusions by specific heat treatments, since incompatibilities exist at grain boundaries and stress concentrations are particularly evident around inclusions. Moreover, they studied the influence of temperature on crack growth and showed that a low propagation rate is obtained for martensitic materials, because the deformation is due to the movement of intervariant interfaces, and that propagation rate increases with temperature. Nayan et al. (2008) performed tensile fatigue tests on cylindrical NiTi specimens and studied the evolution of yield stress, hysteresis area and Young's modulus.

15.2.2 Fatigue methodologies

The literature present two main approaches to evaluate the fatigue behavior of SMAs:

1. *total-life fatigue methodology*, which provides insights into the effects of stress- or strain-life approaches as well as effects of test temperature, transformation temperature and applied mean stress or strain (Coffin, 1953; Wöhler, 1870). Since total-life tests are experimentally easy to conduct, the literature is rich with examples, especially with tests conducted under constant strain conditions. In fact, because of material superelastic behavior, where significant (superelastic) global strain can occur at essentially constant stress, expressing lifetimes in terms of applied strains, rather than stresses, is far more appropriate (Robertson et al., 2012; Runciman et al., 2011). Additionally, it is apparent that, unlike conventional metallic materials, the amplitude of the alternating strain has a significant effect on the fatigue-life than the applied mean strain (Pelton et al., 2008; Tolomeo et al., 2000);

2. *damage-tolerant methodology*, which assumes a distribution of pre-existing cracks and considers the growth of a single dominant crack as a function of the number of cycles and applied stress (Paris et al., 1961).

Few studies have been conducted in the damage-tolerant framework, since the NiTi industry is currently dominated by commercial products with geometrically small feature sizes (e.g., cardiovascular stents), where the emphasis is placed on preventing the fatigue crack nucleation rather than controlling the crack growth (Robertson et al., 2012). Consequently, the following Sections focus only on the total-life fatigue methodology since we are interested in the fatigue-life assessment of biomedical components.

In the total-life fatigue framework, SMA mechanical fatigue behavior is analyzed through one- or three-dimensional criteria. Data are generally collected in terms of the number of cycles to failure as a function of the applied alternating and mean stresses or strains (Wöhler, 1870). Following (Wagner et al., 2004), three types of fatigue can be defined in terms of the number of cycles to failure:

1. *high-cycle fatigue*, typically occurring for small strain amplitudes. The response of the material remains elastic and the number of cycles to failure is higher than one million;

2. *intermediate fatigue*, occurring for intermediate strain amplitudes. No stress-induced martensite exists, but some martensite plates exist locally due to fatigue micro-crack initiation;

3. *low-cycle fatigue*, occurring for high strain amplitudes. Most of the structure undergoes stress-induced martensitic transformation and the number of cycles to failure highly depends on the strain amplitude.

One-dimensional criteria

In the total fatigue framework, stress- or strain-life fatigue behavior of NiTi has been investigated for different types of uniaxial loading, e.g., (Dolce and Cardone, 2001; Kang et al., 2012; Kim and Miyazaki, 1997; Maletta et al., 2012; McNichols et al., 1981; Melton and Mercier, 1979; Nayan et al., 2008, 2009; Nemat-Nasser and Guo, 2006; Pelton et al., 2013, 2003; Reinhoehl et al., 2000; Soul et al., 2010; Tobushi et al., 1998; Wagner et al., 2008; Wang et al., 2008).

Melton and Mercier (1979) firstly proposed a Manson-Coffin law to model their fatigue results and showed that the fatigue limit at room temperature decreases for increasing martensite starting temperature.

A complete study on the uniaxial strain-life fatigue of NiTi is due to the works by Pelton (2011); Pelton et al. (2003, 2008), who investigated diamond-shaped NiTi samples, processed to emulate the commercial processing of stents. Specifically, Pelton (2011); Pelton et al. (2008) investigated the effects of mean strain and strain amplitude on diamond-shaped samples cycled in bending up to 10^7 cycles and compared the fatigue results with radial pulsatile fatigue testing of commercially available NiTi self-expanding stents.
Figure 15.1(a) shows the strain amplitude versus the number of cycles to failure diagram for conditions of zero (white markers) and non-zero (black markers) mean strain from the diamond specimen compression testing. Only conditions that led to fracture are shown. The diagram can be separated into low-cycle

(10^3 to 10^5 cycles) and high-cycle (>10^5 cycles) regions. The fatigue strain limit at the high-cycle data is 0.4%. The inset in Figure 15.1(a) shows also a diamond-shaped subcomponent designed to simulate a representative unit cell of a commercial stent (8 mm length, 0.33 mm width and 0.35 mm thick), and hence to assess the pulsatile fatigue properties of a NiTi biomedical device.
Figure 15.1(b) replots the diamond fatigue-life data from Figure 15.1(a) as a constant-life diagram in terms of mean strain versus strain amplitude. In addition to the 'diamond' fatigue data, results from micro-dogbone specimens are also included (Pelton et al., 2008). Specimens that survived 10^7 cycles are shown as open symbols, whereas specimens that fractured are shown as solid symbols. A trend line, representing the 10^7 cycle life boundary, is drawn to connect the lowest strain amplitude that resulted in fracture. For mean strains between 1.5 and 3%, there is an increase in fatigue-life from 0.4 to 0.6% strain amplitude; a dotted line at 0.6% strain amplitude is drawn between 3 and 7% mean strain to indicate that there are insufficient fracture data for a complete analysis. Above 7% mean strain, the constant-life data exhibit a negative slope. Mechanistically, it is clear that enhanced fatigue-life between 1.5 and 7% mean strains is due to microstructural effects of stress-induced martensite. Hence, within this strain range, mean strain should be more accurately viewed as the volume fraction of stress-induced martensite. Such investigations demonstrate that the composite structure of stress-induced martensite plus austenite is able to accommodate a greater amount of strain amplitude, leading to longer fatigue-lives, than either austenite or deformed martensite.
The overwhelming conclusion from the recent studies by Pelton (2011); Pelton et al. (2003, 2008) is that NiTi fatigue can not be modeled with traditional Goodman or Soderberg type analyses, typically used with conventional engineering materials.

Due to the great interest of NiTi alloys in the biomedical field, several studies have been devoted to the functional and structural fatigue properties of tubes, similar to that used for manufacturing of endovascular stents or stent components (Stankiewicz et al., 2007; Tabanli et al., 2001; Tolomeo et al., 2000; Zipse et al., 2011). In particular, Tabanli et al. (2001) analyzed the effects of mean stress and strain, revealing that classic fatigue criteria for common metals cannot be applied to NiTi-based SMAs, as a consequence of stress-induced mechanisms.

Three-dimensional criteria

Unlike tension/compression/bending loading, there are no corresponding comprehensive fatigue data available in the literature for the torsional fatigue loading of NiTi, although a few studies pertain to torsional behavior under non-cyclic loads (Adler et al., 1990; Imbeni et al., 2003; McNaney et al., 2003; Olier et al., 2004; Predki et al., 2006). Runciman et al. (2011) analyzed the Coffin-Manson approach by defining an equivalent strain obtained from multiaxial loading conditions and determined the torsional strain-life fatigue curve for the superelastic NiTi tubing used for stents, at several strain ratios.

In the three-dimensional framework, it is worth to remember the work by Moumni et al. (2005) who firstly proposed an energy approach, where the dissipated energy of the pseudoelastic hysteresis cycle is used as a parameter for lifetime estimation. The criterion is validated for tensile/compressive experiments, but not for other loading cases. Later, Morin et al. (2010) extended such a criterion to account for the influence of the hydrostatic pressure.

15.3 Thermal fatigue of shape memory alloys

Thermal fatigue is defined as cycling through the transformation temperatures multiple times; in the simplest cases, there is no application of external stress or strain.
Differential scanning calorimetry is an elucidating method to monitor the changes in transformation temperature due to stress-free thermal cycling. As an example, Figure 15.2 illustrates the behavior of annealed Ni50.5Ti49.5 upon cooling to $150\,^{\circ}\mathrm{C}$ and subsequent heating to $120\,^{\circ}\mathrm{C}$ repeated for 100 cycles (Pelton,

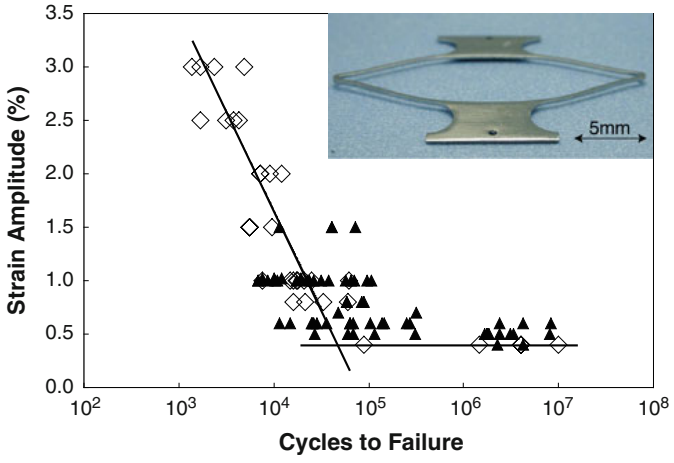

(a)

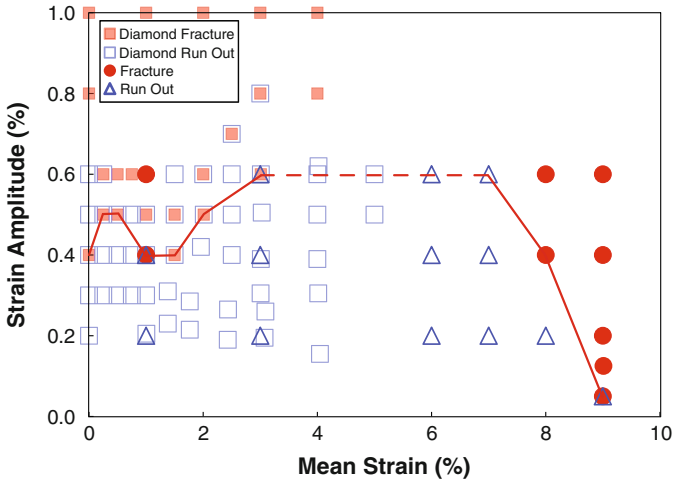

(b)

Figure 15.1: Experimental fatigue tests on diamond stent subcomponents taken from Pelton (2011). (a) Strain amplitude vs. number of cycles to failure diagram; (b) constant-life diagram in terms of mean strain and strain amplitude.

2011). Such results show that martensite and austenite peaks decrease in temperature whereas the R-phase transformation temperature increases with increasing numbers of cycles.
In the following, we do not enter into details; for a recent comprehensive review, the reader is referred to (Pelton, 2011).

15.4 Shape memory alloy biomedical devices and fatigue

An increasing number of medical devices is manufactured from NiTi (Duerig et al., 1999). Many of such devices, particularly endovascular stents, undergo tens to hundreds of millions of loading cycles in a corrosive physiological environment during their lifetime. In particular, such devices must withstand at least 10 years service without exhibiting failure (US Food and Drug Administration, 2010). A rapid computation shows that 70 artery pulses per minutes impose 40 million cycles per year and, consequently, 400 million cycles during its lifetime. However, fracture occurrences of up to 50% have been reported

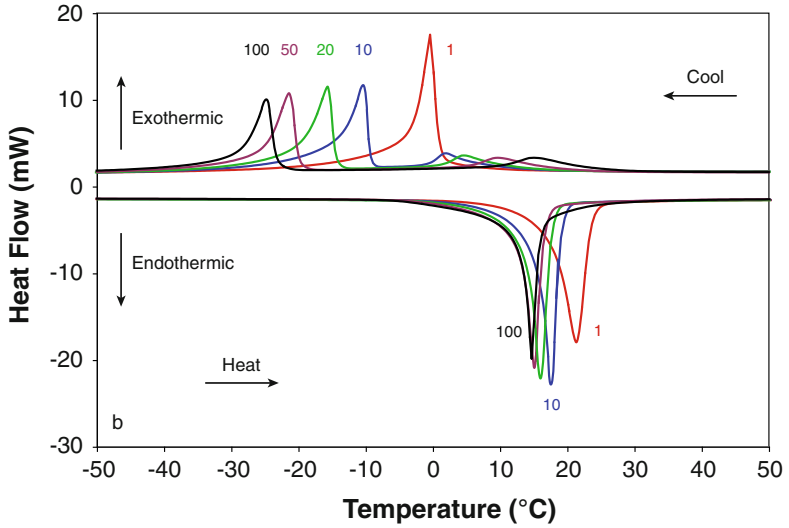

Figure 15.2: Differential scanning calorimetry thermograms of heating and cooling cycles 1, 10, 20, 50, and 100 for annealed Ni50.5Ti49.5, taken from (Pelton, 2011).

in some stents after only one year (Pelton et al., 2008). This indicates a clear need to gain a deeper understanding of stent fracture and fatigue behavior and to develop failure prediction methods to aid stent design refinements.

The majority of fatigue data on NiTi-based SMAs to support such life-prediction procedures is based on cyclic testing under uniaxial loading (Robertson et al., 2012), even if many medical devices, for example endovascular stents, are subjected to more complex modes of loading in the body (Runciman et al., 2011). Moreover, much of the early work on NiTi fatigue has been conducted at fully-reversed stresses or strains. However, self-expanding stents may undergo a large single strain excursion (up to 10%) during constraint into a delivery system and then the opposite strain excursion during deployment into the anatomical location. The physiological movements from the cardiac systolic-diastolic cycle and musculoskeletal motion provide the imposed strain amplitude, as illustrated in Figure 15.3(a). Figures 15.3(b) and (c) show a Cordis NiTi SMART stent with partial deployment from a delivery system and as deployed in a mock arterial vessel respectively.

Additionally, another important aspect in biomedical applications is the the ratio between the length scales of the mescoscopic structure of grains and of the macroscopic structure of the device. The thermomechanical processing of NiTi tubing and devices results, in fact, in a grain size of approximately 100 nm in the stents and stent subcomponents (Pelton et al., 2008). As such, the average number of grains per cross-section is 1000 (compared with typical stainless steel stent material that has 10 grain diameters per section). Moreover, many of the early fatigue studies on NiTi were conducted on fully annealed material with grain sizes of approximately 100 mm and with low defect density (Robertson et al., 2012). These studies provide insight into many of the fundamental mechanisms; however, they are incomplete with respect to providing a definitive microstructure mechanics explanation that could be used to predict fatigue behavior of modern medical devices that exclusively use thermo-mechanically processed NiTi material.

In order to bridge the gap between the existing experiments and the fatigue design of such components, numerical and experimental investigation have gained a lot of interest in the engineering community (Auricchio et al., 2010; Azaouzi et al., 2013, 2012a; Grujicic et al., 2012; Harvey, 2011; Wu et al., 2007).
As an example, the utility of data by Pelton et al. (2008), described in Section 15.2.2, is in the prediction of stent lifetimes. Accordingly, as validation of the pulsatile fatigue behavior, Pelton et al. (2008) conducted radial distension to fracture proof tests on 10 mm diameter Cordis SMART stents. Figure 15.4 shows

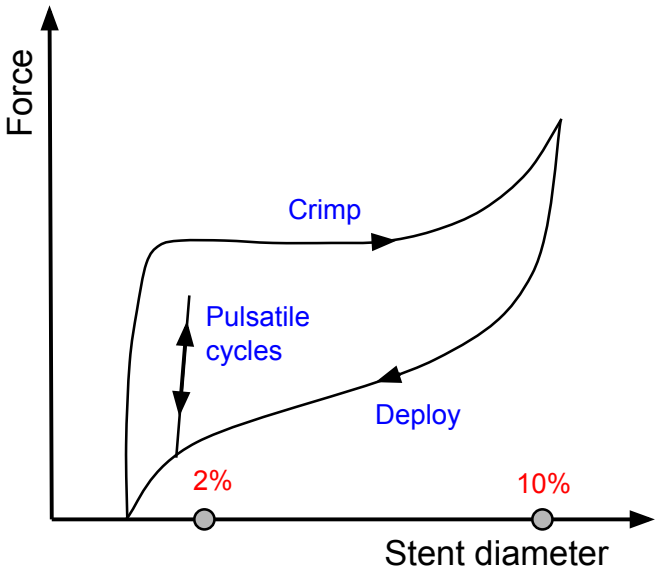

(a)

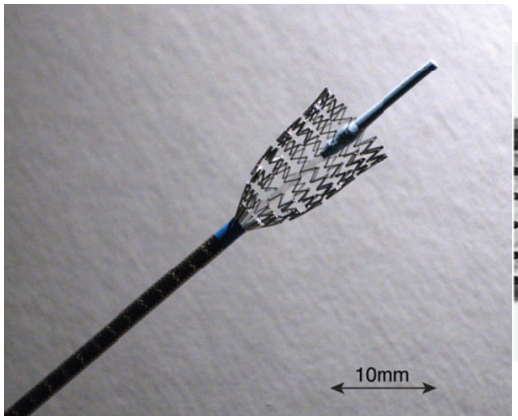

(b)

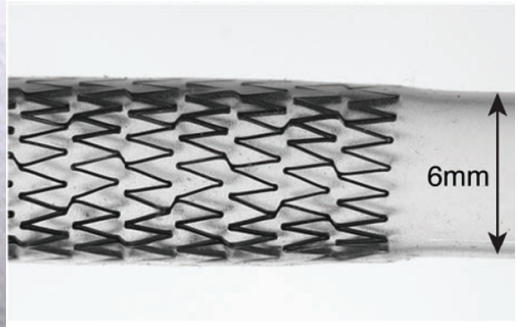

(c)

Figure 15.3: (a) Stress-strain data for a NiTi stent, schematically illustrating the initial crimp stress, deployment and subsequent in vivo cycles; (b) Cordis NiTi SMART stent being deployed from a delivery catheter; the strain on the stent inside the catheter can be about 10%, taken from (Pelton et al., 2008; Robertson et al., 2012); (c) illustration of a 9 mm diameter Cordis NiTi SMART stent in a 6 mm diameter mock vessel, which simulates a constant in-vivo mean strain, taken from (Pelton et al., 2008; Robertson et al., 2012).

the experimental stent pulsatile fatigue data, overlaid on the diamond data. White circles represent test conditions that survived 10^7 pulsatile cycles; red circles represent conditions that led to fracture at $< 10^7$ pulsatile fatigue cycles. Stent fatigue testing is consistent with the diamond data, whereby fracture tends to occur above the 0.4% strain amplitude (dotted line) for a range of mean strains. The shaded box represents mean and amplitude strains for typical oversizing and pulsatile fatigue conditions. The results shown in Figure 15.4 demonstrate the incorporation of the diamond subcomponent testing analysis as a useful and accurate indicator of NiTi stent lifetimes for radial dilation fatigue conditions.

Recently, Petrini et al. (2013) presented a numerical and experimental approach based on tests performed on NiTi specimens, obtained from the same tubes and with the same procedure used in the produc-

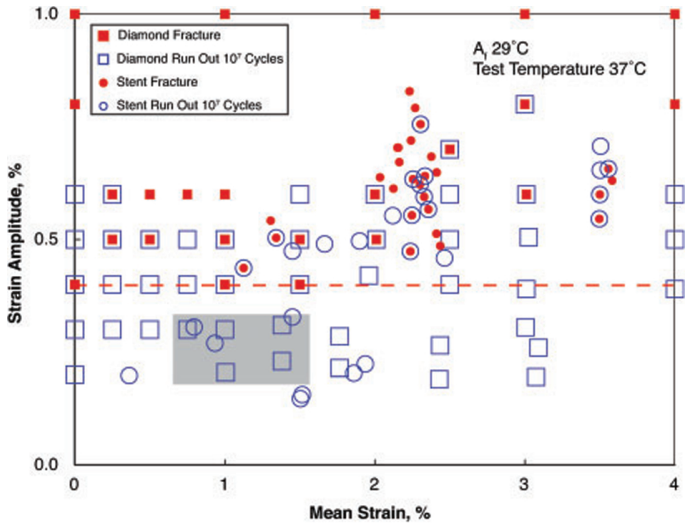

Figure 15.4: Experimental fatigue tests taken from Pelton et al. (2008). Stent pulsatile fracture data are overlaid on the diamond fatigue data from Figure 15.1(b).

tion of commercial peripheral stents and on the validation of numerical stent models for the prediction of fatigue behavior through the comparison with experimental tests. Meoli et al. (2013) presented a computational approach to evaluate the fatigue behavior of NiTi pheriperal stents. Results reveal the influence of the stent oversizing on fatigue behavior and highlight the impact of stent design on fatigue performance. Hsiao and Yin (2013) investigated a simple concept of stent design aimed at enhancing pulsatile fatigue-life.

Conclusions and future work

Motivated by the increasing number of shape memory material based applications and by the consequent growing involvement of industrial players in the field, the present thesis has investigated several research issues involving the advanced constitutive, numerical and fatigue modeling of elastoplastic materials, shape memory alloys and shape memory polymers. As such, the present thesis has pursued a multi-disciplinary approach, ranging from theoretical mathematics and computational science to experimental validation and fatigue modeling.

To conclude this thesis, the key points presented in the previous chapters are summarized, and future research tasks pertaining to these are suggested. We remark that only the chapters containing new results are here recalled.

PART I: Constitutive and numerical modeling of elastoplastic and shape memory materials

The first part of the thesis has presented the following new results.

Motivated by the similarities between the structures of equations representing shape memory and elastoplastic materials behavior, Chapter 3 has presented a detailed analysis of several computational approaches available from the literature and relevant to the numerical solution of the initial boundary-value problem for J_2 elastoplasticity. The aim was to critically review a number of existing algorithmic schemes, ranging from the classical return-map and Augmented Lagrangian approaches to complementary problem function-based algorithms. Then, Chapter 4 has presented the numerical investigation of two integration algorithms for J_2 elastoplasticity with linear isotropic kinematic hardening, i.e., the return-mapping and the Fischer-Burmeister algorithms. The proposed numerical analysis has been carried out through several kinds of numerical tests and has provided a comparison in terms of precision and efficiency. Possible difficulties in the Fischer-Burmeister scheme and solution strategies have been addressed. The obtained results have revealed that these two algorithms can be equally used for numerical simulations of elastoplastic bodies and, therefore, encourage further investigations of the Fischer-Burmeister scheme for its application to more complex constitutive models, e.g., involving non-linear kinematic hardening or describing the behavior of smart materials, as shape memory materials. Future work will deal with the investigation of other numerical schemes for elastoplasticity.

Focused on shape memory alloy modeling, Chapter 6 has proposed the derivation of an explicit integration scheme for solving the constitutive equations of the model by Boyd and Lagoudas (1996) and Lagoudas et al. (2012). The scheme has been tested for a simple uniaxial test. The results encourage further works focusing on a comparison between explicit and implicit integration schemes.

Then, Chapter 7 has developed a refined, flexible and general three-dimensional phenomenological constitutive model for shape memory alloys taking into account several physical phenomena. The model has been treated numerically through the effective and efficient procedure based on the Fischer-Burmeister function, already investigated in Chapter 4. Moreover, the one-dimensional phase diagram and model calibration based on a simple physical interpretation have been addressed.

Chapter 8 has been devoted to a detailed numerical and experimental investigation of shape memory alloys to assess the reliability of the 'flexible' model, introduced in Chapter 7, as well as the effectiveness of its

numerical counterpart. Numerical robustness and efficiency have been carefully investigated. Possible difficulties and the adopted solutions have been described. Extensive numerical tests have been performed to show robustness as well as efficiency of the proposed integration algorithm and the quantitative validation of the proposed model with experimental data available from the literature has been addressed to confirm model reliability. Then, a numerical and experimental investigation of NiTi actuators springs has been conducted in SAES Getters. The modified Souza-Auricchio and the 'flexible' models have revealed good predictions of global SMA behavior, by allowing to take advantage of these preliminary results for future design purposes. The present work will be used as a starting point for an ongoing detailed investigation about the calibration technique, the study of the effect of the variation of geometry properties and material treatment as well as of the application of compression loads.

Focused on shape memory polymers, Chapter 9 has first presented the results of an experimental investigation, conducted in Versalis (ENI), on semi-crystalline polyethylene-based shape memory polymers with different densities. Experimental data have been analyzed to show the main features of material behavior, in particular related to material orientation and thermal retraction. Then, a simple new one-dimensional model has been introduced to predict material behavior at temperatures below the melting temperature. The model has been demonstrated to be able to describe qualitative aspects of material behavior, involving both orientation and thermal retraction, as well as to predict experimental orientation processes for semi-crystalline polyethylene-based polymers with different densities. In future works, the model will be extended to include viscous effects as well as material orientation at temperatures above the melting temperature. Moreover, it will be expanded to a three-dimensional and finite strain framework to possibly simulate important industrial processes, e.g., packaging.

PART II: Fatigue modeling of elastoplastic and shape memory materials

The second part of the thesis has presented the following new results.

Focused on metallic biomedical device fatigue behavior, Chapter 13 has explored the fatigue of stainless steel components of microsize by analyzing several experimental data from the literature. The specimens were either smooth or notched and presented features similar to those characterizing cardiovascular stents. In fact, 316L stainless steel for biomedical devices is employed in structures of very small sizes. The Chapter has investigated several fatigue criteria for infinite and finite lifetime, associated with hot-spot as well as volume element approaches. The results have demonstrated that the volume element approach is efficient in the presence of high stress gradients and size effects. The provided criteria can be used in the numerical fatigue-life assessment of 316L stainless steel stents. The idea of introducing the material variability as a probability density function will be the object of future work.

In order to effectively demonstrate the reliability of the proposed criteria, Chapter 14 has presented the numerical fatigue-life assessment of cardiovascular balloon-expandable stents. To this purpose, the present work has investigated the fatigue behavior of a classical 316L stainless steel coronary stent design through a complete and general computational approach, consisting of a mechanical and a fatigue analysis. The fatigue analysis has been conducted through the application of the high-cycle fatigue criterion by Dang Van, calibrated as explained in Chapter 13. The advantages and limitations of the proposed method have been highlighted, and possible research directions for the development of numerical approaches for the fatigue-life assessment of balloon-expandable stents have been briefly discussed. The obtained results provide useful information either to be used for product improvement or for clinicians to make life-saving decisions and encourage further investigations of such an approach for future research developments in the framework of the numerical fatigue-life assessment of stents. This approach is in fact not limited to 316L stainless steel: further applications will concern other metallic materials as, e.g., cobalt-chromium alloys.

Focused on shape memory alloy fatigue behavior, Chapter 15 has reviewed the actual knowledge on the fatigue of shape memory alloys, with a special focus on the fatigue of cardiovascular stents. Future work will involve the introduction of a numerical fatigue-life assessment of self-expandable stents.

Appendix A

Some elements of convex analysis

This Appendix presents a brief introduction to convex analysis. For further details, the reader is referred to, e.g., (Frémond, 2012; Rockafellar, 1970).

A.1 Convex sets

Definition A.1.1. *Let C be a set of linear space V. The set is convex if:*

$$\forall x \in C, \quad \forall y \in C, \quad \forall \alpha \in (0,1), \quad \alpha x + (1-\alpha) y \in C \tag{A.1}$$

As an example, segment $[0,1]$ of space $V = \Re$ is convex; the interior of a circle is a convex set of space $V = \Re^2$, while the exterior is not convex.

A.2 Convex functions

Let $\overline{\Re} = \Re \cup \{+\infty\}$. The regular addition is completed by:

$$\begin{cases} \forall a \in \Re, & a + (+\infty) = +\infty \\ & +\infty + (+\infty) = +\infty \end{cases} \tag{A.2}$$

while multiplication by positive numbers is completed by:

$$\forall a \in \Re, \quad a > 0, \quad a \times (+\infty) = +\infty \tag{A.3}$$

Therefore, it is forbidden to multiply either by 0 or by negative numbers.

Definition A.2.1. *Let f an application from linear space V into $\overline{\Re}$. The function is convex if:*

$$\forall x \in V, \ \forall y \in V, \ \forall \alpha \in (0,1), \quad f(\alpha x + (1-\alpha) y) \leq \alpha f(x) + (1-\alpha) f(y) \tag{A.4}$$

A.2.1 Examples of convex functions

Let $V = \Re$. Functions, f_p, such that:

$$x \in \Re \quad \rightarrow \quad f_p(x) = \frac{1}{p} |x|^p, \quad \text{with} \quad p \in \Re, \quad p \geq 1 \tag{A.5}$$

are convex.

Let $V = \Re$. The *indicator function*, I, of segment $[0, 1]$, from V into $\overline{\Re}$, defined as:

$$I(x) = \begin{cases} 0 & \text{if } x \in [0, 1] \\ +\infty & \text{otherwise} \end{cases} \tag{A.6}$$

is convex and it is shown in Figure A.1(a).
More generally, we define the indicator function of a set, $C \subset V$, as:

$$I_C(x) = \begin{cases} 0 & \text{if } x \in C \\ +\infty & \text{otherwise} \end{cases} \tag{A.7}$$

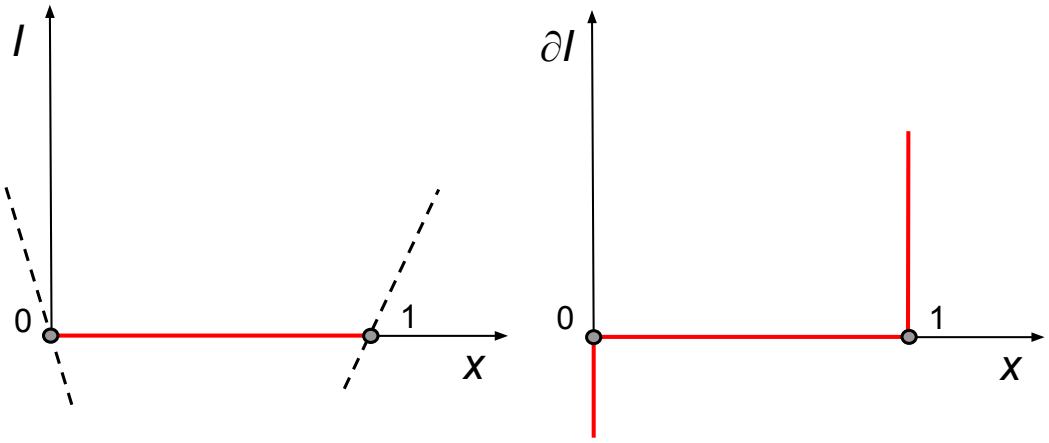

(a) (b)

Figure A.1: (a) Indicator function, I, of segment $[0, 1]$. The subgradients at points 0 and 1 are the slopes of the lines which are under the curve representing the function and in contact with the curve at points 0 and 1; (b) subdifferential set, ∂I, of the indicator function, I, of segment $[0, 1]$ (Frémond, 2012).

We can easily connect the convex function and convex set notions by showing that:

Theorem A.2.1. *A set $C \subset V$ is convex if and only if its indicator function, I_C, is convex.*

A.3 Linear spaces in duality

Definition A.3.1. *Two linear spaces, V and V^*, are in duality if there exists a bilinear form $\langle \cdot, \cdot \rangle$ defined on $(V \times V^*)$ such that:*

$$\begin{cases} \text{for any} \quad x \in V, \quad x \neq 0 \quad \text{there exists} \quad y^* \in V^*, \quad \text{such that} \quad \langle x, y^* \rangle \neq 0 \\ \text{for any} \quad y^* \in V^*, \quad y^* \neq 0 \quad \text{there exists} \quad x \in V, \quad \text{such that} \quad \langle x, y^* \rangle \neq 0 \end{cases} \tag{A.8}$$

A.3.1 Examples of linear spaces in duality

Let $V = \Re$ and $V^* = \Re$. Spaces V and V^* are in duality with the bilinear form which is the usual product $\langle x, y \rangle = x \cdot y$.

Let $V = \Re^n$ and $V^* = \Re^n$. Spaces V and V^* are in duality with the bilinear form which is the usual scalar product $\langle x, y \rangle = \mathbf{x} \cdot \mathbf{y}$, with $\mathbf{x} \in \Re^n$ and $\mathbf{y} \in \Re^n$.

Let $V = S$ and $V^* = S$, where S is the linear space of symmetric matrices (3×3). Spaces V and V^* are in duality with the bilinear form $\langle e, s \rangle = e : s$, with $e \in V$ and $s \in V^*$. Linear spaces V and V^* are also in duality with the bilinear form $\langle\langle e, s \rangle\rangle = e_{11}s_{11} + e_{22}s_{22} + e_{33}s_{33} + e_{12}s_{12} + e_{13}s_{13} + e_{23}s_{23}$.

A.4 Subgradients and subdifferential set of convex functions

The convex function f_p, given in Eq. (A.5), is differentiable for $p > 1$, but not for $p = 1$, since it is equal to the absolute value function which has no derivative at the origin. Similarly, the indicator function, I, of segment $[0, 1]$, given in Eq. (A.6), is not differentiable, because its value is $+\infty$ at some points and it has no derivative at points 0 and 1. Thus, it seems that we have to loose all the calculus properties related to derivatives. Fortunately, it is possible to define generalized derivatives and keep a large amount of properties related to derivatives (Frémond, 2012).

Consider the function, f, shown in Figure A.2, which is convex but not differentiable at point A. We note, in fact, that at a point where the function has a derivative, the curve is everywhere above the tangent; on the contrary, at point A, there exist several lines demonstrating such a property. The slopes of the lines are the subgradients which generalize the derivative.

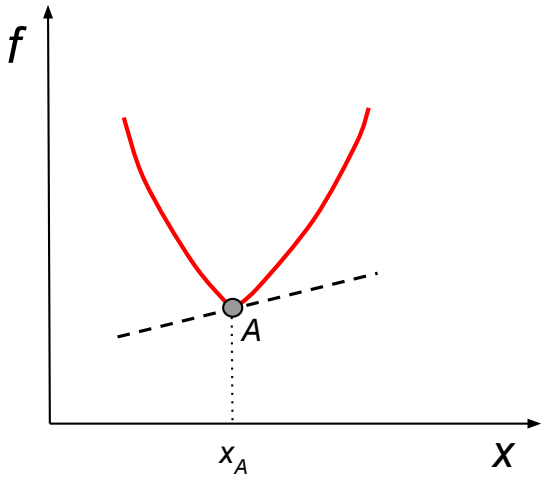

Figure A.2: The convex function, f, has generalized derivatives at point A. The slopes of the lines passing through A and under the curve representing f are the subgradients which constitute the subdifferential set (Frémond, 2012).

Definition A.4.1. *Let convex function f be defined on V in duality with V^*. A subgradient of f at point $x \in V$ is an element $x^* \in V^*$ which satisfies:*

$$\forall z \in V, \quad \langle z - x, x^* \rangle + f(x) \leq f(z) \tag{A.9}$$

The set of the x^* which satisfy definition (A.9) is the *subdifferential* set of f at point x, denoted with $\partial f(x)$. Subgradient depends on f, but also on the bilinear form $\langle \cdot, \cdot \rangle$.

A.4.1 Properties of the subdifferential set

The subdifferential set keeps usual properties of the derivative. For a convex function we define the first property as follows.

Theorem A.4.1. *Let convex function $f \neq +\infty$. If this function is subdifferentiable at point x, i.e., if $\partial f(x) \neq \emptyset$, then it is finite at that point: $f(x) < +\infty$.*

This theorem applies in numerous constitutive laws where we have the relationship $B \in \partial I(\beta)$: because $\partial I(\beta)$ is not empty, we have $I(\beta) < +\infty$ which implies that $I(\beta) = 0$ and $0 \leq \beta \leq 1$ (see Figure A.1(a)).

Moreover, we define the second property, as follows.

Theorem A.4.2. *Let f be a convex function. We have:*

$$\forall y^* \in \partial f(y), \quad \forall z^* \in \partial f(z), \quad \langle y - z, y^* - z^* \rangle \geq 0 \tag{A.10}$$

A.4.2 Examples of subdifferential sets

The subdifferential set of the indicator function, I, of segment $[0,1]$, shown in Figure A.1(b), is defined as:

$$\partial I(x) = \begin{cases} \Re^- & \text{if } x = 0 \\ \Re^+ & \text{if } x = 1 \\ \{0\} & \text{if } x \in (0,1) \\ \emptyset & \text{otherwise} \end{cases} \tag{A.11}$$

A.5 Dual functions

Let V and V^* be in duality with the bilinear form $\langle \cdot, \cdot \rangle$. Let f be a convex function of V into V^*, the *dual function* f^* of f is a function of V^* into $\overline{\Re}$, defined by:

$$f^*(y^*) = \sup \left[\langle x, y^* \rangle - f(x) \;\middle|\; x \in V \right] \tag{A.12}$$

It is possible to prove:

Theorem A.5.1. *Dual function f^* is convex. If function f is subdifferentiable at point x, the properties:*

$$y^* \in \partial f(x), \quad x \in \partial f^*(y^*), \quad \textit{and} \quad f(x) + f^*(y^*) = \langle x, y^* \rangle \tag{A.13}$$

are equivalent.

A.5.1 Examples of dual functions

Let $V^* = \Re$ and the bilinear form be the usual multiplication $\langle x, y \rangle = xy$. The dual function of the indicator function, I, of segment $[0,1]$ is defined by:

$$I^*(y) = \sup \left[xy - I(x) \;\middle|\; x \in V = \Re \right] = \sup \left[xy \;\middle|\; x \in [0,1] \right] \tag{A.14}$$

and it is called *support function* of segment $[0,1]$. It is easy to get:

$$I^*(y) = \begin{cases} y & \text{if } y \geq 0 \\ 0 & \text{if } y \leq 0 \end{cases} \tag{A.15}$$

We note that function I^* is the *positive part function*, i.e.,

$$I^*(y) = \sup [y, 0] \tag{A.16}$$

A.5.2 Internal energy, potential and free enthalpy

The *Helmholtz free-energy* depends on temperature, T, and on other state quantities, $\boldsymbol{\eta}$, i.e., $\Psi = \Psi(T, \boldsymbol{\eta})$.

The dual function of its opposite function, which is convex, i.e.,

$$(-\Psi)^*(y, \boldsymbol{\eta}) = \sup \left[xy - (-\Psi)(x, \boldsymbol{\eta}) \;\middle|\; x \in V = \Re \right] \tag{A.17}$$

defines the *internal energy*, e, depending on entropy, η, and on $\boldsymbol{\eta}$, as follows:

$$e(\eta, \boldsymbol{\eta}) = (-\Psi)^*(\eta, \boldsymbol{\eta}) \tag{A.18}$$

It results also the equivalent relationships:

$$\begin{cases} T \in \partial e\left(\eta, \boldsymbol{\eta}\right) \\ \eta \in -\partial \Psi\left(T, \boldsymbol{\eta}\right) \\ e\left(\eta, \boldsymbol{\eta}\right) = \eta T + \Psi\left(T, \boldsymbol{\eta}\right) \end{cases} \tag{A.19}$$

where the subdifferential sets are with respect to η and T, with $\boldsymbol{\eta}$ a fixed parameter.

Another example of dual function is the *potential* or *Gibbs free-energy*, G, defined with dual function of the Helmholtz free-energy, Ψ, with respect to density, $1/\tau$. We define the function, $\Psi^*\left(p, T\right)$, by:

$$\Psi^*\left(p, T\right) = \sup_x \left[p\frac{1}{x} - \Psi\left(x, T\right) \ \middle| x \in V = \Re \right] \tag{A.20}$$

where p is the pressure, function $1/\tau \to \Psi\left(\tau, T\right)$ is convex, and potential G is given by:

$$G\left(p, T\right) = -\Psi^*\left(p, T\right) \tag{A.21}$$

with:

$$G\left(p, T\right) = -p\,\frac{1}{\tau} + \Psi\left(\tau, T\right) \quad \Leftrightarrow \quad \frac{1}{\tau} = \frac{\partial \Psi^*}{\partial p} \quad \Leftrightarrow \quad p = \frac{\partial \Psi}{\partial\left(1/\tau\right)} \tag{A.22}$$

The *free enthalpy*, $\widehat{G}$, is defined with the specific free-energy, $\widehat{\Psi} = \tau\Psi$, as follows:

$$-\,\widehat{G}\left(P, T\right) = \widehat{\Psi}^*\left(-P, T\right) = \sup_x \left[-Px - \widehat{\Psi}\left(x, T\right) \right] \tag{A.23}$$

with:

$$\widehat{G}\left(P, T\right) = P\tau + \widehat{\Psi}\left(\tau, T\right) \quad \Leftrightarrow \quad \tau = \frac{\partial \widehat{G}}{\partial P} \quad \Leftrightarrow \quad P = -\frac{\partial \widehat{\Psi}}{\partial \tau} \tag{A.24}$$

A.6 Concave functions

A function f is *concave* if its opposite $-f$ is convex. For concave function, *uppergradients*, instead of subgradients, are defined and satisfy:

$$\forall z \in V, \quad \left\langle z - x, x^* \right\rangle + f\left(x\right) \geq f\left(z\right) \tag{A.25}$$

In such a case, the set of the uppergradients at point x is denoted as *upperdifferential set*, $\widehat{\partial} f\left(x\right)$.

A.6.1 Examples of concave functions

The Helmholtz free-energy, $\Psi = \Psi\left(T, \boldsymbol{\varepsilon}, \boldsymbol{\beta}, \nabla\boldsymbol{\beta}\right)$, is a concave function of temperature, T, because it is the dual function of the opposite of the internal energy, $e = e\left(\eta, \boldsymbol{\varepsilon}, \boldsymbol{\beta}, \nabla\boldsymbol{\beta}\right)$, which is a concave function of entropy, η. It results that the heat capacity, $-\partial^2\Psi/\partial T^2$, is non-negative.

Appendix B

AceGen and AceFEM packages

B.1 Overview on traditional finite element environments

Nowadays, numerical simulations are well-established in several engineering fields such as automotive, aerospace, or civil engineering.

The need of numerical methods which can provide a general tool for arbitrary problems in Mechanics of Solids has a long history. Most of the existing numerical methods for solving partial differential equations can be classified into two main classes: *finite difference method* (FDM) and *finite element method* (FEM). Unfortunately, the applicability of such numerical methods is often limited. As an example, the use of traditional commercial finite element (FE) environments, e.g., FEAP (Taylor, 2013) or ABAQUS (SIMULIA, 2012), offers a possibility to analyze a variety of problems and to incorporate user-defined elements and material modes. However, it is time-consuming to develop and test new user-defined pieces of softwares and numerical procedures, since a lot of time is spent to derive characteristic quantities like gradients, Jacobean, or Hessian.

The basic numerical tests on a single FE or on a small patch of elements can be done most efficiently by using general symbolic-numeric environments or *computer algebra* (CA) systems, such as Mathematica[1] (Wolfram, 2013a) or Maple (Maplesoft, 2013). However, the symbolic level of analysis becomes very inefficient if iterative procedures have to be performed, or if a large number of elements have to be considered as for real industrial simulations. Consequently, in order to assess element performances under real conditions, the easiest way is to perform tests on sequential machines with good debugging capabilities (typically personal computers and programs written in FORTRAN or C/C++ language).

For such reasons, during the development of new numerical models, the classical approach, based on the element re-coding in different languages, would be extremely time-consuming and it is never done.

In order to avoid the above troubles, the hybrid symbolic-numerical (HSN) approach combines different techniques inside one system and offers a multi-language and multi-environment generation of numerical codes. Consequently, the automatically-generated codes can be then incorporated into the FE environment that is most suitable for the specific step of the research process.

Motivated by such a framework and by the necessity of the development of numerical models for elasto-plastic and shape memory materials, the present thesis makes use of a couple of innovative Mathematica packages, called AceGen (Wolfram, 2013c) and AceFEM (Wolfram, 2013b), recently released by Wolfram Research in order to bring to Mathematica a robust and optimized architecture for a rapid numerical prototyping and a FE analysis. The combination of the FE environment, AceFEM, with its HSN code generator, AceGen, represents an ideal tool for the development of new numerical models. Such packages have been

[1] Mathematica is a well known software program largely used in several technical computing like scientific, engineering and other mathematical fields (Wolfram, 2013a).

written and developed by Joze Korelc, Professor at the Faculty of Civil and Geodetic Engineering of the University of Ljubljana (Korelc, 2002, 2009).

B.2 Introduction to AceGen and AceFEM packages

This Section presents an overview on AceGen and AceFEM packages, pointing out all their main innovative features (Korelc, 2002, 2009; Wolfram, 2013b,c).

B.2.1 AceGen package

AceGen features and advantages

The AceGen package has been designed in order to approach several problems, especially those where the general strategy of an efficient formulation of numerical procedures, such as the analytical sensitivity analysis of complex multi-field problems, has not yet been established.

The great advantage of such a HSN tool stands on its new and innovative approach which exploits the symbolic and algebraic capabilities of Mathematica, avoiding all the typical troubles of such symbolic software during the analysis of complex mechanical models. The main task is to derive automatically formulas that are required during numerical procedures and that can lead to uncontrollable growth of expressions and inefficient programs in case of symbolic softwares.
Such an automatic code generation is called *simultaneous stochastic simplification* of numerical code and combines the CA system Mathematica with an automatic differentiation technique and an automatic theorem proving by examples. Moreover, AceGen multi-language capabilities can be exploited for a rapid prototyping of numerical procedures in several script languages, such as Mathematica, Matlab, language codes in Fortran/Fortran90 or C/C++.

Mathematica-AceGen combination

The AceGen package is written in the symbolic language of Mathematica and consists of about 300 functions and 20000 lines of Mathematica's source code.
Since AceGen runs in parallel with Mathematica, we can use all the capabilities of Mathematica. The major algebraic computations that can be directly implemented also with the built-in Mathematica functions and optimized by AceGen are:

- analytical differentiation;
- symbolic evaluation;
- symbolic solution to the system of linear equations;
- symbolic integration;
- symbolic solution to the system of algebraic equations.

AceGen codes and commercial FE environments

The AceGen package provides a collection of pre-arranged modules for the automatic creation of an interface between the generated FE code and several FE environments like Abaqus, Feap, Elfen, and AceFEM.

The interfacing phase of the automatically generated code and the FE environment is a two-stage process. At the first stage user-subroutine codes are generated and each of them performs a specific task. The input/output arguments of the generated subroutines are environment- and language-dependent; however, they should contain the same information. Due to fundamental differences among the FE environments,

the required information is not readily available. Thus, at the second stage the contents of the 'splice-file' that contains additional environment-dependent interface and supplementary routines is added to the user-subroutines codes. The 'splice-file' code ensures proper data transfer from the environment to the user-subroutine and back. Automatic interface is already available for a collection of basic tasks required in the FE analysis. There are several possibilities in the case of need for an additional functionality. Standard user-subroutines can be used as templates by giving them a new name and, if necessary, additional arguments. The additional subroutines can be called directly from the environment or from the enhanced 'splice-file'. The additional subroutines can be generated independently just by using the AceGen code generator and can be called directly from the environment or from the enhanced 'splice-file'. Since the complexity of the problem description mostly appears in a symbolic input, we can keep the number of data structures that appear as arguments of the user-subroutines at minimum.
Figure B.1 presents the structure of the HSN system AceGen for multi-language and multi-environment code generation.

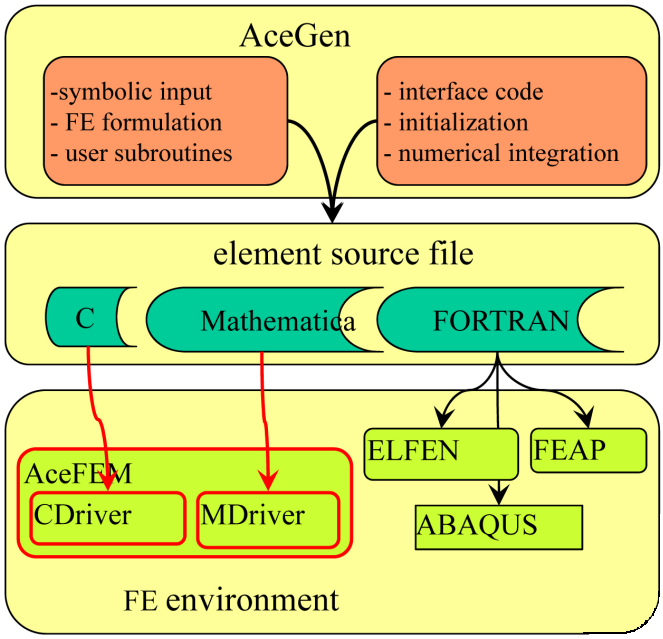

Figure B.1: Structure of the HSN system AceGen for multi-language and multi-environment FE code generation, taken from (Korelc, 2002, 2009).

B.2.2 AceFEM package

AceFEM overview

The AceFEM package is a general FE environment which exploits the symbolic capabilities of Mathematica to solve multi-physics and multi-field problems, while maintaining numerical efficiency of commercial FE environments.

The AceFEM package can employ specific own elements or general codes created by AceGen and it is designed to solve steady-state or transient FE and similar problems implicitly by means of Newton-Raphson type procedures. The idea is to design a FE environment where code complexity is shifted out of the FE environment to a symbolic module, which provides all the necessary formulation-dependent codes by automatic code-generation. The shift concerns the numerical algorithms (at the local element level)

and data structures like the organization of environment and the nodal or element data. One of the most important and original issue is that the AceFEM package contains a lot of useful pre-arranged procedures, written and executed directly inside Mathematica and usually not numerically intensive. As an example, it is easily possible to:

- generate mesh;
- control solutions procedures;
- run interactive post-processing analysis;
- create graphic post-processing of the results.

Moreover, AceFEM includes a numerical module which exists as Mathematica package and as an external program written in C language, connected with Mathematica via the MathLink protocol. This peculiar and unique capability allows the user to solve different large-scale problems with several unknowns. Figure B.2 shows the structure of the AceFEM package (Korelc, 2002, 2009).

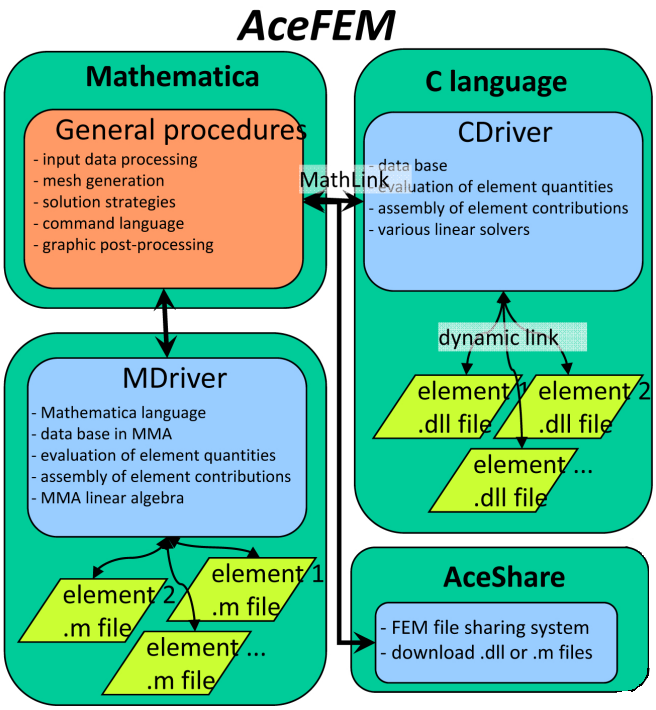

Figure B.2: Structure of the AceFEM package, taken from (Korelc, 2002, 2009).

AceShare

The AceFEM package has a built-in FE library including standard solid, structural, thermal and contact elements. Such elements can be accessed through the AceShare system, which is a built-in FE file sharing software and allows to:

- browse the online FEM libraries;
- create a user-defined library that can be posted on the internet in order to be used by other users of the AceFEM system.

Bibliography

Abbo, A. and S. Sloan (1996). An automatic load stepping algorithm with error control. *Int. J. Numer. Methods Eng. 39*, 1737–1759.

Abeyaratne, R. and J. Knowles (1990). On the driving traction acting on a surface of strain discontinuity in a continuum. *J. Mech. Phys. Solids 38*(3), 345–360.

Abrahamson, E., M. Lake, N. Munshi, and K. Gall (2003). Shape Memory Mechanics of an Elastic Memory Composite Resin. *J. Intel. Mat. Syst. Str. 14*(10), 623–632.

Adler, P., W. Yu, A. Pelton, and R. Zadno (1990). On the tensile and torsional properties of pseudoelastic NiTi. *Scripta Metall. Mater. 24*, 943–947.

AHA (2010). Circulation 121. e46-e215.

Ahn, J. (2007). A vibrating string with dynamic frictionless impact. *Appl. Numer. Math. 57*, 861–884.

Akel, S. and Q. Nguyen (1989). Determination of the limit response in cyclic plasticity. In E. Onate (Ed.), *Proceedings of the 2nd International Conference on Computational Plasticity: Models, Software and Applications*, pp. 639–650. Pineridge Press, Swansea.

Alain, R., P. Violan, and J. Mendez (1997). Low cycle fatigue behavior in vacuum of a 316L type austenitic stainless steel between 20 and 600 °C. Part I: fatigue resistance and cyclic behavior. *Mater. Sci. Eng. A 229*, 87–94.

Allen, M. and E. Isaacson (1998). *Numerical Analysis for Applied Science*. John Wiley & Sons.

Amiable, S., S. Chapuliot, A. Constantinescu, and A. Fissolo (2006). A comparison of lifetime prediction methods for a thermal fatigue experiment. *Int. J. Fatigue 28*(7), 692–706.

Amiable, S., S. Chapuliot, A. Constantinescu, and A. Fissolo (2009a). A computational lifetime prediction for a thermal shock experiment. Part I: thermomechanical modeling and lifetime prediction. *Fatigue Fract. Eng. Mater. Struct. 29*, 209–217.

Amiable, S., S. Chapuliot, A. Constantinescu, and A. Fissolo (2009b). A computational lifetime prediction for a thermal shock experiment. Part II: discussion on different fatigue criteria. *Fatigue Fract. Eng. Mater. Struct. 29*, 219–227.

Andreasen, G. and T. Hilleman (1971). An evaluation of 55 cobalt substituted Nitinol wire for use in orthodontics. *JADA 82*, 1373– 5.

Areias, P., D. Dias-da Costa, E. Pires, and J. Infante Barbosa (2012). A new semi-implicit formulation for multiple-surface flow rules in multiplicative plasticity. *Comput. Mech. 49*, 545–564.

Arghavani, J., F. Auricchio, R. Naghdabadi, and A. Reali (2011). On the robustness and efficiency of integration algorithms for a 3D finite strain phenomenological SMA constitutive model. *Int. J. Numer. Methods Eng. 85*, 107–134.

Arghavani, J., F. Auricchio, R. Naghdabadi, A. Reali, and S. Sohrabpour (2010). A 3D phenomenological

constitutive model for shape memory alloys under multiaxial loadings. *Int. J. Plasticity 26*, 976–991.

Armero, F. and A. Pérez-Foguet (2002a). On the formulation of closest-point projection algorithms in elastoplasticity - Part I: The variational structure. *Int. J. Numer. Methods Eng. 53*, 297–329.

Armero, F. and A. Pérez-Foguet (2002b). On the formulation of closest-point projection algorithms in elastoplasticity - Part II: Globally convergent schemes. *Int. J. Numer. Methods Eng. 53*, 331–374.

Artioli, E., F. Auricchio, and L. Beirao da Veiga (2006). A novel optimal exponential-based integration algorithm for von-Mises plasticity with linear hardening: Theoretical analysis on yield consistency, accuracy, convergence and numerical investigations. *Int. J. Numer. Methods Eng. 67*, 449–498.

Artioli, E., F. Auricchio, and L. Beirao da Veiga (2007). Generalized midpoint integration algorithms for J2 plasticity with linear hardening. *Int. J. Numer. Methods Eng. 72*, 422–463.

Atli, B., F. Gandhi, and G. Karst (2009). Thermomechanical Characterization of Shape Memory Polymers. *J. Intel. Mat. Syst. Str. 20*(1), 87–95.

Attanasi, G., F. Auricchio, and M. Urbano (2011). Theoretical and Experimental Investigation on SMA Superelastic Springs. *J. Mater. Eng. Perform. 20*(4-5), 706–711.

Auricchio, F. (2001). A robust integration-algorithm for a finite-strain shape-memory alloy superelastic model. *International Journal of Plasticity 17*(7), 971–990.

Auricchio, F. and E. Bonetti (2013). A new flexible 3D macroscopic model for shape memory alloys. *Discrete Contin. Dyn. Syst. Ser. S 6*(2), 277–291.

Auricchio, F., A. Coda, A. Reali, and M. Urbano (2009). SMA numerical modeling versus experimental results: parameter identification and model prediction capabilities. *J. Mater. Eng. Perform. 18*, 649–654.

Auricchio, F., M. Conti, S. Morganti, and A. Reali (2010). Shape Memory Alloy: from Constitutive Modeling to Finite Element Analysis of Stent Deployment. *CMES 57*(3), 225–243.

Auricchio, F., A. Morganti, S. andReali, and M. Urbano (2011). Theoretical and Experimental Study of the Shape Memory Effect of Beam in Bending Conditions. *J. Mater. Eng. Perform. 20*, 712–718.

Auricchio, F., S. Morganti, and A. Reali (2009). SMA numerical modeling versus experimental results. In *Proceedings of European Symposium on Martensitic Transformations (ESOMAT 2009)*, pp. 1–6.

Auricchio, F. and L. Petrini (2004a). A three-dimensional model describing stress-temperature induced solid phase transformations: solution algorithm and boundary value problems. *Int. J. Numer. Methods Eng. 6*, 807–836.

Auricchio, F. and L. Petrini (2004b). A three-dimensional model describing stress-temperature induced solid phase transformations: thermomechanical coupling and hybrid composite applications. *Int. J. Numer. Methods Eng. 61*, 716–737.

Auricchio, F., A. Reali, and U. Stefanelli (2007). A three-dimensional model describing stress-induced solid phase transformation with permanent inelasticity. *Int. J. Plasticity 23*, 207–226.

Auricchio, F., A. Reali, and U. Stefanelli (2009). A macroscopic 1D model for shape memory alloys including asymmetric behaviors and transformation-dependent elastic properties. *Comput. Methods in Appl. Mech. Eng. 198*, 1631–1637.

Auricchio, F. and U. Stefanelli (2004). Numerical Analysis of a three-dimensional super-elastic constitutive model. *Int. J. Numer. Methods Eng. 61*, 142–155.

Auricchio, F. and R. Taylor (1997). Shape-memory alloys: modelling and numerical simulations of the finite-strain superelastic behavior. *Comput. Methods in Appl. Mech. Eng. 143*(1-2), 175–194.

Azaouzi, M., N. Lebaal, A. Makradi, and S. Belouettar (2013). Optimization based simulation of self-expanding Nitinol stent. *Mater. Design 50*, 917–928.

Azaouzi, M., A. Makradi, and S. Belouettar (2012a). Deployment of a self-expanding stent inside an artery: A finite element analysis. *Mater. Design 41*, 410–420.

Azaouzi, M., A. Makradi, and S. Belouettar (2012b). Fatigue life prediction of cardiovascular stent using finite element method. *Comput. Methods Biomech. Biomed. Engin. 15*(S1), 93–95.

Aziz, S., J. Morris, R. Perry, and R. Stables (2007). Stent expansion: a combination of delivery balloon underexpansion and acute stent recoil reduces predicted stent diameter irrespective of reference vessel size. *Heart 93*, 1562–1566.

Baddoo, N. (2008). Stainless steel in construction: A review of research, applications, challenges and opportunities. *J. Constr. Steel Res. 64*, 1199–1206.

Baer, G., T. S. Wilson, D. L. Matthews, and D. Maitland (2007). Shape-memory behavior of thermally stimulated polyurethane for medical applications. *J. Appl. Polym. Sci. 103*(6), 3882–3892.

Baghani, M., R. Naghdabadi, J. Arghavani, and S. Sohrabpour (2012). A thermodynamically-consistent 3D constitutive model for shape memory polymers. *Int. J. Plasticity 35*(0), 13–30.

Bairstow, L. (1910). The elastic limits of iron and steel under cyclic variations of stress. *Philos.Trans. R. SOC. 210*, 35–55.

Balakrishna, S. and L. Biegler (1992). Targeting Strategies for the Synthesis and Energy Integration of Nonisothermal Reactor Networks. *Ind. Eng. Chem. Res. 31*, 2152–2164.

Ball, J. and R. James (1987). Fine phase mixtures as minimizers of energy. *Arch. Ration. Mech. An. 100*, 13–52.

Barbe, F., L. Decker, D. Jeulin, and G. Cailletaud (2001). Intergranular and intragranular behavior of polycrystalline aggregates. Part 1: FE model. *Int. J. Plasticity 17*(4), 513–536.

Barot, G. and I. Rao (2006). Constitutive modeling of the mechanics associated with crystallizable shape memory polymers. *Z. Angew. Math. Mech. 57*(4), 652–681.

Barot, G., I. Rao, and K. Rajagopal (2008). A thermodynamic framework for the modeling of crystallizable shape memory polymers. *Int. J. Eng. Sci. 46*(4), 325–351.

Barras, C. and K. Myers (2010). Nitinol - Its use in vascular surgery and other applications. *EJVES Extra 19*, 564–569.

Barrera, O., M. A., M. Abbadi, M. Azaouzi, and S. Belouettar (2012). On high-cycle fatigue of 316L stents. *Comput. Methods Biomech. Biomed. Engin. 0*, 1–12.

Bartel, T. and K. Hackl (2009). A micromechanical model for martensitic transformations in shape-memory alloys based on energy relaxation. *ZAMM 89*, 792–809.

Bartel, T. and K. Hackl (2010). Multiscale modeling of martensitic phase transformations: on the numerical determination of heterogeneous mesostructures within shape-memory alloys induced by precipitates. *Techn. Mech. 30*, 324–342.

Bartel, T., A. Menzel, and B. Svendsen (2011). Thermodynamic and relaxation-based modeling of the interaction between martensitic phase transformations and plasticity. *J. Mech. Phys. Solids 59*, 1004–1019.

Basquin, O. (1910). The exponential law of endurance tests. *Proc. of the ASTM 10*, 625–630.

Bauschinger, J. (1886). Über die Veränderung der Elasticitätsgrenze und der Festigkeit des Eisens und

Stahls durch Strecken und Quetschen, durch Abkühlen und durch oftmals wiederholte Beanspruchung. *Mittheilungen aus dem Mechanisch-Technischem Laboratorium der Tech. Hochschule, München 13*, 1.

Bazant, Z. (1984). *Mechanics of Engineering Materials*, Chapter 3 - Microplane model for strain controlled inelastic behavior, pp. 45–59. John Wiley and Sons.

Bekker, A. and L. Brinson (1997). Temperature-induced phase transformation in a shape memory alloy: phase diagram based kinetics approach. *J. Mech. Phys. Solids 45*(6), 949–988.

Ben-Tal, A. and A. Nemirovski (2001). *Lectures on Modern Convex Optimization*. Society for Industrial and Applied Mathematics.

Benallal, A. and D. Marquis (1987). Constitutive equations for non-proportional cyclic elastoviscoplasticity. *J. Eng. Mater. - T. ASME 109*, 326–336.

Bentachfine, S., G. Pluvinage, J. Gilgert, Z. Azari, and D. Bouami (1999). Notch effect in low cycle fatigue. *Int. J. Fatigue 21*(5), 421–430.

Bertsekas, D. (1982). *Constrained Optimization and Lagrange Multiplier Methods*. Academic Press, New York.

Besson, J., G. Cailletaud, J. Chaboche, and S. Forest (2010). *Non-Linear Mechanics of Materials*. Springer.

Bhattacharyya, A. and H. Tobushi (2000). Analysis of the isothermal mechanical response of a shape memory polymer rheological model. *Polym. Eng. Sci. 40*(12), 2498–2510.

Bićanić, N. and C. Pearce (1996). Computational aspects of a softening plasticity model for plain concrete. *Mech. Cohes. Frict. Mat. 1*, 75–94.

Bilotta, A., L. Leonetti, and G. Garcea (2012). An algorithm for incremental elastoplastic analysis using equality constrained sequential quadratic programming. *Comput. Struct. 102-103*, 97–107.

Bisbos, C. and P. Pardalos (2007). Second-order cone and semi-definite representations of material failure criteria. *J. Optimiz. Theory App. 134*, 275–301.

Boisse, P., P. Bussy, and P. Ladeveze (1990). A new approach in nonlinear mechanics - the large time increment method. *Int. J. Numer. Methods Eng. 29*(3), 647–663.

Bombac, D., M. Brojan, P. Fajfar, F. Kosel, and R. Turk (2007). Review of marterials in medical applications. *Mater. Geoenv. 54*, 471–499.

Bouvet, C., S. Calloch, and C. Lexcellent (2002). Mechanical behavior of a Cu-Al-Be shape memory alloy under multiaxial proportional and non-proportional loadings. *J. Eng. Mater-T. ASME 124*, 112–124.

Bouvet, C., S. Calloch, and C. Lexcellent (2004). A phenomenological model for pseudoelasticity of shape memory alloys under multiaxial proportional and non-proportional loadings. *Eur. J. Mech. A-Solid 23*, 37–61.

Boyd, J. and D. Lagoudas (1994). Thermomechanical response of shape memory composites. *J. Intel. Mat. Syst. Str. 5*(3), 333–346.

Boyd, J. and D. Lagoudas (1996). A thermodynamical constitutive model for shape memory materials. Part I: The monolithic shape memory alloy. *International Journal of Plasticity 12*(6), 805–842.

Brézis, H. (1973). *Opérateurs Maximaux Monotones et Semi-groupes de Contractions dans les Espaces de Hilbert*. North-Holland, Amsterdam.

Brinson, L. (1993). One-dimensional constitutive behavior of shape memory alloys: thermomechanical derivation with non-constant material functions and redefined martensite internal variables. *J. Intel. Mat. Syst. Str. 4*, 229–242.

Brocca, M., L. Brinson, and Z. Bazant (2002). Three-dimensional constitutive model for shape memory alloys based on microplane model. *J. Mech. Phys. Solids 50*(5), 1051–1077.

Buehler, W. J., J. V. Gilfrich, and R. C. Wiley (1963). Effect of Low-Temperature Phase Changes on the Mechanical Properties of Alloys near Composition TiNi. *J. Appl. Phys. 34*(5), 1475–1477.

Bui, H., K. Dang Van, and C. Stolz (1981). Relations entre grandeurs microscopiques et macroscopiques. *CR. Acad. Sci. 294*, 1155–1158.

Bullen, W., A. Head, and W. Wood (1953). Structural changes during the fatigue of metals. *Proc. Roy. Soc. A216*, 332.

Bundhoo, V., E. Haslam, B. Birch, and E. Park (2009). A shape memory alloy-based tendon-driven actuation system for biomimetic artificial fingers. Part I: design and evaluation. *Robotica 27*, 131–146.

Cao, J., W. Zhuang, S. Wang, K. Ho, N. Zhang, J. Lin, and T. Dean. (2009). An integrated crystal plasticity FE system for microforming simulation. *J. Multiscale Modelling 1*, 107.

Casciati, F. and L. Faravelli (2004). Experimental characterisation of a Cu-based shape memory alloy toward its exploitation in passive control devices. *J. Phys. IV 115*, 299–306.

Casciati, F., L. Faravelli, and L. Petrini (1998). Energy dissipation in shape memory alloy devices. *Comput-aided Civ. Inf. 13*, 433–442.

Cast3M (2013). *Documentation Cast3M*. http://www-cast3m.cea.fr.

Cernoch, T., M. Landa, V. Novk, P. Sedlk, and P. Sittner (2004). Acoustic characterization of the elastic properties of austenite phase and martensitic transformations in Cu-Al-Ni shape memory alloy. *J. Alloy Compd 378*(1-2), 140–144.

Chaboche, J., K. Dang Van, and K. Cordier (1979). Modelisation of the strain memory effect on the cycle hardening of 316L stainless steel. In *Proceedings SMIRT 5*, Volume M.

Charkaluk, E., A. Bignonnet, A. Constantinescu, and K. Dang Van (2002). Fatigue design of structures under thermomechanical loadings. *Fatigue Fract. Eng. Mater. Struct. 25*(12), 1199–1206.

Charkaluk, E., L. Bodelot, and R. Seghir (2009). Shakedown, dissipation and fatigue of metals. In *Proceedings of the 7th EUROMECH Solid Mechanics Conference (EUROMECH 2009)*.

Charkaluk, E. and A. Constantinescu (2009). Dissipative aspects in high cycle fatigue. *Mech. Mater. 41*(5), 483–494.

Chemisky, Y., G. Chatzigeorgiou, P. Kumar, and D. Lagoudas (2014). A constitutive model for cyclic actuation of high-temperature shape memory alloys. *Mech. Mater. 68*, 120–136.

Chemisky, Y., A. Duval, E. Patoor, and T. Ben Zineb (2011). Constitutive model for shape memory alloys including phase transformation, martensitic reorientation and twins accommodation. *Mech. Mater. 43*, 361–376.

Chen, C. and O. Mangasarian (1995). Smoothing methods for convex inequalities and linear complementarity problems. *Math. Program. 71*(1), 51–69.

Chen, J. and S. Pan (2012). A survey on SOC complementarity functions and solution methods for SOCPs and SOCCPs. *Pac. J. Optim. 8*, 33–74.

Chen, Y. and D. Lagoudas (2008a). A constitutive theory for shape memory polymers. Part I: Large deformations. *J. Mech. Phys. Solids 56*(5), 1752–1765.

Chen, Y. and D. Lagoudas (2008b). A constitutive theory for shape memory polymers. Part II: A linearized model for small deformations. *J. Mech. Phys. Solids 56*(5), 1766–1778.

Christensen, P. (2002). A non-smooth Newton method for elastoplastic problems. *Computer Methods in Applied Mechanics and Engineering 191*, 1189–1219.

Ciarlet, P. (1993). *Mathematical Elasticity: Three-Dimensional Elasticity*, Volume 1. Elsevier.

Coda, A., L. Toia, G. Ischia, and S. Gialanella (2006). Effect of thermomechanical treatments on the microstructure of NiTi wires: A TEM study. In *Proceedings of the International Conference on Shape Memory and Superelastic Technologies (SMST 2006)*.

Coffin, L. (1953). A study of the effects of cyclic thermal stresses on a ductile metal. *Trans. A.S.M.E. 53-A76*, 931–950.

Comi, C., A. Corigliano, and G. Maier (1991). Extremum properties of finite-step solutions in elastoplasticity with nonlinear mixed hardening. *Int. J. Solids Struct. 27*(8), 965–981.

Commend, S., A. Truty, and T. Zimmermann (2004). Stabilized finite elements applied to elastoplasticity: I. mixed displacement-pressure formulation. *Comput. Methods in Appl. Mech. Eng. 193*(33-35), 3559–3586.

Connolley, T., P. McHugh, and M. Bruzzi (2005). A review of deformation and fatigue of metals at small size scales. *Fatigue Fract. Eng. Mater. Struct. 28*(12), 1119–1152.

Constantinescu, A., E. Charkaluk, G. Lederer, and L. Verger (2004). A computational approach to thermomechanical fatigue. *Int. J. Fatigue 26*, 805–818.

Constantinescu, A., K. Dang Van, and E. Charkaluk (2003). A unified approach for high and low cycle fatigue based on shakedown concepts. *Fatigue Fract. Eng. Mater. Struct. 26*, 561–568.

Constantinescu, A. and L. Verger (2002). Indentification of a viscoplastic material behaviour under anisothermal conditions. In D. Petit, D. Ingham, Y. Jarny, and F. Plourde (Eds.), *Eurotherm Seminar 68: Inverse problems and experimental design in thermal and mechanical engineering (ETS 2002)*, pp. 221–228.

Contrafatto, L. and G. Ventura (2004). Numerical analysis of Augmented Lagrangian algorithms in complementary elastoplasticity. *Int. J. Numer. Methods Eng. 60*, 2263–2287.

Crossland, B. (1956). Effect of large hydrostatic pressure on the torsional fatigue strength of an alloy steel. In *Proceedings of the International Conference on Fatigue of Metals*, pp. 138–149.

Cuomo, M. and L. Contrafatto (2000). Stress rate formulation for elastoplastic models with internal variables based on augmented Lagrangian regularization. *Int. J. Solids Struct. 37*, 3935–3964.

Cuschieri, A. (1991). Variable curvature shape-memory spatula for laparoscopic surgery. *Surg. Endosc. 5*, 179–181.

Daghia, F., M. Fabrizio, and D. Grandi (2010). A non isothermal Ginzburg-Landau model for phase transitions in shape memory alloys. *Meccanica 45*(6), 797–807.

Daghia, F., A. Giammarruto, and G. Pascale (2011). Combined use of FBG sensors and SMA actuators for concrete beams repair. *Struct. Control Health Monit. 18*(8), 908–921.

Daghia, F., D. Inman, F. Ubertini, and E. Viola (2008). Shape memory alloy hybrid composite plates for shape and stiffness control. *J. Intel. Mat. Syst. Str. 19*(5), 609–619.

Daghia, F., D. Inman, F. Ubertini, and E. Viola (2010). Active shape change of an SMA hybrid composite plate. *Smart Struct. Syst. 6*(2), 91–100.

Dai, K., X. Hou, Y. Sun, R. Tang, S. Qiu, and C. Ni (1993). Treatment of intra-articular fractures with shape memory compression staples. *Injury 24*(10), 651–655.

Dang Van, K. (1973). Sur la résistance á la fatigue des métaux. *Sciences Technique Armement 47*(3), x–x.

Dang Van, K. (1999). High-cycle metal fatigue in the context of mechanical design. In K. Van and I. Papadopoulos (Eds.), *CISM Courses and Lectures no 392*, pp. 57–88. Springer-Verlag.

Dang Van, K., A. Bignonnet, and J. Fayard (2003). Assessment of welded structures by a structural multiaxial fatigue approach. In M. d. F. Andrea Carpinteri and A. Spagnoli (Eds.), *Biaxial/Multiaxial Fatigue and Fracture 6th International Conference on Biaxial/Multiaxial Fatigue and Fracture*, Volume 31 of *European Structural Integrity Society*, pp. 3 – 21. Elsevier.

Dang Van, K., B. Griveau, and O. Message (1989). On a New Multiaxial Fatigue Limit Criterion: Theory and Application. In M. Brown and K. Miller (Eds.), *Biaxial and Multiaxial Fatigue (EGF 3)*, pp. 479–496. Mechanical Engineering Publications, London.

Dang Van, K., H. Maitournan, and J. Flavenot (2009). Fatigue Design of Notched Components by a Multiscale Approach Based on Shakedown. In G. Pluvinage and A. Sedmak (Eds.), *Security and Reliability of Damaged Structures and Defective Materials*, NATO Science for Peace and Security Series C: Environmental Security, pp. 325–336. Springer Netherlands.

Davies, V. (1935). Discussion of The Strength of Metals under Combined Alternating Stresses by H.J. Gough and H.V. Pollard. In *Proceedings of the Institution of Mechanical Engineers*, Volume 131.

de Aguiar, R., W. de Castro Leao Neto, M. Savi, and P. Calas Lopes Pacheco (2013). Shape memory alloy helical springs performance: Modeling and experimental analysis. *Mater. Sci. Forum 758*, 147–156.

de Aguiar, R., M. Savi, and P. Pacheco (2010). Experimental and numerical investigations of shape memory alloy helical springs. *Smart Mater. Struct. 9*, 1–19.

De Beule, M., P. Mortier, S. Carlier, B. Verhegghe, R. Van Impe, and P. Verdonck (2008). Realistic finite element-based stent design: The impact of balloon folding. *J. Biomech. 41*(2), 383–389.

de Souza Neto, E., D. Perić, and D. Owen (1994). A model for elastoplastic damage at finite strains: algorithmic issues and applications. *Eng. Computations 11*, 257–281.

de Souza Neto, E., D. Peric, and D. Owen (2008). *Computational Methods for Plasticity: Theory and Applications*. Wiley, U.K.

Dennis, J. and R. Schnabel (1983). *Numerical Methods for Unconstrained Optimization and Nonlinear Equations*. Prentice-Hall, Englewood Cliffs, New York.

Devincre, B., L. Kubin, and T. Hoc (2006). Physical analyses of crystal plasticity by DD simulations. *Scripta Materialia 54*(5), 741–746.

Dhakal, B., A. Saleeb, M. Hosseini, and S. Padula II (2013). Large scale simulation of NiTi helical spring actuators under repeated thermomechanical cycles. *Smart Mater. Struct. 22*, 1–20.

Di Bucchianico, A. (2008). *Coefficient of Determination (R2)*. John Wiley & Sons, Ltd.

Disegi, J., R. Kennedy, and R. Pilliar (1999). *Cobalt-base Alloys for Biomedical Applications*. ASMT International.

Dolce, M. and D. Cardone (2001). Mechanical behaviour of shape memory alloys for seismic applications 2. Austenite NiTi wires subjected to tension. *Int. J. Mech. Sci. 43*(11), 2657–2677.

Donnelly, E. (2012). *Geometry effect in the fatigue behaviour of microscale 316L stainless steel specimens*. Ph. D. thesis, National University of Ireland, Galway.

dos Santos, H., F. Auricchio, and M. Conti (2012). Fatigue life assessment of cardiovascular balloon-expandable stents: A two-scale plasticity-damage model approach. *J. Mech. Behav. Biomed. 15*, 78–92.

Dowling, N. (1972). Fatigue failure predictions for complicated stress-strain histories. *JOM 7*, 71–87.

Duerig, T., K. Melton, D. Stoekel, and C. Wayman (Eds.) (1990). *Engineering Aspects of Shape Memory Alloys*. Butterworth-Heinemann, London.

Duerig, T., A. Pelton, and D. Stoeckel (1999). An overview of nitinol medical applications. *Mater. Sci. Eng. A 273-275*, 149–160.

Dumont, G. and C. Kuhl (2005). Finite element simulation for design optimization of shape memory alloy spring actuators. *Eng. Computation 22*, 835–848.

Dumoulin, C. and B. Cochelin (2000). Mechanical behaviour of balloon expandable stents. *J. Biomech. 33*, 1461–1470.

Dutko, M., D. Péric, and D. Owen (1993). Universal anisotropic yield criterion based on superquadratic functional representation: Part I. Algorithmic issues and accuracy analysis. *Comput. Methods in Appl. Mech. Eng. 109*, 73–93.

Eggeler, G., E. Hornbogen, A. Yawny, A. Heckmann, and M. Wagner (2004). Structural and functional fatigue of NiTi shape memory alloys. *Mater. Sci. Eng. A 378*(1-2), 24–33.

El Feninat, F., G. Laroche, M. Fiset, and D. Mantovani (2002). Shape memory materials for biomedical applications. *Adv. Eng. Mater. 4*, 91–104.

Elber, W. (1970). Fatigue crack closure under cyclic tension. *Engng. Fract. Mech. 2*, 37–45.

Ellyin, F. (1989). Cyclic strain energy density as a criterion for multiaxial fatigue failure. *Biaxial and Multiaxial Fatigue*, 571–583.

Endosmart (consultation: february 2013). http://www.endosmart.com/en/.

Ewing, J. and J. Humfrey (Ewing1903). The Fracture of Metals under Repeated Alternations of Stress. *Philos.Trans. R. SOC. 200*, 241–253.

Faiella, G., V. Antonucci, F. Daghia, S. Fascia, and M. Giordano (2011). Fabrication and thermo-mechanical characterization of a shape memory alloy hybrid composite. *J. Intel. Mat. Syst. Str. 22*(3), 245–252.

Falk, F. (1980). Model free-energy, mechanics and thermodynamics of shape memory alloys. *Acta Metall. 28*, 1773–1780.

Falk, F. (1983). One-dimensional model of shape memory alloys. *Arch. Mech. 35*, 63–84.

Falk, F. and P. Konopka (1990). Three-dimensional Landau theory describing the martensitic transformation of shape memory alloys. *J. Phys-Paris 2*, 61–77.

Feltner, C. and J. Morrow (1961). Micro-plastic strain hysteresis energy a criterion for fatigue fracture. *J. Basic Eng. Trans. A.S.M.E. 83*, 15–22.

Feng, X. and Q. Sun (2007). Shakedown analysis of shape memory alloy structures. *Int. J. Plasticity 23*(2), 183–206.

Ferjani, M., D. Averbuch, and A. Constantinescu (2011a). A computational approach for the fatigue design of threaded connections. *Int. J. Fatigue 33*, 610–623.

Ferjani, M., D. Averbuch, and A. Constantinescu (2011b). Semianalytical solution for the stress distribution in notched tubes. *Int. J. Fatigue 33*(4), 557–567.

Findley, W. (1957). Fatigue of Metals Under Combinations of Stresses. *Trans. A.S.M.E. 79*, x–x.

Firstov, G., J. Van Humbeeck, and Y. Koval (2006). High temperature shape memory alloys: Problems and prospects. *Int. J. Plasticity 17*, 1041–1047.

Fischer, A. (1992). A special Newton-type optimization method. *Optim. 24*, 269–284.

Fischer, F. and K. Tanaka (1992). A micromechanical model for the kinetics of martensitic transformation. *Int. J. Solids Struct. 29*(14-15), 1723–1728.

Forest, S., F. Barbe, and G. Cailletaud (2001). Intergranular and intragranular behavior of polycrystalline aggregates. Part 2: Results. *Int. J. Plasticity 17*(4), 537–563.

Frémond, M. (2002). *Non-smooth Thermomechanics*. Springer-Verlag, Berlin.

Frémond, M. (2012). *Phase Change in Mechanics*, Volume 13 of *Lecture Notes of the Unione Matematica Italiana*. Springer.

Gall, K., M. Dunn, Y. Liu, D. Finch, M. Lake, and N. Munshi (2002). Shape memory polymer nanocomposites. *Acta Mater. 50*(20), 5115–5126.

Gao, X. and L. Brinson (2002). A simplified multivariant SMA model based on invariant plane nature of martensitic transformation. *J. Intel. Mat. Syst. Str. 1*(13), 795–810.

Gao, X., M. Huang, and L. Brinson (2000). A multivariant micromechanical model for SMAs Part 1. Crystallographic issues for single crystal model. *Int. J. Plasticity 16*(10-11), 1345–1369.

Gao, X., R. Qiao, and L. Brinson (2007). Phase diagram kinetics for shape memory alloys: a robust finite element implementation. *Smart Mater. Struct. 16*, 2102–2115.

Gerber, W. (1874). Bestimmung der zulassigen Spannungen in Eisen-Constructionen. *Z. Bayer Archit. Ing. Ver. 6*(6), 101–110.

Gerland, M. and P. Violan (1986). Secondary cyclic hardening and dislocation structures in type 316 stainless steel at 600 °C. *Mater. Sci. Eng. 84*(0), 23–33.

Gervaso, F., C. Capelli, L. Petrini, S. Lattanzio, L. Di Virgilio, and F. Migliavacca (2008). On the effects of different strategies in modelling balloon-expandable stenting by means of finite element method. *J. Biomech. 41*, 1206–1212.

Glenn, R. and J. Lee (1997). Accelerated pulsite fatigue testing of Ni-Ti coronary stents. In A. Pelton, D. Hodgson, S. Russell, and T. Duerig (Eds.), *Proceedings of the Second International Conference on Shape Memory and Superelastic Technologies (SMST 1997)*. SMST Society, Pacific Grove, California, CA, USA.

Goodman, J. (1899). *Mechanics applied to Engineering*. Longmans, Green & Company.

Gopal, V. and L. Biegler (1999). Smoothing Methods for Complementarity Problems in Process Engineering. *AICHE J. 45*(7), 1535–1547.

Gough, H. and H. Pollard (1935). The Strength of Metals under Combined Alternating Stresses. In *Proceedings of the Institution of Mechanical Engineers*, Volume 131, pp. 3–103.

Gough, H., H. Pollard, and W. Clenshaw (1951). Some experiments on the resistance of metals to fatigue under combined stresses. Technical report, Aeronautical Research Council Reports, R and M 2522, HMSO, London.

Grabe, C. and O. Bruhns (2008). On the viscous and strain rate dependent behavior of polycrystalline NiTi. *Int. J. Solids Struct. 45*(7-8), 1876–1895.

Grabe, C. and O. Bruhns (2009). Path dependence and multiaxial behavior of a polycrystalline NiTi alloy within the pseudoelastic and pseudoplastic temperature regimes. *Int. J. Plasticity 25*, 513–545.

Grogan, J., S. Leen, and P. McHugh (2013). Influence of statistical size effects on the plastic deformation of coronary stents. *J. Mech. Behav. Biomed. 20*, 61–76.

Grover, H., S. Bishop, and L. Jackson (1951). Fatigue strength of aircraft materials. Axial load fatigue tests on unnotched sheet specimens of 24S-T3, 75S-T6 aluminum alloys and of SAE 4130 steel. Technical report, NACA TN 2324.

Gruber, P. and J. Valdman (2009). Solution of One-Time-Step Problems in Elastoplasticity by a Slant Newton Method. *SIAM J. Sci. Comput. 31*(2), 1558–1580.

Grujicic, M., B. Pandurangan, A. Arakere, and J. Snipes (2012). Fatigue-Life Computational Analysis for the Self-Expanding Endovascular Nitinol Stents. *J. Mater. Eng. Perform. 21*, 2218–2230.

Gurtin, M., E. Fried, and L. Anand (2010). *The Mechanics and Thermodynamics of Continua*, Volume 158. Cambridge University Press.

Haigh, B. (1917). Experiments on the Fatigue of Brasses. *J. Inst. Metals 18*, 55–86.

Han, W. and B. Reddy (1999). *Plasticity: Mathematical Theory and Numerical Analysis*. Springer-Verlag.

Harewood, F. and P. McHugh (2007). Modeling of size dependent failure in cardiovascular stent struts under tension and bending. *Annals of Biomedical Engineering 35*(9), 1539–1553.

Harker, P. and J. Pang (1990). Finite-dimensional variational inequality and nonlinear complementarity problems: A survey of theory, algorithms and applications. *Math. Program. 48*, 161–220.

Hartl, D. (2009). *Modeling of shape memory alloys considering rate-independent and rate-dependent irrecoverable strains*. Ph. D. thesis, Texas A&M University.

Hartl, D., G. Chatzigeorgiou, and D. Lagoudas (2010). Three-dimensional modeling and numerical analysis of rate-dependent irrecoverable deformation in shape memory alloys. *Int. J. Plasticity 26*, 1485–1507.

Hartl, D. and D. Lagoudas (2009). Constitutive modeling and structural analysis considering simultaneous phase transformation and plastic yield in shape memory alloys. *Smart Mater. Struct. 18*, 1–17.

Harvey, S. (2011). Nitinol Stent Fatigue in a Peripheral Human Artery Subjected to Pulsatile and Articulation Loading. *J. Mater. Eng. Perform. 20*, 697–705.

Haslinger, J. and P. Neittaanmäki (1988). *Finite element approximation for optimal Shape Design: Theory and Applications*. Wiley, Chichester.

Hayashi, S. (2004). *Studies on second order cone complementarity problems*. Ph. D. thesis, Kyoto University.

Helm, D. (2007). Numerical simulation of martensitic phase transitions in shape memory alloys using an improved integration algorithm. *Int. J. Numer. Methods Eng. 69*, 1997–2035.

Helm, D. and P. Haupt (2003). Shape memory behaviour: modelling within continuum thermomechanics. *Int. J. Solids Struct. 40*(4), 827–849.

Hibbert, B. and E. O'Brien (2011). Coronary stent fracture. *183*(11), E756.

Hill, R. (1950). *The mathematical theory of plasticity*. Clarendon Press, Oxford.

Hjiaj, M., J. Fortin, and G. de Saxcé (2003). A complete stress update algorithm for the non-associated Drucker-Prager model including treatment of the apex. *Int. J. Eng. Sci. 41*, 1109–1143.

Hohenemser, K. and W. Prager (1933). *Dynamik der Stabwerke. Eine Schwingungslehre für Bauingenieure*. Springer.

Hsiao, H. and M. Yin (2013). An intriguing design concept to enhance the pulsatile fatigue life of self-expanding stents. *Biomedical Microdevices*, 1–9.

Hu, J. and S. Chen (2010). A review of actively moving polymers in textile applications. *J. Mater. Chem. 20*, 3346–55.

Hu, J., Y. Zhu, H. Huang, and J. Lu (2012). Recent advances in shape-memory polymers: Structure, mechanism, functionality, modeling and applications. *Prog. in Polym. Sci. 37*(12), 1720–1763.

Huang, J., J. Yeh, S.-L. Jeng, C. Chen, and R. Kuo (2006). High-Cycle Fatigue Behavior of Type 316L Stainless Steel. *Mat. Trans. 47*, 409–417.

Huang, M., X. Gao, and L. Brinson (2000). A multivariant micromechanical model for SMAs Part 2. Polycrystal model. *Int. J. Plasticity 16*(10-11), 1371–1390.

Huo, Y. (1989). A mathematical model for the hysteresis in shape memory alloys. *Continuum Mech. Thermodyn. 1*, 283–303.

Idelsohn, S., J. Peña, D. Lacroix, J. Planell, F. Gil, and A. Arcas (2004). Continuous mandibular distraction osteogenesis using superelastic shape memory alloy (SMA). *J. Mater. Sci. 15*(4), 541–546.

Imbeni, V., A. Mehta, S. Robertson, T. Duerig, A. Pelton, and R. Ritchie (2003). On the mechanical behavior of Nitinol under multiaxial loading conditions and in situ synchrotron X-rays. In *Proceedings of the international conference on Shape Memory and Superelastic Technologies (SMST 2003)*, Pacific Grove, CA, pp. 267–276.

Ivshin, Y. and T. Pence (1994). A constitutive model for hysteretic phase transition behavior. *Int. J. Eng. Sci. 32*, 681–704.

Janke, L., C. Czaderski, M. Motavalli, and J. Ruth (2005). Applications of shape memory alloys in civil engineering structures - overview, limits and new ideas. *Mat. Struct. 38*, 578–592.

Ju, F., Z. Xia, and K. Sasaki (2008). On the finite element modelling of balloon-expandable stents. *J. Mech. Behav. Biomed. Mater. 1*(1), 86–95.

Kachanov, L. (1986). *Introduction to continuum damage mechanics*. Kluwer Academic, Dordrecht.

Kadkhodaei, M., M. Salimi, R. Rajapakse, and M. Mahzoon (2007). Modeling of shape memory alloys based on microplane theory. *J. Intel. Mat. Syst. Str. 19*, 541–550.

Kang, G., Q. Kan, C. Yu, D. Song, and Y. Liu (2012). Whole-life transformation ratchetting and fatigue of super-elastic NiTi Alloy under uniaxial stress-controlled cyclic loading. *Mater. Sci. Eng. A 535*(0), 228–234.

Kanzow, C. (1996). Some non-interior continuation methods for linear complementarity problems. *SIAM J. Matrix Anal. Appl. 17*, 851–868.

Karush, W. (1939). Minima of Functions of Several Variables with Inequalities as Side Constraints. Master's thesis, Department of Mathematics, University of Chicago, Chicago, Illinois.

Khandelwal, A. and V. Buravalla (2009). Models for shape memory alloy behavior: An overview of modeling approaches. *Int. J. Struct. Changes Sol. 1*, 111–148.

Khidir, E., N. Mohamed, M. Nor, and M. Mustafa (2008). A new method for actuating parallel manipulators. *Sensors Actuat. A 147*, 593–599.

Khonakdar, H., S. Jafari, S. Rasouli, J. Morshedian, and H. Abedini (2007). Investigation and Modeling of Temperature Dependence Recovery Behavior of Shape-Memory Crosslinked Polyethylene. *Macromolecular Theory and Simulations 16*(1), 43–52.

Kianzad, S., A. Amini, and S. Karkouti (2011). Force control of laparoscopy grasper using antagonistic shape memory alloy. In *Proceedings of the First Middle East Conference on Biomedical Engineering (MECBME 2011)*, Sharjah, pp. 335–338.

Kiefer, B., T. Bartel, , and A. Menzel (2012). Implementation of numerical integration schemes for the simulation of magnetic SMA constitutive response. *Smart Mater. Struct. 21*, 1–8.

Kim, B., S. Lee, J. Lee, S. Baek, Y. Choi, J. Lee, and M. Xu (1998). Polyurethane ionomers having shape memory effects. *Polymer 39*(13), 2803–2808.

Kim, B., S. Lee, and M. Xu (1996). Polyurethanes having shape memory effects. *Polymer 37*(26), 5781–5793.

Kim, J., T. Kang, and W. Yu (2010). Thermo-mechanical constitutive modeling of shape memory polyurethanes using a phenomenological approach. *Int. J. Plasticity 26*(2), 204–218.

Kim, Y. and S. Miyazaki (1997). Fatigue life of Ti-50 at.% Ni and Ti-40Ni-10Cu (at.%) shape memory alloy wires. In *Proceedings of the 2nd International Conference on Shape Memory and Superelastic Technologies (SMST 1997)*, Asilomar, CA, USA, pp. 473–478.

Koiter, W. (1960). *Progress in Solid Mechanics*, Chapter General theorems for elasto-plastic solids, pp. 167–221.

Kolesov, I., K. Kratz, A. Lendlein, and H. Radusch (2009). Kinetics and dynamics of thermally-induced shape-memory behavior of crosslinked short-chain branched polyethylenes. *Polymer 50*(23), 5490–5498.

Korelc, J. (2002). Multi-language and multi-environment generation of nonlinear finite element codes. *Eng. Comput. 18*(4), 312–327.

Korelc, J. (2009). *AceFEM/AceGen Manual 2009*. http://www.fgg.uni-lj.si/Symech/.

Korsunsky, A., D. Dini, F. Dunne, and M. Walsh (2007). Comparative assessment of dissipated energy and other fatigue criteria. *Int. J. Fatigue 29*(9-11), 1990–1995.

Kourambas, J., F. Delvecchio, R. Munver, and G. Preminger (2000). Nitinol stone retrieval-assisted ureteroscopic management of lower pole renal calculi. *Urology 56*(6), 935–939.

Krabbenhoft, K., A. Lyamin, and S. Sloan (2007). Formulation and solution of some plasticity problems as conic programs. *Int. J. Solids Struct. 44*, 1533–1549.

Krabbenhoft, K., A. Lyamin, S. Sloan, and P. Wriggers (2007). An interior point algorithm for elastoplasticity. *Int. J. Numer. Methods Eng. 69*, 592–626.

Krempl, E. and F. Khan (2003). Rate (time)-dependant deformation behavior: an overview of some properties of metal and solid polymers. *Int. J. Plasticity 19*, 1069–1095.

Kuhn, H. and A. Tucker (1951). Nonlinear programming. In B. U. of California Press (Ed.), *Proceedings of the 2nd Berkeley Symposium*, pp. 481–492.

Laamouri, A., H. Sidhom, and C. Braham (2013). Evaluation of residual stress relaxation and its effect on fatigue strength of AISI 316L stainless steel ground surfaces: Experimental and numerical approaches. *Int. J. Fatigue 48*, 109–121.

Lagoudas, D. (Ed.) (2008). *Shape Memory Alloys. Modeling and Engineering Applications*. Springer.

Lagoudas, D., Z. Bo, and M. Qidwai (1996). A unified thermodynamic constitutive model for SMA and finite element analysis of active metal matrix composites. *Mech. Compos. Mater. St. 3*(2), 153–179.

Lagoudas, D., P. Entchev, P. Popov, E. Patoor, L. Brinson, and X. Gao (2006). Shape memory alloys, Part II: Modeling of polycrystals. *Mech. Mater. 38*, 430–462.

Lagoudas, D., D. Miller, L. Rong, and P. Kumar (2009). Thermomechanical fatigue of shape memory alloys. *Smart Mater. Struct. 18*(8), 1–12.

Lagoudas, D. and S. Shu (1999). Residual deformations of active structures with SMA actuators. *Int. J. Mech. Sci. 41*, 595–619.

Lagoudas, D., B. Volk, and Y. Chen (2010). Analysis of the finite deformation response of shape memory polymers: II. 1D calibration and numerical implementation of a finite deformation, thermoelastic model. *Smart Mater. Struct. 19*(7), 075006.

Lagoudas, D. C., D. Hartl, Y. Chemisky, L. Machado, and P. Popov (2012). Constitutive model for the numerical analysis of phase transformation in polycrystalline shape memory alloys. *Int. J. Plasticity 32-33*, 155–183.

Lally, C., F. Dolan, and P. Prendergast (2005). Cardiovascular stent design and vessel stresses: a finite element analysis. *J. Biomech. 38*(8), 1574–1581.

Lally, C., F. Dolan, and P. Prendergast (2006). Cardiovascular stent design and vessel stresses: a finite element analysis. *J. Biomech. 39*, 1760.

Lang, Y. and L. Biegler (2002). Distributed Stream Method for Tray Optimization. *AICHE J. 48*(3), 582–595.

Langer, B. (1937). Fatigue failure from stress cycles of varying amplitude. *J. Appl. Mech. 59*, 160–162.

Laster, Z., A. MacBean, P. Ayliffe, and L. Newlands (2001). Fixation of a frontozygomatic fracture with a shape-memory staple. *Brit. J. Oral Max. Surg. 39*(4), 324–325.

Lê, M.-B. (2013). *Propagation de fissure par fatigue dans un matériau pré-écroui, en présence de contraintes résiduelles*. Ph. D. thesis, École Polytechnique.

Le Pécheur, A., F. Curtit, M. Clavel, J. Stephan, C. Rey, and P. Bompard (2012). Thermo-mechanical FE model with memory effect for 304L austenitic stainless steel presenting microstructure gradient. *Int. J. Fatigue 45*, 106–115.

Leclercq, S. and C. Lexcellent (1996). A general macroscopic description of the thermomechanical behavior of shape memory alloys. *J. Mech. Phys. Solids 44*, 953–980.

Lemaitre, J. and J. Chaboche (1994). *Mechanics of Solid Materials*. Cambridge University Press.

Lemaitre, J. and R. Desmorat (2005). *Engineering Damage Mechanics: Ductile, Creep, Fatigue and Brittle Failures*. Springer.

Lemaitre, J., J. Sermage, and R. Desmorat (1999). A two scale damage concept applied to fatigue. *International Journal of Fracture 97*, 67–81.

Lendlein, A. and S. Kelch (2002). Shape-Memory Polymers. *Angew. Chem. 41*(12), 2034–2057.

Lexcellent, C., M. Boubakar, C. Bouvet, and S. Calloch (2006). About modelling the shape memory alloy behaviour based on the phase transformation surface identification under proportional loading and anisothermal conditions. *Int. J. Solids Struct. 48*, 613–626.

Lexcellent, C., B. Goo, Q. Sun, and J. Bernardini (1996). Characterization, thermomechanical behaviour and micromechanical-based constitutive model of shape-memory Cu-Zn-Al single crystals. *Acta Mater. 44*(9), 3773–3780.

Lexcellent, C., S. Leclercq, B. Gabry, and G. Bourbon (2000). The two way shape memory effect of shape memory alloys: an experimental study and a phenomenological model. *Int. J. Plasticity 16*, 1155–1168.

Leyffer, S. (2006). Complementarity constraints as nonlinear equations: Theory and numerical experience. In *Optimization with Multivalued Mappings*. Springer US.

Li, J., Q. Luo, Z. Xie, Y. Li, and Y. Zeng (2010). Fatigue life analysis and experimental verification of coronary stent. *Heart Vessels 25*(4), 333–337.

Liang, C. and C. Rogers (1990). One-dimensional thermomechanical constitutive relations for shape mem-

ory materials. *J. Intel. Mat. Syst. Str. 1*(2), 207–234.

Liang, C. and C. Rogers (1992). Design of shape memory alloy actuators. *J. Mech. Design 114*, 223.

Likhacev, A. and Y. Koval (1992). On the differential equation describing the hysteretic behavior of shape-memory alloys. *Scripta Metall. Mater. 27*, 223–227.

Lim, T. and D. McDowell (1999). Mechanical behavior of an Ni-Ti shape memory alloy under axial-torsional proportional and nonproportional loading. *J. Eng. Mater.-T. ASME 121*, 9–18.

Lin, P., H. Tobushi, K. Tanaka, T. Hattori, and M. Makita (1994). Pseudoelastic behaviour of TiNi shape memory alloy subjected to strain variations. *Mech. Mater. 5*, 694–701.

Lin, T. (1957). Analysis of elastic and plastic straines of a FCC crystal. *J. Mech. Phys. Solids 5*, 143.

Liu, Y., K. Gall, M. Dunn, A. Greenberg, and J. Diani (2006). Thermomechanics of shape memory polymers: Uniaxial experiments and constitutive modeling. *Int. J. Plasticity 22*(2), 279–313.

Liu, Y., K. Gall, M. Dunn, and P. McCluskey (2004). Thermomechanics of shape memory polymer nanocomposites. *Mech. Mater. 36*(10), 929–940.

Long, K., T. Scott, H. Qi, C. Bowman, and M. Dunn (2009). Photomechanics of light-activated polymers. *J. Mech. Phys. Solids 57*(7), 1103–1121.

Lubliner, J. (1984). A Maximum-Dissipation Principle in Generalized Plasticity. *ACTA Mech. 52*, 225–237.

Lubliner, J. (1986). Normality Rules in Large-Deformation Plasticity. *Mech. Mater. 5*, 29–34.

Lubliner, J. (1990). *Plasticity theory*. MacMillan, New York.

Luenberger, D. (1984). *Linear and Nonlinear Programming*. Addison-Wesley Publishing Company, Reading, Mass.

Luig, P. and O. Bruhns (2008). On the modeling of shape memory alloys using tensorial internal variables. *Mat. Sci. Eng. A-Struct. 481-482*, 379–383.

Luo, Z., J. Pang, and D. Ralph (1996). *Mathematical Programs with Equilibrium Constraints*. Cambridge University Press.

Machado, L. G. and M. A. Savi (2003). Medical applications of shape memory alloys. *Braz. J. Med. Biol. Res. 36*(6), 683–691.

Maier, G. (1970). A matrix structural theory of piece-wise linear plasticity with interacting yield planes. *Meccanica 6*, 55–66.

Maitournam, M., K. Dang Van, and J. Flavenot (2009). Fatigue Design of Notched Components with Stress Gradients and Cyclic Plasticity. *Adv. Eng. Mater. 11*(9), 750–754.

Maitournam, M., B. Pommier, and J. Thomas (2002). Determination of the asymptotic response of a structure under cyclic thermomechanical loading . *CR. Mec. 330*(10), 703–708.

Maletta, C., E. Sgambitterra, F. Furgiuele, and A. Casati, R.and Tuissi (2012). Fatigue of pseudoelastic NiTi within the stress-induced transformation regime: a modified Coffin-Manson approach. *Smart Mater. Struct. 21*(11), 1–7.

Mandel, J. (1964). Contribution Theorique a l'Etude de l'Ecrouissage et des Lois de l'Ecoulement Plastique. In *Proceedings of the Eleventh International Congress on Applied Mechanics*, pp. 502–509.

Mandel, J., B. Halphen, and J. Zarka (1977). Adaptation d'une Structure Elastoplastique a Ecrouissage Cinematique. *Mechanics Res. Commun. 4*, 309–314.

Manson, S. (1953). Behaviour of materials under conditions of thermal stresses. Technical report,

N.A.C.A., TN 2933.

Maplesoft (2013). *Maplesoft Documentation, www.maplesoft.com/products/maple/ 2013*.

Marketz, F. and F. Fischer (1996). Modelling the mechanical behavior of shape memory alloys under variant coalescence. *Comp. Mater. Sci. 5*(1-3), 210–226.

Marrey, R., R. Burgermeister, R. Grishaber, and R. Ritchie (2006). Fatigue and life prediction for cobalt-chromium stents: a fracture mechanics analysis. *Biomaterials 27*, 1988–2000.

Martin, D. and F. Boyle (2013). Finite element analysis of balloon-expandable coronary stent deployment: Influence of angioplasty balloon configuration. *Int. J. Numer. Method Biomed. Eng. x*, xx–xx.

Martin, J., B. Reddy, and T. Griffin (1987). Applications of mathematical programming concepts to incremental elastic-plastic analysis. *Engineering Structures 9*, 171–176.

Masud, A. and K. Xia (2006). A variational multiscale method for inelasticity: Application to superelasticity in shape memory alloys. *Comput. Methods in Appl. Mech. Eng. 195*(33-36), 4512–4531.

McDowell, D. and F. Dunne (2010). Microstructure-sensitive computational modeling of fatigue crack formation. *Int. J. Fatigue 32*(9), 1521–1542.

McGarry, J., B. O'Donnell, P. McHugh, and J. McGarry (2004). Analysis of the mechanical performance of a cardiovascular stent design based on micromechanical modelling. *Computational Materials Science 31*, 421–438.

McNaney, J., V. Imbeni, Y. Jung, P. Papadopoulos, and R. Ritchie (2003). An experimental study of the superelastic effect in a shape-memory Nitinol alloy under biaxial loading. *Mech. Mater. 35*, 969–986.

McNichols, J., P. Brookes, and J. Cory (1981). NiTi fatigue behavior. *J. Appl. Phys. 52*, 7742–7744.

Melan, E. (1936). Theorie statisch unbestimmter systeme aus ideal-plastischen baustoff. *Sitzungsberichte Akademie der Wissenschaften, Wien 1*, 145–195.

Melton, K. and O. Mercier (1979). Fatigue of NiTi thermoelastic martensites. *Acta Metall. 27*(1), 137–144.

Meoli, A., E. Dordoni, L. Petrini, F. Migliavacca, G. Dubini, and G. Pennati (2013). Computational Modelling of In Vitro Set-Ups for Peripheral Self-Expanding Nitinol Stents: The Importance of Stent-Wall Interaction in the Assessment of the Fatigue Resistance. *Cardiov. Eng. Tech. 4*(4).

Miner, M. (1945). Cumulative damage in fatigue. *J. Appl. Math. 12*, 159–164.

Miyazaki, S., T. Imai, Y. Igo, and K. Otsuka (1986). Effect of cyclic deformation on the pseudoelasticty characteristics of Ti-Ni alloys. *Metall. Mater. Trans. A 17*, 115–120.

Miyazaki, S., Y. Sugaya, and K. Otsuka (1988). Effects of various factors on fatigue life of Ti-Ni alloys. In *Proceedings of the MRS Int. Meet. on Advanced materials*, Volume 9, Tokyo, Japan, pp. 251–256.

Mohammad, K., E. Zainudin, M. Salit, N. Zahari, and A. Ali (2013). Experimental Determination of the Fatigue Behavior of Austenitic 316L Stainless Steel under Fatigue and Creep-Fatigue Tests at High Temperature. *Int. J. Metal Steel Research Tech. 1*(1), 1–11.

Monkman, G. (2000). Advances in shape memory polymer actuation. *Mechatronics 10*, 489–498.

Montenegro-Santillan, R., T. Alegre-Domingo, V. Faus-Matoses, and V. Faus-Llacer (2013). An in vitro comparison of cyclic fatigue resistance of ProTaper universal and GT series X files. *Med. Oral Patol. Oral Cir. Bucal 18*(3), e533–e5366.

Moreau, J. (1976). Application of convex analysis to the treatment of elastoplastic systems. In *Applications of Methods of Functional Analysis to Problems in Mechanics*. Springer, Berlin.

Morhácová, E. (1995). Relation between monte carlo simulations of grain growth and real structures.

Crystal Research and Technology 30(1), K9–K12.

Morin, C., Z. Moumni, and W. Zaki (2010). Cyclic behavior and fatigue design of shape memory alloy devices. In *Proceedings of Plasticity 2010*.

Morin, C., Z. Moumni, and W. Zaki (2011a). A constitutive model for shape memory alloys accounting for thermomechanical coupling. *Int. J. Plasticity 27*, 748–767.

Morin, C., Z. Moumni, and W. Zaki (2011b). Thermomechanical coupling in shape memory alloys under cyclic loadings: Experimental analysis and constitutive modeling. *Int. J. Plasticity 27*(12), 1959–1980.

Morlacchi, S., G. Pennati, L. Petrini, G. Dubini, and F. Migliavacca (2014). Influence of plaque calcifications on coronary stent fracture: A numerical fatigue life analysis including cardiac wall movement. *Journal of Biomechanics* (0), –.

Morrow, J. (1965). Cyclic plastic strain energy and fatigue of metals. *Int. Frict. Damp. Cyclic Plasticity STP 378*, 45–87.

Mortier, P., G. Holzapfel, M. Beule, D. Loo, Y. Taeymans, P. Segers, P. Verdonck, and B. Verhegghe (2010). A Novel Simulation Strategy for Stent Insertion and Deployment in Curved Coronary Bifurcations: Comparison of Three Drug-Eluting Stents. *Ann. Biomed. Eng. 38*(1), 88–99.

Moumni, Z., A. Van Herpen, and P. Riberty (2005). Fatigue analysis of shape memory alloys: energy approach. *Smart Mater. Struct. 14*, 287–292.

Moumni, Z., W. Zaki, and Q. Nguyen (2008). Theoretical and numerical modeling of solid-solid phase change: Application to the description of the thermomechanical behavior of shape memory alloys. *Int. J. Plasticity 24*, 614–645.

Murphy, B., H. Cuddy, F. Harewood, T. Connolley, and P. McHugh (2006). The influence of grain size on the ductility of micro-scale stainless steel stent struts. *Journal of Materials Science: Materials in Medicine 17*(1), 1–6.

Murphy, B., P. Savage, P. McHugh, and D. Quinn (2003). The Stress-Strain Behavior of Coronary Stent Struts is Size Dependent. *Annals of Biomedical Engineering 31*, 686–691.

Nayan, N., D. Roy, V. Buravalla, and U. Ramamurty (2008). Unnotched fatigue behavior of an austenitic Ni-Ti shape memory alloy. *Mater. Sci. Eng. A 497*(1-2), 333–340.

Nayan, N., D. Roy, V. Buravalla, and U. Ramamurty (2009). Effect of mechanical cycling on the stress-strain response of a martensitic Nitinol shape memory alloy. *Mater. Sci. Eng. A 525*, 60–7.

Nemat-Nasser, S. and W. Guo (2006). Superelastic and cyclic response of NiTi SMA at various strain rates and temperatures. *Mech. Mater. 38*, 463–474.

Neuber, H. (1946). *Theory of Notch Stresses*. Edwards.

Nguyen, Q. (2003). On shakedown analysis in hardening plasticity. *J. Mech. Phys. Solids 51*(1), 101–125.

Nguyen, Q. and B. Halphen (1975). Sur les matériaux standard généralisés. *J. Mecanique 14*, 39–63.

Nguyen, T., H. Qi, F. Castro, and K. Long (2008). A thermoviscoelastic model for amorphous shape memory polymers: Incorporating structural and stress relaxation. *J. Mech. Phys. Solids 56*(9), 2792–2814.

Nishihara, T. and M. Kawamoto (1945). The strength of metals under combined alternating bending and torsion with phase difference. *Memoirs of the College of Science and Engineering, Kyoto Imperial University 11*, 85–112.

Nocedal, J. and S. Wright (1999). *Numerical Optimization*. Springer.

Norwich, D. (2011). A Study of the Properties of a Room Temperature Martensitic Binary Nitinol Alloy Above and Below its Martensite to Austenite Transformation Temperature. *J. Mater. Eng. Perform. 20*, 529–534.

Olier, P., P. Matheron, and J. Sicre (2004). Experimental study of torsion behavior of NiTi alloy. *J. Phys. IV 115*, 185–194.

Orgeas, L. and D. Favier (1998). Stress-induced martensitic transformation of a NiTi alloy in isothermal shear, tension and compression. *Acta Mater. 46*(15), 5579–5591.

Ortin, J. (1992). Preisach modeling of hysteresis for a pseudoelastic Cu-Zn-Al single crystal. *J. Appl. Phys. 71*, 1454–1461.

Ortiz, M. and J. Simo (1986). An analysis of a new class of integration algorithms for elastoplastic constitutive relations. *Int. J. Numer. Methods Eng. 23*, 353–366.

Otsuka, K. and X. Ren (2005). Physical metallurgy of Ti-Ni-based shape memory alloys. *Prog. Mater. Sci. 50*, 511–678.

Otsuka, K. and C. Wayman (Eds.) (1998). *Shape Memory Materials*. Cambridge University Press, Cambridge.

Owen, D. and E. Hinton (1980). *Finite Elements in Plasticity*. Pineridge Press, Swansea.

Pachera, M. (2011). Studio della memoria di forma nei materiali polimerici. Master's thesis, Università degli Studi di Pavia.

Paiva, A., M. Savi, A. Braga, and P. Pacheco (2005). A constitutive model for shape memory alloys considering tensile-compressive asymmetry and plasticity. *Int. J. Solids Struct. 42*(11-12), 3439–3457.

Pakula, T. and M. Trznadel (1985). Thermally stimulated shrinkage forces in oriented polymers: 1. Temperature dependence. *Polymer 26*(7), 1011–1018.

Palmgren, A. (1924). Die Lebensdauer von Kugellagern. *Zeitschrift des Vereins Deutscher Ingenieure 68*, 339–341.

Pandini, S., S. Passera, M. Messori, K. Paderni, M. Toselli, A. Gianoncelli, E. Bontempi, and T. Riccò (2012). Two-way reversible shape memory behaviour of crosslinked poly(ϵ-caprolactone). *Polymer 53*, 1915–1924.

Panico, M. and L. Brinson (2007). A three-dimensional phenomenological model for martensite reorientation in shape memory alloys. *J. Mech. Phys. Solids 55*(11), 2491–2511.

Papadopoulos, I. (1987). *Fatigue Polycyclique des Métaux : Une Nouvelle Approche*. Ph. D. thesis, Ecole Nationale des Ponts et Chaussées, Paris, France.

Papadopoulos, I. V. (2001). Long life fatigue under multiaxial loading. *Int. J. Fatigue 23*(10), 839–849.

Papapadopulos, P. and R. Taylor (1994). On the application of multi-step integration methods to infinitesimal elastoplasticity. *Int. J. Numer. Methods Eng. 37*, 3169–3184.

Paris, P., M. Gomez, and W. Anderson (1961). A rational analytic theory of fatigue. *The Trend in Engineering 13*, 9–14.

Patoor, E., A. Eberhardt, and M. Berveiller (1996). Micromechanical modelling of superelasticity in shape memory alloys. *J. Phys. IV 6*, 277–292.

Patoor, E., D. Lagoudas, P. Entchev, L. Brinson, and X. Gao (2006). Shape memory alloys, Part I: General properties and modeling of single crystals. *Mech. Mater. 38*, 391–429.

Pearson, S. (1975). Initiation of fatigue cracks in commercial aluminium alloys and the subsequent propa-

gation of very short cracks. *Eng. Fract. Mech. 7*, 235–247.

Peigney, M. and J. Seguin (2013). An incremental variational approach to coupled thermo-mechanical problems in anelastic solids. Application to shape-memory alloys. *Int. J. Solids Struct. 50*(24), 4043–4054.

Peigney, M., J. Seguin, and E. Herve-Luanco (2011). Numerical simulation of shape memory alloys structures using interior-point methods. *Int. J. Solids Struct. 48*, 2791–2799.

Peigney, M. and C. Stolz (2003). An optimal control approach to the analysis of inelastic structures under cyclic loading. *J. Mech. Phys. Solids 51*(4), 575–605.

Pelton, A. (2011). Nitinol Fatigue: A Review of Microstructures and Mechanisms. *J. Mater. Eng. Perform. 20*(4-5), 613–617.

Pelton, A., J. Fino-Decker, L. Vien, C. Bonsignore, P. Saffari, M. Launey, and M. Mitchell (2013). Rotary-bending fatigue characteristics of medical-grade Nitinol wire. *J. Mech. Behav. Biomed. Mater. 1*, 19–32.

Pelton, A., X. Gong, and T. Duerig (2003). Fatigue testing of diamond-shaped specimens. In *Proceedings of the Materials and the Processes for Medical Devices Conference*, pp. 199–204.

Pelton, A., V. Schroeder, M. Mitchell, X.-Y. Gong, M. Barney, and S. Robertson (2008). Fatigue and durability of Nitinol stents. *J. Mech. Behav. Biomed. 1*, 153–164.

Pelton, A., D. Stöckel, and T. Duerig (2000). Medical Uses of Nitinol. *Mat. Sci. Forum 327-328*, 63–70.

Peng, X., B. Chen, X. Chen, J. Wang, and H. Wang (2012). A constitutive model for transformation, reorientation and plastic deformation of shape memory alloys. *Acta Mech. Solida Sin. 25*(3), 285–298.

Pérez-Foguet, A., A. Rodríguez-Ferran, and A. Huerta (2001). Consistent tangent matrices for substepping schemes. *Comput. Methods in Appl. Mech. Eng. 190*, 4627–4647.

Perry, M., S. Oktay, and J. Muskivitch (2002). Finite element analysis and fatigue of stents. *Minim. Invasive Ther. Allied Technol. 11*(4), 165–171.

Petrini, L., E. Dordoni, W. Wu, C. Guala, C. Silvestro, F. Migliavacca, and G. Pennati (2013). Fatigue resistance of Nitinol peripheral stents. In *Proceedings of 6th ECCOMAS Conference on Smart Structures and Materials (SMART 2013)*.

Petrini, L. and F. Migliavacca (2011). Biomedical Applications of Shape Memory Alloys. *J. Metall. 2011*, 1–15.

Petryk, H. (2003). Incremental energy minimization in dissipative solids. *CR. Mec. 331*, 469–474.

Peultier, B., T. Ben Zineb, and E. Patoor (2006). Macroscopic constitutive law for SMA: Application to structure analysis by FEM. *Mech. Mater. 38*, 510–524.

Peultier, B., T. Ben Zineb, and E. Patoor (2008). A simplified micromechanical constitutive law adapted to the design of shape memory applications by finite element methods. *Mat. Sci. Eng. A-Struct. 481-482*, 384–388.

Pham, M., C. Solenthaler, K. Janssens, and S. Holdsworth (2011). Dislocation structure evolution and its effects on cyclic deformation response of AISI 316L stainless steel. *Mater. Sci. Eng. A 528*(7-8), 3261–3269.

Pilch, J., L. Heller, and P. Sittner (2009). http://department.fzu.cz/ofm/roundrobin.

Pilkey, W. and D. Pilkey (2008). *Petersonś Stress Concentration Factors*. John Wiley & Sons Inc.

Poilane, C., P. Delobelle, C. Lexcellent, S. Hayashi, and H. Tobushi (2000). Analysis of the mechanical behavior of shape memory polymer membranes by nanoindentation, bulging and point membrane

deflection tests. *Thin Solid Films 379*, 156–165.

Polak, J., K. Obrtlik, and M. Hajek (1994). Cyclic plasticity in type 316L austenitic stainless steel. *Fatigue Fract. Engng Mater. Struct. 17*, 773–782.

Popov, P. and D. Lagoudas (2007). A 3D constitutive model for shape memory alloys incorporating pseudoelasticity and detwinning of self-accommodated martensite. *Int. J. Plasticity 23*, 1679–1720.

Predki, W., M. Klönne, and A. Knopik (2006). Cyclic torsional loading of pseudoelastic NiTi shape memory alloys: Damping and fatigue failure. *Mater. Sci. Eng. A 417*(1-2), 182–189.

Puchi-Cabrera, E., M. Staia, C. Tovar, and E. Ochoa-Pérez (2008). High cycle fatigue behavior of 316L stainless steel. *Int. J. Fatigue 30*(12), 2140–2146.

Qi, H., T. Nguyen, F. Castro, C. Yakacki, and R. Shandas (2008). Finite deformation thermo-mechanical behavior of thermally induced shape memory polymers. *J. Mech. Phys. Solids 56*(5), 1730–1751.

Qidwai, M. and D. Lagoudas (2000a). Numerical implementation of a shape memory alloy thermomechanical constitutive model using return mapping algorithm. *Int. J. Numer. Methods Eng. 47*, 1123–1168.

Qidwai, M. and D. Lagoudas (2000b). On thermomechanics and transformation surfaces of polycrystalline NiTi shape memory alloy material. *Int. J. Plasticity 16*, 1309–1343.

Quarteroni, A., R. Sacco, and F. Saleri (2007). *Numerical Mathematics*. Springer.

Rabothov, Y. (1969). *Creep problems in structural members*. North-Holland.

Raniecki, B., C. Lexcellent, and K. Tanaka (1992). Thermodynamic models of pseudoelastic behaviour of shape memory alloys. *Arch. Mech. 44*, 261–284.

Reddy, B. and J. Martin (1991). Algorithms for the solution of internal variable problems in plasticity. *Comput. Methods in Appl. Mech. Eng. 93*, 253–273.

Reese, S., M. Bol, and D. Christ (2010). Finite element-based multi-phase modelling of shape memory polymer stents. *Comput. Methods in Appl. Mech. Eng. 199*(21-22), 1276–1286.

Reinhoehl, M., D. Bradley, R. Bouhot, and J. Proft (2000). The influence of melt practice on final fatigue properties of superelastic NiTi wires. In *Proceedings of the International Conference on Shape Memory and Superelastic Technologies (SMST 2000)*, Pacific Grove, CA, pp. 397–403.

Robertson, S., A. Pelton, and R. Ritchie (2012). Mechanical fatigue and fracture of Nitinol. *Int. Mater. Rev. 57*(1), 1–37.

Rockafellar, R. (1970). *Convex Analysis*. Princeton University Press, Princeton.

Romano, G., L. Rosati, and F. Marotti de Sciarra (1993). Variational principles for a class of finite step elastoplastic problems with non-linear mixed hardening. *Comput. Methods in Appl. Mech. Eng. 109*, 293–314.

Runciman, A., D. Xu, A. Pelton, and R. Ritchie (2011). An equivalent strain/Coffin-Manson approach to multiaxial fatigue and life prediction in superelastic Nitinol medical devices. *Biomaterials 32*, 4987–4993.

Saai, A., H. Louche, L. Tabourot, and H. Chang (2010). Experimental and numerical study of the thermomechanical behavior of Al bi-crystal in tension using full field measurements and micromechanical modeling. *Mech. Mater. 42*(3), 275–292.

Sadjadpour, A. and K. Bhattacharya (2007). A micromechanics-inspired constitutive model for shape-memory alloys: the one-dimensional case. *Smart Mater. Struct. 16*, S51–S62.

Sai, K. (2010). Multi-mechanism models: present state and future trends. *Int. J. Plasticity 27*, 250–281.

Saint-Sulpice, L., S. Arbab Chirani, and S. Calloch (2009). A 3D super–elastic model for shape memory alloys taking into account progressive strain under cyclic loadings. *Mech. Mater. 41*, 12–26.

Saleeb, A., B. Dhakal, S. Padula II, and D. Gaydosh (2013). Calibration of a three-dimensional multimechanism shape memory alloy material model for the prediction of the cyclic attraction character in binary NiTi alloys. *J. Intel. Mat. Syst. Str. 4*, 70–88.

Saleeb, A., S. Padula II, and A. Kumar (2011). A multi-axial, multimechanism based constitutive model for the comprehensive representation of the evolutionary response of SMAs under general thermomechanical loading conditions. *Int. J. Plasticity 5*, 655–687.

Savi, M. and A. Braga (1993). Chaotic vibrations of an oscillator with shape memory. *J. Braz. Soc. Mech. Sci. & Eng. 15*, 1–20.

Schievano, S., A. Taylor, C. Capelli, P. Lurz, J. Nordmeyer, F. Migliavacca, and P. Bonhoeffer (2010). Patient specific finite element analysis results in more accurate prediction of stent fractures: Application to percutaneous pulmonary valve implantation. *J. Biomech. 43*(4), 687 – 693.

Schijve, J. (2009). *Fatigue of Structures and Materials*. Netherlands, Springer Science & Business Media, B.V.

Schmidt-Baldassari, M. (2003). Numerical concepts for rate-independent single crystal plasticity. *Comput. Methods in Appl. Mech. Eng. 192*, 1261–1280.

Schwartz, J., O. Fandeur, and C. Rey (2010). Fatigue crack initiation modeling of 316LN steel based on non local plasticity theory. *Procedia Eng. 2*(1), 1353–1362.

Schwartz, M. (Ed.) (2002). *Encyclopedia of Smart Materials*, Volume 1-2. John Wiley & Sons, Inc.

Sedlák, P., M. Frost, B. Benešová, T. Ben Zineb, and P. Šittner (2012). Thermomechanical model for NiTi-based shape memory alloys including R-phase and material anisotropy under multi-axial loadings. *Int. J. Plasticity 39*, 132–151.

Shaikh, F., R. Maddikunta, M. Djelmami-Hani, J. Solis, S. Allaqaband, and T. Bajwa (2008). Stent fracture, an incidental finding or a significant marker of clinical in-stent restenosis? *Catheter. Cardiovasc. Interv. 71*(5), 614–618.

Shaw, J. and S. Kyriakides (1995). Thermomechanical aspects of NiTi. *J. Mech. Phys. Solids 43*(8), 1243–1281.

Sianos, G., S. Hofma, J. Ligthart, F. Saia, A. Hoye, P. Lemos, and P. Serruys (2004). Stent Fracture and Restenosis in the Drug-Eluting Stent Era. *Catheter. Cardiovasc. Interv. 61*(1), 111–116.

Simo, J. (1998). Numerical analysis of classical plasticity. In P. Ciarlet and J. Lions (Eds.), *Handbook for Numerical Analysis*, Volume 4. Elsevier, Amsterdam.

Simo, J. and T. Hughes (1998). *Computational Inelasticity*. Springer.

SIMULIA (2012). *Abaqus 6.12. Analysis User's Manual*.

Sines, G. (1959). Behavior of metals under complex static and alternating stresses. In G. Sines and J. Waisman (Eds.), *Metal Fatigue*, pp. 145–469. McGraw Hill, New York.

Sittner, P., Y. Hara, and M. Tokuda (1995). Experimental study on the thermoelastic martensitic transformation in shape memory alloy polycrystal induced by combined external forces. *Metall. Mater. Trans. A 26*, 2923–2935.

Sittner, P., L. Heller, J. Pilch, P. Sedlak, M. Frost, Y. Chemisky, A. Duval, B. Piotrowski, T. Ben Zineb, E. Patoor, F. Auricchio, S. Morganti, A. Reali, G. Rio, D. Favier, Y. Liu, E. Gibeau, C. Lexcellent, L. Boubakar, D. Hartl, S. Oehler, D. Lagoudas, and J. Van Humbeeck (2009). Roundrobin SMA mo-

deling. In P. Sittner, L. Heller, and V. Paidar (Eds.), *The 8th European Symposium on Martensitic Transformations (ESOMAT 2009)*, pp. 08001. EDP Sciences.

Skelton, R. (1991). Energy criterion for high temperature low cycle fatigue failure. *Mater. Sci.Tech. SER 7*, 427–439.

Skelton, R. (1993). Cyclic hardening, softening, and crack growth during high temperature fatigue. *Mater. Sci.Tech. SER 9*, 1001–1008.

Sloan, S. (1987). Substepping schemes for the numerical integration of elastoplastic stress-strain relations. *Int. J. Numer. Methods Eng. 24*, 893–911.

Soderberg, C. (1939). Factor of safety and working stress. *Trans. A.S.M.E. 52*, 13–28.

Soul, H., A. Isalgue, A. Yamny, V. Torra, and F. Lovey (2010). Pseudoelastic fatigue of NiTi wires: frequency and size effects on damping capacity. *Smart Mater. Struct. 19*, 1–7.

Souza, A., E. Mamiya, and N. Zouain (1998). Three-dimensional model for solids undergoing stress-induced phase transformations. *Eur. J. Mech. A-Solid 17*, 789–806.

Srivastava, V., S. Chester, and L. Anand (2010). Thermally actuated shape-memory polymers: Experiments, theory, and numerical simulations. *J. Mech. Phys. Solids 58*(8), 1100–1124.

Stachowiak, G. and P. McCormick (1987). Two stage yielding in a NiTi alloy. *Scripta Metall. Mater. 21*, 403–406.

Stachowiak, G. and P. McCormick (1988). Shape memory behaviour associated with the R and martensitic transformations in a NiTi alloy. *Mater. T. JIM 36*(2), 291–297.

Stankiewicz, J., S. Robertson, and R. Ritchie (2007). Fatigue-crack growth properties of thin-walled superelastic austenitic Nitinol tube for endovascular stent. *J. Biomed. Mater. Res. B 81*, 685–91.

Stephens, R., A. Fatemi, R. Stephens, and H. Fuchs (2000). *Metal fatigue in engineering*. Willy Interscience Publication.

Stupkiewicz, S. and H. Petryk (2012). A robust model of pseudoelasticity in shape memory alloys. *Int. J. Numer. Methods Eng. 93*(7), 747–769.

Subash, S. (1998). *Fatigue of Materials*. Cambridge University Press.

Sun, Q. and K. Hwang (1993a). Micromechanics modelling for the constitutive behavior of polycrystalline shape memory alloys I. Derivation of general relations. *J. Mech. Phys. Solids 41*(1), 1–17.

Sun, Q. and K. Hwang (1993b). Micromechanics modelling for the constitutive behavior of polycrystalline shape memory alloys II. Study of the individual phenomena. *J. Mech. Phys. Solids 41*(1), 19–33.

Sun, Q. and Z. Li (2002). Phase transformation in superelastic NiTi polycrystalline micro-tubes under tension and torsion - from localization to homogeneous deformation. *Int. J. Solids Struct. 39*, 3797–3809.

Suresh, S. (1998). *Fatigue of Materials*. Cambridge University Press.

Sweeney, C., P. McHugh, J. McGarry, and S. Leen (2012). Micromechanical methodology for fatigue in cardiovascular stents. *Int. J. Fatigue 44*, 202–216.

Szymczak, H., S. Weiss, and A. Meissner (2009). Fatigue and endurance of coronary stents. *Materialwissenschaft und Werkstofftechnik 40*(1-2), 61–64.

Tabanli, R., N. Simha, and B. Berg (2001). Mean strain effects on the fatigue properties of superelastic NiTi. *Metall. Mater. Trans. A 32*, 1866–9.

Tabibian, S., E. Charkaluk, A. Constantinescu, F. Szmytka, and A. Oudin (2013). TMF-LCF life assessment

of a Lost Foam Casting A319 aluminum alloy. *Int. J. Fatigue 53*(0), 75–81.

Talamazzi, P. (2012). Applicazioni di un modello di memoria di forma alla termoretrazione di polietileni. Master's thesis, Università degli Studi di Pavia.

Tanaka, K. and R. Iwasaki (1985). A phenomenological theory of transformation superplasticity. *Engng. Fract. Mech. 4*(21), 709–720.

Tanaka, K. and S. Nagaki (1982). A thermomechanical description of materials with internal variables in the process of phase transitions. *Archive of Applied Mechanics 51*(5), 287–299.

Tanaka, K., F. Nishimura, T. Hayashi, H. Tobushi, and C. Lexcellent (1995). Phenomenological analysis on subloops and cyclic behavior in shape memory alloys under mechanical and/or thermal loads. *Mech. Mater. 19*(4), 281–292.

Tarnita, D., D. Tarnita, and D. Bolcu (2011). *Biomedical engineering - From theory to applications*, Chapter 18 - Orthopaedic Modular Implants Based on Shape Memory Alloys, pp. 1–39.

Taylor, G. (1938). Plastic strain in metals. *J. Inst. Met. 62*, 307–324.

Taylor, R. (2013). *A finite-element analysis program, http://www.ce.berkeley.edu/projects/feap/*. University of California at Berkeley.

Tey, S., W. Huang, and W. Sokolowski (2001). Influence of long-term storage in cold hibernation on strain recovery and recovery stress of polyurethane shape memory polymer foam. *Smart Mater. Struct. 10*, 321–325.

Thamburaja, P. (2005). Constitutive equations for martensitic reorientation and detwinning in shape-memory alloys. *J. Mech. Phys. Solids 53*(4), 825–856.

Thamburaja, P. and L. Anand (2001). Polycrystalline shape-memory materials: effect of crystallographic texture. *J. Mech. Phys. Solids 49*, 709–737.

Thompson, N., N. Wadsworth, and N. Louat (1956). The origin of fatigue fracture in copper. *Philos. Mag. 1*(2), 113–126.

Tin-Loi, F. (1999). A smoothing scheme for a minimum weight problem in structural plasticity. *Structural Optimization 17*, 279–285.

Tin-Loi, F. and J. Pang (1993). Elastoplastic analysis of structures with nonlinear hardening: a nonlinear complementarity approach. *Comput. Methods in Appl. Mech. Eng. 107*, 299–312.

Tobin, R. (1992). Uniqueness results and algorithm for Stackelberg-Cournot-Nash equilibria. *Ann. Oper. Res. 34*, 21–36.

Tobushi, H., T. Hachisuka, S. Yamada, and P. Lin (1997). Rotating-bending fatigue of a TiNi shape-memory alloy wire. *Mech. Mater. 26*, 35–42.

Tobushi, H., K. Okumura, S. Hayashi, and N. Ito (2001). Thermomechanical constitutive model of shape memory polymer. *Mech. Mater. 33*(10), 545–554.

Tobushi, H., Y. Shimeno, T. Hachisuka, and K. Tanaka (1998). Influence of strain rate on superelastic properties of TiNi shape memory alloy. *Mech. Mater. 30*(2), 141–150.

Toi, Y., J. Lee, and M. Taya (2002a). Finite element analysis of superelastic behavior of shape memory alloy devices (part 1: small deformation analysis of tensile and bending behaviors). *Trans. Jpn Soc. Mech. Eng. A 68*(676), 1688–1694.

Toi, Y., J. Lee, and M. Taya (2002b). Finite element analysis of superelastic behavior of shape memory alloy devices (part 2: finite deformation analysis of beams and helical springs). *Trans. Jpn Soc. Mech.*

Eng. A 68(676), 1695–1701.

Toi, Y., J. Lee, and M. Taya (2004). Finite element analysis of superelastic, large deformation behavior of shape memory alloy helical springs. *Comput. Struct. 82*, 1685–93.

Tolomeo, D., S. Davidson, and M. Santinoranout (2000). Cyclic properties of superelastic nitinol: design implications. In *Proceedings of the International Conference on Shape Memory Superelastic Technologies (SMST 2000)*, Pacific Grove, CA, USA, pp. 409–417.

Trznadel, M. and M. Kryszewski (1988). Shrinkage and related relaxation of internal stresses in oriented glassy polymers. *Polymer 29*(3), 418–425.

Tütüncü, R. H., K. C. Toh, and M. J. Todd (2003). Solving semidefinite-quadratic-linear programs using SDPT3. *Math. Program. 95*(2), 189–217.

Urbano, M. and A. SMAq (2006). A Novel Instrument for the Characterization of SMA Wires. In *Proceedings of the International Conference on Shape Memory and Superelastic Technologies (SMST2006)*, Pacific Groove, California, USA, pp. 177–184.

US Food and Drug Administration (2010, April 18th). *Non-clinical engineering tests and recommended labeling for intravascular stents and associated delivery systems: guidance for industry and FDA staff.* US Department of Health and Human Services; Food and Drug Administration, Centre for Devices and Radiological, Health.

Van Humbeeck, J. (1991). Cycling effects, fatigue and degradation of shape memory alloys. *J. Phys. IV 1*(C4), 189–197.

Van Humbeeck, J. (2010). Introduction to shape memory alloys. In *Proceedings of the School and Symposium on Smart Structural Systems Technologies (S3T)*, Porto, Portugal, pp. 3–23.

Voit, W., T. Ware, R. Dasari, P. Smith, L. Danz, D. Simon, S. Barlow, S. Marder, and K. Gall (2010). High-Strain Shape-Memory Polymers. *Adv. Funct. Mater. 20*(1), 162–171.

Volk, B., D. Lagoudas, Y. Chen, and K. Whitley (2010). Analysis of the finite deformation response of shape memory polymers: I. Thermomechanical characterization. *Smart Mater. Struct. 19*(7), 075005.

Volk, B., D. Lagoudas, and D. Maitland (2011). Characterizing and modeling the free recovery and constrained recovery behavior of a polyurethane shape memory polymer. *Smart Mater. Struct. 20*(9), 094004.

Wackers, P., M. Alquezar-Getan, A. Constantinescu, H. Maitournam, and V. Arrieta (2010). A Modeling Approach to Predict Fretting Fatigue on Highly Loaded Blade Roots. *J. Eng. Gas Turbines Power 132*(8), 1–9.

Wagner, M., N. Nayan, and U. Ramamurty (2008). Healing of fatigue damage in NiTi shape memory alloys. *J. Phys. D: Appl. Phys. 41*(18), 1–4.

Wagner, M., T. Sawaguchi, G. Kausträter, D. Höffken, and G. Eggeler (2004). Structural fatigue of pseudoelastic NiTi shape memory wires. *Mater. Sci. Eng. A 378*(1-2), 105–109.

Wagner, M. and W. Windl (2008). Lattice stability, elastic constants and macroscopic moduli of NiTi martensites from first principles. *Acta Mater. 56*, 6232–6245.

Wang, S., W. Zhuang, D. Balint, and J. Lin (2009). A crystal plasticity study of the necking of micro-films under tension. *Journal of Multiscale Modelling 1*, 331.

Wang, X., B. Xu, and Z. Yue (2008). Phase transformation behavior of pseudoelastic NiTi shape memory alloys under large strain. *J. Alloys Compd. 463*(1-2), 417–422.

Ware, T., W. Voit, and K. Gall (2010). Radiation crosslinked shape-memory polymers. *Polymer 51*(15),

3551–3559.

Wayman, C. and J. Harrison (1989). The origins of the shape memory effect. *JOM 41*(9), 26–28.

Wei, Z., R. Sandstrom, and S. Miyazaki (1998a). Shape memory materials and hybrid composites for smart systems: Part I Shape-memory materials. *J. Mater. Sci. 33*(15), 3743–3762.

Wei, Z., R. Sandstrom, and S. Miyazaki (1998b). Shape memory materials and hybrid composites for smart systems: Part II Shape-memory hybrid composites. *J. Mater. Sci. 33*(15), 3763–3783.

Weiss, S. and A. Meissner (2006). Fatigue and Microstructure of Coronary Artery Stents. *Materialwissenschaft und Werkstofftechnik 37*(9), 755–761.

Weiss, S., A. Meissner, and A. Fischer (2009). Microstructural changes within similar coronary stents produced from two different austenitic steels. *J. Mech. Behav. Biomed. 2*, 210–216.

Weldon, L. (2001). The effects of passivation processes on the mechanical performance of stainless steels for stent applications. Master's thesis, NUI, Galway, Ireland.

Westbrook, K., V. Parakh, T. Chung, P. Mather, L. Wan, M. Dunn, and H. Qi (2010). Constitutive Modeling of Shape Memory Effects in Semicrystalline Polymers With Stretch Induced Crystallization. *J. Eng. Mater. - T. ASME 132*(4), 1–9.

Wieners, C. (2008). SQP methods for incremental plasticity with kinematic hardening. In *IUTAM symposium on theoretical, computational and modeling aspects of inelastic media*, Volume 11(4), pp. 143–153. Springer, Berlin.

Wiersma, S., F. Dolan, and D. Taylor (2006). Fatigue and fracture in materials used for micro-scale biomedical components. *Biomedical Materials and Engineering 16*(2), 137–146.

Wiersma, S. and D. Taylor (2005). Fatigue of materials used in microscopic components. *Fatigue Fract. Eng. Mater. Struct. 28*(12), 1153–1160.

Wilson, T. S., J. P. Bearinger, J. L. Herberg, J. E. Marion, W. J. Wright, C. L. Evans, and D. J. Maitland (2007). Shape memory polymers based on uniform aliphatic urethane networks. *J. Appl. Polym. Sci. 106*(1), 540–551.

Winters, G. and M. Nutt (2003). *Stainless Steel for Medical and Surgical Applications*. ASMT International.

Wöhler, A. (1870). Über die Festigkeitsversuche mit Eisen and Stahl. *Zeitschrift Bauwesen 20*, 73–106.

Wolfram (2013a). *Mathematica Documentation, www.wolfram.com*.

Wolfram (2013b). *Wolfram AceFEM Documentation, www.wolfram.com/products/applications/acefem/*.

Wolfram (2013c). *Wolfram AceGen Documentation, www.wolfram.com/products/applications/acegen/*.

Wu, W., M. Qi, X. Liu, D. Yang, and W. Wang (2007). Delivery and Release of Nitinol Stent in Carotid Artery and their Interactions: a Finite Element Analysis. *J. Biomech. 40*, 3034–3040.

Xu, W. and G. Li (2010). Constitutive modeling of shape memory polymer based self-healing syntactic foam. *Int. J. Solids Struct. 47*(9), 1306–1316.

Yang, B., W. Huang, C. Li, and L. Li (2006). Effects of moisture on the thermomechanical properties of a polyurethane shape memory polymer. *Polymer 47*(4), 1348–1356.

You, X., T. Connolley, P. Mchugh, H. Cuddy, and C. Motz (2006). A combined experimental and computational study of deformation in grains of biomedical grade 316LVM stainless steel. *Acta Materialia 54*, 4825–4840.

Zaki, W. (2012a). An efficient implementation for a model of martensite reorientation in martensitic shape

memory alloys under multiaxial non-proportional loading. *Int. J. Plasticity 37*, 72–94.

Zaki, W. (2012b). Time integration of a model for martensite detwinning and reorientation under non-proportional loading using Lagrange multipliers. *Int. J. Solids Struct. 49*(21), 2951–2961.

Zaki, W. and Z. Moumni (2007a). A 3D model of the cyclic thermomechanical behavior of shape memory alloys. *J. Mech. Phys. Solids 55*(11), 2427–2454.

Zaki, W. and Z. Moumni (2007b). A three-dimensional model of the thermomechanical behavior of shape memory alloys. *J. Mech. Phys. Solids 55*(11), 2455–2490.

Zaki, W., S. Zamfir, and Z. Moumni (2010). An extension of the ZM model for shape memory alloys accounting for plastic deformation. *Mech. Mater. 42*, 266–274.

Zarka, J., J. Frelat, G. Inglebert, and P. Kasmai-Navidi (1998). *A new approach to inelastic analyses of structures*. Dordrecht, PAYS-BAS.

Zhang, H., S. He, X. Li, and P. Wriggers (2004). A new algorithm for numerical solution of 3D elastoplastic contact problems with orthotropic friction law. *Comput. Mech. 34*, 1–14.

Zhang, L., J. Li, H. Zhang, and S. Pan (2013). A second order cone complementarity approach for the numerical solution of elastoplasticity problems. *Comput. Mech. 51*(1), 1–18.

Zhu, C. (1995). A finite element-mathematical programming method for elastoplastic contact problems with friction. *Finite Elem. Anal. Des. 20*, 273–282.

Zhu, G., G. Liang, Q. Xu, and Q. Yu (2003). Shape-memory effects of radiation crosslinked poly(ϵ-caprolactone). *J. Appl. Polym. Sci. 90*(6), 1589–1595.

Zhu, G., S. Xu, J. Wang, and L. Zhang (2006). Shape memory behaviour of radiation-crosslinked PCL/PMVS blends. *Radiat. Phys Chem. 75*(3), 443–448.

Zhu, G. M., Q. Y. Xu, G. Z. Liang, and H. F. Zhou (2005). Shape-memory behaviors of sensitizing radiation-crosslinked polycaprolactone with polyfunctional poly(ester acrylate). *J. Appl. Polym. Sci. 95*(3), 634–639.

Zipse, A., M. Schlun, G. Dreher, J. Zum Gahr, and N. Rebelo (2011). Accelerated Fatigue Testing of Stent-Like Diamond Specimens. *J. Mater. Eng. Perform. 20*(4-5), 579–583.

Publications

The published and submitted results of the present research are as follows.

International Journal Articles

1. F. Auricchio, E. Bonetti, **G. Scalet**, F. Ubertini. *Theoretical and numerical modeling of shape memory alloys accounting for multiple phase transformations and martensite reorientation*, accepted for publication in the International Journal of Plasticity.

2. F. Auricchio, **G. Scalet**, M. Urbano. *A Numerical/Experimental Study of Nitinol Actuator Springs*. Journal of Materials Engineering and Performance, doi:10.1007/s11665-014-0883-1, 1-9, 2014.

International Conference Proceedings

1. F. Auricchio, **G. Scalet**, M. Urbano. *Further Numerical/Experimental Investigations Of Nitinol Actuator Springs*. Proceedings of the International Conference on Shape Memory and Superelastic Technologies (SMST 2014), May, 12-16, 2014, Pacific Grove, California. Accepted abstract.

2. F. Auricchio, **G. Scalet**. *Computational treatment of non-smooth problems: shape memory alloys and elasto-plastic materials*. Proceedings of EUROMECH - Colloquium 548 Direct and variational methods for nonsmooth problems in mechanics, June 24-26, 2013, Amboise, France.

3. F. Auricchio, **G. Scalet**, M. Urbano. *A Numerical/Experimental Study of Nitinol Actuator Springs*. Proceedings of the International Conference on Shape Memory and Superelastic Technologies (SMST 2013), May, 21-24, 2013, Prague, Czech Republic. ASM International. Pages 113-114.

4. F. Auricchio, E. Bonetti, **G. Scalet**, F. Ubertini. *Refined shape memory alloys model taking into account martensite reorientation*. CD-ROM Proceedings of the 6th European Congress on Computational Methods in Applied Sciences and Engineering (ECCOMAS 2012), September 10-14, 2012, Vienna, Austria. Eds.: Eberhardsteiner, J.; Böhm, H.J.; Rammerstorfer, F.G. Publisher: Vienna University of Technology, Austria. Pages 3349-3362. ISBN: 978-3-9502481-9-7. Scopus: 2-s2.0-84871639131.

5. F. Auricchio, E. Bonetti, M. Conti, S. Morganti, A. Reali, **G. Scalet**, M. Aiello, A. Valentini. *Shape-Memory Alloys: 3D Constitutive Modeling and Biomedical Device Investigation*. CD-ROM Book of Abstracts of the 8th European Solid Mechanics Conference (ESMC 2012), July 9-13, 2012, Graz, Austria. Eds.: G.A. Holzapfel, R.W. Ogden, Verlag d. Technischen Universität Graz. Pages 1-2. ISBN: 978-3-851-25223-1 (Plenary Lecture)

Submitted International Journal Articles

1. F. Auricchio, A. Constantinescu, **G. Scalet**. *Fatigue of 316L stainless steel notched μm-size components*, under revision.

2. F. Auricchio, A. Constantinescu, M. Conti, **G. Scalet**. *A computational approach for the lifetime prediction of cardiovascular balloon-expandable stents*, submitted.

3. **G. Scalet**, F. Auricchio, E. Bonetti, L. Castellani, D. Ferri, M. Pachera, F. Scavello. *An experimental, theoretical and numerical investigation of shape memory polymers*, submitted.